Institute for Space and Nuclear Power Studies
School of Engineering
The University of New Mexico
Albuquerque, New Mexico 87131-1341

"HPTAM", A TWO-DIMENSIONAL HEAT PIPE TRANSIENT ANALYSIS MODEL, INCLUDING THE STARTUP FROM A FROZEN STATE

JEAN-MICHEL TOURNIER AND MOHAMED S. EL-GENK

FINAL REPORT NO. UNM-ISNPS-4-1995

NASA Grant No. NAG3-941
to
Institute for Space and Nuclear Power Studies
University of New Mexico
Farris Engineering Center, Rm. 239
Albuquerque, NM 87131

September 1995

Acknowledgments

This research has been funded by NASA Lewis Research Center under Grant N°. NAG3–941 for a number of years. When funding was discontinued in March 1994, work was completed with internal funds by the Institute for Space and Nuclear Power Studies (ISNPS). The authors are grateful to NASA Lewis for the financial support to undertake this challenging and demanding research. We wish to thank Mr. Albert Juhasz, the NASA Lewis Technical Officer of the Grant for his continuous support and constructive suggestions and input throughout the development of HPTAM. We are also grateful to NASA Lewis Management Mr. Joseph Sovie, and Dr. Henry Brandhorst for their encouragement and support. Finally, we wish to acknowledge the help of the ISNPS staff, and the financial support provided by the ISNPS. Without it, completing the development and documentation of HPTAM would not have been possible.

ABSTRACT

Heat pipes are highly reliable and efficient energy transport devices, which are being considered for many terrestrial and space power thermal–management applications, such as high–performance aeronautics and space nuclear and solar dynamic power systems. In this work, a two–dimensional Heat Pipe Transient Analysis Model, "HPTAM", was developed to simulate the transient operation of fully–thawed heat pipes and the startup of heat pipes from a frozen state. The model incorporates: (a) sublimation and resolidification of working fluid; (b) melting and freezing of the working fluid in the porous wick; (c) evaporation of thawed working fluid and condensation as a thin liquid film on a frozen substrate; (d) free–molecule, transition and continuum vapor flow regimes, using the Dusty Gas Model; (e) liquid flow and heat transfer in the porous wick; and (f) thermal and hydrodynamic couplings of phases at their respective interfaces. HPTAM predicts the radius of curvature of the liquid meniscus at the liquid–vapor interface and the radial location of the working fluid level (liquid or solid) in the wick. It also includes the transverse momentum jump condition (capillary relationship of Pascal) at the liquid–vapor interface and geometrically relates the radius of curvature of the liquid meniscus to the volume fraction of vapor in the wick. The present model predicts the capillary limit and partial liquid recess (dryout) in the evaporator wick, and incorporates a liquid pooling submodel, which simulates accumulation of the excess liquid in the vapor core at the condenser end.

HPTAM can handle both rectangular and cylindrical geometries. The model divides the heat pipe into three transverse regions: wall, wick, and vapor regions, and solves the complete form of governing equations in these regions. The heat pipe wick can be a wire–screened mesh, an isotropic porous medium such as a powder or a bed of spheres, or an open annulus separated from the vapor core by a thin sheet (with small holes to provide capillary forces). HPTAM incorporates several working fluids such as lithium, sodium, potassium and water, as well as various wall materials (tungsten, niobium, zirconium, stainless–steel, copper and carbon). Evaporation, condensation, sublimation and resolidification rates are calculated using the kinetic theory relationship with an accommodation coefficient of unity. To predict the flow of liquid in the porous wick of the heat pipe, HPTAM uses the Brinkman–Forchheimer–extended Darcy model. This model was successfully benchmarked against experimental data for natural convection of molten gallium in a porous bed of glass beads. Also, HPTAM handles the phase–change of

working fluid in the wick using a modified fixed–grid homogeneous enthalpy method. The technique employs a mushy–cell temperature range as small as 2×10^{-8} K (limited by machine accuracy only), without requiring under–relaxation of the temperatures and generating numerical instabilities. Instead of using the harmonic mean discretization scheme (HMDS) of Patankar, a simple method, based on the frozen volume fraction, was developed to calculate the heat fluxes at the boundaries of the mushy cell. This method improved the accuracy of the solution and reduced the oscillations in temperature time histories (usually encountered when the HMDS is used) by one–to–two orders of magnitude.

Because of the physical complexity of the problem, advanced numerical methods were considered. Two segregated solution techniques, one based on the non–iterative Pressure Implicit Splitting Operator (PISO), and the other based on the SIMPLEC segregated iterative technique, were developed and tested for their stability and effectiveness in reducing the CPU time while maintaining the accuracy of results. Various linear–system solvers were also examined to determine which one was most efficient for solving the problem at hand. Based on the results of these examinations, the segregated solution technique using the SIMPLEC procedure was selected for HPTAM. To solve the five–point linear Poisson equations resulting from the discretization of the mass balance equations, a direct solution routine using Gaussian elimination was developed. The banded version of the solver allowed significant decreases in computation time and memory storage requirement. The iterative Strongly Implicit Solver was chosen to solve the five–point linear equations resulting from the discretization of the energy and momentum balance equations.

The development of this comprehensive model was guided by continuous benchmarking of the model predictions with available experimental and numerical results. The accuracy of the physical and numerical schemes for modeling heat and mass transfers in the wick was verified using various benchmark problems, namely: (a) natural convection of liquid in a square cavity; (b) natural convection of molten gallium in a porous bed of glass beads; (c) one–dimensional pure conduction solidification problem; (d) two–dimensional pure conduction problem of freezing in a corner; and (e) the freezing of tin in a rectangular cavity in the presence of natural convection. Numerical results of the frozen startup of a radiatively–cooled water heat pipe are presented, which demonstrate the soudness of the physical model and numerical approach used in HPTAM. The results illustrate the importance of the sublimation and recondensation processes during the first period of the

transient and the combined effects of phase–change and liquid hydrodynamics in the wick during the startup of the low–temperature heat pipe. The startup is characterized by partial recess of liquid in the evaporator wick after the capillary limit has been reached. After enough working fluid was melted by resolidification and condensation in the adiabatic and condenser sections of the heat pipe, resaturation of the wick was established before complete dryout of the evaporator occurred, leading to a successful startup. Also, the heat pipe model was validated using transient experimental data of a fully–thawed water heat pipe constructed at the Institute for Space and Nuclear Power Studies. The calculated steady–state vapor and wall axial temperature profiles and the transient power throughput and vapor temperature were in good agreement with measurements. Results illustrated the importance of the hydrodynamic coupling of the vapor and liquid phases and showed the appearance during the heatup transient (disappearance during cooldown) of a pool of excess liquid at the condenser end. Finally, the effects of input power and initial liquid inventory in the water heat pipe on the wet point and liquid pooling, and on the vapor and liquid pressure and temperature distributions were investigated in details.

TABLE OF CONTENTS

Page

Acknowledgments ii
ABSTRACT iii
LIST OF FIGURES xii
LIST OF TABLES xviii
NOMENCLATURE xix
1. INTRODUCTION 1
1.1. SUMMARY ON HEAT PIPE MODELING 4
1.2. OBJECTIVES 16
2. BACKGROUND 20
2.1. PRINCIPLE OF HEAT PIPE OPERATION AND LIMITS 20
2.2. STARTUP OF HEAT PIPES FROM A FROZEN STATE 28
2.3. LITERATURE REVIEW ON HEAT PIPE MODELING 32
2.3.1. Vapor Model of Bowman et al. (1987–1988) 33
2.3.2. Vapor Model of Issacci et al. (1988–1991) 34
2.3.3. The Model of Tilton et al. (1986–1987) 36
2.3.4. The Model of Faghri et al. (1989–1990) 36
2.3.5 The Model of Jang et al. (1988, 1990a) 37
2.3.6 The Model of Cao and Faghri (1992, 1993a, 1993b) 38
2.3.7 The Model of Costello et al. (1988) 39
2.3.8 The Model of Peery and Best (1987) 40
2.3.9 The Model of Ransom and Chow (1987) 42
2.3.10 The Model of Hall et al. (1988–1994) 43
2.3.11 The Model of Seo and El–Genk (1989) 45
2.4. LITERATURE REVIEW ON EXPERIMENTAL DATA 47
2.4.1 High–Temperature Heat Pipe Experiments 47
2.4.2 Low–Temperature Heat Pipe Experiments 50
3. MODEL FORMULATION AND DESCRIPTION 53
3.1. GOVERNING EQUATIONS IN THE LIQUID/WICK REGION 54
3.1.1. Conservation of Mass 56
3.1.2. Conservation of Radial Momentum 56
3.1.3. Conservation of Axial Momentum 56
3.1.4. Conservation of Enthalpy in the Liquid/Wick Region 57

3.2. GOVERNING EQUATIONS IN THE VAPOR REGION OF LOW-TEMPERATURE HEAT PIPES 58
3.2.1. Conservation of Mass 58
3.2.2. Conservation of Radial Momentum 58
3.2.3. Conservation of Axial Momentum 59
3.2.4. Conservation of Energy 60
3.3. GOVERNING EQUATIONS IN THE PIPE WALL REGION 60
3.4. INTERFACIAL AND BOUNDARY CONDITIONS 61
3.4.1. Liquid–Vapor Interfacial Jump Conditions 61
3.4.2. Radius of Curvature of the Liquid Meniscus in the Wick 63
3.4.3. Interfacial Phase–Change Mass Rates 65
3.4.4. Other Boundary Conditions 66
3.4.5. Initial Conditions and Mathematical Closure 66
3.5. FREEZE–AND–THAW MODELING 68
3.6. LIQUID–POOLING SUBMODEL 70
3.7. FREE–MOLECULE AND TRANSITION FLOWS REGIMES 73
3.8. THERMOPHYSICAL PROPERTIES AND STATE EQUATIONS 76
4. METHOD OF SOLUTION 81
4.1. SOLUTION PROCEDURE 82
4.1.1. Definition of Domain, Variables and Extrapolations 85
4.1.2. Discretization of the Conservation Equations 91
4.1.3. Homogeneous Enthalpy Equation in the Porous Wick 92
4.1.4. Heat balance at the Liquid–Vapor Interface 101
4.1.5. Coupling of Enthalpy Jump Condition with the Kinetic Theory Relationship 102
4.1.6. Modeling of the Condenser Cooling Jacket 105
4.1.7. Thermal Boundary Conditions at the Walls 106
4.1.8. Radial Momentum Conservation Equations 109
4.1.9. Axial Momentum Conservation Equations 112
4.1.10. Mass Conservation Equations 115
4.1.11. Vapor–Wick Interfacial Model 122
4.1.12. Liquid Pooling Submodel 124
4.2. DESCRIPTION OF NUMERICAL SOLUTION ALGORITHMS 131
4.3. SOLVERS FOR 5–POINT LINEAR EQUATIONS 135
4.4. PERFORMANCE OF NUMERICAL SOLUTION ALGORITHMS 140
5. BENCHMARK OF WICK MODEL 146

5.1. NATURAL CONVECTION IN A SQUARE CAVITY....146
5.2. NATURAL CONVECTION OF MOLTEN GALLIUM IN A POROUS BED OF GLASS BEADS....150
5.3. ONE-DIMENSIONAL SOLIDIFICATION PROBLEM....151
5.4. TWO-DIMENSIONAL FREEZING IN A CORNER....155
5.5. FREEZING OF TIN IN A RECTANGULAR ENCLOSURE WITH NATURAL CONVECTION....157
6. STARTUP OF A WATER HEAT PIPE FROM A FROZEN STATE....161
6.1. DESCRIPTION OF THE TEST CASE....161
6.2. TRANSIENT OPERATION WITH FROZEN EVAPORATOR....161
6.3. THE MELTING PROCESS OF THE EVAPORATOR....164
6.4. THE MELTING PROCESS OF THE CONDENSER....167
7. TRANSIENT CALCULATIONS OF FULLY-THAWED WATER HEAT PIPE AND COMPARISON WITH EXPERIMENTAL DATA....173
7.1. DESCRIPTION OF THE WATER HEAT PIPE EXPERIMENT AND MODELING....173
7.2. COMPARISON OF THE MODEL WITH WATER HEAT PIPE EXPERIMENT....175
7.3. WICK VOID FRACTION AND LIQUID POOLING RESULTS....179
8. ANALYSIS OF WET POINTS AND LIQUID POOLING (WATER HEAT PIPE)....186
8.1. LIQUID POOLING AT END OF CONDENSER....187
8.2. TRANSIENT RESPONSE OF WATER HEAT PIPE....190
8.3. HEAT PIPE CHARACTERISTIC PERIOD....195
8.4. TRANSIENT VAPOR PRESSURE RECOVERY....195
8.5. VAPORIZATION RATES AND TEMPERATURE PROFILES....195
8.6. VISCOUS DISSIPATION....198
9. STEADY-STATE OPERATION OF FULLY-THAWED LITHIUM HEAT PIPE....200
9.1. PRESSURE PROFILES AND VAPOR PRESSURE RECOVERY....201
9.2. VAPOR PORE VOID FRACTION....201
9.3. TEMPERATURE PROFILES....201
9.4. VISCOUS DISSIPATION....204
9.5. EVAPORATION / CONDENSATION RATES....204
10. SUMMARY AND CONCLUSIONS....208
11. RECOMMENDATIONS FOR FUTURE WORK....213

REFERENCES 214
APPENDIX A. MODELING OF HEAT AND MASS TRANSFERS IN POROUS MEDIA 236
A-1. MODELING OF FLOW THROUGH POROUS MEDIA 236
A-1.1. Darcy's Law 237
A-1.2. Forchheimer's Extension 237
A-1.3. Brinkman's Extension 240
A-1.4. Transient and Convective Inertia Terms 242
A-1.5. Local Volume–Averaging Technique 243
A-2. MODELING OF HEAT TRANSFER IN A PARTIALLY–FROZEN POROUS MEDIUM 246
A-2.1. Volume–Averaged Homogeneous Enthalpy Formulation 247
A-2.2. Effective Thermal Conductivity Tensor 249
A-3. CONSERVATION OF MASS 251
A-4. HYDRODYNAMIC PROPERTIES OF WIRE–SCREENED WICKS 252
A-4.1. Surface Porosity of Wire–Screened Wick 254
A-4.2. Coefficient of Shrinkage 254
A-4.3. Volume Porosity of Wire–Screened Wick 255
A-4.4. Permeability of Wire–Screened Wick 257
A-4.5. Verification of Wire–Screened Wick Model 259
A-4.6. Effective Pore Radius of a Wire–Screened Wick 259
A-4.7. Relationship Between Mesh Number and Wire Diameter 261
A-5. EFFECTIVE THERMAL CONDUCTIVITY OF POROUS WICK 263
A-5.1. Theoretical Models of Effective Thermal Conductivity 263
A-5.2. Comparison of Theoretical Models with Experimental Data 266
APPENDIX B. FREE–MOLECULE AND TRANSITION FLOWS REGIMES 272
B-1. MEAN FREE PATH AND KINETIC THEORY 272
B-2. EVALUATION OF THE MOLECULAR DIAMETER OF SPHERICAL NON–POLAR MOLECULES 272
B-2.1. Transport Coefficient Method (Dynamic Viscosity) 273
B-2.2. Van der Waals Method 275
B-2.3. Close–Packed Solid–Phase Density (metallic fluids) 275
B-2.3.1. Close–Packed Simple Cubic Lattice (6 nearest neighbors) 275
B-2.3.2. Close–Packed Body–Centered Cubic Lattice 275

B-2.3.3. Close–Packed Face–Centered Cubic Lattice 276
B-3. EVALUATION OF THE MOLECULAR DIAMETER OF LITHIUM.....277
B-3.1. Transport Coefficient Method (Dynamic Viscosity).....277
B-3.2. Van der Waals Method.....277
B-3.3. Close–Packed Solid–Phase Density.....277
B-4. EVALUATION OF THE MOLECULAR DIAMETER OF POTASSIUM.....278
B-4.1. Transport Coefficient Method (Dynamic Viscosity).....278
B-4.2. Van der Waals Method.....278
B-4.3. Close–Packed Solid–Phase Density.....278
B-5. EVALUATION OF THE MOLECULAR DIAMETER OF SODIUM.....279
B-5.1. Transport Coefficient Method (Dynamic Viscosity).....279
B-5.2. Van der Waals Method.....279
B-5.3. Close–Packed Solid–Phase Density.....279
B-6. EVALUATION OF THE MOLECULAR DIAMETER OF WATER.....280
APPENDIX C. AN OVERVIEW OF NUMERICAL TECHNIQUES.....282
C-1. DIFFUSION/CONVECTION DISCRETIZATION SCHEMES.....283
C-2. STAGGERED GRID ARRANGEMENTS.....284
C-3. NON–STAGGERED GRIDS AND FINITE–ELEMENTS.....285
C-4. EQUIVALENCE OF UNDER–RELAXATION AND TRANSIENT FORMULATIONS.....286
C-5. SIMPLE–TYPE PROCEDURES.....288
C-6. RESIDUAL NORM REDUCTION TECHNIQUE.....292
C-7. EFFECTIVE PARABOLIC BLOCK CORRECTION PROCEDURE.....294
C-8. THE CELS SOLVER FOR TREATING THE TEMPERATURE–VELOCITY COUPLING.....296
C-9. THE LINE–BY–LINE ITERATIVE TECHNIQUE.....300
C-10. ADDITIVE BLOCK–CORRECTION METHOD.....300
C-11. ACM VERSUS BRANDT–TYPE MULTIGRID ALGORITHM.....303
C-12. NON–ITERATIVE SPLITTING METHODS.....304
C-12.1. Alternating Direction Implicit Approximations (ADI).....305
C-12.2. Marker–And–Cell Formulation and Projection Algorithms.....311

C-12.3. Non–Iterative PISO Procedure (Pressure–Implicit with Splitting of Operators).....315

LIST OF FIGURES

Figure **Page**

2.1. Illustration and Principle of Operation of a Conventional Heat Pipe.....21
2.2. Operation Limits of a Heat Pipe.....22
2.3. Vapor Pressure of Some Heat Pipe Working Fluids.....24
2.4. Figure of Merit of Some Heat Pipe Working Fluids.....26
2.5. Progression of the Frozen Startup of a Low–Temperature Heat Pipe.....30
3.1. Physical Model of Heat Pipe and Boundary Conditions.....55
3.2. Illustration of Liquid–Vapor Interfacial Geometry.....64
3.3. Pore Void Fraction as a Function of the Cosine of Contact Angle of the Liquid Meniscus (Seo and El–Genk 1989).....64
3.4. Illustration of Liquid Pooling at End of Condenser.....71
3.5. Vapor Flow Chart for Liquid–Metal Working Fluids.....75
3.6. Vapor Flow Chart for Sodium Working Fluid.....75
3.7. Vapor Flow Chart for Water Working Fluid.....76
3.8. Enthalpies of Solid, Saturated Liquid and Saturated Vapor Phases of Working Fluids as a Function of Temperature.....80
4.1a. Numerical Grid Layout for Circular Heat Pipe.....86
4.1b. Details of the Numerical Grid for Condenser Cooling Jacket.....87
4.2. Grid Layout for a Mass Cell.....88
4.3. Grid Layout for a Radial Momentum Cell.....90
4.4. Grid Layout for an Axial Momentum Cell.....90
4.5. Variation of the Fluid Frozen Volume Fraction with Temperature.....95
4.6. Numerical Grid Layout in the Vicinity of the Solid–Liquid Interface.....98
4.7. Numerical Grid Layout of Heat Pipe Wick During Startup from a Frozen State.....123
4.8. Simplified Flow Chart for Algorithm HPTAM–Revised.....134
4.9. Illustration of Band Storage of a Linear System Matrix which Results from Discretization of Conservation Equations on a Two–Dimensional Domain.....136
4.10. CPU Time on a DEC VAX 6320 to Solve a Linear System of $N_r x N_z$ Equations with the Banded Gauss–Elimination Solver.....138
4.11. CPU Time on a DEC VAX 6320 to Solve a Linear System of N Equations with the Iterative SIS Solver.....139

4.12. Comparison of the Banded Gauss–Elimination Solver and Iterative SIS Solver in terms of CPU Time on a DEC VAX 6320, to Solve a Linear System of NrxNz Equations.....139
4.13. Comparison of Calculated Transient Response of Effective Power Throughput with Water Heat Pipe Experimental Data.....143
4.14. Comparison of Calculated and Experimental Transient Responses of Vapor Temperature for the Water Heat Pipe.....143
4.15. Calculated Extent of Liquid Pooling at the End of the Condenser in Water Heat Pipe as a Function of Time.....144
4.16. Calculated Centerline Vapor Velocity at the Evaporator Exit as a Function of Time.....144
5.1. Temperature Profile Along The Horizontal Mid–Plane for Natural Convection in a Square Cavity (Pr=1, $Gr=10^4$).....147
5.2. Vertical Velocity Profile along the Horizontal Mid–Plane for Natural Convection in a Square Cavity (Pr=1, $Gr=10^4$).....147
5.3. Flow Field for Natural Convection in a Square Cavity, at Pr=1 and $Gr=10^4$.....148
5.4. Temperature Profile along the Horizontal Mid–Plane for Natural Convection in a Square Cavity (Pr=1, $Gr=10^5$).....149
5.5. Vertical Velocity Profile along the Horizontal Mid–Plane for Natural Convection in a Square Cavity (Pr=1, $Gr=10^5$).....149
5.6. Flow Field for Natural Convection in a Square Cavity, at Pr=1 and $Gr=10^5$.....150
5.7. Measured and Predicted Temperature Profiles for Natural Convection of Pure Gallium in a Porous Bed of Glass Beads (Exp. 1, Beckermann and Viskanta 1988).....151
5.8. Crust Thickness as a Function of Time for the Slab Solidification Problem (St=0.25, no Liquid Superheat).....153
5.9. Temperature Histories at x/L=0.09 for the Slab Solidification Problem (St=0.25, no Liquid Superheat).....153
5.10. Crust Thickness as a Function of Time for the Slab Solidification Problem (St=0.25, with Liquid Superheat).....154
5.11. Temperature histories at x/L=0.09 for the Slab Solidification Problem (St=0.25, with Liquid Superheat).....154
5.12. Freezing Constant at Various Liquid Superheats and Stefan Numbers for the Slab Solidification Problem.....156

5.13. Comparison of Analytical and Numerical Front Locations for Freezing in a Corner (Rathjen and Jiji 1971).....156
5.14. Comparison of Measured and Calculated Temperature Profiles in the Liquid at Time 0.077h, for Solidification of Pure Tin.....158
5.15. Comparison of Measured and Calculated Temperature Profiles in the Liquid at Time 0.529h, for Solidification of Pure Tin.....158
5.16. Comparison of Measured and Calculated Freezing Front Locations at Preselected Times, for Solidification of Pure Tin.....159
5.17. Calculated Liquid Flow Field at Time 0.529h, for Solidification of Pure Tin.....159
5.18. Calculated Liquid Flow Field at Time 1.468h, for Solidification of Pure Tin.....160
6.1. Solid and Liquid Phases Distributions in the Wick during Startup of the Water Heat Pipe.....162
6.1. Solid and Liquid Phases Distributions in the Wick during Startup of the Water Heat Pipe (Cont.).....163
6.2. Calculated Mass of Ice in the Water Heat Pipe during Startup from a Frozen State.....165
6.3. Calculated Vaporization Rate during Startup of the Water Heat Pipe as a Function of Time.....165
6.4. Calculated Mid–Evaporator Wick Temperature at Wall during Startup of the Water Heat Pipe as a Function of Time.....166
6.5. Calculated Condenser Output Power during Startup of the Water Heat Pipe as a Function of Time.....166
6.6. Calculated Vapor Pressure at Evaporator End during Startup of the Water Heat Pipe as a Function of Time.....168
6.7. Calculated Normalized Working Fluid Level at Evaporator End during Startup of the Water Heat Pipe as a Function of Time.....168
6.8. Axial Vapor Velocity along the Centerline of the Water Heat Pipe during Formation of a Thin Liquid Film.....169
6.9. Calculated Axial Distribution of the Pore Vapor Fraction in the Wick during Liquid Recess.....169
6.10. Calculated Axial Distribution of the Pore Vapor Fraction in the Wick during Resaturation of the Evaporator Wick.....171
6.11. Calculated Axial Distributions of Liquid and Vapor Pressures during Resaturation of the Evaporator Wick.....171

6.12. Calculated Axial Distributions of Liquid and Vapor Pressures Shortly After Resaturation of the Evaporator Wick. 172
7.1. Water Heat Pipe Experimental Setup (El–Genk and Huang 1993). 174
7.2. Comparison of Calculated Transient Response of Effective Power Throughput with Water Heat Pipe Experimental Data. 177
7.3. Comparison of Calculated and Experimental Transient Response of Vapor Temperature for the Water Heat Pipe. 177
7.4. Comparison of Calculated and Experimental Vapor and Wall Temperature Profiles along the Water Heat Pipe at Different Times during the Heatup Transient. 178
7.5. Calculated Normalized Vapor Void Fraction in the Wick at Different Locations along the Heat Pipe, as a Function of Time. 180
7.6. Calculated Liquid and Vapor Pressures of the Water Heat Pipe as a Function of Time. 180
7.7. Extent of Liquid Pooling at the End of the Condenser in Water Heat Pipe as a Function of Time. 181
7.8. Calculated Axial Distribution of the Vapor Pressure at Steady–State. 181
7.9. Calculated Axial Distributions of the Interfacial Pressures at Steady–State for the Water Heat Pipe. 183
7.10. Calculated Axial Distributions of the Wick Void Fraction at Different Times during the Cooldown Transient of the Water Heat Pipe. 183
7.11. Calculated Axial Distributions of Evaporation–Condensation Rates at Different Times during the Cooldown Transient of Water Heat Pipe. 184
7.12. Calculated Centerline Vapor Velocity at the end of the Evaporator as a Function of Time. 184
8.1. Total Interfacial Pressure Profiles at Various Times for the Water Heat Pipe Analyzed in Case 4. 188
8.2. Vapor Pore Void Fraction Distributions at Various Times for the Water Heat Pipe Analyzed in Case 4. 189
8.3a. Total Interfacial Pressure Profiles for Water Heat Pipe at the Time of First Wet Point for Case 1. 191
8.3b. Vapor Pore Void Fraction Distribution for Water Heat Pipe at the Time of First Wet Point for Case 1. 191
8.4a. Total Interfacial Pressure Profiles for Water Heat Pipe at the Time of First Wet Point for Case 2. 192

8.4b. Vapor Pore Void Fraction Distribution for Water Heat Pipe at the Time of First Wet Point for Case 2. 192
8.5. Transient Variation of Input and Output Powers for the Water Heat Pipe Analyzed in Case 4. 193
8.6. Transient Variation of Wall Temperatures for the Water Heat Pipe Analyzed in Case 4. 193
8.7. Transient Variation of Vapor Pore Void Fractions for the Water Heat Pipe Analyzed in Case 4. 194
8.8. Extent of Liquid Pool as a Function of Time for the Water Heat Pipe Analyzed in Case 4. 194
8.9a. Normalized Vapor Pressure Distribution at Various Times During the Heatup Transient for the Water Heat Pipe Analyzed in Case 4. 196
8.9b. Transient Variation of Reference Vapor Pressure at Evaporator End for the Water Heat Pipe Analyzed in Case 4. 196
8.10a. Evaporation/Condensation Rates at Various Times During the Heatup Transient for the Water Heat Pipe Analyzed in Case 4. 197
8.10b. Transient Variation of the Condensation Mass Flux at Mid–Condenser for the Water Heat Pipe Analyzed in Case 4. 197
8.11. Liquid and Wall Temperatures Profiles at 2 Different Times During the Heatup Transient for the Heat Pipe Analyzed in Case 4. 199
9.1. Steady–State Vapor Pressure Distribution Along the Lithium Heat Pipe Analyzed. 200
9.2. Steady–State Liquid Pressure Distribution Along the Lithium Heat Pipe Analyzed. 201
9.3. Total Interfacial Pressure Profiles at Steady–State Along the Lithium Heat Pipe Analyzed. 203
9.4. Pore Void Fraction Distribution at Steady–State Along the Lithium Heat Pipe Analyzed. 203
9.5. Liquid/Wick and Wall Temperatures Profiles at Steady–State for the Lithium Heat Pipe Analyzed. 205
9.6. Viscous Dissipation Profile in the Vapor Phase at Steady–State for the Lithium Heat Pipe Analyzed. 205
9.7. Viscous Dissipation Profile in the Liquid Phase at Steady–State for the Lithium Heat Pipe Analyzed. 206
9.8. Evaporation/Condensation Rates Distribution at Steady–State Along the Lithium Heat Pipe Analyzed. 206

9.9. A Two–Dimensional Illustration of the Spacial Discretization and Mass Flow Field at Steady–State for the Lithium Heat Pipe Analyzed.....207
9.10. A Two–Dimensional Illustration of the Spacial Discretization and Velocity Field at Steady–State for the Lithium Heat Pipe Analyzed.....207
A-1. Schematic of a Woven Wire Screen (Top and Front Views).....253
A-2. Surface Porosity of a Screen Wick as a Function of Wire Diameter–to–Mesh Size Ratio.....256
A-3. Coefficient of Shrinkage of a Screen Wick as a Function of Wire Diameter–to–Mesh Size Ratio.....256
A-4. Volume Porosity of Screen Wicks as a Function of Wire Diameter–to–Mesh Size Ratio and Normalized Clearance.....258
A-5. Normalized Permeability of Screen Wicks as a Function of Wire Diameter–to–Mesh Size Ratio and Normalized Clearance.....258
A-6. Effective Pore Radius of the Screen Wick as a Function of Wire Diameter and Mesh Number.....262
A-7. Effective Thermal Conductivity of Wicks for a Conductivity Ratio $k_m / k_f = 0.1$ as a Function of Volume Porosity.....267
A-8. Effective Thermal Conductivity of Wicks for a Conductivity Ratio $k_m / k_f = 4$ as a Function of Volume Porosity.....267
A-9. Effective Thermal Conductivity of Wicks for a Conductivity Ratio $k_m / k_f = 24$ (Water–Stainless Steel) as a Function of Porosity.....269
A-10. Effective Thermal Conductivity of Wicks for a Conductivity Ratio $k_m / k_f = 75$ as a Function of Volume Porosity.....269
A-11. Effective Thermal Conductivity of Wicks for a Conductivity Ratio $k_m / k_f = 623$ (Water–Copper) as a Function of Volume Porosity.....270

LIST OF TABLES

Table		Page
1.1.	Summary of Previous Heat Pipe Modeling Efforts	5
3.1.	Mathematical Closure of the Physical Model	67
3.2.	References and Temperature Range of Validity for the Thermophysical Properties of Working Fluids (Solid, Liquid and Vapor Phases)	77
3.3.	References and Temperature Range of Validity for the Thermophysical Properties of Structural Materials	78
7.1.	Design and Operational Parameters of Experimental Water Heat Pipe Analyzed	176
8.1.	Design and Operational Parameters of Water Heat Pipes Analyzed	186
8.2.	Comparison of Operational Parameters of Water Heat Pipes Investigated	187
9.1.	Design and Operational Parameters of Lithium Heat Pipe Analyzed	200
A-1.	Comparison of Calculated and Measured Porosity and Permeability for various Square–Mesh Wire Screens	260
A-2.	Comparison of Common Manufacturing Values of the Wire Diameter with Correlation Equation (A-44), as a Function of Mesh Number	262
B-1.	Some Properties of Heat Pipe Working Fluids (Vargaftik 1975, Reynolds 1979, and Schlunder 1984)	276
B-2.	Lattice Parameters of Solid Potassium at Various Temperatures	278
B-3.	Lattice Parameters of Solid Sodium at Various Temperatures	279
B-4.	Energy Potential Parameters for Water Vapor as Determined by Monchick and Mason (1961) from Various Fitting Methods	281

NOMENCLATURE

English

a	cubic lattice parameter (m)
a	radius of pipe (m)
a_c	accommodation coefficient
A	cross–sectional area (m^2)
b	distance between nearest neighbors in lattice (m)
b_0	molar volume (m^3/mole)
C	inertia coefficient, Equations (2), (A–3)
C_p	specific heat (J/kg.K)
C_v	heat capacity at constant volume (J/kg.K)
d	wire diameter of screen (m)
D	diffusion coefficient ($W/m^2.K$)
D	pipe diameter (m)
$\overline{\overline{D}}$	deformation rates tensor
$\vec{F}$	external acceleration (m/s^2)
F_{rad}	wall view factor
g	gravity acceleration, g=9.81 m/s^2
Gr	Grashof number, $Gr=g\beta_P L^3(T_H-T_C)/\nu_L^2$
h	enthalpy (J/kg)
h_{fg}	latent heat of vaporization (J/kg)
h^{REF}	reference enthalpy of liquid phase (J/kg)
H	height of the cavity (m)
H_{fus}	latent heat of fusion (J/kg)
H^J	convective heat transfer coefficient ($W/m^2.K$)
k	Boltzmann constant, $k=1.3804 \times 10^{-23}$ J/K
k	thermal conductivity (W/m.K)
K	permeability of wick (m^2)
Kn	Knudsen number ($Kn = \lambda/D$)
L	effective pipe length (m)
L	mesh size of screen, L=1/N (m)
L	width of the cavity (m)
m	molecular mass (kg)

M	molecular weight (kg/mole)
$\dot{\bar{m}}$	evaporation/condensation/sublimation/resolidification mass flux ($kg/m^2.s$)
$\dot{\bar{M}}^J$	water jacket mass flow rate (kg/s)
n	molecular density ($molecules/m^3$)
N	screen mesh number, N=1/L (1/inch)
N_a	Avogadro number, $N_a = 6.0225 \times 10^{23}$ molecules/mole
N_{first}	axial location of first identifiable liquid film
N_{last}	axial location of last cell bearing a liquid film
N_{mush}	axial location of first interfacial mushy cell
N_z	number of axial numerical cells
P	pressure (Pa)
P_c	critical pressure (Pa)
Pr	Prandtl number, $Pr=\nu_L/\alpha_L$
$\vec{q}$	mean filter velocity in wick (m/s)
$\vec{Q}$	conduction heat flux (W/m^2)
r	radial coordinate
R	radius (m)
R	radius of curvature of screen wire (m)
Ra	Rayleigh number, Ra=Pr Gr
R_c	radius of curvature of interfacial liquid meniscus (m)
R_g	universal gas constant, $R_g = kN_a = 8.314$ J/mol.K
R_i	radial location of numerical cell interface (m)
R_{int}	radius of liquid– / solid–vapor interface (m)
R_p	wick effective pore radius (m)
R_{wk}	radius of screen wick surface (m)
R_o	initial radius of solid–vapor interface (m)
St	Stefan number, $St = C_p^S(T_{fus}-T_C)/H_{fus}$
t	time (s)
t	thickness of one screen layer, $t=2d+\eta$ (m)
T	temperature (K)
T_c	critical temperature (K)
T_C	cold wall temperature (K)
T_{fus}	fluid fusion temperature (K)
T_H	hot wall temperature (K)
$Tint$	temperature of liquid– / solid–vapor interface (K)
Tin^J	water jacket inlet temperature (K)

T_o initial liquid temperature (K)

T_o^* dimensionless liquid superheat, $T_o^* = k_L(T_o - T_{fus})/[k_S(T_{fus} - T_C)]$

T_{REF} reference temperature for evaluating enthalpy of liquid phase (K)

T_{sp} ambient temperature (K)

T^* dimensionless temperature, $T^*=kT/\varepsilon$

u, v radial and axial front locations (m)

$\vec{U}$ velocity field

v_a average molecular speed (m/s)

V_r^{int} radial velocity of displacement of L–V interface (m/s)

Vol wick cell volume (m^3)

Vol_o wick cell volume when $R_{int}=R_{wk}$ (m^3)

Vol_α volume of phase α in interfacial wick cell (m^3)

V_p volume of hemispherical pores at wick surface (m^3)

V^* dimensionless axial velocity, $V^*=Lq_z/\nu_L$

w width of the screen openings (m)

x coordinate along the width of the cavity (m)

z axial coordinate (m)

z coordinate along the height of the cavity (m)

Z_j axial location of numerical cell interface (m)

Greek

α thermal diffusivity, $\alpha=k/(\rho C_p)$ (m^2/s)

α_p vapor pore volume fraction in wick at liquid–vapor interface

β normalized clearance of screen, $\beta=\eta/(2d)$

β_P liquid thermal expansion coefficient (1/K)

β_T liquid isothermal compressibility factor (1/Pa)

γ ratio of specific heat capacities

γ volume fraction of frozen fluid in wick voids

Γ convection–diffusion enthalpy flux (W/m^2)

δ solid crust thickness (m)

δT half width of mushy region (K)

ΔR_i radial size of numerical cell (m)

Δt discretization time step (s)

Δx discretization mesh size (m)

ΔZ_j axial size of numerical cell (m)

ε volume porosity (void fraction) of wick

ε energy potential parameter (J)

ε_i local volume porosity, Equation (4.70)

ε_{rad} wall emissivity

ζ figure of merit of working fluid, $\zeta=\rho_L(h_V-h_L)\sigma / \mu_L$ (W/m^2)

η screen interlayer clearance (m)

θ geometrical angle, Figure A–1a

ϑ dimensionless temperature, $\vartheta=(T-T_C)/(T_o-T_C)$

θ_L dimensionless temperature, $\theta_L=(T_L-T_C)/(T_H-T_C)$

λ molecular mean free path (m), Equation (B-1)

μ dynamic viscosity (kg/m.s)

μ_c cosine of contact angle of liquid meniscus at liquid–vapor interface, $\mu_c=R_p/R_c$

ν kinematic viscosity, $\nu=\mu/\rho$ (m^2/s)

ρ density (kg/m^3)

ρ_s close–packed solid phase density (kg/m^3)

σ surface tension of liquid (N/m)

σ effective molecular diameter (m)

σ_{rad} Stefan–Boltzmann constant, $\sigma=5.67x10^{-8}$ W / $m^2.K^4$

τ dimensionless time, $\tau = \alpha_S t/L^2$

τ exponential period (s)

ϕ viscous dissipation

φ_L dimensionless temperature, $\varphi_L=(T_L-T_{fus})/(T_H-T_{fus})$

ω wire diameter–to–mesh size ratio, $\omega=d/L$

Ω^* kinetic theory collision integral

Subscript / Superscript

a adiabatic region

c condenser region

e evaporator region

eff effective property of wick

equ equilibrium

f working fluid

fus fusion

i radial number of wick cell

int liquid– / solid– vapor interface

j	axial cell number
L	liquid phase of fluid
m	porous matrix
n	temporal discretization number
o	wall outer surface
p	pore
r	radial component
S	frozen (solid) phase of fluid
sat	saturation
v	vapor phase, liquid inner surface
V	vapor phase of fluid
v0	vapor phase, at beginning of evaporator
w	wall region
W	outer wall surface
wk	porous wick
z	axial component
*	best estimate at new time
'	correction

Operators

div	divergence of vector
∂	partial derivative
Δ	Laplacien of vector
$\vec{q}$	vector
$\|\vec{q}\|$	norm of vector
$\vec{\nabla}$	gradient of scalar
$\vec{\vec{\nabla}}$	gradient of vector operator
$\bullet$	scalar product of vector

1. INTRODUCTION

Heat pipes can transport relatively large amounts of energy over a significant distance with a small temperature drop between the heat source and the heat sink. Since heat pipes have no moving parts and operate passively in vacuum and in microgravity environments, they are highly reliable and efficient energy transport devices and are being considered for many terrestrial and space power thermal–management applications, such as high–performance aeronautics and space nuclear and solar dynamic power systems.

Water and alkali metal heat pipes are currently being considered for passive cooling of commercial nuclear reactors after shutdown. They are also being developed for solar dynamics, nuclear space power systems and space platforms such as the space station Freedom, either as the primary transport sub–system of for radiative heat rejection. Nuclear space power systems may employ thermoelectric elements, thermionic elements, closed Brayton cycle, or Free Piston Stirling Engines (the latter are being considered for a lunar outpost), to convert thermal power to electrical power. Heat pipes operating at temperatures in excess of 700 K employ liquid–metal working fluids while those operating at lower temperature may employ non–liquid metal fluids such as water or ammonia.

In the temperature range of 300–500 K, water provides the best alternative for a working fluid. Water heat pipes have been used in numerous terrestrial and space applications, such as solar water heaters, cooling of molds during casting of aluminum and plastics, and cooling of electronic components on board satellites.

Between 500 K and 700 K, there does not exist, to date, any working fluid with attractive properties. Mercury has suitable vapor pressure and high figure of merit in this temperature range, unfortunately, it is highly toxic and its use is not recommended.

In the temperature range of 700–1600 K, candidate heat pipe working fluids of interest for high–performance space power applications are the alkali metals, potassium, sodium, and lithium. Examples of these applications include heat transport from the reactor to the power converter, heating and cooling of electrodes in thermionic converters, and heat rejection. Additional uses of high temperature heat pipes are cooling of radiation shield, electromagnetic pumps, control drums and drive motors, and thermal conditioning of liquid–metal pumped loops during the startup and shutdown of power systems (Merrigan

1985). These potential applications have received the most attention in recent years with the onset of advanced space power programs such as the SP–100 (Cox et al. 1991) and Dynamic Isotope Power Subsystem (DIPS) studies (Dix 1991). An advantage of using sodium or potassium working fluids in the temperature range 700–1100 K is their relatively low melting temperature (98 °C and 64 °C, respectively), which is favorable for space applications. The NaK–78 alloy has a melting temperature well below that of sodium and potassium (-10 °C), which is the reason why this particular working fluid was selected as the primary coolant for all Russian (Romachka and Topaz) and American (SNAP–10A) nuclear power systems launched in space since the late 1950's. At very high temperatures (above 1200 K), lithium is a good choice as a heat pipe working fluid because of its high latent heat of vaporization and high surface tension. Also, because of the very low vapor pressure of this fluid, lithium heat pipes can operate at a much higher temperature than potassium and sodium heat pipes without overpressurization of the container.

One of the concerns with the utilization of heat pipes in space and in some terrestrial applications is understanding their transient behavior during startup from a frozen state. The startup of high–temperature heat pipes from the frozen state has been extensively and experimentally investigated (Deverall et al. 1970; Ivanovskii et al. 1982; Jang et al. 1990a; Faghri et al. 1991; Jang 1995), and successful startup of such heat pipes is consistently achieved. However, experiments on the startup of low–temperature heat pipes are rare. Heat pipes using high vapor pressure working fluids (such as water and ammonia) typically exhibit a uniform temperature startup, whereas those using fluids with low vapor pressures (such as liquid metals, sodium, potassium and lithium) exhibit a frontal startup. Deverall et al. (1970) successfully started a water heat pipe from a frozen state. Because of the relatively high vapor pressure of water, even near the melting temperature, choked and/or supersonic vapor flows were not encountered during the startup. Experimental results showed that the heat pipe became immediately active where the ice was melted.

Previous investigations of the frozen startup of heat pipes generally assume uniform distribution of the working fluid in the wick. Such assumption is found to be invalid experimentally for low–temperature heat pipes. Redistribution of frozen working fluid in low–temperature heat pipes occurs during startup due to sublimation and resolidification of vapor (Kuramae 1992; and Ochterbeck and Peterson 1993). Such processes may prevent successful re–startup of the heat pipe during cyclic operation. The vapor resolidifies in the cooler parts of the heat pipe and cannot return back to the evaporator. Eventually, the wick might completely dryout in the evaporator. In cases of low–temperature heat pipes with

large evaporator–to–condenser length ratio, complete blockage of the vapor channel was observed, due to resolidification of working fluid (Ochterbeck and Peterson 1993).

The startup characteristics of low–temperature and high–temperature heat pipes from a frozen state differ significantly due to differences in the vapor pressure of the working fluid near the melting point. In low–temperature heat pipes, although the vapor pressure is large enough so that the startup difficulties associated with the viscous and sonic limits are avoided, significant migration of the working fluid from the evaporator to the colder regions in the heat pipe occurs. Once the solid working fluid is melted in the evaporator, dryout may occur due to immediate vaporization of the fluid. In the case of high–temperature working fluids, the vapor flow in the heat pipe remains in the free–molecule regime for temperatures well above the melting temperature. This has the beneficial effect of minimizing the transport of the solid working fluid to the condenser by sublimation / resolidification. The large thermal conductivity of liquid–metal working fluids also allows melting of the working fluid in adiabatic and condenser sections by conduction, before large scale evaporation of the liquid occurs.

Attempts have been made to fill the heat pipe with noncondensible gas to make it start more readily. A significant decrease in startup time was noted by Ivanovskii et al. (1982) for increasing amounts of noncondensible gas loading in sodium heat pipes. The effect of noncondensible gas on the startup of a water heat pipe was also investigated by Ochterbeck and Peterson (1993). The gas–vapor interface, observed visually, was found to be quite sharp. In the region containing the gas, resolidification and condensation of water vapor did not occur. A frontal startup, characteristic of high–temperature and gas–loaded heat pipes, was observed in the gas–loaded water heat pipe.

The wide interest in heat pipes has stimulated the development of numerous steady–state and transient models. Because the transient operation of heat pipes and the startup of heat pipes from a frozen state involve several highly non–linear and tightly coupled heat and mass transfer processes in the vapor, wick and wall regions, mathematical modeling of these problems is quite complex. An analytical solution is unattainable, and except when simplifying assumptions are made, the numerical solution could be tedious and require large computation time. The following section reviews the previous and major heat pipe modeling efforts, which included a variety of simplifying assumptions in the governing equations, and a spectrum of numerical techniques to solve these equations.

1.1. SUMMARY ON HEAT PIPE MODELING

Heat pipe models can be classified into four categories: (a) models which simulate the vapor flow region only; (b) models which simulate vapor, wick and wall regions but ignore the liquid flow in the wick and the momentum coupling at the liquid–vapor (L–V) interface; (c) liquid/vapor counter–current flow models which neglect the momentum coupling at the L–V interface; (d) models which have the capability to predict the radius of curvature of the liquid meniscus at the L–V interface in order to insure proper hydrodynamic coupling of the liquid and vapor phases. Only a few models, however, attempted to simulate the non–continuum vapor flow regimes occurring in high–temperature heat pipes operating in the low temperature range, and the change of phase of the working fluid in the wick during the startup of heat pipe from a frozen state. Table 1.1 summarizes the capabilities and important characteristics of major heat pipe models developed after the year 1987.

In an attempt to describe the operation of heat pipe, Bowman (1987), Bowman and Hitchcock (1988), Klein and Catton (1987) and Issacci et al. (1988, 1990 and 1991) have developed two–dimensional transient models of vapor flow, which decoupled the vapor from the liquid–wick and wall regions, except for a simplified interfacial energy balance.

Bowman and Hitchcock (1988) studied the vapor flow in the laminar and turbulent regimes. The emphasis was placed on studying highly compressible vapor flow situations, including subsonic and supersonic flow fields with shock waves and flow reversal. Bowman and Hitchcock solved the full unsteady compressible, Reynolds–averaged turbulent Navier–Stokes equations in cylindrical coordinates, using the Explicit MacCormack finite difference method. In their calculations, they had to use very small time steps in order to avoid numerical instabilities. Bowman and Hitchcock (1988) experimentally investigated vapor flow dynamics using isothermal air injection and suction at the walls of a porous pipe made from polyethylene beads. Based on this work, Bowman (1987) established functional relationships of the friction coefficient for a simple, steady one–dimensional model for highly compressible and sonic vapor flows.

Researchers at the University of California Los Angeles (Klein and Catton 1987; Issacci et al. 1988, 1990 and 1991) also studied the heat pipe vapor dynamics, using a two–dimensional approach. Originally, they solved the two–dimensional, laminar compressible

TABLE 1.1. Summary of Previous Heat Pipe Modeling Efforts.

Model		Bowman and Hitchcock (1988)	Issacci et al. (1988-1991)	Tilton (1987)	Faghri and Buchko (1991)
Vapor region	free-molecule flow regime	(not included)	(not included)	(not included)	(not included)
	continuum flow regime	2-D transient compressible Reynolds-averaged turbulent equations	2-D transient compressible laminar Navier-Stokes equations	1-D steady incompressible friction model Uniform vapor temperature from saturated vapor state	2-D steady compressible laminar Navier-Stokes equations
Liquid-vapor interface	evaporation/ condensation	uniform injection and suction	from radial energy balance	from radial energy balance	from radial energy balance
	temperature	isothermal	vapor saturation temperature	uniform, equal to vapor temperature	vapor saturation temperature
	capillary effect	(not included)	(not included)	(not included)	(not included)
	pooling of excess liquid	(not included)	(not included)	(not included)	(not included)
Wick region	heat transfer	(not included)	simple radial thermal resistance	obtain rate of energy storage per unit length from global energy balance Radial conduction	2-D steady conduction
	liquid flow	(not included)	(not included)	liquid flow rate from steady mass balance	2-D steady Darcy-extended flow equations
	liquid recess	(not included)	(not included)	(not included)	(not included)
	solid-liquid phase-change	(not included)	(not included)	(not included)	(not included)
Wall region		(not included)	simple radial thermal resistance	Radial conduction	2-D steady conduction
Numerical solution		Explicit MacCormack finite difference method Severe time step restrictions Obtained experimentally friction coefficients for 1-D steady compressible flow	SIMPLER and CONDIF schemes with SOR iterative method were unstable Boundary Cs. smoothed out Non-linear filtering technique could capture shock waves	Explicit discretization of energy equations Internal iterations to resolve vapor temperature coupling Time step restrictions	PHOENICS iterative method combined with SIMPLEST technique for momentum equations

TABLE 1.1. Summary of Previous Heat Pipe Modeling Efforts (Continued).

Model		Cao and Faghri (1990)	Jang (1988)	Jang et al. (1990a)	Cao and Faghri (1993a)
Vapor region	free-molecule flow regime	(not included)	sonic limited transport	no heat or mass transfer (front location defined by transition temperature)	self-diffusion rarefied vapor flow model
	continuum flow regime	2-D transient compressible Navier-Stokes equations	1-D steady compressible flow equations	1-D transient compressible flow equations	(not included)
Liquid-vapor interface	evaporation/ condensation	from interfacial energy balance	from kinetic theory	from interfacial energy balance	from kinetic theory
	temperature	vapor saturation temperature	vapor saturation temperature	vapor saturation temperature	vapor saturation temperature
	capillary effect	(not included)	(not included)	(not included)	(not included)
	pooling of excess liquid	(not included)	(not included)	(not included)	(not included)
Wick region	geometry	saturated with liquid	rectangular leading edge	circular heat pipe	circular heat pipe
	heat transfer	2-D transient conduction	2-D transient conduction	2-D transient conduction	2-D transient conduction
	liquid flow	(not included)	(not included)	(not included)	(not included)
	liquid recess	(not included)	(not included)	(not included)	(not included)
	solid-liquid phase-change	(not included)	equivalent heat capacity method (pure conduction)	equivalent heat capacity method (pure conduction)	fixed-grid temperature transformation (conduction)
Wall region		2-D transient conduction	2-D transient conduction	2-D transient conduction	2-D transient conduction
Numerical solution		SIMPLE method combined with vapor state equation (ideal gas) to include vapor compressibility	Finite element method of solution	Iterative solution procedure ADI for conduction, Beam and Warming method for vapor flow	Combine TDMA and Gauss-Seidel methods Under-relaxation of temperature (phase-change)

TABLE 1.1. Summary of Previous Heat Pipe Modeling Efforts (Continued).

Model		Cao and Faghri (1993b)	Peery and Best (1987)	Costello et al. (1988)
Vapor region	free-molecule flow regime	Self-diffusion rarefied vapor flow model (front location defined by transition temperature)	(not included)	friction factor function of Knudsen number
	continuum flow regime	2-D transient compressible Navier-Stokes equations	Saturated vapor 1-D transient compressible flow equations	Saturated vapor 1-D transient compressible flow equations
Liquid-vapor interface	evaporation/ condensation	from kinetic theory	from kinetic theory	from kinetic theory
	temperature	vapor saturation temperature	(not included)	(not included)
	capillary effect	(not included)	liquid and vapor pressures are equal at condenser end	liquid and vapor pressures are equal at condenser end
	pooling of excess liquid	(not included)	(not included)	(not included)
Wick region	geometry	circular heat pipe	rectangular H2O heat pipe	startup of LM heat pipe
	heat transfer	2-D transient conduction	1-D transient energy balance	1-D transient energy balance
	liquid flow	(not included)	1-D transient compressible flow	1-D transient compressible flow
	liquid recess	(not included)	(not included)	(not included)
	solid-liquid phase-change	fixed-grid temperature transforming model (pure conduction)	(not included)	homogeneous enthalpy method (radial lumped model)
Wall region		2-D transient conduction	2-D transient conduction	2-D transient conduction
Numerical solution		Iterative solution procedure Under-relaxation of temperature (phase-change model)	Numerical instabilities due to coupling of energy equations and kinetic theory Also, velocities obtained from continuity equation alone Inadequate solution procedure	KACHINA method for vapor flow, modified SIMPLER for liquid flow Severe time step restrictions (KACHINA) Numerical instabilities due to coupling of energy equations and kinetic theory

TABLE 1.1. Summary of Previous Heat Pipe Modeling Efforts (Continued).

Model		Ransom and Chow (1987)	Hall et al. (1988-1994)	Seo and El–Genk (1989)
Vapor region	free-molecule flow regime	(not included)	treat all flow regimes with 1-D Dusty Gas Model (effect of non-condensable gas included)	(not included)
	continuum flow regime	1-D transient area-averaged phasic model (RELAP–5)		quasi-steady state, 1-D compressible approximation
Liquid-vapor interface	evaporation/ condensation	from interfacial energy balance (?)	from kinetic theory (predicts also resolidification rates)	from interfacial energy balance
	temperature	vapor saturation temperature (?)	from interfacial energy balance	continuity of temperature (?)
	capillary effect	Pascal capillary relationship (vapor volume fraction function of radius of curvature of liquid meniscus)	Pascal capillary relationship (vapor volume fraction function of radius of curvature of liquid meniscus)	Pascal capillary relationship (vapor volume fraction function of radius of curvature of liquid meniscus)
	pooling of excess liquid	(not included)	calculates axial distribution of liquid volume fraction	(not included)
Wick region	geometry	fully-thawed lithium heat pipe	startup of circular lithium heat pipe	fully-thawed lithium heat pipe
	heat transfer	1-D transient area-averaged phasic model (RELAP–5)	Neglect thermal mass of wick matrix	Neglect thermal mass of wick matrix
	liquid flow		1-D transient area-averaged heat and mass transfer (radial heat transfer lumped)	2-D transient incompressible flow and heat transfer
	liquid recess	(not included)	calculates axial distribution of vapor volume fraction in wick	(not included)
	solid-liquid phase-change	(not included)	phase–change B. C. at liquid–solid front (radial layers, axial front model)	(not included)
Wall region		(not included)	1-D transient area-averaged heat conduction (radial lumped model)	2-D transient conduction
Numerical solution		Iterative semi-implicit RELAP–5 solution scheme Phasic pressure difference evaluated explicitly Severe time step restrictions	1-D model allows the use of specialized block-diagonal matrix inversion Linearization errors of gas mixture state equation and capillary pressure relationship reduced by updating the Jacobian during iterations	SIMPLE–type numerical solution technique Iterative scheme to resolve interfacial couplings

Navier–Stokes equations using the SIMPLER algorithm. This method, however, was limited to low–compressibility flows. Issacci et al. (1991) showed that a centered–difference scheme, when used with non–linear filtering, yielded a second–order, stable solution and captured shocks without oscillations. This non–linear filtering technique was used to analyze the startup vapor dynamics of a sodium heat pipe with a high heat input flux. The startup transient involved multiple wave reflections from the line of symmetry in the evaporator section. It is not clear, however, how this code could model free–molecule and/or transition flow conditions without any special treatment.

Although the vapor flow models of Bowman and Hitchcock (1988) and Issacci et al. (1988, 1990 and 1991) have provided valuable information on the vapor flow dynamics, they are of limited use for the design and transient analysis of heat pipes, because of the thermal and hydrodynamic decouplings of the vapor from the wick region.

Traditionally, the second category regroups heat pipe models that have been developed for design purposes. These models pay attention to only these phenomena that influence the performance of heat pipes. The experimental investigations of Ivanovsky et al. (1982) and Tilton et al. (1986) suggested that during steady–state or slow transients, heat pipe operation can be described solely by vapor dynamics and energy balance in the various heat pipe regions. Following these observations, Tilton et al. (1986), Faghri and Chen (1989) and Cao and Faghri (1990) at Wright State University solved the two–dimensional heat conduction equations in the wall and liquid–wick regions, which were thermally coupled to either a one– or two–dimensional vapor flow model.

In their two–dimensional steady–state model, Faghri and Chen (1989) assumed thermodynamic equilibrium at the L–V interface (the interfacial temperature is equal to the vapor saturation temperature) and evaluated the evaporation/condensation rates from the energy balance at the interface. With this model, Faghri and Chen evaluated the effects of axial conduction, vapor compressibility and viscous dissipation on the operation of water and sodium heat pipes. Cao and Faghri (1990) extended Faghri and Chen's model to perform transient calculations. They used the SIMPLE method, and incorporated the effect of vapor compressibility by treating the vapor pressure as a dependent variable and directly applying the state equation to obtain the density while iterating.

Jang (1988), Jang et al. (1990a) and Cao and Faghri (1993a, 1993b and 1992) also modeled the startup of heat pipes from a frozen state. Jang (1988) developed a pure–conduction transient model for rectangular heat pipe cooled leading edges, and compared its

predictions with Camarda's (1977) experimental results. Evaporation and condensation rates were evaluated from the kinetic theory to account for the thermal resistance at the L–V interface. Different startup periods were considered, including free–molecule and continuum vapor flow conditions. During the first period, Jang (1988) obtained the vapor temperature by equating the evaporative heat input to the sonic limited heat transport. When continuum flow is established along the heat pipe, one–dimensional steady compressible equations were used in the vapor core. Later, Jang et al. (1990a) improved the model by solving the one–dimensional transient compressible flow equations for the continuum vapor flow, and developed a model for the frontal startup of circular heat pipes from a frozen state. The phase change of the working fluid was modeled by using the fixed–grid heat capacity method. Jang and co–workers used the transition temperature at a Knudsen number of 0.01 to characterize the axial location of the free–molecule flow front, and assumed no heat or mass transfers at the boundaries of the rarefied vapor zone. Unfortunately, these assumptions do not allow the vapor to accumulate progressively in the heat pipe core, so that the vapor flow would never reach the continuum regime.

Cao and Faghri (1993a) improved the model of Jang et al. (1990a) by using a rarefied self–diffusion vapor model to simulate the early startup period of high–temperature heat pipes. After the melting front has reached the vapor–wick interface, evaporation and condensation rates were calculated using a modification of the kinetic theory of gases. Cao and Faghri (1993b) extended the model by using a two–region description of the vapor core. The continuum vapor flow region was modeled using the two–dimensional compressible Navier–Stokes equations, while the rarefied vapor flow region was simulated by a self–diffusion model, the two vapor regions being coupled with appropriate boundary conditions at the axial front defined by the transition temperature. Based on the results of their model, Cao and Faghri (1992) developed an approximate flat–front analytical solution for the startup of high–temperature heat pipes, and proposed a frozen–startup operation limit which indicated the possibility of dryout in the evaporator. This limit was obtained by comparing the rate of increase of the mass of liquid in the wick (due to axial propagation of the melting front) with the rate of loss of the working fluid by resolidification of vapor on the frozen substrate. The two rates were found to be similar for a number of heat pipes, indicating that resolidification of working fluid is a potential factor for failure of the startup of high–temperature heat pipes also.

Some of the above models have focused on the modeling of free–molecule flow regimes in the vapor and have provided valuable information concerning the startup of high–

temperature heat pipes. Unfortunately, all of these models treated the wick as a pure conducting medium, assumed a uniform distribution of the working fluid, and neglected liquid flow, hydrodynamic coupling between the liquid and vapor phases, and solid–vapor mass transfers. Therefore, these models are not capable of predicting the operation limits of the heat pipe, such as capillary, entrainment, dryout of the wick, and the redistribution of working fluid by sublimation and resolidification during the startup of heat pipes. Tilton (1987) and Cao and Faghri (1990) recognized that the hydrodynamics of both the liquid and vapor phases must be modeled in order to predict these operation limits.

Investigators of the third heat pipe model category have included modeling of the liquid flow and treated the vapor flow as compressible.

In their models, Costello et al. (1988) and Peery and Best (1987) treated the liquid and vapor flows in the heat pipe as one–dimensional and compressible flow problems, and evaluated the evaporation and condensation rates at the L–V interface using modified forms of the kinetic theory relationship. The evaporator end of the heat pipe contained a porous node to store excess liquid fluid, while the excess liquid in the condenser end was assumed to exist in slug form. At the condenser end, the liquid pressure in the wick was assumed to be equal to the vapor pressure in the core. Costello et al. (1988), on contract for Los Alamos National Laboratory, developed a heat pipe model to predict the transient behavior of liquid–metal heat pipes during startup from the frozen state and operational shutdowns. The friction factor was a function of the Knudsen number to simulate free–molecule and transition flow conditions occurring during startup at low temperature. At each axial location, the liquid and vapor pressure difference was tested against the maximum capillary pressure head. If the pressure difference exceeded the capillary pressure, the node was flagged as being dried out. Although their model is quite comprehensive, Costello and co–workers did not report any calculation results. It is believed that the temporal discretization scheme associated with the KACHINA algorithm limited the time step for calculations. Peery and Best (1987) developed a model to simulate the transient operation of a rectangular water heat pipe tested at Texas A&M University. Even so Peery and Best used oversimplifying assumptions, their model suffered from numerical instability, and the authors could only report calculations of small transients (up to 2 seconds). Extremely small time steps (10^{-4} s) were required to solve iteratively for the coupled energy and kinetic theory equations. This constraint on the time step was previously reported by Subbotin when using his model for predicting evaporation / condensation rates. In conclusion, Costello et al. and Peery and Best did not succeed. The numerical instabilities

encountered by these authors are attributed to the numerical methods they used, which were not suitable to handle the complexity of the problem, particularly the coupling with the kinetic theory relationship.

Later, Faghri and Buchko (1991) extended the capability of their two–dimensional steady–state model (Faghri and Chen 1989) by including the effect of liquid flow in the wick. They used the steady Darcy–extended flow equations for a saturated and isotropic porous medium, but computed the pressure profiles along the heat pipe independently.

Unfortunately, all the investigators mentioned above ignored the hydrodynamic coupling at the L–V interface. Such decoupling of the liquid and vapor momentum equations can result in erroneous liquid and vapor flow rates and pressures. This uncertainty is attributed to the fact that neither of these models satisfy the local interfacial force balance at the L–V interface. As pointed out by Hall and Doster (1989), it is necessary to accurately model the capillary phenomena along the entire length of the heat pipe and thus, adequately satisfy the local capillary relationship of Pascal. Setting the liquid and vapor pressures equal at an assumed axial location and computing the phasic pressure distributions independently does not allow the capillary pressure difference to adjust to system parameters. Consequently, models using this approach could not accurately calculate the vapor and liquid flow rates and pressures during a transient, and were not capable of predicting the capillary and dryout operation limits.

The fourth category regroups the heat pipe models that use a geometric approach for modeling the radius of curvature of the liquid meniscus. Ransom and Chow (1987), Hall and co–workers (1988–1994) and Seo and El–Genk (1989) incorporated liquid flow and thermal expansion, hydrodynamically coupled the liquid and vapor phases, and predicted the vapor volume distribution in the wick. They used the capillary relationship of Pascal to relate the phasic pressures. The pore radius, R_p, is fixed by the geometry of the wick, and the radius of curvature of the liquid meniscus at the L–V interface, R_c, is related to the amount of vapor in the wick. The maximum pressure difference occurs when R_c is equal to the pore radius; in this case, the volume of vapor in the wick forms a hemisphere of radius R_p in each pore of the wick surface. These geometrical considerations allow to express the vapor void fraction in the wick in terms of R_c, the wick surface porosity, and the diameter of the vapor core.

The Advanced Thermal Hydraulic Energy Network Analyser (ATHENA) heat pipe model of Ransom and Chow (1987) is a modification of the reactor transient code RELAP–5 (a general purpose thermal hydraulic transient simulation code for two–fluid, two–phase stratified flow systems). In this model, the two–fluid heat pipe formulation is obtained from the one–dimensional area–averaged phasic momentum equations by retaining distinct phasic pressures. Results reported by Ransom and Chow suggest the soundness of their model and the stability of the iterative semi–implicit numerical scheme used. However, to minimize the number of changes to the original solution scheme of RELAP–5, the phasic pressure difference was evaluated explicitly, which led to severe time step restrictions, much less than the Courant–Friedrichs–Lewy (CFL) limit, and resulted in large computational time for each run. The authors pointed out that in the case of liquid flooding, the diphasic interface is flat and the pressure difference between the phases is equal to zero, while this pressure difference is equal to a maximum corresponding to $R_c = R_p$ when the vapor volume fraction exceeds the volume of a hemisphere of radius R_p times the number of pores available at the surface of the wick. These specifications define the variation of the interphase pressure difference in terms of the vapor volume fraction in the heat pipe. However, only the relationship corresponding to normal conditions was considered in the model, so that wick flooding or dryout conditions were not modeled.

Hall (1988) and Hall and co–workers (1990–1994) developed the THROHPUT (Thermal Hydraulic Response Of Heat Pipes Under Transients) code to model the transient behavior of a circular lithium heat pipe during startup from a frozen state and operational shutdowns. Their model predicted the solid, liquid and vapor volume fractions along the heat pipe, so that liquid pooling and recess were modeled. The THROHPUT code predicts the evaporation, condensation and resolidification rates using the kinetic theory equation proposed by Collier (1981). However, the two–dimensional conservation equations were averaged over the radial direction, yielding a one–dimensional axial model. The important radial effects and interphase transfer terms were treated in separate lumped submodels. Melting and freezing processes were modeled with a discontinuous heat flux at the liquid–solid boundaries. Hall and co–workers assumed that the phases existed in radial layers in order to simplify the radial submodel. Four specific configurations were considered: cold state (all solid), startup or melting (wall–liquid–solid), normal operation (all liquid), and shutdown or freezing (wall–solid–liquid). The governing equations were discretized on a staggered grid and linearized using an implicit Taylor series expansion about the old time step. Because the model of Hall is basically one–dimensional, it was possible to solve the linearized coupled finite–difference equations directly, using specialized block–diagonal

matrix inversion methods. Hall and Doster (1988) attempted to simulate a Los Alamos experiment (Merrigan et al. 1986) of the frozen startup of a 4 m–long lithium heat pipe. In order to simulate the first 50 seconds of the thaw transient the authors needed 5 hours of CPU time on a VAX 11/750. In further developments, Hall and Doster (1989, 1990) used the Dusty Gas Model of Cunningham and Williams to treat free–molecule and transition flow regimes as well as continuum flow regime in the vapor core. Also, they incorporated an axial melt front submodel in THROHPUT. Hall (1988) and Hall and Doster (1989, 1990) showed that using multiple passes (updating the Jacobian at each pass) to update the highly nonlinear equations (particularly the gas mixture state equation and the capillary pressure relationship) reduced the linearization errors, which had limited the time step size. With this new numerical approach, a 2–hour–long transient was simulated using approximately 24 hours of CPU time on a VAX 8600.

In some stages of the THROHPUT calculations, it was found that there was not enough total vapor pressure to support the capillary pressure difference. In early versions of the code, this was viewed as a shortcoming, and Hall forced the liquid pressure equal to zero to prevent any negative liquid pressure in the wick. However, when adjacent liquid nodes showed the same condition, there was no pressure difference between them, resulting in no axial liquid flow. To remedy this problem, Hall and Doster (1989, 1990) assumed that some of the capillary pressure was directed axially when there was a difference in liquid volume fraction between two nodes. This treatment caused their model to predict dryout of the evaporator when this did not occur experimentally for the same conditions. In an attempt to resolve this problem and reproduce the experimental results, Hall and co–workers (Hall 1988; and Hall and Doster 1990) varied the values of the evaporation and condensation accommodation coefficients used in the calculation. The code could satisfy each of several experimental criteria separately by adjusting these coefficients, but no pair of coefficients could meet all of the requirements simultaneously. In a recent paper, Hall et al. (1994) performed in–depth literature reviews of experimental measurements of evaporation / condensation accommodation coefficients and of the possibility of tension in the liquid phase. They found that values of the accommodation coefficients close to unity could be measured for both liquid–metal and non–liquid metal working fluids when care was taken in the experiments to avoid surface contamination, the presence of non–condensable gas, and other forms of experimental errors. Furthermore, Hall et al. (1994) found several references which described the effect of tension in the liquid (that is, the possibility of negative liquid pressure) and validated its physical existence. In the later version of the THROHPUT code, Hall et al. (1994) allowed negative liquid pressure in the

wick and used unity accommodation coefficients to calculate the evaporation, condensation and resolidification rates. With these modifications, the model results were greatly improved and agreed reasonably well with the experimental data of Merigan et al. (1986) for the frozen startup of a lithium heat pipe.

Seo and El–Genk (1989) at the University of New Mexico developed a transient model for simulating the operation of fully–thawed liquid–metal heat pipes. They assumed the liquid flow in the wick region to be two–dimensional, transient, incompressible and laminar. However, a quasi–steady state, compressible one–dimensional approximation was used to simulate the vapor flow. Seo and El–Genk used the laminar two–dimensional Navier–Stokes equations and retained only these terms that could be discretized using the axial variables of the vapor. While the authors recognized the limitations of such an approach, their goal was to design a fast running heat pipe code for incorporation in the Space Nuclear Power System Analysis Model (SNPSAM), of SP–100 space nuclear power system (Seo 1988). Seo and El–Genk used the geometric Pascal relationship to explicitly satisfy the interfacial local force balance, and the capillary limit was detected when the effective radius of curvature of the liquid meniscus in the wick became equal to the geometrical pore radius. The equations were discretized implicitly using a conventional finite difference method, and an iterative solution scheme was used to resolve the interfacial couplings. To verify the model predictions, results were compared with the experimental data of Merrigan et al. (1986) for a 4 m–long cylindrical lithium heat pipe. During normal operation, a high–frequency RF coil heated the evaporator section, while the condenser section was cooled radiatively. After shutdown, both the evaporator and condenser sections were radiatively cooled. The model prediction of the wall temperature distribution after shutdown before the working fluid reached its freezing point agreed well with the experimental results, except at the end of the condenser region. It was found experimentally that during normal operation, excess working fluid pooled into the vapor core and filled approximately the last 50 cm of the condenser, causing higher measured temperatures at this end of the heat pipe. It is not clear how pooling effects were treated in the model.

Although Ransom and Chow (1987) and Seo and El–Genk (1989) incorporated the effects of liquid flow, interfacial hydrodynamic coupling and thermal expansion, their models lacked the capability of predicting liquid pooling at the end of the condenser. Also, these investigators did not model the phase–change of working fluid in the wick during the startup from a frozen state, nor the free–molecule and transition vapor flow regimes.

THROHPUT (Hall and co–workers 1988–1994) is one of the most comprehensive heat pipe models to date. It is the only model with provisions for predicting liquid recess, partial dryout and resaturation of wick, and pooling of excess liquid in the vapor core. However, THROHPUT has certain drawbacks. Because this model is basically one–dimensional, it does not deal with freezing and melting of the working fluid mechanistically, hence, its predictions during startup and shutdown transients are only approximate. Furthermore, because heat transfer through the metallic matrix of the wick was not modeled separately, THROHPUT cannot be used to predict the startup of low–temperature heat pipes from a frozen state.

In conclusion, to the best of our knowledge, there has not been a detailed, accurate and efficient transient analysis model for the startup of heat pipes from a frozen state. Some of the processes characteristics of the startup of heat pipes from a frozen state, such as the redistribution of working fluid by sublimation and resolidification, liquid flow and liquid recess in the wick, partial dryout and resaturation of wick, and pooling of excess liquid, have not been considered or been seriously investigated by the scientific community. Furthermore, due to the complexity and nonlinearity of the thaw process of a heat pipe, an analytical solution is unattainable and the numerical solution could be rather involved and CPU time consuming. For example, Jang et al. (1990a) modeled the phase–change of the working fluid using the fixed–grid heat capacity method. Because this method is only applicable to a special case of the general form of the energy equation, it is prone to numerical instabilities and inaccurately calculates the melting front location and the temperature profiles in the solid and liquid regions. Cao and Faghri (1993a, 1993b) used a fixed–grid temperature transforming method to predict the freezing and melting of working fluid in the wick (Cao and Faghri 1990b). Their numerical scheme, however, required strong under–relaxation of the temperature and a large computation time when the mushy cell temperature range (δT) was small. Also, because of the sharp thermal conductivity jump at the liquid–solid interface, their model predicted wiggly temperature time histories.

1.2. OBJECTIVES

The objectives of this work are to develop and validate a two–dimensional, transient heat pipe model, and to devise a stable and efficient solution technique for simulating the transient operation of liquid–metal and non–liquid metal heat pipes. The model must be capable of simulating the startup of wick–type heat pipes from fully–thawed or frozen conditions. The heat pipe wick could be an annular wire–screened mesh, or an isotropic

porous medium such as a powder or a bed of spheres. In addition to simulating the melting and/or freezing processes of the working fluid, the model must include liquid flow in the porous wick and hydrodynamic coupling of the liquid and vapor phases in order to predict the operation limits of the heat pipe, such as capillary limit and liquid recess (dryout) in the evaporator wick, and the pooling of excess liquid in the vapor core. Of special interest is to quantify the importance of sublimation and resolidification processes during the startup of low–temperature heat pipes from a frozen state. These processes can cause significant redistribution of the working fluid in the wick and the occurrence of early dryout of the evaporator wick.

Because of the physical complexity of the problem, an advanced numerical method is required. Another objective of this work is to develop a stable, accurate and efficient solution technique in terms of computation time. Also, efficient linear–system solvers must be devised to solve the five–point linear equations resulting from the discretization of the energy, mass and momentum balance equations. These solvers must be optimized in terms of computation time and memory storage requirement.

The last (but not least) objective is to verify the soundness and accuracy of the physical and numerical schemes using available analytical and experimental data. Of particular importance are the validations of the freeze–and–thaw model and of the modeling of heat and mass transfers in the porous wick. Finally, the heat pipe model will be validated using transient experimental data of a fully–thawed water heat pipe constructed at the Institute for Space and Nuclear Power Studies (El–Genk and Huang 1993).

The statement of objectives is followed by a quick description of the following chapters.

The physical models and the governing equations of the problem in HPTAM are described in Chapter 3. HPTAM can handle both rectangular (symmetric and non–symmetric slabs) and cylindrical geometries. The model divides the heat pipe into three transverse regions: wall, liquid/wick, and vapor regions, and solves the complete form of governing equations in these regions, together with the mass, momentum (capillary relationship of Pascal) and energy jump conditions at the liquid–vapor (L–V) interface. The calculated quantities are the wall temperature, temperatures in the solid, liquid and vapor phases, pressures and mass fluxes in the liquid and vapor phases, the radius of curvature of the liquid meniscus at the L–V interface, and the radial location of the working fluid level (liquid or solid) in the wick. To predict the flow of liquid in the porous wick of the heat pipe, HPTAM uses the

Brinkman–Forchheimer–extended Darcy flow model (Section 3.1), while the volume–averaged homogeneous enthalpy model is used to model the heat transfer. Evaporation, condensation, sublimation and resolidification rates are calculated in terms of interfacial pressures and temperatures from the kinetic theory relationship with an accommodation coefficient of unity. HPTAM incorporates several working fluids such as lithium, sodium, potassium and water, as well as various wall materials (tungsten, niobium, zirconium, stainless–steel and copper).

The model handles the phase–change of working fluid in the wick using a modified fixed–grid homogeneous enthalpy method, as described in Section 3.2. The technique employs a mushy–cell temperature range as small as 2×10^{-8} K (limited by machine accuracy only), without requiring under–relaxation of the temperatures and generating numerical instabilities. The simple method, based on the frozen fraction, developed to calculate the heat fluxes at the boundaries of the mushy cell, improves accuracy and reduces oscillations in temperature time histories by one–to–two orders of magnitude. Section 3.3 describes the liquid pooling submodel, which simulates accumulation of the excess liquid in the vapor core at the condenser end due to thermal expansion of the liquid during heatup.

When modeling the transient operation of low–temperature heat pipes, the vapor is always in the continuum flow regime. In such case, HPTAM solves the two–dimensional Navier–Stokes flow equations in the vapor and obtains the vapor temperature from the saturation state. However, when dealing with high–temperature heat pipes operating at low temperatures, free–molecule and transition vapor flow regimes may occur in the heat pipe. Therefore, HPTAM uses the 1–D Dusty Gas Model in the vapor to model the transient operation of liquid–metal heat pipes (Section 3.4).

Because of the physical complexity of the problem, advanced numerical methods are required. Chapter 4 compares several different segregated solution techniques, one based on the non–iterative Pressure Implicit Splitting Operator (PISO) of Issa (1986), another of the SIMPLEC segregated iterative type, in terms of their effectiveness in reducing the CPU time while maintaining the accuracy of results. Also, various linear–system solvers are tested to determine which one is most efficient.

The development of this comprehensive model has been guided by continuous benchmarking of the model predictions with available experimental and numerical results. The accuracy of the physical and numerical schemes for modeling heat and mass transfers

in the wick is checked in Chapter 5, using various benchmark problems, namely the problems of natural convection of liquid in a square cavity (Section 5.1), natural convection of molten gallium in a porous bed of glass beads (Section 5.2), the one–dimensional pure conduction solidification problem (Section 5.3), the two–dimensional pure conduction problem of freezing in a corner (Section 5.4), and the freezing of tin in a rectangular cavity in the presence of natural convection (Section 5.5).

Numerical results of the frozen startup of a radiatively–cooled water heat pipe are presented in Chapter 6. These results demonstrate the soudness of the physical model and numerical approach used in HPTAM, and illustrate the effects of resolidification and sublimation, and combined phase–change and liquid hydrodynamics in the wick on the startup of low–temperature heat pipes.

In Chapter 7, the heat pipe model is validated using transient experimental data of a fully–thawed water heat pipe constructed at the Institute for Space and Nuclear Power Studies (El–Genk and Huang 1993). Results illustrate the effect of the hydrodynamic coupling of the vapor and liquid phases and the appearance during the heatup transient (disappearance during cooldown) of a pool of excess liquid at the condenser end. The effects of input power and initial liquid inventory on the location of the wet point and liquid pooling effects, and on the vapor and liquid pressure and temperature distributions are illustrated in Chapter 8.

Chapter 9 presents steady–state results of a lithium heat pipe operating at a temperature level of 1250 K and a power throughput of 6.5 kWt. Results show that high evaporation and condensation rates can generate significant recovery of vapor pressure and non–negligible viscous dissipation rates in the vapor space.

Finally, summary and conclusions of this study are presented in Chapter 10, along with some recommendations for future numerical and experimental work (Chapter 11).

The next chapter reviews important background information on the startup of heat pipes from a frozen state, the transient operation of fully–thawed heat pipes and operation limits, and discusses in detail the previous heat pipe modeling efforts and related experimental work.

2. BACKGROUND

Heat pipes are highly reliable and efficient energy transport devices. They have no moving parts and can operate passively under vacuum and zero–gravity environments. Heat pipes can transport relatively large amounts of thermal energy over a significant distance with a small temperature drop between the heat source and the heat sink. Energy transport is achieved by means of the evaporation of a liquid working fluid at the heat source (evaporator section) and condensation of the vapor produced at the heat sink (condenser section). Capillary forces developed in a porous structure (or wick) return the liquid condensate back to the evaporator section.

Thermosyphons are the ancestor of heat pipes and have been used for the first time by Perkins in 1897. They are wickless heat pipes which rely on gravitational pull to return the liquid from the condenser to the evaporator. In 1942 Gaugler invented a heat pipe that worked in a similar manner to Perkin's device, but with a wick structure. In 1963, Grover and co–workers at the Los Alamos Scientific Laboratory began serious research on heat pipes. Since 1963, research on heat pipes has grown steadily all over the world.

The next section describes the principle of heat pipe operation in more details. Considerations for selection of the working fluid for a given temperature range of operation are given, based on the fluid properties and operation limits of the heat pipe. Section 2.2 describes the startup from a frozen state of low–temperature and high–temperature heat pipes. Finally, Sections 2.3 and 2.4 review in details the previous heat pipe modeling and experimental efforts.

2.1. PRINCIPLE OF HEAT PIPE OPERATION AND LIMITS

Figure 2.1 shows a schematic of a conventional circular heat pipe. The heat pipe consists of a metallic pipe or tube, which serves as a container, closed at both ends. The liquid phase of the working fluid is confined to a thin capillary structure, a homogeneous porous medium or a wire–screened wick. The center of the pipe is occupied by the vapor phase of the working fluid. The heated portion of the heat pipe is called the "evaporator," and the cooled section, usually located at the opposite end of the heat pipe, is called the "condenser". The evaporator and condenser can be separated by a thermally insulated

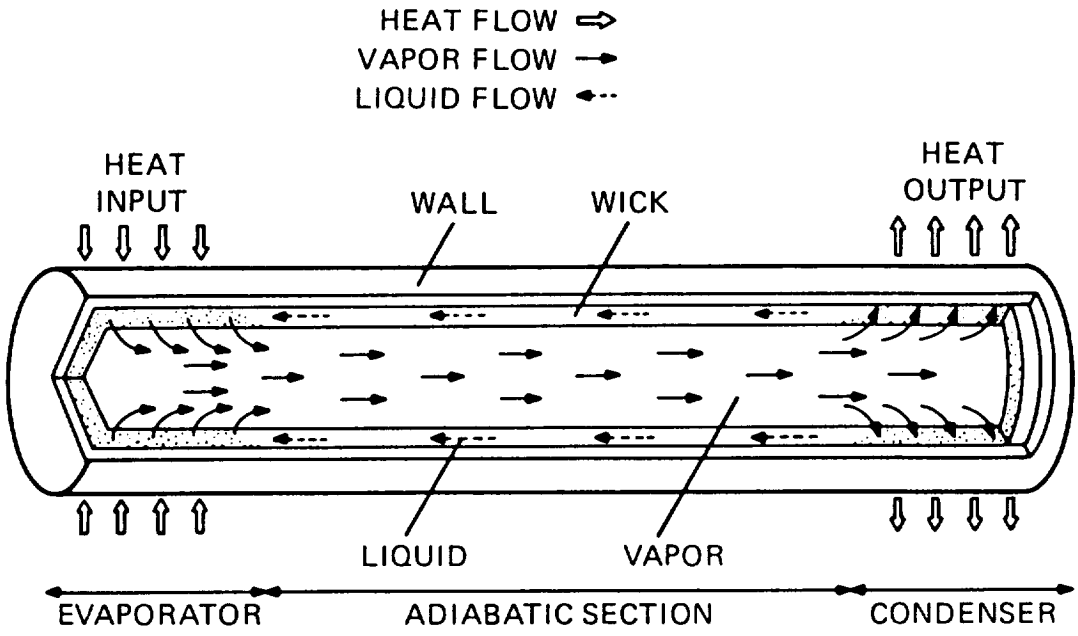

FIGURE 2.1. Illustration and Principle of Operation of a Conventional Heat Pipe.

("adiabatic") section. Heat added to the evaporator section is conducted radially through the pipe wall and the wick, and evaporates the liquid. The vapor pressure in the evaporator of the heat pipe is higher than that in the condenser, forcing the vapor to flow from the evaporator to the condenser, where it condenses. The liquid condensate returns to the evaporator by capillary effect. The radius of curvature of the liquid meniscus in the wick structure of the evaporator is lower than that in the condenser. This difference in these radii creates the capillary force that returns the liquid from the condenser to the evaporator through the wick structure.

Heat pipes can operate over a broad range of temperatures, by selecting appropriate working fluids. The best choices of wick geometry and working fluid are that which maximize the various operation limits of the heat pipe over the temperature range of interest, and minimize the mass of the system. This last criteria is of particular importance for space applications, because of today's prohibitive launch cost of space systems per unit of mass. The heat pipe operation limits are: the viscous limit, the sonic limit, the capillary limit, the entrainment limit, and the boiling limit. These limits are illustrated in Figure 2.2.

The viscous limit arises at low temperature with working fluids of very low vapor pressure. Such fluids are usually frozen at room temperature, for example lithium and sodium. The viscous limit occurs when the vapor pressure of the working fluid is too low

to counter the pressure losses in the vapor along the heat pipe. The sonic limit arises when the vapor velocity reaches the sonic velocity at the exit of the evaporator section. In such case, the maximum (sonic limited) power throughput transported by the vapor is proportional to the vapor cross–sectional flow area and to the vapor pressure of the fluid, and is inversely proportional to the square root of the vapor temperature. When the vapor flow is maximum, or choked, changes in the condenser heat rejection rate cannot be transmitted upstream to the evaporator section. This means that further reduction in the condenser temperature or pressure will not increase the vapor flow rate, but will cause the vapor velocity to become supersonic in the condenser section, often exhibiting pressure recovery in the form of a shock front. Therefore, sonic limited heat pipes are characterized by very large axial temperature gradients.

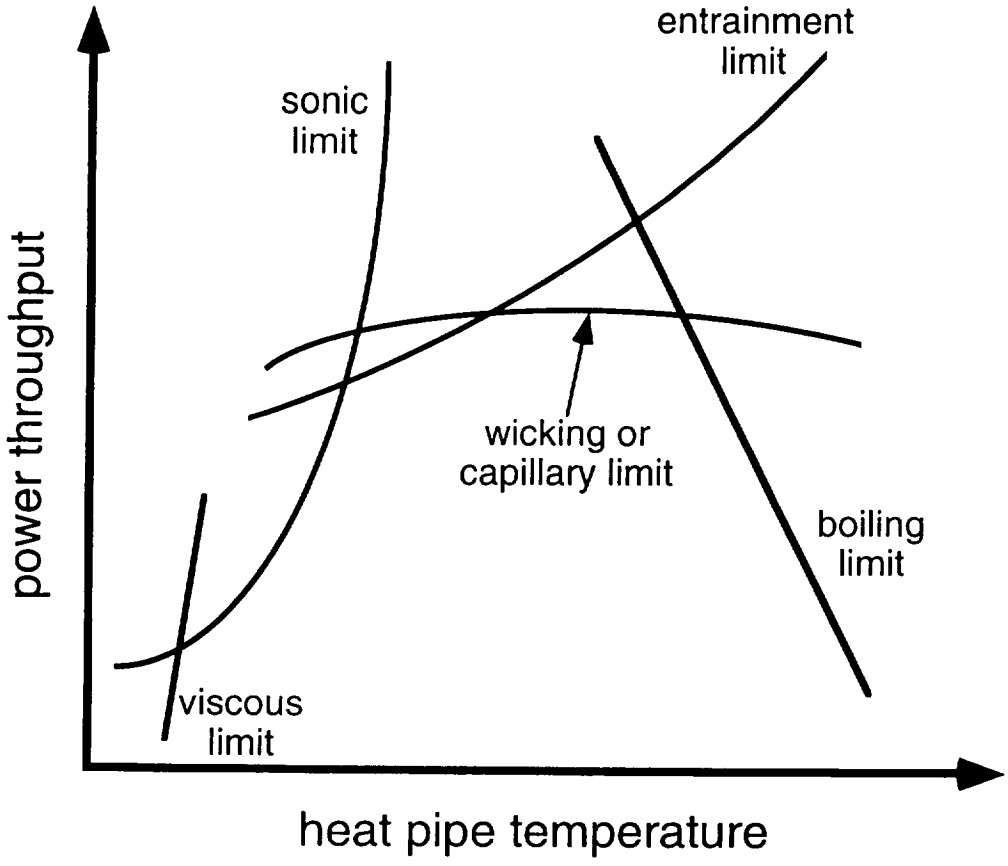

FIGURE 2.2. Operation Limits of a Heat Pipe.

Clearly, both the viscous and sonic limits are strong increasing functions of the vapor temperature, and can be enhanced by increasing the vapor flow area or reducing the vapor velocity. Therefore, an adequate working fluid is one which has a suitable vapor pressure level over the operation temperature range of interest. Too low a vapor pressure would cause the heat pipe to be viscous or sonic limited. Figure 2.3 shows the vapor pressure of a number of working fluids as a function of temperature. In the 800 K–1000 K temperature range, for example, the vapor pressure of potassium varies between 7 and 80 kPa, while that of sodium ranges between 1 and 18 kPa; the vapor pressure of lithium is below 100 Pa in this temperature range. While the choice of potassium will result in a 20 kWt sonic limit in a pipe with a diameter of 3 cm, the sonic limit for sodium will be 4 kWt while that for lithium will be as low as 400 Wt (at the lower end of the temperature range, 800 K).

When selecting the working fluid, care must also be taken that the vapor pressure of the fluid is not too high (that is, less than a few bars). Too high a vapor pressure would cause the heat pipe to be limited by the boiling limit in the wick, or to be blocked by the approach of the critical point, and could cause mechanical rupture of the heat pipe container. In the 800 K–1000 K temperature range, the vapor pressure of potassium and sodium is less than 1 bar (10^5 Pa), and boiling limit and mechanical resistance of the container are not a concern at this low pressure level. As an illustration, a 0.3–mm thick nickel tube of radius 2 cm could withstand a radial pressure differential of 10 bars.

The capillary (or wicking) operation limit of the heat pipe arises when the maximum capillary pressure capability of the porous wick cannot overcome the combined liquid and vapor pressure losses along the heat pipe. The capillary pressure head is proportional to the surface tension of the liquid and inversely proportional to the minimum radius of curvature of the liquid meniscus in the wick. The maximum capillary pressure head arises when the radius of curvature of the liquid meniscus equals the effective pore size of the wick structure. To pursue the selection of working fluid further, one can use the figure of merit. The latter is defined as the product of surface tension, liquid density and latent heat of vaporization, divided by the dynamic viscosity of the liquid phase, and is shown in Figure 2.4 as a function of temperature for several working fluids. Clearly, it is preferable to use the working fluid which exhibits the highest figure of merit. The higher the liquid transport capability (the product of liquid density and latent heat of vaporization) the slower the liquid flow in the wick, the lower the liquid viscosity the smaller the liquid pressure

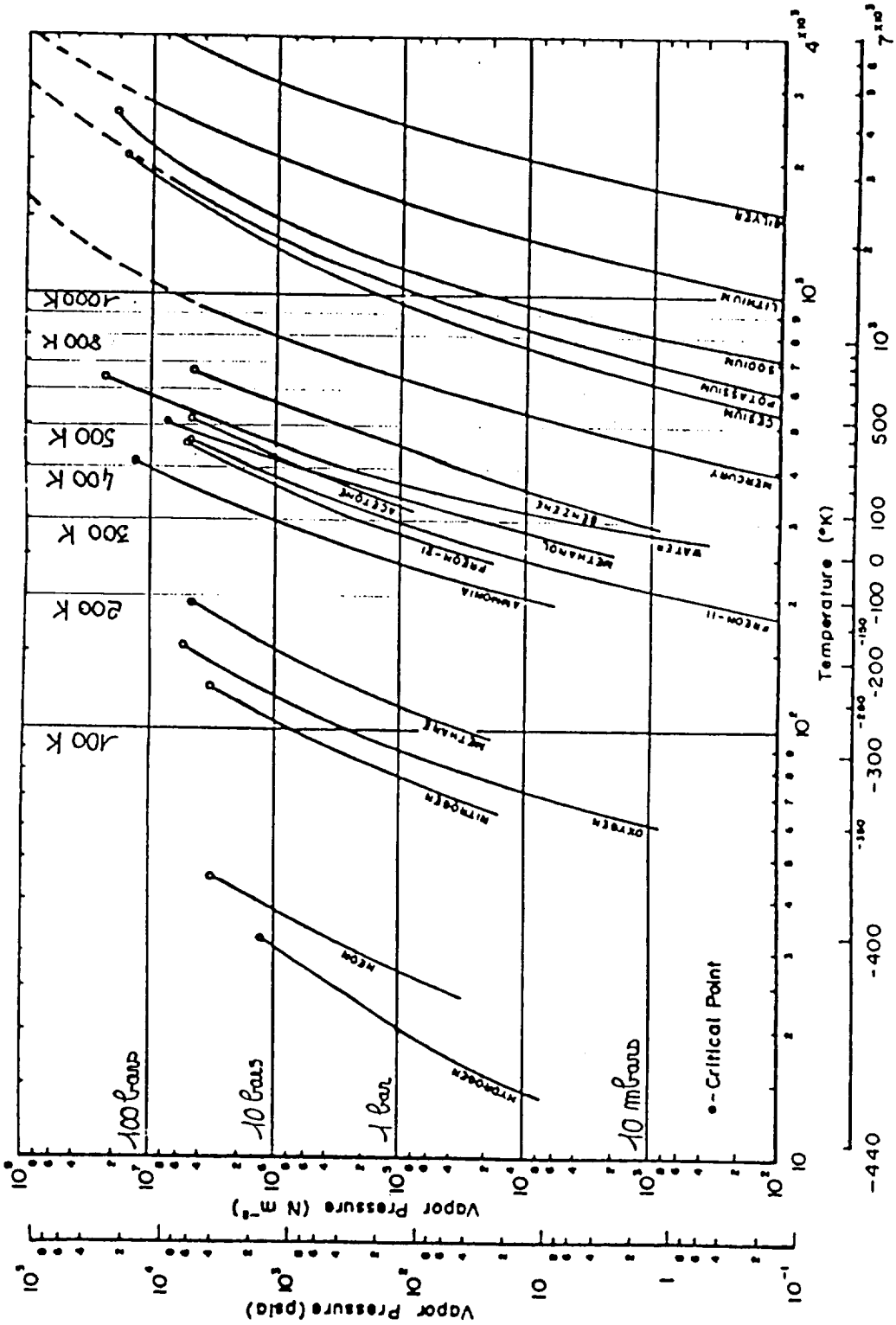

FIGURE 2.3. Vapor Pressure of Some Heat Pipe Working Fluids.

losses. Finally, the higher the surface tension of the liquid the larger the capillary pressurehead, and all these factors contribute to a larger capillary operation limit. In the 800 K to 1000 K temperature range, for example, potassium and sodium working fluids are much preferable than cesium. As shown in Figure 2.4, cesium has a much lower figure of merit than sodium and potassium. Also, the vapor pressure of cesium is larger, which leads to a lower boiling limit.

Note that the figure of merit chart must be used carefully. While it combines several desirable properties which characterize the liquid transport capability and the capillary limit, it does not provide any information concerning the viscous and sonic operation limits of the heat pipe. For example, sodium has a figure of merit as much as twice that of potassium, while the figure of merit of lithium beats that of sodium by one order of magnitude. This is because lithium working fluid has very high latent heat of vaporization and surface tension. However, sodium and potassium are preferred working fluids in the temperature range of 800 K–1000 K, because of their much larger vapor pressures than lithium at these temperatures. The fact that lithium has such a high figure of merit makes it the best choice of working fluids at higher temperatures (1100 K–1700 K), where its vapor pressure is higher. Above 1700 K, silver would be preferable, as apparent in Figures 2.3 and 2.4.

The last operation limit of the heat pipe is the entrainment limit. This limit arises when the shear stress exerted by the vapor at the liquid–vapor interface in the wick overcomes the liquid surface tension forces. As a result, the vapor carries away liquid droplets back to the condenser, thus preventing the liquid from replenishing the evaporator wick. Entrainment arises in the presence of very high and supersonic vapor velocities which occur usually in sonic limited heat pipes, and depends strongly on the geometry of the separative interface between the liquid and vapor phases.

There exists a number of heat pipe wick geometries, and only the most popular are reviewed in this section. The most common type of wick is the homogeneous wick, which is made of a wrapped wire–screened mesh or a ceramic or metallic powder. Heat pipes with homogeneous wicks are easily constructed. The main limitation of such wicks is to introduce large liquid pressure losses, as the liquid must flow through a tight low–porosity structure. The capillary limit can be enhanced by increasing the capillary pressure capability of the wick. This is achieved by reducing the effective pore size of the wick structure, till an optimum value of the capillary limit is reached, due to the associated

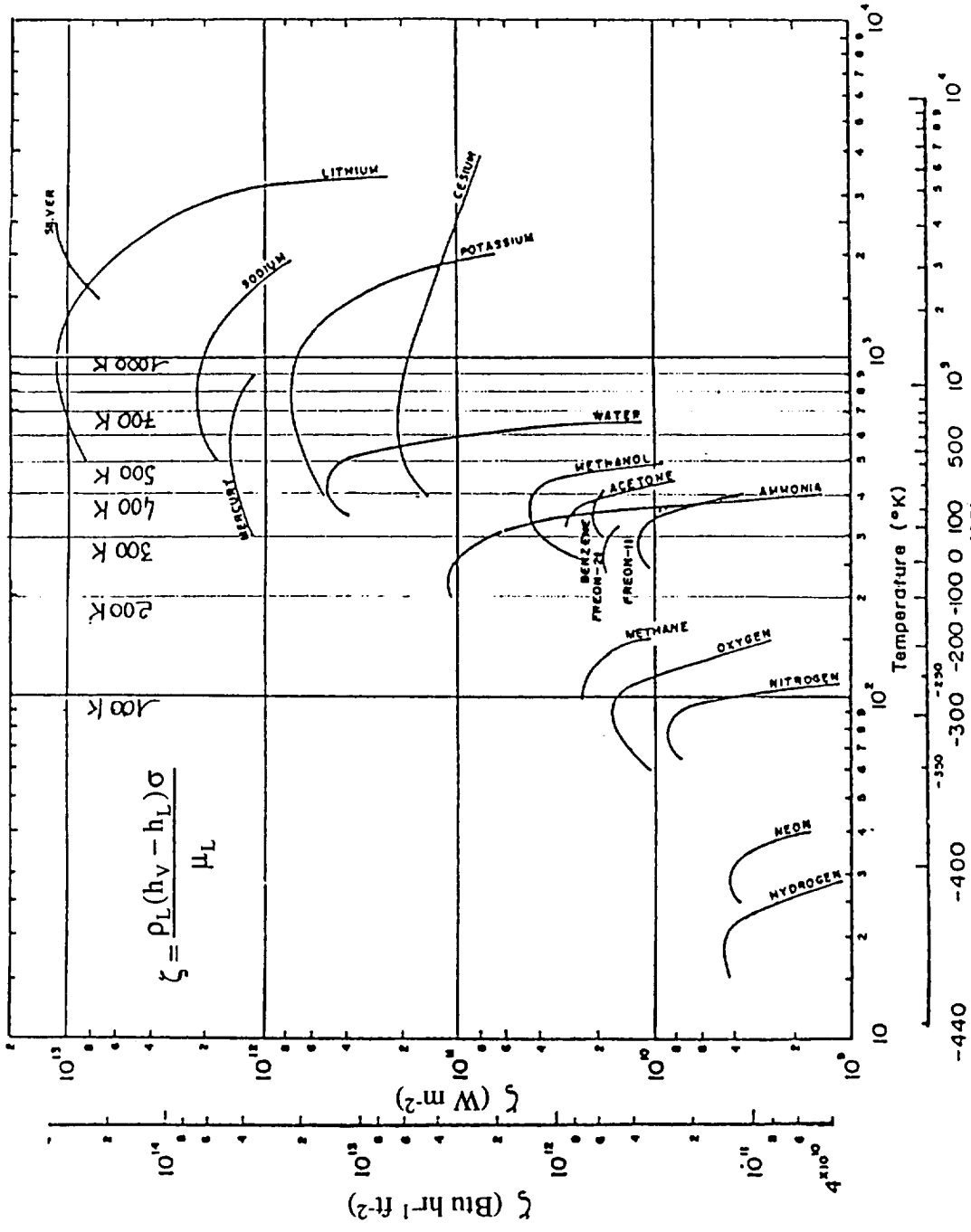

FIGURE 2.4. Figure of Merit of Some Heat Pipe Working Fluids.

decrease in the wick permeability (that is, increased liquid flow resistance through the wick). A possible solution to this geometrical limitation is to increase the effective liquid flow cross–sectional area by adding longitudinal grooves in the pipe wall.

Pipe–grooving is the only manufacturing technique characterized by a high mass–production at low cost. In the case of a simple grooved heat pipe, performance is quite sensitive to the groove geometry. Grooves must be deep enough to insure suitable liquid flow rates, but narrow to provide sufficient capillary driving forces. The entrainment limit is usually low because of the direct contact between the liquid and vapor phases. The performance of the heat pipe can be enhanced by covering the grooves with a metallic wire–screened wick structure.

The combination of grooves and screen wick resolves the limitations associated with both wick designs considered separately. The existence of grooves significantly reduces the liquid pressure losses associated with the homogeneous wick design, while the presence of the screen wick considerably enhances the poor capillary driving force and low entrainment limit characteristics of the bare grooved heat pipe. In such a configuration, the role of the grooves is essentially to reduce the liquid pressure losses by increasing the liquid flow cross–sectional area. This area is maximized when the longitudinal grooves are connected together, which results in a small annular spacing between the pipe container and the wick structure. However, this solution is only applicable to heat pipes which utilize liquid–metal working fluids. Non–liquid metal fluids have too low a thermal conductivity and nucleate boiling may develop in the annular spacing, blocking the operation of heat pipe.

Another important configuration is that of heat pipes using arteries in the vapor space. While the use of arteries greatly increases the complexity of the design and the fabrication cost, it has the potential of offering very high performances. The function of the artery, which has become a popular feature of heat pipes considered for space applications, is to provide a low pressure–drop path for circulating the liquid from the condenser to the evaporator section, where it is redistributed in a thin layer through the circumferential wick. This last characteristic has the additional effect of enhancing the boiling limit. Also entrainment effects are reduced because of the partial separation of liquid and vapor flows. However, arteries may fail to operate when filled with vapor, a phenomena referred to as depriming. To remedy this problem, several arteries (3 to 4) are usually introduced in the heat pipe for redundancy, reducing the vapor flow cross–sectional area and increasing the

vapor velocity. This has the detrimental effect of reducing the sonic limit, as well as the entrainment limit in some cases.

After the working fluid and wick geometry have been selected for the application of interest, the structural material for the container and the wick structure must be chosen. The role of the container is to isolate the working fluid from the environment and maintain the pressure differential across the wall. The material selected for the wick should have preferably high thermal conductivity and strength–to–weight ratio in order to minimize the radial thermal resistance and mass of the system. Also, the wick material must have good compatibility and wettability properties with the working fluid, and should be easy and cheap to fabricate. Compatibility is an important issue in heat pipes design, since no chemical reaction can be tolerated between the working fluid and the structural material of the heat pipe. This is particularly important considering that the working fluid in a heat pipe is in a diphasic form and always very pure, an environment which greatly enhances corrosion reactions. Non–condensable gases which may be generated, even in small quantity, could significantly reduce the heat pipe performance, and possibly lead to its complete blockage.

The performance of a heat pipe depends not only on the type of wick and working fluid used, but also to a great extent on the thermal external conditions imposed upon it, particularly during the startup. When the capillary limit, the entrainment limit, or the boiling limit is encountered, the wick structure in the evaporator dries out, leading to operation failure of the heat pipe. In addition to these limitations, startup difficulties may occur at low temperature when the heat pipe working fluid is frozen.

2.2. STARTUP OF HEAT PIPES FROM A FROZEN STATE

The startup of high–temperature (liquid–metal) heat pipes from a frozen state differs significantly from that of low–temperature heat pipes, due to differences in the vapor pressure of the working fluid near the melting point. In low–temperature heat pipes, the vapor pressure is large enough to avoid the viscous and sonic limits and allow significant migration of the working fluid to colder regions in the heat pipe. Once the solid working fluid is melted in the evaporator, dryout may occur due to immediate vaporization of the fluid.

The startup process of a low–temperature heat pipe may be divided into several successive steps (Figure 2.5). Initially, the working fluid in the wick is frozen. As thermal power is applied to the evaporator section, the frozen working fluid sublimates and transports as a continuum flow to the condenser where it resolidifies (Figure 2.5a). This sublimation / resolidification process depletes the frozen working fluid in the evaporator and accumulates it in the condenser (Figure 2.5b). As the wall temperature continues to increase, the working fluid at the evaporator wall begins to melt (Figure 2.5c). The melting front progresses radially and axially with time. As the melting front reaches the liquid–vapor (L–V) interface (Figure 2.5d), the following processes take place:

(a) evaporation depletes working fluid in the evaporator and could cause the wick to dryout. In cases where the density of the working fluid decreases upon melting, potential dryout of the wick decreases, and vice versa.

(b) a thin liquid film of vapor condensate forms on a frozen substrate in the condenser. The drainage of the film back to the evaporator, which is governed by the capillary effect and frictional drag at the film–solid interface, could prevent or postpone dryout (Figure 2.5d).

In addition to the two–dimensional progression of the melt front toward the condenser, melting may also occur in the condenser and adiabatic sections at the liquid film/solid interface and proceeds radially outward. Eventually, the heat pipe becomes fully–thawed and liquid circulation in the wick is established (Figure 2.5e).

Because of the relatively high vapor pressure of low–temperature working fluids, even near the melting temperature, choked and/or supersonic vapor flows are not encountered during the startup.

In the case of high–temperature working fluids, however, the vapor flow in the heat pipe remains in the free–molecule and transition vapor flow regimes for temperatures well above the melting temperature. This has the beneficial effects of limiting migration of the solid working fluid to the condenser (by sublimation and resolidification), and allowing for melting the working fluid by conduction heat transfer before large scale evaporation of the liquid occurs. However, the startup of high–temperature heat pipes generally involves very high vapor velocities. In most cases, the sonic limit is reached and supersonic velocities exist along the condenser, which could cause entrainment of liquid droplets and prevent the liquid from returning to the evaporator. A typical liquid–metal heat pipe has a

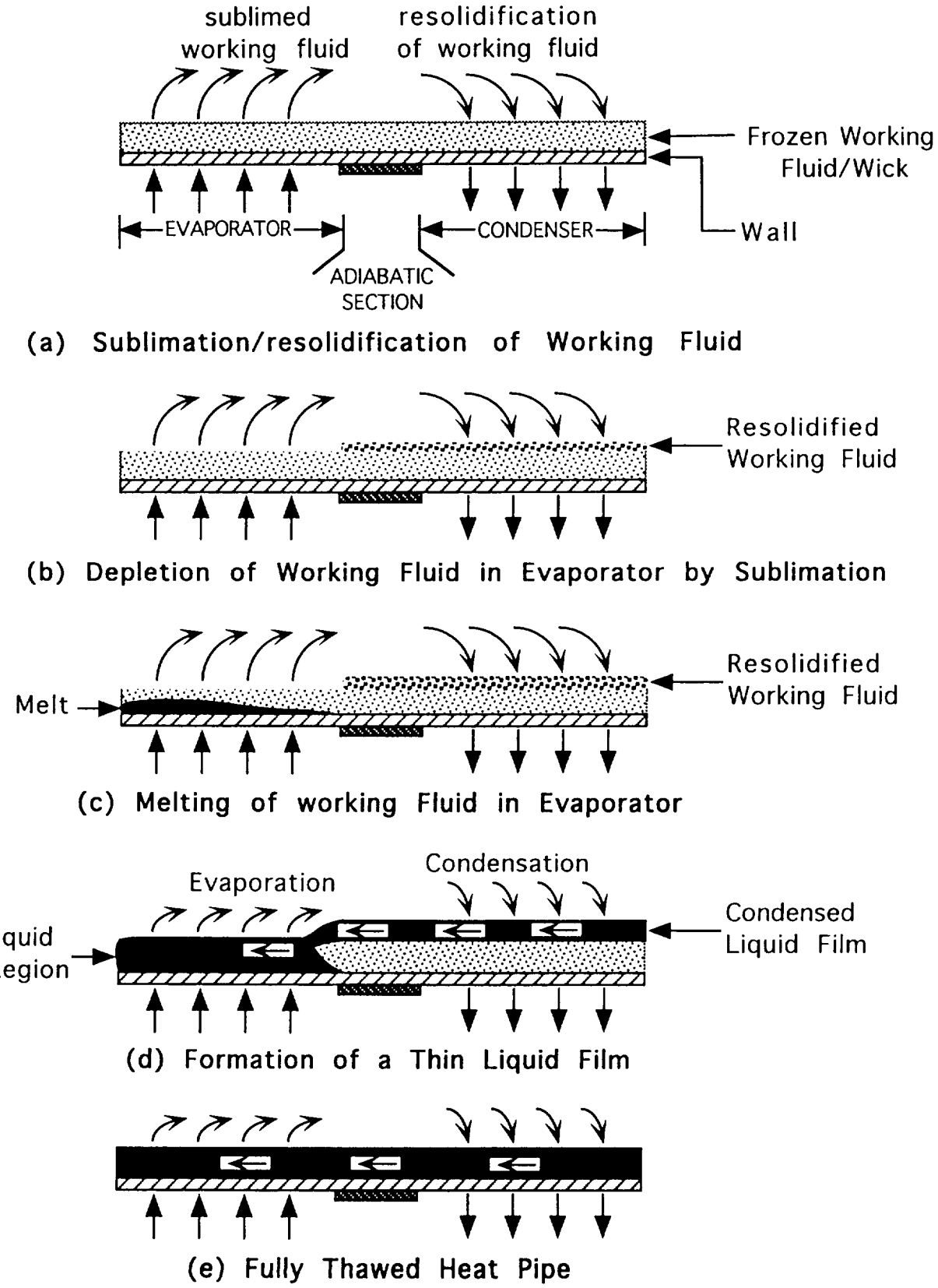

FIGURE 2.5. Progression of the Frozen Startup of a Low–Temperature Heat Pipe.

sonic limit of several kilowatts at high operating temperature, but of only a fraction of a watt at room temperature. Therefore, the heat pipe operation must pass through a region of very low heat transfer rates (to the condenser) during the startup.

One way of achieving a successful startup of high–temperature heat pipes would be to subject the evaporator to a very small input power, progressively increased as the temperature of the heat pipe rises, to avoid reaching the viscous or sonic limit at any time. However, such startup scenario would probably take several hours (if not days) before the operating temperature would be reached. In fact, the startup of heat pipes from a frozen state is primarily a function of the heat rejection rate at the condenser. The rejection rate must be low enough to enable the heat transferred by the vapor to melt the working fluid in the condenser section, and to allow the liquid to return to the evaporator before the wick is depleted of working fluid.

Three types of startup failures of high–temperature heat pipes have been observed experimentally (Deverall et al. 1970), all related to the sonic limit. When the temperature is low and the condenser heat rejection rate is high, very low vapor densities in the heat pipe result in choked vapor flow and limited heat transfer to the condenser section. The first type of startup failure occurs when relatively high heat rejection rates are applied to the condenser. In this case, the limited heat transfer rate is not sufficient to raise the condenser temperature above the fusion temperature of the working fluid, and the vapor freezes out in the condenser wick. The evaporator eventually dries out, since the working fluid cannot return from the frozen condenser. Dryout of the evaporator wick is followed by a local rise in temperature which eventually damages the heat pipe.

The second type of startup failure of high–temperature heat pipes occurs at moderate condenser heat rejection rates. Further increases in the evaporator input power or temperature cannot raise the temperature of the condenser (due to the sonic limited heat transfer rate), but generate very high (supersonic) vapor velocities along the condenser, which eventually sweep the liquid out of the wick structure (entrainment limit) and cause dryout of the evaporator wick. When the entrainment limit occurs, it is often possible to hear the impingement of liquid droplets on the condenser end cap.

The third type of startup failure arises when moderate heat input and rejection rates are applied to the evaporator and condenser, simultaneously. The low temperature level and moderate heat rejection rate at the condenser result in choked vapor flow. Due to the

limited heat transfer rate, the condenser temperature does not rise, and the vapor pressure remains negligible in that section. A moderate heat input to the evaporator causes the evaporator temperature to rise rapidly, since the heat transfer rate to the condenser is limited by the sonic flow. Eventually the vapor pressure in the evaporator becomes so large that the capillary pumping capability of the wick cannot overcome the pressure losses along the heat pipe, and the flow of liquid returning to the evaporator is not sufficient to prevent dryout of the wick.

Despite the aforementioned difficulties, successful startup of high–temperature heat pipes can be achieved, even when the heat transfer rate to the condenser is choked (sonic limited). If the heat rejection rate at the condenser is low enough, as in the case of a radiative condition for example, the condenser can heat up gradually, with a corresponding increase in vapor density and decrease in the vapor velocity at the evaporator exit, before the entrainment or capillary limit could occur.

This concludes the background information on the startup of heat pipes from a frozen state. The next section gives a detailed account of previous heat pipe modeling efforts reported in the literature.

2.3. LITERATURE REVIEW ON HEAT PIPE MODELING

Because heat pipes are highly reliable and efficient energy transport devices, they have been considered for many terrestrial and space thermal management applications. Such wide interest in heat pipes has stimulated the development of numerous steady–state and transient models. Because the transient operation of heat pipes and the startup of heat pipes from a frozen state involve several highly non–linear and tightly coupled heat and mass transfer processes in the vapor, wick and wall regions, mathematical modeling of these problems is quite complex. To the best of the authors knowledge, no complete treatment of the processes taking place and described earlier (Section 2.2) has been reported. An analytical solution is unattainable, and except when simplifying assumptions are made, the numerical solution could be tedious and require large computation time. This section reviews the previous and major heat pipe modeling efforts in details. These models included a variety of simplifying assumptions in the governing equations, and a spectrum of numerical techniques to solve these equations (Table 1.1). A literature review of heat pipe models developed prior to the year 1988 can be found in the Ph.D. Thesis of Hall (1988), Jang (1988) and Seo (1988).

Heat pipe models can be classified into four categories:

(a) models which simulate the vapor flow region only;

(b) models which simulate vapor, wick and wall regions but ignore the liquid flow in the wick and the momentum coupling at the liquid–vapor (L–V) interface;

(c) liquid/vapor counter–current flow models which neglect the momentum coupling at the L–V interface; and

(d) models which have the capability to predict the radius of curvature of the liquid meniscus at the L–V interface in order to insure proper hydrodynamic coupling of the liquid and vapor phases.

Only a few models, however, attempted to simulate the non–continuum vapor flow regimes occurring in high–temperature heat pipes operating in the low temperature range, and the change of phase of the working fluid in the wick during the startup of heat pipes from a frozen state.

The next subsections describe the heat pipe models of the first group, which have focused on the heat pipe vapor dynamics. In an attempt to describe the operation of heat pipe, Bowman (1987), Bowman and Hitchcock (1988), Klein and Catton (1987) and Issacci et al. (1988, 1990 and 1991) have developed two–dimensional transient models of vapor flow, which decoupled the vapor from the liquid–wick and wall regions, except for a simplified interfacial energy balance.

2.3.1. Vapor Model of Bowman et al. (1987–1988)

Bowman and Hitchcock (1988) studied the vapor flow in the laminar and turbulent regimes. The emphasis was placed on studying highly compressible vapor flow situations, including subsonic and supersonic flow fields with shock waves and flow reversal. Bowman and Hitchcock solved the full unsteady compressible, Reynolds–averaged turbulent Navier–Stokes equations in cylindrical coordinates. The vapor was assumed to behave like a perfect gas. Because the governing equations were solved numerically using the Explicit MacCormack finite difference method, the time step used in the calculations was severely limited by a Courant–Friedrichs–Lewy–type condition, to avoid numerical instabilities. Bowman and Hitchcock (1988) experimentally investigated vapor flow dynamics using isothermal air injection and suction at the walls of a porous pipe made from polyethylene beads. Comparison of the model predictions with experimental data was

good for axial Mach numbers as high as 1.7. Based on this work, Bowman (1987) established functional relationships of the friction coefficient for a simple, steady one–dimensional model for highly compressible and sonic vapor flows. Bowman used the compressible, one–dimensional, adiabatic and steady vapor flow model employing the influence coefficients of Shapiro. As a result of the numerical and experimental studies conducted, expressions for the friction coefficient as functions of the local axial Reynolds number, Mach number, pipe aspect ratio, and radial Reynolds number were developed. These expressions were shown to give excellent results when used in the one–dimensional vapor compressible model and compared with experimental data. Based on experimental measurements, the flow was found to be always laminar in the evaporator section, and fully turbulent in most of the condenser section (for axial Reynolds numbers ranging from 2000 to 10^6).

2.3.2. Vapor Model of Issacci et al. (1988–1991)

Researchers at the University of California Los Angeles (Klein and Catton 1987; Issacci et al. 1988, 1990 and 1991) also studied the heat pipe vapor dynamics, using a two–dimensional approach. They solved the two–dimensional, laminar compressible Navier–Stokes equations in a cylinder or slab. To provide mathematical closure to the system of equations in the vapor region, the input heat flux and the temperature of the outer surface were specified in the evaporator and condenser sections respectively. The evaporation mass flux was estimated by dividing the heat input power by the latent heat of vaporization, and the condensation rate was approximated by equating the heat of condensation to the heat conducted radially across the wick. The interfacial vapor temperature was assumed to be the saturation temperature corresponding to the interfacial vapor pressure. In the early stage of their research, the authors used the SIMPLE method of Patankar (Issacci et al. 1988), upgraded eventually to the SIMPLER algorithm. However, because the SIMPLE–type methods are limited to low–compressibility flows, the authors resorted to using the CONDIF scheme for differentiating the convective terms (Issacci et al. 1990). A Successive Over–Relaxation iterative method was used to solve the different equations, and it was found that the sharp boundary conditions at the evaporator exit and entrance of the condenser were perturbing the numerical scheme. These boundary conditions were smoothed out to solve the problem. However, the numerical scheme was stable only for low heat input fluxes, and the authors considered various filtering techniques. Issacci et al. (1991) showed that a centered–difference scheme, when used with non–linear filtering, yielded a second–order, stable solution and captured shocks without oscillations. This

non–linear filtering technique was used to analyze the startup vapor dynamics of a sodium heat pipe with a high heat input flux. The startup transient involved multiple wave reflections from the line of symmetry in the evaporator section. It is not clear, however, how this code could model free–molecule and/or transition flow conditions that occur during the frozen startup of liquid–metal heat pipes, without any special treatment.

Although the vapor flow models of Bowman and Hitchcock (1988) and Issacci et al. (1988, 1990 and 1991) have provided valuable information on the vapor flow dynamics, they are of limited use for the design and transient analysis of heat pipes, because of the thermal and hydrodynamic decouplings of the vapor from the wick region.

The characteristics of steady–state operation of heat pipe have been extensively studied, both experimentally and theoretically. They include geometrical configurations, materials of construction, heat transfer operation limits and life expectancy (Baker and Tower 1989; and Woloshun et al. 1989). The experimental investigations of Ivanovsky et al. (1982) and Tilton et al. (1986) suggested that during steady–state or slow transients, heat pipe operation can be described solely by vapor dynamics and energy balance in the various heat pipe regions. During normal heat pipe operation, heat is primarily transported radially by conduction through the liquid–saturated wick, while phase change occurs at the L–V interface. Temperature gradients exist at the L–V interface in the evaporator and condenser regions and along the vapor core region, but in most cases they are small enough to be neglected.

Traditionally, the second category regroups heat pipe models that have been developed for design purposes. These models pay attention to only these phenomena that influence the performance of heat pipes. At present there are 4 such models at different stages of development (Tilton 1987; Faghri and Chen 1989; Cao and Faghri 1990; Jang 1988; Jang et al. 1990a; Cao and Faghri 1993a, 1993b, and 1992). The models of this second group ignore liquid flow in the wick as well as the interfacial phenomena such as capillary effect and interfacial momentum exchange. Tilton et al. (1987), Faghri and Chen (1989) and Cao and Faghri (1990) at Wright State University solved the two–dimensional heat conduction equations in the wall and liquid–wick regions, which were thermally coupled to either a one– or two–dimensional vapor flow model.

2.3.3. The Model of Tilton et al. (1986–1987)

Tilton et al. (1986) studied numerically and experimentally the transient response of an Inconel 617 sodium heat pipe subjected to adverse radiative heating of the condenser. The first experiment used a sliding cylindrical shell radiant heater to simulate Laser illumination of the condenser end, while an actual CO_2 Laser was used for the second test. The outer surface temperature of the wall along the pipe was recorded as a function of time. Tilton and co–workers assumed that the effective heat capacity of the cross section of the heat pipe was axially uniform, and they made use of the global energy balance for the heat pipe to calculate the rate of energy storage per unit length, by assuming that the heat pipe responded isothermally at any given time. The heat pipe was divided into axial sections of identical length, and by writing the sectional energy balance (and neglecting liquid and vapor mass accumulation terms) the authors obtained a set of equations that related evaporation/condensation flow rates to the external input/output heat fluxes. The vapor axial flow rate was then obtained from steady–state mass conservation in the vapor core region. The vapor pressure profile was then calculated using the steady one–dimensional momentum balance with frictional and dynamic coefficients for laminar incompressible flows, and the vapor temperature profile was obtained by assuming the vapor state to be saturated. In his thesis, Tilton (1987) improved the heat pipe model by considering radial conduction across the wall and liquid–wick regions. The L–V interfacial temperature was assumed to be equal to the axially uniform vapor core temperature. The radial heat flux at the L–V interface was equated to the phase change rate multiplied by the latent heat of vaporization. Global mass conservation in the vapor core made it possible to calculate the (uniform) vapor temperature through the equation of state. Internal iterations were necessary to resolve the vapor temperature coupling. However, because the energy equations were discretized explicitly, the size of the time step was limited in the calculations to avoid numerical instabilities. Tilton (1987) pointed out that his performance model must be used only for heat pipes operating at high temperature and for low heat input rates and slow transients, under which conditions the vapor axial temperature variation and L–V interfacial resistance can be neglected.

2.3.4. The Model of Faghri et al. (1989–1990)

In their two–dimensional steady–state model, Faghri and Chen (1989) assumed thermodynamic equilibrium at the L–V interface (the interfacial temperature is equal to the vapor saturation temperature) and evaluated the evaporation/condensation rates from the

energy balance at the interface. They used the iterative method developed by Spalding and Rosten (1985) for the generalized PHOENICS code, combined with the SIMPLEST technique to accelerate the convergence of the vapor momentum equations. With this model, Faghri and Chen evaluated the effects of axial conduction, vapor compressibility and viscous dissipation on the operation of water and sodium heat pipes. Cao and Faghri (1990) extended Faghri and Chen's model to perform transient calculations. They used the SIMPLE method, and incorporated the effect of vapor compressibility by treating the vapor pressure as a dependent variable and directly applying the state equation to obtain the density while iterating. These authors simulated the transient operation of sodium heat pipes and demonstrated the ability of their model to handle highly–compressible and supersonic flow conditions in the vapor region. However, they neglected liquid flow in the wick and the hydrodynamic coupling between the liquid and vapor phases. Jang (1988), Jang et al. (1990a) and Cao and Faghri (1993a, 1993b and 1992) also modeled the startup of heat pipes from a frozen state.

2.3.5 The Model of Jang et al. (1988, 1990a)

Jang (1988) developed a pure–conduction transient model for rectangular heat pipe cooled leading edges, and compared its predictions with Camarda's (1977) experimental results. The capillary structure was assumed to be saturated and liquid flow in the capillary structure was neglected. Evaporation and condensation rates were evaluated from the kinetic theory to account for the thermal resistance at the L–V interface. Different startup periods were considered, including free–molecule and continuum vapor flow conditions. During the first period, Jang (1988) obtained the vapor temperature by equating the evaporative heat input to the sonic limited heat transport. When continuum flow is established along the heat pipe, one–dimensional steady compressible equations were used in the vapor core. Later, Jang et al. (1990a) improved the model by solving the one–dimensional transient compressible flow equations for the continuum vapor flow, and developed a model for the frontal startup of circular heat pipes from a frozen state. The phase change of the working fluid was modeled by using the fixed–grid heat capacity method. Because this method is only applicable to a special case of the general form of the energy equation, it is prone to numerical instabilities and inaccurately calculates the melting front location and the temperature profiles in the solid and liquid regions. Jang and co–workers derived the Darcy–extended momentum equations in the wick, but neglected the flow of liquid in their numerical solution. They used the transition temperature at a Knudsen number of 0.01 to characterize the axial location of the free–molecule flow front,

and assumed no heat or mass transfers at the boundaries of the rarefied vapor zone. Unfortunately, these assumptions do not allow the vapor to accumulate progressively in the heat pipe core, so that the vapor flow would never reach the continuum regime.

2.3.6 The Model of Cao and Faghri (1992, 1993a, 1993b)

Cao and Faghri (1993a) improved the model of Jang et al. (1990a) by using a rarefied self–diffusion vapor model to simulate the early startup period of high–temperature heat pipes. After the melting front has reached the vapor–wick interface, evaporation and condensation rates were calculated using a modification of the kinetic theory of gases. Cao and Faghri (1993b) extended the model by using a two–region description of the vapor core. The continuum vapor flow region was modeled using the two–dimensional compressible Navier–Stokes equations, while the rarefied vapor flow region was simulated by a self–diffusion model, the two vapor regions being coupled with appropriate boundary conditions at the axial front defined by the transition temperature. Based on the results of their model, Cao and Faghri (1992) developed an approximate flat–front analytical solution for the startup of high–temperature heat pipes, and proposed a frozen–startup operation limit which indicated the possibility of dryout in the evaporator. This limit was obtained by comparing the rate of increase of the mass of liquid in the wick (due to axial propagation of the melting front) with the rate of loss of the working fluid by resolidification of vapor on the frozen substrate. The two rates were found to be similar for a number of heat pipes, indicating that resolidification of working fluid is a potential factor for failure of the startup of high–temperature heat pipes also. Cao and Faghri (1993a, 1993b) used a fixed–grid temperature transforming method to predict the freezing and melting of working fluid in the wick (Cao and Faghri 1990b). Their numerical scheme, however, required strong under–relaxation of the temperature and a large computation time when the mushy cell temperature range (δT) was small. Also, because of the sharp thermal conductivity jump at the liquid–solid interface, their model predicted wiggly temperature time histories. In reference (1993a), Cao and Faghri used a width of the mushy region as large as 1 K, claiming that it is small enough to simulate the phase–change of pure substances. However, only the least challenging cases of identical (or almost identical) liquid and solid properties had been investigated during the development of their phase–change model (Cao and Faghri 1990b).

Some of the above models (in the second category) have focused on the modeling of free–molecule and transition flow regimes in the vapor and have provided valuable information concerning the startup of high–temperature heat pipes. Under normal conditions, the

transient response of heat pipes is dictated by thermal capacity and conductance of the shell, capillary structure and working fluid, and is only slightly influenced by liquid and vapor dynamics. However, when drying or resaturation occurs in the wick, when the working fluid is frozen or in a thermodynamic near–critical state, working fluid dynamics may become very significant. Unfortunately, all of the heat pipe models above treated the wick as a pure conducting medium, assumed a uniform distribution of the working fluid, and neglected liquid flow, hydrodynamic coupling between the liquid and vapor phases, and solid–vapor mass transfers. Therefore, these models are not capable of predicting the operation limits of the heat pipe, such as capillary, entrainment, dryout of the wick, and the redistribution of working fluid by sublimation and resolidification during the startup of heat pipes from a frozen state. Tilton (1987) and Cao and Faghri (1990) recognized that the hydrodynamics of both the liquid and vapor phases must be modeled in order to predict these operation limits.

Investigators of the third model category have considered modeling of the liquid flow and treated the vapor flow as compressible. Faghri and Buchko (1991) extended the capability of their two–dimensional steady–state model (Faghri and Chen 1989) by including the effect of liquid flow in the wick. They used the steady Darcy–extended flow equations for a saturated and isotropic porous medium, but computed the pressure profiles along the heat pipe independently. In their models, Costello et al. (1988) and Peery and Best (1987) treated the liquid and vapor flows in the heat pipe as one–dimensional and compressible flow problems, and evaluated the evaporation and condensation rates at the L–V interface using modified forms of the kinetic theory relationship. The evaporator end of the heat pipe contained a porous node to store excess liquid fluid, while the excess liquid in the condenser end was assumed to exist in slug form. At the condenser end, the liquid pressure in the wick was assumed to be equal to the vapor pressure in the core.

2.3.7 The Model of Costello et al. (1988)

Costello et al. (1988), on contract for Los Alamos National Laboratory, developed a heat pipe model to predict the transient behavior of liquid–metal heat pipes during startup from the frozen state and operational shutdowns. The friction factor was a function of the Knudsen number to simulate free–molecule and transition flow conditions that occur during startup at low temperature. The flow equations in the vapor region were solved using an iterative scheme based on the KACHINA method developed by Harlow and Amsden (1971). The liquid flow equations in the wick were solved using a modified version of the

SIMPLER algorithm developed by Patankar (1980). At each axial location, the liquid and vapor pressure difference was tested against the maximum capillary pressure head. If the pressure difference exceeded the capillary pressure, the node was flagged as being dried out. Freezing and melting processes in the wick were treated by an enthalpy method. The two–dimensional energy equation was solved in the wall and wick regions with a radial lumped model to determine the radial temperature profile. Although their model is quite comprehensive, Costello and co–workers did not report any calculation results. It is believed that the temporal discretization scheme associated with the KACHINA algorithm limited the time step for calculations. The use of this iterative semi–implicit solution algorithm implies that computer running times would be prohibitive for modeling realistic operational transients.

2.3.8 The Model of Peery and Best (1987)

Peery and Best (1987) developed a model to simulate the transient operation of a rectangular water heat pipe tested at Texas A&M University. The two–dimensional transient conduction equation was used to model the heat transfer through the heat pipe wall, while the liquid and vapor flows were treated as one–dimensional and compressible. Both fluid phases were assumed to be saturated. Evaporation and condensation rates were evaluated using a modified form of the kinetic theory relationship. Once the temperatures and phase–change mass rates were obtained by solving the coupled energy and kinetic theory equations, the one–dimensional continuity equations were solved in the fluid regions for the vapor and liquid axial velocities. The pressure distributions were then obtained from the one–dimensional momentum equations. Even so Peery and Best used oversimplifying assumptions, their model suffered from numerical instability, and the authors could only report calculations of small transients (up to 2 seconds). Extremely small time steps (10^{-4} s) were required to solve iteratively for the coupled energy and kinetic theory equations. This constraint on the time step was previously reported by Subbotin when using his model for predicting evaporation / condensation rates.

In conclusion, Costello et al. (1988) and Peery and Best (1987) did not succeed. The numerical instabilities encountered by these authors are attributed to the numerical methods they used, which were not suitable to handle the complexity of the problem, particularly the coupling with the kinetic theory relationship. Also, it is well known that determination of the velocities from the continuity equation alone (as it was done in the model of Peery and

Best) is not only inaccurate but also a source of instabilities that become amplified with time.

Unfortunately, all the investigators mentioned above ignored the hydrodynamic coupling at the L–V interface. Such decoupling of the liquid and vapor momentum equations can result in erroneous liquid and vapor flow rates and pressures. This uncertainty is attributed to the fact that neither of these models satisfy the local interfacial force balance at the L–V interface. The simplified form of the Pascal relationship (which neglects the effect of flow) reads as:

$$P_V - P_L = 2\frac{\sigma}{R_c}\cos\theta_w \quad , \tag{2.1}$$

where σ is the surface tension of the liquid, θ_w is the wetting angle between the liquid and the wick matrix, and R_c is the radius of curvature of the liquid meniscus at the L–V interface. incorporation of Equation (2.1) into the model poses an additional constraint on the solution procedure as the later must implicitly calculate R_c. Instead of this approach, Costello et al. (1988) and Peery and Best (1987) employed a global pressure relation given below to check if the capillary limit had been exceeded:

$$\left(P_V - P_L\right)_{max} \le 2\frac{\sigma}{R_p}\cos\theta_w \quad , \tag{2.2}$$

where R_p is the effective pore radius of the wick at the L–V interface. These models assumed that the heat pipe was operational as long as Equation (2.2) was satisfied.

As pointed out by Hall and Doster (1989), it is necessary to accurately model the capillary phenomena along the entire length of the heat pipe and thus, adequately satisfy the local capillary relationship of Pascal, Equation (2.1). Setting the liquid and vapor pressures equal at an assumed axial location and computing the phasic pressure distributions independently does not allow the capillary pressure difference to adjust to system parameters. Consequently, models using this approach could not accurately calculate the vapor and liquid flow rates and pressures during a transient, and were not capable of predicting the capillary and dryout operation limits.

The fourth category regroups the heat pipe models that use a geometric approach for modeling the radius of curvature of the liquid meniscus. Ransom and Chow (1987), Hall

and co–workers (1988–1994) and Seo and El–Genk (1989) incorporated liquid flow and thermal expansion, hydrodynamically coupled the liquid and vapor phases, and predicted the vapor volume distribution in the wick. They used the capillary relationship of Pascal (Equation 2.1) to relate the phasic pressures. The pore radius, R_p, is fixed by the geometry of the wick, and the radius of curvature of the liquid meniscus at the L–V interface, R_c, is related to the amount of vapor in the wick. The maximum pressure difference occurs when R_c is equal to the pore radius; in this case, the volume of vapor in the wick forms a hemisphere of radius R_p in each pore of the wick surface. These geometrical considerations allow to express the vapor void fraction in the wick in terms of R_c, the wick surface porosity, and the diameter of the vapor core.

2.3.9 The Model of Ransom and Chow (1987)

The Advanced Thermal Hydraulic Energy Network Analyser (ATHENA) heat pipe model of Ransom and Chow (1987) is a modification of the reactor transient code RELAP–5 (a general purpose thermal hydraulic transient simulation code for two–fluid, two–phase stratified flow systems). In this model, the two–fluid heat pipe formulation is obtained from the one–dimensional area–averaged phasic momentum equations by retaining distinct phasic pressures. The Pascal relationship (Equation 2.2) is used to relate the phasic pressures. Ransom and Chow reported steady–state pressure and axial velocity distributions for a lithium heat pipe with a wick material having a pore radius of 2.5 μm and operating at an evaporator input flux of 4.3 kW/cm^2. The results suggest the soundness of the model and the stability of the iterative semi–implicit numerical scheme used. However, to minimize the number of changes to the original solution scheme of RELAP–5, the phasic pressure difference was evaluated explicitly, which led to severe time step restrictions, much less than the Courant–Friedrichs–Lewy (CFL) limit, and resulted in large computational time for each run. It is not clear how the evaporation and condensation mass rates were evaluated. We can only assume that the thermodynamic equilibrium condition used by RELAP–5 was extended for modeling heat pipe operation as well. The authors pointed out that in the case of liquid flooding, the diphasic interface is flat and the pressure difference between the phases is equal to zero, while this pressure difference is equal to a maximum corresponding to $R_c = R_p$ when the vapor volume fraction exceeds the volume of a hemisphere of radius R_p times the number of pores available at the surface of the wick. These specifications define the variation of the interphase pressure difference in terms of the vapor volume fraction in the heat pipe. However, only the relationship corresponding to normal conditions was considered in the model, so that wick flooding or

dryout conditions were not modeled. Finally, Ransom and Chow (1987) did not model the phase–change of working fluid in the wick during startup from a frozen state, nor the free–molecule and transition vapor flow regimes.

2.3.10 The Model of Hall et al. (1988–1994)

Hall (1988) and Hall and co–workers (1990–1994) developed the THROHPUT (Thermal Hydraulic Response Of Heat Pipes Under Transients) code to model the transient behavior of a circular lithium heat pipe during startup from a frozen state and operational shutdowns. Hall and co–workers incorporated liquid flow in the wick, hydrodynamic coupling of the liquid and vapor phases, and the effect of noncondensible gas in the vapor core (air). Their model predicted the solid, liquid and vapor volume fractions along the heat pipe, so that liquid pooling and recess were modeled. The THROHPUT code predicts the evaporation, condensation and resolidification rates using the kinetic theory equation proposed by Collier (1981). However, the two–dimensional conservation equations were averaged over the radial direction, yielding a one–dimensional axial model. The important radial effects and interphase transfer terms were treated in separate lumped submodels. For simplicity, specific heat capacities were assumed to be constant, and the thermal mass of the wick matrix was neglected. This was justified because the screen wick material has thermal properties that are similar to solid and liquid lithium, and because of the presence of an open annulus between the wall and the screen wick. Melting and freezing processes were modeled with a discontinuous heat flux at the liquid–solid boundaries. Hall and co–workers assumed that the phases existed in radial layers in order to simplify the radial submodel. Four specific configurations were considered: cold state (all solid), startup or melting (wall–liquid–solid), normal operation (all liquid), and shutdown or freezing (wall–solid–liquid). The THROHPUT model assumes that the radial temperature distributions are parabolic in each non–vapor layer. The three coefficients for each layer are determined by forcing the equations to satisfy the temperature and heat flux boundary conditions, and to match the layer average temperature with that computed in the axial model. If a liquid–solid interface exists, it is forced to be at the melting temperature and to satisfy a phase–change jump condition for a moving interface. The capillary pressure relationship is not applied if a node is solid or in the process of melting. The governing equations were discretized on a staggered grid and linearized using an implicit Taylor series expansion about the old time step. Because the model of Hall is basically one–dimensional, it was possible to solve the linearized coupled finite–difference equations directly, using specialized block–diagonal matrix inversion methods. Hall and Doster (1988) attempted to

simulate a Los Alamos experiment (Merrigan et al. 1986) of the frozen startup of a 4 m–long lithium heat pipe. In order to simulate the first 50 seconds of the thaw transient the authors needed 5 hours of CPU time on a VAX 11/750. In further developments, Hall and Doster (1989, 1990) used the Dusty Gas Model of Cunningham and Williams to treat free-molecule flow regime as well as continuum flow regime in the vapor core. Also, they incorporated an axial melt front submodel in THROHPUT. In the new model, the axial progression of the melt front was modeled by combining the radial model with a lumped–parameters axial treatment (Hall 1988). Finally, the evaporation–condensation model was extended to include recondensation at the evaporating surface, and used accommodation coefficients to account for non–ideal behavior. Hall (1988) and Hall and Doster (1989, 1990) showed that using multiple passes (updating the Jacobian at each pass) to update the highly nonlinear equations (particularly the gas mixture state equation and the capillary pressure relationship) reduced the linearization errors, which had limited the time step size. With this new numerical approach, a 2–hour–long transient was simulated using approximately 24 hours of CPU time on a VAX 8600.

In some stages of the THROHPUT calculations, it was found that there was not enough total vapor pressure to support the capillary pressure difference. In early versions of the code, this was viewed as a shortcoming, and Hall forced the liquid pressure equal to zero to prevent any negative liquid pressure in the wick. However, when adjacent liquid nodes showed the same condition, there was no pressure difference between them, resulting in no axial liquid flow. To remedy this problem, Hall and Doster (1989, 1990) assumed that some of the capillary pressure was directed axially when there was a difference in liquid volume fraction between two nodes. This treatment caused their model to predict dryout of the evaporator when this did not occur experimentally for the same conditions. In an attempt to resolve this problem and reproduce the experimental results, Hall and co–workers (Hall 1988; and Hall and Doster 1990) varied the values of the evaporation and condensation accommodation coefficients used in the calculation. The code could satisfy each of several experimental criteria separately by adjusting these coefficients, but no pair of coefficients could meet all of the requirements simultaneously. This behavior prompted the authors to suggest that the accommodation coefficients were dependent on temperature, liquid level, wick porosity, gas velocity and flow regime, and could be much smaller than one for liquid–metals. To justify their findings, Hall and co–workers mentioned the experimental results of a number of researchers who measured condensation heat transfer in liquid–metals to be a fraction of the predictions of Nusselt theory. Other investigators found that the accommodation coefficient strongly depended upon surface contamination

(Hall and Doster 1990). In a recent paper, Hall et al. (1994) performed in–depth literature reviews of experimental measurements of evaporation / condensation accommodation coefficients and of the possibility of tension in the liquid phase. They found that values of the accommodation coefficients close to unity could be measured for both liquid–metal and non–liquid metal working fluids when care was taken in the experiments to avoid surface contamination, the presence of non–condensable gas, and other forms of experimental errors. Furthermore, Hall et al. (1994) found several references which described the effect of tension in the liquid (that is, the possibility of negative liquid pressure) and validated its physical existence. The first experiment that exhibited tension in the liquid was performed by the French chemist Marcellin Berthelot in the 19th century. Other examples can be found in nature, as for example water–filled cavities in minerals and the rising of sap in trees. In the later version of the THROHPUT code, Hall et al. (1994) allowed negative liquid pressure in the wick (the effect of pressure on liquid density, or isothermal compressibility, is negligible when compared with the effect of temperature, or thermal expansion) and used unity accommodation coefficients to calculate the evaporation, condensation and resolidification rates. With these modifications, the model results were greatly improved and agreed reasonably well with the experimental data of Merigan et al. (1986) for the frozen startup of a lithium heat pipe.

In summary, THROHPUT (Hall and co–workers 1988–1994) is one of the most comprehensive heat pipe models to date. It is the only model with provisions for predicting liquid recess, partial dryout and resaturation of wick, and pooling of excess liquid in the vapor core. However, THROHPUT has certain drawbacks. Because this model is basically one–dimensional, it does not deal with freezing and melting of the working fluid mechanistically, hence, its predictions during startup and shutdown transients are only approximate. Furthermore, because heat transfer through the metallic matrix of the wick was not modeled separately, THROHPUT cannot be used to predict the startup of low–temperature heat pipes from a frozen state.

2.3.11 The Model of Seo and El–Genk (1989)

Seo and El–Genk (1989) at the University of New Mexico developed a transient model for simulating the operation of fully–thawed liquid–metal heat pipes. They assumed the liquid flow in the wick region to be two–dimensional, transient, incompressible and laminar. However, a quasi–steady state, compressible one–dimensional approximation was used to simulate the vapor flow. Seo and El–Genk used the laminar two–dimensional Navier–

Stokes equations and retained only these terms that could be discretized using the axial variables of the vapor. In the same spirit, the second derivative of the axial liquid velocity in the momentum conservation equations was neglected compared to its radial gradient. While the authors recognized the limitations of such an approach, their goal was to design a fast running heat pipe code for incorporation in the Space Nuclear Power System Analysis Model (SNPSAM), of SP–100 space nuclear power system (Seo 1988). The two–dimensional transient conduction equation was solved in the wall region, and specific heat capacities were assumed to be constant for simplicity. The model was developed for liquid–metal working fluids and employed an annular wick structure covered by a screen mesh, so that there was no need to consider the thermal mass of the screen wick. The evaporation and condensation rates were obtained from the energy balance at the L–V interface by dividing the liquid radial heat flux in the wick by the latent heat of vaporization. Seo and El–Genk used the geometric Pascal relationship to explicitly satisfy the interfacial local force balance, and the capillary limit was detected when the effective radius of curvature of the liquid meniscus in the wick became equal to the geometrical pore radius. In addition, Seo and El–Genk incorporated implicitly the dependence of surface tension on liquid temperature in their model. The equations were discretized implicitly using a conventional finite difference method, and an iterative solution scheme was used to resolve the interfacial couplings. The Poisson equation was formed in the liquid region by combining the continuity and momentum conservation equations, and was solved for the pressure of the liquid phase. To verify the model predictions, results were compared with the experimental data of Merrigan et al. (1986) for a 4 m–long cylindrical lithium heat pipe. During normal operation, a high–frequency RF coil heated the evaporator section, while the condenser section was cooled radiatively. After shutdown, both the evaporator and condenser sections were radiatively cooled. The model prediction of the wall temperature distribution after shutdown before the working fluid reached its freezing point agreed well with the experimental results, except at the end of the condenser region. It was found experimentally that during normal operation, excess working fluid pooled into the vapor core and filled approximately the last 50 cm of the condenser, causing higher measured temperatures at this end of the heat pipe. It is not clear how pooling effects were treated in the model, when the interfacial liquid meniscus flattens at some point along the heat pipe. Finally, Seo and El–Genk did not model the phase–change of working fluid in the wick during startup from a frozen state, nor the free–molecule and transition vapor flow regimes. Also, their model could not handle highly compressible flow conditions and propagation of shock waves in the vapor core region.

In summary, there has not been a detailed, accurate and efficient transient analysis model for the startup of heat pipes from a frozen state. Some of the processes occurring during the startup of heat pipes from a frozen state, such as sublimation and resolidification, liquid flow and liquid recess in the wick, partial dryout and resaturation of wick, and pooling of excess liquid, have not been incorporated nor explicitly investigated.

To verify the heat pipe models and assess the accuracy of the numerical schemes employed, it is preferable to compare the model predictions with experimental data. The next section summarizes the experiments reported in the literature for low–temperature and high–temperature heat pipes.

2.4. LITERATURE REVIEW ON EXPERIMENTAL DATA

Heat pipes using low vapor pressure working fluids (such as liquid metals, sodium, potassium and lithium) typically exhibit a frontal startup, whereas those using fluids with high vapor pressures (such as water and ammonia) exhibit a uniform temperature startup. The startup characteristics of low–temperature and high–temperature heat pipes from a frozen state differ significantly due to differences in the vapor pressure of the working fluid near the melting point. In low–temperature heat pipes, although the vapor pressure is large enough so that the startup difficulties associated with the viscous and sonic limits are avoided, significant migration of the working fluid from the evaporator to the colder regions of the heat pipe occurs. Once the solid working fluid is melted in the evaporator, dryout may occur due to immediate vaporization of the fluid.

2.4.1 High–Temperature Heat Pipe Experiments

The startup of high–temperature heat pipes from the frozen state has been extensively and experimentally investigated (Deverall et al. 1970; Ivanovskii et al. 1982; Jang et al. 1990a; Faghri et al. 1991; Jang 1995), and successful startup of such heat pipes is consistently achieved. The vapor flow in high–temperature heat pipes remains in the free–molecule regime for temperatures well above the melting temperature. This has the beneficial effects of minimizing the transport of the solid working fluid to the condenser by sublimation / resolidification. The large thermal conductivity of liquid–metal working fluids also allows melting of the working fluid in adiabatic and condenser sections by conduction, before large scale evaporation of the liquid occurs.

Camarda (1977) evaluated analytically and experimentally the performance of a sodium heat pipe for cooling the leading edges of Earth reentry vehicles. The pipe wick consisted of seven alternate layers of 100– and 200–mesh stainless steel screens, and the transient operation of the heat pipe during a space shuttle reentry was simulated by using radiant heaters consisting of quartz iodine lamps. Tolubinsky et al. (1978) have investigated experimentally the frozen startup of sodium and potassium heat pipes subject to continuous radiation heating and high–frequency heating of the evaporator. They showed that the latter mode of heating considerably reduced the startup time.

BECHTEL NATIONAL, under DOE contract (Preliminary Heat Pipe Testing Program 1981) has analyzed the capability of sodium and potassium heat pipes to survive the cyclic operation associated with solar receiver power systems, for such transient as fast startup and cloud passing. They selected Incoloy 800H for the container material, and the heat pipes were equipped with a stainless–steel parallel–tent mesh structure. Insulation was simulated with an array of radiant quartz lamps.

Intensive performance investigations and startup and shutdown studies of liquid–metal heat pipes have been carried out at the Los Alamos National Laboratory (Kemme 1966; Deverall et al. 1970; Kemme et al. 1978; Merrigan 1985; Merrigan et al., 1985 and 1986). Kemme (1966) compared the performance of axially–grooved pipes charged with potassium, sodium and lithium working fluids in the temperature range 750–1150 K. Particular attention was devoted to startup and low temperature operation. The heat transport capability of the heat pipe was significantly improved when the grooves were covered with a wire–screened mesh, which increased the capillary and entrainment limits. Deverall et al. (1970) studied the effect of sonic vapor velocity and related startup problems, and reported temperature measurements of a mercury heat pipe. They demonstrated the effects of noncondensable gas and heat rejection rate at the condenser on the startup. Other attempts have been made to fill the heat pipe with noncondensible gas to make it start more readily. A significant decrease in startup time was noted by Ivanovskii et al. (1982) for increasing amounts of noncondensible gas loading in sodium heat pipes.

Kemme et al. (1978) investigated the thermal performance of mercury, potassium, sodium and lithium heat pipes with various wick structures. A 4–m–long lithium/molybdenum heat pipe was tested experimentally by Merrigan et al. (1985 and 1986) in transient and steady–state operations at temperatures up to 1500 K. Tests conducted included startup from the frozen state, high power steady–state operation, and shutdown with continuous radiation

thermal loading. Tilton et al. (1986) studied analytically and experimentally the transient response of an Inconel 617, sodium heat pipe subject to adverse thermal heating of the condenser. The first experiment used a sliding cylindrical shell radiant heater to simulate Laser illumination of the condenser end, while an actual CO_2 Laser was used for a second test. The outer surface temperature of the wall along the pipe was recorded as a function of time.

Jang (1995) investigated experimentally the frozen startup of a stainless steel / potassium heat pipe with a 40–mesh screen wick. A total of 9 Chromel–alumel thermocouples were installed on the outer surface of the wall. The heat pipe was tested in a vacuum chamber to simulate radiation heat transfer at the condenser, and the evaporator of the heat pipe was radiatively heated by an annular, radiation–shielded silicon carbide heater. Jang (1995) estimated the transition temperature between free–molecule and continuum vapor flow regimes using a Knudsen number of 0.01. Experimental data showed that the heat pipe was inactive until the evaporator end cap temperature reached the transition temperature. Then, the evaporation of liquid became significant and a continuum flow front propagated axially along the heat pipe, until the condenser end cap temperature reached the transition temperature. After that point, the entire heat pipe became active and eventually reached steady–state operation. Jang (1995) observed that the startup period could be significantly reduced by increasing the evaporator heat input. At a power throughput approximately equal to 80% of the heat pipe capillary limit, dryout of the evaporator occurred before the condenser was completely melted. However, successful startup was achieved later as the wick became resaturated with liquid again.

Faghri et al. (1991) also investigated the startup of a sodium heat pipe with multiple evaporator heat source. They measured the outer wall temperature along the heat pipe, and the vapor temperature using a multipoint thermocouple probe. The startup behavior of the sodium heat pipe, which was radiatively cooled in vacuum, was always frontal in nature, with a sharp temperature dropoff in temperature across the vapor front. The low condenser heat rejection rate prevented supersonic vapor velocities and caused the condenser temperature to slowly rise to the steady–state value. Experimental measurements showed that the moving vapor temperature front was much steeper than the outer wall temperature front, and the vapor temperature was more uniform in the hot zone than the wall temperature. When the heat pipe was tested in air, the duration of the startup period was about halved, because the convective losses by natural convection increased the condenser heat rejection rate. The startup of the sodium heat pipe in air was sonic limited, and the

very steep vapor temperature dropoff in the condenser indicated the existence of supersonic vapor flow in that section. However, evaporator dryout never occurred, and the startup was always successful.

2.4.2 Low–Temperature Heat Pipe Experiments

Experiments on the startup of low–temperature heat pipes are rare. Deverall et al. (1970) successfully started a water heat pipe from a frozen state. Because of the relatively high vapor pressure of water, even near the melting temperature, choked and/or supersonic vapor flows were not encountered during the startup. Experimental results showed that the heat pipe became immediately active where the ice was melted. Redistribution of frozen working fluid in low–temperature heat pipes occurred during startup due to sublimation and resolidification of vapor (Faghri 1992; Kuramae 1992; Ochterbeck and Peterson 1993). Such processes may prevent successful re–startup of the heat pipe during cyclic operation. The vapor resolidifies in the cooler parts of the heat pipe and cannot return back to the evaporator. Eventually, the wick might completely dryout in the evaporator.

Faghri (1992) measured the wall and vapor temperature profiles along a water / copper heat pipe and investigated the frozen startup and shutdown transients. The wick of the heat pipe was made of two layers of 50 mesh copper wire–screen. Three flexible heaters were installed side by side along the evaporator section of the heat pipe, and the condenser was cooled with a chiller using ethylene glycol as the coolant. The input power to the evaporator was 20 W, well below the capillary limit of the heat pipe. After sitting the heat pipe in a -21°C freezer for at least 12 hours, startup was attempted with no chiller coolant flow. After the ice was melted in the evaporator, water evaporated and resolidified onto the frozen adiabatic and condenser sections of the heat pipe. Eventually the evaporator wick dried out because the still partially frozen adiabatic section could not provide any condensate return. Faghri (1992) was able to start the frozen water heat pipe successfully by pulsing the power input. As soon as the temperature difference between any two vapor thermocouples exceeded 3 K, the input power was turned off. This allowed the working fluid in the frozen section immediately adjacent to the hot zone to melt and rewet the wick. Once the vapor temperatures became uniform again (within 1 K), another power pulse was applied. In an another experiment, Faghri (1992) froze the water heat pipe from room temperature by supplying the condenser chiller with -15°C coolant. Because the evaporator temperature was always above that of the condenser during the freeze–out transient, a significant portion of the working fluid was displaced by evaporation and

sublimation from the evaporator to the condenser where it resolidified. The reduced amount of ice in the evaporator led to an early dryout after the re–startup of the heat pipe. In cases of low–temperature heat pipes with large evaporator–to–condenser length ratio, complete blockage of the vapor channel was observed, due to resolidification of working fluid (Ochterbeck and Peterson 1993).

Reinarts and Best (1990) attempted the startup of a rectangular water heat pipe with a conventional 100–mesh screen, from frozen and thawed conditions. They measured vapor pressure and temperature and surface wick temperature in the condenser and the evaporator regions and observed wick dryout and subsequent rewetting.

The effect of noncondensible gas on the startup of a water heat pipe was also investigated by Ochterbeck and Peterson (1993). The gas–vapor interface, observed visually, was found to be quite sharp. In the region containing the gas, resolidification and condensation of water vapor did not occur. A frontal startup, characteristic of high–temperature and gas–loaded heat pipes, was observed in the gas–loaded water heat pipe.

Several other experiments have been performed which involved fully–thawed water heat pipes. Fox and Thomson (1970) have measured the axial and radial temperature distributions in the vapor region of a water heat pipe. They have compared two different wire–screened wick designs, a dual wick in which generation of superheated vapor occurred, and a conventional 100–mesh wick, for which the steady–state vapor flow observed was isothermal. Feldman and Munje (1978) evaluated the thermal performance of gravity–assisted circular pipes with and without circumferential grooves. Gernert (1986) presented axial variations of vapor and pipe wall surface temperatures of a water heat pipe with a copper sintered–powder wick and multiple heat sources under steady–state conditions. Faghri and Thomas (1989) compared the performance characteristics of circular and annular water heat pipes having longitudinal grooves at various tilt angles. Jang et al. (1990b) measured the axial variation of the wall surface temperature in a water heat pipe with longitudinal grooves, during heatup transients from ambient conditions to steady–state.

Recently, El–Genk and Huang (1993) investigated the transient response of a horizontal water heat pipe. The copper heat pipe employed a double–layered, 150 mesh copper screen wick. The vapor temperature was measured along the centerline of the heat pipe using a special probe made of a thin–walled brass tube instrumented with eleven thermocouples,

equally spaced along the heat pipe. An additional eleven thermocouples were attached to the outer surface of the heat pipe wall. The evaporator section was uniformly heated using a flexible electric tape, while the condenser section was convectively cooled using a water jacket. Results showed that the transient response of the heat pipe could be described by an exponential function of time. El–Genk and Huang (1993) determined the time constants of the vapor temperature and effective power throughput during heatup and cooldown transients, as functions of the electric input power and the water flow rate in the condenser cooling jacket. In a follow–up study, El–Genk et al. (1995) experimentally investigated the effects of inclination angle on the transient response of a gravity–assisted copper / water heat pipe, subjected to step changes in input power and varied condenser cooling rates. At steady–state, the effective power throughput, determined from the heat balance in the condenser cooling jacket, was 443 W. The difference between the electric input to the electric tape and the steady–state effective power throughput (132 W) was approximately equal to the heat losses from the surface of the insulation in the evaporator section to ambient by natural convection (El–Genk and Huang 1993).

It is apparent that only a few startup experiments of low–temperature and high–temperature heat pipes have been attempted in the literature, and that most experiments conducted have basically been performance tests, rather than phenomenological investigations. It is not an easy task to monitor phenomena occurring within a short distance in a closed pipe. For example, because of practical limitations, no direct measurements of the actual progression of the melting front and mass transfers associated with sublimation and resolidification were possible. Experimental data available are limited to wall temperatures in most cases, with few attempts made to measure the vapor pressure or temperature inside the heat pipe. Therefore, there is a need for systematic theoretical and experimental studies of the transient behavior of liquid–metal and non–liquid metal heat pipes. The outcome of these studies would be useful to better benchmark calculation models for the design of reliable heat pipes for space and terrestrial applications. The transient modes of interest are power step changes, reversed heat pipe operation due to a condenser external heating, and the startup of heat pipes from a frozen state.

3. MODEL FORMULATION AND DESCRIPTION

In this work, a two–dimensional Heat Pipe Transient Analysis Model, "HPTAM", is developed to simulate the transient operation of fully–thawed heat pipes and the startup of heat pipes from a frozen state. This chapter describes the physical model used in HPTAM. The model incorporates the following processes: (a) sublimation of working fluid in the evaporator and resolidification in the condenser; (b) melting and freezing of the working fluid in the porous wick; (c) evaporation of thawed working fluid and condensation as a thin liquid film on a frozen substrate; (d) liquid flow and heat transfer in the porous wick; (e) thermal and hydrodynamic couplings of vapor, liquid and solid phases at their respective interfaces; (f) accumulation of excess liquid in a liquid pool at the end of the condenser; and (g) free–molecule, transition and continuum flow regimes in the vapor region.

HPTAM is a fully two–dimensional heat pipe model which has the capability of handling both rectangular (flat–plate heat pipe) and cylindrical geometries. Nevertheless, the analysis throughout this work focuses on heat pipes having a cylindrical geometry. The model divides the cylindrical heat pipe into three radial regions: wall, wick, and vapor regions (Figure 3.1), and solves the complete form of governing equations in these regions. The heat pipe wick can be a wire–screened mesh, an isotropic porous medium such as a powder or a bed of spheres, or an open annulus separated from the vapor core by a thin sheet (with small holes to provide capillary forces). To predict the flow of liquid in the porous wick of the heat pipe, HPTAM uses the Brinkman–Forchheimer–extended Darcy model (Section 3.1). The properties of wicks (such as permeability and effective thermal conductivity) are calculated, based on analysis of experimental data. The model employs the complete form of the Navier–Stokes compressible flow equations in the vapor region of low–temperature heat pipes (Section 3.2), and solves the two–dimensional transient conduction equation in the pipe wall (Section 3.3).

Section 3.4 describes the interfacial and boundary conditions of the problem. Evaporation, condensation, sublimation and resolidification rates are calculated using the kinetic theory relationship with an accommodation coefficient of unity. The model predicts the radius of curvature of the liquid meniscus at the liquid–vapor interface, and the radial location of the working fluid level (liquid or solid) in the wick, and includes the transverse momentum jump condition (capillary relationship of Pascal) at the liquid–vapor (L–V) interface. The

radius of curvature of the liquid meniscus is geometrically related to the volume fraction of vapor in the wick. These features allow the model to predict the capillary limit and partial liquid recess (dryout) in the evaporator wick.

In Section 3.5, the modified fixed–grid homogeneous enthalpy method used to handle the phase–change of working fluid in the wick is described. The volume of working fluid in the heat pipe varies with temperature, due to thermal expansion of the liquid phase. A liquid pooling submodel is developed and incorporated into HPTAM, which simulates (de)wetting phenomena and the accumulation of excess liquid in the vapor core at the condenser end. This liquid pooling model is described in Section 3.6.

During the startup of high–temperature heat pipes (utilizing liquid–metal working fluids), rarefied and transition flow regimes arise in the vapor region. These flow regimes are described in Section 3.7.

Finally, the model accounts for the change in physical properties with temperature and in density upon melting and offers several choices of working fluids, such as lithium, sodium, potassium and water, and of structural materials, including tungsten, niobium, zirconium, stainless–steel, carbon and copper. The liquid and vapor state equations and the thermophysical properties of the fluids and structural materials of the heat pipe are described in the last Section of this chapter (Section 3.8).

3.1. GOVERNING EQUATIONS IN THE LIQUID/WICK REGION

The liquid/wick region is constituted of the liquid phase of the working fluid and the solid structural phase of the wick, whether it is an annular wire–screened mesh or a homogeneous porous medium. HPTAM models the wick as an isotropic and homogeneous porous medium. Most analytical studies of flow through porous media have dealt primarily with a mathematical formulation based on Darcy's law, which neglects the effects of solid boundaries and inertial forces on fluid flow through porous media. These effects are particularly important for high–porosity media. To account for these effects, Forchheimer and Brinkman extended Darcy's law, and other investigators introduced the transient and convective inertia effects into their generalized flow equation (see APPENDIX A). The flow of liquid in the porous region of the heat pipe is modeled using the Brinkman–Forchheimer–extended Darcy flow model (Scheidegger 1974), while the volume–averaged homogeneous model described by Cheng (1978) is used to model the

heat transfer (see APPENDIX A). The model assumes thermal and hydrodynamic equilibrium in the porous medium, and neglects the thermal dispersion diffusivity since heat conduction is the only significant mode of heat transfer in this region. The form of the Brinkman–Forchheimer–extended Darcy's flow equations can be partly justified through analytical volume–averaging of the microscopic conservation equations, which provides a mean to identify the apparent viscosity in the Brinkman's term. It is then postulated that Darcy's term and Forchheimer's extension are the necessary constitutive relationships to model the unknown terms arising from the volume–averaging process (APPENDIX A).

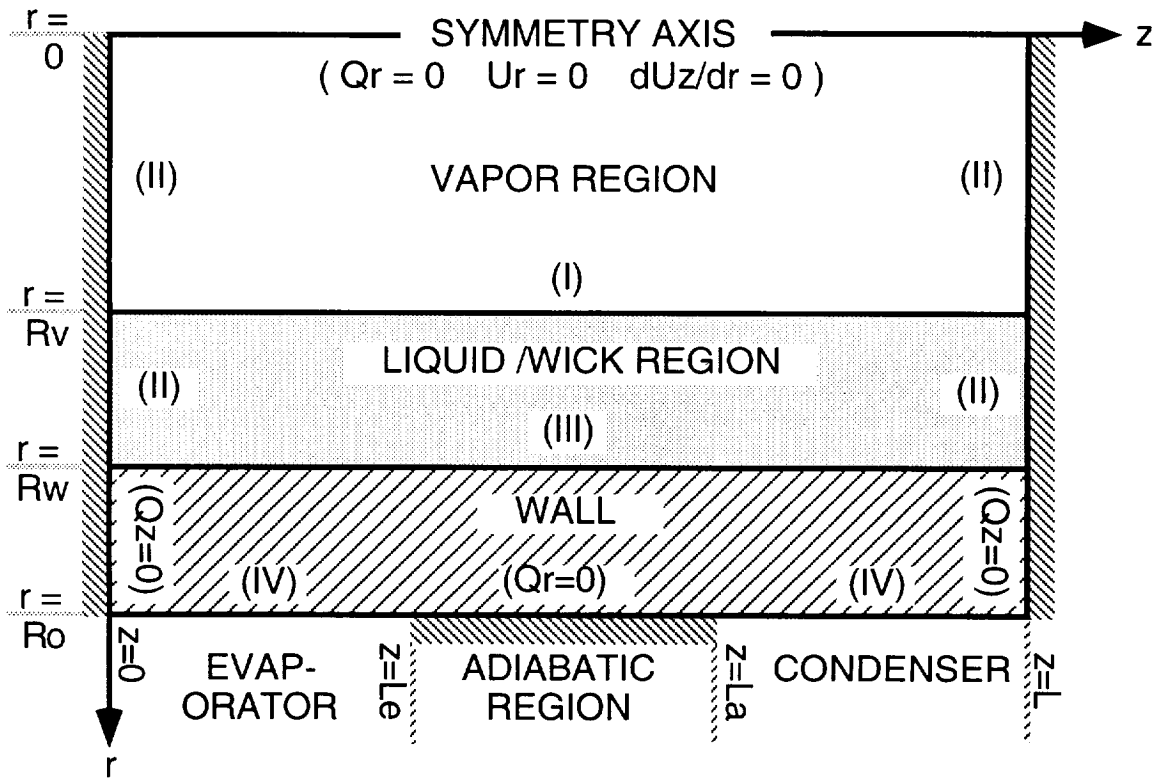

FIGURE 3.1. Physical Model of Heat Pipe and Boundary Conditions.

HPTAM uses the Brinkman–Forchheimer–extended Darcy's flow equations for modeling liquid flow in a fully–saturated isotropic porous wick. The resulting governing equations in the liquid/wick region of the heat pipe are best rewritten in terms of the mean filter (area–averaged) velocity $\bar{q}$ instead of the pore velocity (actual fluid velocity), and are given in the following subsections.

3.1.1. Conservation of Mass

The continuity equation in the wick of the heat pipe has the following form:

$$\varepsilon \frac{\partial \rho_L}{\partial t} + \operatorname{div}\left[\rho_L \vec{q}\right] = 0 \tag{3.1}$$

3.1.2. Conservation of Radial Momentum

The radial momentum balance in the wick can be written:

$$\frac{1}{\varepsilon}\frac{\partial\left(\rho_L q_r\right)}{\partial t} + \frac{1}{\varepsilon^2}\operatorname{div}\left(\rho_L q_r \vec{q}\right) = \rho_L F_r - \frac{\partial P_L}{\partial r} - \left[\frac{\mu_L}{K_r} + \frac{C}{\sqrt{K_r}}\left|\rho_L \vec{q}\right|\right] q_r + \frac{\mu_L}{\varepsilon}\Delta q_r \tag{3.2}$$

where

$$\Delta q_r = \frac{1}{r}\frac{\partial}{\partial r}\left[r\frac{\partial q_r}{\partial r}\right] - \frac{q_r}{r^2} + \frac{\partial}{\partial z}\left[\frac{\partial q_r}{\partial z}\right] .$$

3.1.3. Conservation of Axial Momentum

The axial momentum balance in the wick can be written:

$$\frac{1}{\varepsilon}\frac{\partial\left(\rho_L q_z\right)}{\partial t} + \frac{1}{\varepsilon^2}\operatorname{div}\left(\rho_L q_z \vec{q}\right) = \rho_L F_z - \frac{\partial P_L}{\partial z} - \left[\frac{\mu_L}{K_z} + \frac{C}{\sqrt{K_z}}\left|\rho_L \vec{q}\right|\right] q_z + \frac{\mu_L}{\varepsilon}\Delta q_z \tag{3.3}$$

where

$$\Delta q_z = \frac{1}{r}\frac{\partial}{\partial r}\left[r\frac{\partial q_z}{\partial r}\right] - \frac{q_z}{r^2} + \frac{\partial}{\partial z}\left[\frac{\partial q_z}{\partial z}\right] .$$

The parameters ε, K_r and K_z are the effective porosity and radial and axial permeabilities of the liquid–wick region, respectively. Two additional permeability terms have been introduced into the axial and transverse momentum conservation equations (3.2) and (3.3)

to account for the enhanced pressure losses in a homogeneous porous medium, as demonstrated by Darcy's experiment (Scheidegger 1974). The third, fourth and fifth terms on the right–hand side of the momentum Equations (3.2) and (3.3) are commonly referred to as the *Darcy,* the *Forchheimer,* and the *Brinkman* terms, respectively. The permeability K and the "inertia coefficient" C are functions of the microstructure of the porous medium, and can be determined from the measured static pressure drop and mass flow rates. Experimental investigations (Ergun 1952; and Beavers and Sparrow 1969) for uni–directional flows of water and gases through packed columns and fibrous materials showed that the *Darcy's* and the *Forchheimer's* extensions can accurately express the relationship between flow rate and pressure drop in porous media.

The form of Equations (3.1), (3.2) and (3.3) can be partly justified analytically through volume–averaging of the microscopic conservation equations (Cheng 1978; and Gray and O'Neill 1976), which explains why these equations have been used with success in recent years to model flow of liquids in porous media (Beckermann and Viskanta 1988; and Raw and Lee 1991). The final attractive feature of these equations is that they approach the empirical representation of flow in a porous medium (the Forchheimer–extended Darcy flow model) as the permeability, K, decreases, and reduce to the standard Navier–Stokes equations as the porosity ε goes to 1 and the permeability goes to infinity.

Expressions for the hydrodynamic properties of wicks, such as volume porosity ε, permeability K and inertia coefficient C are given in APPENDIX A-4.

3.1.4. Conservation of Enthalpy in the Liquid/Wick Region

In the present model, the volume–averaged homogeneous enthalpy method is used to predict the transport of energy in the heat pipe wick, assuming local thermal and hydrodynamic equalibrium between phases and negligible thermal dispersion coefficients. The resulting enthalpy conservation equation has the form (see APPENDIX A):

$$\frac{\partial}{\partial t}\left[\varepsilon\left(\rho h\right)_L + (1-\varepsilon)\left(\rho h\right)_m\right] + \mathrm{div}\left[\left(\rho h\right)_L \vec{q}\right] = \frac{\partial P_L}{\partial t} + q_r\frac{\partial P_L}{\partial r} + q_z\frac{\partial P_L}{\partial z} - \mathrm{div}\left(\bar{\bar{Q}}\right) + \frac{1}{\varepsilon}\Phi_L, \tag{3.4}$$

where Φ_L is the viscous dissipation:

$$\Phi_L = 2\mu_L\left[\left(\frac{\partial q_r}{\partial r}\right)^2 + \left(\frac{q_r}{r}\right)^2 + \left(\frac{\partial q_z}{\partial z}\right)^2\right] + \mu_L\left[\frac{\partial q_r}{\partial z} + \frac{\partial q_z}{\partial r}\right]^2 - \frac{2}{3}\mu_L\left[\mathrm{div}\left(\vec{q}\right)\right]^2, \qquad (3.5)$$

and $\vec{q} = \left[q_r\ , q_z\right]$, $\vec{Q} = \left[-k_r^{eff}\frac{\partial T}{\partial r}\ , -k_z^{eff}\frac{\partial T}{\partial z}\right]$,

and *div* is the divergence operator defined as $\mathrm{div}\left(\vec{q}\right) = \frac{1}{r}\frac{\partial\left(rq_r\right)}{\partial r} + \frac{\partial q_z}{\partial z}$.

Note that since we are only concerned here with slow liquid flows in the wick generated by gravity or capillary forces, viscous dissipation and compressible effects can be neglected in the liquid. In this case, the right–hand side of Equation (3.4) reduces to the divergence of the heat flux vector.

3.2. GOVERNING EQUATIONS IN THE VAPOR REGION OF LOW–TEMPERATURE HEAT PIPES

For the case of high–vapor pressure (or low–temperature) working fluids such as water, the vapor flow is in the continuum regime, and HPTAM uses the two–dimensional transient compressible Navier–Stokes flow equations.

3.2.1. Conservation of Mass

The continuity equation in the vapor region of the heat pipe has the following form:

$$\frac{\partial \rho_v}{\partial t} + \mathrm{div}\left[\rho_v \vec{U}^v\right] = 0 \qquad (3.6)$$

3.2.2. Conservation of Radial Momentum

The radial momentum balance in the vapor can be written:

$$\frac{\partial\left(\rho_v U_r^v\right)}{\partial t} + \operatorname{div}\left(\rho_v U_r^v \vec{U}^v\right) =$$
$$\rho_v F_r - \frac{\partial P_v}{\partial r} + \left[\overrightarrow{\operatorname{Div}}\left(2\mu_v \bar{\bar{D}}\right)\right]_r - \frac{2}{3}\frac{\partial}{\partial r}\left[\mu_v \operatorname{div}\left(\vec{U}^v\right)\right] \tag{3.7}$$

where

$$\left[\overrightarrow{\operatorname{Div}}\left(2\mu_v \bar{\bar{D}}\right)\right]_r = \frac{1}{r}\frac{\partial}{\partial r}\left[2\mu_v r \frac{\partial U_r^v}{\partial r}\right] - 2\mu_v \frac{U_r^v}{r^2} + \frac{\partial}{\partial z}\left[\mu_v\left(\frac{\partial U_r^v}{\partial z} + \frac{\partial U_z^v}{\partial r}\right)\right] \quad . \tag{3.8}$$

3.2.3. Conservation of Axial Momentum

The axial momentum balance in the vapor can be written:

$$\frac{\partial\left(\rho_v U_z^v\right)}{\partial t} + \operatorname{div}\left(\rho_v U_z^v \vec{U}^v\right) =$$
$$\rho_v F_z - \frac{\partial P}{\partial z} + \left[\overrightarrow{\operatorname{Div}}\left(2\mu_v \bar{\bar{D}}\right)\right]_z - \frac{2}{3}\frac{\partial}{\partial z}\left[\mu_v \operatorname{div}\left(\vec{U}^v\right)\right] \tag{3.9}$$

where

$$\left[\overrightarrow{\operatorname{Div}}\left(2\mu_v \bar{\bar{D}}\right)\right]_z = \frac{\partial}{\partial z}\left[2\mu_v \frac{\partial U_z^v}{\partial z}\right] + \frac{1}{r}\frac{\partial}{\partial r}\left[\mu_v r\left(\frac{\partial U_r^v}{\partial z} + \frac{\partial U_z^v}{\partial r}\right)\right] \quad . \tag{3.10}$$

Note that the model incorporates acceleration effects in the axial and radial directions (Equations 3.2, 3.3, 3.7 and 3.9). The two–dimensional cylindrical model can handle heat pipe operation in microgravity conditions (space applications) or in an axial force field; this is possible through the axial external acceleration term F_z in Equations (3.3) and (3.9). Rotating circular heat pipes, also, can be modeled through the radial acceleration term F_r in Equations (3.2) and (3.7). However, the model cannot handle a non–symmetric problem such as a horizontal circular pipe in a uniform gravity field. The latter is a truly three–dimensional problem, that could be solved approximately by assuming that non–axial gravity contributions are small enough not to disturb the circumferential symmetry of the

liquid flow in the annular wick, because the width of the liquid annulus is very small (less than a few millimeters). In such case, F_r is taken to be zero.

3.2.4. Conservation of Energy

The enthalpy conservation equation in the continuum vapor region has the form:

$$\frac{\partial}{\partial t}(\rho h)_v + \mathrm{div}\left(\rho h \vec{U}\right)_v = \frac{\partial P_v}{\partial t} + U_r^v \frac{\partial P_v}{\partial r} + U_z^v \frac{\partial P_v}{\partial z} - \mathrm{div}\left(\vec{Q}_v\right) + \Phi_v \quad , \tag{3.11}$$

where Φ_V is the viscous dissipation:

$$\Phi_v = 2\mu_v\left[\left(\frac{\partial U_r^v}{\partial r}\right)^2 + \left(\frac{U_r^v}{r}\right)^2 + \left(\frac{\partial U_z^v}{\partial z}\right)^2\right] + \mu_v\left[\frac{\partial U_r^v}{\partial z} + \frac{\partial U_z^v}{\partial r}\right]^2 - \frac{2}{3}\mu_v\left[\mathrm{div}\left(\vec{U}^v\right)\right]^2$$

, (3.12)

and $\vec{U}^v = \left[U_r^v \ , U_z^v\right]$, $\vec{Q}_v = \left[-k_v \frac{\partial T}{\partial r} \ , -k_v \frac{\partial T}{\partial z}\right]$

For the case of high–vapor pressure (or low–temperature) working fluids such as water, it is a good approximation to assume the vapor phase to be saturated. This approximation is valid for continuum–flow conditions in the vapor, when the vapor pressure of the fluid is high, and to some extent for transition and free–molecule flow regimes. In this case, the vapor temperature is evaluated in terms of the vapor pressure along the saturation line, and there is no need to solve the vapor energy conservation equation.

3.3. GOVERNING EQUATIONS IN THE PIPE WALL REGION

The wick region is thermally coupled to the annular wall of the heat pipe. The energy balance equation in the heat pipe wall region reduces to the well–known transient conduction form of Equation (3.4):

$$\frac{\partial}{\partial t}\left(\rho h\right)_w + \mathrm{div}\left(\vec{Q}_w\right) = 0 \quad . \tag{3.13}$$

3.4. INTERFACIAL AND BOUNDARY CONDITIONS

In two–phase flow, the interface between the liquid and vapor phases is a surface of discontinuity and local jump conditions must be derived, which relate the values of the flow parameters on both sides of the interface. Both the local instantaneous governing equations and jump conditions were developed in their general and conservative form by following the procedure described by Delhaye (1974 and 1976).

3.4.1. Liquid–Vapor Interfacial Jump Conditions

The derivation of the interfacial jump conditions starts with the integral balance laws written for a fixed control volume containing both phases. These integral laws are then transformed by means of the Leibnitz rule and Gauss theorems to obtain a sum of two volume integrals and a surface integral. The volume integrals lead to the well–known monophasic local instantaneous equations (compressible Navier–Stokes equations) in each continuous phase. The surface integral furnishes the local instantaneous jump conditions at the interface. The continuity of the normal mass fluxes at this interface (evaporation/ condensation) yields:

$$\dot{\bar{m}} = \rho_L U_r^L = \rho_V U_r^V \quad . \tag{3.14}$$

The Marangoni and capillary effects arise in the linear momentum jump conditions by taking into account the surface tension force acting on the contour of the diphasic separative interface. The normal momentum jump condition at the L–V interface relates the static pressure drop across the interface to the capillary pressure head in the wick and the normal viscous stress discontinuity as:

$$\begin{aligned} &\left(P_L - P_V\right) + 2\frac{\sigma}{R_c} + \left(\frac{1}{\varepsilon\rho_L} - \frac{1}{\rho_V}\right)\dot{\bar{m}}^2 = \\ &2\left[\mu_L \frac{\partial U_r^L}{\partial r} - \mu_V \frac{\partial U_r^V}{\partial r}\right] - \frac{2}{3}\left[\mu_L \operatorname{div}\left(\vec{U}^L\right) - \mu_V \operatorname{div}\left(\vec{U}^V\right)\right] \end{aligned} \tag{3.15}$$

The first two terms on the left hand side represent the capillary relationship of Pascal, which has been used in almost all previous heat pipe models reported in the literature, only to check if the capillary limit has been exceeded. The Pascal relationship is only valid for incompressible and inviscid phases with no mass transfer at the interface, therefore it is not

necessarily applicable to heat pipe modeling. The third term on the left hand side accounts for change of momentum at the L–V interface. Other terms on the right account for radial stresses in the liquid and vapor phases. These terms are very small in a heat pipe and can be neglected. In Equation (3.15), the two principal radii of curvature are assumed identical (and equal to R_c) because, for small mesh size in the wick, the interfacial pores are very small and are locally hemispherical.

The transverse momentum jump condition relates the tangential velocities of the phases at the L–V interface to the axial gradient of the surface tension (Marangoni effect, $\partial\sigma/\partial z$) and the discontinuity in shear stress:

$$\dot{\bar{m}}\left(U_z^L - U_z^V\right) + \mu_L\left(\frac{\partial U_r^L}{\partial z} + \frac{\partial U_z^L}{\partial r}\right) - \mu_V\left(\frac{\partial U_r^V}{\partial z} + \frac{\partial U_z^V}{\partial r}\right) + \frac{\partial \sigma}{\partial z} = 0 \quad . \tag{3.16}$$

In the present model, this transverse momentum jump condition is simplified by assuming the continuity of the tangential velocities at the interface. This simplification is physically acceptable when dealing with viscous phases separated with a solid wire–screened mesh or a homogeneous porous medium (this is the case of a no–slip condition at the L–V interface). Therefore, the transverse momentum jump condition (3.16) is replaced by the following equations:

$$U_z^L = U_z^V = 0 \quad . \tag{3.17}$$

The enthalpy jump condition relates the enthalpy phase change due to evaporation/condensation across the L–V interface to the discontinuities of the conduction flux, kinetic energy and energy dissipated by viscous stress:

$$\begin{aligned} &Q_r^V - Q_r^L + \dot{\bar{m}}\left(h^V - h^L\right) + \mu_L\left(\frac{\partial U_r^L}{\partial z} + \frac{\partial U_z^L}{\partial r}\right)U_z^L - \mu_V\left(\frac{\partial U_r^V}{\partial z} + \frac{\partial U_z^V}{\partial r}\right)U_z^V + \frac{\partial}{\partial z}\left(\sigma V_r^{int}\right) \\ &+ \frac{\dot{\bar{m}}}{2}\left[\left(U_z^V\right)^2 - \frac{1}{\varepsilon^2}\left(U_z^L\right)^2 + \dot{\bar{m}}^2\left(\frac{1}{\rho_V^2} - \frac{1}{\left(\varepsilon\rho_L\right)^2}\right)\right] + 2\dot{\bar{m}}\left[\frac{\mu_L}{\varepsilon\rho_L}\frac{\partial U_r^L}{\partial r} - \frac{\mu_V}{\rho_V}\frac{\partial U_r^V}{\partial r}\right] = 0 \end{aligned} \tag{3.18a}$$

Making use of Equation (3.17) and neglecting the viscous stress terms in Equation (3.18a) leads to the simplified form:

$$Q_r^V - Q_r^L + \dot{\bar{m}}\left(h^V - h^L\right) + \frac{\dot{\bar{m}}^3}{2}\left(\frac{1}{\rho_V^2} - \frac{1}{\left(\varepsilon\rho_L\right)^2}\right) = 0 \qquad (3.18b)$$

Equations (3.14) through (3.18) specify the discontinuities of mass, momentum and enthalpy fluxes at the L–V interface. However, an additional equation is needed at this interface to formulate a closed form solution of the governing equations and boundary conditions (see Figure 3.1). This relation is obtained by assuming continuous temperature at the L–V interface:

$$T^L = T^V = T\,int \quad . \qquad (3.19)$$

3.4.2. Radius of Curvature of the Liquid Meniscus in the Wick

In Equation (3.15), the radius of curvature of the liquid meniscus at the interface, R_c, is geometrically related to the amount of vapor in the wick. Because the meniscus is concave at the L–V interface, the wick is partially filled with vapor (Figure 3.2). The maximum capillary pressure head occurs when the radius of curvature of the liquid meniscus in the wick, R_c, equals the pore radius, R_p. Assuming hemispherical pores, the maximum volume of vapor in the wick forms a hemisphere of radius R_p in each pore of the wick surface. For this condition, the volume of vapor in the hemispherical pores of the wick interfacial cell (iL,j) is:

$$V_p^j = \varepsilon\left(\frac{2\pi R_{int}^j \Delta Z_j}{\pi R_p^2}\right)\left(\frac{2}{3}\pi R_p^3\right) = \frac{4}{3}\pi R_p \varepsilon R_{int}^j \Delta Z_j \quad . \qquad (3.20)$$

The void fraction α_p (the volume of vapor in the wick interfacial pores over the total volume of the pores V_p) is a geometric function of the cosinus of contact angle of the liquid meniscus ($\mu_c = R_p / R_c$) as (Seo and El–Genk 1989):

$$\alpha_p = \frac{1}{\mu_c^3}\left[1 - \left(1 + \frac{\mu_c^2}{2}\right)\sqrt{1 - \mu_c^2}\right], \qquad (3.21)$$

where α_p and μ_c vary between 0 and 1, as explained later. Equation (3.21) is inversed using the following approximations derived by Seo (1988) and Seo and El–Genk (1989),

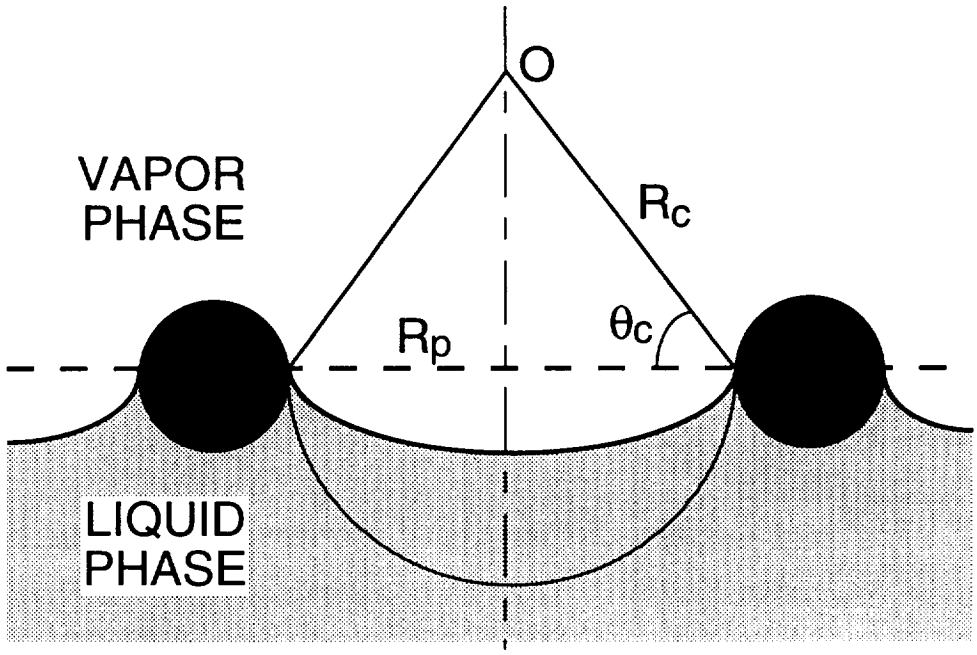

FIGURE 3.2. Illustration of Liquid–Vapor Interfacial Geometry.

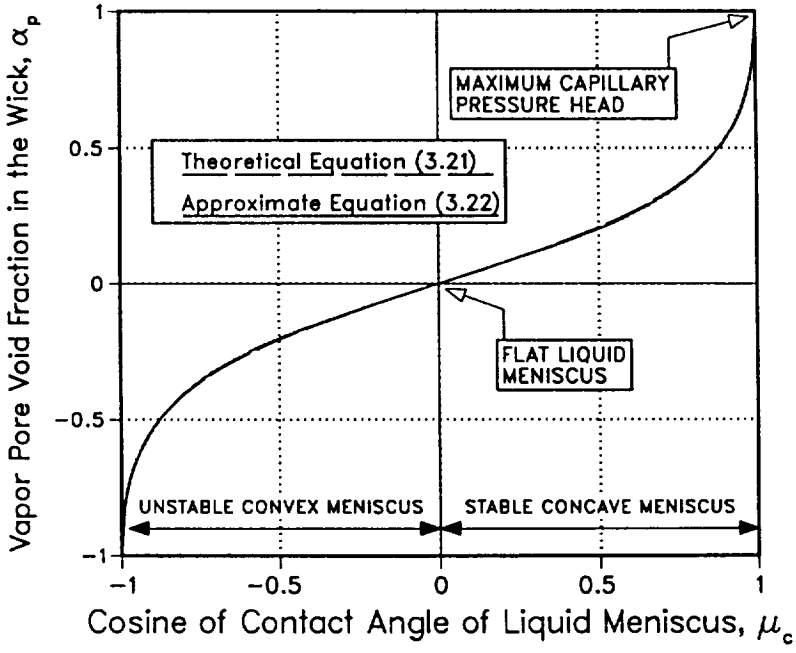

FIGURE 3.3. Pore Void Fraction as a Function of the Cosine of Contact Angle of the Liquid Meniscus (Seo and El–Genk 1989).

reproduced here to correct an error in the second formula ("0.413" instead of "0.443"):

$$\mu_c = \frac{8}{3}\alpha_p (1 - 1.723\,\alpha_p^2) \qquad \text{for} \quad \alpha_p < 0.25 \quad ,$$

$$\mu_c = \frac{8}{3}\left[0.443 - 0.0529\,\alpha_p - \frac{1}{3.5}\,\mathrm{EXP}(\,0.56 - 3.5\,\alpha_p\,)\right] \qquad \text{for} \quad \alpha_p \geq 0.25 \qquad (3.22)$$

Figure 3.3 shows the pore void fraction as a function of the cosine of contact angle of the liquid meniscus, using both the theoretical Equation (3.21) and the approximate relationship (3.22). As this figure shows, Equation (3.22) is a very good approximation of the inverse of Equation (3.21).

3.4.3. Interfacial Phase–Change Mass Rates

To account for the phase change thermal resistance at the L–V and S–V interfaces, evaporation, condensation, sublimation and resolidification mass rates are calculated from an extension of the kinetic theory of gases to non–flat interfaces:

$$\dot{\overline{m}} = \rho_V U_r^V = a_{cc}\left(\frac{M}{2\pi R_g T\mathrm{int}}\right)^{1/2}\left[P_V - P_V^{equ}\right] \ , \qquad (3.23)$$

where P_V^{equ}, the pressure of a vapor bubble in thermal equalibrium with the surrounding liquid, is given as (Defay and Prigogine 1966):

$$P_V^{equ} = P_{sat}(T\mathrm{int}).\mathrm{EXP}\left[-\frac{2\sigma}{R_c}\left(\frac{M}{R_g T\mathrm{int}}\right)\frac{1}{\rho_L}\right] \ . \qquad (3.24a)$$

A positive $\dot{\overline{m}}$ indicates condensation or resolidification, while a negative value indicates vaporization (evaporation or sublimation). For all practical cases, however, the term in squared brackets is negligible, so that the exponential term is very close to unity. Therefore, Equation (3.24a) simplifies to:

$$P_V^{equ} = P_{sat}(T\mathrm{int}) \ . \qquad (3.24b)$$

3.4.4. Other Boundary Conditions

Equations (3.1) through (3.13) are solved subject to the interfacial jump conditions described in the previous subsections and to the boundary conditions delineated in Figure (3.1). The jump conditions (I) are represented by Equations (3.14) through (3.19), (3.16) excluded, while the boundary conditions (II) and (III) are given, respectively, as:

$$Q_z = 0, \quad U_r = U_z = 0, \quad \text{and} \quad Q_r^L = Q_r^W, \quad T^L = T^W, \quad U_r^L = U_z^L = 0 \cdot \qquad (3.25)$$

That is, the liquid and vapor velocities are taken equal to zero at all solid boundaries of the numerical domain (no–slip condition). Both ends of the heat pipe are assumed insulated, and isoflux, adiabatic, isothermal or radiative boundary conditions (IV) are applied independently at the outer wall of the evaporator, adiabatic and condenser sections, respectively.

3.4.5. Initial Conditions and Mathematical Closure

The governing equations, jump relations and boundary conditions, together with the equations of states for both the liquid and vapor phases, thermophysical properties for the wall and both fluid phases, and the initial conditions specified by the user provide all necessary relations to obtain a closed mathematical system of equations (see Table 3.1). Initially, at the startup from a frozen state, the vapor, solid and wall temperatures are uniform and equal, and the vapor pressure is equal to the saturation pressure of the working fluid calculated at the heat pipe temperature. The radius of the solid–vapor (S–V) interface is uniform and smaller than that of the screen/wick surface ($R_{int}^j = R_o \leq R_{wk}$) when modeling the startup of a water heat pipe from a frozen state (due to the decrease in water density upon freezing), and can be larger than that of the screen/wick surface ($R_{int}^j = R_o \geq R_{wk}$) for a liquid–metal heat pipe (due to the increase in density upon freezing of the working fluid).

The model calculates the wall temperatures, the temperatures, pressures, and mass fluxes (or velocities) of the liquid and vapor, and the radii of curvature of the liquid meniscus at the L–V interface (or vapor void fractions in the wick along the pipe).

One should not overlook the fact that the proper choice of boundary conditions is always governed by the mathematical nature of the equations, which results from the highest order

TABLE 3.1. Mathematical Closure of the Physical Model.

Region / Equations	Unknown	Boundary Conditions / **Jump Conditions**
WALL		
Enthalpy	T_W	2 wall boundary conditions (insulated ends)
		1 outer wall boundary condition
		1 radial heat balance at wick/wall interface
LIQUID/WICK		
Enthalpy	T_L	2 wall boundary conditions (insulated ends)
		1 temperature condition at wick/wall interface
		1 radial heat balance at L/V interface
Radial momentum	q_r	3 wall boundary conditions ($q_r = 0$)
		1 radial mass balance at L/V interface
Axial momentum	q_z	3 wall boundary conditions ($q_z = 0$)
		1 axial velocity condition at L/V interface ($q_z = 0$)
VAPOR		
Enthalpy	T_V	2 wall boundary conditions (insulated ends)
		1 symmetric boundary condition (insulated)
		1 temperature condition at L/V interface
Radial momentum	U_r^V	2 wall boundary conditions ($U_r^V = 0$)
		1 symmetric boundary condition ($U_r^V = 0$)
		1 radial momentum balance at L/V interface
Axial momentum	U_z^V	2 wall boundary conditions ($U_z^V = 0$ on pipe ends)
		1 symmetric boundary condition ($\partial U_z^V / \partial r = 0$)
		1 axial momentum balance at L/V interface
Additional Unknowns		Additional Equations
Radius of Curvature	R_c	Kinetic Theory Relationship, Equation (3.23)
Liquid Density	ρ_L	Equation of State, $\rho_L=F(P_L,T_L)$
Vapor Density	ρ_V	Equation of State, $\rho_V=G(P_V,T_V)$

derivatives. As a consequence, the solution considered globally depends strongly on the dissipative terms in the Navier–Stokes equations (conductive heat flux, and viscous stresses). This property is obviously related to the problem of uniqueness of the solution in the inviscid case. All the governing equations (mass, momentum and energy balances) possess the following form:

$$\frac{\partial}{\partial t}(\rho\phi) + \mathrm{div}\left(\rho\bar{U}\phi\right) = \mathrm{div}\left(\Gamma\bar{\nabla}\phi\right) + S \quad \cdot \tag{3.26}$$

The various terms in Equation (3.26) represent, from left to right, accumulation, convection, diffusion and source effects. When diffusion is included, the conservation equations (energy, radial and axial momentum) possess second (highest) order derivatives. Since they are solved in a two–dimensional (cylindrical or rectangular) space, every one of them requires 2x2=4 boundary conditions, one on each boundary of the domain to which they apply. Note that these considerations do not apply to the mass balance Equations (3.1) and (3.6), which are of first order. The continuity equation is an extra equation to be satisfied by the additional degree of freedom, the density or the pressure, these two quantities being related through the equation of state of the fluid.

3.5. FREEZE–AND–THAW MODELING

To handle the startup from the frozen state and subsequent freezing during cooldown, HPTAM incorporates the volume–averaged homogeneous enthalpy method (see APPENDIX A-2). In this formulation, the enthalpy is used as a dependent variable along with the temperature, and there is no need to satisfy explicitly interfacial conditions at the phase–change boundary. An enthalpy equation for each phase (the porous matrix, liquid and frozen phases) is derived analytically using the volume–averaging technique (Gray and O'Neill 1976; and Cheng 1978). These equations contain some unknown convective and dispersive terms, which involve the deviations of the fluid velocity and temperatures from their intrinsic averages, as well as surface integrals of temperatures and interphasic exchange quantities over the separative interfaces between the three phases. In the approach known as the *homogeneous model*, the evolution equation of the overall spatial average temperature is formed by adding the energy equations associated with each phase; the various interphasic exchange terms simply cancel each others.

The volume–averaged homogeneous enthalpy method is used in the present model to predict the thaw (or freezing) of the working fluid in the heat pipe wick, assuming local thermal and hydrodynamic equalibrium between phases and negligible thermal dispersion coefficients. The volume–averaged homogeneous enthalpy method offers several advantages: (a) it employs a fixed–grid numerical scheme; (b) it accounts for the complicated interfacial structures of the various constituents and is valid for any volume fractions of the wick porous matrix and the liquid and frozen phases of the working fluid; and (c) it does not necessitate implicit tracking of the liquid–solid (L–S) interface. This method is also preferred because it can be easily incorporated into the conventional fully–thawed enthalpy conservation scheme. This is an important advantage, particularly since the change–of–phase is only one of the multiple processes involved in the physical operation of heat pipes. The resulting enthalpy conservation equation has the form (see APPENDIX A-2):

$$\frac{\partial}{\partial t}\left[\varepsilon\gamma(\rho h)_S + \varepsilon(1-\gamma)(\rho h)_L + (1-\varepsilon)(\rho h)_m\right] + \mathrm{div}\left[(\rho h)_L \vec{q}\right] = \frac{\partial P_L}{\partial t} + q_r\frac{\partial P_L}{\partial r} + q_z\frac{\partial P_L}{\partial z} - \mathrm{div}\left(\vec{Q}\right) + \frac{1}{\varepsilon}\Phi_L \,, \tag{3.27}$$

where the subscripts S, L and m refer to the frozen phase, liquid phase and solid matrix respectively, ε is the porosity (void fraction) of the porous matrix, and γ is the fraction of the frozen fluid in the voids of the porous matrix. Since we are only concerned here with slow liquid flows in the wick generated by gravity or capillary forces, viscous dissipation and compressible effects can be neglected in the liquid. In this case, the right–hand side of Equation (3.27) reduces to the divergence of the heat flux vector. The main difficulty of the enthalpy formulation is that an appropriate procedure is required to insure that the velocities are null in the solid phase. The idea is to derive a flow equation which reduces to the proper form of the Brinkman–Forchheimer–extended Darcy equations in a liquid control element, yields zero velocity in a frozen volume element, and provides a transition zone in the mushy element which, though artificial, maintains mass and momentum balances. This is best achieved by a gradual slow–down technique, which treats each volume element undergoing phase–change as a porous medium with known liquid volume fraction (Voller and Prakash 1987; and Beckermann and Viskanta 1988). This technique replaces the wick porosity, ε, appearing in Equations (3.1) to (3.3), (A-6) and (A-41) with the liquid volume fraction in the wick, $\varepsilon(1-\gamma)$; thus, the permeability and liquid velocity

approach zero near the frozen region, as the momentum Equations (3.2) and (3.3) reduce to the hydrostatic pressure equations.

Finally, the *parallel* theoretical model (Equation A-45) and Maxwell's Equation (A-47) for randomly packed and sized cylinders are used to calculate the effective axial and radial thermal conductivities of the screen wick, respectively (see APPENDIX A-5). The model of Veinberg (Equation A-52) for distributed spheres is used to calculate the effective thermal conductivity of isotropic porous media such as ceramic powder, metallic felt or sintered metal.

3.6. LIQUID–POOLING SUBMODEL

An effect that has been overlooked in earlier models is the thermal expansion of the liquid during the startup/cooldown of the heat pipe. Liquid thermal expansion is very important for transient modeling of heat pipes utilizing working fluids having high thermal expansion coefficients, such as liquid–metals and water. Experiments have shown that during startup, the liquid volume in the heat pipe increases, causing its excess volume to pool at the end of the condenser and reduce its effective length (Merrigan et al. 1986). Such a behavior could not be accounted for if the liquid flow and thermal expansion are neglected, resulting in erroneous predictions of the liquid and vapor pressures in the heat pipe. Also modeling these phenomena is of paramount importance to accurately predict the wicking limit and dryout conditions.

Figure 3.4 presents a schematic of the liquid model incorporated in the present effort. During the startup of a heat pipe, as the input power to the evaporator increases with time, the temperature of the liquid phase in the evaporator section increases rapidly initially, and hence the working fluid volume increases due to thermal expansion. When the rate of increase in the liquid volume (taking into account vapor condensation in the condenser section) exceeds the liquid flow rate towards the evaporator, the radius of curvature of the liquid meniscus increases. Eventually, the rising concave liquid meniscus at the L–V interface becomes flat at some point along the heat pipe (such occurrence is referred to herein as the *wet point* , as defined by Busse and Kemme, 1978). At the wet point, liquid and vapor interfacial total pressures become equal and the void fraction in the pores of the wick is zero. The position of the wet point can be determined by comparing the vapor pressure recovery with the liquid viscous pressure drop in the condenser region. When the former is small compared with the latter, the wet point occurs at the end of the condenser

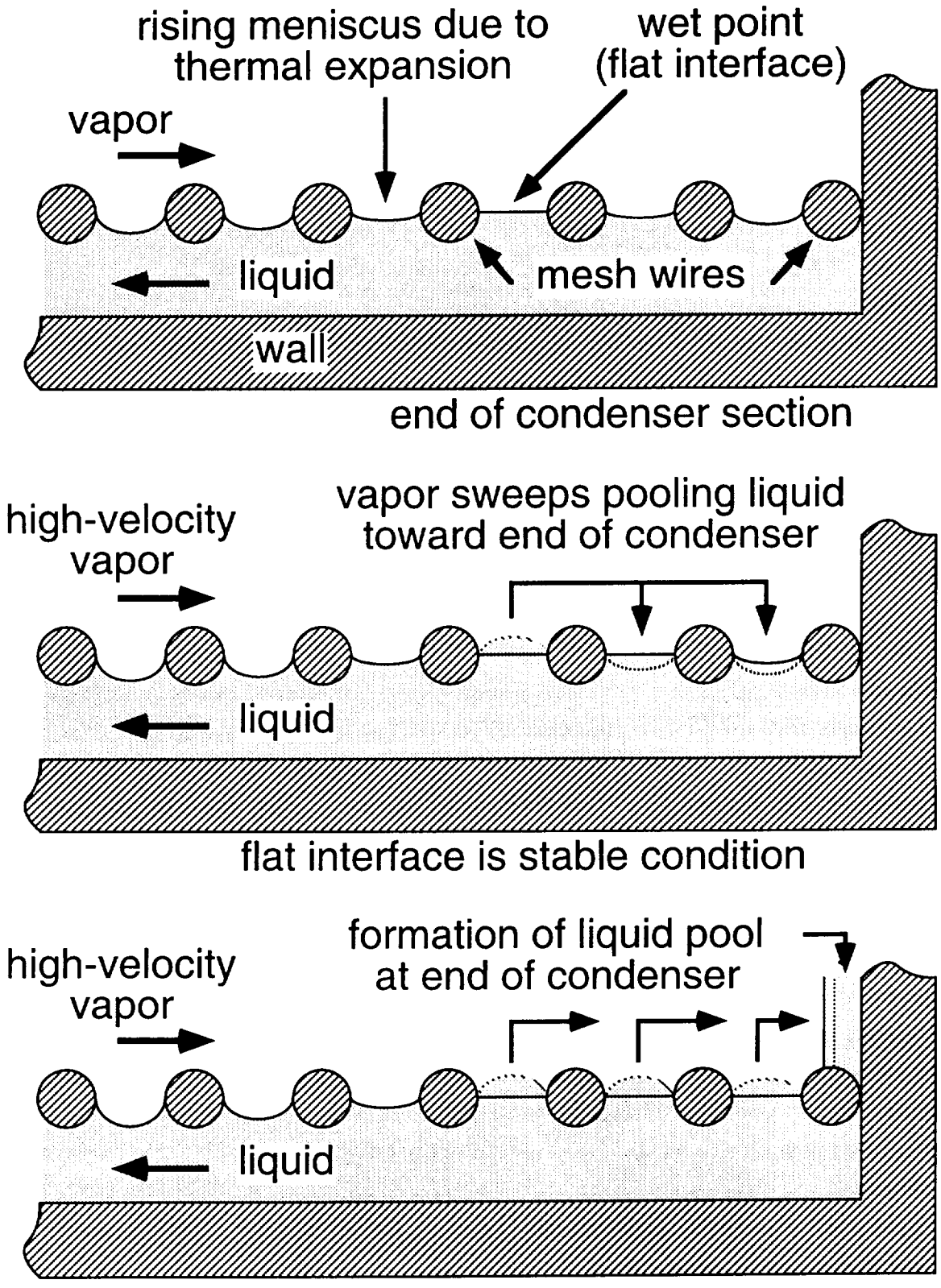

FIGURE 3.4. Illustration of Liquid Pooling at End of Condenser.

region. If the pressure recovery exceeds the liquid pressure drop in the condenser, the wet point moves across the condenser till it eventually appears at the beginning of the condenser region in the case of a much higher pressure recovery. After the first wet point is encountered, further heating of the heat pipe could cause the liquid meniscus at the wet point to become convex, which would correspond to the case of a negative pore void fraction at the L–V interface (Figure 3.3). While such a convex liquid meniscus in the wick might be possible in principle under normal operating conditions, it cannot occur in practice. Because of vapor shear stress and condensation at the L–V interface, such an interface structure is unstable, the excess liquid will be entrained by the vapor stream, transforming the convex meniscus into a coherent liquid plane surface (Busse and Kemme 1978). Therefore, for any practical reasons, the interface is flat at any wet point position in the heat pipe. As the expanding liquid is dragged by the vapor high–velocity flow, the wet point propagates across the condenser region. Eventually, the wet point reaches the end of the condenser, forming a liquid pool. Experiments performed at Los Alamos by Merrigan et al. (1986) using a lithium heat pipe have shown that during startup, excess liquid in the heat pipe pools at the end of the condenser and reduces its effective length.

A submodel has been incorporated into HPTAM to handle these liquid–pooling processes. This submodel assumes that as the transient progresses in time, any excess liquid is swept by the vapor flow towards the end of the condenser, leaving a flat interface and filling up the eventual concave menisci on its way. When a convex liquid meniscus occurs somewhere along the heat pipe, the interface is set flat (the void fraction in the pores of the wick is forced to be zero) at this particular location. The radial momentum jump condition at the L–V interface (Equation 3.15) is used to calculate the pressure in the liquid cell next to the diphasic interface. Then, using the mass balance in this cell, the mass of the liquid pooling into the vapor core is determined. This mass is then transported into the next interfacial liquid cell. Therefore, the wet point moves towards the end of the condenser. When the interface at the end of the condenser becomes flat, excess liquid accumulates in the vapor core and forms a liquid pool. The liquid–pooling submodel also simulates liquid pool recession conditions during the subsequent cooldown of the heat pipe. As the heat pipe cools down, the average liquid temperature and volume decrease due to thermal contraction, and the amount of excess liquid which accumulated at the end of the condenser (liquid pool) is reduced, and eventually vanishes, so that a positive liquid meniscus is restored in the condenser region.

Other phenomena, such as free–molecule and transition flow regimes, need to be considered to model the transient operation of high–temperature heat pipes.

3.7. FREE–MOLECULE AND TRANSITION FLOWS REGIMES

During the startup at low temperature of a frozen or fully–thawed liquid–metal heat pipe, very low pressures arise in the vapor region, and free–molecule and transition flow conditions are prevalent there. The gas flow through a cylindrical channel can be classified into three types, depending on the dimensionless Knudsen number K_n, which is the ratio of the molecules mean free path λ to the channel diameter D (Dushman and Lafferty 1962, chapter 2). The first type of flow is the *viscous flow regime*, which occurs when the mean free path is very small compared to the diameter of the channel, so that molecule–molecule collisions dominate. The second type of flow, the *free–molecule flow regime*, occurs when the mean free path of the gas is large compared to the channel diameter, and is limited by the molecular collisions with the walls. The third type is the *transition flow regime*, for which both molecule–molecule and molecule–wall collisions are important. These three types of flow have been classified as follows:

$$\begin{array}{lll} \text{(1) viscous flow, for} & & K_n < 0.01 \\ \text{(2) transition flow, for} & 0.01 < K_n < 1 & \\ \text{(3) free–molecule flow, for} & 1. < K_n & . \end{array} \qquad (3.28)$$

The values of the Knudsen number, 0.01 and 1.00, are rather arbitrary, since the viscous and transition flow regimes are approached asymptotically; they correspond to a ratio of viscous to total flow conductance of 90% and 7.7% respectively (APPENDIX B).

The flow charts for lithium, sodium, potassium and water heat pipe working fluids give an estimate of the transition temperatures between viscous, transition and free–molecule flows regions, as a function of the vapor core diameter. To draw these flow charts, the mean free path of the vapor molecules is calculated as a function of temperature using Equation (B–1), reproduced here for convenience:

$$\lambda = \frac{M}{\sqrt{2}\pi\sigma^2 N_a}\frac{1}{\rho_v} \quad , \quad D = 2a = \frac{\lambda}{Kn} = \frac{1}{Kn}\frac{k}{\sqrt{2}\pi\sigma^2}\frac{T_{tr}}{P_{sat}(T_{tr})} \qquad (B–1)$$

where M is the molecular weight and σ is the effective diameter of the gas molecules. In this equation, the vapor density is taken as that of the saturated phase. The effective molecular diameters of lithium, sodium, potassium and water heat pipe working fluids are estimated in APPENDIX B.

The resulting flow charts for liquid–metals and water heat pipe working fluids are presented in Figures (3.5) to (3.7). For a liquid–metal heat pipe with a vapor core diameter of 2.2 cm, the transition temperatures between free–molecule, transition and viscous flow regimes are 810K and 1030K for lithium, 540K and 680K for sodium, and 450K and 570K for potassium (Figure 3.5). Clearly, since these liquid–metal fluids are frozen at room temperature and have melting temperatures (453.7 K, 371.0 K and 336.4 K respectively) below their free–molecule transition temperature, a heat pipe startup from frozen conditions belongs to the free–molecule flow regime; therefore it is necessary to include such modeling to predict the transient operation of liquid–metal heat pipes from the frozen state and the fully–thawed condition.

For a water heat pipe, viscous flow conditions are prevalent over the whole temperature and pipe diameter ranges of interest (micro–heat pipes are not being considered here), because of the relatively high vapor pressure of this fluid above its melting temperature (Figure 3.7).

Because funding from NASA Lewis Research Center was discontinued in March 1994, the present report does not include any information concerning the modeling of the free–molecule and transition vapor flow regimes. However, the final version of HPTAM includes the capability of modeling these non–continuum flow regimes and the frozen startup of liquid–metal heat pipes, and this effort is well documented and described in Mr. Tournier's Dissertation (1995).

The thermophysical properties of the wall material and the working fluids, and the state equations of the liquid and vapor phases are described in the next subsection.

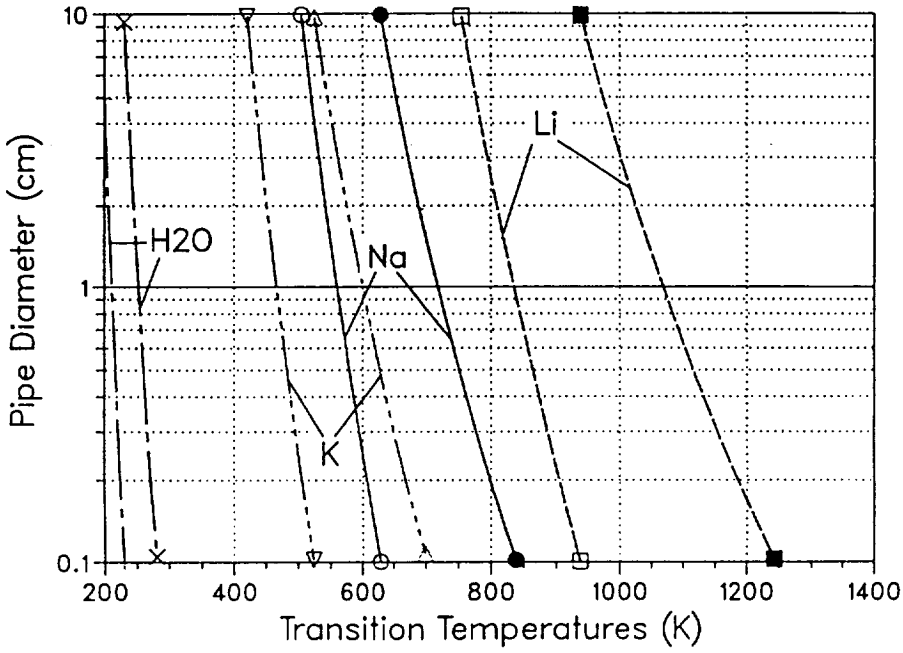

FIGURE 3.5. Vapor Flow Chart for Liquid–Metal Working Fluids.

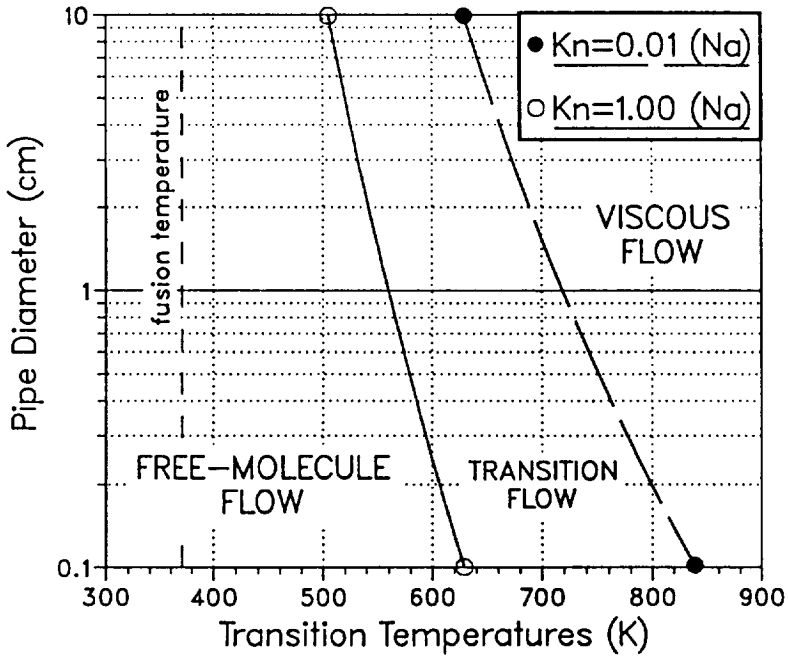

FIGURE 3.6. Vapor Flow Chart for Sodium Working Fluid.

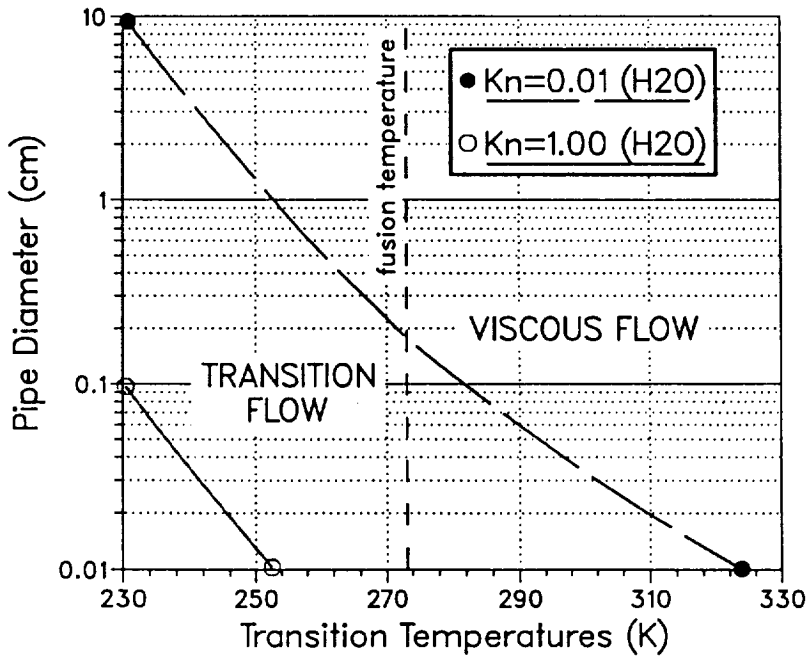

FIGURE 3.7. Vapor Flow Chart for Water Working Fluid.

3.8. THERMOPHYSICAL PROPERTIES AND STATE EQUATIONS

The thermophysical properties of the wall material and the liquid and vapor phases are taken to be temperature dependent (also pressure dependent when relevant). The model incorporates various working fluids such as lithium, sodium, potassium and water, as well as various structural materials including tungsten, niobium, zirconium, stainless–steel, carbon and copper.

Additional wall materials are easily incorporated, as they only require knowledge of density, thermal conductivity and heat capacity as a function of temperature. However, for a new working fluid, a great deal of data is needed, since the properties of the solid, liquid and vapor phases are needed (see Table 3.2). Much of these properties are difficult to locate, particularly for the vapor phase.

TABLE 3.2. References and Temperature Range of Validity for the Thermophysical Properties of Working Fluids (Solid, Liquid and Vapor Phases).

Property of working fluid	lithium	sodium	potassium	water
Melting temperature T_m [Weast 1986]	453.7 K	370.9 K	336.4 K	273.15 K
Saturation vapor pressure $P_{sat}(T)$	T_m—1600 K [Hall 1988]	T_m—1450 K [Vargaftik 1975]	T_m—1400 K [Vargaftik 1975]	T_m—600 K [Irvine and Liley 1984]
Surface tension of liquid phase $\sigma(T)$	T_m—1600 K [Léger 1980]	T_m—1450 K [Vargaftik 1975]	T_m—1400 K [CEA 1963]	300—647 K [Vargaftik 1975]
Density of saturated liquid $\rho_{sat}^{L}(T)$	T_m—1600 K [Léger 1980]	T_m—1450 K [Vargaftik 1975]	T_m—1400 K [Vargaftik 1975]	T_m—647 K [El-Wakil 1981]
Isothermal compressibility of saturated liquid $\beta_T(T)$	T_m—2000 K [Ohse 1985]	T_m—2000 K [Ohse 1985]	T_m—1800 K [Ohse 1985]	300—373 K [Weast 1986]
Dynamic viscosity of liquid phase $\mu_L(T)$	T_m—1500 K [Ohse 1985]	T_m—1500 K [Ohse 1985]	T_m—1500 K [Ohse 1985]	T_m—600 K [El-Wakil 1981]
Thermal conductivity of liquid phase $k_L(T)$	T_m—1500 K [Léger 1980]	T_m—1500 K [CEA 1963]	T_m—1500 K [CEA 1963]	T_m—600 K [El-Wakil 1981]
Specific heat capacity of liquid phase $C_p^L(T)$	T_m—1600 K [Vargaftik 1975]	T_m—1500 K [Vargaftik 1975]	T_m—1500 K [Woloshun et al. 1989]	T_m—647 K [Irvine and Liley 1984]
Dynamic viscosity of (saturated) vapor $\mu_V(T)$	980*—2000 K [Vargaftik 1975]	800*—1500 K [Woloshun et al. 1989]	800*—1500 K [Woloshun et al. 1989]	T_m—600 K [Vargaftik 1975]
Thermal conductivity of (saturated) vapor $k_V(T)$	700*—2500 K [Ohse 1985]	700*—1500 K [Ohse 1985]	700*—1500 K [Ohse 1985]	T_m—620 K [Vargaftik 1975]
Latent heat of vaporization $h_{fg}(T)$	T_m—1600 K [Vargaftik 1975]	T_m—1500 K [Vargaftik 1975]	T_m—1500 K [Vargaftik 1975]	T_m—647 K [Reynolds 1979]
Density of solid phase $\rho_S(T)$	100 K—T_m [Hall 1988]	270 K—T_m [Metals Handbook 1979]	100 K—T_m [Metals Handbook 1979]	100 K—T_m [Touloukian 1970]
Thermal conductivity of solid phase $k_S(T)$	100 K—T_m [Touloukian 1970]	100 K—T_m [Touloukian 1970]	100 K—T_m [Touloukian 1970]	120 K—T_m [Ross et al. 1978]
Latent heat of fusion H_{fus}	432.3 kJ/kg [Metals Handbook 1979]	113.0 kJ/kg [Metals Handbook 1979]	59.5 kJ/kg [Metals Handbook 1979]	333.6 kJ/kg [Moeller 1980]
Specific heat capacity of solid phase $C_p^S(T)$	100 K—T_m [Touloukian 1970]	100 K—T_m [Touloukian 1970]	100 K—T_m [Touloukian 1970]	70 K—T_m [Weast 1986]

*: correlation can be used at lower temperatures.

TABLE 3.3. References and Temperature Range of Validity for the Thermophysical Properties of Structural Materials.

Property of structural material	Melting temperature T_{fus}	Density $\rho_m s$	Thermal conductivity $k_m(T)$	Specific heat capacity $C_p^m(T)$
tungsten	3680 K [Weast 1986]	19350 kg/m^3 [Weast 1986]	120—3000 K [Ho et al. 1968]	273—2600 K [Touloukian 1975]
niobium	2740 K [Weast 1986]	8570 kg/m^3 [Weast 1986]	200—2300 K [Ho et al. 1968]	273—1900 K [Touloukian 1975]
zirconium ($\alpha \angle \beta$ metallic phase change at 1140 K)	2120 K [Weast 1986]	6490 kg/m^3 [Weast 1986]	200—2000 K [Ho et al. 1968]	298—1800 K [Touloukian 1975]
stainless–steel	1700 K [Weast 1986]	7900 kg/m^3 [Weast 1986]	80—1200 K [Metals Handbook 1979]	200—1230 K [Metals Handbook 1979]
carbon	> 3700 K [Weast 1986]	2250 kg/m^3 [Weast 1986]	200—1500 K [Schlunder 1984]	C_p^m= 1506 J/kg.K
copper	1360 K [Weast 1986]	8920 kg/m^3 [Weast 1986]	200—1200 K [Ho et al. 1968]	323—1273 K [Touloukian 1975]

In addition to the thermophysical properties, inverse functions and derivative functions are needed in many cases to perform the numerical solution of the problem. For these reasons, all of the property information is in the form of functional evaluations. Most of these functions were derived by using least–squares regression on table values and experimental data from the literature. Tables 3.2 and 3.3 show the references selected for the various properties of working fluids and structural materials, and give the temperature range of validity of the extrapolated functions. For every property, data from several references were plotted against each other as a function of temperature. In most cases, good agreement was found in between the various references, and a consistent set of data was selected that would cover the widest range of temperature. Due to the limitation in space, only the major dataset reference is given in Tables 3.2 and 3.3. It is important to specify the temperature range of validity since all too often a function obtained by least–squares regression gives nonphysical results (such as very large or negative values) outside the temperature interval of extrapolation.

The density of the liquid phase is calculated as a function of pressure and temperature to account for the fluid thermal expansion and compressibility. Because of the capillary pressure head at the L–V interface, due to the concave meniscus in the wick, the pressure of the liquid phase is less than the corresponding vapor pressure, that is the liquid phase is subcooled. Because the van der Waals state equation cannot practically be used away from the critical point, the density of the liquid phase is obtained in terms of pressure and temperature from the following relation:

$$\rho_L(T,P_L) = \left\{ 1 + \beta_T(T)\left[P_L - P_{sat}(T)\right] \right\} \rho_{sat}^L(T) \quad , \tag{3.29}$$

where β_T is the isothermal compressibility factor of the saturated liquid phase.

The density of the vapor phase is obtained as a function of pressure and temperature using the ideal–gas law:

$$\rho_V(T,P_V) = \frac{M}{R_g T} P_V \quad . \tag{3.30}$$

Enthalpies of the solid, liquid and vapor phases of the working fluid are obtained as illustrated in Figure 3.8. The enthalpy of the liquid phase is taken as that of the saturated liquid phase and is related to the liquid specific heat capacity by:

$$h^L(T) = h^{REF} + \int_{T_{REF}}^{T} C_p^L(T)\, dT \quad . \tag{3.31}$$

The enthalpy of the saturated vapor phase is the sum of the enthalpy of the liquid phase and of the latent heat of vaporization:

$$h^V(T) = h^L(T) + h_{fg}(T) \quad . \tag{3.32}$$

By definition, the heat capacity at constant pressure is the partial derivative of the enthalpy with respect to temperature, so that the vapor specific heat capacity is:

$$C_p^V(T) = C_p^L(T) + \frac{d}{dT}\left[h_{fg}(T)\right] \quad . \tag{3.33}$$

Finally, the enthalpy of the solid phase is related to the enthalpy of the liquid at melting temperature, the heat of fusion and specific heat capacity of the solid by:

$$h^S(T) = h^L(T_{fus}) - H_{fus} - \int_T^{T_{fus}} C_p^S(T)\, dT \quad . \tag{3.34}$$

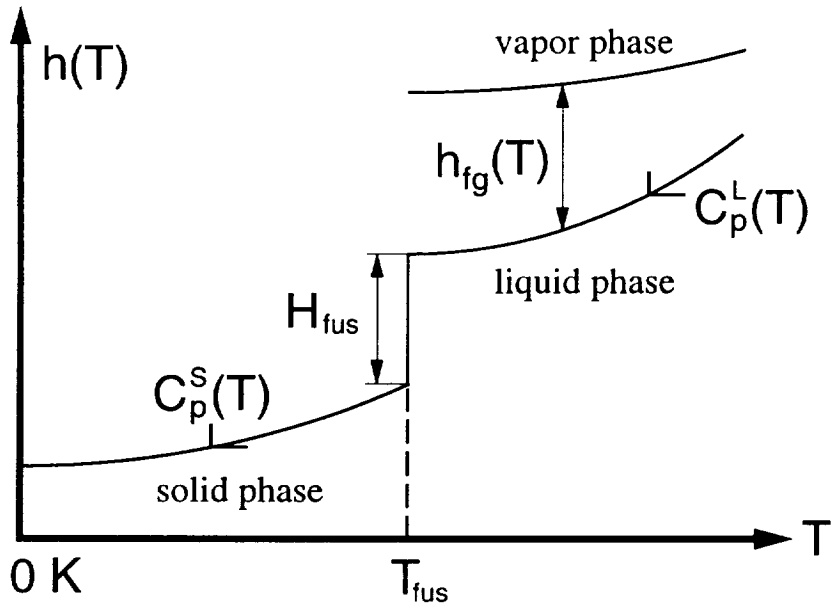

FIGURE 3.8. Enthalpies of Solid, Saturated Liquid and Saturated Vapor Phases of Working Fluids as a Function of Temperature.

This section ends the description of the physical heat pipe model. The next chapter describes in details the discretization of the governing equations and numerical technique used in HPTAM.

4. METHOD OF SOLUTION

Simulating the transient operation of heat pipes involves solving a highly non–linear homogeneous two–phase flow problem, which incorporates the effect of surface tension and the processes of phase change at the liquid–vapor (L–V) interface. The two–dimensional Heat Pipe Transient Analysis Model (HPTAM) developed herein solves the compressible Navier–Stokes equations in the vapor region, and models the liquid flow in the wick with the Darcy–Forchheimer–extended flow equations. The vapor and liquid phases are coupled at the L–V interface through the mass, radial momentum and energy jump conditions. In addition, the evaporation, condensation, sublimation and resolidification rates are calculated from the kinetic theory of gases to account for the thermal resistance at the L–V and S–V interfaces. HPTAM geometrically relates the radii of curvature of the liquid meniscus at the L–V interface to the volume of vapor in the wick, and simulates pooling of excess liquid in the condenser.

Because of the physical complexity of the problem, advanced numerical methods are required. In this work, a stable solution technique for simulating transient operation of a fully–thawed heat pipe is developed, that is accurate and efficient in terms of CPU time. Various segregated solution techniques are implemented, one based on the non–iterative Pressure Implicit Splitting Operator (PISO) of Issa (1986), another of the SIMPLEC segregated iterative type. Their accuracy and computation time requirement are examined using experimental results for the heatup and cooldown transients of a horizontal water heat pipe.

The most efficient technique, HPTAM–Revised, is a SIMPLEC–type segregated solution technique which includes two internal iterative steps to resolve the pressure–velocity and temperature–velocity couplings and reduce the linearization errors of the kinetic theory relationship and equations of state. The solution evaluates the volume of the vapor in the wick explicitly, while the kinetic theory relationship is implicitly coupled with the energy jump condition at the L–V interface. Other solution techniques examined require using a small time step size (< 15 ms) to avoid numerical instabilities. On the other hand, a time step size as high as 500 ms could be used with the HPTAM–Revised technique without developing any numerical instability. While all solution techniques examined performed the same in terms of accuracy, the HPTAM–Revised is 90 times faster than the basic non–iterative SIMPLE–type approach.

The selection of the appropriate linear–system solver also affects the efficiency of the solution technique, particularly when computational grids larger than 10x30 are used. For example, when solving a typical heat pipe problem using a 20x40 size grid, more than 90% of the total CPU time is used by the banded Gauss–elimination solver. Calculations showed that, when the iterative SIS solver is used instead of the banded Gauss–elimination solver for the solution of the 5–point momentum and energy linear systems, the total CPU time was only 48% of that for the technique using the Gauss–elimination solver.

4.1. SOLUTION PROCEDURE

The numerical approach selected to solve this highly non–linear and complex problem is attractive in the sense that it combines the power of the most advanced numerical methods to date and the advantage of algorithmic flexibility. A summary of the method selected follows, with some comments to justify the choices made. The theoretical developments and full justifications are collected in APPENDIX C. To solve the set of governing equations which describe the operation of heat pipes (see Chapter 3), an unsteady finite–difference discretization method, based on the SIMPLEC segregated iterative solution technique, is developed.

Finite–difference methods are simple to formulate, can easily be extended to 2 or 3 dimensions, and require considerably less computational work and storage requirement than finite–element methods. The use of the unsteady formulation makes it possible to solve both the steady and transient problems with the same code. When solving the steady–state equations directly, heavy under–relaxation is usually necessary to resolve the non–linearities and couplings, and it is easily shown that relaxing the steady–state equations is equivalent to the transient formulation (APPENDIX C-4).

The governing equations and boundary conditions are discretized on a staggered grid using the control–volume integration approach proposed by Patankar (1980), instead of the conventional Taylor series technique. The stability enhancing characteristics of the finite difference equations obtained by volume integration of the conservative form of the governing equations, are discussed in detail by several investigators (Patankar 1980; Harlow and Amsden 1971; and Roache 1982). Lax (1954) and others have shown that shock wave speed and strength are correctly predicted when the conservative form of the Navier–Stokes equations is used, and that this is not the case with the non–conservative

form. The point is that all stable, consistent and conservative finite–difference methods applied to the conservative form of the equations satisfy the Rankine–Hugoniot relations and therefore produce the correct jump conditions across a shock.

The final attraction of this integration approach is that it is simple to implement, and the finite–difference forms can be interpreted as integral laws over the control–volume cell: the solution obtained using this approach satisfies global conservation, even on a non–uniform grid. The main drawback of using finite–difference methods is the possibility of developing a "checkerboard" pressure field. Such spurious pressure distribution is prevented by using the well–known Eulerian staggered–grid (APPENDIX C-2). On this grid, the liquid and vapor velocities are determined at the cell boundaries while the other quantities, such as pressures and enthalpies, are evaluated at the cell center. The harmonic average of the thermal conductivity is used at the boundaries of the control volumes to insure continuity of temperature and heat flux at these interfaces.

To resolve the couplings and non–linearities of the flow conservation equations, both direct solution algorithms and non–iterative splitting procedures have been developed. In practical problems, however, a direct solution technique would require a very large amount of computer storage and time (Beam and Warming 1978), even when specialized sparse matrix solvers are employed.

Non–iterative splitting procedures have been considered to speed up calculations and reduce the complexity of programmation as well as storage requirements (APPENDIX C-12). Originally, these methods have been applied to solve multi–dimensional problems as a series of linearized one–dimensional problems (Alternating Direction Implicit approximations). Unfortunately, it was found that such spatial splitting methods have a rather poor accuracy for disturbances which propagate skew to the coordinate axes. This suggests that a more productive approach would be to split by physical phenomena instead, as it is done in the Marker–And–Cell (MAC) formulation and projections algorithm. It is therefore desirable to use segregated iterative solution techniques in which the velocity components and pressure are calculated in a sequential or *segregated* manner.

Most modern iterative numerical methods used to solve the unsteady compressible flow equations, such as the SIMPLE–type procedures (APPENDIX C-5) and PISO (Pressure–Implicit with Splitting of Operators), are based on the Marker–And–Cell (MAC) method (APPENDIX C-12). They make use of the staggered grid and deduce the pressure field

from a Poisson equation obtained by combining the continuity and momentum conservation equations.

Harlow and Amsden (1971) have extended the MAC method to the solution of the conservative form of the unsteady compressible flow equations. The advanced–time density was linearized in terms of the pressure by using the equation of state, and procedures similar to the SIMPLE–type techniques were derived to resolve the pressure–density–velocity couplings. The Implicit Continuous–fluid Eulerian technique of Harlow and Amsden (1971) is suitable for arbitrary equation of state and proved successful for all Mach number.

The SIMPLE–Consistent (SIMPLEC) algorithm of van Doormaal and Raithby (1984) uses a consistent simplification of the momentum correction equations and does not require any pressure under–relaxation (the off–diagonal velocity corrections appearing in the diffusion/convection terms are equated to the diagonal velocity correction). When diffusion and convection phenomena are dominated by pressure gradients and source terms, the consistent approximation in SIMPLEC becomes exact so that this procedure should be used. This applies to flow systems with large pressure gradients such as flows in porous media and heat exchangers. Also SIMPLEC is easy to program and performs as well or better than SIMPLER in terms of CPU time and storage requirements.

Since these modern segregated iterative solution techniques are extremely modular in nature, it is a relatively simple task to test possible variations of the algorithm. Any basic iteration is made of several sequential steps:

(a) *momentum predictor step* : best estimates of the pressure gradients are calculated explicitly, and the momentum conservation equations are solved for the velocity field.

(b) *pressure corrector step* : a simplified (corrected) form of the momentum conservation equations is used to implicitly relate mass flow rates and pressure gradients; the mass flow rates are eliminated in terms of pressures in the continuity equations, and densities are linearized using the equations of state; the resulting Poisson equation is solved for the pressure field.

(c) *energy or enthalpy predictor step* : best estimates of pressures and convective fluxes are evaluated explicitly, and the enthalpy conservation equations are solved for the temperatures.

(d) *properties update* : the thermophysical properties are updated, particularly densities, which are calculated using the equations of state.

While these basic sequential steps are suitable for monophasic fluid flow problems, they must be modified to solve the more complex two–phase flow coupled problem, that of heat pipe. During the pressure corrector step, liquid and vapor volumes around the L–V interface are treated as functions of the wick void fractions. The void fractions are linearized in terms of the cosines of the contact angles using the geometrical Equation (3.22). The latter are implicitly related to the liquid and vapor pressures at the L–V interface through the radial momentum jump condition or extended Pascal relationship (Equation 3.15). The kinetic theory Equation (3.23) is used implicitly to relate the evaporation/condensation mass fluxes and the pressures at the L–V interface. The densities, evaporation/condensation mass fluxes, and radii of curvature of the liquid meniscus for the advanced time are then obtained, with the pressure corrections.

The predictor steps are stabilizing steps for the convective and diffusive terms. The momentum equations are solved for velocities, while the enthalpy equations are linearized and solved for temperatures and evaporation/condensation rates by implicitly coupling the interfacial energy jump condition (3.18b) and Equation (3.23) at the L–V interface. To decouple the radial and axial momentum conservation equations, the convective mass fluxes, the divergence of the velocity field and the cross–derivative viscous terms are evaluated explicitly from the previous step. These cross derivative terms are not important for the stability of the solution (Beam and Warming 1978). If the explicit differentiating of these terms imposes any limitation on the time step, this fact has been masked by more restrictive conditions due to convection, diffusion or strong non–linearities for example.

4.1.1. Definition of Domain, Variables and Extrapolations

The physical domain is divided into a two–dimensional cylindrical grid (r,z) of (Nr+1) by Nz cells. Since azymutal symmetry is assumed in the cylindrical heat pipe, only half of the vapor core is modeled with cells (i=1) through (i=Nv), as shown in Figure 4.1a. The liquid–wick region is represented by cells (i=iL=Nv+1) through (i=NL), and the pipe wall is modeled with cells (i=NL+1) through (i=Nr). The coolant flow in the cooling jacket along the condenser section is represented by a column of cells (i=Nr+1), as shown in Figure 4.1b. In the axial direction, the evaporator section extends from (j=1) to (j=Nevap), the adiabatic section from (j=Nevap+1) to (j=Nadia), and the condenser section from (j=Nadia+1) to (j=Nz). The dimensions of the cell (i,j) are ΔR_i and ΔZ_j , while $Rcell_i$ and $Zcell_j$ are the coordinates of the center of this cell (Fig. 4.2). The surface areas of the sides

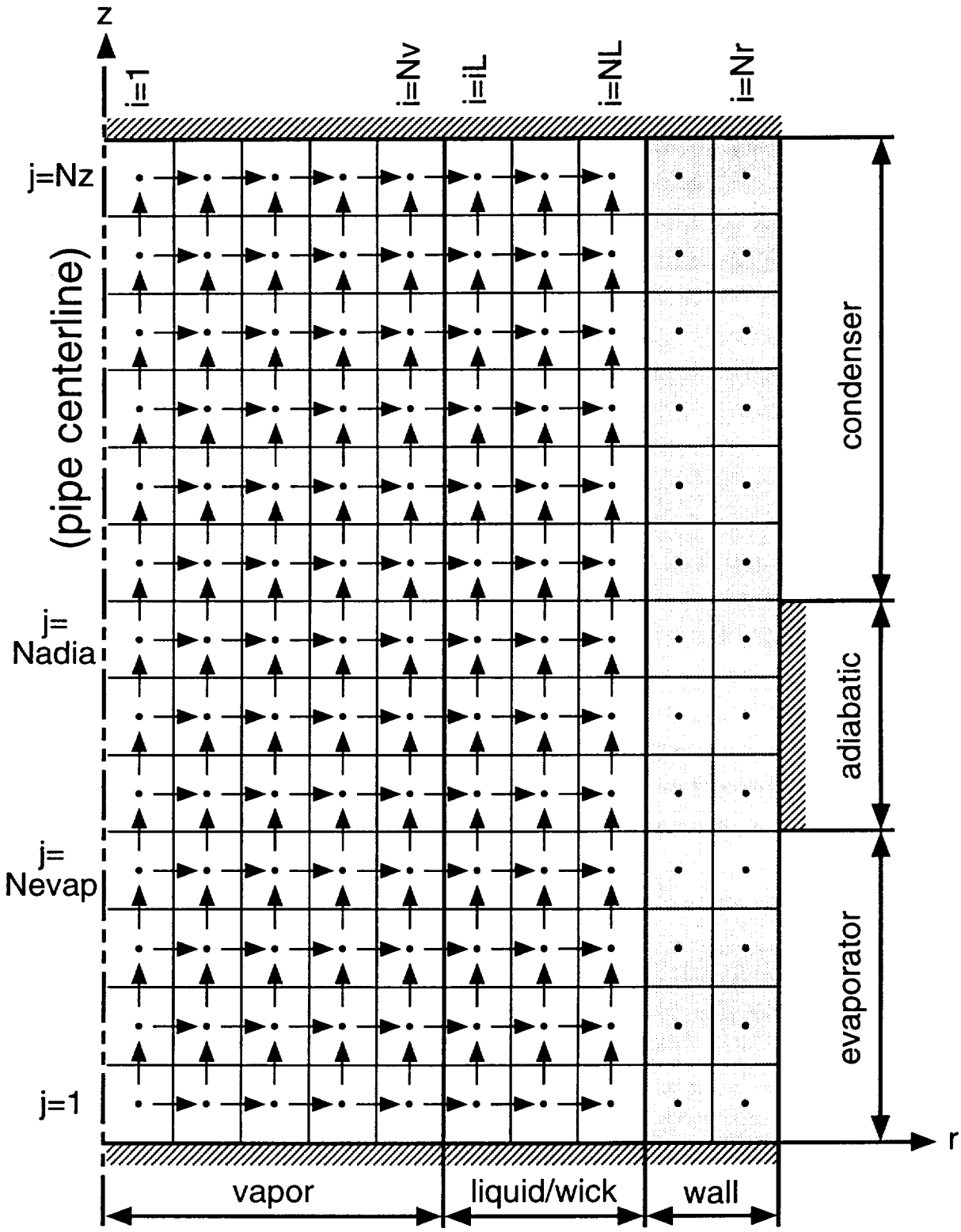

FIGURE 4.1a. Numerical Grid Layout for Circular Heat Pipe.

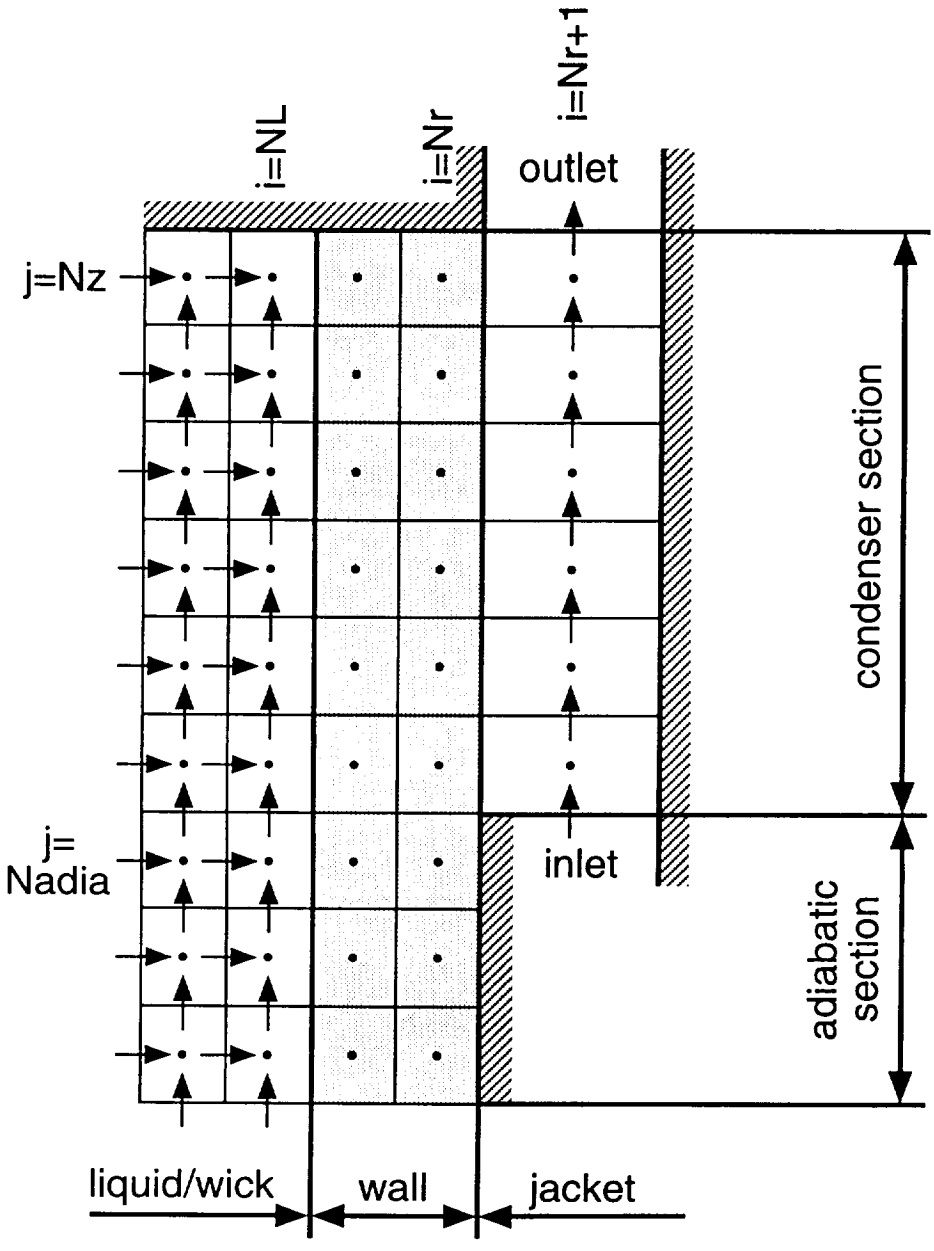

FIGURE 4.1b. Details of the Numerical Grid for Condenser Cooling Jacket.

of cell (i,j) are $A_r^{i,j}$, $A_r^{i-1,j}$, $A_z^{i,j-1}$ and $A_z^{i,j}$ in the radial and axial directions, respectively. The volume of the cell (i,j) is $Vol^{i,j}$. The denomination "cell" refers to the mass balance cell. On the staggered grid, densities, pressures, temperatures and enthalpies are defined at the center of the mass balance cells, while velocities and mass fluxes are defined at the center of the faces of these cells (the latter holds for wick void fractions and cosines of contact angle as well, but along the L–V interface only). The momentum conservation equations are integrated over the momentum cells surrounding the velocity components (Figures 4.2, 4.3 and 4.4). $B_r^{i,j}$, $B_r^{i+1,j}$, and B_z^i are the surface areas of the sides of the radial momentum cell (i,j), whose volume is $Vol_r^{i,j}$. $X_r^{i-1,j}$, $X_r^{i,j}$, and A_z^i are the surface areas of the sides of the axial momentum cell (i,j), whose volume is $Vol_z^{i,j}$. These volumes and areas can be expressed as:

$$
\begin{aligned}
A_r^{i,j} &= 2\pi R_i \Delta Z_j \quad , \quad A_z^i = \pi\left(R_i^2 - R_{i-1}^2\right) \quad , \\
B_r^{i,j} &= 2\pi Rcell_i \Delta Z_j \quad , \quad B_z^i = \pi\left(Rcell_{i+1}^2 - Rcell_i^2\right) \quad , \\
X_r^{i,j} &= \pi R_i\left(\Delta Z_j + \Delta Z_{j+1}\right) \quad , \quad Vol^{i,j} = A_z^i \Delta Z_j \quad , \\
Vol_r^{i,j} &= B_z^i \Delta Z_j \quad , \quad Vol_z^{i,j} = A_z^i \frac{\Delta Z_j + \Delta Z_{j+1}}{2} \quad .
\end{aligned}
\tag{4.1}
$$

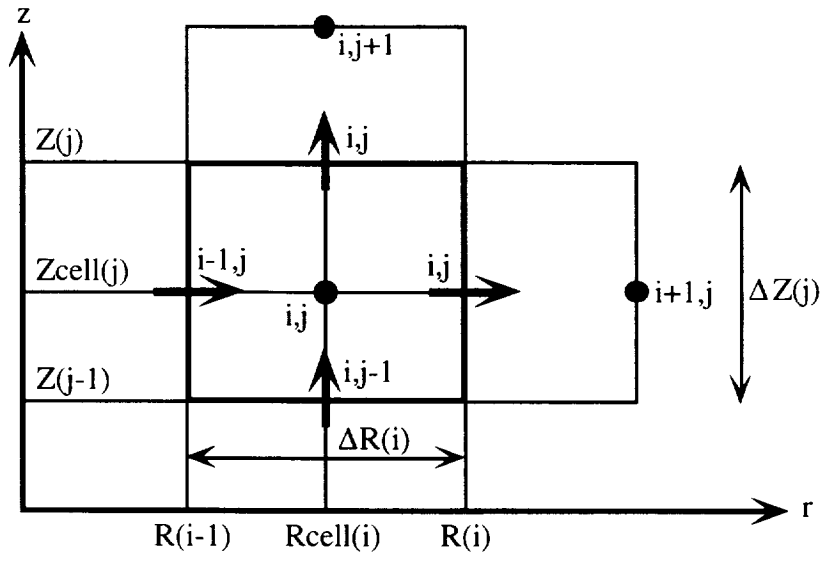

FIGURE 4.2. Grid Layout for a Mass Cell.

The densities, pressures, enthalpies, and heat capacities are extrapolated at the velocity locations using weighting factors, φ_r^i and φ_z^j, such that:

$$\begin{aligned} \rho_r^{i,j} &= \varphi_r^i \rho_{i,j} + (1-\varphi_r^i)\rho_{i+1,j} \quad , \\ \rho_z^{i,j} &= \varphi_z^j \rho_{i,j} + (1-\varphi_z^j)\rho_{i,j+1} \quad . \end{aligned} \tag{4.2}$$

The mass fluxes and velocities are then related by:

$$G_r = \rho_r U_r \text{ , and } \quad G_z = \rho_z U_z \, . \tag{4.3}$$

Other extrapolations are necessary to evaluate the convective mass fluxes at the faces of the radial (G_{Rr}, G_{Rz}) and axial (G_{Zr}, G_{Zz}) momentum cells. By construction, G_{Rr} and G_{Zz} are located at the centers of mass cells (densities locations), while G_{Rz} and G_{Zr} are located at the vertices (grid intersections) of the mass cell grid (Figures 4.3 and 4.4). These extrapolated mass fluxes are expressed as:

$$\begin{aligned} B_r^{i,j} G_{Rr}^{i,j} &= \left(\frac{AzLEFT}{A_z}\right)^i \left(A_r G_r\right)^{i,j} + \left(1 - \frac{AzLEFT}{A_z}\right)^i \left(A_r G_r\right)^{i-1,j} \, , \\ G_{Rz}^{i,j} &= \varphi_r^i G_z^{i,j} + (1-\varphi_r^i) G_z^{i+1,j} \, , \\ X_r^{i,j} G_{Zr}^{i,j} &= \frac{1}{2}\left[\left(A_r G_r\right)^{i,j} + \left(A_r G_r\right)^{i,j+1}\right] \quad , \\ G_{Zz}^{i,j} &= \frac{1}{2}\left[G_z^{i,j} + G_z^{i,j-1}\right] \quad , \qquad \text{where} \\ AzLEFT^i &= \pi\left(Rcell_i^2 - R_{i-1}^2\right) \quad , \qquad \text{and} \\ \varphi_r^i &= 1 - \frac{AzLEFT^i}{B_z^i} \quad , \qquad \varphi_z^j = \frac{\Delta Z_j}{\Delta Z_j + \Delta Z_{j+1}} \quad . \end{aligned} \tag{4.4}$$

These extrapolations are derived so that conservation of mass in the mass cells insures conservation of mass in the radial and axial momentum cells.

$UrCELL_{i,j}$ and $UzCELL_{i,j}$ denote the extrapolated velocities at the centers of mass cells and are given by:

$$UrCELL_{i,j} = \frac{GRr_{i,j}}{\rho_{i,j}} \quad , \text{ and } \quad UzCELL_{i,j} = \frac{GZz_{i,j}}{\rho_{i,j}} \quad . \tag{4.5}$$

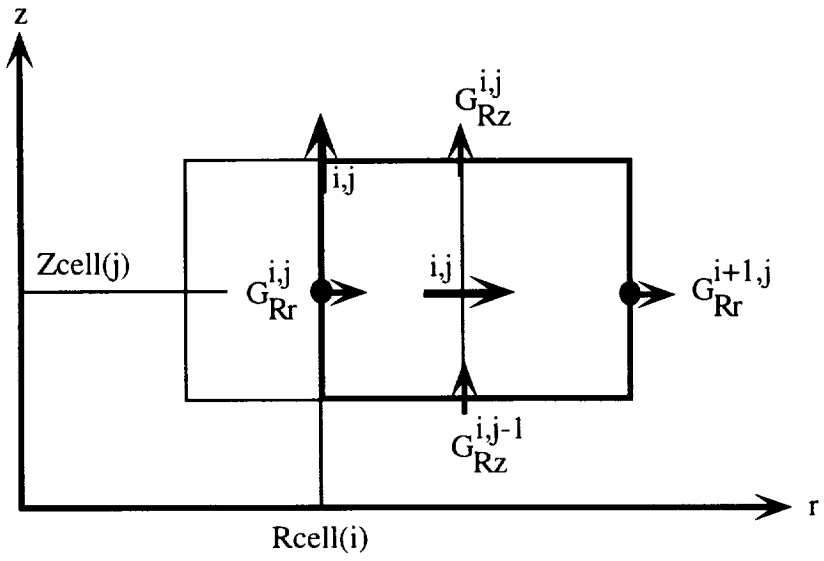

FIGURE 4.3. Grid Layout for a Radial Momentum Cell.

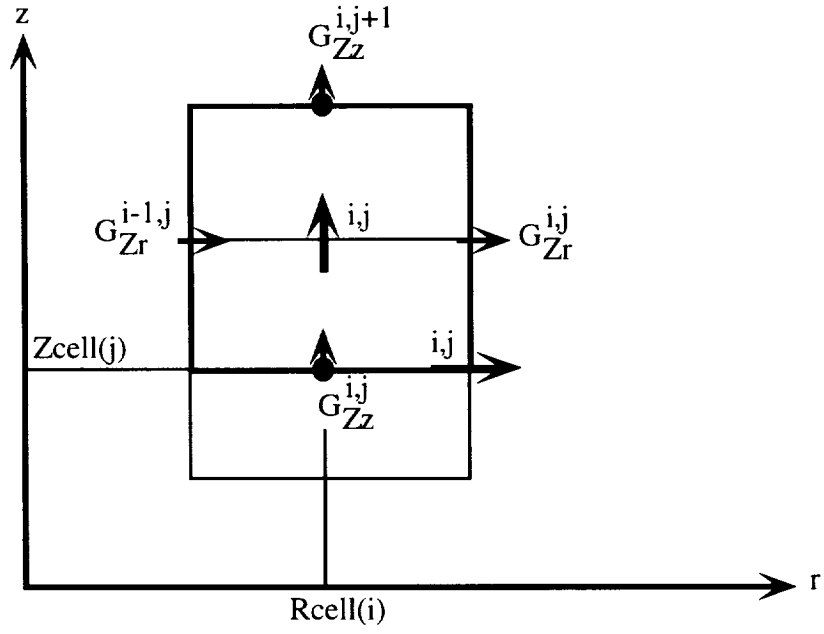

FIGURE 4.4. Grid Layout for an Axial Momentum Cell.

The superscript (n) is used to reference the variables at the old time step $t_n = t_0 + n\Delta t$, such as: $P^n, \rho^n, T^n, Tint^n, h^n, \vec{U}^n, \vec{G}^n, \alpha_p^n, \mu_c^n, Vol^n, \dot{\bar{m}}^n$, which represent in order of appearance pressure, density, temperature, interfacial temperature, enthalpy, velocity field, mass flux, wick void fraction, cosine of contact angle of liquid meniscus, mass cell volume and evaporation/condensation mass fluxes. In the same manner, a superscript (n+1) is used for the variables at the new time step $t_{n+1} = t_n + \Delta t$, while a superscript (*) refers to the best estimate of the new–time variable available at the time of the computation. Since the formulation is partially implicit, the factors α, θ and ψ, which vary between 0 (explicit) and 1 (fully implicit), are introduced such that the *tilted* intermediate–time variables are defined as:

$$\begin{aligned}
\tilde{T}int^* &= \alpha Tint^* + (1-\alpha)Tint^n, \\
\tilde{G}_r^{n+1} &= \psi G_r^{n+1} + (1-\psi)G_r^n, \\
\tilde{\mu}_c^{n+1} &= \theta \mu_c^{n+1} + (1-\theta)\mu_c^n, \\
\tilde{P}^* &= \theta P^* + (1-\theta)P^n.
\end{aligned} \tag{4.6}$$

The factor α is used for temperatures and enthalpies, ψ for densities, velocities and mass fluxes, while θ is used for the other variables such as pressures, wick void fractions and cosines of contact angle. Finally, the *Delta* notation is defined as:

$$\begin{aligned}
&\Delta P^{n+1} = P^{n+1} - P^n, \quad \text{and} \quad \Delta P^* = P^* - P^n, \\
&\text{so that} \quad \tilde{P}^* = \theta P^* + (1-\theta)P^n = P^n + \theta \Delta P^* \quad .
\end{aligned} \tag{4.7}$$

Now, given a *stared* best estimate of a new–time quantity, for example the pressure (P^*), we seek a *primed* correction field (P') such that:

$$P^{n+1} = P^* + P' \, . \tag{4.8}$$

4.1.2. Discretization of the Conservation Equations

The mass balance, momentum and enthalpy conservation equations are integrated over their respective control volume (mass cell, radial and axial momentum cells, and mass cell, respectively), using the Gauss theorem and Green's formula (Delhaye 1976):

$$\iiint_{Vol} \mathrm{div}\left(\vec{U}\right) dV = \oiint_{\partial Vol} \vec{U} \bullet \vec{N}\, dA \quad , \tag{4.9a}$$

and

$$\begin{aligned} \iiint \left(\vec{U} \bullet \vec{\nabla} P\right) dV &= \iiint_{Vol} \left[\mathrm{div}\left(P\vec{U}\right) - P\,\mathrm{div}\left(\vec{U}\right)\right] dV \\ &= \oiint_{\partial Vol} P\vec{U} \bullet \vec{N}\, dA - \iiint_{Vol} P\,\mathrm{div}\left(\vec{U}\right) dV \quad , \end{aligned} \tag{4.9b}$$

where ∂Vol denotes the surface of the volume Vol and $\vec{N}$ is the outward unity vector normal to this surface.

In the following, any omitted grid subscript/superscript must be taken as (i,j). The next subsections describe the discretization of all the governing equations and their associated jump conditions and boundary conditions.

4.1.3. Homogeneous Enthalpy Equation in the Porous Wick

During the enthalpy predictor step of the solution procedure, the liquid and solid enthalpies in the enthalpy conservation Equation (3.27) are linearized in terms of temperature using the heat capacities of the phases (Figure 4.5). Also, the frozen volume fraction γ is related to the cell average temperature T according to Figure 4.6 (Beckermann and Viskanta 1988). The three types of cells are:

(a) *solid cell,* where $T < (T_{fus}-\delta T)$, $\gamma = 1$, and $\partial\gamma/\partial T = 0$.
(b) *mushy cell,* where $(T_{fus}-\delta T) \le T \le (T_{fus}+\delta T)$, $0 \le \gamma \le 1$, and $\partial\gamma/\partial T = -1/(2\delta T)$.
(c) *liquid cell,* where $(T_{fus}+\delta T) < T$, $\gamma = 0$, and $\partial\gamma/\partial T = 0$.

Integration of Equation (3.27) over a control volume (i,j) leads to the following discretized form of the enthalpy conservation equation:

$$
\begin{aligned}
&\frac{\varepsilon}{\Delta t}\left\{Vol^{*}\left[(1-\gamma^{*})(\rho h)_{L}^{*}+\gamma^{*}(\rho h)_{S}^{*}\right]-Vol^{n}\left[(1-\gamma^{n})(\rho h)_{L}^{n}+\gamma^{n}(\rho h)_{S}^{n}\right]\right\}\\
&\quad+\frac{\varepsilon Vol^{*}}{\Delta t}\left\{(1-\gamma^{*})\left(\rho C_{p}\right)_{L}^{*}+\gamma^{*}\left(\rho C_{p}\right)_{S}^{*}+\left[(\rho h)_{S}^{*}-(\rho h)_{L}^{*}\right]\left(\frac{\partial\gamma}{\partial T}\right)^{*}\right\}T'\\
&\qquad+\frac{1-\varepsilon}{\Delta t}Vol_{o}\rho_{m}\left\{(h)_{m}^{*}+\left(C_{p}\right)_{m}^{*}T'-(h)_{m}^{n}\right\}\\
&+\left(A_{r}\tilde{\Gamma}_{r}\right)_{i,j}^{n+1}-\left(A_{r}\tilde{\Gamma}_{r}\right)_{i-1,j}^{n+1}+\left(A_{z}\tilde{\Gamma}_{z}\right)_{i,j}^{n+1}-\left(A_{z}\tilde{\Gamma}_{z}\right)_{i,j-1}^{n+1}=-\tilde{W}_{j}^{FLOOD}\\
&\quad+\left(A_{r}\tilde{q}_{r}^{*}\tilde{P}_{r}^{*}\right)_{i,j}-\left(A_{r}\tilde{q}_{r}^{*}\tilde{P}_{r}^{*}\right)_{i-1,j}+\left(A_{z}\tilde{q}_{z}^{*}\tilde{P}_{z}^{*}\right)_{i,j}-\left(A_{z}\tilde{q}_{z}^{*}\tilde{P}_{z}^{*}\right)_{i,j-1}\\
&\qquad+Vol^{n}\left[\frac{P^{*}-P^{n}}{\Delta t}+\frac{1}{\varepsilon}\tilde{\Phi}_{L}^{*}-\tilde{P}^{*}\tilde{div}\left(\vec{q}^{*}\right)\right]
\end{aligned}
\tag{4.10}
$$

where Γ_r and Γ_z represent the convection–diffusion enthalpy fluxes across the faces of the mass balance cell (i,j). The power loss term for liquid cell (iL,j), $\tilde{W}_j^{FLOOD}$, accounts for the enthalpy of the excess liquid pooling into the vapor core. The second member of Equation (4.10) is calculated explicitly using the most recent *stared* pressure and velocity fields. The derivatives and divergence term at the mass cell centers which appear in the viscous dissipation Φ_L (see Equation (3.5) are discretized as:

$$
\begin{aligned}
&\left[\frac{\partial q_r}{\partial r}\right]_{i,j}\equiv\frac{q_r^{i,j}-q_r^{i-1,j}}{\Delta R_i}\quad,\quad\left[\frac{\partial q_z}{\partial z}\right]_{i,j}\equiv\frac{q_z^{i,j}-q_z^{i,j-1}}{\Delta Z_j}\quad,\\
&\text{and}\qquad div\left(\vec{q}\right)_{i,j}\equiv\left[\frac{\partial q_r}{\partial r}\right]_{i,j}+\frac{UrCELL_{i,j}}{Rcell_i}+\left[\frac{\partial q_z}{\partial z}\right]_{i,j}\quad.
\end{aligned}
\tag{4.11}
$$

The cross–derivatives at the mass cell centers are approximated using the following second–order accurate formulations:

$$
\left[\frac{\partial q_r}{\partial z}\right]_{i,j}\equiv\frac{\frac{1}{\omega_z^j}\left(UrCELL_{i,j+1}-UrCELL_{i,j}\right)+\omega_z^j\left(UrCELL_{i,j}-UrCELL_{i,j-1}\right)}{\frac{1}{2}\left(1+\omega_z^j\right)\left(\Delta Z_j+\Delta Z_{j-1}\right)},\tag{4.12a}
$$

$$
\left[\frac{\partial q_z}{\partial r}\right]_{i,j}\equiv\frac{\frac{1}{\omega_r^i}\left(UzCELL_{i+1,j}-UzCELL_{i,j}\right)+\omega_r^i\left(UzCELL_{i,j}-UzCELL_{i-1,j}\right)}{\frac{1}{2}\left(1+\omega_r^i\right)\left(\Delta R_i+\Delta R_{i-1}\right)},\tag{4.12b}
$$

$$\text{where} \quad \omega_r^i = \frac{\Delta R_i + \Delta R_{i+1}}{\Delta R_i + \Delta R_{i-1}} \quad \text{and} \quad \omega_z^j = \frac{\Delta Z_j + \Delta Z_{j+1}}{\Delta Z_j + \Delta Z_{j-1}} \quad . \tag{4.12c}$$

Equations (4.12) reduce to the well known centered approximations when the grid is uniform. In the boundary cells, the following one–sided approximations are used:

$$\begin{aligned}
&\left[\frac{\partial q_r}{\partial z}\right]_{i,1} \equiv \frac{UrCELL_{i,1}}{\Delta Z_1 / 2} \quad , \quad \left[\frac{\partial q_r}{\partial z}\right]_{i,Nz} \equiv \frac{-UrCELL_{i,Nz}}{\Delta Z_{Nz} / 2} \quad , \\
&\left[\frac{\partial U_z}{\partial r}\right]_{1,j} \equiv 0 \quad , \quad \left[\frac{\partial U_z}{\partial r}\right]_{Nv,j} \equiv \frac{-UzCELL_{Nv,j}}{\Delta R_{Nv} / 2} \quad , \\
&\left[\frac{\partial q_z}{\partial r}\right]_{iL,j} \equiv \frac{UzCELL_{iL,j}}{\Delta R_{iL} / 2} \quad , \quad \left[\frac{\partial q_z}{\partial r}\right]_{Nl,j} \equiv \frac{-UzCELL_{Nl,j}}{\Delta R_{Nl} / 2} \quad .
\end{aligned} \tag{4.12d}$$

The viscous dissipation term in Equation (4.10) is calculated explicitly as:

$$\Phi_{i,j}^L = 2\mu_L \left\{ \left[\frac{\partial q_r}{\partial r}\right]_{i,j}^2 + \left(\frac{UrCELL_{i,j}}{Rcell_i}\right)^2 + \left[\frac{\partial q_z}{\partial z}\right]_{i,j}^2 + \frac{1}{2}\left[\frac{\partial q_r}{\partial z} + \frac{\partial q_z}{\partial r}\right]_{i,j}^2 - \frac{1}{3}\left[\text{div}(\vec{q})\right]_{i,j}^2 \right\} \tag{4.13}$$

In Equation (3.27), enthalpies were linearized in terms of temperatures using the heat capacities at constant pressure C_p according to Figure 3.8:

$$h^{n+1} = h^* + C_p^* T' \tag{4.14}$$

A very small δT must be used to simulate the phase–change of a pure substance. When δT is small, the γ–T relationship closely approximates a step function (Figure 4.5), and many schemes using the enthalpy formulation have experienced numerical difficulties and predicted wiggly temperature time histories (Beckermann and Viskanta 1988; Cao and Faghri 1990b; Cao and Faghri 1993a). The present numerical solution, however, uses a δT as small as 10^{-8} K (limited by machine accuracy), without under–relaxation of the temperature and numerical instabilities. The transitions between the different phases are recognized and treated as follows:

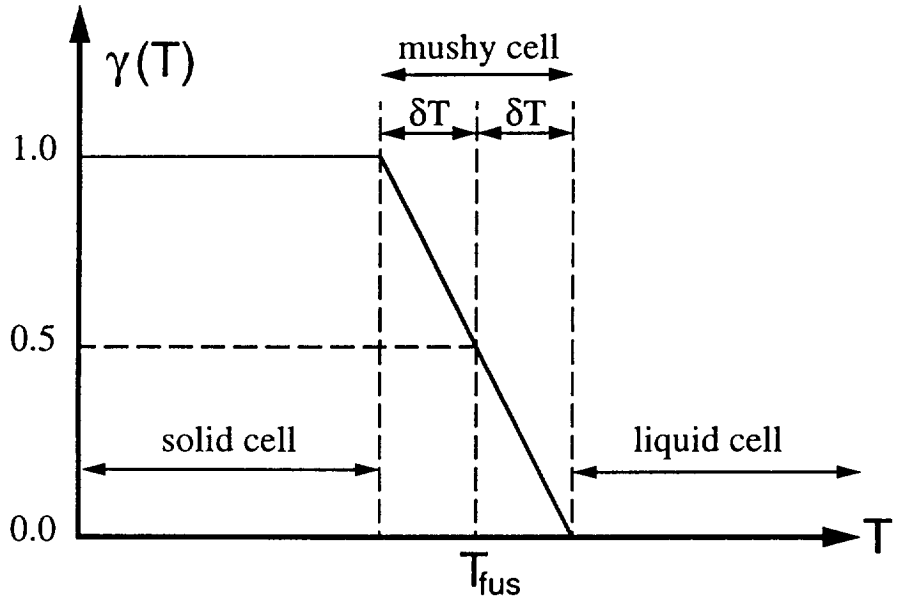

FIGURE 4.5. Variation of the Fluid Frozen Volume Fraction with Temperature.

(a) when the calculated solid fraction $\gamma^* > 1$, the model declares a transition from a mushy to a frozen cell, and sets γ^* and $\partial\gamma/\partial T$ equal to 1 and 0, respectively.

(b) when the calculated solid fraction $\gamma^* < 0$, the model declares a transition from a mushy to a liquid cell, and sets γ^* and $\partial\gamma/\partial T$ both equal to 0.

(c) when $\gamma^* = 1$ and the calculated temperature $T^* \geq (T_{fus} - \delta T)$, the model declares a transition from a frozen to a mushy cell, and sets $T^* = T_{fus} - \delta T$ and $\partial\gamma/\partial T = -1/(2\delta T)$.

(d) when $\gamma^* = 0$ and the calculated temperature $T^* \leq (T_{fus} + \delta T)$, the model declares a transition from a liquid to a mushy cell, and sets $T^* = T_{fus} + \delta T$ and $\partial\gamma/\partial T = -1/(2\delta T)$.

Many numerical schemes have been developed to discretize the convection–diffusion enthalpy fluxes appearing in Equation (4.10), such as central difference, upwind difference, hybrid, exponential, power–law (Patankar 1980) and weighting function (Lee and Tzong 1991) discretization schemes (APPENDIX C-1). The use of the central difference scheme is restricted to the treatment of low Reynolds number flows, because a numerical instability occurs when the convective transport dominates the transport by

diffusion. The upwind and hybrid difference schemes are unconditionally stable, but suffer from severe false numerical diffusion. The exponential sheme developed by Patankar (1980) is applicable to solving equations of conservative form and to the case of uniform thermal conductivity; it is unconditionally stable and performs well in flow regions in which the velocity field aligns closely with the mesh lines. In this scheme, the effects of convection and diffusion are treated separately, and the exponential function is employed to incorporate the effect of fluid flow. To account for the effect of variable thermal conductivity, Patankar (1980) combined the exponential scheme with the harmonic mean scheme. He matched the heat fluxes at the interface between grid cells to obtain the "average" thermal conductivity at this location. Finally, the power–law difference scheme, which is only an approximation of the exponential scheme, reduces the computation time.

The new weighting function scheme of Lee and Tzong (1991) is applicable to both conservative and non–conservative equations and can be implemented on non–uniform grids, an improvement from their former scheme. When applied to the solution of conservation equations, the weighting function scheme reduces to Patankar's exponential scheme in the case of uniform thermal conductivity. A number of higher–order difference schemes (such as QUICK) have been developed also, which have higher accuracy and minimal false numerical diffusion. These schemes, however, are only conditionally stable, more complex to implement, and more CPU time intensive, as they require the solution of unusual nine–point linear systems.

Since heat transfer in the wick is dominated by diffusion, the central difference discretization scheme is appropriate for such a situation and is implemented in the homogeneous enthalpy equation of the present model. By contrast, Cao and Faghri (1990b and 1993a) adopted the upwind difference scheme in their numerical solution, which is unconditionally stable but suffers from severe false numerical diffusion, particularly when heat transfer is dominated by conduction. Therefore, the convection–diffusion enthalpy fluxes Γ_r and Γ_z are expressed as:

$$\begin{aligned}\left(\tilde{\Gamma}_r\right)_{i,j}^{n+1} &= \left(\tilde{G}_r^*\right)_{i,j}\left(h^{n+1}\right)_{i,j}^{r} + \left(Q_r\right)_{i,j}^{n+1}, \\ \left(\tilde{\Gamma}_z\right)_{i,j}^{n+1} &= \left(\tilde{G}_z^*\right)_{i,j}\left(h^{n+1}\right)_{i,j}^{z} + \left(Q_z\right)_{i,j}^{n+1},\end{aligned} \tag{4.15}$$

where the enthalpies are extrapolated at the velocity locations as:

$$\left(h^{n+1}\right)^{r}_{i,j} = \varphi^{i}_{r} h^{n+1}_{i,j} + (1-\varphi^{i}_{r}) h^{n+1}_{i+1,j} \quad ,$$
$$\left(h^{n+1}\right)^{z}_{i,j} = \varphi^{j}_{z} h^{n+1}_{i,j} + (1-\varphi^{j}_{z}) h^{n+1}_{i,j+1} \quad . \tag{4.16}$$

The large numerical error and sometimes poor stability characteristics and convergence rates of existing fixed–grid enthalpy formulations are caused by improper handling of the evolution of the latent heat and discretization of the convection–diffusion enthalpy fluxes appearing in Equation (3.27). The use of the conventional harmonic mean scheme of Patankar (1980) to estimate the heat fluxes at the boundaries of the mushy cell is largely responsible for the loss in accuracy and the generation of wiggly temperature time histories (Lee and Tzong 1991). The larger the change in thermal diffusivity of the working fluid upon melting, the worse are the results. Indeed, the thermal diffusivity of the solid phase is quite different from that of the liquid phase for most materials. For instance, the solid–to–liquid thermal diffusivity ratios (α_S/α_L) for working fluids of common use in heat pipes are 1.60 (lithium), 1.27 (sodium) and 1.85 (potassium). The thermal diffusivity ratio for pure water is as large as 7.45. Because Cao and Faghri (1990b and 1993a) employed the conventional harmonic mean scheme of Patankar (1980) to estimate the heat fluxes at the faces of the control volumes, their numerical scheme suffered from the inaccuracy described above, particularly when they used a small δT. Their model would give reasonable (but inaccurate) front locations and temperature time histories when δT is large, since these authors calculated the thermal conductivity in the mushy cells as a linear function of the solid and liquid thermal conductivities.

The model developed by Raw and Lee (1991) for convection–diffusion change–of–phase problems uses a modified weighting function scheme to handle the sharp viscosity and thermal diffusivity jumps at the liquid–solid interface. Unlike other existing fixed–grid enthalpy formulations, their numerical technique produces smooth streamlines and isotherms, even in the vicinity of the change–of–phase front. However, it is increasingly complex and requires larger computation time. The volume fractions (or dimensionless latent heats) of liquid in the control volumes are related to the node temperatures (or dimensionless sensible heats) in a complex manner when dealing with a two– or three–dimensional problem (Lee and Tzong 1991). This strong coupling necessitates the use of an iterative procedure and a small Successive Over–Relaxation (SOR) factor when solving the discretized enthalpy equations for temperatures.

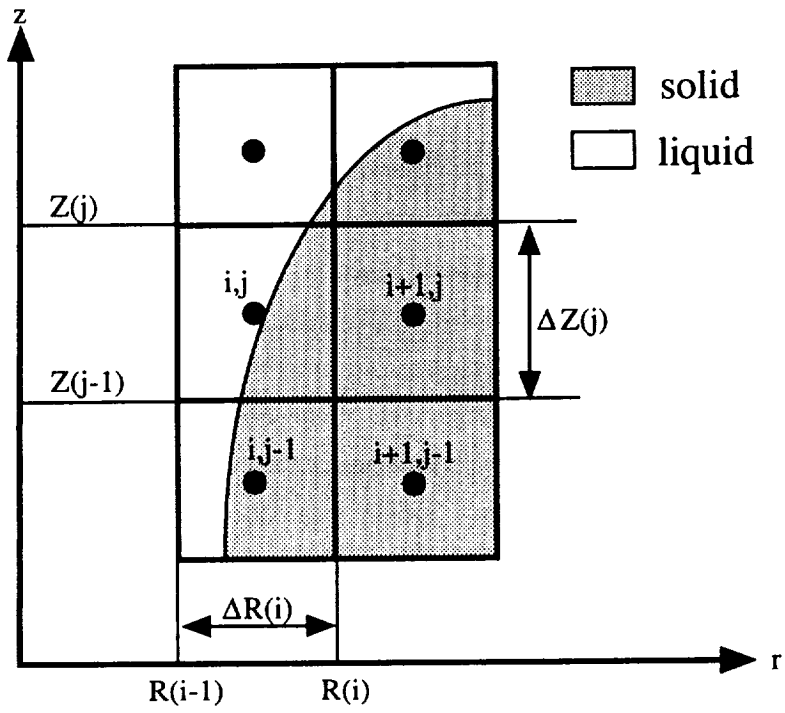

FIGURE 4.6. Numerical Grid Layout in the Vicinity of the Solid–Liquid Interface.

In the present work, a simple method is developed to evaluate the heat fluxes at the boundaries of the mushy cells, based on a one–dimensional analysis estimation of the location of the change–of–phase front. Consider a typical grid layout in the vicinity of the melting front, as depicted in Figure 4.6. The heat fluxes are evaluated at the interfaces of the numerical cells, and the discretization scheme depends on the types of the cells adjacent to the interface (mushy, liquid or solid). Considering the radial heat flux between the mushy cell (i,j) and the monophasic cell (i+1,j) in Figure 4.6, the radius of the melting front, u, is approximated as:

$$u = \sqrt{(1-f)R_{i-1}^2 + f R_i^2} \quad , \tag{4.17a}$$

where

$$f = \left| \gamma_{i,j}^* - \gamma_{i+1,j}^* \right| \quad . \tag{4.17b}$$

The radial heat flux at the interface (i,j) between the cells (i,j) and (i+1,j) is expressed as:

$$Q_r^{i,j} = D_r^{i,j}(T_{i,j} - T_{i+1,j}) \quad , \tag{4.18a}$$

where

$$D_r^{i,j} = \frac{\left(k_{Sm}^{eff}\right)_{i+1,j}}{\Delta R_{i+1}/2 + R_i - u} \quad . \tag{4.18b}$$

The strong dependence of D_r upon $\gamma_{i,j}$ is taken into account by discretizing the heat flux using the following Taylor series:

$$\begin{aligned}(Q_r^{i,j})^{n+1} &= D_r^*(T_{i,j}^* - T_{i+1,j}^*) + D_r^*(T_{i,j}^{'} - T_{i+1,j}^{'}) \\ &+ \frac{\partial D_r}{\partial u}\frac{\partial u}{\partial f}\frac{\partial f}{\partial \gamma_{i,j}}\frac{\partial \gamma_{i,j}^*}{\partial T}(T_{i,j}^* - T_{i+1,j}^*)T_{i,j}^{'}\end{aligned} \tag{4.19a}$$

where the partial derivatives of the right–hand–side of Equation (4.19a) can be expressed as:

$$\begin{aligned}&\frac{\partial D_r}{\partial u} = \frac{D_r^2}{\left(k_{Sm}^{eff}\right)_{i+1,j}}, \quad \frac{\partial u}{\partial f} = \frac{R_i^2 - R_{i-1}^2}{2u}, \quad \text{and} \\ &\frac{\partial f}{\partial \gamma_{i,j}} = 1 \quad \text{when} \quad \gamma_{i+1,j}^* = 0 \quad (f = \gamma_{i,j}^*), \\ &\frac{\partial f}{\partial \gamma_{i,j}} = -1 \quad \text{when} \quad \gamma_{i+1,j}^* = 1 \quad (f = 1 - \gamma_{i,j}^*).\end{aligned} \tag{4.19b}$$

The heat flux in the axial direction between the solid cell (i+1,j) and the mushy cell (i+1,j+1) is calculated in a similar manner. The axial location of the melting front, v, is obtained from:

$$v = (1-g)Z_{j+1} + gZ_j \quad , \tag{4.20a}$$

where

$$g = \left|\gamma_{i+1,j}^* - \gamma_{i+1,j+1}^*\right| \quad . \tag{4.20b}$$

The axial diffusion coefficient, D_z, has the following expression:

$$D_z^{i+1,j} = \frac{\left(k_{Sm}^{eff}\right)_{i+1,j}}{\Delta Z_j / 2 + v - Z_j} \quad . \tag{4.21}$$

Finally, the axial heat flux at the interface (i+1,j) is discretized using the following Taylor series:

$$\begin{aligned}(Q_z^{i+1,j})^{n+1} &= D_z^*(T^*_{i+1,j} - T^*_{i+1,j+1}) + D_z^*(T'_{i+1,j} - T'_{i+1,j+1}) \\ &\quad + \frac{\partial D_z}{\partial v}\frac{\partial v}{\partial g}\frac{\partial g}{\partial \gamma_{i+1,j+1}}\frac{\partial \gamma^*_{i+1,j+1}}{\partial T}(T^*_{i+1,j} - T^*_{i+1,j+1})T'_{i+1,j+1} \quad ,\end{aligned} \tag{4.22a}$$

where

$$\begin{aligned}&\frac{\partial D_z}{\partial v} = -\frac{D_z^2}{\left(k_{Sm}^{eff}\right)_{i+1,j}}, \quad \frac{\partial v}{\partial g} = -\Delta Z_{j+1}, \quad \text{and} \\ &\frac{\partial g}{\partial \gamma_{i+1,j+1}} = 1 \quad \text{when} \quad \gamma^*_{i+1,j} = 0 \quad (g = \gamma^*_{i+1,j+1}), \\ &\frac{\partial g}{\partial \gamma_{i+1,j+1}} = -1 \quad \text{when} \quad \gamma^*_{i+1,j} = 1 \quad (g = 1 - \gamma^*_{i+1,j+1}).\end{aligned} \tag{4.22b}$$

In the two other cases of the heat flux between two monophasic cells, and between two mushy cells, the conventional harmonic mean scheme of Patankar (1980) is used. For example, the axial heat flux between the solid cells (i+1,j) and (i+1,j-1) of Figure 4.6 is discretized as:

$$(Q_z^{i+1,j-1})^{n+1} = D_z^{i+1,j-1}(T^*_{i+1,j-1} - T^*_{i+1,j} + T'_{i+1,j-1} - T'_{i+1,j}) \quad , \tag{4.23a}$$

where the diffusion coefficient, D_z, is given as:

$$D_z^{i+1,j-1} = 2\left[\frac{\Delta Z_j}{\left(k_{Sm}^{eff}\right)_{i+1,j}} + \frac{\Delta Z_{j-1}}{\left(k_{Sm}^{eff}\right)_{i+1,j-1}}\right]^{-1} \quad . \tag{4.23b}$$

The heat flux between the mushy cells (i,j) and (i,j-1) of Figure 4.6 is calculated in a similar manner, except that the effective thermal conductivities of the mushy cells are calculated using the *parallel* model (see APPENDIX A, Equation A–45):

$$k_{i,j}^{eff} = \gamma_{i,j}^{*}(k_{Sm}^{eff})_{i,j} + (1-\gamma_{i,j}^{*})(k_{Lm}^{eff})_{i,j} \quad . \tag{4.24}$$

Similar treatment is applied to the discretization of the heat fluxes at the boundaries of the wick cells. Even though the derived procedure is based on a one–dimensional analysis of the melting front location, it is quite capable of predicting the shape of the liquid–solid interface of truly two–dimensional problems, as will be shown in the solution benchmark section of the thesis (Chapter 5).

4.1.4. Heat balance at the Liquid–Vapor Interface

Making use of the no–slip condition at the L–V interface and neglecting the Marangoni effect, the enthalpy jump condition (3.18a) reduces to:

$$\tilde{\Gamma}_r^V - \tilde{\Gamma}_r^L = \left(\tilde{Q}_r^V + \tilde{\dot{m}}h^V\right) - \left(\tilde{Q}_r^L + \tilde{\dot{m}}h^L\right) = \Delta\tilde{\Gamma}_r \quad , \tag{4.25a}$$

where

$$\Delta\tilde{\Gamma}_r = \left[\frac{1}{(\varepsilon\rho_L)^2} - \frac{1}{\rho_V^2}\right]\frac{\tilde{\dot{m}}^3}{2} \quad + \quad 2\left[\frac{\mu_V}{\rho_V}\frac{\partial U_r^V}{\partial r} - \frac{\mu_L}{\varepsilon\rho_L}\frac{\partial U_r^L}{\partial r}\right]\tilde{\dot{m}} \quad . \tag{4.25b}$$

The conductive fluxes in Equation (4.25a) are discretized as:

$$\begin{aligned} \tilde{Q}_r^V &= D_r^V\left[\tilde{T}_{Nv,j} - \tilde{T}\,int_j\right] \quad , \quad \text{and} \\ \tilde{Q}_r^L &= D_r^L\left[\tilde{T}\,int_j - \tilde{T}_{il,j}\right] \quad , \end{aligned} \tag{4.26a}$$

where the diffusion coefficients are:

$$D_r^V = \frac{2k_{Nv,j}}{\Delta R_{Nv}} \quad , \quad \text{and} \quad D_r^L = \frac{2k_{il,j}}{\Delta R_{il}} \quad . \tag{4.26b}$$

Finally, the enthalpies h^L and h^V in Equation (4.25a) are evaluated explicitly at the saturation temperature of the vapor $Tsat\left(\tilde{P}_v^*\right)$.

4.1.5. Coupling of Enthalpy Jump Condition with the Kinetic Theory Relationship

In the first algorithms tested (Algorithms A and B), the evaporation/condensation mass fluxes in the energy jump condition Equation (4.25a) are evaluated explicitly, from the best available estimates. Because of the sensitivity of the evaporation/condensation rates to the interfacial temperature *Tint*, the stability of the algorithm is enhanced by implicitly coupling the kinetic theory relationship and the energy jump condition in Algorithms HPTAM–PISO and HPTAM–Revised.

The evaporation/condensation mass fluxes are governed by the kinetic theory, Equation (3.23). For convenience, this relation is rewritten here as:

$$\tilde{\dot{m}}_j = \frac{\beta}{\sqrt{\tilde{T}int_j}}\left[\tilde{P}_{Nv,j} - P_{sat}\left(\tilde{T}int_j\right)\right] = \Psi\left(\tilde{T}int_j, \tilde{P}_{Nv,j}\right) \quad , \tag{4.27a}$$

where

$$\beta = a_{cc}\left(\frac{M}{2\pi R_g}\right)^{1/2} . \tag{4.27b}$$

Equation (4.27a) is linearized in terms of the interfacial temperature corrections as:

$$\tilde{\dot{m}}_j^{n+1} \cong \tilde{\dot{m}}_j^* + \alpha\frac{\partial\tilde{\Psi}_j^*}{\partial T int}T int_j' , \tag{4.28a}$$

where

$$\tilde{\dot{m}}_j^* = \Psi\left(\tilde{T}int_j^*, \tilde{P}_{Nv,j}^*\right). \tag{4.28b}$$

and

$$\frac{\partial \tilde{\Psi}_j^*}{\partial T\,int} = -\frac{\beta}{\tilde{T}int_j^*}\left[\frac{dP_{sat}\left(\tilde{T}int_j^*\right)}{dT}\sqrt{\tilde{T}int_j^*} \quad + \quad \frac{\tilde{P}_{Nv,j}^* - P_{sat}\left(\tilde{T}int_j^*\right)}{2\sqrt{\tilde{T}int_j^*}}\right] . \qquad (4.28c)$$

The right–hand side of the enthalpy jump condition Equation (4.25a), a polynom in $\dot{\bar{m}}$, is linearized (the coefficients in squared brackets appearing in Equation 4.25b are evaluated explicitly) as:

$$\Delta\tilde{\Gamma}_r^{n+1} = \Delta_j^{EXP} + \alpha\Delta_j^{IMP}\left[\frac{\partial \tilde{\Psi}_j^*}{\partial T\,int}T\,int_j'\right] \quad , \quad \text{where}$$

$$\Delta_j^{EXP} = \left(COEF_1 + COEF_3\right)\dot{\bar{m}}_j^* \quad , \quad \Delta_j^{IMP} = COEF_1 + 3COEF_3 \quad ,$$

$$COEF_1 = 2\left(\frac{\mu}{\tilde{\rho}}\right)_{Nv,j}^* \frac{\frac{\dot{\tilde{m}}_j^*}{\tilde{\rho}_{Nv,j}^*} - \left(\tilde{U}_r^*\right)_{Nv-1,j}}{\Delta R_{Nv}} + 2\left(\frac{\mu}{\varepsilon\tilde{\rho}}\right)_{iL,j}^* \frac{\frac{\dot{\tilde{m}}_j^*}{\tilde{\rho}_{iL,j}^*} - \left(\tilde{U}_r^*\right)_{Nv+1,j}}{\Delta R_{iL}}, \qquad (4.29)$$

$$\text{and} \quad COEF_3 = \left[\frac{1}{\left(\varepsilon\tilde{\rho}_{iL,j}^*\right)^2} - \frac{1}{\left(\tilde{\rho}_{Nv,j}^*\right)^2}\right]\frac{\left(\dot{\bar{m}}_j^*\right)^2}{2} \quad .$$

The enthalpy jump condition (4.25a) is implicitly discretized and rewritten as:

$$\tilde{\Gamma}_r^V - \tilde{\Gamma}_r^L = \left(\tilde{Q}_r^V + \dot{\tilde{\bar{m}}}h^V\right)^{n+1} - \left(\tilde{Q}_r^L + \dot{\tilde{\bar{m}}}h^L\right)^{n+1} = \Delta\tilde{\Gamma}_r^{n+1} \quad , \qquad (4.30)$$

By using Equations (4.26a) and (4.28a), the radial energy fluxes at the L–V interface are discretized as:

$$\tilde{\Gamma}_r^V = \left[\dot{\bar{m}}_j^* + \alpha\left(\frac{\partial \tilde{\Psi}_j^*}{\partial T\,int}T\,int_j'\right)\right]h_j^V + D_r^V\left[\tilde{T}_{Nv,j}^* - \tilde{T}int_j^*\right] + \alpha D_r^V\left[T_{Nv,j}' - T\,int_j'\right] \quad ,$$

$$\tilde{\Gamma}_r^L = \left[\dot{\bar{m}}_j^* + \alpha\left(\frac{\partial \tilde{\Psi}_j^*}{\partial T\,int}T\,int_j'\right)\right]h_j^L + D_r^L\left[\tilde{T}int_j^* - \tilde{T}_{iL,j}^* \quad\right] + \alpha D_r^L\left[T\,int_j' - T_{iL,j}' \quad\right] \quad . \qquad (4.31)$$

The substitution of Equations (4.29) and (4.31) into Equation (4.30) allows to express the liquid interfacial temperature corrections in terms of temperature corrections for the mass cells as:

$$\alpha T\,int'_j = AINT_j\left[\alpha T'_{iL,j}\right] + BINT_j\left[\alpha T'_{Nv,j}\right] + CINT_j \quad , \quad \text{where}$$

$$AINT_j = \frac{D_r^L}{DINT_j} \quad , \quad BINT_j = \frac{D_r^V}{DINT_j} \quad ,$$

$$CINT_j = \frac{1}{DINT_j}\left[\dot{\bar{m}}_j^*\left(h_j^V - h_j^L\right) + D_r^V\left(\tilde{T}^*_{Nv,j} - \tilde{T}\,int_j^*\right) + D_r^L\left(\tilde{T}^*_{iL,j} - \tilde{T}\,int_j^*\right) - \Delta_j^{EXP}\right] \quad , \tag{4.32}$$

$$\text{and} \qquad DINT_j = D_r^L + D_r^V - \frac{\partial\tilde{\Psi}_j^*}{\partial T\,int}\left(h_j^V - h_j^L - \Delta_j^{IMP}\right) \quad .$$

Equation (4.32) is used to eliminate the interfacial temperature corrections in Equations (4.31), so that finally the radial energy fluxes at the L–V interface can be expressed in terms of temperature corrections for the mass cells only as:

$$\left(\tilde{\Gamma}_r^V\right)_j^{n+1} = AINT_j^V\left[\alpha T'_{iL,j}\right] + BINT_j^V\left[\alpha T'_{Nv,j}\right] + CINT_j^V \quad ,$$

$$\left(\tilde{\Gamma}_r^L\right)_j^{n+1} = AINT_j^L\left[\alpha T'_{iL,j}\right] + BINT_j^L\left[\alpha T'_{Nv,j}\right] + CINT_j^L \quad , \quad \text{where}$$

$$AINT_j^V = \left[h_j^V\frac{\partial\tilde{\Psi}_j^*}{\partial T\,int} - D_r^V\right]AINT_j \quad , \quad BINT_j^V = \left[h_j^V\frac{\partial\tilde{\Psi}_j^*}{\partial T\,int} - D_r^V\right]BINT_j + D_r^V \quad ,$$

$$CINT_j^V = \left[h_j^V\frac{\partial\tilde{\Psi}_j^*}{\partial T\,int} - D_r^V\right]CINT_j + \dot{\bar{m}}_j^* h_j^V + D_r^V\left(\tilde{T}^*_{Nv,j} - \tilde{T}\,int_j^*\right) \quad ,$$

$$AINT_j^L = \left[h_j^L\frac{\partial\tilde{\Psi}_j^*}{\partial T int} + D_r^L\right]AINT_j - D_r^L \quad , \quad BINT_j^L = \left[h_j^L\frac{\partial\tilde{\Psi}_j^*}{\partial T int} + D_r^L\right]BINT_j \quad , \tag{4.33}$$

$$CINT_j^L = \left[h_j^L\frac{\partial\tilde{\Psi}_j^*}{\partial T int} + D_r^L\right]CINT_j + \dot{\bar{m}}_j^* h_j^L + D_r^L\left(\tilde{T}\,int_j^* - \tilde{T}^*_{iL,j}\right) \quad .$$

Finally, the interfacial convection–diffusion energy fluxes in the discretized enthalpy conservation Equation (4.10) are expressed as:

$$\begin{aligned} &\left(\tilde{\Gamma}_r\right)_{Nv,j}^{n+1} = \left(\tilde{\Gamma}_r^V\right)_j^{n+1} \quad \text{for the mass cell } (Nv, j), \text{ and} \\ &\left(\tilde{\Gamma}_r\right)_{Nv,j}^{n+1} = \left(\tilde{\Gamma}_r^L\right)_j^{n+1} \quad \text{for the mass cell } (il, j)\,. \end{aligned} \tag{4.34}$$

Note that in the model the vapor is assumed to be saturated so that there is no need to solve the energy conservation in the vapor region. In that case, the radial conduction flux in the vapor is neglected in the interfacial enthalpy jump condition (Equation 4.30), which results in zero BINT, $BINT^V$ and $BINT^L$ coefficients. From Equation (4.33), it can be seen that the interfacial convection–diffusion energy flux on the wick side becomes an implicit function of the wick cell temperature correction only.

4.1.6. Modeling of the Condenser Cooling Jacket

For the case of a condenser cooled with a water jacket, a column of cells (i=Nr+1) is added to model the water flow in the jacket (Figure 4.1b), which extends from (j=Nadia+1) to (j=Nz). The flow enters the jacket with a constant mass flow rate $\dot{\bar{M}}^J$ and temperature Tin^J. Properties of the cooling water (density ρ^J, heat capacity C_p^J and thermal conductivity k^J) are assumed to be constant. For a cooling water cell (i=Nr+1), the discretized Equation (4.10) reduces to the following form (the jacket is thermally insulated externally):

$$\frac{Vol_{i,j}}{\Delta t}\left(\rho C_p\right)_{i,j}^{J}\left(T_{i,j}^{n+1}-T_{i,j}^{n}\right)-\left(A_r\tilde{\Gamma}_r\right)_{i-1,j}^{n+1}+\left(A_z\tilde{\Gamma}_z\right)_{i,j}^{n+1}-\left(A_z\tilde{\Gamma}_z\right)_{i,j-1}^{n+1}=0. \quad (4.35)$$

Introducing the convective heat transfer coefficient H^J and the jacket inner wall temperature T^W, the radial energy flux at the inner wall can be expressed as:

$$\left(\tilde{\Gamma}_r\right)_{Nr,j}^{n+1}=\left(\tilde{Q}_r\right)_{Nr,j}^{n+1}=k_{Nr,j}\frac{\tilde{T}_{Nr,j}-\tilde{T}_j^W}{\Delta R_{Nr}/2}=H_j^J\left(\tilde{T}_j^W-\tilde{T}_{i,j}\right) \quad . \quad (4.36)$$

The equality in Equation (4.36) is used to eliminate T^W in the radial energy flux so that:

$$\left(\tilde{\Gamma}_r\right)_{Nr,j}^{n+1}=\left(\frac{\Delta R_{Nr}}{2k_{Nr,j}}+\frac{1}{H_j^J}\right)^{-1}\left[\tilde{T}_{i-1,j}^{n+1}-\tilde{T}_{i,j}^{n+1}\right] \quad . \quad (4.37)$$

Since heat transfer along the cooling jacket is dominated by convection, the convection–diffusion energy fluxes Γ_z across the faces of the jacket cells are discretized using the upwind difference scheme (Patankar 1980) as:

$$\left(A_z\tilde{\Gamma}_z\right)_{i,j}^{n+1} \equiv \dot{\bar{m}}^J\tilde{h} - A_z k\frac{\partial\tilde{T}}{\partial z} \equiv \dot{\bar{m}}^J\left[\left(h^J\right)_{i,j}^{*} + \alpha C_p^J T_{i,j}^{'}\right] + A_z^{i,j} D_z^{i,j}\left[\tilde{T}_{i,j}^{n+1} - \tilde{T}_{i,j+1}^{n+1}\right], \quad (4.38a)$$

where the diffusion coefficients are defined as:

$$D_z^{i,j} = \frac{2k^J}{\Delta Z_j + \Delta Z_{j+1}} \quad . \quad (4.38b)$$

At the entrance of the cooling jacket, the axial energy flux is expressed as:

$$\left(A_z\tilde{\Gamma}_z\right)_{i,Nadia}^{n+1} \equiv \dot{\bar{m}}^J\tilde{h} - A_z k\frac{\partial\tilde{T}}{\partial z} \equiv \dot{\bar{m}}^J h^J(Tin^J) + A_z^i D_z^{i,Nadia}\left[Tin^J - \tilde{T}_{i,Nadia+1}^{n+1}\right], \quad (4.39a)$$

where the diffusion coefficient at the entrance is:

$$D_z^{i,Nadia} = \frac{k^J}{\Delta Z_{Nadia+1}/2} \quad . \quad (4.39b)$$

Finally, the axial energy flux at the exit of the cooling jacket is expressed as:

$$\left(A_z\tilde{\Gamma}_z\right)_{i,Nz}^{n+1} \equiv \dot{\bar{m}}^J\tilde{h} \equiv \dot{\bar{m}}^J\left[\left(h^J\right)_{i,Nz}^{*} + \alpha C_p^J T_{i,Nz}^{'}\right] . \quad (4.40)$$

4.1.7. Thermal Boundary Conditions at the Walls

In the case of a cylindrical heat pipe, the vapor centerline boundary (r=0) is a line of symmetry. Also, the heat pipe end caps, z=0, and z=Z(Nz), are thermally insulated (Figure 4.1a), so that:

$$\left(\tilde{\Gamma}_r\right)_{0,j}^{n+1} = 0 \quad , \quad \text{and} \quad \left(\tilde{\Gamma}_z\right)_{i,0}^{n+1} = \left(\tilde{\Gamma}_z\right)_{i,Nz}^{n+1} = 0 \quad . \quad (4.41)$$

The radial wall boundary condition (IV) delineated in Figure (3.1) can be either isoflux, isothermal, radiative or convective, and is applied independently in the evaporator, adiabatic section and condenser. In this subsection, i=Nr and ΔX stands for $\Delta R_i/2$. The radial energy flux leaving the wall cell (i,j) by conduction can be expressed in terms of the outer wall temperature T^W, as:

$$\left(\tilde{\Gamma}_r\right)_{i,j}^{n+1} = k_{i,j}\frac{\tilde{T}_{i,j}^{n+1} - \tilde{T}_j^W}{\Delta X} \quad . \tag{4.42}$$

a. Isoflux thermal boundary condition

In the case of a given radial thermal energy flux, $\left(\tilde{\Gamma}_r\right)_{i,j}^{n+1}$ is simply equated to its specified (explicit) value.

b. Isothermal boundary condition

In the case of a given outer wall temperature T^W, Equation (4.42) is used as it is to express the radial thermal energy flux.

c. Radiative boundary condition

In the case of a radiative boundary condition, we have formally:

$$\left(\tilde{\Gamma}_r\right)_{i,j}^{n+1} = k_{i,j}\frac{\tilde{T}_{i,j}^{n+1} - \tilde{T}_j^W}{\Delta X} = (\sigma\varepsilon F)_{rad}\left[\left(\tilde{T}_j^W\right)^4 - T_{sp}^4\right] \quad . \tag{4.43}$$

In order to eliminate T^W in the radial energy flux, we must linearize the right–hand side of Equation (4.43). Because of good thermal conductivity of the container metallic material, the temperature drop across the wall is relatively small, so that we can write:

$$\delta\tilde{T} \equiv \tilde{T}_{i,j} - \tilde{T}_j^W \langle\langle \tilde{T}_{i,j} \quad . \tag{4.44}$$

To a first approximation, this gives:

$$\left(\tilde{T}_j^W\right)^4 = \left(\tilde{T}_{i,j} - \delta\tilde{T}\right)^4 = \left(\tilde{T}_{i,j}\right)^4\left(1 - \frac{\delta\tilde{T}}{\tilde{T}_{i,j}}\right)^4 \cong \left(\tilde{T}_{i,j}\right)^4\left(1 - 4\frac{\delta\tilde{T}}{\tilde{T}_{i,j}}\right) \quad . \tag{4.45}$$

If this approximation (Equation 4.45) is used to eliminate the fourth power of the wall temperature in Equation (4.43), we find that:

$$\left[\frac{k_{i,j}}{\Delta X}+4\tilde{T}_{i,j}^{3}(\sigma\varepsilon F)_{rad}\right]\delta\tilde{T}=(\sigma\varepsilon F)_{rad}\left[\tilde{T}_{i,j}^{4}-T_{sp}^{4}\right] \quad , \tag{4.46}$$

so that the radial energy flux at the wall can be expressed as:

$$(\Gamma_r)_{i,j}^{n+1}=\left[\frac{1}{(\sigma\varepsilon F)_{rad}}+4\frac{\Delta X}{k_{i,j}}\tilde{T}_{i,j}^{3}\right]^{-1}\left[\tilde{T}_{i,j}^{4}-T_{sp}^{4}\right] \quad , \tag{4.47}$$

Equation (4.47) is linearized around the best estimate $\tilde{T}_{i,j}^{*}$ in terms of temperature corrections:

$$(\Gamma_r)_{i,j}^{n+1}=\frac{\tilde{T}_{i,j}^{*4}-T_{sp}^{4}}{DENOM^{*}}+\left[DENOM^{*}\tilde{T}_{i,j}^{*}-3\frac{\Delta X}{k_{i,j}}\left(\tilde{T}_{i,j}^{*4}-T_{sp}^{4}\right)\right]\left(\frac{2\tilde{T}_{i,j}^{*}}{DENOM^{*}}\right)^{2}\left[\alpha T_{i,j}^{'}\right], \tag{4.48}$$

where $\quad DENOM^{*}=\dfrac{1}{(\sigma\varepsilon F)_{rad}}+4\dfrac{\Delta X}{k_{i,j}}\tilde{T}_{i,j}^{*3} \quad .$

Finally, the energy conservation discretized Equations (4.10) can be written in terms of the mass cell temperature corrections in the following form:

$$aP_{i,j}^{T}T_{i,j}^{'}+aE_{i,j}^{T}T_{i+1,j}^{'}+aW_{i,j}^{T}T_{i-1,j}^{'}+aN_{i,j}^{T}T_{i,j+1}^{'}+aS_{i,j}^{T}T_{i,j-1}^{'}=S_{i,j}^{T} \quad , \tag{4.49}$$

for i=1 to NrMAX, and j=1 to Nz (NrMAX=Nr+1 for the case of a condenser cooling jacket, Nr otherwise). We obtain by construction:

$$\begin{aligned}
&aW_{1,j}^{T}=aN_{i,Nz}^{T}=aS_{i,1}^{T}=0 \quad ,\\
&aE_{NrMAX,j}^{T}=0 \quad \text{for} \quad j=Nadia+1 \quad \text{to} \quad Nz \, ,\\
&aE_{Nr,j}^{T} \quad =0 \quad \text{for} \quad j=1 \quad \text{to} \quad Nadia \, , \quad \text{and}\\
&aS_{Nr+1,Nadia+1}^{T}=0 \quad \text{for a cooling jacket} \quad .
\end{aligned} \tag{4.50}$$

Equations (4.49) are solved for mass cell temperature corrections using the very efficient iterative Strongly–Implicit–Solver (SIS) (see Section 4.3). The interfacial temperature corrections are then computed from Equations (4.32), and the new tilted evaporation/condensation rates are obtained from Equation (4.28).

4.1.8. Radial Momentum Conservation Equations

After multiplying Equations (3.2) by the porosity ε, integration of these equations leads to the following discretized form:

$$\begin{aligned}&\frac{Vol_r}{\Delta t}\left[\rho_r^* U_r^{n+1} - \rho_r^n U_r^n\right] \;+\; DIAG_R^{i,j}\tilde{U}_r^{n+1} \\ &+\left(B_r\tilde{\Gamma}_{Rr}\right)_{i+1,j}^{n+1} - \left(B_r\tilde{\Gamma}_{Rr}\right)_{i,j}^{n+1} + \left(B_z\tilde{\Gamma}_{Rz}\right)_{i,j}^{n+1} - \left(B_z\tilde{\Gamma}_{Rz}\right)_{i,j-1}^{n+1} = EXPL_R^{i,j},\end{aligned} \tag{4.51}$$

where

$$EXPL_R^{i,j} = \varepsilon Vol_r\left[\tilde{\rho}_r^* F_r - \frac{\tilde{P}_{i+1,j}^* - \tilde{P}_{i,j}^*}{(\Delta R_{i+1} + \Delta R_i)/2}\right] - \frac{2}{3}Vol_r\frac{\left[\mu\tilde{div}(\vec{U})\right]_{i+1,j}^* - \left[\mu\tilde{div}(\vec{U})\right]_{i,j}^*}{(\Delta R_{i+1} + \Delta R_i)/2}$$
$$+B_z^j\left[\mu_{VRTX}^{i,j}\frac{\tilde{U}_z^{i+1,j} - \tilde{U}_z^{i,j}}{(\Delta R_{i+1} + \Delta R_i)/2} - \mu_{VRTX}^{i,j-1}\frac{\tilde{U}_z^{i+1,j-1} - \tilde{U}_z^{i,j-1}}{(\Delta R_{i+1} + \Delta R_i)/2}\right],$$

and

$$DIAG_R^{i,j} = \varepsilon Vol_r\left[\frac{\mu_r}{K_r} + \frac{C}{\sqrt{K_r}}\left|\tilde{\vec{G}}^*\right|_r^{i,j}\right] + 2\mu_r\left(\iiint_{Vol_r}\frac{dV}{r^2}\right), \quad \text{with}$$

$$\iiint_{Vol_r}\frac{dV}{r^2} = 2\pi\int_{Z_{j-1}}^{Z_j} dz\int_{Rcell_i}^{Rcell_{i+1}}\frac{dr}{r} = \left(2\pi\Delta Z_j\right)Log_e\frac{Rcell_{i+1}}{Rcell_i}\quad .$$

The magnitude of the mass flux at the radial velocity location (i,j) is consistently extrapolated as:

$$\left|\tilde{\vec{G}}^*\right|_r^{i,j} = \sqrt{\left[\tilde{G}_r^*\right]_{i,j}^2 + \left[\varphi_r^i\left(\tilde{G}_{Zz}^*\right)_{i,j} + \left(1-\varphi_r^i\right)\left(\tilde{G}_{Zz}^*\right)_{i+1,j}\right]^2}\quad . \tag{4.52}$$

At the velocity locations, the dynamic viscosities are extrapolated as follows:

$$\mu_r^{i,j} = \frac{\Delta R_i + \Delta R_{i+1}}{\dfrac{\Delta R_i}{\mu_{i,j}} + \dfrac{\Delta R_{i+1}}{\mu_{i+1,j}}}\quad , \quad \text{and} \quad \mu_z^{i,j} = \frac{\Delta Z_j + \Delta Z_{j+1}}{\dfrac{\Delta Z_j}{\mu_{i,j}} + \dfrac{\Delta Z_{j+1}}{\mu_{i,j+1}}}\quad . \tag{4.53}$$

The dynamic viscosities at the grid vertices are given by:

$$\mu_{VRTX}^{i,j} = \frac{\Delta Z_j + \Delta Z_{j+1}}{\dfrac{\Delta Z_j}{\mu_r^{i,j}} + \dfrac{\Delta Z_{j+1}}{\mu_r^{i,j+1}}} \quad \text{inside the domain, while}$$

$$\mu_{VRTX}^{i,0} = \mu_r^{i,1}\,, \quad \mu_{VRTX}^{i,Nz} = \mu_r^{i,Nz}\,, \quad \mu_{VRTX}^{Nl,j} = \mu_z^{Nl,j}\,, \tag{4.54}$$

$$\text{and} \quad \mu_{VRTX}^{0,j} = 0 \quad \text{on the grid boundaries.}$$

The last identity holds for a cylindrical heat pipe since there is no shear stress along the vapor centerline (symmetry axis).

It has been long known that, though not detected by von Neumann stability analysis, a behavior very much characteristic of numerical instability can occur if the choice of grid spacing permits the convective transport to dominate the diffusive one (early fluid codes were limited to low Reynolds numbers). This physical implausibility has been identified by Patankar and Spalding (Patankar 1980) as the positiveness of non–diagonal coefficients of the matrix. The same authors refer to their proposed remedy as a *high lateral flux* correction. While the much used donor cell representation is numerically dissipative, the high lateral flux correction is derived from the exact solution of a theoretical steady–state one–dimensional flow with constant properties, and is physically more satisfactory (see APPENDIX C–1). In this work, the convection–diffusion momentum fluxes Γ_{Rr} and Γ_{Rz} across the faces of the radial momentum control volumes are discretized implicitly using the power law approximation of the exponential scheme of Patankar (1980) as:

$$\left(\tilde{\Gamma}_{Rr}\right)_{i,j}^{n+1} \equiv \frac{1}{\varepsilon} G_r \tilde{U}_r - 2\mu \frac{\partial \tilde{U}_r}{\partial r} \equiv \frac{1}{\varepsilon}\left(\tilde{G}_{Rr}^{*}\right)_{i,j}\left[\tilde{U}_r^{i-1,j}\right]^{n+1} + \mathrm{FPAT}\left(\mathrm{Pe}_{Rr}^{i,j}\right) D_{Rr}^{i,j}\left[\tilde{U}_r^{i-1,j} - \tilde{U}_r^{i,j}\right]^{n+1},$$

$$\left(\tilde{\Gamma}_{Rz}\right)_{i,j}^{n+1} \equiv \frac{1}{\varepsilon} G_z \tilde{U}_r - \mu \frac{\partial \tilde{U}_r}{\partial z} \equiv \frac{1}{\varepsilon}\left(\tilde{G}_{Rz}^{*}\right)_{i,j}\left[\tilde{U}_r^{i,j}\right]^{n+1} + \mathrm{FPAT}\left(\mathrm{Pe}_{Rz}^{i,j}\right) D_{Rz}^{i,j}\left[\tilde{U}_r^{i,j} - \tilde{U}_r^{i,j+1}\right]^{n+1},$$

where the diffusion and Peclet coefficients are defined as:

$$D_{Rr}^{i,j} = \frac{2\mu_{i,j}}{\Delta R_i} \quad , \qquad \mathrm{Pe}_{Rr}^{i,j} = \frac{1}{\varepsilon}\frac{\left(\tilde{G}_{Rr}^{*}\right)_{i,j}}{D_{Rr}^{i,j}} \quad , \qquad \text{and}$$

$$D_{Rz}^{i,j} = \frac{\mu_{VRTX}^{i,j}}{\left(\Delta Z_j + \Delta Z_{j+1}\right)/2} \quad , \qquad \mathrm{Pe}_{Rz}^{i,j} = \frac{1}{\varepsilon}\frac{\left(\tilde{G}_{Rz}^{*}\right)_{i,j}}{D_{Rz}^{i,j}} \quad . \tag{4.55}$$

The function FPAT has the form (Patankar 1980):

$$FPAT(Pe) = \frac{Pe}{e^{Pe} - 1} \cong MAX\left\{0, \left(1 - \frac{|Pe|}{10}\right)^5\right\} + MAX\{0, -Pe\} \quad . \tag{4.56}$$

Along the axial boundaries of the domain, the convection–diffusion momentum fluxes Γ_{Rz} have the following form:

$$\begin{aligned} \left(\tilde{\Gamma}_{Rz}\right)_{i,0}^{n+1} &\equiv -\ \mu \frac{\partial \tilde{U}_r}{\partial z} \equiv -\mu_{VRTX}^{i,0} \frac{\left[\tilde{U}_r^{i,1}\right]^{n+1} - 0}{\Delta Z_1 / 2} = -D_{Rz}^{i,0}\left[\tilde{U}_r^{i,1}\right]^{n+1}, \\ \left(\tilde{\Gamma}_{Rz}\right)_{i,Nz}^{n+1} &\equiv -\ \mu \frac{\partial \tilde{U}_r}{\partial z} \equiv -\mu_{VRTX}^{i,Nz} \frac{0 - \left[\tilde{U}_r^{i,Nz}\right]^{n+1}}{\Delta Z_{Nz} / 2} = D_{Rz}^{i,Nz}\left[\tilde{U}_r^{i,Nz}\right]^{n+1} . \end{aligned} \tag{4.57}$$

The form of the radial momentum conservation equations in the vapor region is identical to that in the wick region where the volume porosity, ε, is taken as one, and the radial permeability, K_r, is infinite. Finally, the discretized form of the radial momentum conservation Equations (4.51) is written in terms of the radial velocity corrections in the following form:

$$aP_{i,j}^r\left(U_r'\right)_{i,j} + aE_{i,j}^r\left(U_r'\right)_{i+1,j} + aW_{i,j}^r\left(U_r'\right)_{i-1,j} + aN_{i,j}^r\left(U_r'\right)_{i,j+1} + aS_{i,j}^r\left(U_r'\right)_{i,j-1} = S_{i,j}^r \ , \tag{4.58}$$

for i=1 to Nv-1, i=iL to NL-1 and j=1 to Nz. Note that Equation (4.58) does not apply at the L–V interface (i=Nv). At this particular location, the evaporation/condensation rates are governed by the kinetic theory of gases, Equation (3.23). However, the interfacial radial velocity corrections appear in equations (4.58) and must be treated correctly. Of course, we have by construction:

$$aE_{Nl-1,j}^r = aW_{l,j}^r = aN_{i,Nz}^r = aS_{i,l}^r = 0 \quad . \tag{4.59}$$

During the radial momentum predictor step, Equations (4.58) are solved for the radial velocity corrections. In this case, the interfacial radial velocity corrections are evaluated

explicitly, using best available estimates. After computation of the radial velocity corrections, the radial mass fluxes are updated using the following corrections:

$$G_r' = \rho_r^* U_r' \quad . \tag{4.60}$$

4.1.9. Axial Momentum Conservation Equations

After multiplying Equations (3.4) by the porosity ε, integration of these equations leads to the following discretized form:

$$\begin{aligned} &\frac{Vol_z}{\Delta t}\left[\rho_z^* U_z^{n+1} - \rho_z^n U_z^n\right] \quad + \quad DIAG_Z^{i,j}\tilde{U}_z^{n+1} \\ &+\left(X_r\tilde{\Gamma}_{Zr}\right)_{i,j}^{n+1} - \left(X_r\tilde{\Gamma}_{Zr}\right)_{i-1,j}^{n+1} + \left(A_z\tilde{\Gamma}_{Zz}\right)_{i,j+1}^{n+1} - \left(A_z\tilde{\Gamma}_{Zz}\right)_{i,j}^{n+1} = EXPL_Z^{i,j} \end{aligned} \quad , \tag{4.61}$$

where

$$EXPL_Z^{i,j} = \varepsilon Vol_z\left[\tilde{\rho}_z^* F_z - \frac{\tilde{P}_{i,j+1}^* - \tilde{P}_{i,j}^*}{\left(\Delta Z_{j+1} + \Delta Z_j\right)/2}\right] - \frac{2}{3} Vol_z \frac{\left[\mu \tilde{div}\left(\vec{U}\right)\right]_{i,j+1}^* - \left[\mu \tilde{div}\left(\vec{U}\right)\right]_{i,j}^*}{\left(\Delta Z_{j+1} + \Delta Z_j\right)/2}$$

$$+\left[X_r^{i,j}\mu_{VRTX}^{i,j}\frac{\tilde{U}_r^{i,j+1} - \tilde{U}_r^{i,j}}{\left(\Delta Z_{j+1} + \Delta Z_j\right)/2} - X_r^{i-1,j}\mu_{VRTX}^{i-1,j}\frac{\tilde{U}_r^{i-1,j+1} - \tilde{U}_r^{i-1,j}}{\left(\Delta Z_{j+1} + \Delta Z_j\right)/2}\right], \quad \text{and}$$

$$DIAG_Z^{i,j} = \varepsilon Vol_z\left[\frac{\mu_z}{K_z} + \frac{C}{\sqrt{K_z}}\left|\vec{\tilde{G}}^*\right|_z^{i,j}\right] \quad .$$

The magnitude of the mass flux at the axial velocity location (i,j) is consistently extrapolated as:

$$\left|\vec{\tilde{G}}^*\right|_z^{i,j} = \sqrt{\left[\tilde{G}_z^*\right]_{i,j}^2 + \left[\varphi_z^j\left(\tilde{G}_{Rr}^*\right)_{i,j} + \left(1-\varphi_z^j\right)\left(\tilde{G}_{Rr}^*\right)_{i,j+1}\right]^2} \quad . \tag{4.62}$$

The convection–diffusion momentum fluxes Γ_{Zr} and Γ_{Zz} across the faces of the axial momentum control volumes are discretized using the power law approximation of the exponential scheme of Patankar (1980) as:

$$\left(\tilde{\Gamma}_{Zr}\right)_{i,j}^{n+1} \equiv \frac{1}{\varepsilon} G_r \tilde{U}_z - \mu \frac{\partial \tilde{U}_z}{\partial r} \equiv \frac{1}{\varepsilon}\left(\tilde{G}^*_{Zr}\right)_{i,j}\left[\tilde{U}_z^{i,j}\right]^{n+1} + FPAT\left(Pe_{Zr}^{i,j}\right) D_{Zr}^{i,j}\left[\tilde{U}_z^{i,j} - \tilde{U}_z^{i+1,j}\right]^{n+1},$$

$$\left(\tilde{\Gamma}_{Zz}\right)_{i,j}^{n+1} \equiv \frac{1}{\varepsilon} G_z \tilde{U}_z - 2\mu \frac{\partial \tilde{U}_z}{\partial z} \equiv \frac{1}{\varepsilon}\left(\tilde{G}^*_{Zz}\right)_{i,j}\left[\tilde{U}_z^{i,j-1}\right]^{n+1} + FPAT\left(Pe_{Zz}^{i,j}\right) D_{Zz}^{i,j}\left[\tilde{U}_z^{i,j-1} - \tilde{U}_z^{i,j}\right]^{n+1}, \tag{4.63a}$$

where the diffusion and Peclet coefficients are defined as:

$$D_{Zr}^{i,j} = \frac{\mu_{VRTX}^{i,j}}{\left(\Delta R_i + \Delta R_{i+1}\right)/2}, \qquad Pe_{Zr}^{i,j} = \frac{1}{\varepsilon}\frac{\left(\tilde{G}^*_{Zr}\right)_{i,j}}{D_{Zr}^{i,j}}, \qquad \text{and}$$

$$D_{Zz}^{i,j} = \frac{2\mu_{i,j}}{\Delta Z_j}, \qquad Pe_{Zz}^{i,j} = \frac{1}{\varepsilon}\frac{\left(\tilde{G}^*_{Zz}\right)_{i,j}}{D_{Zz}^{i,j}}. \tag{4.63b}$$

Along the radial boundaries of the domain, the convection–diffusion momentum fluxes Γ_{Zr} have the following form:

$$\left(\tilde{\Gamma}_{Zr}\right)_{0,j}^{n+1} \equiv -\mu \frac{\partial \tilde{U}_z}{\partial r} \equiv -\mu_{VRTX}^{0,j} \frac{\left[\tilde{U}_z^{1,j}\right]^{n+1} - 0}{\Delta R_1 / 2} = -D_{Zr}^{0,j}\left[\tilde{U}_z^{1,j}\right]^{n+1},$$

$$\left(\tilde{\Gamma}_{Zr}\right)_{Nl,j}^{n+1} \equiv -\mu \frac{\partial \tilde{U}_z}{\partial r} \equiv -\mu_{VRTX}^{Nl,j} \frac{0 - \left[\tilde{U}_z^{Nl,j}\right]^{n+1}}{\Delta R_{Nl} / 2} = D_{Zr}^{Nl,j}\left[\tilde{U}_z^{Nl,j}\right]^{n+1}. \tag{4.64}$$

The form of the axial momentum conservation equations in the vapor region is identical to that in the wick region where the volume porosity, ε, is taken as one, and the axial permeability, K_z, is infinite. At the L–V interface, the flux Γ_{Zr} has different expressions on the vapor and liquid side. The interface is assimilated to a wall axially (no–slip condition), but the radial mass transfer must be accounted for. The fluxes Γ_{Zr} have the following expressions at the L–V interface:

$$\left(\tilde{\Gamma}_{Zr}^{L}\right)_{Nv,j}^{n+1} \equiv \left[\frac{1}{\varepsilon} G_r \tilde{U}_z - \mu \frac{\partial \tilde{U}_z}{\partial r}\right]_{int}^{L}$$
$$= \frac{1}{\varepsilon}\left(\tilde{G}^*_{Zr}\right)_{Nv,j}\left[\tilde{U}_z^{iL,j}\right]^{n+1} - FPAT\left(Pe_{Zr}^{L,j}\right) D_{Zr}^{L,j}\left[\tilde{U}_z^{iL,j} - 0\right]^{n+1}, \tag{4.65a}$$

$$\left(\tilde{\Gamma}_{Zr}^{V}\right)_{Nv,j}^{n+1} \equiv \left[G_r \tilde{U}_z - \mu \frac{\partial \tilde{U}_z}{\partial r} \right]_{int}^{V} \qquad (4.65b)$$

$$= \left(\tilde{G}_{Zr}^{*}\right)_{Nv,j} \left[\tilde{U}_z^{Nv,j}\right]^{n+1} - FPAT\left(Pe_{Zr}^{V,j}\right) D_{Zr}^{V,j} \left[0 - \tilde{U}_z^{Nv,j}\right]^{n+1},$$

where the interfacial diffusion and Peclet coefficients are defined as:

$$D_{Zr}^{L,j} = \frac{\mu_z^{iL,j}}{\Delta R_{iL}/2} \quad , \qquad Pe_{Zr}^{L,j} = -\frac{1}{\varepsilon} \frac{\left(\tilde{G}_{Zr}^{*}\right)_{Nv,j}}{D_{Zr}^{L,j}} \quad , \qquad \text{and}$$

$$D_{Zr}^{V,j} = \frac{\mu_z^{Nv,j}}{\Delta R_{Nv}/2} \quad , \qquad Pe_{Zr}^{V,j} = \frac{\left(\tilde{G}_{Zr}^{*}\right)_{Nv,j}}{D_{Zr}^{V,j}} \quad . \qquad (4.65c)$$

Finally, the discretized form of the axial momentum conservation Equations (4.61) can be written in terms of the axial velocity corrections in the form:

$$aP_{i,j}^{z}\left(U_z^{'}\right)_{i,j} + aE_{i,j}^{z}\left(U_z^{'}\right)_{i+1,j} + aW_{i,j}^{z}\left(U_z^{'}\right)_{i-1,j} + aN_{i,j}^{z}\left(U_z^{'}\right)_{i,j+1} + aS_{i,j}^{z}\left(U_z^{'}\right)_{i,j-1} = S_{i,j}^{z} \quad , \qquad (4.66)$$

for i=1 to NL and j=1 to Nz-1. Note that the vapor (i=1 to Nv) and liquid (i=iL=Nv+1 to NL) regions are decoupled since we assumed a no–slip condition at the L–V interface (Equation 3.17). We have by construction:

$$aE_{Nv,j}^{z} = aW_{iL,j}^{z} = 0 \,, \quad \text{and}$$
$$aE_{Nl,j}^{z} = aW_{1,j}^{z} = aN_{i,Nz-1}^{z} = aS_{i,1}^{z} = 0 \quad . \qquad (4.67)$$

During the axial momentum predictor step, Equations (4.66) are solved for the axial velocity corrections. Then, the axial mass fluxes are updated using the following corrections:

$$G_z^{'} = \rho_z^{*} U_z^{'} \quad . \qquad (4.68)$$

4.1.10. Mass Conservation Equations

The solution of the mass balance equations is the most essential step for resolving the pressure–density–velocity couplings in the liquid and vapor regions. A combination of the continuity equations and of an approximation of the momentum conservation equations is used to formulate the Poisson equation, which is solved for the pressure corrections. The discretized forms of the radial and axial momentum conservation Equations (4.58) and (4.66) are derived as described in the previous sections, using the most recent updates of the new–time pressure and velocity fields. It is apparent that solution of these equations leads to the correct new–time velocity field only if the pressure field is correct. Since it is not usually the case, the velocity and pressure fields are corrected simultaneously so as to satisfy the following momentum correction equations:

$$aP^r_{i,j}\left(U'_r\right)_{i,j} + aE^r_{i,j}\left(U'_r\right)_{i+1,j} + aW^r_{i,j}\left(U'_r\right)_{i-1,j} + aN^r_{i,j}\left(U'_r\right)_{i,j+1} + aS^r_{i,j}\left(U'_r\right)_{i,j-1}$$
$$= S^r_{i,j} - \varepsilon_i \theta \mathrm{Vol}^{i,j}_r \frac{P'_{i+1,j} - P'_{i,j}}{\left(\Delta R_{i+1} + \Delta R_i\right)/2} \quad , \tag{4.69a}$$

$$aP^z_{i,j}\left(U'_z\right)_{i,j} + aE^z_{i,j}\left(U'_z\right)_{i+1,j} + aW^z_{i,j}\left(U'_z\right)_{i-1,j} + aN^z_{i,j}\left(U'_z\right)_{i,j+1} + aS^z_{i,j}\left(U'_z\right)_{i,j-1}$$
$$= S^z_{i,j} - \varepsilon_i \theta \mathrm{Vol}^{i,j}_z \frac{P'_{i,j+1} - P'_{i,j}}{\left(\Delta Z_{j+1} + \Delta Z_j\right)/2} \quad . \tag{4.69b}$$

The local volume porosity, ε_i, has been introduced into Equations (4.69) so that the form of these equations applies to both the vapor region and the liquid–wick region. The local volume porosity, ε_i, is simply defined as:

$$\begin{aligned} &\varepsilon_i = 1 \quad \text{if} \quad i \le Nv \qquad \text{(vapor region)}, \\ &\varepsilon_i = \varepsilon \quad \text{if} \quad i \ge iL = Nv + 1 \quad \text{(wick region)}. \end{aligned} \tag{4.70}$$

In order to form a pentadiagonal Poisson equation and avoid costly matrix inversions, the off–diagonal velocity corrections in Equations (4.69) must be eliminated. In the SIMPLE algorithm, these corrections are neglected. This approximation is used in Algorithms A and B. The SIMPLEC (SIMPLE–Consistent) procedure of van Doormaal and Raithby (1984) assumes that the off–diagonal corrections are equal to the diagonal correction. This is a consistent approximation of the momentum correction equations, which does not require

any pressure under–relaxation (APPENDIX C-5). When diffusion and convection phenomena are dominated by pressure gradients and source terms, the consistent approximation in SIMPLEC becomes exact, and hence this procedure should be used. Furthermore, SIMPLEC performs as well or better than SIMPLER in terms of CPU time and storage requirement. Indeed, when the SIMPLEC approximation was used in the third Algorithm HPTAM–PISO in place of the SIMPLE approximation, it resulted in greater numerical stability and much faster convergence rates. Therefore, the SIMPLEC approximation was selected for Algorithm HPTAM–PISO. The SIMPLEC–approximated momentum correction equations take the following form:

$$\left[aP^r_{i,j} + aE^r_{i,j} + aW^r_{i,j} + aN^r_{i,j} + aS^r_{i,j}\right]\left(U'_r\right)_{i,j} = S^r_{i,j} - \varepsilon_i \theta Vol^{i,j}_r \frac{P'_{i+1,j} - P'_{i,j}}{\left(\Delta R_{i+1} + \Delta R_i\right)/2} \quad , \quad (4.71a)$$

$$\left[aP^z_{i,j} + aE^z_{i,j} + aW^z_{i,j} + aN^z_{i,j} + aS^z_{i,j}\right]\left(U'_z\right)_{i,j} = S^z_{i,j} - \varepsilon_i \theta Vol^{i,j}_z \frac{P'_{i,j+1} - P'_{i,j}}{\left(\Delta Z_{j+1} + \Delta Z_j\right)/2} \quad . \quad (4.71b)$$

The velocity and mass flux corrections are related by:

$$G'_r = \rho^*_r U'_r \quad \text{and} \quad G'_z = \rho^*_z U'_z \quad . \quad (4.72)$$

At the L–V interface, the liquid and vapor radial velocity corrections are expressed in terms of the evaporation/condensation mass flux corrections as:

$$\left(U'_r\right)^L_{Nv,j} = \frac{\left(G'_r\right)_{Nv,j}}{\rho^*_{Nv+1,j}} \quad \text{and} \quad \left(U'_r\right)^V_{Nv,j} = \frac{\left(G'_r\right)_{Nv,j}}{\rho^*_{Nv,j}} \quad . \quad (4.73)$$

When solving the continuity equations, the evaporation/condensation mass flux corrections can be either neglected (as in Algorithms A and B), or written implicitly in terms of vapor pressure corrections using the kinetic theory relationship (Equation 4.27a), as it is done in Algorithms HPTAM–PISO and HPTAM–Revised. In this case, Equation (4.27a) is linearized as:

$$\left(\tilde{G}^{n+1}_r\right)_{Nv,j} \equiv \tilde{\dot{m}}^{n+1}_j = \left(\tilde{G}^*_r\right)_{Nv,j} + \psi\left(G'_r\right)_{Nv,j} = \dot{m}^*_j + \theta \frac{\partial \tilde{\Psi}^*_j}{\partial P_{Nv}} P'_{Nv,j} \, , \quad (4.74a)$$

where

$$\left(\tilde{G}_r^*\right)_{Nv,j} = \dot{\tilde{m}}_j^* = \Psi\left(\tilde{T}int_j^*, \tilde{P}_{Nv,j}^*\right) \quad , \tag{4.74b}$$

and

$$\left(G_r^{'}\right)_{Nv,j} = \frac{\theta}{\psi}\frac{\partial\tilde{\Psi}_j^*}{\partial P_{Nv}} P_{Nv,j}^{'} = \frac{\theta}{\psi}\frac{\beta}{\sqrt{\tilde{T}int_j^*}} P_{Nv,j}^{'} \quad . \tag{4.74c}$$

It is worth noting that the interfacial radial velocity corrections appear in the momentum correction Equations (4.69) for the radial momentum cells (i=Nv-1) and (i=Nv+1). Because the evaporation/condensation rates are governed by the kinetic theory of gases, we found that a consistent approximation (Equation 4.71) causes relatively slow convergence rates when it is used in the iterative Algorithm HPTAM–PISO. To remedy this problem, Equations (4.73) and (4.74) can be used to implicitly evaluate the interfacial radial velocity corrections in the radial momentum correction equations (i=Nv-1). The SIMPLE–Consistent approximation is used for the other off–diagonal radial velocity corrections. In the radial momentum correction equations (i=Nv+1), the interfacial radial velocity corrections are evaluated explicitly, after the pressure corrections in the vapor region have been calculated using the following formulation:

(a) for i=Nv-1

$$\left[aP_{i,j}^r + aW_{i,j}^r + aN_{i,j}^r + aS_{i,j}^r\right]\left(U_r^{'}\right)_{i,j} =$$
$$S_{i,j}^r - \theta Vol_r^{i,j}\frac{P_{i+1,j}^{'} - P_{i,j}^{'}}{(\Delta R_{i+1} + \Delta R_i)/2} - \frac{\theta}{\psi}\frac{aE_{i,j}^r}{\rho_{Nv,j}^*}\frac{\partial\tilde{\Psi}_j^*}{\partial P_{Nv}} P_{i+1,j}^{'} \tag{4.75a}$$

(b) for i=Nv+1

$$\left[aP_{i,j}^r + aE_{i,j}^r + aN_{i,j}^r + aS_{i,j}^r\right]\left(U_r^{'}\right)_{i,j} =$$
$$S_{i,j}^r - \varepsilon\theta Vol_r^{i,j}\frac{P_{i+1,j}^{'} - P_{i,j}^{'}}{(\Delta R_{i+1} + \Delta R_i)/2} - aW_{i,j}^r\left(U_r^{'}\right)_{Nv,j}^L \, . \tag{4.75b}$$

Indeed, when this procedure was used in HPTAM–Revised, in place of the SIMPLEC approximation, it resulted in faster convergence rate and greater numerical stability. Therefore, this SIMPLEC–corrected procedure was selected for Algorithm HPTAM–Revised.

Now that the radial and axial mass flux corrections $G_r^{'}$ and $G_z^{'}$ are related to the pressure corrections by the momentum corrections equations, the mass balance Equation (3.1) can be integrated as:

$$\begin{aligned} &\frac{\varepsilon_i}{\Delta t}\left[(\rho Vol)_{i,j}^{n+1}-(\rho Vol)_{i,j}^{n}\right] \;-\; \tilde{m}_j^{INJECT} \\ &+\left(A_r\tilde{G}_r\right)_{i,j}^{n+1}-\left(A_r\tilde{G}_r\right)_{i-1,j}^{n+1}+\left(A_z\tilde{G}_z\right)_{i,j}^{n+1}-\left(A_z\tilde{G}_z\right)_{i,j-1}^{n+1}=0\,, \end{aligned} \qquad (4.76)$$

where $\tilde{m}_j^{INJECT}$ is the mass injection source for the liquid mass cells (iL,j). This term is used later in modeling the liquid pooling phenomena.

The transient term is linearized using the Taylor series linearization. The resulting equation can be written as:

$$\begin{aligned} &\frac{\varepsilon_i}{\Delta t}\left[Vol_{i,j}^{*}\left(\rho^{*}+\rho^{'}\right)_{i,j}+\rho_{i,j}^{*}Vol_{i,j}^{'}\right] \\ &+\;\psi\left[\left(A_r\tilde{G}_r^{'}\right)_{i,j}-\left(A_r\tilde{G}_r^{'}\right)_{i-1,j}+\left(A_z\tilde{G}_z^{'}\right)_{i,j}-\left(A_z\tilde{G}_z^{'}\right)_{i,j-1}\right] \\ &=-\left[\left(A_r\tilde{G}_r^{*}\right)_{i,j}-\left(A_r\tilde{G}_r^{*}\right)_{i-1,j}+\left(A_z\tilde{G}_z^{*}\right)_{i,j}-\left(A_z\tilde{G}_z^{*}\right)_{i,j-1}\right]+\tilde{m}_j^{INJECT}. \end{aligned} \qquad (4.77)$$

The equations of state are linearized to express the density corrections in terms of the pressure corrections as:

$$\begin{aligned} &\rho_{i,j}^{n+1}=\rho_{i,j}^{*}+\rho_{i,j}^{'}=\rho_{i,j}^{*}+\left(\frac{\partial\rho}{\partial P}\right)_T^{*}P_{i,j}^{'} \quad , \quad \text{where} \\ &\rho_{i,j}^{*}=\rho\left(P_{i,j}^{*},T_{i,j}^{*}\right) \quad \text{and} \quad \left(\frac{\partial\rho}{\partial P}\right)_T^{*}=\left(\frac{\partial\rho}{\partial P}\right)_T\left(P_{i,j}^{*},T_{i,j}^{*}\right) \quad . \end{aligned} \qquad (4.78)$$

The volumes of the mass cells are kept fixed (independent of time), except those adjacent to the L–V interface (Equations 3.20–3.22). In the case of a concave liquid meniscus, there is some vapor in the wick, and the change in the liquid and vapor volumes adjacent to the L–V interface due to the variation of the cosinus of contact angle can be expressed in terms of the wick void fraction as:

$$\varepsilon \mathrm{Vol}'_{iL,j} = -V_p^j\left(\alpha'_p\right)_j \quad , \tag{4.79a}$$

$$\mathrm{Vol}'_{Nv,j} = V_p^j\left(\alpha'_p\right)_j \quad . \tag{4.79b}$$

The wick void fraction is geometrically related to the cosine of contact angle of the liquid meniscus through Equation (3.21). This equation (technically its approximation, Equation 3.22) is linearized to express the wick void fraction corrections in terms of the cosine of contact angle corrections as:

$$\left(\alpha_p^{n+1}\right)_j = \left(\alpha_p^*\right)_j + \left(\alpha'_p\right)_j = \left(\alpha_p^*\right)_j + \left(\frac{\partial \alpha_p}{\partial \mu_c}\right)_j^* \left(\mu'_c\right)_j \quad , \tag{4.80a}$$

where

$$\left(\alpha_p^*\right)_j = \alpha_p\left(\mu_c^*\right)_j \, , \quad \text{and} \quad \left(\frac{\partial \alpha_p}{\partial \mu_c}\right)_j^* = \left(\frac{\partial \alpha_p}{\partial \mu_c}\right)\left(\mu_c^*\right)_j \quad . \tag{4.80b}$$

The radial momentum jump condition, Equation (3.15), is used to relate the wick void fraction to the pressure corrections. This relationship is implicitly discretized as:

$$\begin{aligned} &\left(\tilde{P}_L^{n+1} - \tilde{P}_V^{n+1}\right) + 2\frac{\sigma}{R_p}\tilde{\mu}_c^{n+1} + \left(\frac{1}{\varepsilon\tilde{\rho}_L^*} - \frac{1}{\tilde{\rho}_V^*}\right)\left(\tilde{\dot{m}}^{n+1}\right)^2 \\ &= 2\left[\mu_L \frac{\partial \tilde{U}_r^L}{\partial r} - \mu_V \frac{\partial \tilde{U}_r^V}{\partial r}\right]^* - \frac{2}{3}\left[\mu_L \, \mathrm{div}\left(\tilde{\vec{U}}^L\right) - \mu_V \, \mathrm{div}\left(\tilde{\vec{U}}^V\right)\right]^* . \end{aligned} \tag{4.81}$$

After linearization of the square of the evaporation/condensation rate, Equation (4.81) relates the corrections of the cosine of contact angle of the liquid meniscus, μ_c', to the pressure corrections and evaporation/condensation rate corrections as:

$$\begin{aligned} &\left(\tilde{P}_{iL,j}^* - \tilde{P}_{Nv,j}^*\right) + 2\frac{\sigma_j}{R_p}\left(\tilde{\mu}_c^*\right)_j + \theta\left[\left(P'_{iL,j} - P'_{Nv,j}\right) + 2\frac{\sigma_j}{R_p}\left(\mu'_c\right)_j\right] \\ &+ \left(\frac{1}{\varepsilon\tilde{\rho}_{iL,j}^*} - \frac{1}{\tilde{\rho}_{Nv,j}^*}\right)\tilde{\dot{m}}_j^*\left[\tilde{\dot{m}}_j^* + 2\psi\left(G'_r\right)_{Nv,j}\right] = \mathrm{EXPL}_{int}^j \, , \end{aligned} \tag{4.82a}$$

where

$$EXPL^{j}_{int} = -2\frac{\mu_{iL,j}}{\Delta R_{iL}}\left[\frac{\tilde{\dot{m}}^{*}_{j}}{\tilde{\rho}^{*}_{iL,j}} - \left(\tilde{U}^{*}_{r}\right)_{Nv+1,j}\right] - 2\frac{\mu_{Nv,j}}{\Delta R_{Nv}}\left[\frac{\tilde{\dot{m}}^{*}_{j}}{\tilde{\rho}^{*}_{Nv,j}} - \left(\tilde{U}^{*}_{r}\right)_{Nv-1,j}\right] - \frac{2}{3}\left\{\left[\mu\,\tilde{div}\left(\vec{U}\right)\right]^{*}_{iL,j} - \left[\mu\,\tilde{div}\left(\vec{U}\right)\right]^{*}_{Nv,j}\right\} \quad . \tag{4.82b}$$

Finally, Equation (4.74) is used to eliminate the evaporation/condensation rate corrections in terms of the vapor pressure corrections, which gives:

$$2\frac{\sigma_j}{R_p}\theta\left(\mu_c^{'}\right)_j = \left(COEF^{j}_{int}\right)\theta P^{'}_{Nv,j} - \theta P^{'}_{iL,j} + JUMP^{j}_{int}\,, \quad \text{with}$$

$$COEF^{j}_{int} = 1 - \left(\frac{1}{\varepsilon\tilde{\rho}^{*}_{iL,j}} - \frac{1}{\tilde{\rho}^{*}_{Nv,j}}\right)\frac{2\beta\tilde{\dot{m}}^{*}_{j}}{\sqrt{\tilde{T}int^{*}}}\,, \quad \text{and} \tag{4.83}$$

$$JUMP^{j}_{int} = EXPL^{j}_{int} - \left[\left(\tilde{P}^{*}_{iL,j} - \tilde{P}^{*}_{Nv,j}\right) + 2\frac{\sigma_j}{R_p}\left(\tilde{\mu}^{*}_{c}\right)_j\right] - \left(\frac{1}{\varepsilon\tilde{\rho}^{*}_{iL,j}} - \frac{1}{\tilde{\rho}^{*}_{Nv,j}}\right)\left[\tilde{\dot{m}}^{*}_{j}\right]^{2} \quad .$$

In Equation (4.82) it is apparent that the radial momentum jump source term $JUMP_{int}$ goes to zero upon convergence of the new–time fields.

Finally, by substituting Equations (4.80) and (4.83) into Equations (4.79), the corrections of the liquid and vapor volumes adjacent to the L–V interface can be expressed implicitly as linear functions of the pressure corrections as:

$$\varepsilon Vol^{'}_{iL,j} = -V^{j}_{p}\left(\frac{\partial\alpha_p}{\partial\mu_c}\right)^{*}_{j}\frac{R_p}{2\sigma_j}\left[COEF^{j}_{int}P^{'}_{Nv,j} - P^{'}_{iL,j} + \frac{1}{\theta}JUMP^{j}_{int}\right],$$

$$Vol^{'}_{Nv,j} = V^{j}_{p}\left(\frac{\partial\alpha_p}{\partial\mu_c}\right)^{*}_{j}\frac{R_p}{2\sigma_j}\left[COEF^{j}_{int}P^{'}_{Nv,j} - P^{'}_{iL,j} + \frac{1}{\theta}JUMP^{j}_{int}\right]. \tag{4.84}$$

Now it is possible to express all mass flux corrections and advanced–time volumes and densities in terms of pressure corrections, so that the discretized mass balance Equation (4.77) reduces to the following Poisson equation:

$$aP^{\rho}_{i,j}\left(P^{'}\right)_{i,j} + aE^{\rho}_{i,j}\left(P^{'}\right)_{i+1,j} + aW^{\rho}_{i,j}\left(P^{'}\right)_{i-1,j} + aN^{\rho}_{i,j}\left(P^{'}\right)_{i,j+1} + aS^{\rho}_{i,j}\left(P^{'}\right)_{i,j-1} = S^{\rho}_{i,j} + \tilde{m}^{INJECT}_{j},$$

(4.85)

for i=1 to NL and j=1 to Nz.

We have by construction: $$aE^{\rho}_{Nl,j} = aW^{\rho}_{1,j} = aN^{\rho}_{i,Nz} = aS^{\rho}_{i,1} = 0 \quad , \tag{4.86}$$

since the normal velocity components cancel on all solid boundaries and symmetry axis (r=0 for a cylindrical heat pipe). The Poisson Equations (4.85) are solved for the pressure corrections using a direct banded Gauss–elimination solver (with normalization and partial pivoting). The use of the SIS iterative solver of Lee has proven to be very inefficient for this type of elliptic linear system, even with strong relaxation (see Section 4.3).

At this point, it is useful to make the following observation. Since the evaporation/ condensation rate corrections are functions of the vapor pressure corrections only (see Equation 4.74), the Poisson equations in the vapor cells are coupled to the liquid pressure corrections only through the implicit discretization of the volumes of the vapor cells (i=Nv) (Equation 4.79b, or 4.84), as it is done in Algorithm A. This coupling, however, introduces a non–dominant component to the Poisson linear system, which is responsible for the poor stability characteristics of Algorithm A. Fortunately, the coupling in question is found to be particularly weak because the volume of vapor in the wick is a very small fraction of the vapor core volume, and represents an insignificant fraction of the working fluid inventory in the heat pipe. Therefore, it is very advantageous to evaluate the volumes of vapor cells adjacent to the L–V interface (i=Nv) explicitly in the mass balance equations. This is accomplished in Algorithms B, HPTAM–PISO and HPTAM–Revised by replacing Equation (4.79b) with the following equation:

$$Vol'_{Nv,j} = 0 \quad . \tag{4.87}$$

While this simplification does not affect the accuracy of the solution, it permits decoupling the Poisson equations in the vapor and liquid regions ($aE^{\rho}_{Nv,j} = 0$), hence increasing the stability of the algorithm, and reducing the amount of CPU time (the CPU time required to solve a system of NLxNz linear equations with the banded Gauss–elimination solver is proportional to $NL^{2.67}$x Nz). The saving in the CPU time is particularly evident when internal iterations are needed for the convergence of the mass injection rates, $\tilde{m}_j^{FLOOD}$ to account for pooling of excess liquid.

Now, the new algorithm is as follows. The Poisson Equations (4.85) are solved in the vapor region (i=1 to Nv, and j=1 to Nz) for the vapor pressure corrections. Then the evaporation/condensation rate corrections are calculated using Equations (4.74), and the radial interfacial liquid velocity corrections appearing in Equations (4.75b) can be evaluated from Equations (4.73). At this point, the Poisson Equations (4.85) are discretized in the liquid region (i=iL to NL, and j=1 to Nz). In the equations for the liquid cells adjacent to the L–V interface (i=iL), the vapor pressure corrections are known and treated explicitly:

$$aP^{\rho}_{i,j}\left(P'\right)_{i,j} + aE^{\rho}_{i,j}\left(P'\right)_{i+1,j} + aN^{\rho}_{i,j}\left(P'\right)_{i,j+1} + aS^{\rho}_{i,j}\left(P'\right)_{i,j-1} = S^{\rho}_{i,j} - aW^{\rho}_{i,j}\left(P'\right)_{Nv,j} + \tilde{\dot{m}}^{INJECT}_{j} . \tag{4.88}$$

Once the liquid pressure corrections are obtained, the corrections in the cosine of contact angle, μ_c', are calculated from the radial momentum jump condition, Equation (4.83), and the advanced–time tilted cosines of contact angle are obtained as:

$$\tilde{\mu}_c^{n+1} = \tilde{\mu}_c^{*} + \theta\mu_c' \quad . \tag{4.89}$$

4.1.11. Vapor–Wick Interfacial Model

During the startup of heat pipe from a frozen state, several interfacial conditions may occur at the wick–vapor interface, such as: solid–vapor interface sustaining sublimation or resolidification of working fluid, liquid film on a frozen substrate in the vapor core, liquid–vapor interface sustaining evaporation or condensation of working fluid and a concave liquid meniscus in the wick, and a receded liquid–vapor interface in the wick sustaining maximum capillary pressure head. The way the model recognizes and treats these different interfacial conditions is described in this subsection. First, we introduce the radial location of the liquid– / solid– vapor interface, R_{int}. The volumes of the frozen and liquid phases in the interfacial wick cell (iL,j) are given respectively as:

$$Vol_S^{iL,j} = \gamma_{iL,j} Vol_{LS}^{iL,j} , \quad \text{and} \quad Vol_L^{iL,j} = (1-\gamma_{iL,j}) Vol_{LS}^{iL,j} , \tag{4.90a}$$

where

$$Vol_{LS}^{iL,j} = \varepsilon\pi\left[(R_{wk} + \Delta R_{iL})^2 - (R_{int}^j)^2\right]\Delta Z_j - \alpha_p^j V_p^j , \quad \text{when } R_{int}^j \geq R_{wk} , \tag{4.90b}$$

$$Vol_{LS}^{iL,j} = \varepsilon\pi\left[(R_{wk} + \Delta R_{iL})^2 - R_{wk}^2\right]\Delta Z_j + \pi\left[R_{wk}^2 - (R_{int}^j)^2\right]\Delta Z_j - \alpha_p^j V_p^j, \quad \text{when } R_{int}^j < R_{wk}. \tag{4.90c}$$

In a partially thawed wick, there are three different axial regions: (a) a fully–thawed region, with $R_{int}^j \geq R_{wk}$; (b) a liquid film on a frozen substrate, extending from $j=N_{mush}$ to $j=N_{last}$; and (c) a solid region, whose radius $R_{int}^j < R_{wk}$ (Figure 4.7).

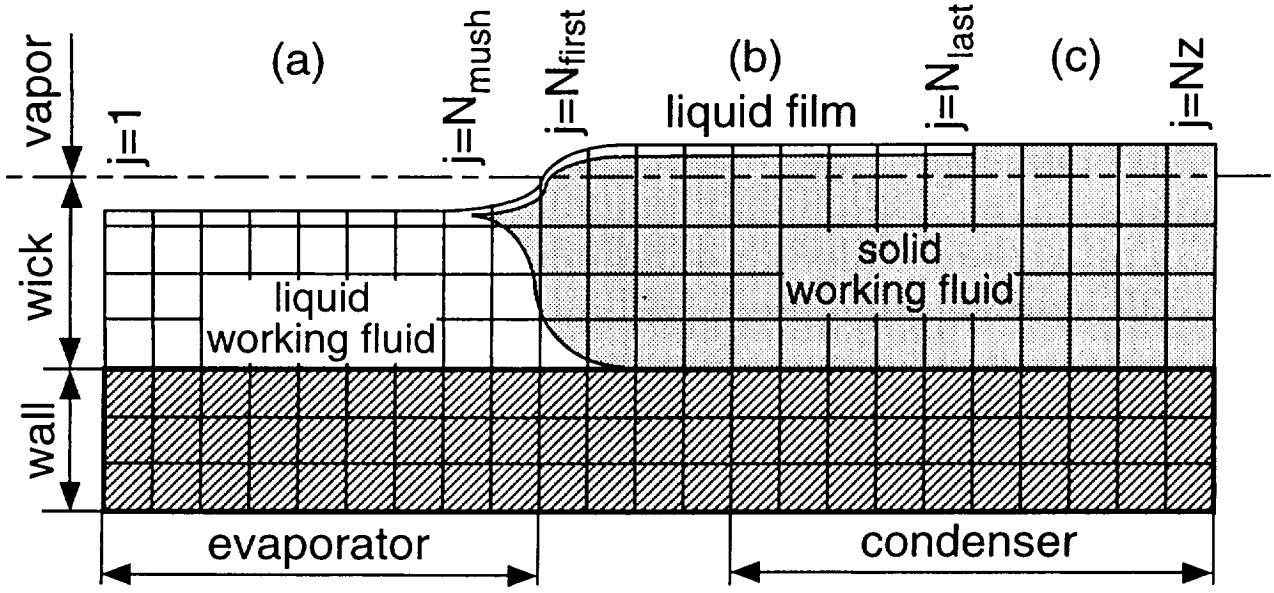

FIGURE 4.7. Numerical Grid Layout of Heat Pipe Wick During Startup from a Frozen State.

The liquid film thickness is determined based on calculated liquid volume fractions in the interfacial wick cells. In the transition zone between regions (a) and (b) (Figure 4.7), the interfacial cells incorporate liquid film at the top, intermediate solid, and liquid substrate ($j=N_{mush}$ to $j=N_{first}-1$); in these cells the model does not differentiate between the liquid film at the top and the liquid substrate. Therefore, to estimate the thickness of the liquid film in these interfacial cells, the film thickness is assumed the same as that calculated in the first cell incorporating only liquid film on a solid substrate ($j=N_{first}$).

In region (a) of Figure 4.7, the liquid and vapor phases are coupled through the momentum jump condition (or capillary relationship), using Equations (4.82)–(4.84). When the calculated cosine of contact angle is greater than 1, which is a sign of recessing liquid in the

wick, the maximum capillary pressure head is assumed, by using Equation (4.82) with a radius of curvature, R_c, equal to the effective pore radius of the wick, R_p (in that case, α_p and μ_c are unity). The mass balance in the interfacial cell is then used to determine the radial location of the liquid level, R_{int}, in the wick. This treatment is also applied to the liquid film ($j \le N_{last}$) where $R_{int}^j \ge R_{wk}$.

In region (b) of Figure 4.7 where $R_{int}^j < R_{wk}$, the coupling between the vapor and liquid film is treated the same as in region (a), except that the L–V interface is flat; thus Equation (4.82) is used with an infinite radius of curvature (in that case, α_p and μ_c are zero). The mass balance in the interfacial cell is then used to determine the location of the vapor–film interface, R_{int}. The film thickness depends on the rate of condensation at the L–V interface, rate of liquid drainage from the film in region (a), and melting rate at the L–S interface of the substrate. The liquid film thickness is used to determine the radial thermal resistance of the film and the drag between the film and the solid substrate. The flow in the liquid film is treated as a one–dimensional flow with a non–slip boundary condition at the L–S interface and a slip boundary condition at the L–V interface.

Finally, in the interfacial wick cells in region (c) of Figure 4.7, which extends from $j=N_{last}+1$ to $j=N_z$, the solid substrate temperature is below the triple point, causing the vapor to resolidify at the S–V interface. The radius of the S–V interface, R_{int}, is determined from the mass balance in the interfacial cells.

4.1.12. Liquid Pooling Submodel

Whenever the cosines of the contact angles are positive, the L–V interface is concave and the interfacial phenomena are treated as described in the previous sections, 4.1.10 and 4.1.11. However, as discussed in Section 3.6, it is possible that the interfacial shear and the thermal expansion of the liquid phase cause the concave liquid meniscus at the L–V interface to rise and flatten at some *wet point* (j) along the heat pipe. Such a condition is recognized by the numerical scheme as:

$$\left(\tilde{\mu}_c^{n+1}\right)_j \le 0 \quad . \tag{4.91}$$

The submodel incorporated into HPTAM to handle liquid–pooling phenomena assumes that as the transient progresses in time, any excess liquid into the vapor core is swept by the

vapor flow towards the end of the condenser, leaving a flat interface and filling up the eventual concave menisci on its way. The flag WET_j is introduced to specify whether the liquid cell (iL,j) is wet (pooling) or not:

$$\begin{aligned} WET_j &= 0 \quad \text{if} \quad \left(\tilde{\mu}_c^{n+1}\right)_j > 0 \quad , \\ WET_j &= 1 \quad \text{if} \quad \left(\tilde{\mu}_c^{n+1}\right)_j \le 0 \quad . \end{aligned} \tag{4.92}$$

Also, jMIN and jMAX stand for the first and last wet liquid cells (iL,j), respectively. Wherever a convex liquid meniscus forms in the heat pipe (WET_j=1), the interface is assumed flat at this particular location, by forcing the cosine of contact angle correction equal to:

$$\left(\mu_c'\right)_j = -\frac{1}{\theta}\left(\tilde{\mu}_c^*\right)_j \quad , \quad \text{so that} \quad \left(\tilde{\mu}_c^{n+1}\right)_j = \left(\tilde{\alpha}_c^{n+1}\right)_j = 0 \quad , \quad \text{if} \quad WET_j = 1 \quad . \tag{4.93}$$

The radial momentum jump condition at the L–V interface (Equation 4.82) is used to calculate the pressure correction in the liquid cell (iL,j) next to the diphasic interface:

$$P'_{il,j} = \left(COEF_{int}^j\right)P'_{Nv,j} + 2\frac{\sigma_j}{R_p}\frac{1}{\theta}\left(\tilde{\mu}_c^*\right)_j + \frac{1}{\theta}JUMP_{int}^j \quad , \quad \text{if} \quad WET_j = 1. \tag{4.94}$$

Equation (4.94) replaces the discretized mass balance Equation (4.88) for the wet cell (iL,j). The pressure Equations (4.85), (4.88) and (4.94) are solved for the liquid pressure corrections in the liquid–wick region (i=iL to NL, and j=1 to Nz), and the corrections of the cosines of the contact angle are evaluated using Equations (4.83) and (4.93) as:

$$\begin{aligned} 2\frac{\sigma_j}{R_p}\theta\left(\mu_c'\right)_j &= \left(COEF_{int}^j\right)\theta P'_{Nv,j} - \theta P'_{il,j} + JUMP_{int}^j \quad , \quad \text{if} \quad WET_j = 0 \quad , \\ \left(\mu_c'\right)_j &= -\frac{1}{\theta}\left(\tilde{\mu}_c^*\right)_j \qquad\qquad\qquad\qquad\qquad\qquad \text{if} \quad WET_j = 1 \quad , \end{aligned} \tag{4.95}$$

The advanced–time cosines of contact angle are updated using Equation (4.89).

During the iterative process, it is possible that new wet points appear, or that former wet points disappear, so that the flags WET_j must be updated using Equations (4.92).

Similarly, the mass injection rates, $\tilde{m}_j^{INJECT}$, which appear as a sink term in the mass balance, Equation (4.85), must be evaluated explicitly and updated, in terms of the mass loss rates due to the removal of excess liquid from the wet liquid cell (iL,j), $\tilde{m}_j^{FLOOD}$. The latter are determined in terms of the pressure corrections using the conservation of mass in the wet cells (iL,j). Because we force a flat interface at the boundary of these cells, excess liquid is pooling into the vapor core in order to insure mass conservation. This mass loss rate $\tilde{m}_j^{FLOOD}$ must appear as a sink term in the mass balance Equation (4.88). In the discretization of this equation, we make use of the fact that the L–V interface is flat to express the volume of the cell as:

$$\varepsilon Vol_{iL,j}^{n+1} = \varepsilon\left(A_z^i \Delta Z_j\right), \quad \text{if} \quad WET_j = 1 \quad . \tag{4.96}$$

Since at this point we know all pressure corrections, the mass loss rates are simply determined as:

$$\tilde{m}_j^{FLOOD} = S_{i,j}^{\rho} - aW_{i,j}^{\rho}\left(P'\right)_{Nv,j} - \left[aP_{i,j}^{\rho}\left(P'\right)_{i,j} + aE_{i,j}^{\rho}\left(P'\right)_{i+1,j} + aN_{i,j}^{\rho}\left(P'\right)_{i,j+1} + aS_{i,j}^{\rho}\left(P'\right)_{i,j-1}\right],$$
$$\text{if} \quad WET_j = 1,$$

$$\tilde{m}_j^{FLOOD} = 0, \quad \text{if} \quad WET_j = 0. \tag{4.97}$$

Now we introduce $\tilde{m}_j^{TRz}$, the mass rate of liquid transported by the vapor flow towards the end of the condenser (at axial velocity location j). Physically we always have $\tilde{m}_{jMIN}^{FLOOD} > 0$ (unless all liquid cells are dry) and the wet cells (iL,j) form a connected set, from j=jMIN to jMAX. The transport rate of excess liquid by the vapor flow can then be calculated as:

$$\tilde{m}_j^{TRz} = \sum_{jMIN}^{j} \tilde{m}_k^{FLOOD}, \quad \text{for} \quad j \in [jMIN, jMAX]. \tag{4.98}$$

There are now several physical cases to consider, depending on the values of the quantities jMAX and $\tilde{m}_{jMAX}^{TRz}$.

CASE 1 $\left(\text{jMAX} < \text{Nz} \quad \text{and} \quad \tilde{\dot{m}}_{\text{jMAX}}^{\text{TRz}} > 0\right)$

These conditions occur *during the heating process of the heat pipe, before the wet point reaches the end of the condenser.* The mass of excess liquid transported by the vapor flow is dumped into the next interfacial dry liquid cell (iL,jMAX+1). Therefore, the mass injection source term for this cell is obtained from:

$$\tilde{\dot{m}}_{\text{jMAX+1}}^{\text{INJECT}} = \tilde{\dot{m}}_{\text{jMAX}}^{\text{TRz}} \quad . \tag{4.99}$$

All the other injection source terms are nul.

CASE 2 $\left(\text{jMAX} = \text{Nz} \quad \text{and} \quad \tilde{\dot{m}}_{\text{jMAX}}^{\text{TRz}} > 0\right)$

These conditions occur *during the heating process of the heat pipe, when the wet point reaches the end of the condenser.* After the L–V interface eventually flattens at the end of the condenser, the excess liquid transported by the vapor flow accumulates in the vapor core and forms a liquid pool. The mass rate of accumulation into the liquid pool is:

$$\tilde{\dot{m}}^{\text{POOL}} = \tilde{\dot{m}}_{\text{jMAX}}^{\text{TRz}} \quad . \tag{4.100}$$

The size of the liquid pool increases with time (all the injection source terms $\tilde{\dot{m}}_{\text{j}}^{\text{INJECT}}$ are nul). Conservation of mass in the liquid pool is expressed as:

$$\frac{M_{\text{POOL}}^{\text{n+1}} - M_{\text{POOL}}^{\text{n}}}{\Delta t} = \tilde{\dot{m}}^{\text{POOL}} \quad , \tag{4.101}$$

where M_{POOL} represents the mass of the liquid pool.

CASE 3 $\left(\text{jMAX} = \text{Nz}\,, \quad \text{and} \quad -\frac{M_{\text{POOL}}^{\text{n}}}{\Delta t} < \tilde{\dot{m}}_{\text{jMAX}}^{\text{TRz}} < 0\right)$

These conditions occur *during the cooldown of the heat pipe, when the liquid pool is receding.* As the heat pipe cools down, the average liquid temperature and volume decrease due to thermal contraction, and the amount of excess liquid which accumulated at the end of

the condenser (liquid pool) is reduced. In this case, Equations (4.100) and (4.101) still apply.

CASE 4 $\left(jMAX = Nz, \quad \text{and} \quad \tilde{\dot{m}}^{TRz}_{jMAX} < -\frac{M^{n}_{POOL}}{\Delta t} < 0 \right)$

These conditions occur *during the cooldown of the heat pipe, just before disappearance of the liquid pool.* Because there is not enough fluid mass in the pool to preserve a flat L–V interface at the end of the condenser (j=Nz), the liquid pool vanishes and the liquid meniscus recedes at (j=Nz), that is, the liquid cell (iL,Nz) dries out (we mean that the cell establishes a concave meniscus). For this case, the numerical treatment can become extremely complex if more than one cell dries out at the same time (within the same time step). Therefore, we assume, for simplicity, that the time step is small enough so that only the last cell (iL,Nz) dries out. In this case $\left(\tilde{\dot{m}}^{TRz}_{Nz-1} \geq 0\right)$, we have:

$$\begin{aligned} &DRY_{Nz} = 1 \quad , \\ &WET_{Nz} = 0 \quad , \quad \text{and} \quad . \\ &\tilde{\dot{m}}^{INJECT}_{Nz} = \tilde{\dot{m}}^{TRz}_{Nz-1} + \frac{M^{n}_{POOL}}{\Delta t} \quad . \end{aligned} \tag{4.102}$$

All the other injection source terms are nul. The flag DRY_{Nz} is necessary to insure that Expression (4.102) of the injection source term is used for all internal iterations within the time step. Upon convergence for this time step, the pool vanishes and its mass is set to zero $\left(M^{n+1}_{POOL} = 0\right)$.

CASE 5 $\left(jMAX < Nz \quad \text{and} \quad \tilde{\dot{m}}^{TRz}_{jMAX} < 0\right)$

These conditions occur *during the cooldown of the heat pipe, after the liquid pool has disappeared.* The liquid cell (iL,jMAX) dries out. For efficiency of the internal iterations, we anticipate the mass injection source term for this cell to be:

$$\begin{aligned} &WET_{jMAX} = 0 \quad , \quad \text{and} \\ &\tilde{\dot{m}}^{INJECT}_{jMAX} = \tilde{\dot{m}}^{TRz}_{jMAX-1} \quad . \end{aligned} \tag{4.103}$$

All the other injection source terms are nul.

CASE 6 $\left(\text{jMIN} > 0 \quad \text{and} \quad \tilde{\dot{m}}_{\text{jMIN}}^{\text{TRz}} < 0\right)$

There is always the possibility that *the first wet cell* (j=JMIN) *dries out* . In this case, we set:

$$\text{WET}_{\text{jMIN}} = 0 \quad . \tag{4.104}$$

Internal iterations are performed until the flags WET_j and injection source terms converge. Note that it is possible that several cells will dry out/wet within one time step.

The liquid–pooling submodel is rather sophisticated owing to the fact that it must identify liquid pool recession and dewetting conditions during the cooldown of the heat pipe, and incorporates both mass and energy transfer processes. For simplicity, we neglect the kinetic energy of the liquid droplets carried by the vapor stream and the work developed by the vapor to extract these droplets from the L–V interface. Therefore, conservation of energy becomes a matter of conserving the enthalpy stored in the liquid droplets. The power loss terms, $\tilde{\dot{W}}_j^{\text{FLOOD}}$, in Equation (4.10) are calculated explicitly in a manner consistent with the derivation of the mass injection rates $\tilde{\dot{m}}_j^{\text{INJECT}}$. $\tilde{\dot{W}}_j^{\text{FLOOD}}$ is the power loss term for the liquid cell (iL,j), which accounts for the enthalpy of the excess liquid pooling into the vapor core. We introduce $\tilde{\dot{W}}_j^{\text{TRz}}$, the power of liquid transported by the vapor flow towards the end of the condenser (at axial velocity location j). These two quantities are related by:

$$\tilde{\dot{W}}_k^{\text{TRz}} = \sum_{\text{jMIN}}^{k} \tilde{\dot{W}}_j^{\text{FLOOD}}, \quad \text{for} \quad k \in [\text{jMIN}, \text{jMAX}], \quad \text{where}$$

$$\begin{aligned} \tilde{\dot{W}}_j^{\text{FLOOD}} &= \tilde{\dot{m}}_j^{\text{FLOOD}} \times h^{\text{L}}\left(\tilde{T}\,\text{int}_j^{*}\right) \quad > 0 \qquad \text{if} \quad \tilde{\dot{m}}_j^{\text{FLOOD}} > 0, \\ \tilde{\dot{W}}_j^{\text{FLOOD}} &= \frac{\tilde{\dot{m}}_j^{\text{FLOOD}}}{\tilde{\dot{m}}_{j-1}^{\text{TRz}}} \tilde{\dot{W}}_{j-1}^{\text{TRz}} \qquad < 0 \qquad \text{if} \quad \tilde{\dot{m}}_j^{\text{FLOOD}} < 0. \end{aligned} \tag{4.105}$$

A positive flooding mass rate corresponds to the case of excess liquid pooling into the vapor core, while a negative one corresponds to the filling up of the interfacial pores with liquid droplets transported by the vapor flow (propagation of wet point). There are again several physical cases to consider, after convergence of the internal Poisson iterations.

CASE 1 $\left(\text{jMAX} < \text{Nz} \quad \text{and} \quad \text{DRY}_{\text{Nz}} = 0 \quad \Rightarrow \tilde{\dot{m}}^{\text{TRz}}_{\text{jMAX}} > 0\right)$

These conditions occur *during the heatup or cooldown of the heat pipe, with no liquid pool at the end of the condenser.* The liquid mass rate $\tilde{\dot{m}}^{\text{TRz}}_{\text{jMAX}}$ transported by the vapor flow is dumped into the next interfacial dry liquid cell (iL,jMAX+1). Therefore, the power loss term for this cell is taken as:

$$\tilde{\dot{W}}^{\text{FLOOD}}_{\text{jMAX+1}} = -\tilde{\dot{W}}^{\text{TRz}}_{\text{jMAX}} < 0 \quad . \tag{4.106}$$

CASE 2 $\left(\text{jMAX} = \text{Nz} \quad \text{and} \quad \tilde{\dot{m}}^{\text{TRz}}_{\text{jMAX}} > 0 \quad \Rightarrow \text{liquid pool grows}\right)$

These conditions occur *during the heating process of the heat pipe, when the wet point has reached the end of the condenser.* The size of the liquid pool increases with time. The enthalpy rate of accumulation in the liquid pool is:

$$\tilde{\dot{W}}^{\text{POOL}} = \tilde{\dot{W}}^{\text{TRz}}_{\text{jMAX}} > 0 \quad . \tag{4.107}$$

CASE 3 $\left(\text{jMAX} = \text{Nz}, \quad \text{and} \quad \tilde{\dot{m}}^{\text{TRz}}_{\text{jMAX}} < 0 \quad \Rightarrow \text{liquid pool decreases}\right)$

These conditions occur during the cooldown of the heat pipe, when the liquid pool is receding. For this case, we have:

$$\begin{aligned} \tilde{\dot{W}}^{\text{POOL}} &= \tilde{\dot{m}}^{\text{TRz}}_{\text{jMAX}}\, h^{n}_{\text{POOL}} < 0, \quad \text{and} \\ \tilde{\dot{W}}^{\text{FLOOD}}_{\text{jMAX}} &= \tilde{\dot{W}}^{\text{POOL}} - \tilde{\dot{W}}^{\text{TRz}}_{\text{jMAX-1}} < 0 \quad . \end{aligned} \tag{4.108}$$

CASE 4 $\left(\text{DRY}_{\text{Nz}} = 1 \quad \Rightarrow \text{jMAX} = \text{Nz} - 1, \quad \text{and} \quad \tilde{\dot{m}}^{\text{TRz}}_{\text{jMAX}} > 0\right)$

These conditions mean that *the liquid pool just vanished during the particular time step.* Because there is not enough fluid mass in the pool to preserve a flat L–V interface at the end of the condenser (j=Nz), the liquid meniscus recedes at (j=Nz), that is, the liquid cell (iL,Nz) dries out. We assumed that the time step is small enough so that only this cell dries out. In this case, we have:

$$\tilde{W}^{POOL} = -\frac{M^{n}_{POOL}\, h^{n}_{POOL}}{\Delta t} < 0 \quad ,$$

$$\tilde{W}^{FLOOD}_{jMAX+1} = \tilde{W}^{POOL} - \tilde{W}^{TRz}_{jMAX} < 0 \quad , \quad \text{and} \quad . \tag{4.109}$$

$$M^{n+1}_{POOL} = 0 \quad , \quad h^{n+1}_{POOL} = 0 \quad .$$

For the case of a liquid pool (jMAX=Nz, CASES 2 and 3), the new–time mass, enthalpy and temperature of the pool are determined from mass and energy balances as:

$$\frac{1}{\Delta t}\left[M^{n+1}_{POOL} - M^{n}_{POOL}\right] = \tilde{m}^{POOL},$$

$$\frac{1}{\Delta t}\left[M^{n+1}_{POOL} h^{n+1}_{POOL} - M^{n}_{POOL} h^{n}_{POOL}\right] = \tilde{W}^{POOL}, \tag{4.110}$$

$$\text{and} \quad T^{n+1}_{POOL} = T_L\left(h^{n+1}_{POOL}\right) \quad .$$

We assume hydrodynamic equilibrium at the vapor–pool interface to calculate the pressure of the liquid pool:

$$P^{n+1}_{POOL} = \frac{1}{\pi R^2_{Nv}} \sum_{i=1}^{Nv} A^i_z \tilde{P}^{n+1}_{i,Nz} \quad . \tag{4.111}$$

Finally, the liquid pool density and thickness are obtained as:

$$\rho^{n+1}_{POOL} = \rho_L\left(T^{n+1}_{POOL}, P^{n+1}_{POOL}\right) \quad , \quad \text{and}$$

$$\Delta Z^{n+1}_{POOL} = \frac{1}{\pi R^2_{Nv}} \frac{M^{n+1}_{POOL}}{\rho^{n+1}_{POOL}} \quad . \tag{4.112}$$

4.2. DESCRIPTION OF NUMERICAL SOLUTION ALGORITHMS

The code is written in Standard Fortran 77 and is easily implemented on any machine supporting a Fortran 77 compiler. In the present effort, HPTAM was successfully implemented on 386 and 486 machines running MS–DOS, machines running VMS operating system (DEC VAX 6320) and UNIX operating system (Sun workstations, AIX–RS6000 IBM, CRAY–YMP).

Various segregated solution algorithms have been considered to accomplish the couplings between the discretized equations. The first algorithm (A) is non–iterative and is formed of the following sequential steps: (a) momentum predictor step, (b) pressure corrector step, and (c) energy predictor step. In step (b) of this algorithm, the SIMPLE procedure is used in the momentum corrections equations to eliminate the off–diagonal velocity corrections, and the evaporation and condensation rates are linearized in terms of the vapor pressures using the kinetic theory relationship. Also, the volumes of both the liquid and vapor cells adjacent to the L–V interface are discretized implicitly using Equations (4.79). The evaporation/condensation rates are evaluated explicitly in step (c).

The implicit discretization of the volumes of the vapor cells adjacent to the L–V interface using Equation (4.79b) introduces a non–dominant component to the Poisson linear system, which is responsible for the poor stability characteristics of Algorithm A.

The second algorithm (B) is identical to Algorithm A except for step (b). In step (b) of Algorithm B, the volumes of the vapor cells (Nv,j) are evaluated explicitly using Equation (4.87) in place of Equation (4.79b). Because the volume of vapor in the wick is a very small fraction of the vapor core volume, and represents an insignificant fraction of the working fluid inventory in the heat pipe, it is found that this simplification does not affect the accuracy of the solution, but increases the stability of the algorithm.

Algorithm B, however, has some limitations. First, it is not suitable to resolve the pressure–velocity coupling and the dependence of the evaporation and condensation rates on both the vapor pressure and L–V interfacial temperature. Also, it has been established that the SIMPLE–Consistent approximation performs much better than the SIMPLE algorithm, particularly when diffusion and convection phenomena are dominated by pressure gradients and source terms.

The third algorithm (HPTAM–PISO) is based on the two–stage PISO (Pressure–Implicit with Splitting of Operators) scheme of Issa (1986). This algorithm is non–iterative and is formed of the following sequential steps: (a) momentum predictor step, (b) pressure corrector step, (c) energy predictor step, and (d) pressure corrector step. Note the additional step (d) to enhance the resolution of the pressure–velocity coupling. In steps (b) and (d) of this algorithm, the SIMPLEC procedure is used in the momentum corrections equations to eliminate the off–diagonal velocity corrections. Finally, the kinetic theory relationship is linearized in step (c) to express the evaporation and condensation rates in

terms of temperatures, as described in section 4.1.5. As before, the volumes of the vapor cells (Nv,j) are evaluated explicitly .

The last algorithm (HPTAM–Revised) is iterative in nature to reduce the linearization errors of the kinetic theory relationship and equations of state, and formed of the following sequential steps:

(a) *enthalpy predictor step:* best estimates of pressures and convective fluxes are used explicitly, frozen fractions in the wick are linearized in terms of temperatures, and the enthalpy conservation equations are solved for the temperatures.
(b) the frozen fractions in the wick are updated in terms of the temperatures.
(c) iterations to (a) are performed till temperatures and frozen fractions have converged.

(d) *pressure corrector step:* a simplified form of the momentum conservation equations is used to implicitly relate the mass flow rates and pressure gradients. The mass flow rates are eliminated in terms of pressures in the continuity equations. The vapor pore void fraction appearing in the interfacial wick cell volumes (Equations 4.90) is related to μ_c through Equation (4.80), and the later is expressed in terms of the liquid and vapor pressures using the capillary relationship, Equation (4.83). The resulting Poisson equation is solved for the pressure field, and the vapor pore void fractions are updated.

(e) *momentum predictor step:* best estimates of the pressure gradients are calculated, and the momentum conservation equations are solved for the velocity field.

(f) *properties update:* the thermophysical properties and densities are updated.

(g) iterations to (d) are performed until velocities and pressures converge (that is until pressure corrections are below a prescribed value).
(h) iterations to (a) are performed until the mass balance is satisfied (then evaporation, condensation, sublimation and resolidification rates and temperatures have converged).

As before, the kinetic theory relationship is linearized in step (a) to express the vaporization and condensation rates in terms of temperatures. In the momentum corrections equations of step (d), the interfacial radial velocity corrections are evaluated from the linearization of the kinetic theory Equations (4.74) and the SIMPLE–Consistent procedure is used to

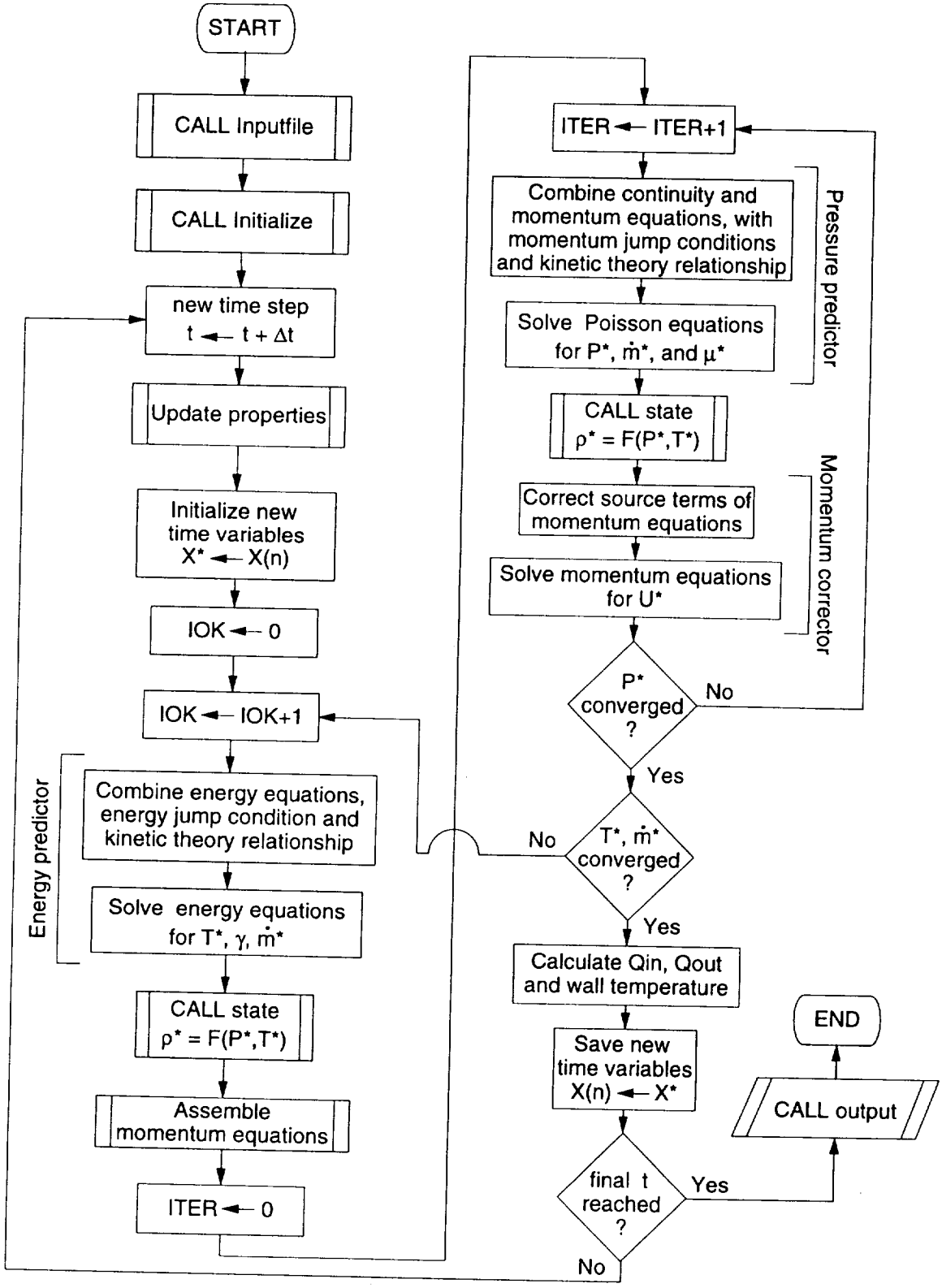

FIGURE 4.8. Simplified Flow Chart for Algorithm HPTAM–Revised.

eliminate the other off–diagonal velocity corrections. This modification considerably improved the convergence rate of the method. Also, the volumes of the vapor cells (Nv,j) are evaluated explicitly, as before. A simplified flow chart of this algorithm HPTAM–Revised is depicted in Figure 4.8.

4.3. SOLVERS FOR 5–POINT LINEAR EQUATIONS

To solve the five–point linear equations resulting from the discretization of the mass, energy and momentum balance equations, a direct solution routine using Gaussian elimination (Golub and van Loan 1984) is developed and tested, which includes partial pivoting and row–normalization options. While this method is very efficient for solving relatively small linear systems, it is very cumbersome for large matrices encountered in fluid flow problems. To solve a set of discretized conservation equations on a rectangular domain of N=NrxNz cells, the computational time increases with the number of equations raised to the third power, that is as $(NrxNz)^3$.

In this case, it is useful to consider the banded version of the solver. A band linear equation solver is organized around a data structure that takes advantage of the many zeros in the pentadiagonal matrix of the linear system. By construction, this matrix has lower and upper bandwidths Nr and can be represented in a (2Nr+1)xN band array (see Figure 4.9). The bandwidth of the matrix is preserved as long as no pivoting is performed. If pivoting is necessary, the matrix can still be represented in a (3Nr+1)xN band array. Fortunately, such permutation of line was never necessary in solving the present heat pipe problem. A quick estimate of the number of flops in the banded Gauss–elimination algorithm shows that the computational time increases as Nr^3xNz. Therefore, the use of the band structure considerably reduces the amount of memory storage and computational time required. More precisely, if we make use of the "corner zeros" in the band storage matrix, the computational time is proportional to $Nr^{8/3}xNz$, which is confirmed by numerical experiments on a DEC VAX 6320 (Figure 4.10). The CPU time (in seconds) needed for the banded Gauss–elimination solver to obtain the solution of a linear system of NrxNz equations is fitted as:

$$CPU_{Gauss} = 1.66x10^{-5} Nr^{2.67} Nz \quad . \tag{4.113}$$

Several 5–point iterative solvers have been examined and tested which combine strongly implicit procedures with successive overrelaxation, additive block (row and column)

The following linear system is considered:

$$aP_{i,j}(T)_{i,j} + aE_{i,j}(T)_{i+1,j} + aW_{i,j}(T)_{i-1,j} + aN_{i,j}(T)_{i,j+1} + aS_{i,j}(T)_{i,j-1} = S_{i,j}$$

for i=1 to Nr, and j=1 to Nz.

If each cell [i,j] is given the cell number k=i+(j-1)xNr, the matrix [a] has lower and upper bandwidthes Nr (Nr<Nz for max. efficiency).

Example for Nr=4, Nz=5 :

[a] is a 20x20 matrix.

The banded matrix [b] has 2Nr+1 diagonals, that is :

[b] is a 20x9 matrix.

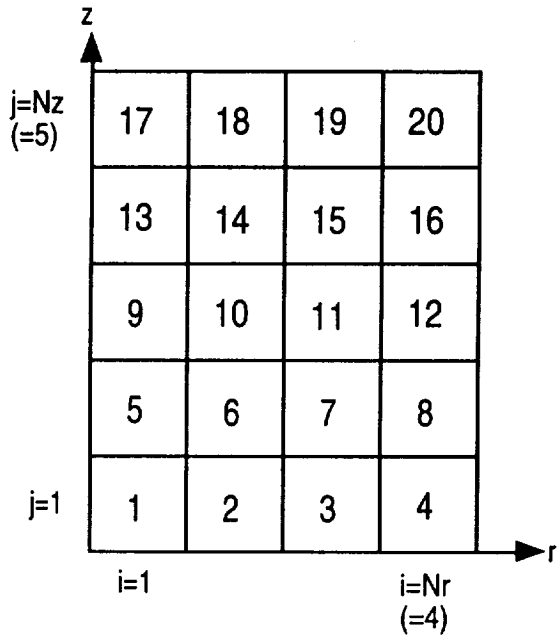

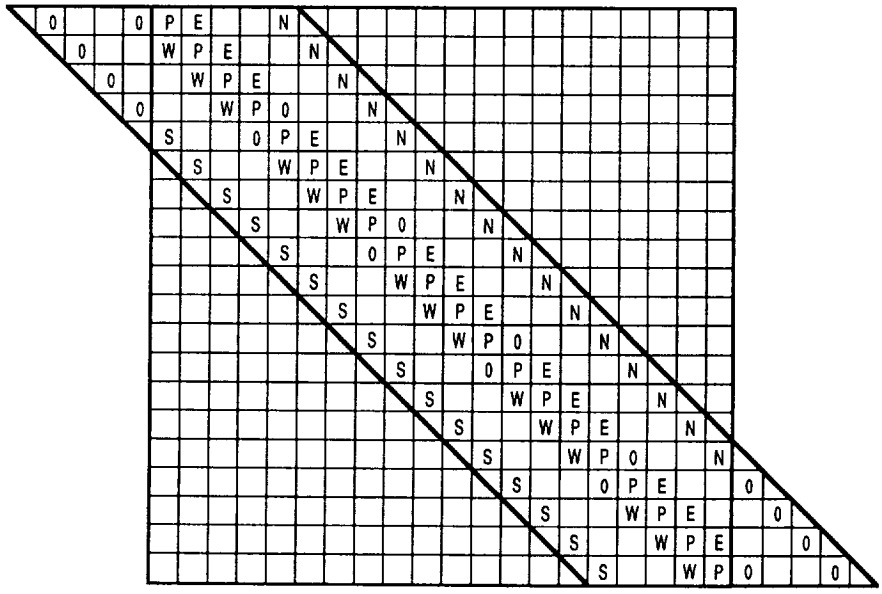

FIGURE 4.9. Illustration of Band Storage of a Linear System Matrix which Results from Discretization of Conservation Equations on a Two–Dimensional Domain.

corrections and conjugate gradient. The Strongly Implicit Solver of Lee (1989) is found to be the most efficient in solving the momentum and energy discretized equations of the present heat pipe problem. The SIS procedure of Lee has the advantage of not requiring a partial cancellation parameter, as most of the implicit iterative solvers do. Also a SOR (strongly Over–Relaxation) factor of unity is found to be the best choice for the convergence of the iterations. The LU decomposition of Lee, combined with the iterative method of solution devised by Stone (1968), is used.

One pass of the selected iterative solver is constituted of the following steps. Given a vector approximation $\mathbf{T}^*$ to the solution of the linear system $[A]\mathbf{T}=\mathbf{S}$, we use Stone's iterative method to obtain a correction $\mathbf{T}'$ to the vector $\mathbf{T}^*$, such that:

$$[A+A'](\mathbf{T}^*+\mathbf{T}') = [A+A']\,\mathbf{T}^* + \mathbf{S} - [A]\mathbf{T}^* \quad ,$$

or

$$[A+A']\mathbf{T}' = \mathbf{S} - [A]\mathbf{T}^* \quad . \tag{4.114}$$

It is apparent that the vector correction is nul upon convergence. The matrix alteration [A'] to the system matrix [A] is obtained from the SIS procedure of Lee (1989) such that:

$$[A+A'] = [L][U] \quad , \tag{4.115}$$

where [L] is a lower triangular matrix and [U] is an upper triangular matrix. Both [L] and [U] have same dimension NxN than the matrix [A]. While [A] has only 5 non–zero elements per line when it originates from the discretization of conservation equations on a two–dimensional domain, the triangular matrices [L] and [U] have only 3 non–zero elements per line, which makes the computations particularly easy. Making use of Equation (4.115) into Equation (4.114), the linear system becomes:

$$[L][U]\mathbf{T}' = \mathbf{R} \quad , \tag{4.116}$$

where $\mathbf{R} = \mathbf{S} - [A]\mathbf{T}^*$ is the residual vector. The linear system (4.116) is readily solved by making use of the properties of triangular matrices:

$$[L]\mathbf{V} = \mathbf{R} \quad ,$$
$$[U]\mathbf{T}' = \mathbf{V} \quad . \tag{4.117}$$

Once $\mathbf{T}'$ is obtained, the vector $\mathbf{T}^*$ is corrected as $\mathbf{T}^* = \mathbf{T}^* + \mathbf{T}'$, and the residual vector is recalculated as $\mathbf{R} = \mathbf{S} - [A]\mathbf{T}^*$. Another iteration is performed if $\mathbf{R}$ does not satisfy the specified convergence criteria.

It is apparent that the iterative algorithm of Stone has the disadvantage of using more computational time than Lee's, since it requires calculation of the residual vector at the end of every iteration. However, knowledge of these residuals permits to closely control the internal iterations of the iterative segregated algorithm HPTAM–Revised, resulting in an overall saving in the CPU time.

The number of flops of the iterative solver SIS is proportional to the number of equations N and to the number of internal iterations. Numerical experiments are performed on a DEC VAX 6320 (Figure 4.11) to obtain the following relation for the CPU time (in seconds):

$$CPU_{SIS} = \frac{5 + ITER}{30{,}000.} \, Nr \, Nz \quad . \tag{4.118}$$

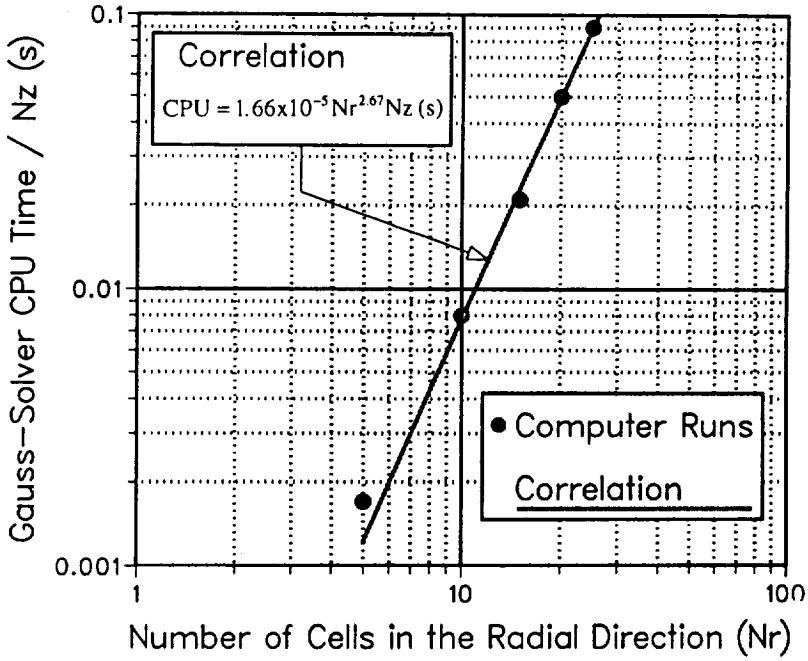

FIGURE 4.10. CPU Time on a DEC VAX 6320 to Solve a Linear System of NrxNz Equations with the Banded Gauss–Elimination Solver.

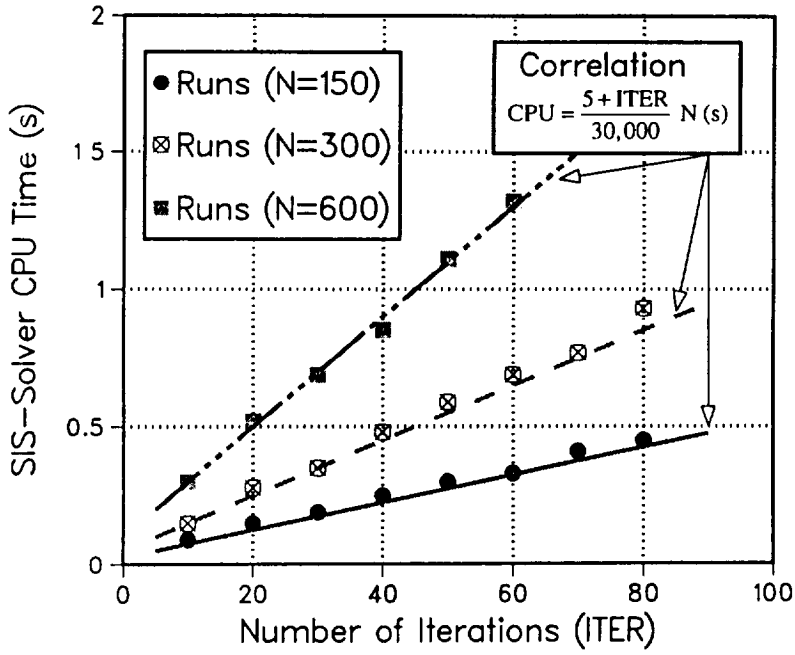

FIGURE 4.11. CPU Time on a DEC VAX 6320 to Solve a Linear System of N Equations with the Iterative SIS Solver.

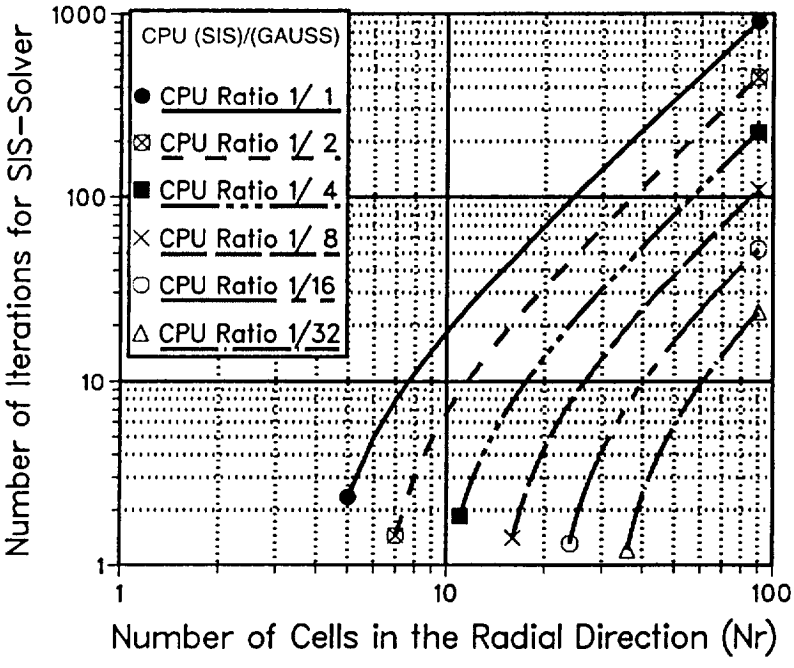

FIGURE 4.12. Comparison of the Banded Gauss–Elimination Solver and Iterative SIS Solver in terms of CPU Time on a DEC VAX 6320, to Solve a Linear System of NrxNz Equations.

Because the SIS solver is iterative in nature, the computational time for this solver is a function of the number of iterations performed. On the other hand, the amount of CPU time necessary when using the direct Gauss algorithm is solely a (strong) function of the size of the discretized domain. To evaluate which solver is more efficient in a given situation, it is useful to plot the ISO–CPU curves in Figure 4.12. For a given number of radial cells Nr (it defines the bandwidth of the matrix), there is an optimal number of internal iterations for the SIS solver such that it is competitive with the Gauss solver in terms of CPU time. It is worth noting that in practice, the amount of CPU time needed for the SIS solver is only a fraction of that needed for the Gauss direct solver. For example, on a 10x30 domain, if 7 iterations of the SIS solver are sufficient to bring the residuals below a satisfactory value, then the saving in the CPU time is about 50% than that for the Gauss algorithm. Since the CPU time required for the Gauss solver is proportional to $Nr^{8/3}$, the maximum number of iterations increases as $Nr^{5/3}$ (Figure 4.12). The saving in the CPU time increases exponentially with the size of the numerical domain.

4.4. PERFORMANCE OF NUMERICAL SOLUTION ALGORITHMS

To verify the system of equations in HPTAM and test the performance of the various algorithms considered, the model is used to simulate the transient results of El–Genk and Huang (1993) for a (fully–thawed) horizontal water heat pipe experiment. The design and operational parameters of the experiment analyzed are given in Section 7.1. In the experiment, the heat pipe was initially at room temperature (296.2 K) when the electrical power to the heating tape in the evaporator section increased in a step–function to 575 W. The cooling water enters the condenser cooling jacket at 294.5 K and 11.33 g/s. After about 10 minutes into the heatup transient, the heat pipe reaches steady–state. After an additional 7 minutes of steady–state operation, the electrical power to the heating tape was turned off, and the heat pipe entered the cooldown phase of the transient. To account for the actual heat input to the heat pipe evaporator section during the heat pipe transient, the calculations are performed using the measured values of the wall temperatures along the evaporator section. The number of numerical cells are: Nv=5 (5 radial cells in the vapor core), NL=iL=6 (1 radial cell in the liquid–wick region), Nr=7 (1 radial cell in the wall), and Nz+1=31 (31 axial cells). More details can be found in Section 7.1.

Because of their simplistic nature, algorithms (A) and (B) are expected to be very inefficient. Indeed, when algorithm (A) is used, the size of the time step is limited to a very

small value (0.5 ms), resulting in a computer time to real time ratio of 4500 on a DEC VAX 6320.

When algorithm (B) is used, the volumes of the vapor cells adjacent to the L–V interface (Nv,j) are explicitly discretized in the mass balance equations. This simplification does not affect the accuracy of the solution, because the change in vapor volume in the wick is negligible and does not affect the pressure field in the vapor core. However, the numerical algorithm is much more stable. This is because implicit discretization of the volumes of the vapor cells (Nv,j) introduces a non–dominant component in the Poisson equation, which decreases the stability of the algorithm. This approach also permits the decoupling of the Poisson equations in the vapor and liquid regions, which reduces the amount of CPU time for the Gauss solver. As a result, algorithm (B) is five time faster than algorithm (A), with a time ratio of 900. The time step could be increased to 2 ms (this is a value 4 times greater than the previous one).

In the algorithm HPTAM–PISO, the implicit coupling of the kinetic theory equation with the energy conservation equations, combined with the Pressure–Implicit Splitting Operator algorithm (PISO) of Issa, allowed to use larger time steps, ranging between 5 and 15 ms. With an increase in CPU time of only 15% per iteration, the overall acceleration factor is greater than 5 (with a computer to real time ratio of 150) when compared with algorithm (B).

While this algorithm is much more efficient (30 times faster) than the original algorithm (A), the size of the time step is still very small and not suitable for simulating heat pipe transients of several minutes. This limitation on the size of the time step is essentially due to the linearization errors of the equation of state of the vapor, and the kinetic theory relationship used to calculate the evaporation/condensation rates. As indicated in the introductory section, the instability characteristic of the kinetic theory equation is the most stringent. This is because it is formulated in terms of the difference of two terms of comparable magnitude.

To minimize the constraint imposed by the kinetic theory relationship, the iterative scheme HPTAM–Revised, is used. During the first pass of this algorithm, the evaporation and condensation rates are taken as that of the previous time step when solving the energy equation (step (a)) and only one pressure–velocity internal iteration (step (g)) is performed. The use of the SIMPLEC–corrected procedure instead of SIMPLEC as in the previous

algorithm decreased the residuals of the momentum equations by one order of magnitude for an identical number of internal iterations (g). In order to model a half–hour transient of the water heat pipe, this iterative algorithm requires 35 hours of CPU time on a DEC VAX 6320, which corresponds to a computer to real time ratio of only 70. The size of the time step used in the calculations ranged between 40 ms to 100 ms.

Figures 4.13 to 4.16 compare the numerical results for the HPTAM–PISO and HPTAM–Revised algorithms. The comparison is very good, except for a difference in the centerline vapor velocity of about 3% during the heatup transient of the heat pipe. The time step used by HPTAM–Revised is generally one order of magnitude larger than that used by HPTAM–PISO. When time steps larger than 0.1 s were used, a loss of accuracy in the calculations resulted for the particular water heat pipe considered, but HPTAM–Revised was still performing in a stable manner.

Figures 4.13 and 4.14 compare the calculated transient response of the effective power throughput, determined from the heat balance in the cooling jacket, and of the vapor temperature with experimental data. The calculated effective power throughput at steady–state (455 W) is almost the same as that reported in the experiment (443 W). However, the transient response of the calculated power throughput is somewhat faster than that in the experiment. This is because in the experiment, a relatively large fraction of the heat generated in the electric tape is initially stored in the insulation surrounding the evaporator and adiabatic sections and in the condenser jacket, therefore slowing down the heat pipe transient. As shown in Figure 4.14, the calculated transient vapor temperature compares very well with experimental measurements. At steady–state, the calculated vapor temperature was only 1.2 K lower than that measured.

Such good agreement between HPTAM and the transient experimental data of the water heat pipe verifies the soundness of the system of equations and the modeling approach used. As described in the previous sections, HPTAM has the additional capability to simulate pooling of excess liquid in the condenser. After the formation of the liquid pool, any liquid volume increase due to thermal expansion is accommodated in the pool. Figure 4.15 shows that at steady state a liquid pool that is 1.7 mm thick forms at the end of the condenser section.

In algorithms (A), (B) and HPTAM–PISO, the discretized energy, balance and momentum equations are solved using the banded Gauss–elimination solver. In the algorithm

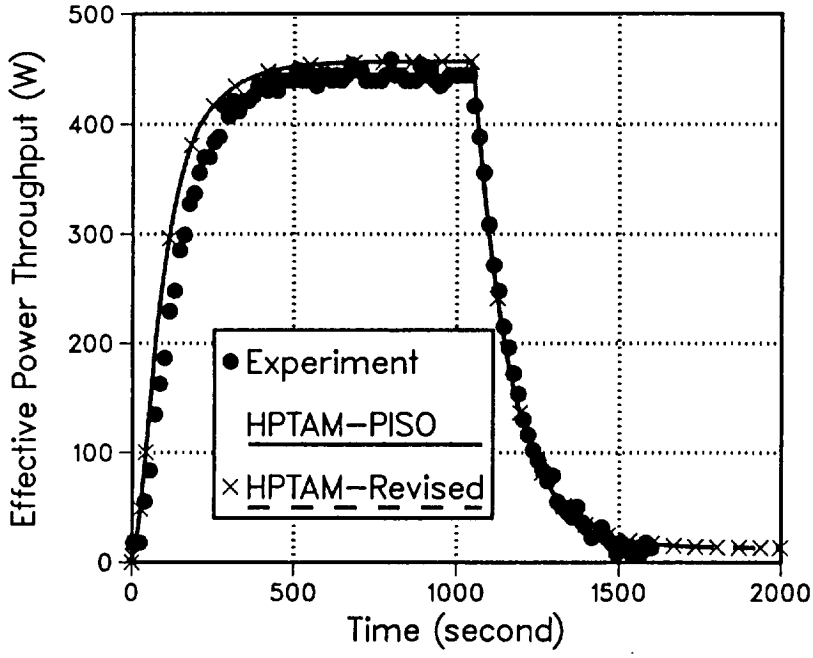

FIGURE 4.13. Comparison of Calculated Transient Response of Effective Power Throughput with Water Heat Pipe Experimental Data.

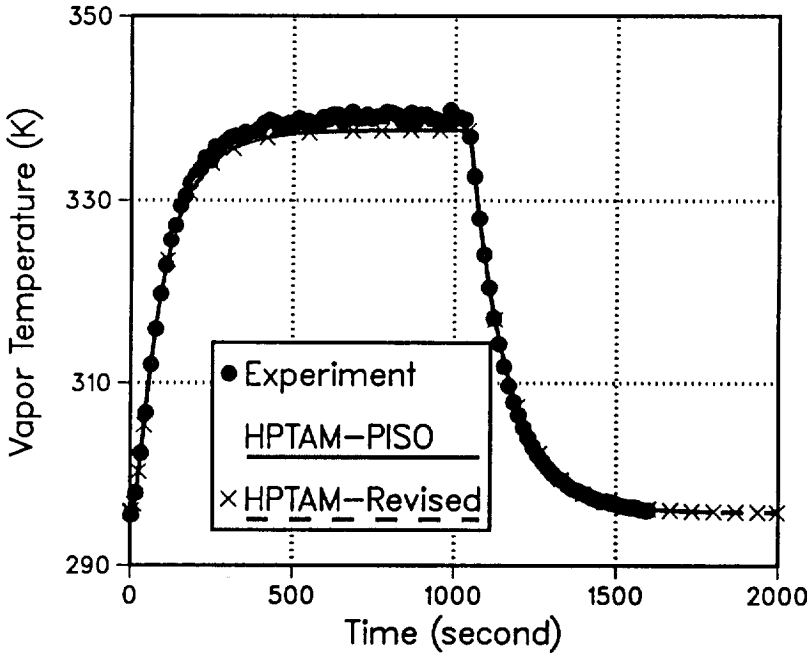

FIGURE 4.14. Comparison of Calculated and Experimental Transient Responses of Vapor Temperature for the Water Heat Pipe.

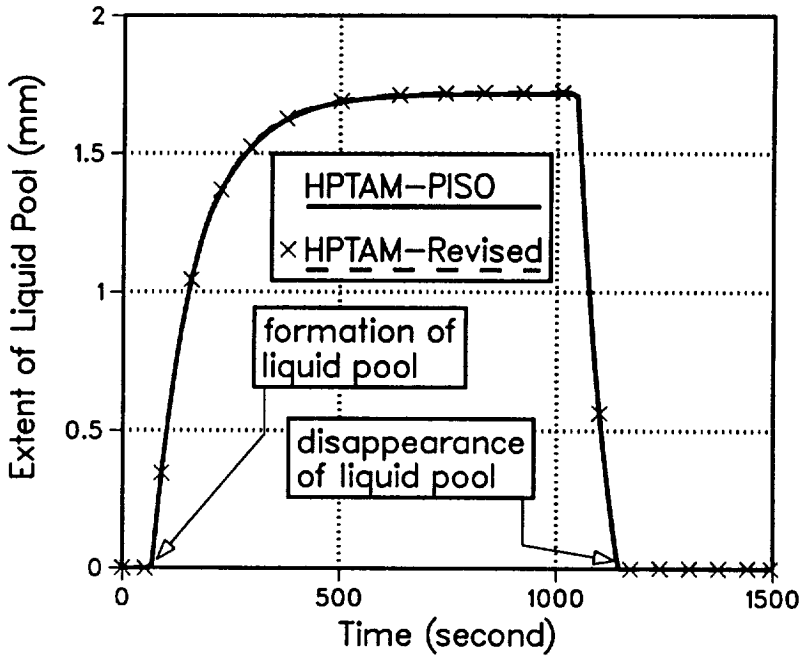

FIGURE 4.15. Calculated Extent of Liquid Pooling at the End of the Condenser in Water Heat Pipe as a Function of Time.

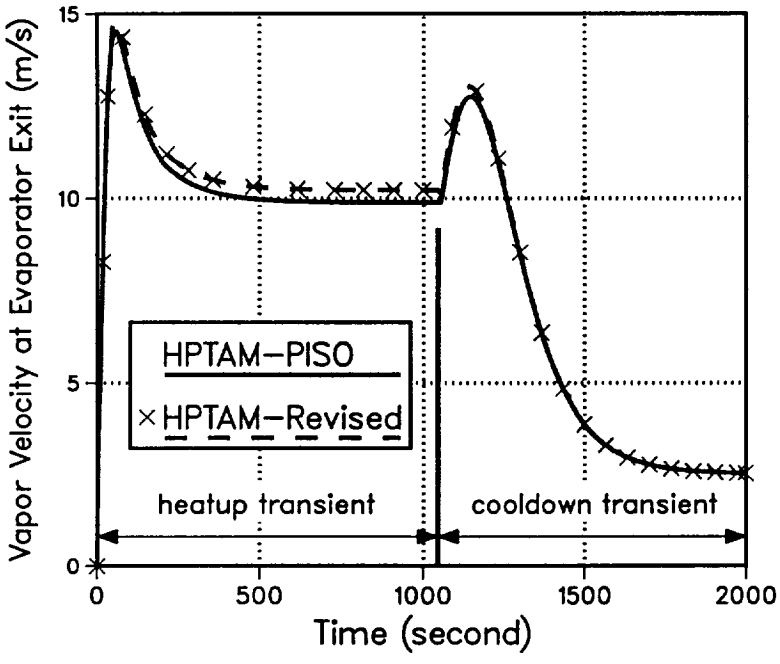

FIGURE 4.16. Calculated Centerline Vapor Velocity at the Evaporator Exit as a Function of Time.

HPTAM–Revised, the iterative SIS solver is used instead, except for the solution of the Poisson equations (the use of such iterative solver is proven to be very inefficient for this type of elliptic linear system of equations, even with strong relaxation). It turned out that the SIS solver is extremely efficient for solving the momentum and energy equations. Typically, the residual of the energy equation decreased by 2 to 4 orders of magnitude, while the residuals of the momentum equations decreased by one order of magnitude, for every iteration of the solver.

Despite these favorable results, the use of the SIS solver decreased the CPU time by only 10–20%, simply because the numerical domain (8x31) was relatively small. For a reasonable number of iterations (typically 3 to 4 for step (g), and 4 to 6 for step (h)), between 50% and 65% of the CPU time is used up by the 5–point linear system solvers. Because of this significant fraction of the CPU, the use of the SIS solver could result in significant savings for larger computational domains.

In the next chapter, the physical and numerical schemes for modeling heat and mass transfers in the wick are validated.

5. BENCHMARK OF WICK MODEL

In order to verify the modeling approach, it is preferable to compare the model results with experimental data. The development of HPTAM has been guided by continuous benchmarking of its predictions with available experimental and numerical results. The accuracy of the freeze–and–thaw model of the wick region of the heat pipe is checked using several benchmark problems, namely: (a) natural convection of liquid in a square cavity (Prakash and Patankar 1985); (b) natural convection of molten gallium in a porous bed of glass beads (Beckermann and Viskanta 1988); (c) one–dimensional pure conduction solidification (Ozisik 1980); (d) two–dimensional pure conduction freezing in a corner (Rathjen and Jiji 1971); and (e) freezing of tin in a rectangular cavity in the presence of natural convection (Wolff and Viskanta 1988). Predictions of the present freeze–and–thaw model for each of the above problems are presented and discussed in the following subsections, and compared with numerical and experimental values reported in the literature.

5.1. NATURAL CONVECTION IN A SQUARE CAVITY

This problem is a standard test case for verifying the accuracy of computational schemes. The square cavity has differentially–heated vertical side–walls and insulated horizontal boundaries. The properties of the fluid are assumed constant, except the density which is a linear function of the temperature (using a constant thermal expansion coefficient, β_P). A dimensionless analysis of the problem shows that the solution is dependent only on Prandtl (Pr) and Grashof (Gr) numbers. No analytical solution is available for this problem, and the results of the present model can only be compared to those of other numerical models. Such a comparison is made in this section with the results obtained by the SIMPLE finite–difference method of Patankar using a fine 32x32 grid, and by the finite–element method using equal–order velocity–pressure interpolation on a 19x19 grid (Prakash and Patankar 1985).

Calculations are performed with the present model on a uniform 24x24 numerical grid with a fixed Prandtl number of 1, and Grashof numbers of 10^3, 10^4 and 10^5. Calculated mid–plane temperature and vertical velocity profiles and flow field are presented for $Gr=10^4$ and $Gr=10^5$, in Figures 5.1 to 5.6. For lower values of the Grashof number, the present

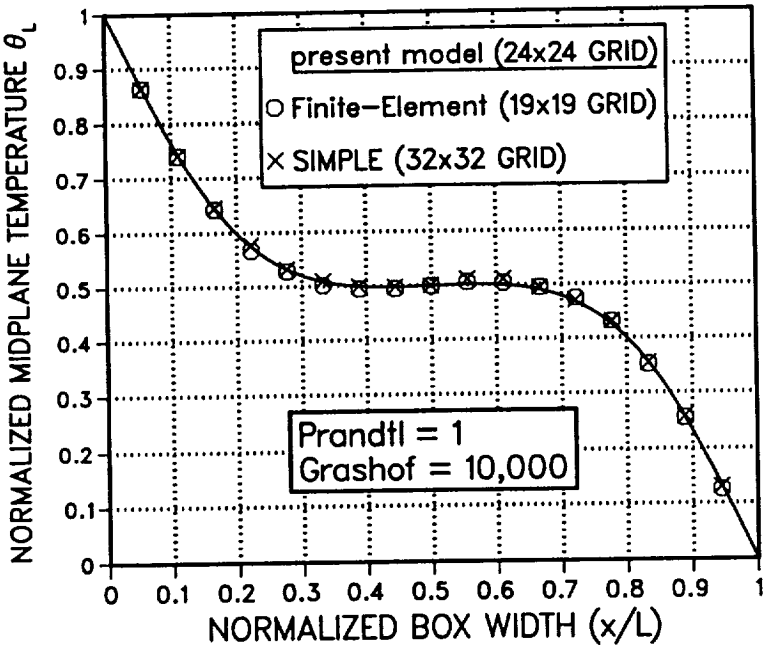

FIGURE 5.1. Temperature Profile Along The Horizontal Mid-Plane for Natural Convection in a Square Cavity (Pr=1, Gr=10^4).

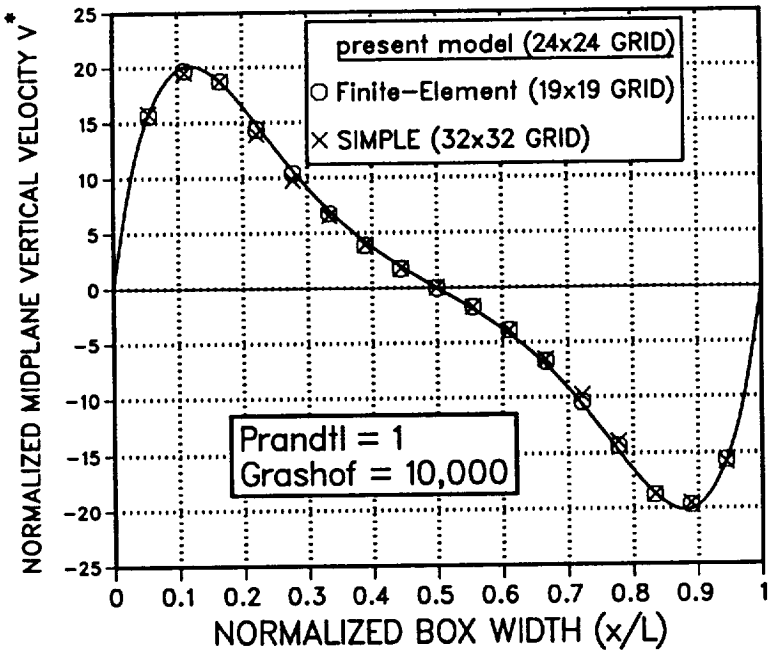

FIGURE 5.2. Vertical Velocity Profile along the Horizontal Mid-Plane for Natural Convection in a Square Cavity (Pr=1, Gr=10^4).

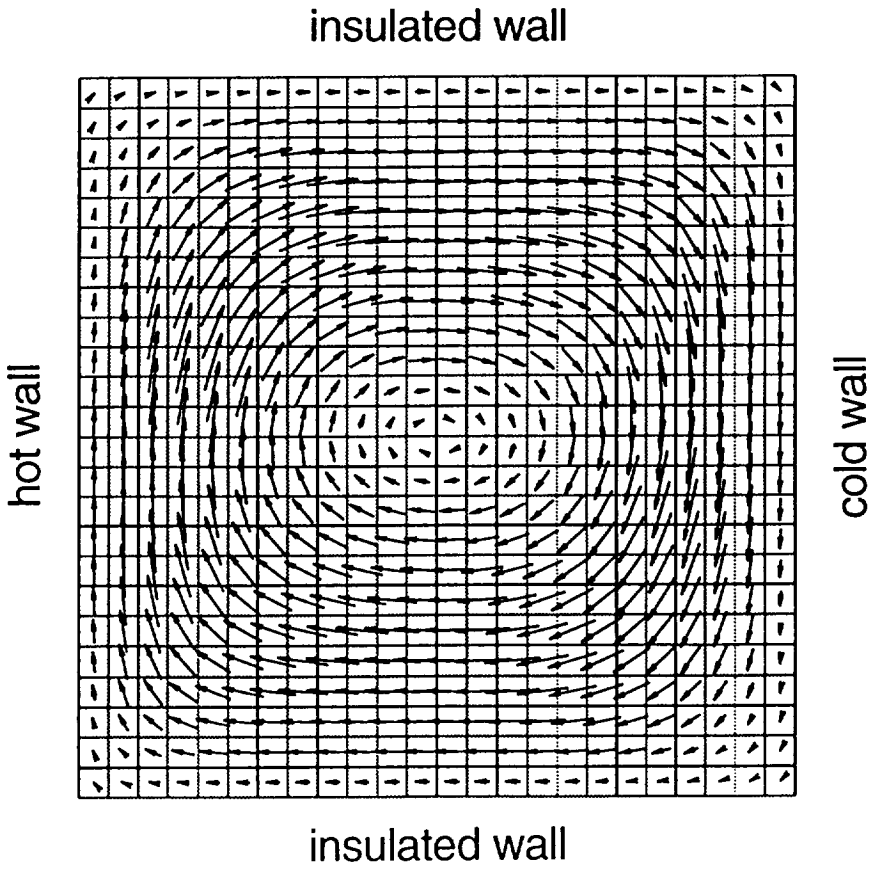

FIGURE 5.3. Flow Field for Natural Convection in a Square Cavity, at Pr=1 and $Gr=10^4$.

model produces very accurate results, even with coarser grids. For the numerically most challenging case of $Gr=10^5$, calculated mid–plane temperature and vertical velocity profiles (Figures 5.4 and 5.5) agree to within 4% with that reported by other investigators (Prakash and Patankar 1985). At such high Grashof number, the convective cell in the cavity has a stagnant eye of elongated shape (Figure 5.6), which is characterized by a uniform temperature profile along a large portion of the horizontal mid–plane (Figure 5.4). Most of the heat is transported by strong convection currents around the stagnant eye, characterized by vertical velocity peaks located very close to the vertical side–walls (Figure 5.5). The calculations confirm that the continuum conservation Equations (3.1)–(3.6) developed for multiphase problems transform, as they must, to well–established single–phase conservation equations.

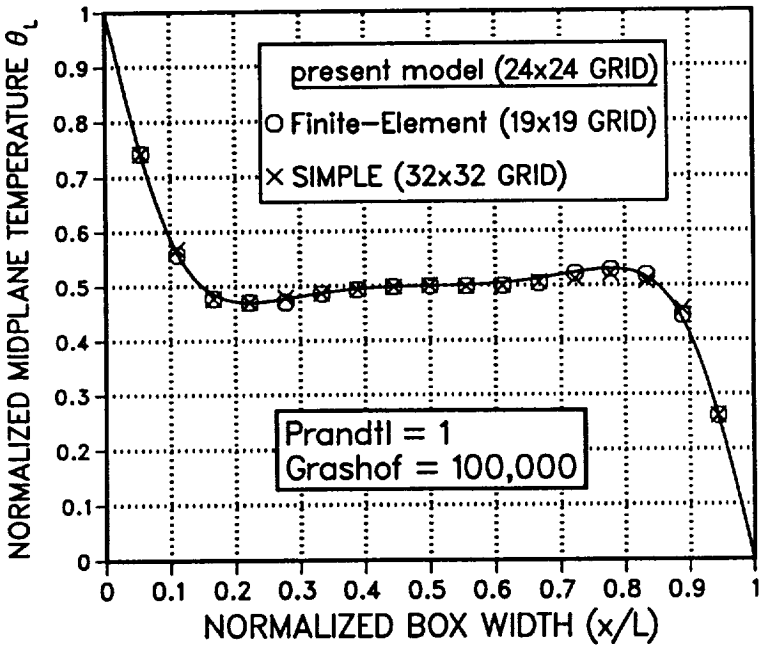

FIGURE 5.4. Temperature Profile along the Horizontal Mid–Plane for Natural Convection in a Square Cavity (Pr=1, Gr=10^5).

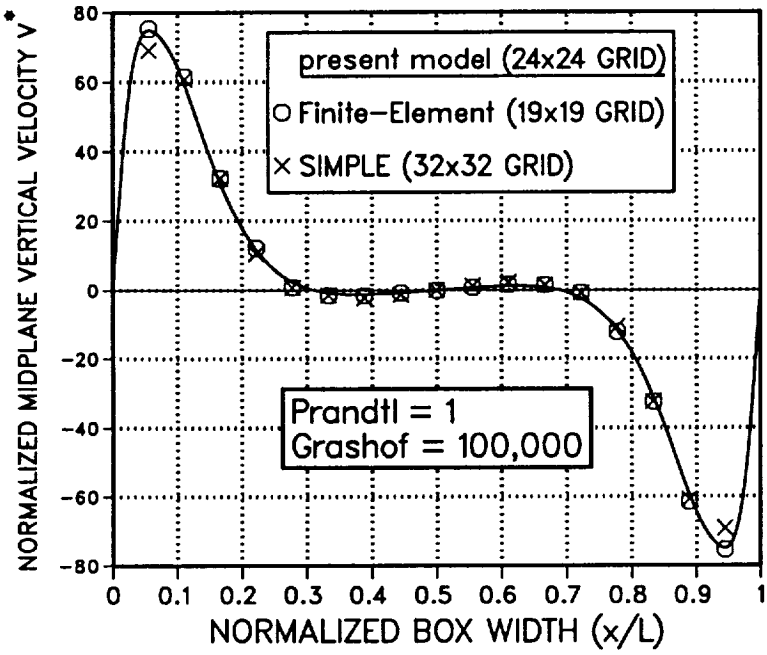

FIGURE 5.5. Vertical Velocity Profile along the Horizontal Mid–Plane for Natural Convection in a Square Cavity (Pr=1, Gr=10^5).

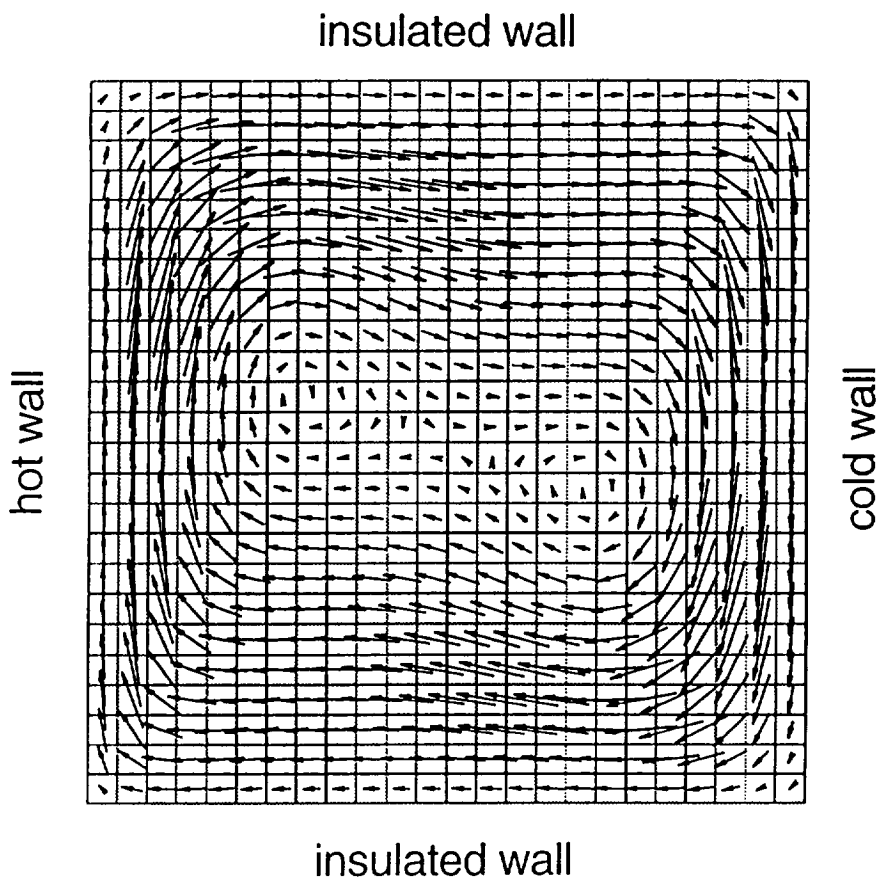

FIGURE 5.6. Flow Field for Natural Convection in a Square Cavity, at Pr=1 and $Gr=10^5$.

5.2. NATURAL CONVECTION OF MOLTEN GALLIUM IN A POROUS BED OF GLASS BEADS

In this section, the work of Beckermann and Viskanta (1988) is used to verify the Brinkman–Forchheimer–extended Darcy's model for predicting liquid flow in porous media. These authors studied numerically and experimentally the phase–change of pure gallium in a porous bed of randomly–packed glass beads, 6 mm in diameter. The well insulated rectangular test cell was 47.6 mm in height and width, and 38.1 mm in depth. The two vertical side–walls, which served as isothermal heat source and heat sink, were multipass heat exchangers machined out of a copper plate. The first experiment performed by Beckermann and Viskanta (Experiment 1) was a pure natural convection flow experiment. The temperatures of the hot and cold walls of the cavity were held constant above the melting temperature of gallium, at 325.05 K and 303.65 K, respectively. Figure 5.7 shows that the difference between the measured and predicted steady–state temperature profiles is less than 7% of the temperature difference across the test cell.

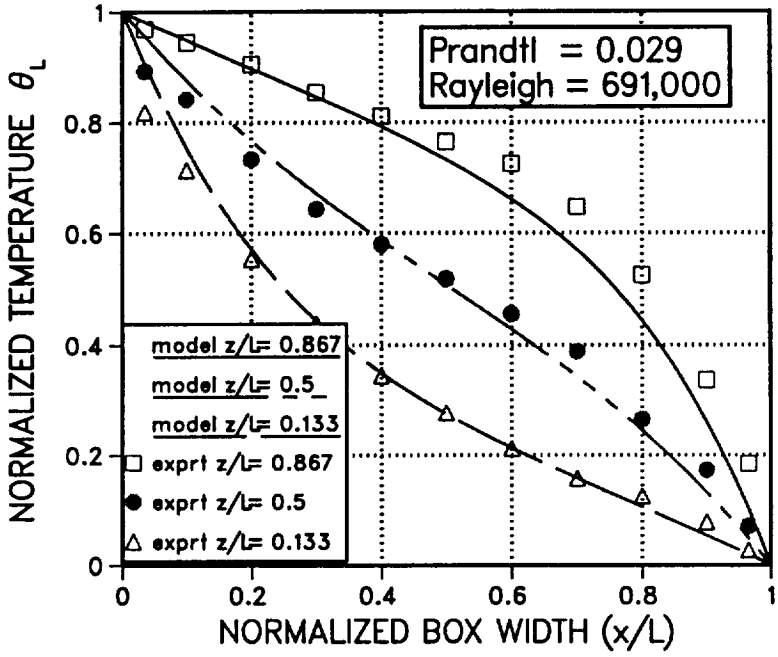

FIGURE 5.7. Measured and Predicted Temperature Profiles for Natural Convection of Pure Gallium in a Porous Bed of Glass Beads (Exp. 1, Beckermann and Viskanta 1988).

5.3. ONE-DIMENSIONAL SOLIDIFICATION PROBLEM

The analytical solution of the problem of pure conduction, one–dimensional solidification (Ozisik 1980) is used herein to verify the present freeze–and–thaw model of the heat pipe wick. The liquid and solid phases have constant, but different, thermophysical properties. Initially, the semi–infinite slab is liquid at a temperature T_o above the fusion temperature of the fluid, T_{fus}. The solidification process is initiated by lowering the wall temperature to a value T_C below T_{fus}. A dimensionless analysis of the problem shows that the solution is dependent only on three parameters, the ratio of solid and liquid thermal diffusivities, α_S/α_L, the Stefan number, St, and the dimensionless liquid superheat, T_o^*. In the dimensionless form, the crust thickness growths with time according to the relation (Ozisik 1980):

$$\frac{\delta(\tau)}{L} = 2\lambda\sqrt{\tau}\ , \tag{5.1}$$

where the freezing constant, λ, is given by the following transcendental equation:

$$\frac{\exp(-\lambda^2)}{\mathrm{erf}(\lambda)} - T_0^* \left(\frac{\alpha_S}{\alpha_L}\right)^{1/2} \frac{\exp(-\lambda^2 \alpha_S / \alpha_L)}{\mathrm{erfc}(\lambda\sqrt{\alpha_S / \alpha_L})} - \frac{\sqrt{\pi}}{St}\lambda = 0 \quad . \tag{5.2}$$

The temperature profiles in the solid and liquid are given by:

$$\frac{T_S(t) - T_C}{T_{fus} - T_C} = \frac{\mathrm{erf}(X^*)}{\mathrm{erf}(\lambda)}, \quad \text{for} \quad x \le \delta(t) \quad (X^* \le \lambda) \ , \tag{5.3a}$$

and

$$\frac{T_L(t) - T_o}{T_{fus} - T_o} = \frac{\mathrm{erfc}(X^*\sqrt{\alpha_S / \alpha_L})}{\mathrm{erfc}(\lambda\sqrt{\alpha_S / \alpha_L})}, \quad \text{for} \quad x \ge \delta(t) \quad (X^* \ge \lambda) \ . \tag{5.3b}$$

In Equations (5.3a) and (5.3b), the similarity variable $X^* = x / \sqrt{4\alpha_S t}$.

Numerical calculations are performed on a uniform grid of 50 cells, for a fluid with thermal diffusivities ratio $\alpha_S/\alpha_L=2$, and Stefan number St = 0.25 (the model used the following thermophysical properties: $\rho_S=\rho_L=1000$ kg/m^3; $C_p^S=C_p^L=1000$ J/kg.K; $k_S=100$ W/m.K; $k_L=50$ W/m.K; $H_{fus}=10^5$ J/kg; $T_{fus}=400$ K). Figures 5.8 to 5.11 compare the results of the present model with the exact analytical solution for the cases of no initial liquid superheat ($T_o^*=0$) and with liquid superheat ($T_o^*=0.25$). Also shown are the results of Beckermann and Viskanta's model (1988), which uses the conventional harmonic mean scheme of Patankar (1980) to estimate the heat fluxes (no special treatment is performed in the vicinity of the solidification front). Results of the present model compare well with the exact analytical solution, while the conventional harmonic mean scheme underpredicts the crust thickness and generates oscillations of large amplitude in the temperature time history. The larger the change in thermal conductivity of the working fluid upon freezing, the larger the amplitude of these oscillations. The peaks of the oscillations correspond to when the solidification front crosses an interface between two numerical cells.

Note that the present model does not produce perfectly smooth crust thickness and temperature histories, particularly for freezing problems with small Stefan number and large initial liquid superheat. This is because the average nodal temperature of a cell

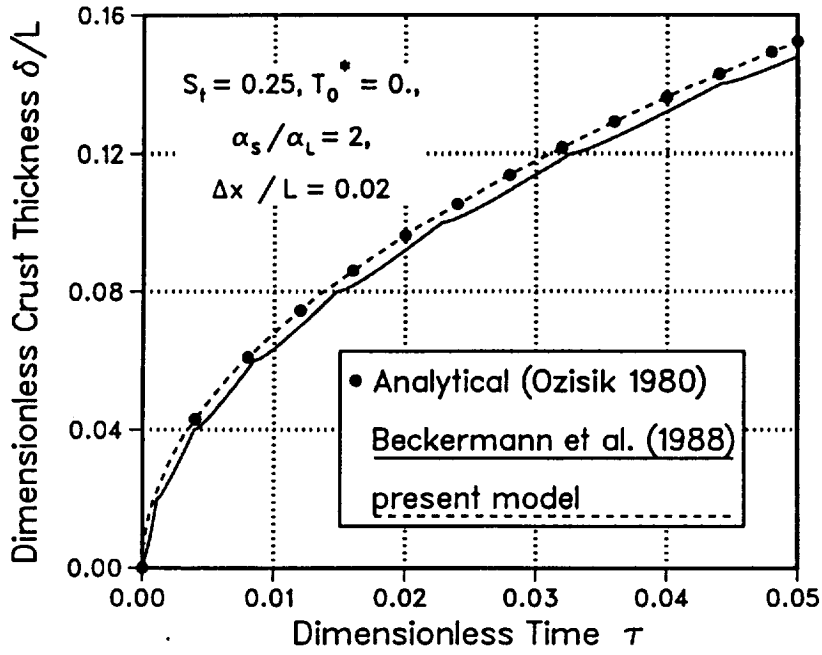

FIGURE 5.8. Crust Thickness as a Function of Time for the Slab Solidification Problem (St=0.25, no Liquid Superheat).

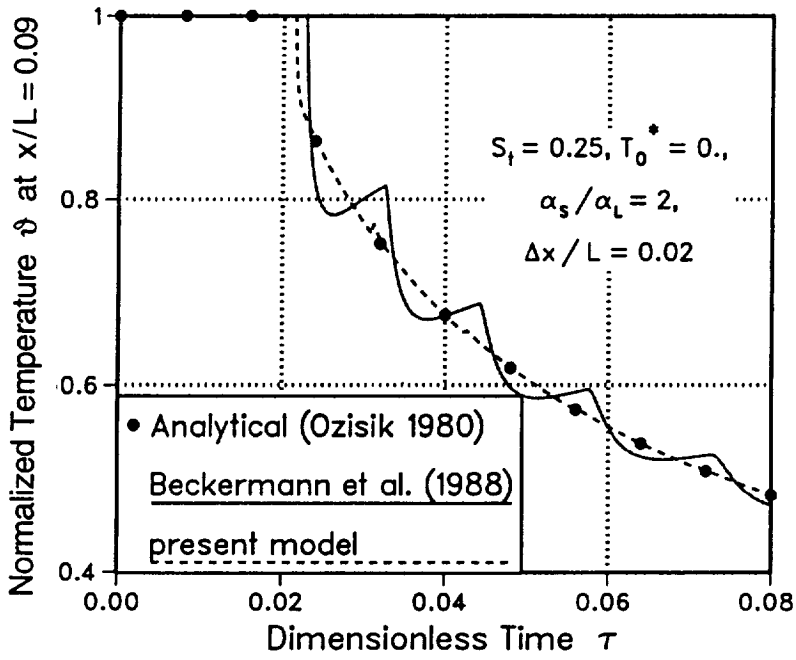

FIGURE 5.9. Temperature Histories at x/L=0.09 for the Slab Solidification Problem (St=0.25, no Liquid Superheat).

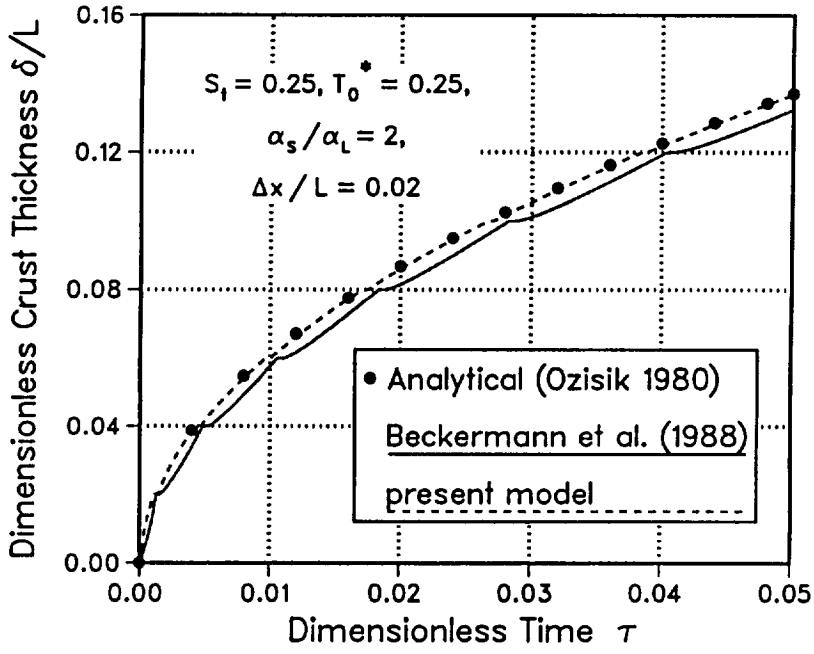

FIGURE 5.10. Crust Thickness as a Function of Time for the Slab Solidification Problem (St=0.25, with Liquid Superheat).

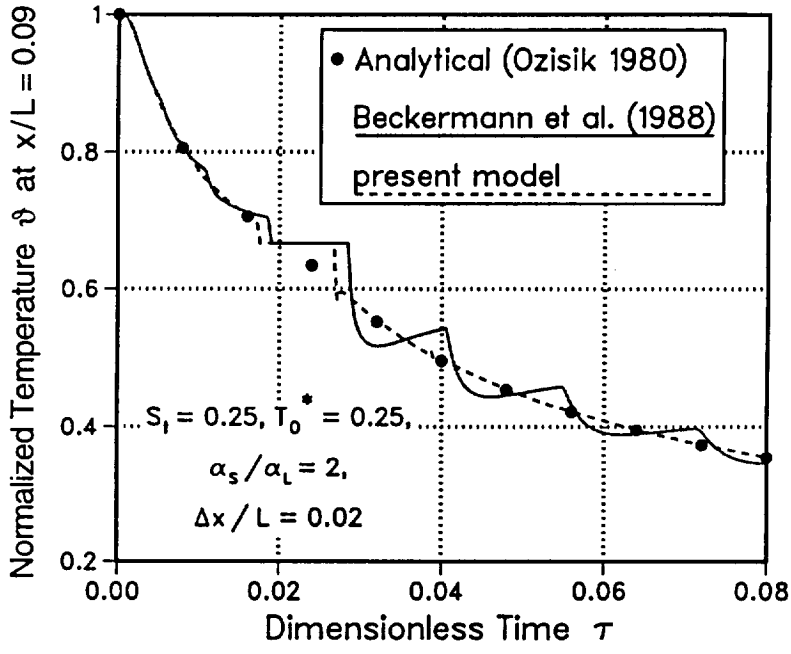

FIGURE 5.11. Temperature histories at x/L=0.09 for the Slab Solidification Problem (St=0.25, with Liquid Superheat).

undergoing phase–change is artificially set to the fusion temperature of the fluid, so that the change in the heat storage in the mushy cell is not predicted accurately. However, the present model is a good improvement over the classical fixed–grid enthalpy formulation, which uses the harmonic mean scheme; it reduces the amplitude of the wiggles in the temperature time histories by one–to–two orders of magnitude in all cases.

The freezing constant predicted by the present model was also computed for increasing Stefan numbers and liquid superheats and compared with the exact analytical solution and the numerical solution of Beckermann and Viskanta (1988) over a larger spectrum of conditions. As shown in Figure 5.12, the present model predicts the freezing constant quite well over the full range of Stefan numbers and liquid superheats investigated. However, the enthalpy model using the harmonic mean discretization scheme (referred to as Beckermann and Viskanta 1988) underpredicts the freezing constant, with the error increasing as the Stefan number decreases and/or the liquid superheat increases. The slower the transient, the flatter the temperature gradients in the vicinity of the freezing front, and the larger the numerical error introduced by the harmonic mean scheme.

An obvious alternative to the numerical error, step–like and weavy patterns characteristics of the fixed–grid enthalpy method is to decrease the numerical mesh size, so that the time over which the nodal temperature of the mushy cell is held at T_{fus} is reduced. Numerical calculations show that the magnitude of the oscillations decreases as the mesh size is decreased and/or the Stefan number increased, and the solution appears essentially smooth. As expected, the conventional enthalpy formulations provide accurate numerical results as long as the mesh size is sufficiently small.

5.4. TWO–DIMENSIONAL FREEZING IN A CORNER

The present freeze–and–thaw model is also verified using an approximate analytical solution for the two–dimensional (pure conduction) freezing problem in a corner (Rathjen and Jiji 1971). Initially, the liquid is at 12.5 K above its fusion temperature. Freezing is initiated by lowering the temperature of the two corner faces 25 K below the fusion temperature, which corresponded to a Stefan number, St= 0.5, and an initial liquid superheat, T_o^*=0.25 (the model used the following thermophysical properties: $\rho_S=\rho_L$=1000 kg/m^3; C_p^S=2000 J/kg.K; C_p^L=1000 J/kg.K; k_S=100 W/m.K; k_L=50 W/m.K; $H_{fus}=10^5$ J/kg; T_{fus}=400 K). The analytical solution is presented in Figure 5.13 in terms of the similarity variables X* and Z*, so that the freezing front profile is

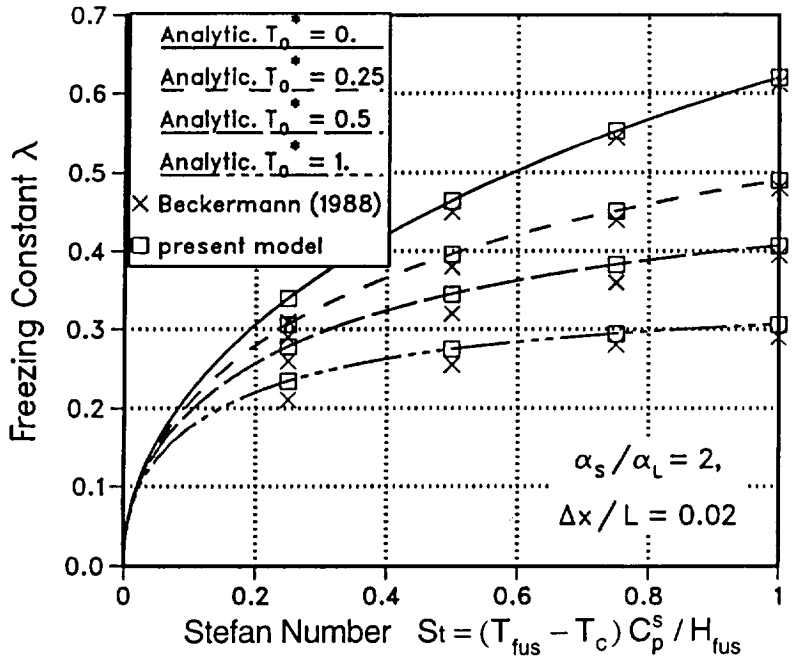

FIGURE 5.12. Freezing Constant at Various Liquid Superheats and Stefan Numbers for the Slab Solidification Problem.

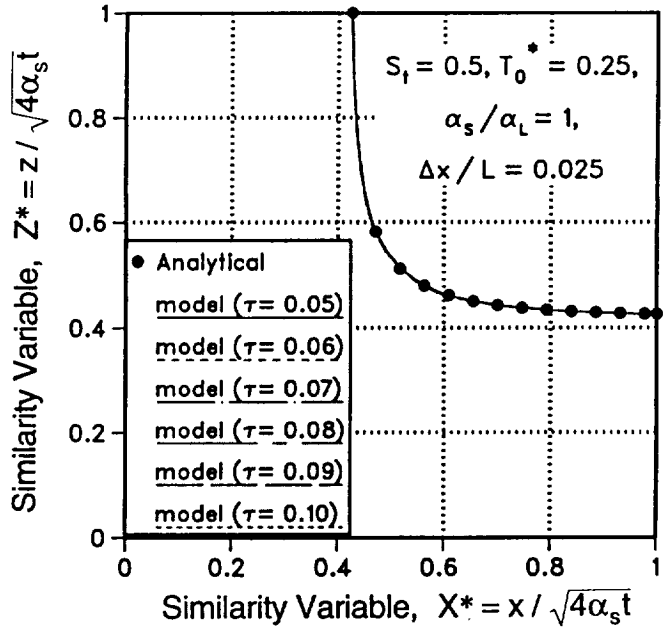

FIGURE 5.13. Comparison of Analytical and Numerical Front Locations for Freezing in a Corner (Rathjen and Jiji 1971).

stationary. Even though the present solution procedure is based on a one–dimensional analysis of the melting front location, it accurately predicts the shape of the liquid–solid interface of truly two–dimensional problems. As shown in Figure 5.13, the numerical predictions are in excellent agreement with the analytical solution.

5.5. FREEZING OF TIN IN A RECTANGULAR ENCLOSURE WITH NATURAL CONVECTION

The experimental work of Wolff and Viskanta (1988) is also used to benchmark the freeze–and–thaw model. These investigators studied the freezing of pure tin in a rectangular enclosure with differentially heated vertical side–walls and insulated horizontal boundaries, in the presence of natural convection. The rectangular test cell had inside dimensions of 66.6 mm in height, 88.9 mm in width, and 126 mm in depth. The hot side–wall temperature was kept at T_H=506.15 K. Initially, the fluid in the test cell was liquid, at this temperature (T_o=T_H). The phase–change process was initiated by lowering the cold wall temperature to a value of 502.15 K, which corresponded to a Stefan number (St) of 0.013.

The temperatures in the liquid and the locations of the freezing front were measured using a movable thermocouple probe and L–shaped glass rod, respectively. Figures 5.14 and 5.15 show the measured and predicted temperature profiles in the liquid at two different times in the transient. The scatter in the data is due to disturbances introduced by the measurements probes and to the uncertainty in thermocouple measurements (± 0.1 K), since the liquid superheat in the experiment was only 1.1 K (pure tin has a melting temperature of 505.05 K). Despite these difficulties in the measurements, the model predictions compare well with experimental data. Also, it is worth noting that the temperature profiles calculated by HPTAM are closer to the experimental data than that calculated by Wolff and Viskanta (1988), and Raw and Lee (1991).

Figure 5.16 shows the measured and predicted freezing fronts at preselected times. The early discrepancy between calculations and experimental data is because the specified cold wall temperature was not actually achieved in the experiment until approximately 0.033h. Also, imperfect insulation at the bottom of the test cell speeded up the solidification rate there, as remarked by Wolff and Viskanta (1988). Nevertheless, the front locations predicted by HPTAM compare also well with experimental data, and are similar to that calculated by Raw and Lee (1991). Figures 5.17 and 5.18 show the calculated liquid flow

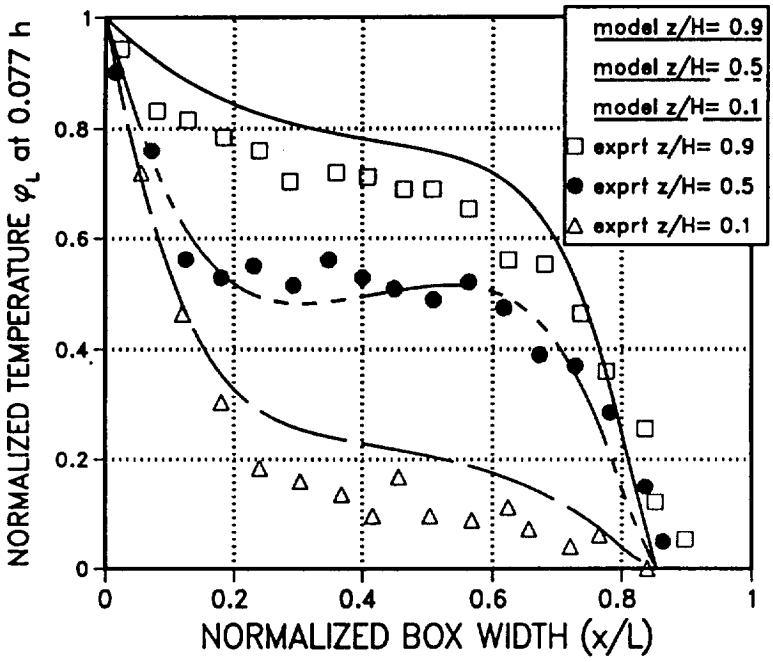

FIGURE 5.14. Comparison of Measured and Calculated Temperature Profiles in the Liquid at Time 0.077h, for Solidification of Pure Tin.

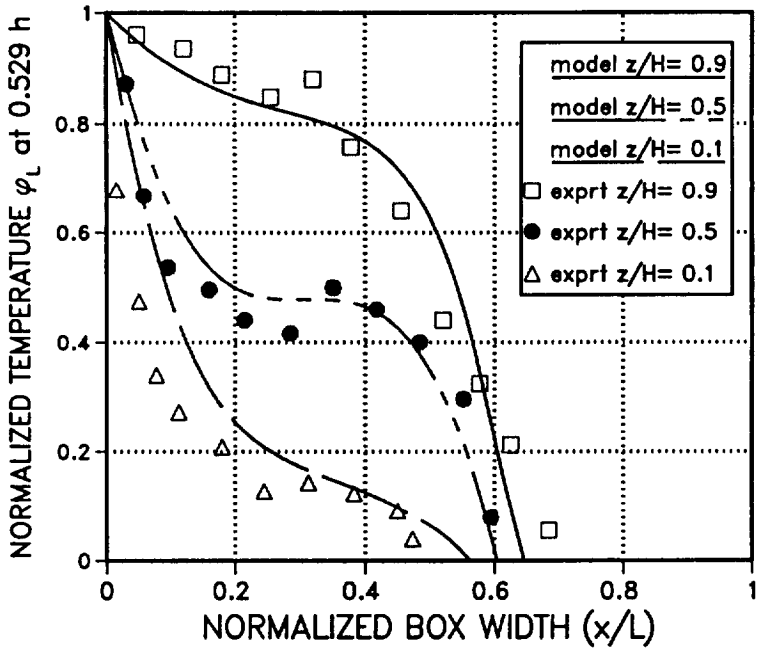

FIGURE 5.15. Comparison of Measured and Calculated Temperature Profiles in the Liquid at Time 0.529h, for Solidification of Pure Tin.

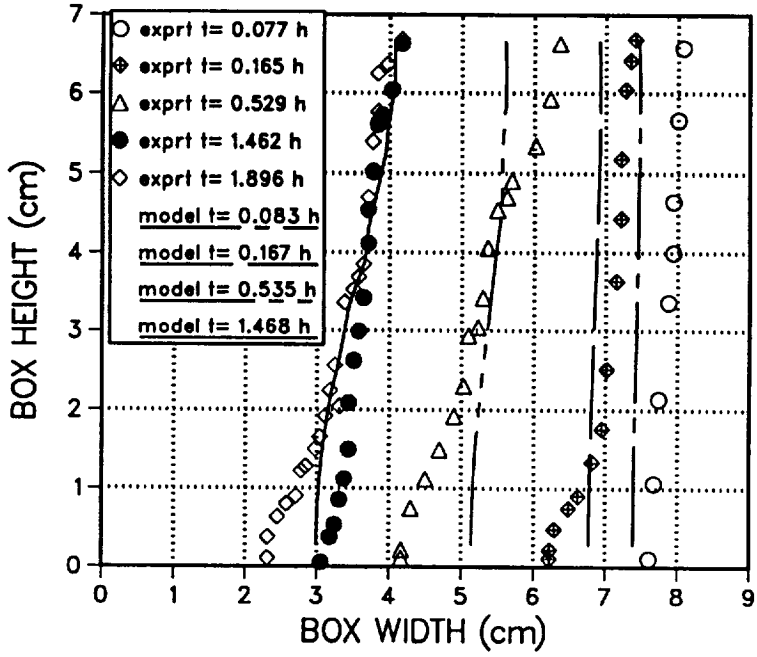

FIGURE 5.16. Comparison of Measured and Calculated Freezing Front Locations at Preselected Times, for Solidification of Pure Tin.

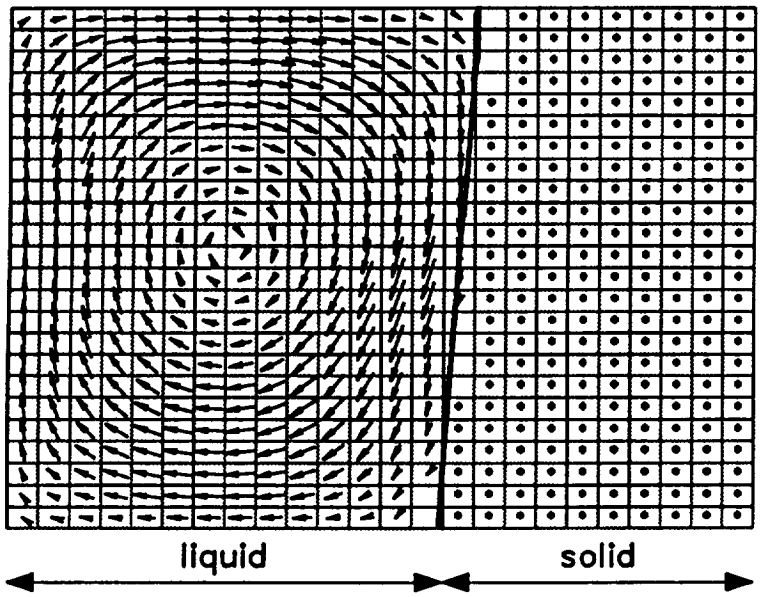

FIGURE 5.17. Calculated Liquid Flow Field at Time 0.529h, for Solidification of Pure Tin.

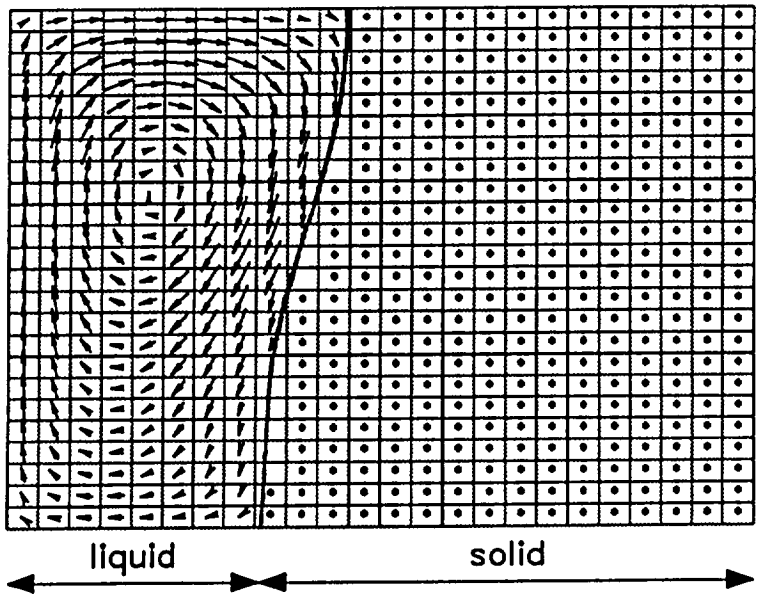

FIGURE 5.18. Calculated Liquid Flow Field at Time 1.468h, for Solidification of Pure Tin.

field in the cavity at two different times in the transient. As expected, the freezing front moves slower near the top of the cavity where the liquid, heated by the hot wall, impinges. The solidification rate increases toward the bottom of the cavity, since the liquid cools down as it descends along the interface.

This ends this chapter on the benchmark of the wick model. In the next chapter, results of the startup of a water heat pipe from a frozen state are presented and discussed.

6. STARTUP OF A WATER HEAT PIPE FROM A FROZEN STATE

This chapter presents the results of the startup of a water heat pipe from a frozen state. The calculation illustrates the importance of the sublimation and recondensation processes during the first period of the transient. The startup is characterized by partial recession of liquid in the evaporator wick after the capillary limit has been reached. After enough working fluid was melted by resolidification and condensation in the adiabatic and condenser sections of the heat pipe, resaturation of the wick was established before complete dryout of the evaporator occurred, leading to a successful startup.

6.1. DESCRIPTION OF THE TEST CASE

The copper heat pipe, 22 mm I.D., 25 mm O.D., has a 100–inch^{-1} mesh copper screen wick (ε=0.75, d=109 μm, R_p=72 μm), 1–mm thick. The evaporator, adiabatic, and condenser sections are 0.3 m, 0.1 m, and 0.6 m long, respectively. The evaporator is heated uniformly and the condenser is radiatively cooled to an ambient temperature of 260 K. The emissivity and view factor of the condenser are taken as 1 and 2, respectively. The view factor accounts for the increased radiative area due to the condenser fin. Because water expands upon freezing, it is assumed that the ice extends initially 0.046 mm above the screen surface (Figure 6.1a); the mass of working fluid in the heat pipe is 48.0 g (Figure 6.2).

6.2. TRANSIENT OPERATION WITH FROZEN EVAPORATOR

The frozen heat pipe is initially at 260 K when the input power to the evaporator was increased in a step–function to 50 W. After about 20 s, 36 W are consumed in the sublimation–resolidification process of the ice (Figure 6.3), and the other 14 W are used to raise the temperature of the heat pipe structure and solid working fluid in the evaporator (Figure 6.4). Most of the heat generated by resolidification along the adiabatic and condenser sections of the heat pipe is used to raise the temperature in these sections. As a result, the power radiated away at the condenser wall increases steadily, as shown in Figure 6.5. After about 140 s, when the heat pipe temperature reaches the fusion temperature of ice, the fraction of the power throughput radiated away at the condenser wall is still small, only 5.3 W (Figure 6.5). This is characteristic of radiative heat transfer, which increases with the fourth power of the temperature. The sublimation–resolidification

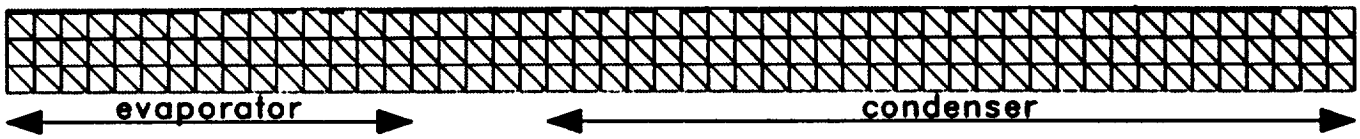

(a) Time = 0 s

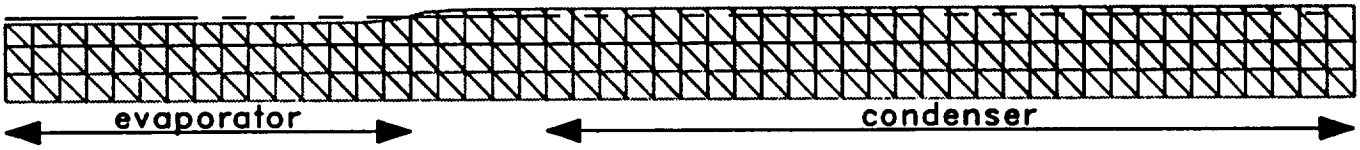

(b) Time = 140 s

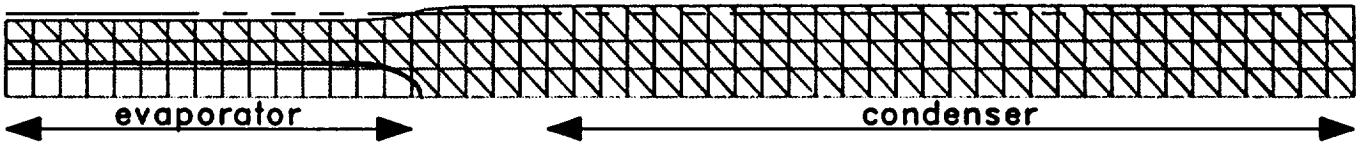

(c) Time = 188 s

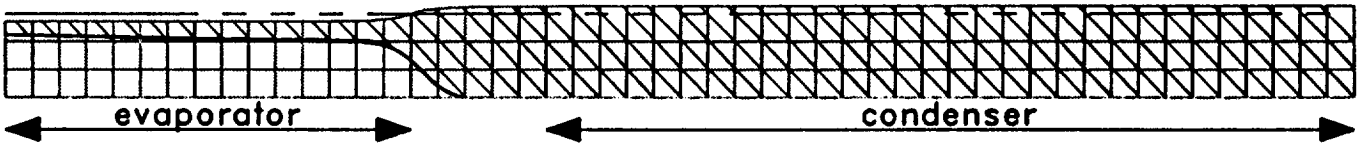

(d) Time = 225 s

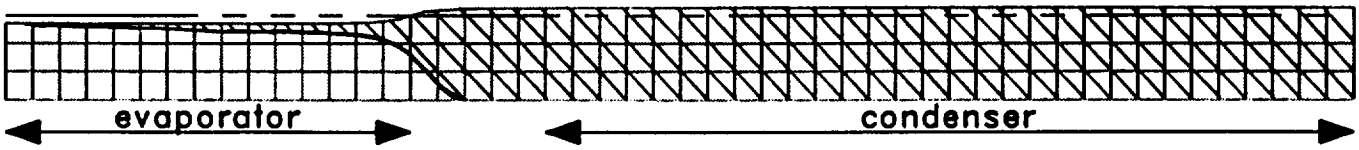

(e) Time = 247 s

FIGURE 6.1. Solid and Liquid Phases Distributions in the Wick during Startup of the Water Heat Pipe.

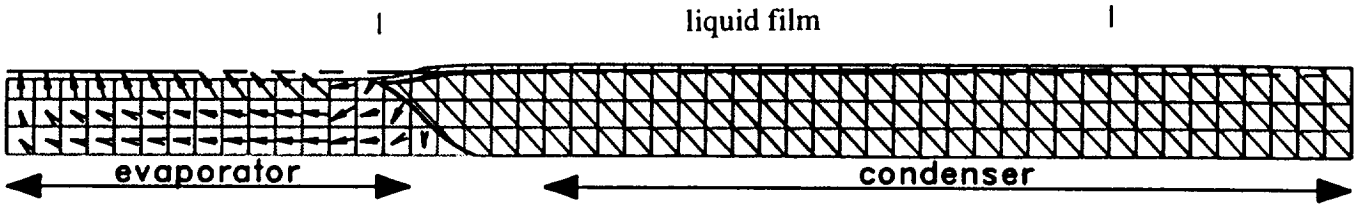

(f) Time = 251 s

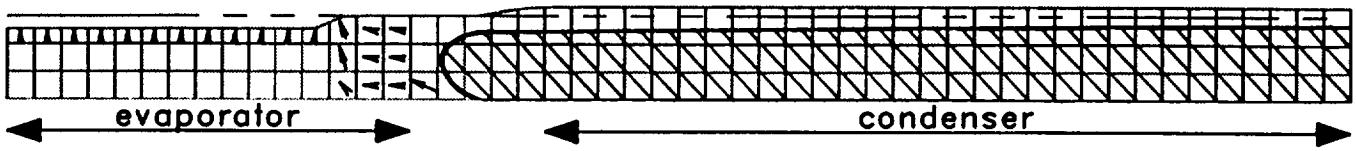

(g) Time = 309 s

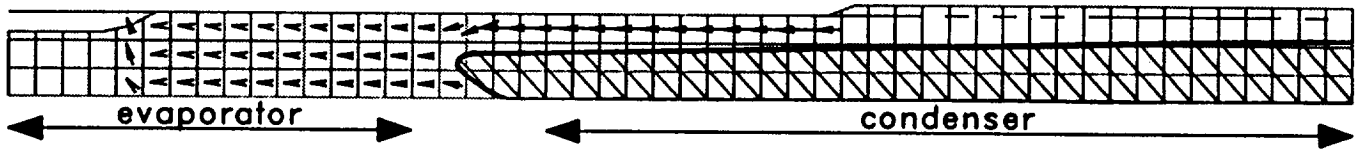

(h) Time = 369 s

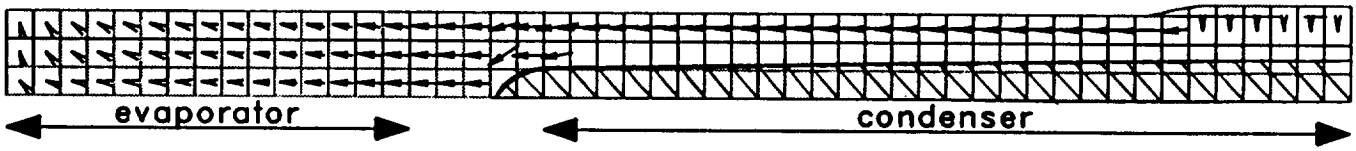

(i) Time = 429 s

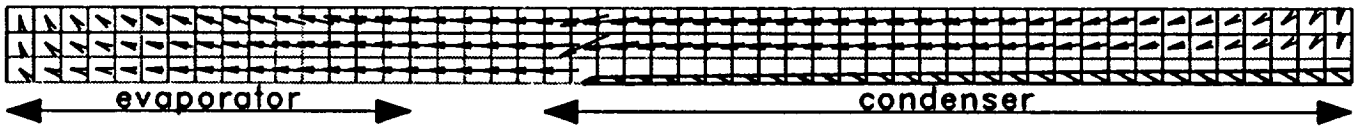

(j) Time = 506 s

FIGURE 6.1. Solid and Liquid Phases Distributions in the Wick during Startup of the Water Heat Pipe (Cont.).

process partially depletes the frozen working fluid in the evaporator and accumulates it in the adiabatic and condenser sections (Figure 6.1b). During the first 140 s of the transient, when the working fluid is still frozen in the evaporator, the heat pipe can be considered to operate like a fully–thawed heat pipe during heatup transient (Figures 6.4 to 6.6), with the differences that the heat transport mechanism is sublimation–resolidification instead of evaporation–condensation, and that the displaced working fluid cannot circulate back to the evaporator. That is, the loss of working fluid by sublimation will eventually lead to complete dryout of the evaporator and startup failure. Note the slight increase in the sublimation rate with time (Figure 6.3) due to the slow decreases in the radial thermal resistance and heat storage capacity of the evaporator wick. The normalized working fluid level at the evaporator end of the wick, $[R_{int}(1)-R_{wk}] / \Delta R_{il}$, is plotted in Figure 6.7. A value of zero corresponds to a wick saturated with working fluid, while a positive value means that the working fluid extends above the screen surface, in the vapor core, and a negative value represents a fluid level receded within the wick. As shown in Figure 6.7, the level of ice in the evaporator decreases at uniform rates during the first 140 s of the startup transient. The rate takes a larger value as soon as the level starts receding within the wick, because of the smaller volume porosity of the screen wick.

6.3. THE MELTING PROCESS OF THE EVAPORATOR

As the wall temperature continues to increase, the working fluid at the evaporator wall begins to melt. The melting front progresses essentially radially with time, as shown in Figures 6.1c and 6.1d. Most of the heat input (41 W) is consumed in the thaw of the working fluid, and the importance of the sublimation–resolidification process quickly diminishes, transporting only 5.4 W (Figure 6.3). This reduction in the sublimation rate is responsible for the slower rate of decrease in the evaporator ice level (Figure 6.7) during the melting process of the evaporator, from 142 s to 247 s.

During the thaw process of the heat pipe, from 142 s to 530 s (Figure 6.2), the temperature of the condenser remained close to the fusion temperature of the working fluid, and the radiative output power remained essentially constant at 5.3 W (Figure 6.5). Also, the evaporator temperature remained within only a few Kelvins of the fusion temperature (Figures 6.4 and 6.6), so that the startup of the water heat pipe was essentially uniform in temperature. This is characteristic of the startup of low–temperature heat pipes, which become immediately active upon heatup, as sublimation and evaporation of working fluid (and their counterparts, resolidification and condensation) have the potential of transporting

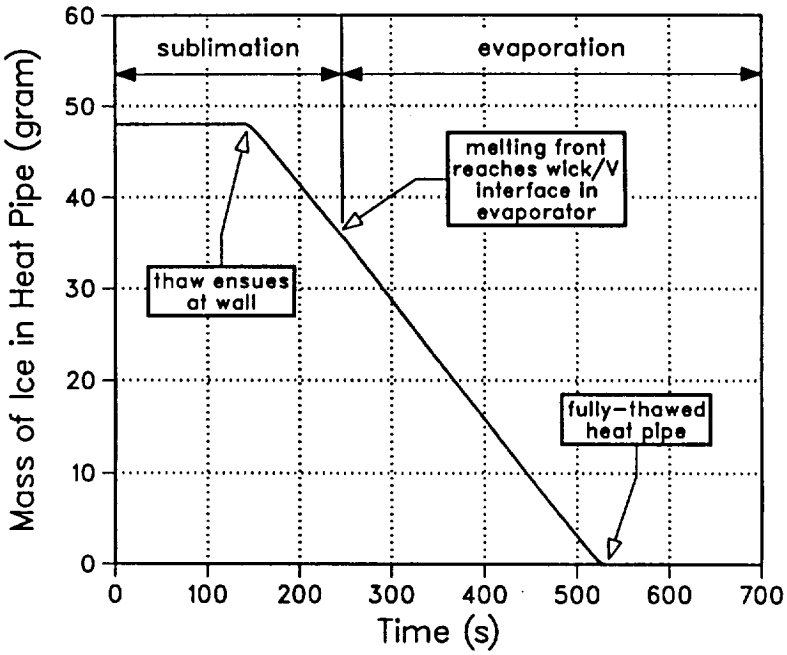

FIGURE 6.2. Calculated Mass of Ice in the Water Heat Pipe during Startup from a Frozen State.

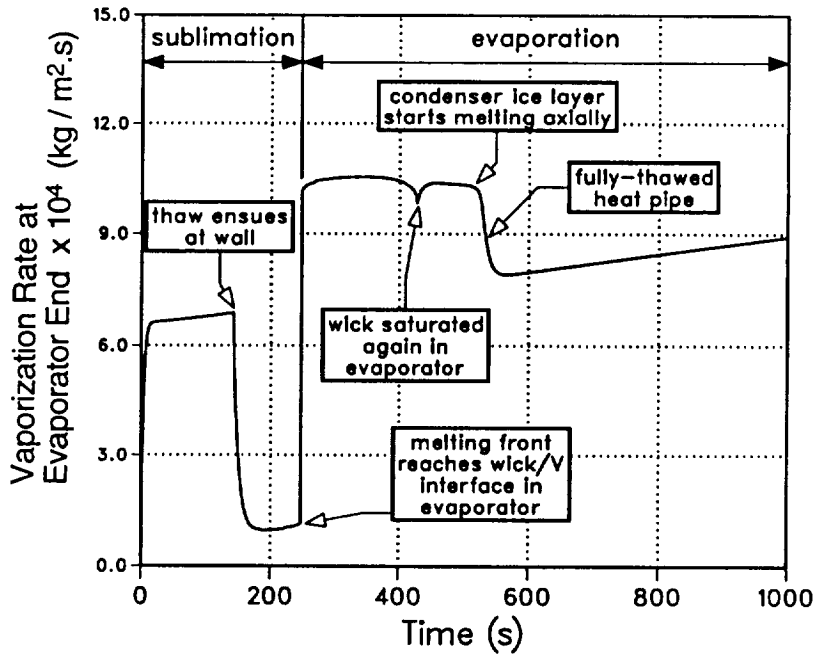

FIGURE 6.3. Calculated Vaporization Rate during Startup of the Water Heat Pipe as a Function of Time.

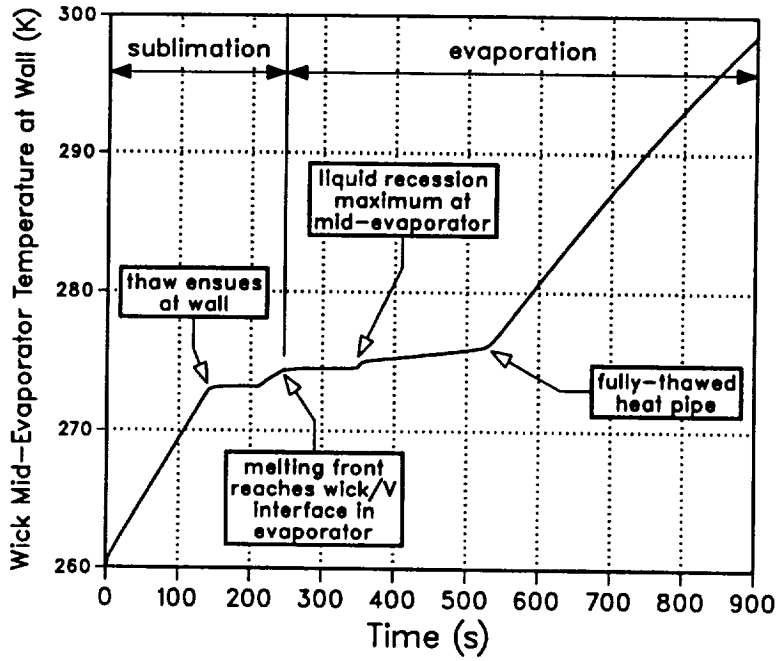

FIGURE 6.4. Calculated Mid-Evaporator Wick Temperature at Wall during Startup of the Water Heat Pipe as a Function of Time.

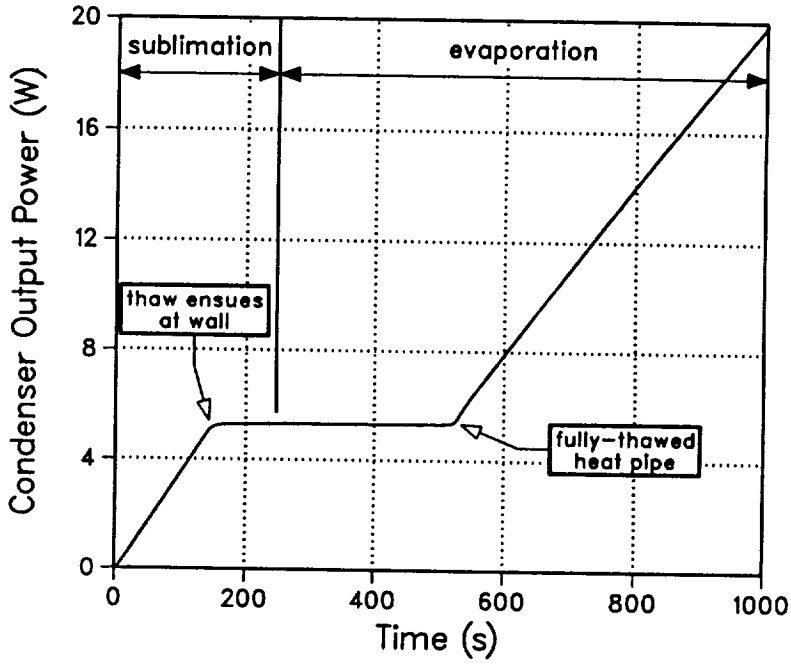

FIGURE 6.5. Calculated Condenser Output Power during Startup of the Water Heat Pipe as a Function of Time.

large amounts of energy without encountering any vapor transport limitations, as in the case of high–temperature heat pipes.

After 248 s, the thaw front reaches the wick–vapor interface first at the evaporator end (Figures 6.1d and 6.1e). Within only a few seconds, most of the wick–vapor interface in the evaporator is thawed (Figure 6.1f). Consequently, most of the heat input is used to evaporate the working fluid (the power throughput is essentially 50 W), as indicated by the jump in the rate of evaporation in Figure 6.3. Most of the heat deposited by condensation and resolidification along the adiabatic and condenser sections of the heat pipe is consumed in the thaw of the working fluid (about 40 W), causing the melting front to proceed radially outward in the condenser and adiabatic sections (Figures 6.1f to 6.1j).

6.4. THE MELTING PROCESS OF THE CONDENSER

After the thaw front reached the wick–vapor interface in the evaporator, simultaneous melting and condensation occurred at the L–V interface in the adiabatic and condenser sections, forming a liquid film near the leading edge of the frozen fluid (Figure 6.1f). Figure 6.8 shows the axial vapor velocity along the centerline of heat pipe during the formation of the liquid film. The vapor velocity peaks at the axial location corresponding to the thaw front at the wick–vapor interface. At 248.0 s, the liquid film extends to the end of the adiabatic section, and resolidification still occurs along the S–V interface in the condenser (Figure 6.8). After an additional 1.4 s, the liquid film extends to the middle of the condenser, and covers all of the condenser at t=252.4 s.

Evaporation depletes the working fluid in the evaporator, and the vapor pore volume fraction in the wick (or the cosinus of contact angle of the liquid meniscus) rises, eventually reaching a value of 1 (Figure 6.9). At 267 s, the capillary pressure head reached its maximum value along the evaporator, however, the frictional drag at the film–solid interface slowed liquid return, causing a liquid recess in the evaporator wick (Figure 6.7).

As melting proceeded radially outward in the adiabatic and condenser sections, enough working fluid thawed and began to replenish the liquid in the evaporator; this occurred before the wick would have dried out in the evaporator (Figures 6.1g and 6.1h), causing unsuccessful startup. At 300 s, the vapor pore void fraction recovered at the beginning of the adiabatic section (Figure 6.10), and liquid flowed to refill progressively the wick towards the evaporator end (Figures 6.1g to 6.1h). During that phase, evaporation kept

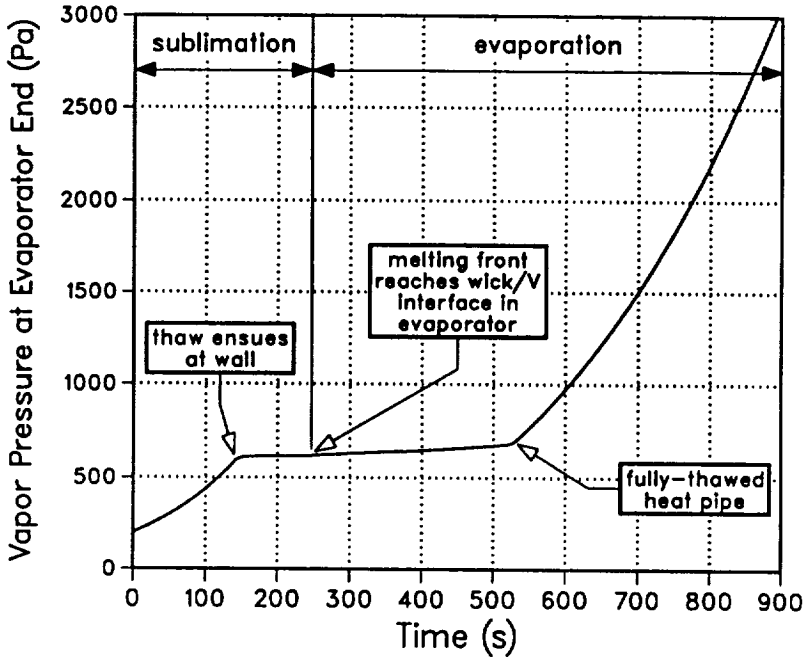

FIGURE 6.6. Calculated Vapor Pressure at Evaporator End during Startup of the Water Heat Pipe as a Function of Time.

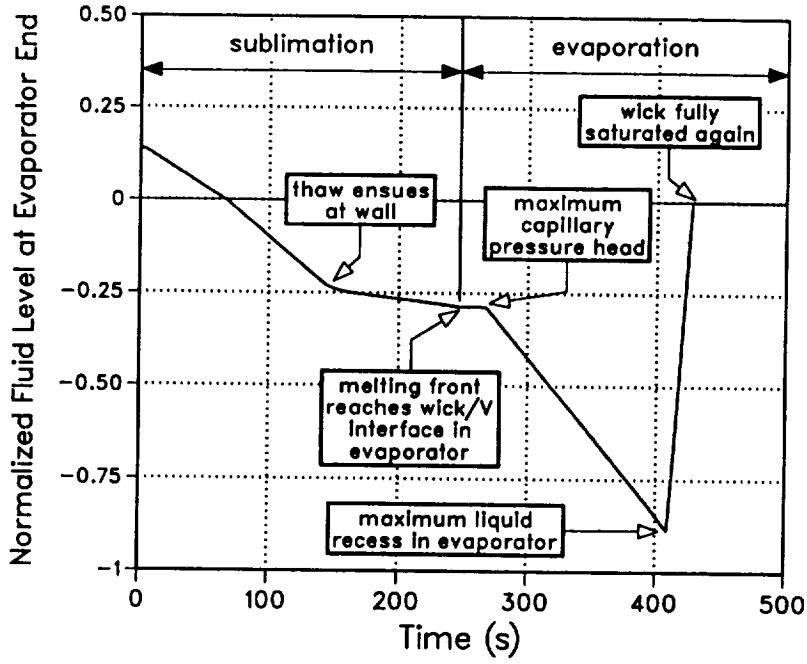

FIGURE 6.7. Calculated Normalized Working Fluid Level at Evaporator End during Startup of the Water Heat Pipe as a Function of Time.

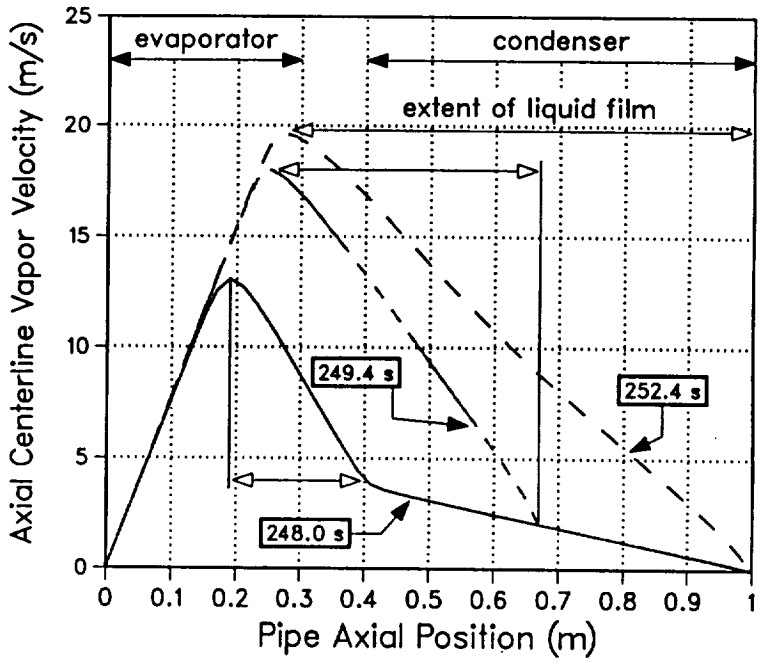

FIGURE 6.8. Axial Vapor Velocity along the Centerline of the Water Heat Pipe during Formation of a Thin Liquid Film.

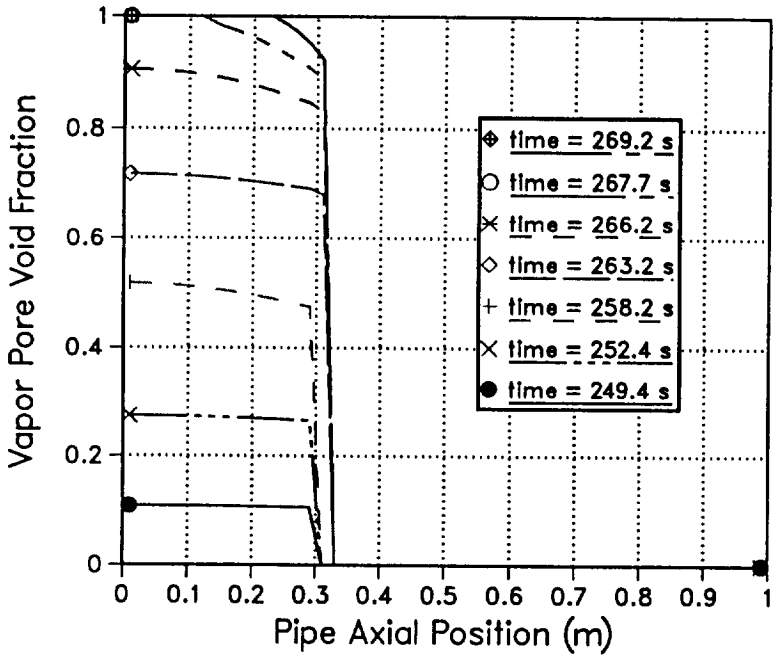

FIGURE 6.9. Calculated Axial Distribution of the Pore Vapor Fraction in the Wick during Liquid Recess.

depleting the working fluid in the unsaturated portion of the evaporator, and the liquid level receded further down in the wick (Figure 6.7). Figure 6.11 shows the vapor and liquid pressure distributions along the heat pipe at two different times during resaturation of the wick. The vapor pressure is almost uniform along the heat pipe, at a value corresponding to the saturation at the fusion temperature of the working fluid, and this during the entire thaw process of the heat pipe (Figure 6.6). The liquid pressure corresponds to the maximum capillary pressure head of the heat pipe along the unsaturated portion of the condenser, and is equal to the vapor pressure along the portion of the wick covered with the liquid film. At time 410 s, the liquid reached its lowest level in the wick at the evaporator end of the heat pipe (Figure 6.7), and the wick became fully saturated with liquid at 429 s (Figures 6.1i and 6.7). Resaturation of the wick caused a temporary decrease in the evaporation rate (Figure 6.3), as some of the heat input was consumed in heating the cold liquid returning to the evaporator from the condenser section.

Figure 6.12 shows the vapor and liquid pressure distributions along the heat pipe at time 439 s, shortly after resaturation of the wick. The vapor pore void fraction has recovered along the entire length of the evaporator section (Figure 6.10), and the heat pipe operation is not limited by the capillary limit anymore. Liquid and Vapor interfacial pressures are equal along the shorter extent of the liquid film. The extent of the liquid film in the condenser decreased with time due to the reduction in the working fluid volume as it melted (Figures 6.1g to 6.1i). At 506 s, the liquid film disappeared, shortly after the wick became fully saturated with liquid (Figure 6.1j). This was expected, since the heat pipe was nearing the condition for which the liquid charge of working fluid was calculated (that is, a fully-saturated wick with liquid fluid at the fusion temperature of the working fluid).

At 511 s, the thin ice crust along the condenser began to melt rapidly, uncovering the wall and causing the portion of the power throughput consumed in the thaw of the working fluid to drop quickly from 42 W to zero (in about 23 s). The portion used to raise the temperature of the heat pipe structure and liquid in the condenser increased accordingly. As a result, the condensation rate decreased, causing the vapor pressure to increase faster, and the evaporation rate in the evaporator to temporarily drop (Figure 6.3).

At 534 s, the heat pipe is fully–thawed, and a larger portion of the input power is consumed in raising the thermal inertia of the heat pipe structure and working fluid, causing the evaporation rate to drop even faster (Figure 6.3). After about 30 s, a uniform radial temperature gradient was established in the condenser and proper circulation of liquid to the

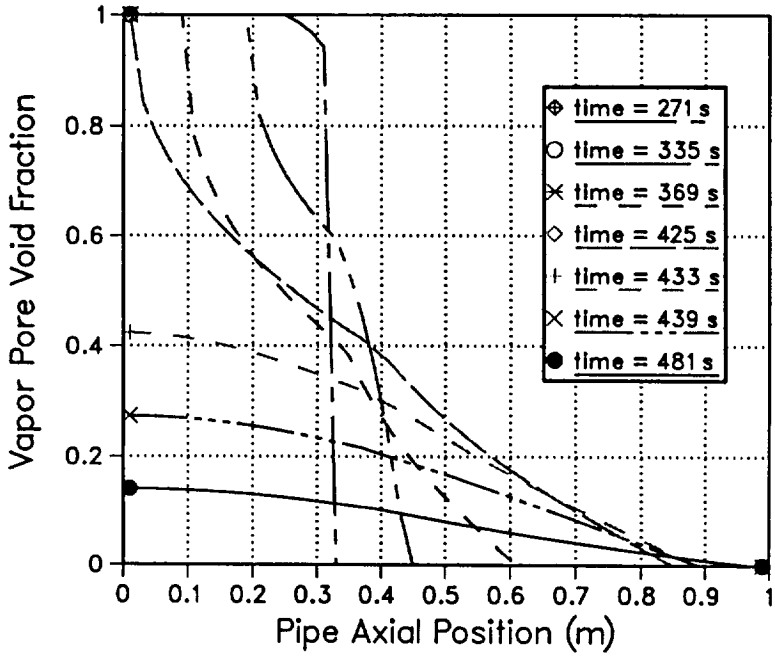

FIGURE 6.10. Calculated Axial Distribution of the Pore Vapor Fraction in the Wick during Resaturation of the Evaporator Wick.

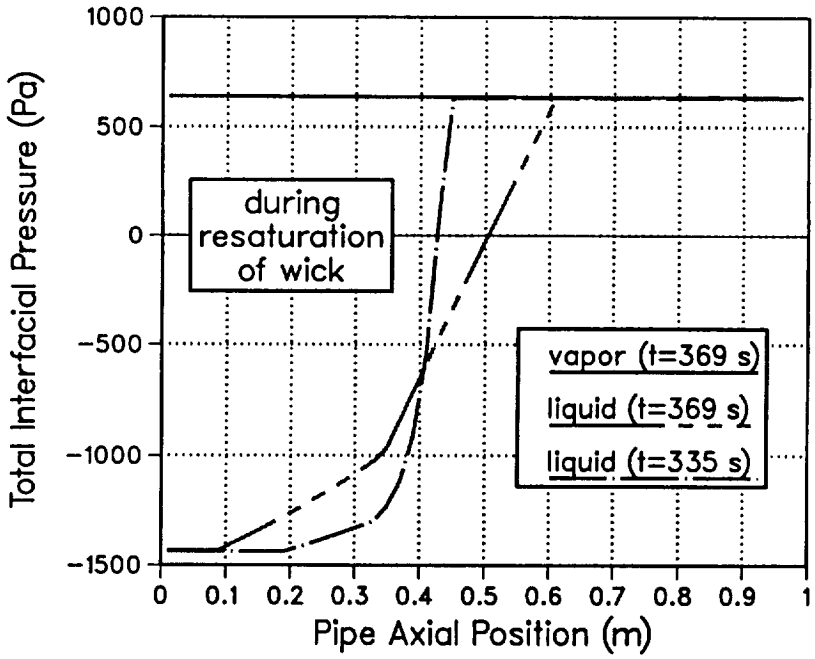

FIGURE 6.11. Calculated Axial Distributions of Liquid and Vapor Pressures during Resaturation of the Evaporator Wick.

C-3

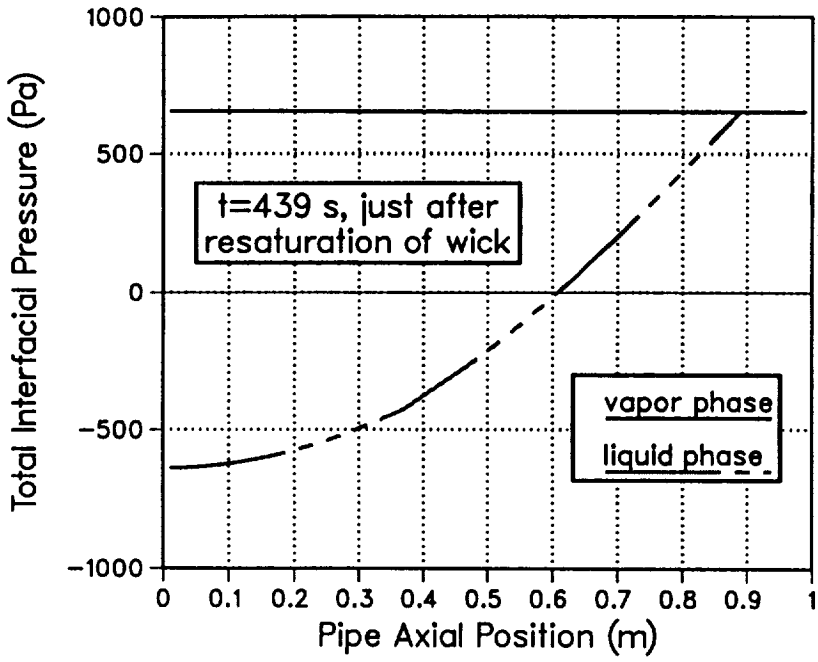

FIGURE 6.12. Calculated Axial Distributions of Liquid and Vapor Pressures Shortly After Resaturation of the Evaporator Wick.

evaporator was fully resumed. Beyond this point, the heat pipe temperature and the condenser output power rose gradually (Figures 6.4 to 6.6), approaching steady–state when the rate of heat rejection in the condenser equals the power input to the evaporator.

This ends the presentation and discussion of the results of the frozen startup of a water heat pipe. In the next chapter, the model is benchmarked using transient experimental data of a fully–thawed horizontal water heat pipe.

7. TRANSIENT CALCULATIONS OF FULLY–THAWED WATER HEAT PIPE AND COMPARISON WITH EXPERIMENTAL DATA

The fully–thawed heat pipe model is benchmarked using transient experimental data of a horizontal water heat pipe. The calculated steady–state vapor and wall axial temperature profiles and the transient power throughput and vapor temperature are in good agreement with measurements. Also presented and discussed are the calculated axial distributions of liquid and vapor pressures, effective radius of curvature of the liquid meniscus at the liquid–vapor interface, and liquid pooling and recession following a step function heatup and cooldown transients of the water heat pipe.

7.1. DESCRIPTION OF THE WATER HEAT PIPE EXPERIMENT AND MODELING

To verify the system of equations in HPTAM, the model predictions are compared with the transient results of El–Genk and Huang (1993) for a horizontal water heat pipe experiment. The copper heat pipe, 1.73 cm I.D., 1.91 cm O.D., employs a double–layered, 150 mesh copper screen wick. The lengths of the evaporator, adiabatic, and condenser sections are 60 cm, 9 cm, and 20 cm, respectively (Figure 7.1). The vapor temperature is measured along the centerline of the heat pipe using a special probe made of a thin walled brass tube (3.2 mm O.D.) instrumented with eleven thermocouples, equally spaced along the heat pipe. An additional eleven thermocouples are attached to the outer surface of the heat pipe wall to measure its temperature at the same axial location as the vapor temperature thermocouples. The evaporator section is uniformly heated using a flexible electric tape and the condenser section is convectively cooled using a water jacket. More details on the heat pipe design and experimental setup can be found in El–Genk and Huang (1993).

The experimental heat pipe was initially at room temperature (296.2 K) when the electrical power to the heating tape in the evaporator section increased in a step–function to 575 W. The cooling water enters the condenser cooling jacket at 294.5 K and 11.33 g/s. After about 10 minutes into the heatup transient, the heat pipe reaches steady–state. At steady–state, the effective power throughput, determined from the heat balance in the condenser cooling jacket, was 443 W. The difference between the electric input to the electric tape and the steady–state effective power throughput (132 W) was approximately equal (within 5%) to the heat losses from the surface of the insulation in the evaporator section to ambient

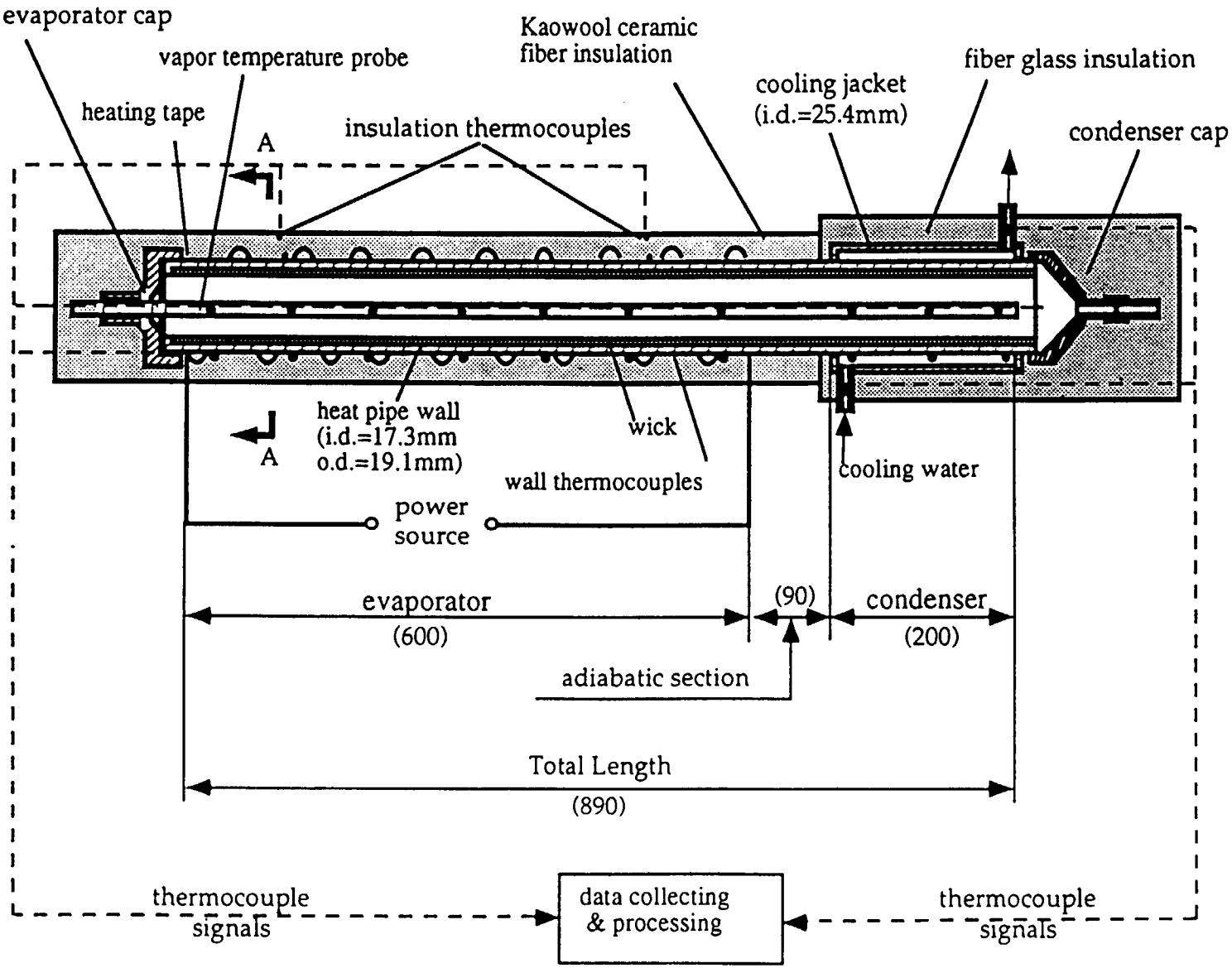

FIGURE 7.1. Water Heat Pipe Experimental Setup (El–Genk and Huang 1993).

by natural convection (El–Genk and Huang 1993). After about 7 minutes of steady–state operation, the electrical power to the heating tape was turned off (t=1040 s), and the cooldown of the heat pipe was observed.

Because the water flow rate in the cooling jacket is relatively small, a transient one–dimensional water jacket submodel was thermally coupled to the condenser wall in HPTAM in order to calculate the axial distribution of the coolant bulk temperature in the jacket. At steady–state, the average convective heat transfer coefficient in the jacket determined from the experiment was 1800 W / m^2.K; this value is used in the model during the simulation. The wick thickness assumed is 0.75 mm, and wick effective pore radius, porosity and permeability were taken as 54 μm, 0.9 and 1.5×10^{-9} m^2, respectively. The effective thermal conductivity of the liquid–wick region is calculated using the equation given by Chi (1976) for distributed cylinders having an effective porosity of 0.5. The evaporation accommodation coefficient in Equation (3.18) was taken as 0.1 for water vapor, and the initial vapor void fraction in the wick was assumed uniform along the heat pipe, with a value of 0.15.

7.2. COMPARISON OF THE MODEL WITH WATER HEAT PIPE EXPERIMENT

To account for the actual heat input to the heat pipe evaporator section during the experiment, transient calculations were performed using the measured transient wall temperatures along the evaporator section. This approach gives good estimate of the input heat flux in the evaporator region, without the complexity and uncertainty associated with modeling the thermal response of the electric heater and of the insulation along the evaporator section. Comparison with the experimental results shown later confirm the validity of using the transient wall temperatures to determine the heat input to the evaporator region of the heat pipe. In the experiment, the wall temperature in the evaporator section was measured at 7 axial locations and found to be uniform. The design and operational parameters of the experimental water heat pipe analyzed are listed in Table 7.1.

Figures 7.2 and 7.3 compare the calculated transient response of the vapor temperature and of the effective power throughput, determined from the heat balance in the cooling jacket, with experimental data. The calculated effective power throughput at steady–state (455 W)

TABLE 7.1. Design and Operational Parameters of Experimental Water Heat Pipe Analyzed.

Design Parameter	Value	Operational Parameter	Value
Heat pipe length L (cm)	89	Initial pipe temperature (K)	296.2
Evaporator length L_e (cm)	60	Initial pore void fraction	0.15
Condenser length L_c (cm)	20	Startup mode	Evaporator wall temperature specified
Adiabatic length L_a (cm)	9		
Pipe outer diameter (mm)	19.10	Shutdown mode	Step function
Wall thickness (mm)	0.90	Evaporator wall temperature	Uniform
Liquid/wick thickness (mm)	0.75	Evaporator maximum heat flux (W/cm^2)	1.25
Effective pore radius (μm)	54	Maximum power throughput (W)	450
Wick porosity ε	0.7	Condenser cooling method	Convective
Wick permeability (m^2)	1.5×10^{-9}	Jacket coolant flow rate (gram/s)	11.33
Wall material	Copper	Jacket coolant inlet temperature (K)	294.5
Working fluid	Water	Jacket heat transfer coefficient (W/m^2K)	1800.

is almost the same as that reported in the experiment (443 W). However, the transient response of the calculated power throughput is somewhat faster than that in the experiment. This is because in the experiment, a relatively large fraction of the heat generated in the electric tape is initially stored in the insulation surrounding the evaporator and adiabatic sections and in the condenser jacket, therefore slowing down the heat pipe transient. As shown in figure 7.3, the calculated transient vapor temperature compares very well with experimental measurements. At steady–state, the calculated vapor temperature was only 1.2 K lower than that measured. Such good agreements at steady–state suggest that the model can predict the thermal resistance of the heat pipe quite well. Figure 7.4 compares the calculated wall and vapor temperatures along the heat pipe with those measured at different times during the heatup transient; again the comparison is good. The difference between calculated and measured wall temperatures in the condenser section is attributed to the fact that an axially uniform convective heat transfer coefficient is used along the cooling

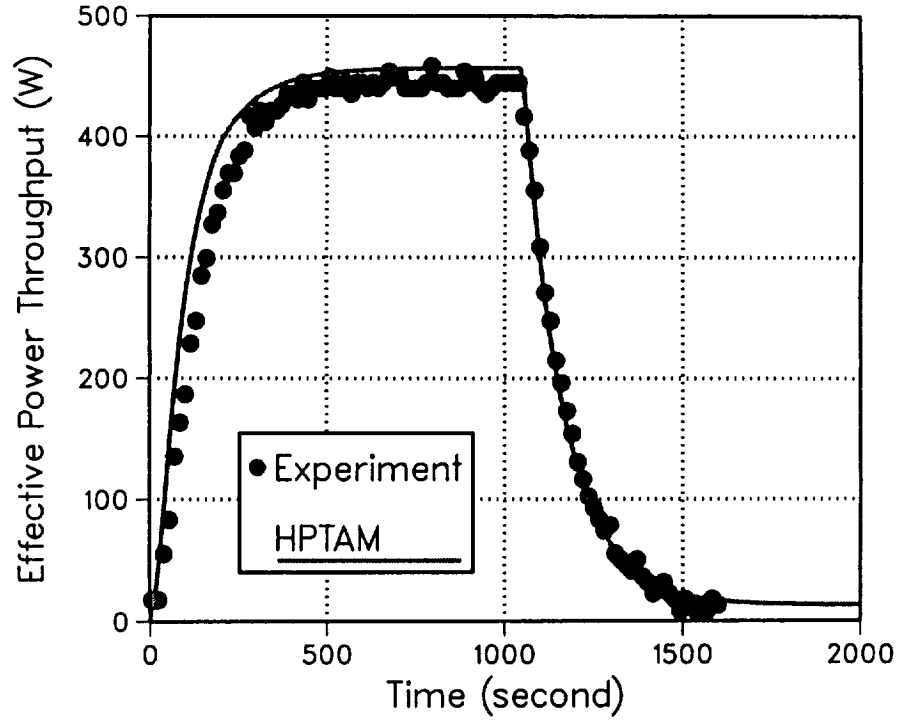

FIGURE 7.2. Comparison of Calculated Transient Response of Effective Power Throughput with Water Heat Pipe Experimental Data.

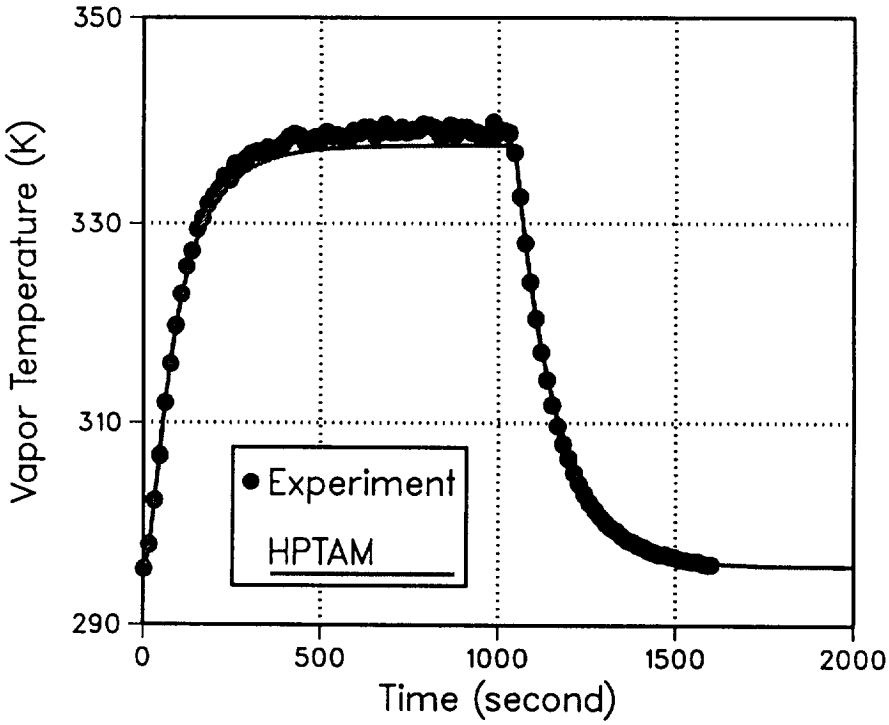

FIGURE 7.3. Comparison of Calculated and Experimental Transient Response of Vapor Temperature for the Water Heat Pipe.

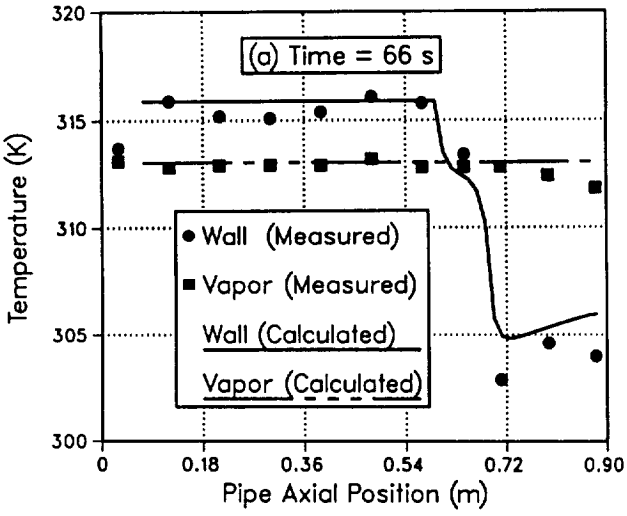

(a) Time = 66 s

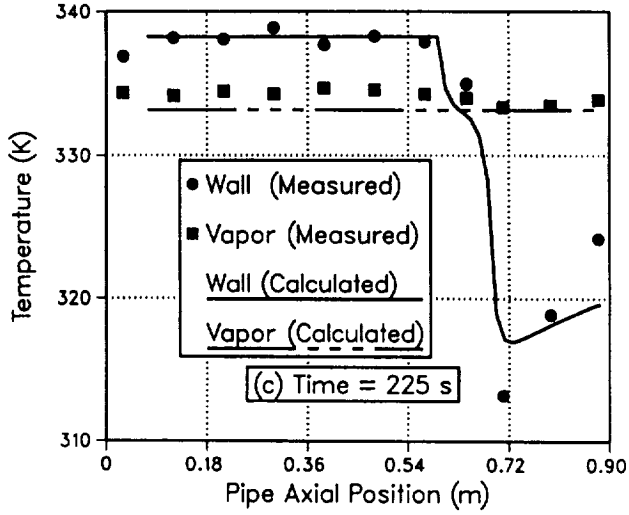

(c) Time = 225 s

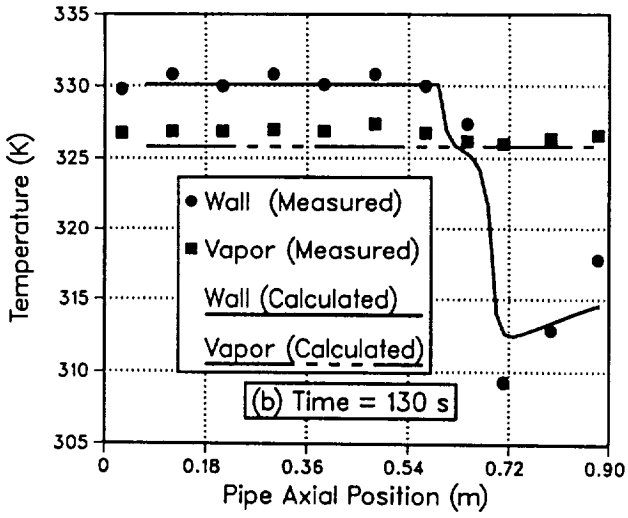

(b) Time = 130 s

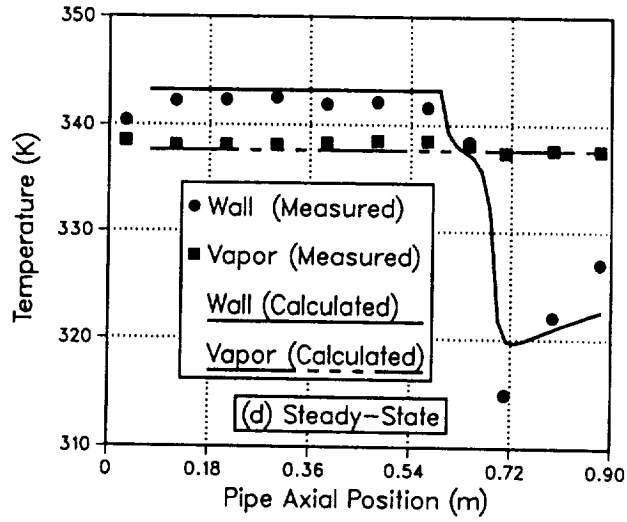

(d) Steady–State

FIGURE 7.4. Comparison of Calculated and Experimental Vapor and Wall Temperature Profiles along the Water Heat Pipe at Different Times during the Heatup Transient.

jacket. Also, the condensation rate at the L–V interface decreases along the condenser, due to the increase in the cooling water temperature. Finally, the effects of end bases that are observed in the experiments during the heatup transient (Figure 7.4a) are not calculated numerically since both ends of the heat pipe are assumed thermally insulated. As figure 7.4 shows, the calculated vapor temperature is nearly uniform along the heat pipe and in good agreement with experimental values. Such good agreement between HPTAM and the transient experimental data of the water heat pipe verifies the soundness of the system of equations and the modeling approach used for fully–thawed heat pipes.

7.3. WICK VOID FRACTION AND LIQUID POOLING RESULTS

In Figure 7.5, the vapor pore void fraction, α_p, is normalized to its initial value of 0.15. At the beginning of the heatup transient, the liquid temperature and volume increase rapidly, causing the vapor void fraction in the wick to decrease at a relatively uniform rate (Figure 7.5). Because of the evaporation and condensation in the heat pipe, the void fraction decreases (or the radius of curvature of the liquid meniscus increases) faster in the condenser than in the evaporator. In the evaporator, liquid evaporation competes with the liquid compressibility effect by removing mass, while condensation adds up to the increase in fluid volume along the condenser. During this period of decreasing wick void fraction, the liquid pressure is lower than the vapor pressure. The pressure difference decreases with time and eventually vanishes after about one minute into the transient (Figure 7.6). At this time, a wet point appears and excess liquid begins to accumulate at the end of the condenser section, forming a water pool (Figure 7.7). At the wet point, the L–V interface is flat (or the pore void fraction is zero) and the liquid and vapor total pressures are equal. The first wet point appears at the end of the condenser because the full length of the condenser became operational before liquid pooling could occur. The situation would have been different if a larger amount of working fluid had been introduced in the heat pipe (see Chapter 8). After the formation of the liquid pool, any increase in liquid volume due to thermal expansion is accommodated in the pool (Figure 7.7). Essentially, the structure of the L–V interface is governed by evaporation, condensation, and the liquid flow return. as shown in Figure 7.5, the vapor void fraction recovers along the heat pipe, except in the flooded portion of the condenser. As the effective power throughput in the water heat pipe increases, the pressure losses in the liquid–wick region increase, and the wick void fraction at the beginning of the evaporator rises in order to provide the necessary capillary pressure head needed to circulate the liquid in the wick. Before reaching steady–state, the rate of

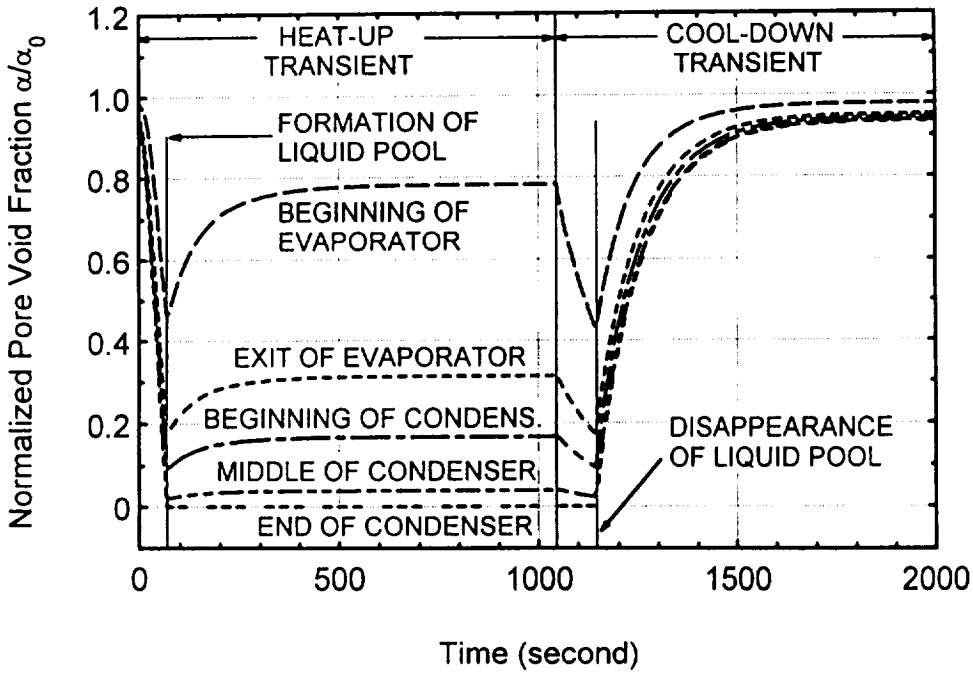

FIGURE 7.5. Calculated Normalized Vapor Void Fraction in the Wick at Different Locations along the Heat Pipe, as a Function of Time.

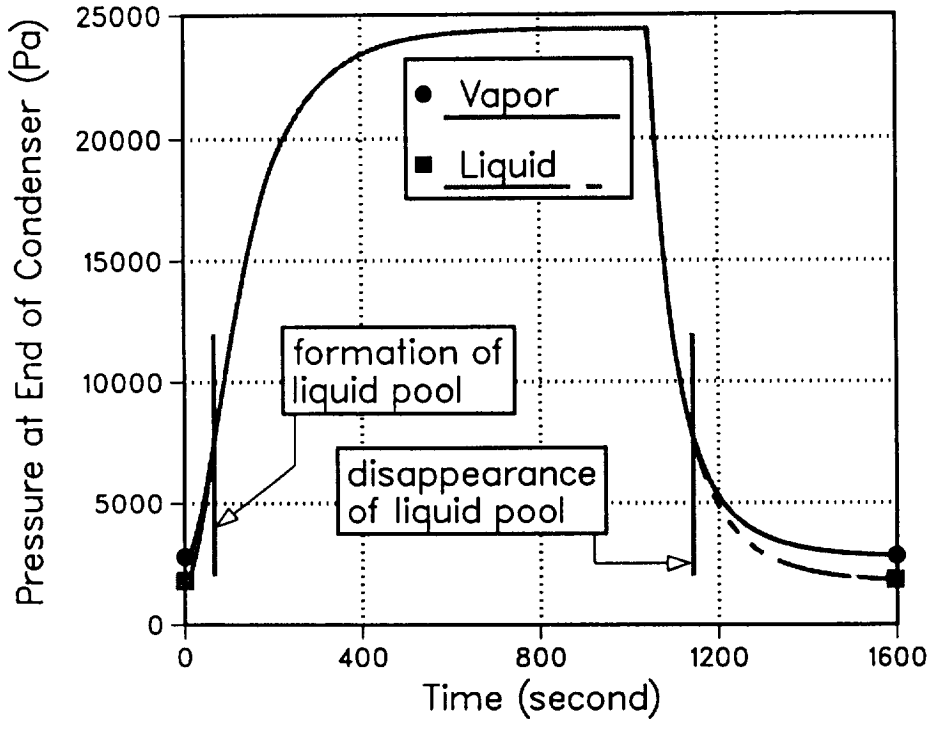

FIGURE 7.6. Calculated Liquid and Vapor Pressures of the Water Heat Pipe as a Function of Time.

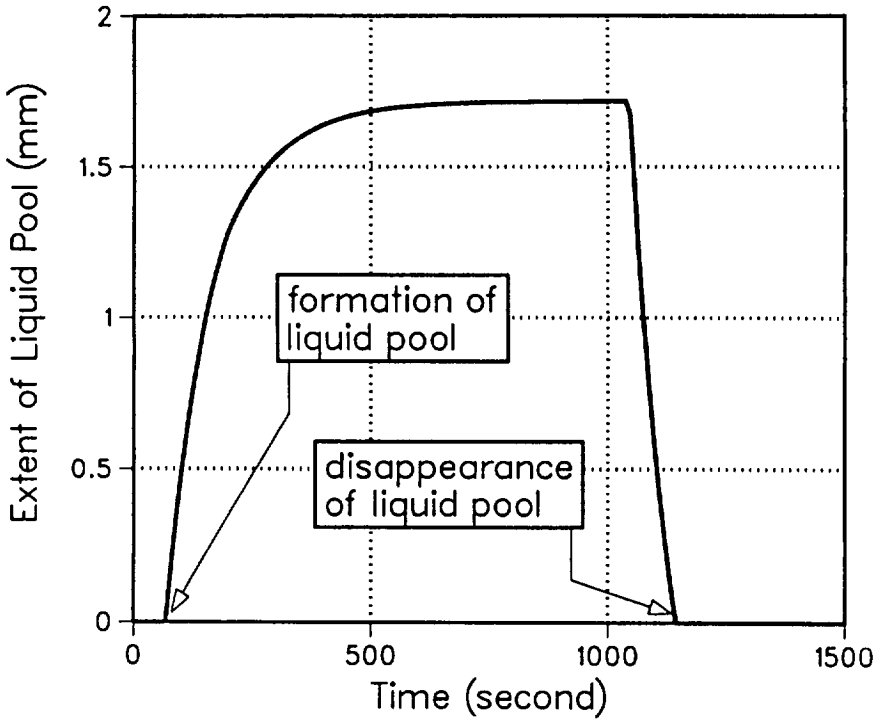

FIGURE 7.7. Extent of Liquid Pooling at the End of the Condenser in Water Heat Pipe as a Function of Time.

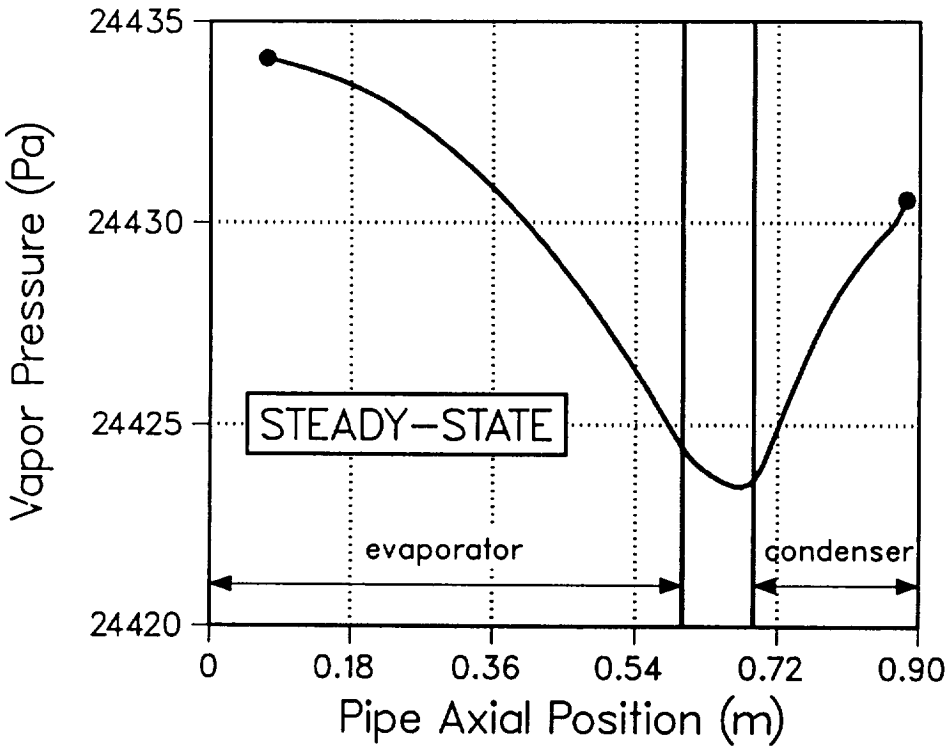

FIGURE 7.8. Calculated Axial Distribution of the Vapor Pressure at Steady–State.

evaporation is greater than the liquid flow return from the condenser to the evaporator. In the condenser, the vapor pressure recovers, as the rate of liquid removal is greater than the rate of condensation.

At steady–state, the liquid pool extends to about 1.7 mm (Figure 7.7). Figures 7.8 and 7.9 show the calculated axial distributions of the liquid and vapor pressures at steady–state. At a power throughput of 455 W, a vapor pressure recovery of 66% occurs along the condenser section. Figure 7.9 shows that the liquid pressure losses in the wick region are much larger than the vapor pressure losses. This is expected since the liquid is flowing across a relatively tight wire–screen wick. Figure 7.9 also shows that the vapor and liquid total pressures are equal at the end of the condenser, where it is flooded. As delineated in Figure 7.10, at steady–state, the vapor void fraction in the wick is highest (or liquid meniscus radius of curvature is smallest) at the beginning of the evaporator and decreases to zero at the end of the condenser. Figure 7.11 shows the axial distribution of the evaporation and condensation rates along the heat pipe. At steady–state, evaporation is uniform along the evaporator, while condensation decreases along the condenser due to the increase in temperature along the cooling jacket (Figure 7.4). Some evaporation and condensation occurs in the adiabatic section due to the effect of axial conduction in the wall and liquid–wick regions.

After 17 minutes of heatup transient (1040 s), the electrical power to the heating tape was shut off. However, the water was kept running in the cooling jacket. During the first period of the cooldown, the wick void fraction decreases (or the liquid meniscus rises) along the heat pipe, as shown in Figures 7.5 and 7.10. Subsequent decrease in liquid volume due to thermal compressibility causes the liquid pool to recede (Figure 7.7). As Figure 7.11 shows, the rate of evaporation decreases faster than the rate of condensation, causing the mass of vapor in the heat pipe to decrease with time. This inequality between evaporation and condensation rates causes the vapor void fraction in the wick to decrease faster in the condenser than in the evaporator. After 1142 s of the transient, the liquid pool disappears (Figure 7.7).

From then on, the structure of the L–V interface is generally governed by the thermal compressibility of the liquid phase. Because the liquid temperature and volume decrease rapidly, the vapor void fraction in the wick increases at a relatively uniform rate (Figures 7.5 and 7.10), and so does the difference between the vapor and liquid pressures (Figure 7.6). The difference between the vapor void fraction in the evaporator and the condenser is

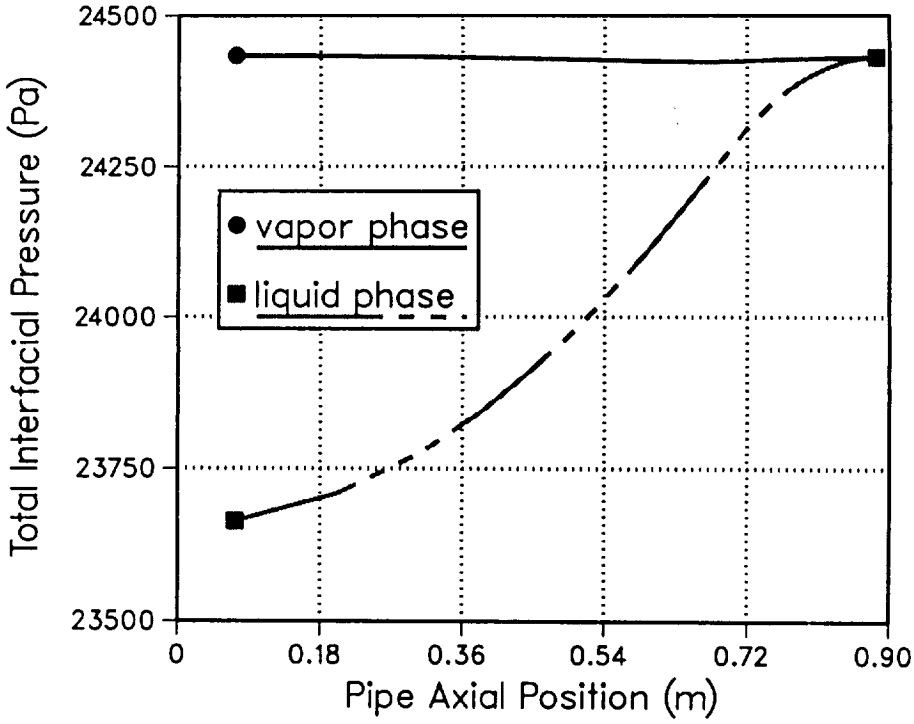

FIGURE 7.9. Calculated Axial Distributions of the Interfacial Pressures at Steady–State for the Water Heat Pipe.

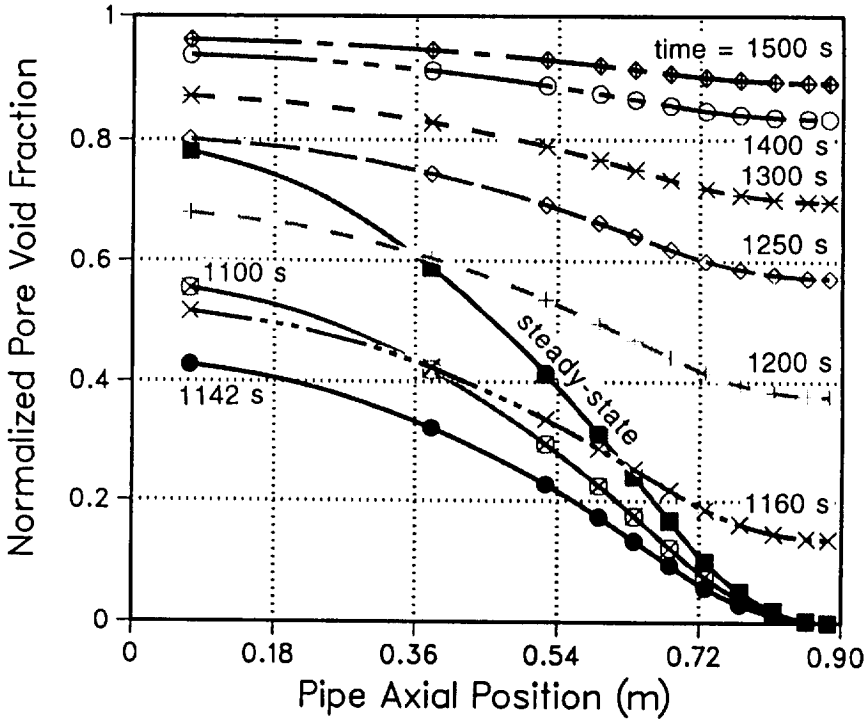

FIGURE 7.10. Calculated Axial Distributions of the Wick Void Fraction at Different Times during the Cooldown Transient of the Water Heat Pipe.

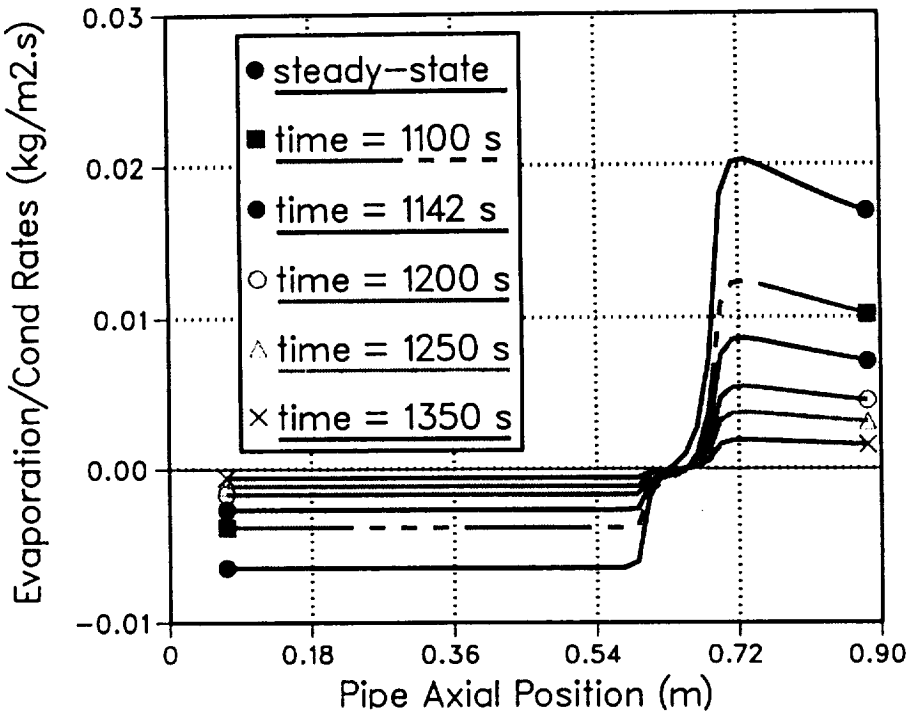

FIGURE 7.11. Calculated Axial Distributions of Evaporation–Condensation Rates at Different Times during the Cooldown Transient of Water Heat Pipe.

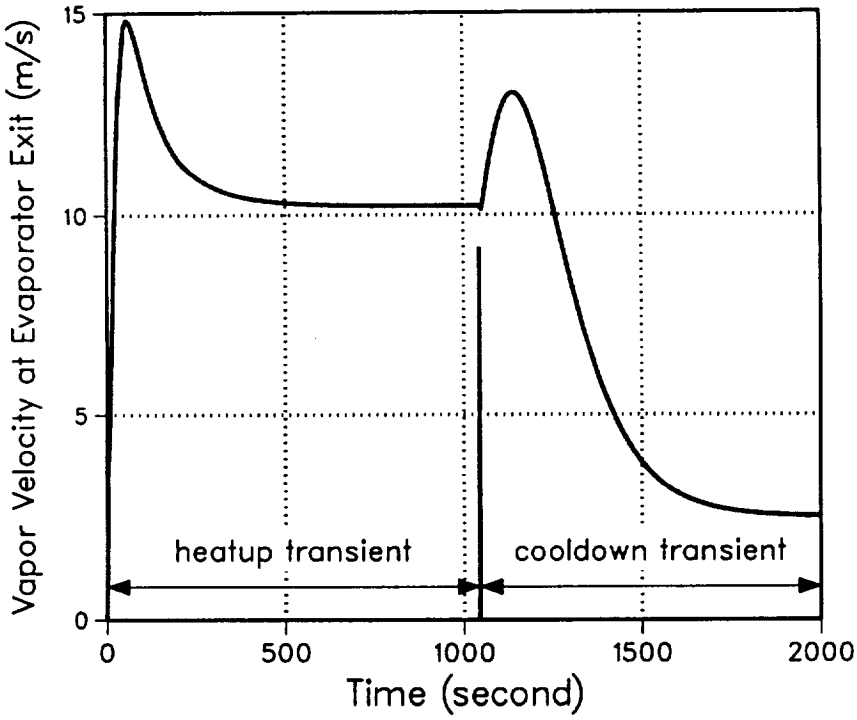

FIGURE 7.12. Calculated Centerline Vapor Velocity at the end of the Evaporator as a Function of Time.

governed by the evaporation/condensation rates, or the power transported through the heat pipe. As the heat pipe cools down, the wick void fraction along the heat pipe becomes more uniform and returns to its initial value of 0.15.

Figure 7.12 shows the transient variation of the centerline vapor velocity at the exit of the evaporator. During the heatup and cooldown transient phases, the vapor velocity increases above its full–power steady–state value of 10 m/s, for short periods of time. The first peak occurs because the heat transport capability of the heat pipe increases faster than the mass of vapor in the core. The second peak occurs at the beginning of the cooldown phase and is related to the imbalance between evaporation and condensation. After the electrical power in the evaporator was cut off, the rate of evaporation decreased faster than the rate of condensation. As a result, the vapor traveled fast toward the L–V interface along the condenser section, resulting in a rapid decrease in vapor mass in the evaporator and increase in the vapor velocity.

After 2000 s of transient, steady–state operation is established again; however, the temperatures are slightly different from the initial condition. As Figure 7.2 shows, the steady–state power throughput is about 13 W, with a centerline vapor velocity of 2.5 m/s (Figure 7.12). Also, Figure 7.5 shows a vapor void fraction distribution that is not quite uniform. This is because the temperature is not uniform along the heat pipe. After cooldown, the temperature of the evaporator wall equals room temperature (296.2 K), while the condenser wall is slightly cooler because the cooling water enters the condenser jacket at 294.5 K.

In the next chapter, the effects of input power and initial liquid inventory in the heat pipe on the wet point and liquid pooling, and on the vapor and liquid pressure and temperature distributions are investigated in details.

8. ANALYSIS OF WET POINTS AND LIQUID POOLING (WATER HEAT PIPE)

Results of the transient operation of a water heat pipe subject to various heating conditions and having different working fluid inventories are presented. In this chapter, the liquid/wick region is treated as a liquid open–annulus. Design and operational parameters of the heat pipe for the four cases analyzed are listed in Tables 8.1 and 8.2. At the startup, the heat pipe is initially at a temperature of 300 K, and the 20–cm–long evaporator is heated uniformly with an exponential period τ = 5 s, while the 80–cm–long condenser is convectively cooled by a water jacket. For the purpose of determining the temperature distributions in the various regions as well as the distributions of the vapor and liquid pressures, the numerical scheme employs 6, 2, and 2 radial cells in the vapor, liquid/wick and wall regions respectively, and 6, 6, and 18 axial cells in the evaporator, adiabatic and condenser regions, respectively. As indicated in Table 8.2, four cases are investigated,

TABLE 8.1. Design and Operational Parameters of Water Heat Pipes Analyzed.

Design Parameter	Value	Operational Parameter	Value
Heat pipe length L (cm)	120	Initial pipe temperature (K)	300
Evaporator length L_e (cm)	20	Initial pore void fraction	0.02 – 0.20
Condenser length L_c (cm)	80	Startup mode	Exponential
Adiabatic length L_a (cm)	20		heating
Pipe outer diameter (mm)	25	Shutdown mode	Step function
Wall thickness (mm)	1.0	Evaporator radial heat flux	Uniform
Liquid/wick thickness (mm)	1.0	Evaporator maximum heat flux (W/cm^2)	1 – 5
Effective pore radius (μm)	50	Evaporator exponential heating period τ	5 s
Wick porosity ε	0.7	Condenser cooling method	Convective
Wall material	Copper	Water jacket average temperature (K)	300
Working fluid	Water	Jacket heat transfer coefficient (W/m^2K)	1000

TABLE 8.2. Comparison of Operational Parameters of Water Heat Pipes Investigated.

PARAMETER	Case 1	Case 2	Case 3	Case 4
Evaporator heat flux (W/cm^2)	1	2	2	5
Initial pore void fraction	0.02	0.10	0.12	0.20
Liquid inventory (gram)	82.805	82.332	82.295	82.148
Vapor pressure recovery at time of wet point	0.5%	36.8%	no wet point	66.0%

each with different working fluid inventory and maximum evaporator heat flux. In these cases, the maximum evaporator heat flux ranged from 1 W/cm^2 to 5 W/cm^2. The masses of working fluid introduced in the pipe were such that initially the liquid meniscus at the liquid–vapor (L–V) interface is concave everywhere, so that the pressure of the vapor phase is greater than that of the liquid phase. A greater mass of working fluid corresponds to a smaller initial vapor pore void fraction at the L–V interface. As the liquid water in the heat pipe heats up, the excess volume due to thermal expansion will be accommodated in the pores of the wick, and it may flatten the L–V interface at some point during the transient; such occurrence is referred to herein as the "wet point". Results on the effects of water inventory and maximum heat flux on the "wet point" location and potential liquid pooling at the end of the condenser are presented in the following sections.

8.1. LIQUID POOLING AT END OF CONDENSER

Figures 8.1a and 8.2a show the interfacial pressures and pore void fraction distributions of Case 4 at the occurrence of the first wet point. Because the vapor pressure recovery in the condenser is relatively high (66%), the wet point is located close to the beginning of the condenser region. At the wet point, the L–V interface is flat and the pore void fraction is zero. Further thermal expansion of the liquid phase increases the liquid pressure causing the wet point to advance along the condenser region (Figures 8.1b and 8.2b). Eventually, the wet point reaches the end of the condenser, and the excess liquid begins to accumulate at the end of the condenser (Figures 8.1c and 8.2c). Notice that wetting of the entire

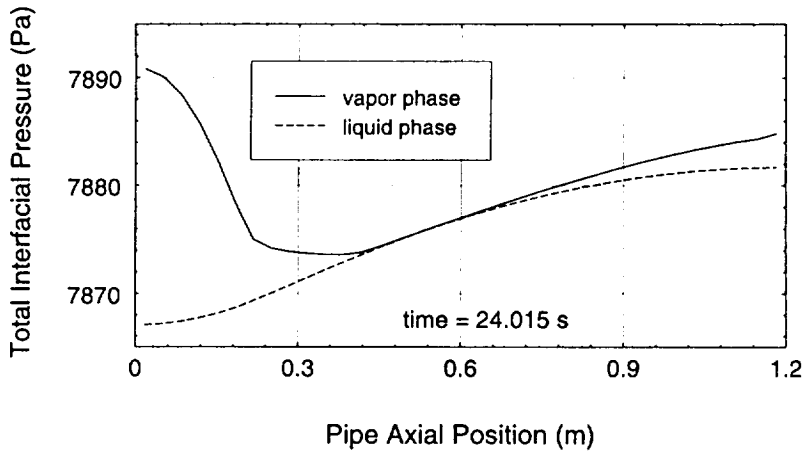

a) Occurrence of First Wet Point in the Condenser Region

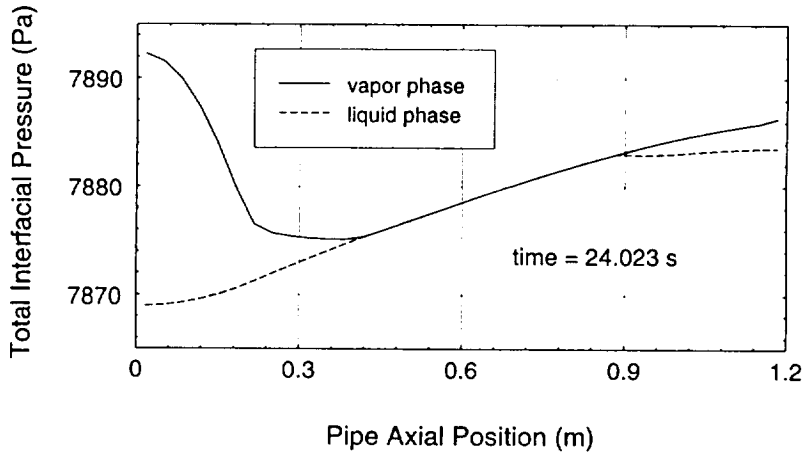

b) Propagation of the Wet Point towards the Condenser

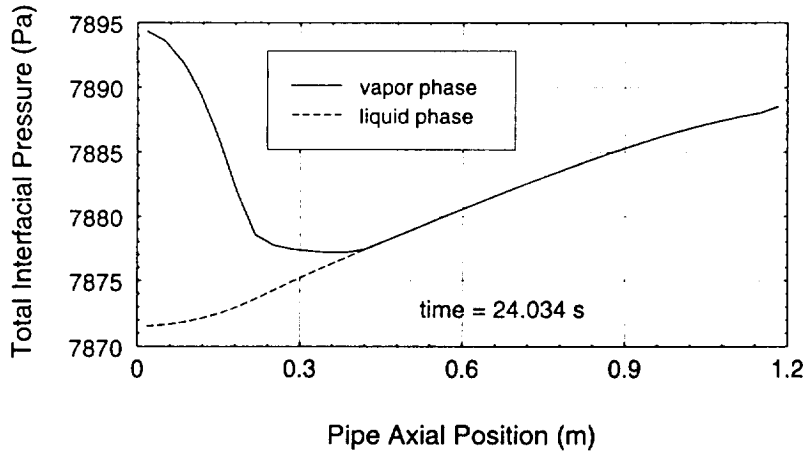

c) The Entire Condenser is Wet: a Liquid Pool Starts Forming at the End.

FIGURE 8.1. Total Interfacial Pressure Profiles at Various Times for the Water Heat Pipe Analyzed in Case 4.

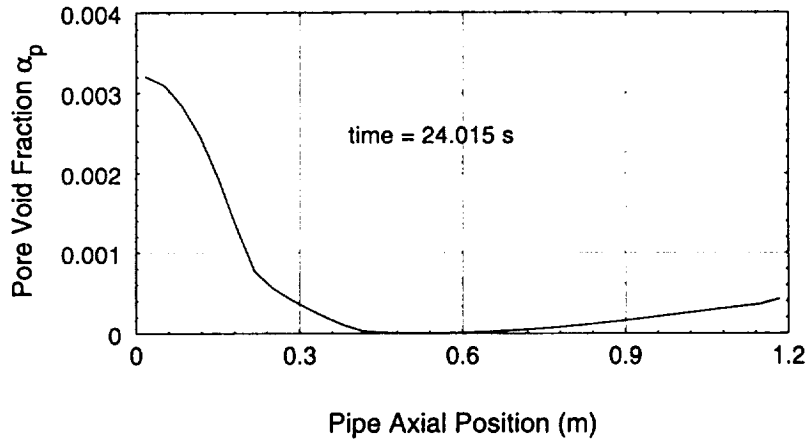

a) Occurrence of First Wet Point in the Condenser Region

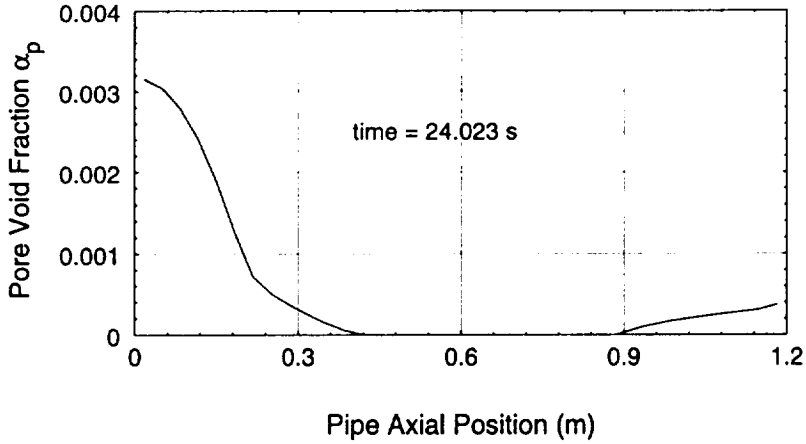

b) Propagation of the Wet Point towards the Condenser

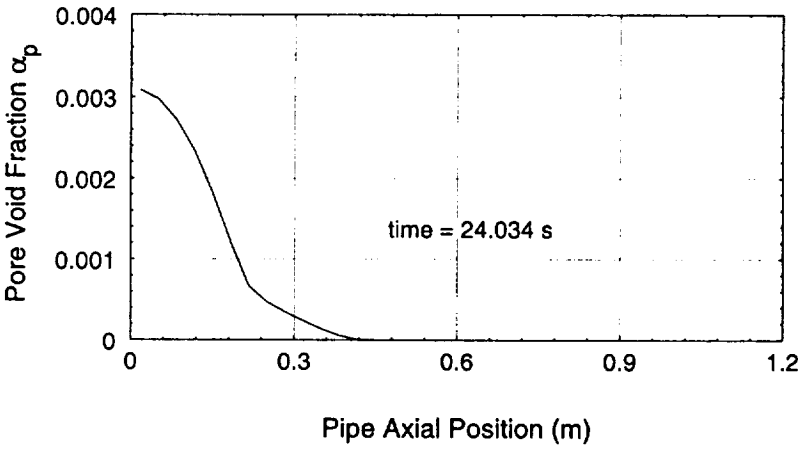

c) The Entire Condenser is Wet: a Liquid Pool Starts Forming at the End.

FIGURE 8.2. Vapor Pore Void Fraction Distributions at Various Times for the Water Heat Pipe Analyzed in Case 4.

condenser occurs within a very short time, only 19 ms after the occurrence of the first wet point. Also, the maximum pore void fraction (or smallest radius of curvature of the liquid meniscus) occurs at the beginning of the evaporator, and before flooding of the wick occurs (wet point), the void fraction recovers along the condenser.

The effects of varying the liquid inventory and the evaporator input power on the position of the wet point are delineated in Figures 8.3 and 8.4. When the vapor pressure recovery is small compared to the liquid viscous pressure drop in the condenser region, the wet point occurs at the end of the condenser region (Case 1, Figure 8.3). If the pressure recovery exceeds the liquid pressure drop in the condenser, the wet point occurs at some intermediate position in the condenser (Case 2, Figure 8.4). For Case 3, the mass of the working fluid was low enough that such flooding of the wick at the L–V interface does not occur even after 2 minutes into the transient, at which time steady–state operation is reached. Therefore, by decreasing the operating maximum evaporator heat flux and/or the liquid inventory in the heat pipe, pooling of liquid at the end of the condenser can be avoided.

8.2. TRANSIENT RESPONSE OF WATER HEAT PIPE

As shown in Figures 8.5 to 8.7, in Case 4, the heat pipe reached steady–state after about 110 s. Figure 8.5 shows that at the beginning of the transient, the input power to the evaporator is higher than the output power to the condenser, by the amount stored in the wall, liquid and vapor regions. As the transient progresses, the output power approaches the input power and the difference between the two disappears as the heat pipe reaches steady–state, at a power throughput of 785 W. After 120 s (or 10 s after reaching steady–state), the evaporator input power is cut off, and the heat pipe begins to cool down. The heat pipe returns to its initial temperature and void fraction distribution, 100 s after the power is cut off (Figures 8.6 and 8.7). At 24 s after the initiation of the transient, a liquid pool forms at the end of the condenser (Figure 8.8). This pool, however, remains relatively small, extending to a maximum of 0.58 mm at full–power (steady–state). After the input power is cut off, the pool recedes very quickly, and disappears in about 11 s. Also, the pore void fraction increases and the condenser becomes fully dewetted (Figure 8.7).

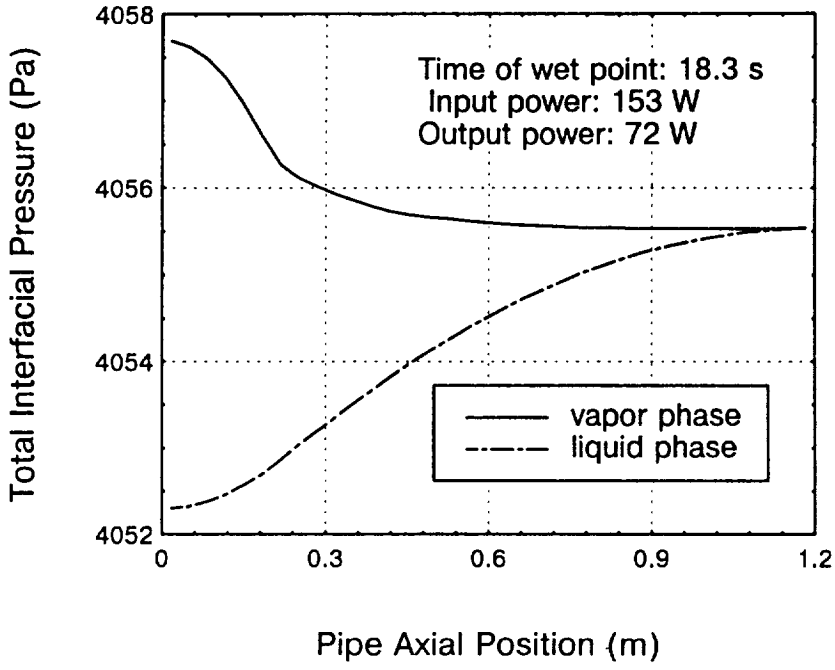

FIGURE 8.3a. Total Interfacial Pressure Profiles for Water Heat Pipe at the Time of First Wet Point for Case 1.

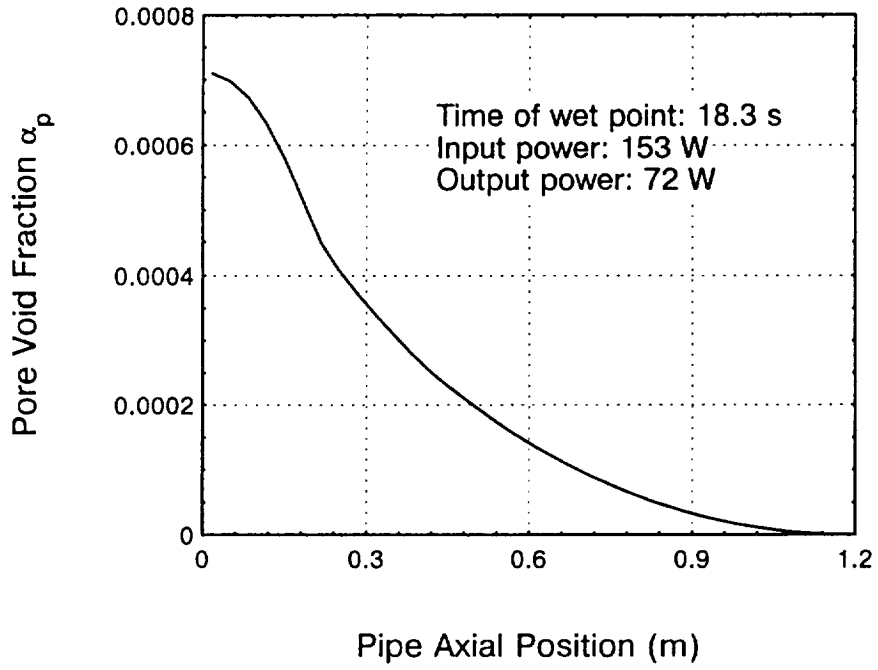

FIGURE 8.3b. Vapor Pore Void Fraction Distribution for Water Heat Pipe at the Time of First Wet Point for Case 1.

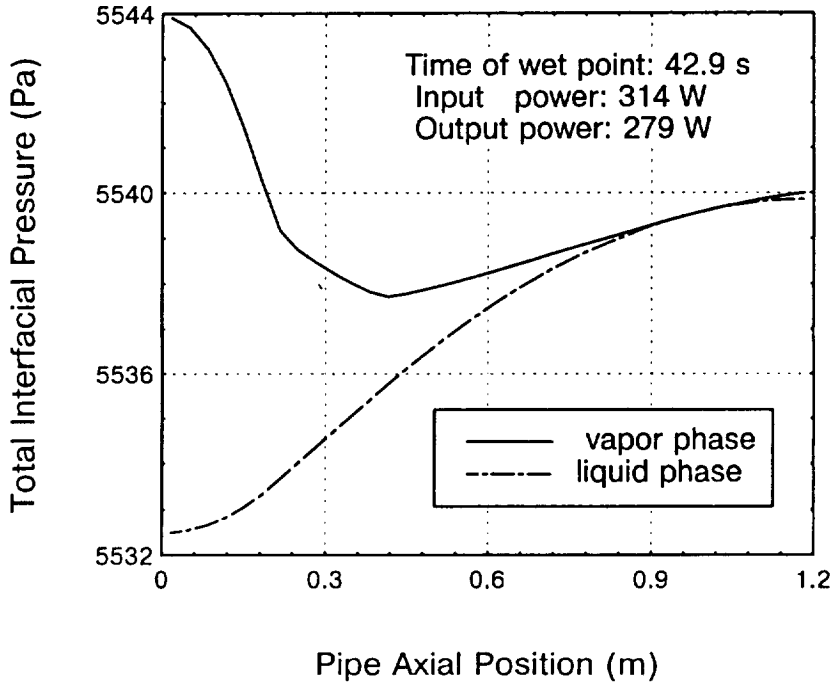

FIGURE 8.4a. Total Interfacial Pressure Profiles for Water Heat Pipe at the Time of First Wet Point for Case 2.

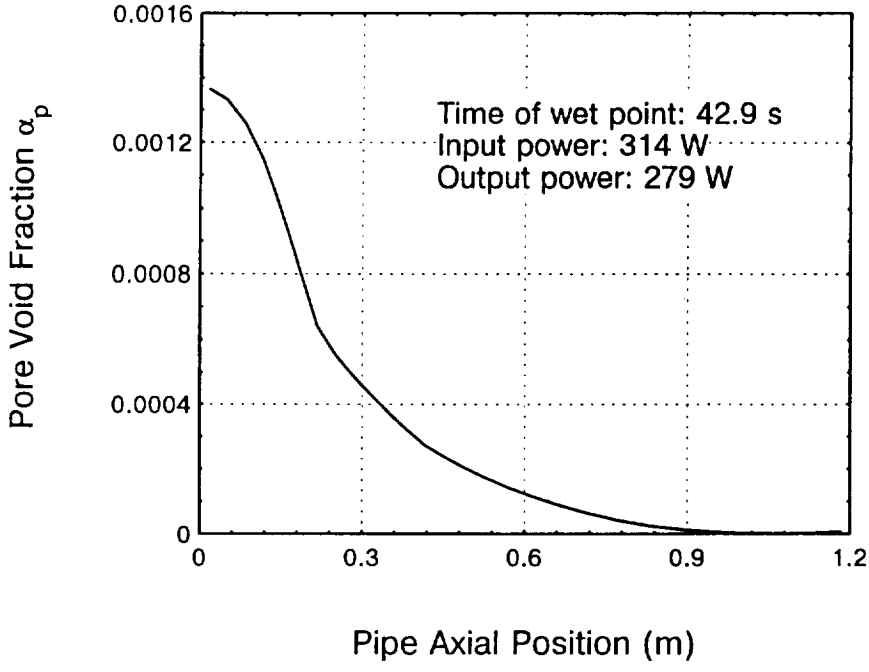

FIGURE 8.4b. Vapor Pore Void Fraction Distribution for Water Heat Pipe at the Time of First Wet Point for Case 2.

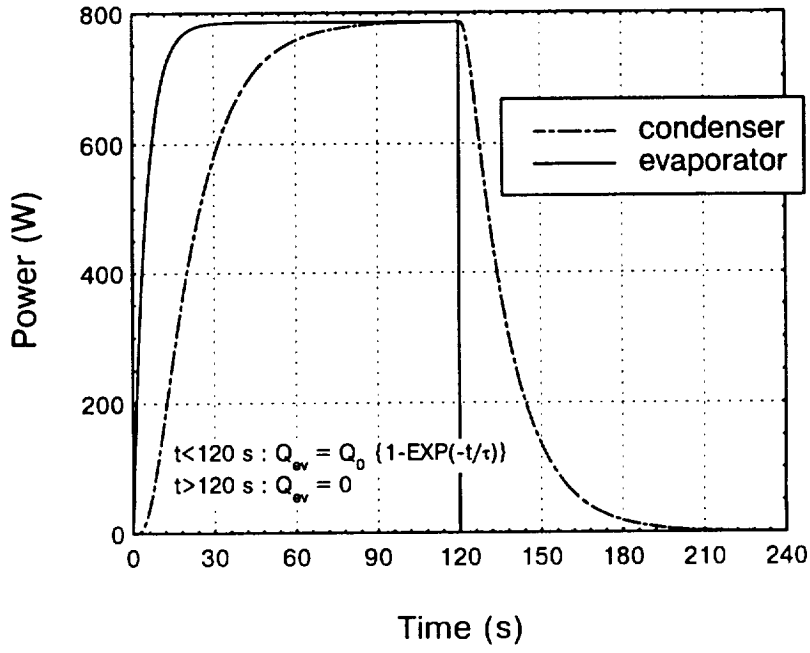

FIGURE 8.5. Transient Variation of Input and Output Powers for the Water Heat Pipe Analyzed in Case 4.

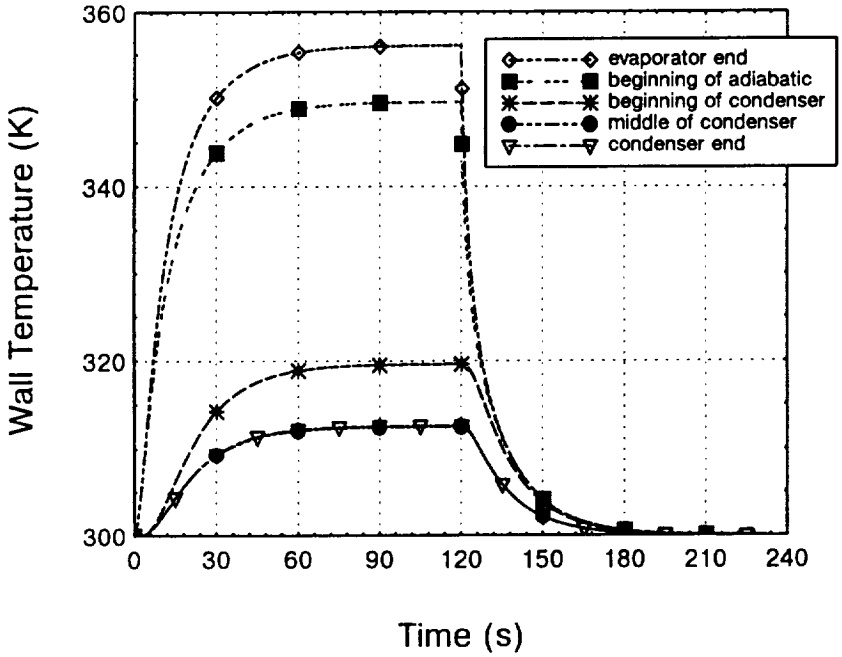

FIGURE 8.6. Transient Variation of Wall Temperatures for the Water Heat Pipe Analyzed in Case 4.

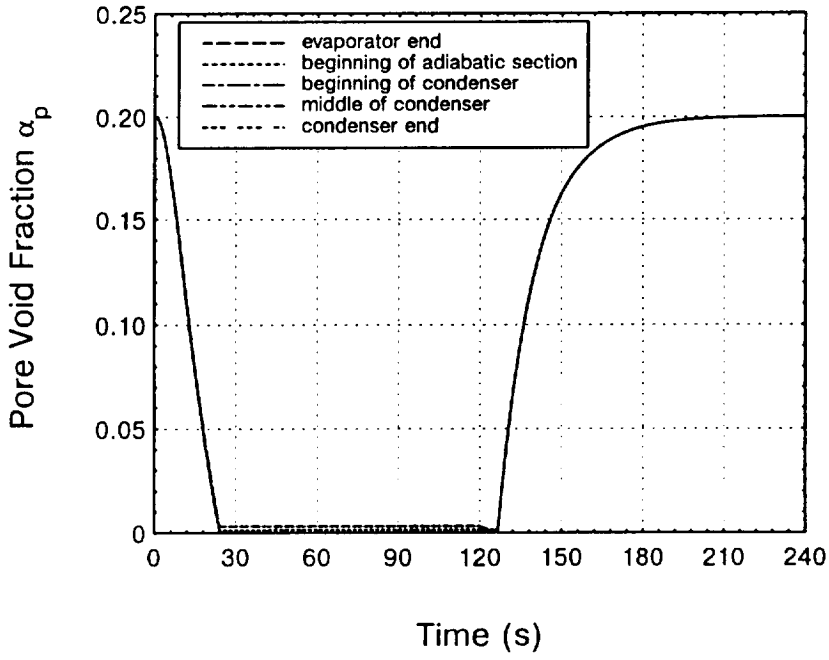

FIGURE 8.7. Transient Variation of Vapor Pore Void Fractions for the Water Heat Pipe Analyzed in Case 4.

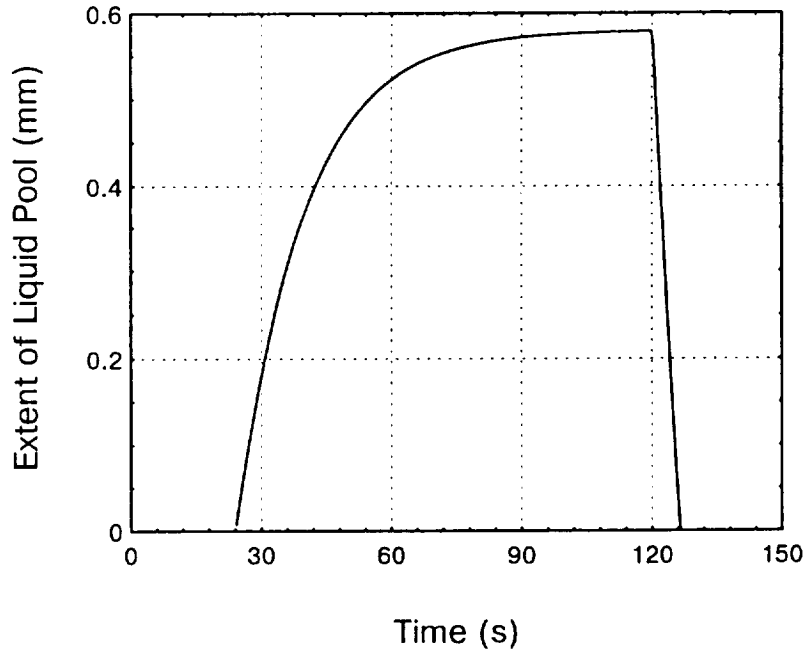

FIGURE 8.8. Extent of Liquid Pool as a Function of Time for the Water Heat Pipe Analyzed in Case 4.

8.3. HEAT PIPE CHARACTERISTIC PERIOD

It is interesting to analyze the transient response of the heat pipe in terms of its characteristic periods. Indeed it is found that, except during the early startup until the formation of the liquid pool (from 0 s to 24 s) and during the pool recession phase (from 120 s to 131 s), the condenser output power, evaporation/condensation mass fluxes and pore void fractions varied at a characteristic exponential period $\tau = 14.9 \pm 0.1$ s. This period applies both during the exponential heating phase and the step–function cooldown phase, and is therefore characteristic of the water heat pipe analyzed (Case 4). This period is expected to vary with the pipe geometry, temperature levels of interest (since most properties, such as heat capacity and thermal conductivity, are temperature dependent) and the type of condenser cooling (convective or radiative); further work will investigate these effects.

8.4. TRANSIENT VAPOR PRESSURE RECOVERY

Issacci et al. (1988) and Faghri and Chen (1989), in their simulation of the steady–state operation of water and sodium heat pipes, have reported pressure recoveries up to 90% of the vapor pressure drop along the condenser and flow reversal at the end of the condenser. This behavior intensifies as the input power, and consequently the radial Reynolds number of the vapor increases. Similar behavior is also detected by our model. Figure 8.9a shows the vapor pressure axial profile, normalized with respect to the maximum vapor pressure at the beginning of the evaporator (Figure 8.9b), at different times during the heatup transient. As the input power is increased with time, both the pressure level and the vapor pressure recovery in the condenser region increase dramatically. The vapor pressure recovery in the condenser reached a maximum value of 72% at steady–state, at a power throughput of 785 W (after 120 s of transient). Because the vapor pressure at this input power is 3 times that at startup, a small time step is needed to accurately predict the heat pipe transient response. The time step must be much smaller than both the exponential heating period (5 s) and heat pipe's characteristic period (14.9 s). These calculations were performed with a time step of 25 ms.

8.5. VAPORIZATION RATES AND TEMPERATURE PROFILES

Figure 8.10a shows the variation in the radial evaporation/condensation mass flux at the L–V interface along the heat pipe at different times during the transient. After a very short transient time (less than 2 s), the radial mass flux profile becomes uniform in both the

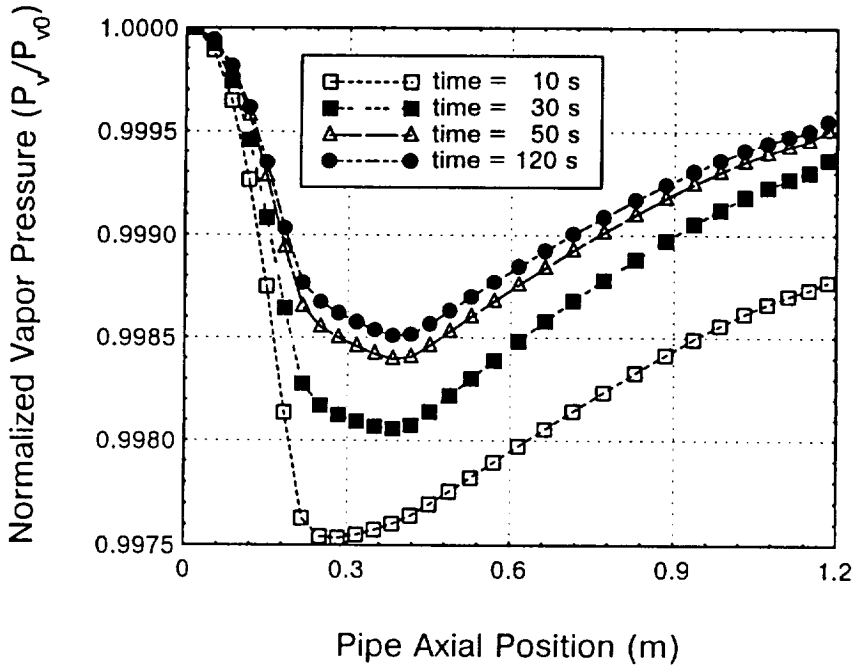

FIGURE 8.9a. Normalized Vapor Pressure Distribution at Various Times During the Heatup Transient for the Water Heat Pipe Analyzed in Case 4.

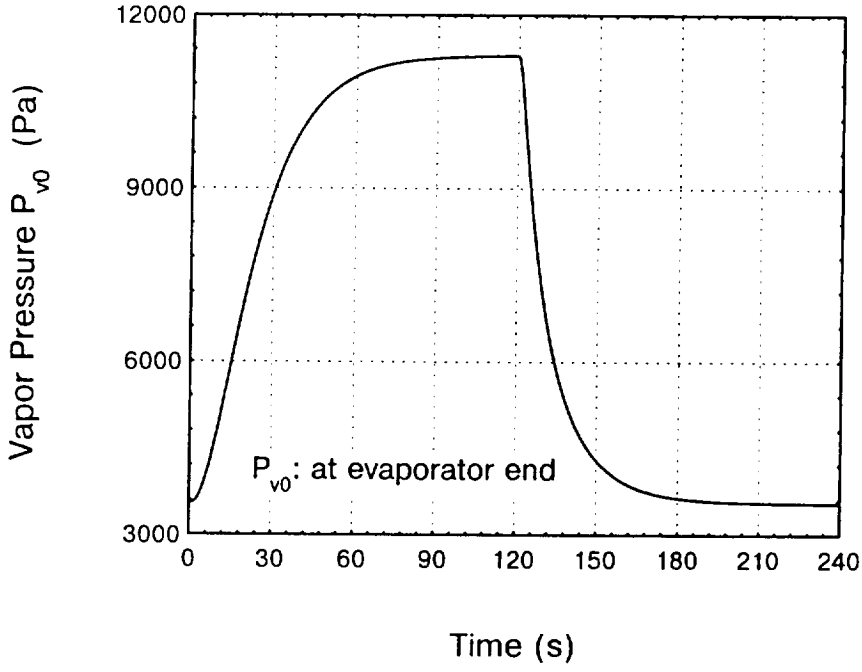

FIGURE 8.9b. Transient Variation of Reference Vapor Pressure at Evaporator End for the Water Heat Pipe Analyzed in Case 4.

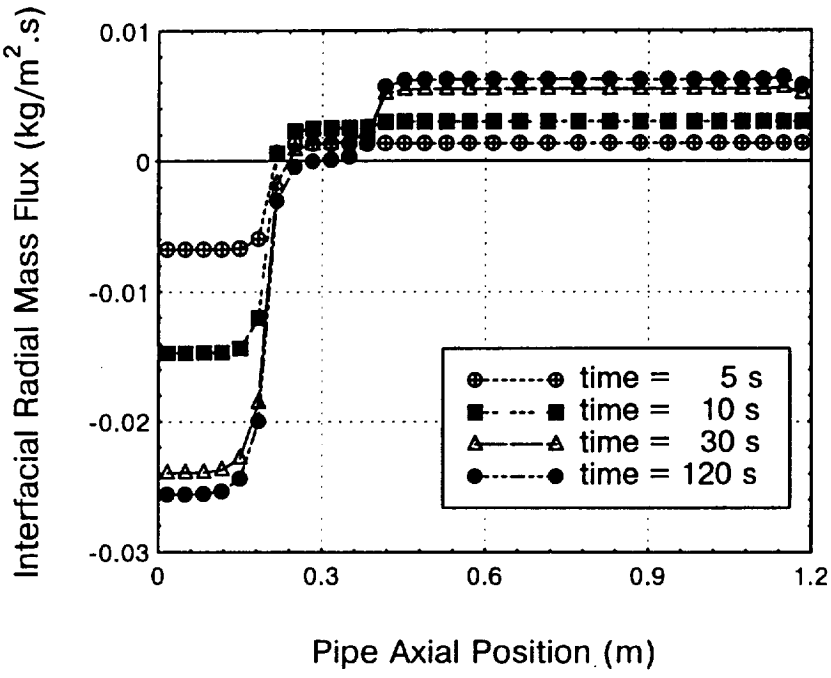

FIGURE 8.10a. Evaporation/Condensation Rates at Various Times During the Heatup Transient for the Water Heat Pipe Analyzed in Case 4.

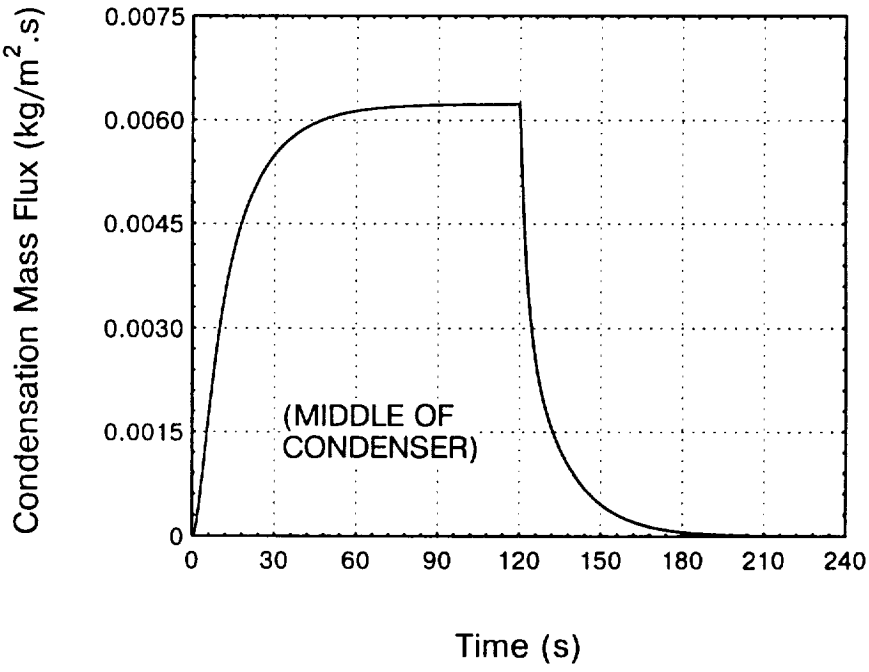

FIGURE 8.10b. Transient Variation of the Condensation Mass Flux at Mid–Condenser for the Water Heat Pipe Analyzed in Case 4.

evaporator and condenser regions. However, condensation also occurs along the adiabatic section during the transient because the liquid and wall temperatures are cooler in this region. The condensation mass flux in the adiabatic region progressively disappears with time as the heat pipe reaches steady–state (at 120 s). Results in Figure 8.10 show that during the transient the evaporation and condensation mass fluxes in the evaporator and condenser regions, respectively, increase with time, reaching their highest values at steady–state. It is interesting to note that during steady state operation, the evaporation–condensation mass flux at the L–V interface is uniform in both the evaporator and condenser regions, as it is assumed by simplified theories.

Figure 8.11 shows the calculated outer wall and liquid axial temperature profiles at different times during the heatup transient. These temperatures are axially uniform in the evaporator, adiabatic section and condenser, with sharp changes at the transitions between these regions. These results suggest that the heat is transferred mainly by radial conduction in the wall and liquid/wick regions, and that axial conduction insignificantly affects the water heat pipes transient. The radial temperature drop across the wall is also negligible (0.2 K) due to the high thermal conductivity of the container material (about 400 W/m.K for copper). However, the radial temperature drop in the liquid/wick region in the evaporator is significant (42 K) because of the poor thermal conductivity of water (about 0.65 W/m.K), hence justifying using a two–dimensional modeling approach of the heat pipe. With a wick porosity of 0.70, the added conductance of the copper mesh has effectively increased the conductivity of the working fluid in the wick region by only a factor of 1.85. This poor conductance of the water/wick region results in a relatively large temperature drop along the pipe (44 K at the maximum steady–state power throughput of 785 W).

Because the liquid flow in the wick is very slow, conduction is the dominant mode of heat transfer in this region. It is worth noting that the radial temperature difference between the outer wall surface and liquid at the L–V interface in the adiabatic section is negligible at steady–state, but it is as much as 9 K after 10 s into the transient.

8.6. VISCOUS DISSIPATION

Results show that the viscous dissipation peaks at the midplane and vanishes towards the axial ends of the heat pipe. While the viscous dissipation in the liquid phase is three orders of magnitude smaller than that in the vapor region, the latter peaks up to 180 W/m^3 in the

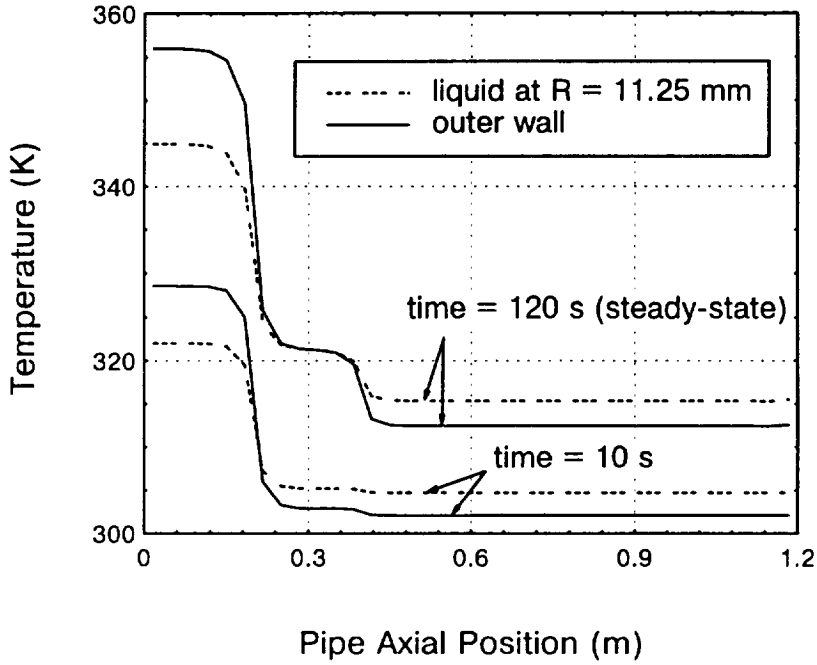

FIGURE 8.11. Liquid and Wall Temperatures Profiles at 2 Different Times During the Heatup Transient for the Heat Pipe Analyzed in Case 4.

vapor region, at the end of the condenser. Consequently, the primary effect of viscous dissipation is to increase the vapor temperature near the center of the pipe. This effect is however three orders of magnitude smaller than that for liquid–metal heat pipes, and is negligible for water heat pipes.

This chapter ends the analysis of the transient operation of low–temperature (water in the present case) heat pipes. The next chapter presents steady–state results of a lithium heat pipé operating at a temperature level of 1250 K and a power throughput of 6.5 kWt. Results show that high evaporation and condensation rates can generate significant recovery of vapor pressure and non–negligible viscous dissipation rates in the vapor space.

9. STEADY-STATE OPERATION OF FULLY-THAWED LITHIUM HEAT PIPE

Steady-state results of a lithium heat pipe operating at a temperature of 1250 K are presented herein. The lithium heat pipe evaporator is uniformly heated, while its condenser is radiatively cooled. At such a high temperature, viscous flow conditions are prevalent in the vapor core region. Design and operational parameters of the lithium/niobium heat pipe analyzed are listed in Table 9.1. In the radial direction, 5, 3, and 2 computational cells are used in the vapor, liquid/wick and wall regions respectively, while 8, 4, and 8 axial cells are used in the evaporator, adiabatic and condenser regions, respectively (Figure 9.10). Note that, even so modeling of the liquid/wick region as a porous medium has been incorporated into the heat pipe transient model, the sample calculations presented in this chapter (and the preceding Chapter 8) were performed for a liquid open-annulus.

TABLE 9.1. Design and Operational Parameters of Lithium Heat Pipe Analyzed.

Design Parameter	Value	Operational Parameter	Value
Heat pipe length L (cm)	150	Initial pipe temperature (K)	1250
Evaporator length L_e (cm)	60	Initial pore void fraction	0.1
Condenser length L_c (cm)	60	Mass of working fluid (gram)	35.538
Adiabatic length L_a (cm)	30		
Pipe outer diameter (mm)	26.72	Evaporator radial heat flux	Uniform
Wall thickness (mm)	1.60	Evaporator maximum heat flux (W/cm^2)	12.8
Liquid/wick thickness (mm)	0.76	Input power (W)	6470
Effective pore radius (μm)	50	Condenser cooling method	Radiative
Wick porosity ε	0.7	Space/ambient temperature (K)	300
Wall material	Niobium	Wall emissivity	1
Working fluid	Lithium	View factor	1

9.1. PRESSURE PROFILES AND VAPOR PRESSURE RECOVERY

Issacci et al. (1988) and Faghri and Chen (1989), in their simulation of the steady–state operation of water and sodium heat pipes, have reported pressure recoveries up to 90% of the vapor pressure drop along the condenser and flow reversal at the end of the condenser. This behavior intensifies as the input power, and consequently the radial Reynolds number of the vapor increases. Similar behavior is also detected by our model. Figure (9.1) shows the axial profile of the vapor pressure at steady–state. The vapor pressure recovery in the condenser reached a value of 49%, at a power throughput of 6470 W.

At steady–state, radial gradients of static pressure are negligible in both the liquid and vapor regions. This is found to be always true in the vapor region, but untrue in the liquid region during transient operation. At steady–state the returning liquid flow from the condenser to the evaporator is fully established as shown in Figures (9.9) and (9.10), and there is no radial pressure gradient in the liquid region (Figure 9.2). Note that the flow is found to be symmetric since the evaporator and condenser lengths are equal.

9.2. VAPOR PORE VOID FRACTION

The mass of working fluid introduced in the heat pipe is such that at steady–state, no liquid pooling occur red. As shown in Figure (9.3), the total interfacial pressure of the vapor phase is greater than that of the liquid phase, and the liquid meniscus at the L–V interface is concave everywhere, even in the condenser region, so that the pore void fraction is positive (Figure 9.4). Note the recovery of the pore void fraction along the condenser, which follows the vapor pressure recovery in this region.

9.3. TEMPERATURE PROFILES

Figure (9.5) shows the calculated steady–state temperature distributions in the wall and liquid–wick regions of the lithium heat pipe. The total radial temperature drop across the wall and the liquid–wick combined thicknesses is about 6 K in both the evaporator and condenser regions at a steady–state throughput power of 6470 W. Such a small temperature drop is due to the high thermal conductivity of the container material (niobium) and the liquid lithium. The maximum temperature difference along the pipe wall is 22 K, which is small compared with the pipe average temperature of 1250 K (see Figure 9.5).

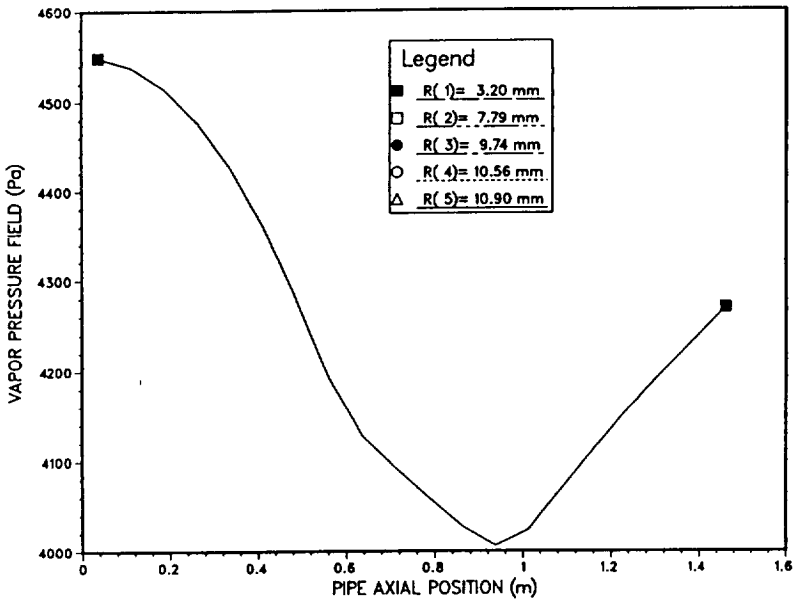

FIGURE 9.1. Steady–State Vapor Pressure Distribution Along the Lithium Heat Pipe Analyzed.

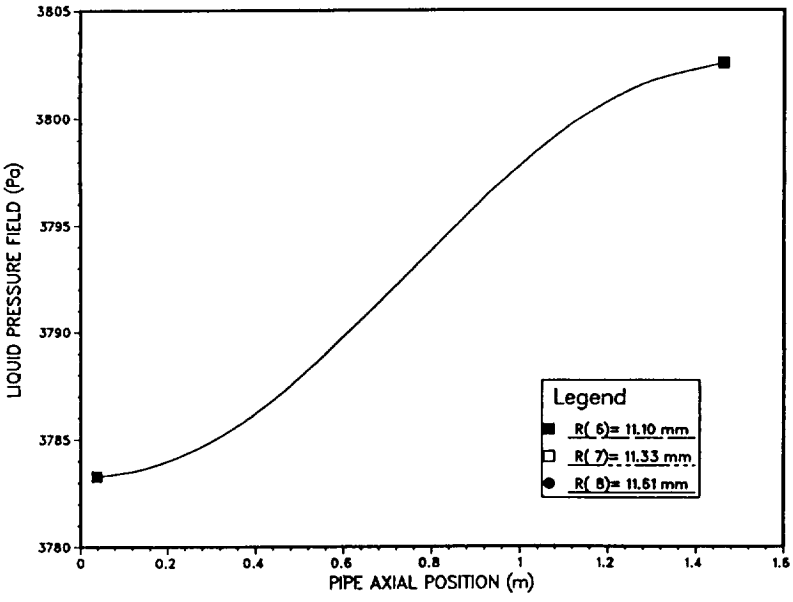

FIGURE 9.2. Steady–State Liquid Pressure Distribution Along the Lithium Heat Pipe Analyzed.

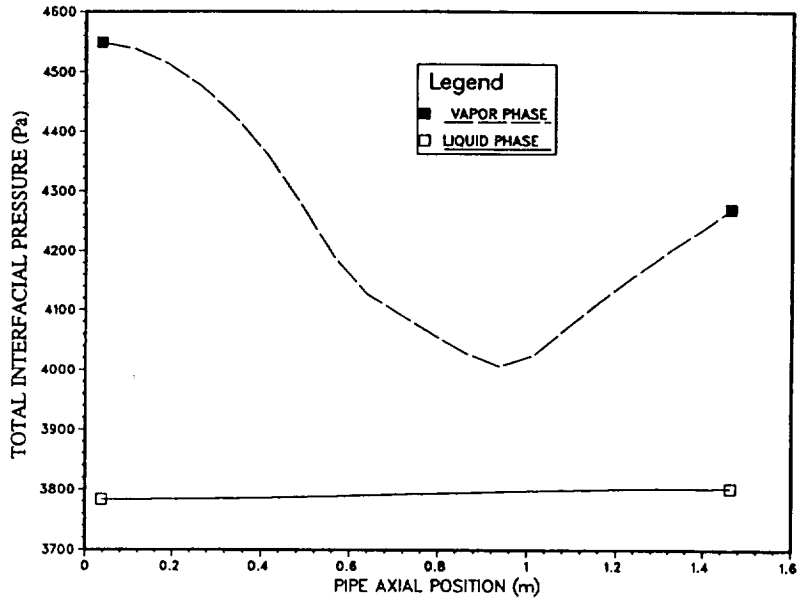

FIGURE 9.3. Total Interfacial Pressure Profiles at Steady–State Along the Lithium Heat Pipe Analyzed.

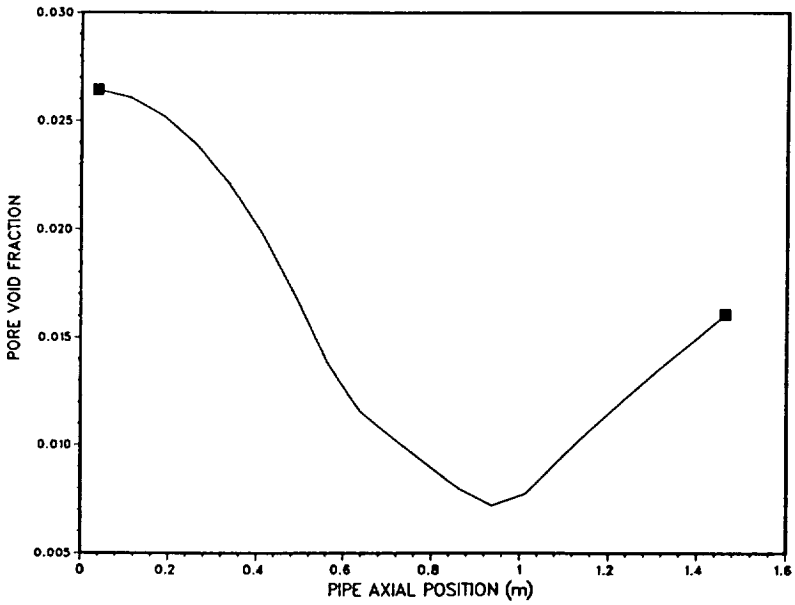

FIGURE 9.4. Pore Void Fraction Distribution at Steady–State Along the Lithium Heat Pipe Analyzed.

These results suggest that the heat is transferred mainly by radial conduction in the wall and liquid–wick regions, and that axial conduction insignificantly affects the heat pipe transient. Because the liquid flow in the wick is very slow, conduction is the only mode of heat transfer in this region. It is worth noting that the radial temperature difference between the outer wall surface and liquid at the L–V interface in the adiabatic section is negligible at steady–state.

9.4. VISCOUS DISSIPATION

Results presented in Figures (9.6) and (9.7) show that the viscous dissipation profile in both the liquid and vapor regions peaks at the axial midplane and vanishes towards the ends of the heat pipe. As expected, this axial profile is similar to that of the velocity field. Radially, the peak of the viscous dissipation is located in the vicinity of the liquid–vapor interface, where the shear stress is maximum. Very close to the interface, the axial velocity is too small, while the shear stresses are negligible near the centerline of the pipe. While viscous dissipation is less than 7 W/m^3 in the liquid phase (Figure 9.7), it peaks at about 230 kW/m^3 in the vapor region (Figure 9.6). Consequently, the primary effect of viscous dissipation is to increase the vapor temperature near the center of the pipe. These results clearly suggest that while viscous dissipation in the liquid phase could be neglected, it is not negligible in the vapor region of liquid–metal heat pipes. Neglecting viscous dissipation in the vapor could underpredict the vapor temperatures. Note that the vapor viscous dissipation curve at R=10.56 mm indicates that flow reversal is occurring at the end of the condenser region. Similar results have been reported by other investigators (Issacci et al. 1988; and Faghri and Chen 1989).

9.5. EVAPORATION / CONDENSATION RATES

Figure (9.8) presents the axial profile of the evaporation/condensation mass flux along the lithium heat pipe. It is interesting to note that at steady–state, the evaporation/ condensation mass flux at the L–V interface is uniform in both the evaporator and condenser regions, as it is assumed by simplified theories. The evaporator and condenser lengths of the heat pipe are equal, and there is no evaporation or condensation along the adiabatic section of the heat pipe.

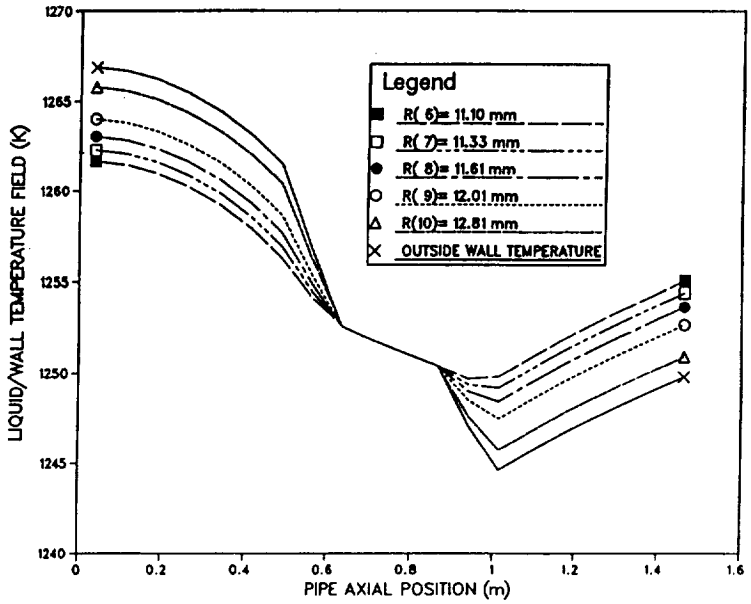

FIGURE 9.5. Liquid/Wick and Wall Temperatures Profiles at Steady–State for the Lithium Heat Pipe Analyzed.

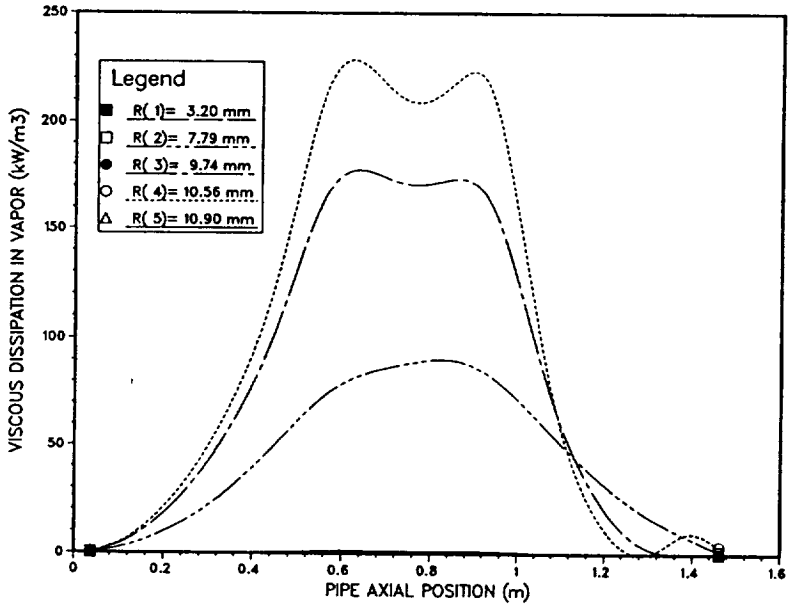

FIGURE 9.6. Viscous Dissipation Profile in the Vapor Phase at Steady–State for the Lithium Heat Pipe Analyzed.

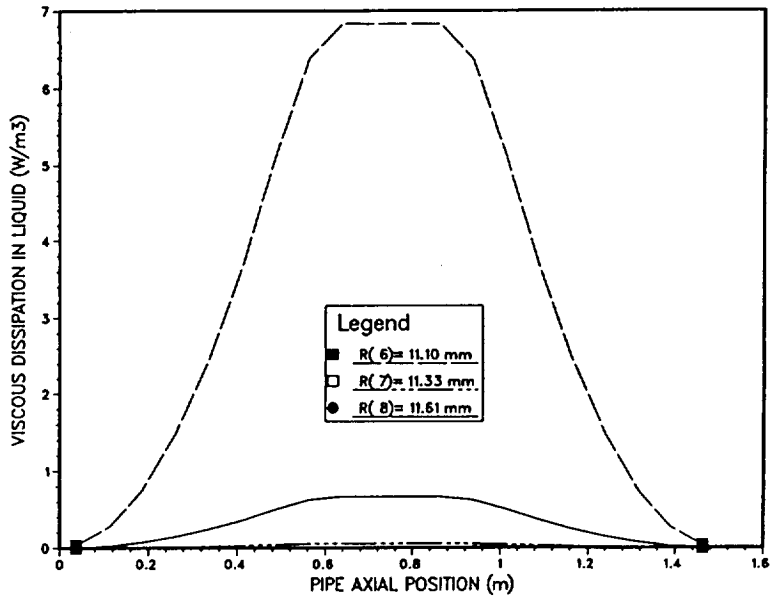

FIGURE 9.7. Viscous Dissipation Profile in the Liquid Phase at Steady–State for the Lithium Heat Pipe Analyzed.

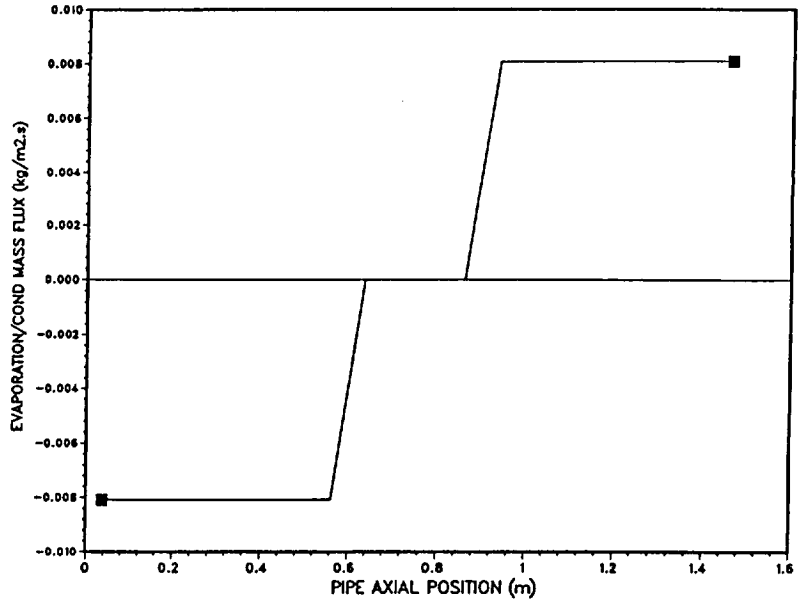

FIGURE 9.8. Evaporation/Condensation Rates Distribution at Steady–State Along the Lithium Heat Pipe Analyzed.

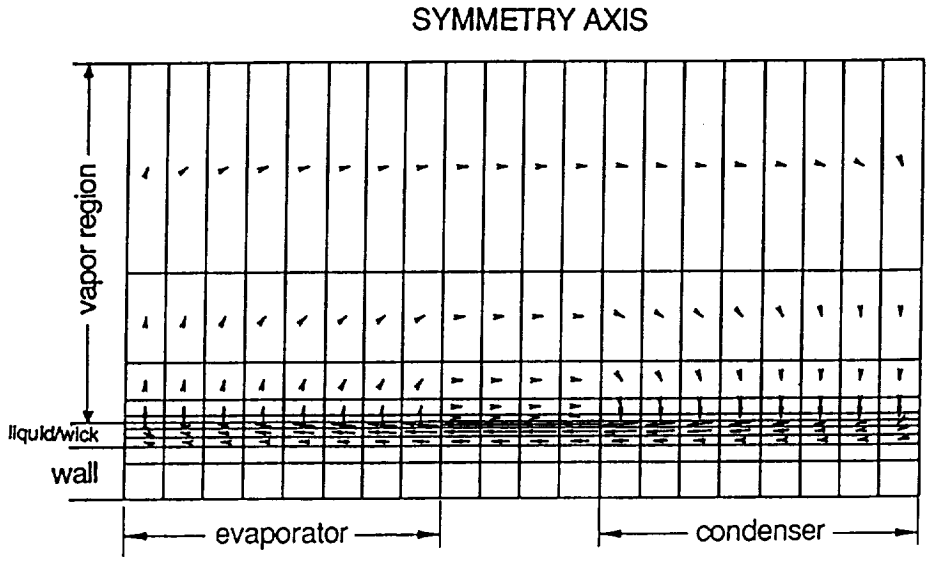

maximum axial mass flow = 7.52 kg/m^2.s
maximum radial mass flow = 0.013 kg/m^2.s

FIGURE 9.9. A Two–Dimensional Illustration of the Spacial Discretization and Mass Flow Field at Steady–State for the Lithium Heat Pipe Analyzed.

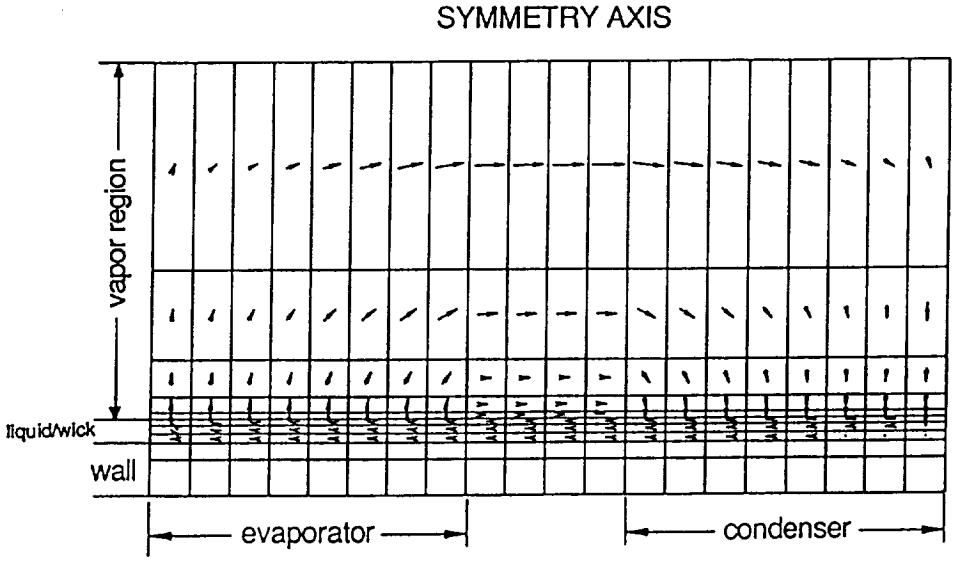

maximum axial velocity = 491.6 kg/m^2.s
maximum radial velocity = 4.69 kg/m^2.s

FIGURE 9.10. A Two–Dimensional Illustration of the Spacial Discretization and Velocity Field at Steady–State for the Lithium Heat Pipe Analyzed.

10. SUMMARY AND CONCLUSIONS

Heat pipes are highly reliable and efficient energy transport devices, which are being considered for many terrestrial and space power thermal–management applications, such as high–performance aeronautics and space nuclear and solar dynamic power systems. In this work, a two–dimensional Heat Pipe Transient Analysis Model, "HPTAM", was developed to simulate the transient operation of fully–thawed heat pipes and the startup of heat pipes from a frozen state. The model incorporates: (a) sublimation and resolidification of working fluid; (b) melting and freezing of the working fluid in the porous wick; (c) evaporation of thawed working fluid and condensation as a thin liquid film on a frozen substrate; (d) free–molecule, transition and continuum vapor flow regimes, using the Dusty Gas Model; (e) liquid flow and heat transfer in the porous wick; and (f) thermal and hydrodynamic couplings of phases at their respective interfaces. HPTAM predicts the radius of curvature of the liquid meniscus at the liquid–vapor interface and the radial location of the working fluid level (liquid or solid) in the wick. It also includes the transverse momentum jump condition (capillary relationship of Pascal) at the liquid–vapor interface and geometrically relates the radius of curvature of the liquid meniscus to the volume fraction of vapor in the wick. The present model predicts the capillary limit and partial liquid recess (dryout) in the evaporator wick, and incorporates a liquid pooling submodel, which simulates accumulation of the excess liquid in the vapor core at the condenser end.

HPTAM can handle both rectangular and cylindrical geometries. The model divides the heat pipe into three transverse regions: wall, wick, and vapor regions, and solves the complete form of governing equations in these regions. The heat pipe wick can be a wire–screened mesh, an isotropic porous medium such as a powder or a bed of spheres, or an open annulus separated from the vapor core by a thin sheet (with small holes to provide capillary forces). HPTAM incorporates several working fluids such as lithium, sodium, potassium and water, as well as various wall materials (tungsten, niobium, zirconium, stainless–steel, copper and carbon). Evaporation, condensation, sublimation and resolidification rates are calculated using the kinetic theory relationship with an accommodation coefficient of unity.

To predict the flow of liquid in the porous wick of the heat pipe, HPTAM uses the Brinkman–Forchheimer–extended Darcy model. A submodel was developed to calculate

the effective hydrodynamic properties of wire–screened wicks, such as volume porosity, permeability and effective pore size. This submodel was verified using measured characteristics of wicks found in the literature. Also several models for calculating the effective thermal conductivity of wicks were reviewed and compared with experimental data. Based on the results, Maxwell's equation for distributed cylinders is recommended to calculate the effective radial thermal conductivity of wire–screened wicks, while the parallel model is best for calculating the axial thermal conductivity of such wicks. The model of Veinberg for distributed spheres is most accurate for estimating the effective thermal conductivity of isotropic porous media such as ceramic powder, metallic felt or sintered metal. The Brinkman–Forchheimer–extended Darcy model was successfully benchmarked against experimental data for natural convection of molten gallium in a porous bed of glass beads.

HPTAM handles the phase–change of working fluid in the wick using a modified fixed–grid homogeneous enthalpy method. The large numerical error and sometimes poor stability characteristics and convergence rates of existing fixed–grid enthalpy formulations are caused by improper handling of the evolution of the latent heat and discretization of the convection–diffusion energy fluxes. A very small δT must be used to simulate the phase–change of a pure substance. When δT is small, the γ–T relationship closely approximates a step function, and many schemes using the enthalpy formulation have experienced numerical difficulties. The present numerical technique, however, employs a mushy–cell temperature range as small as 2×10^{-8} K (limited by machine accuracy only), without requiring under–relaxation of the temperatures and generating numerical instabilities. The use of the conventional harmonic mean discretization scheme (HMDS) of Patankar to estimate the heat fluxes at the boundaries of the mushy cell is largely responsible for the loss in accuracy and the generation of wiggly temperature time histories. The larger the change in thermal diffusivity of the working fluid upon melting, the worse are the results. Indeed, the thermal diffusivity of the solid phase is quite different from that of the liquid phase for most materials. Instead of using the HMDS, a simple method, based on the frozen volume fraction, was developed to calculate the heat fluxes at the boundaries of the mushy cell. This method improved the accuracy of the solution and reduced the oscillations in temperature time histories (usually encountered when the HMDS is used) by one–to–two orders of magnitude.

The wide interest in heat pipes has stimulated the development of numerous models. Because the transient operation of heat pipes and the startup of heat pipes from a frozen

state involve several highly non–linear and tightly coupled heat and mass transfer processes in the vapor, wick and wall regions, mathematical modeling of these problems is quite complex. Even so they used oversimplifying assumptions, several investigators encountered numerical instabilities (Costello et al. 1988; and Peery and Best 1987) when attempting to model the operation of heat pipes. Extremely small time steps (10^{-4} s) were required to solve iteratively for the coupled energy and kinetic theory equations. This constraint on the time step was previously reported by Subbotin when using his model for predicting evaporation / condensation rates.

Not the least contribution of this work was to develop a stable solution procedure that is accurate and efficient in terms of CPU time. Two segregated solution techniques, one based on the non–iterative Pressure Implicit Splitting Operator (PISO), and the other based on the SIMPLEC segregated iterative technique, were developed and tested for their stability and effectiveness in reducing the CPU time while maintaining the accuracy of results. The most efficient technique, HPTAM–Revised, is a SIMPLEC–type segregated solution technique which includes two internal iterative steps to resolve the pressure–velocity and temperature–velocity couplings and reduce the linearization errors of the kinetic theory relationship and equations of state. The solution evaluates the volume of the vapor in the wick explicitly, while the kinetic theory relationship is implicitly coupled with the energy jump condition at the L–V interface. Other solution techniques examined required using a small time step size (< 15 ms) to avoid numerical instabilities. On the other hand, a time step size as high as 500 ms could be used with the HPTAM–Revised technique without developing any numerical instability. While all solution techniques examined performed the same in terms of accuracy, the HPTAM–Revised is about 90 times faster than the basic non–iterative SIMPLE–type approach.

Various linear–system solvers were also examined to determine which one was most efficient for solving the problem at hand. To solve the five–point linear Poisson equations resulting from the discretization of the mass balance equations, a direct solution routine using Gaussian elimination was developed. The banded version of the solver allowed significant decreases in computation time and memory storage requirement. The selection of the appropriate linear–system solver clearly affects the efficiency of the solution technique, particularly when computational grids larger than 10x30 are used. For example, when solving a typical heat pipe problem using a 20x40 size grid, more than 90% of the total CPU time is used by the banded Gauss–elimination solver. Calculations showed that, when the iterative SIS solver is used instead of the banded Gauss–elimination solver for the

solution of the 5–point momentum and energy linear systems, the total CPU time was only 48% of that for the technique using the Gauss–elimination solver.

The development of this comprehensive model was guided by continuous benchmarking of the model predictions with available experimental and numerical results. The accuracy of the physical and numerical schemes for modeling heat and mass transfers in the wick was verified using various benchmark problems, namely: (a) natural convection of liquid in a square cavity; (b) natural convection of molten gallium in a porous bed of glass beads; (c) one–dimensional pure conduction solidification problem; (d) two–dimensional pure conduction problem of freezing in a corner; and (e) the freezing of tin in a rectangular cavity in the presence of natural convection.

Numerical results of the frozen startup of a radiatively–cooled water heat pipe are presented, which demonstrate the soudness of the physical model and numerical approach used in HPTAM. The results illustrate the importance of the sublimation and recondensation processes during the first period of the transient and the combined effects of phase–change and liquid hydrodynamics in the wick during the startup of the low–temperature heat pipe. The startup is characterized by partial recess of liquid in the evaporator wick after the capillary limit has been reached. After enough working fluid was melted by resolidification and condensation in the adiabatic and condenser sections of the heat pipe, resaturation of the wick was established before complete dryout of the evaporator occurred, leading to a successful startup. The present analysis identified the following processes occurring sequentially during the startup of a radiatively cooled water heat pipe from a frozen state:

- depletion of solid working fluid in the evaporator and accumulation in the adiabatic and condenser sections via sublimation / resolidification;
- thaw of working fluid in the evaporator and decrease of liquid inventory in wick due to evaporation and volume decrease upon melting;
- formation of a liquid film on the solid substrate in adiabatic and condenser regions due to condensation of vapor;
- outward radial propagation of thaw front in adiabatic and condenser regions;
- recovery of liquid saturation in evaporator wick due to liquid circulation from condenser;
- completion of heat pipe thaw and resumption of normal operation.

Results also showed that the sublimation/resolidification process in the low–temperature heat pipe has the beneficial effect of transporting a portion of the heat input from the evaporator to the condenser, thus reducing the temperature difference between these two regions, and accelerating the thaw process during the startup from a frozen state.

Previous investigations of the frozen startup of heat pipes generally assumed uniform distribution of the working fluid in the wick. Such assumption is found to be invalid for low–temperature heat pipes. As the present calculations show, redistribution of frozen working fluid in low–temperature heat pipes occurs during startup due to sublimation and resolidification of vapor. Such phenomena has also been observed experimentally (Kuramae 1992; and Ochterbeck and Peterson 1993). These processes may prevent successful re–startup of the heat pipe during cyclic operation. The vapor resolidifies in the cooler parts of the heat pipe and cannot return back to the evaporator. Eventually, the wick might completely dryout in the evaporator. In cases of low–temperature heat pipes with large evaporator–to–condenser length ratio, complete blockage of the vapor channel could occur due to resolidification of working fluid (Ochterbeck and Peterson 1993).

The heat pipe model was validated using transient experimental data of a fully–thawed water heat pipe constructed at the Institute for Space and Nuclear Power Studies. The calculated steady–state vapor and wall axial temperature profiles and the transient power throughput and vapor temperature were in good agreement with measurements. Results illustrated the importance of the hydrodynamic coupling of the vapor and liquid phases and showed the appearance during the heatup transient (disappearance during cooldown) of a pool of excess liquid at the condenser end. These pooling phenomena were observed by Merrigan et al. (1986) who studied experimentally the startup and shutdown transients of a 4 m–long cylindrical lithium heat pipe. They found that during normal operation, excess working fluid pooled into the vapor core and filled approximately the last 50 cm of the condenser. Finally, the effects of input power and initial liquid inventory in the water heat pipe on the wet point and liquid pooling, and on the vapor and liquid pressure and temperature distributions were investigated in details.

11. RECOMMENDATIONS FOR FUTURE WORK

It is apparent that only a few startup experiments of low–temperature and high–temperature heat pipes have been attempted in the literature, and that most experiments conducted have basically been performance tests, rather than phenomenological investigations. It is not an easy task to monitor phenomena occurring within a short distance in a closed pipe. For example, because of practical limitations, no direct measurements of the actual progression of the melting front and mass transfers associated with sublimation and resolidification were possible. Experimental data available are limited to wall temperatures in most cases, with few attempts made to measure the vapor pressure or temperature inside the heat pipe. Therefore, there is a need for systematic theoretical and experimental studies of the transient behavior of liquid–metal and non–liquid metal heat pipes. The outcome of these studies would be useful to better benchmark calculation models for the design of reliable heat pipes for space and terrestrial applications. The transient modes of interest are power step changes, reversed heat pipe operation due to a condenser external heating, and the startup of heat pipes from a frozen state.

Space experiments, which investigate the effect of microgravity in startup from a frozen state, will be a welcome input for benchmarking the present model "HPTAM" and other models in literature. Such research is necessary for future applications of heat pipe analysis code to space thermal management and spacecraft thermal control system's operation.

REFERENCES

ASM Metals Reference Book: A Handbook of Data about Metals and Metalworking (1981), American Society for Metals, Ed.

Baker, K. W. and L. K. Tower (1989) "The NASA Lewis Heat Pipe Code with Application to SP–100 GES Heat Pipes," in *Space Nuclear Power Systems 1988,* M. S. El–Genk and M. D. Hoover, Eds., Orbit Book Company, Malabar, FL., Vol. IX, pp. 387–394.

Baliga, B. R., and S. V. Patankar (1983) "A Control Volume Finite–Element Method for Two–Dimensional Fluid Flow and Heat Transfer," *Numerical Heat Transfer*, 6: 245–261.

Banaszek, J. (1989) "Comparison of Control Volume and Galerkin Finite Element Methods for Diffusion–Type Problems," *Numerical Heat Transfer*, Part B, 16: 59–78.

Beam, R. M., and R. F. Warming (1976) "An Implicit Finite–Difference Algorithm for Hyperbolic Systems in Conservation–Law Form," *Journal of Computational Physics*, 22: 87–110.

Beam, R. M., and R. F. Warming (1978) "An Implicit Factored Scheme for the Compressible Navier–Stokes Equations," *AIAA Journal*, 16 (4): 393–402.

Beavers, G. S., and E. M. Sparrow (1969) "Non–Darcy Flow through Fibrous Porous Media," *Journal of Applied Mechanics*, 36 (4): 711–714 (December 1969).

Beckermann, C., and R. Viskanta (1988) "Natural Convection Solid–Liquid Phase Change in Porous Media," *International Journal of Heat and Mass Transfer*, 31 (1): 35–46.

Bergman, T. L., and B. W. Webb (1990) "Simulation of Pure Metal Melting with Buoyancy and Surface Tension Forces in the Liquid Phase," *International Journal of Heat and Mass Transfer*, 33 (1): 139–149.

Bowman, W. J. (1987) *Simulated Heat Pipe Vapor Dynamics*, Ph. D. Thesis, the School of Engineering of the Air Force Institute of Technology, Air University, AFIT/DS/ENY/87.

Bowman, W. J. and J. E. Hitchcock (1988) "Transient Compressible Heat Pipe Vapor Dynamics," in *Proceedings of the 25th ASME National Heat Transfer Conference*, held in Houston, TX, 24–27 July 1988, HTD–96, Vol. 1, pp. 329–337.

Bowman, W. J., W. B. McClure, M. C. Towne, and D. P. Rizzetta (1990) "Transient Heat Pipe Modeling, Paper 2," in *Proceedings of the 28th Aerospace Sciences Meeting*, held in Reno, Nevada, 8–11 January 1990, Paper N°. AIAA 90–0061, pp. 1–7.

Braaten, M. E., and S. V. Patankar (1989) "A Block–Corrected Subdomain Solution Procedure for Recirculating Flow Calculations," *Numerical Heat Transfer*, Part B, 15: 1–20.

Brandt, A. (1980) "Multi–Level Adaptive Computations in Fluid Dynamics," *AIAA Journal*, 18 (10): 1165–1172.

Brandt, A. (1984) *Multigrid Techniques: 1984 Guide with Applications to Fluid Dynamics*, prepared as Lectures Notes for the Computational Fluid Dynamics Lecture Series at the von–Karmen Institute for Fluid Dynamics, Rhode–Saint–Genèse, Belgium, March 26–30, 1984.

Briley, W. R. (1974) "Numerical Method for Predicting Three–Dimensional Steady Viscous Flow in Ducts," *Journal of Computational Physics*, 14: 8–28.

Briley, W. R., and H. McDonald (1975) "Solution of the Three–Dimensional Compressible Navier–Stokes Equations by an Implicit Technique," in *Proceedings of the Fourth International Conference on Numerical Methods in Fluid Dynamics*, held at the University of Colorado, June 24–28, 1974, R. D. Richtmeyer Ed. . Lecture Notes in Physics, Vol. 35, pp. 105–110, Springer–Verlag.

Briley, W. R., and H. McDonald (1977) "Solution of the Multidimensional Compressible Navier–Stokes Equations by a Generalized Implicit Method," *Journal of Computational Physics*, 24: 372–397.

Brinkman, H. C. (1947a) "A Calculation of the Viscous Force Exerted by a Flowing Fluid on a Dense Swarm of Particles," *Applied Sciences Research*, Vol. A1, pp. 27–34.

Brinkman, H. C. (1947b) "On the Permeability of Media Consisting of Closely Packed Porous Particles," *Applied Sciences Research*, Vol. A1, pp. 81–86.

Burdi, G. F. (1964) *SNAP Technology Handbook*, Volume 1: Liquid–Metals, report NAA–SR–8617, Atomics International, Canoga Park, CA.

Busse, C. A., and J. E. Kemme (1978) "The Dry–Out Limits of Gravity–Assist Heat Pipes with Capillary Flow," in *Proceedings of the 3rd International Heat Pipe Conference*, held in Palo Alto, Paper N°. AIAA–78–383, pp. 41–48.

Camarda, C. J. (1977) *Analysis and Radiant Heating Tests of a Heat Pipe Cooled Leading Edge*, NASA Report TN–8468 (accession number N77–28967), Langley Research Center, Hampton, VA (August 1977).

Cao, Y., and A. Faghri (1990a) "Transient Two–Dimensional Compressible Analysis for High–Temperature Heat Pipes with Pulsed Heat Input," *Numerical Heat Transfer*, Part A, 18: 483–502.

Cao, Y., and A. Faghri (1990b) "A Numerical Analysis of Phase–Change Problems Including Natural Convection," *ASME Journal of Heat Transfer*, 112: 812–816.

Cao, Y., and A. Faghri (1992) "Closed–Form Analytical Solutions of High–Temperature Heat Pipe Startup and Frozen Startup Limitation," *ASME Journal of Heat Transfer*, 114: 1028–1035.

Cao, Y., and A. Faghri (1993a) "Simulation of the Early Startup Period of High–Temperature Heat Pipes from the Frozen State by a Rarefied Vapor Self–Diffusion Model," *ASME Journal of Heat Transfer*, 115: 239–246.

Cao, Y., and A. Faghri (1993b) "A Numerical Analysis of High–Temperature Heat Pipe Startup from the Frozen State," *ASME Journal of Heat Transfer*, 115: 247–254.

CEA (1963) *Principales Propriétés Physiques du Sodium, du Potassium et de leurs Alliages*, Report DRP/ML/FAR R/143, CEA–Saclay, France (December 1963).

Chang, W. S. (1990) "Porosity and Effective Thermal Conductivity of Wire Screens," *ASME Journal of Heat Transfer*, 112: 5–9 (February 1990).

Chang, W. S., and G. T. Colwell (1985) "Mathematical Modeling of the Transient Operating Characteristics of a Low–Temperature Heat Pipe," *Numerical Heat Transfer*, 8: 169–186.

Chatwani, A. U., and A. Turan (1991) "Improved Pressure–Velocity Coupling Algorithm Based on Minimization of Global Residual Norm," *Numerical Heat Transfer*, Part B, 20: 115–123.

Cheng, P. (1978) "Heat Transfer in Geothermal Systems," in *Advances in Heat Transfer* (Edited by T. F. Irvine, Jr., and J. P. Hartnett), Vol. 14, pp. 1–105. Academic Press, New York.

Chi, S. W. (1976) *Heat Pipe Theory and Practice*, Hemisphere Publishing Corporation, Washington, D. C.; Chapter 2, pp. 47–51

Chorin, A. J. (1968) "Numerical Solution of the Navier–Stokes Equations," *Mathematics of Computation*, 22: 745–762.

Collier, J. G. (1981) *Convective Boiling and Condensation*, McGraw–Hill Inc., New York, pp. 316–328.

Colwell, G. T. and J. G. Hartley (1985) *Modeling of Transient Heat Pipe Operation*, NASA–CR–175496 Report (accession number N85–21571), Georgia Institute of Technology, Atlanta, GA (February 1985).

Combarnous, M. A., and S. A. Bories (1975) "Hydrothermal Convection in Saturated Porous Media," in *Advances in Hydroscience* (Edited by V. T. Chow), Vol. 10, pp. 231–243. Academic Press, New York (1975).

Connell, S. D., and P. Stow (1986a) "A Discussion and Comparison of Numerical Techniques Used to Solve the Navier–Stokes and Euler Equations," *International Journal for Numerical Methods in Fluids*, 6: 155–163.

Connell, S. D., and P. Stow (1986b) "The Pressure Correction Method," *Computers and Fluids*, 14 (1): 1–10.

Costello, F. A., M. Merrigan, and T. R. Scollon, Jr. (1986) "Detailed Transient Model of a Liquid–Metal Heat Pipe," Presented at the *Transient Heat Pipe Modeling Workshop*, held in Los Alamos, NM, 4–5 March 1986.

Costello, F. A., R. S. Reid, M. A. Merrigan, and A. F. Montague (1988) "Detailed Transient Model of a Liquid–Metal Heat Pipe," in *Space Nuclear Power Systems 1987*, M. S. El–Genk and M. D. Hoover, Eds., Orbit Book Company, Malabar, FL., Vol. VI, pp. 197–204.

Cox, C. M., M. M. Mahaffey, and G. L. Smith (1991) "Sp–100 Design, Safety, and Testing," *Proceedings of the 8th Symposium on Space Nuclear Power Systems*, held in Albuquerque, New Mexico, January 6–10, 1991 (ISNPS publisher), Part 1, pp. 292–300.

Cunningham, R. E., and R. J. J. Williams (1980) *Diffusion in Gases and Porous Media*, Plenum Press, New York.

Darcy, H. (1856) *Les Fontaines Publiques de la Ville de Dijon*, Dalmont, Paris (France). See also Muskat (1937).

Defay, R., and I. Prigogine (1966) *Surface Tension and Adsorption*, English Edition, John Wiley and Sons, Inc., New York, NY, Chapter XV.

Delhaye, J. M. (1974) "Jump Conditions and Entropy Sources in Two–Phase Systems. Local Instant Formulation," *International Journal of Multiphase Flow*, 1: 395–409.

Delhaye, J. M. (1976) "Local Instantaneous Equations," *Two–Phase Flows and Heat–Transfer*, **1**: 59–79, S. Kakac and T. N. Veziroglu, Eds. (*Proceedings of NATO*

Advanced Study Institute on Two–Phase Flows and Heat–Transfer, congress held in Istanbul, Turkey, 16–27 August, 1976).

Deverall, J. E., J. E. Kemme, and L. W. Florschuetz (1970) *Sonic Limitations and Startup Problems of Heat Pipes*, Los Alamos Scientific Laboratory Report LA–4518 (accession number N71–18944), Los Alamos, NM, November 1970.

Dix, T. E. (1991) "DIPS Space Exploration Initiative Safety," *Proceedings of the 8th Symposium on Space Nuclear Power Systems*, held in Albuquerque, New Mexico, January 6–10, 1991 (ISNPS publisher), Part 1, pp. 264–269.

Doster, J. M. and M. L. Hall (1989) "Numerical Modeling of High–Temperature Liquid–Metal Heat Pipes," in *Proceedings of the 1989 Joint ASME/AIChE National Heat Transfer Conference*, held in Philadelphia, Pennsylvania, August 5–8, 1989, Vol. 89–HT–13, pp. 1–9.

Douglas, J. (1955) "On the Numerical Integration of Uxx+Uyy=Ut by Implicit Methods," *Journal of the Society of Industrial and Applied Mathematics*, 3 (1): 42–65 (March 1955).

Douglas, J., and J. E. Gunn (1964) "A General Formulation of Alternating Direction Methods – Part I. Parabolic and Hyperbolic Problems," *Numerische Mathematiks*, Vol. 6, pp. 428–453.

Douglas, J., and B. F. Jones (1963) "On Predictor–Corrector Methods for Non–Linear Parabolic Differential Equations," *Journal of the Society of Industrial and Applied Mathematics*, 11 (1): 195–204 (March 1963).

Dunn, P. D., and D. A. Reay (1978) *Heat Pipes*, Pergamon Press, New York, 2nd Edition, Chapter 3, pp. 107–108.

Dushman, S., and J. M. Lafferty (1962) *Scientific Foundations of Vacuum Technique*, 2nd Edition, John Wiley & Sons, New York.

Eisenberg, D., and W. Kauzmann (1969) *The Structure and Properties of Water*, Oxford University Press.

El–Genk, M. S., and L. Huang (1993) "An Experimental Investigation of the Transient Response of a Water Heat Pipe," *International Journal of Heat and Mass Transfer*, 36 (15): 3823–3830.

El–Genk, M. S., L. Huang and J.–M. Tournier (1995) "Transient Experiments of an Inclined Copper–Water Heat Pipe," *Journal of Thermophysics and Heat Transfer*, 9 (1): 109–116.

El–Wakil, M. M. (1981) *Nuclear Heat Transport*, 3rd Edition, published by the American Nuclear Society.

Ergun, S. (1952) "Fluid Flow through Packed Columns," *Chemical Engineering Progress*, 48 (2): 89–94 (February 1952).

Faghri, A. (1992) "Frozen Startup Behavior of Low–Temperature Heat Pipes," *International Journal of Heat and Mass Transfers*, 35 (7): 1681–1694.

Faghri, A. and M. Buchko (1991) "Experimental and Numerical Analysis of Low–Temperature Heat Pipes with Multiple Heat Sources," *ASME Journal of Heat Transfer*, 113 (3): 728–734.

Faghri, A., M. Buchko, and Y. Cao (1991) "A Study of High–Temperature Heat Pipes with Multiple Heat Sources and Sinks, Part I: Experimental Methodology and Frozen Startup Profiles," *ASME Journal of Heat Transfer*, 113 (4): 1003–1009.

Faghri, A., and M. M. Chen (1989) "A Numerical Analysis of the Effects of Conjugate Heat Transfer, Vapor Compressibility, and Viscous Dissipation in Heat Pipes," *Numerical Heat Transfer*, Part A, 16: 389–405.

Faghri, A., and S. Thomas (1989) "Performance Characteristics of a Concentric Annular Heat Pipe: Part I – Experimental Prediction and Analysis of the Capillary Limit," *ASME Journal of Heat Transfer*, 111 (4): 844–850 (November 1989).

Feldman, K. T., Jr., and S. Munje (1978) "Experiments with Gravity–Assisted Heat Pipes with and without Circumferential Grooves," in *Proceedings of the 3rd International Heat Pipe Conference*, Paper N°. AIAA–78–378, pp. 15–20.

Ferrell, J. K., E. G. Alexander, and W. T. Piver (1973) "Vaporization Heat Transfer in Heat Pipe Wick Materials," in *Progress in Astronautics and Aeronautics*, Vol 31: Thermal Control and Radiation, pp. 3–18, Alpine Press, Inc.

Fox, R. D., and W. J. Thomson (1970) "Internal Measurements of a Water Heat Pipe," in *Proceedings of the Intersociety Energy Conversion Engineering Conference*, held in Las Vegas, Nevada, September 21–25, 1970 (ANS publisher), pp. 7–72 to 7–76.

Galpin, P. F., and G. D. Raithby (1986) "Numerical Solution of Problems in Incompressible Fluid Flow: Treatment of the Temperature–Velocity Coupling," *Numerical Heat Transfer*, 10: 105–129.

Galpin, P. F., J. P. van Doormaal, and G. D. Raithby (1985) "Solution of the Incompressible Mass and Momentum Equations by Application of a Coupled Equation Line Solver," *International Journal for Numerical Methods in Fluids*, 5: 615–625.

Gary, J. (1964) "On Certain Difference Schemes for Hyperbolic Systems," *Mathematics of Computation*, 18: 1–18.

Georgiadis, J. G., and I. Catton (1986) "Prandtl Number Effect on Bénard Convection in Porous Media," *ASME Journal of Heat Transfer*, 108: 284–290 (May 1986).

Georgiadis, J. G., and I. Catton (1988a) "An Effective Equation Governing Convective Transport in Porous Media," *ASME Journal of Heat Transfer*, 110: 635–641 (August 1988).

Georgiadis, J. G., and I. Catton (1988b) "Dispersion in Cellular Thermal Convection in Porous Layers," *International Journal of Heat and Mass Transfer*, 31 (5): 1081–1091.

Gernert, N. J. (1986) "Analysis and Performance Evaluation of Heat Pipes with Multiple Heat Sources," in *Proceedings of the AIAA/ASME 4th Joint Thermophysics and Heat Transfer Conference*, held in Boston, MA, June 2–4, 1986, pp. 1–7.

Goda, K. (1979) "A Multistep Technique with Implicit Difference Schemes for Calculating Two– or Three–Dimensional Cavity Flows," *Journal of Computational Physics*, 30: 76–95.

Golub, G. H., and C. F. van Loan (1984) *Matrix Computations*, 2nd Edition, The Johns Hopkins University Press, Baltimore and London.

Gourlay, A. R., and J. L. Morris (1968) "Finite–Difference Methods for Non–Linear Hyperbolic Systems," *Mathematics of Computation*, 22: 28–39.

Gray, W. G., and K. O'Neill (1976) "On the General Equations for Flow in Porous Media and their Reduction to Darcy's Law," *Water Resources Research*, 12 (2): 148–154 (April 1976).

Hall, M. L. (1988) *Numerical Modeling of the Transient Thermohydraulic Behavior of High–Temperature Heat Pipes for Space Reactor Applications*, Ph. D. Thesis, Nuclear Engineering, North Carolina State University, Raleigh, NC.

Hall, M. L., and J. M. Doster (1987) "Transient Thermohydraulic Heat Pipe Model," in *Trans. of 4th Symposium on Space Nuclear Power Systems*, CONF–870102–Summs., held in Albuquerque, NM, January 12–16, 1987, pp. 397–410.

Hall, M. L., and J. M. Doster (1988) "Transient Thermohydraulic Heat Pipe Model," in *Space Nuclear Power Systems 1987*, M. S. El–Genk and M. D. Hoover, Eds., Orbit Book Company, Malabar, FL., Vol. VI, pp. 205–218.

Hall, M. L., and J. M. Doster (1989) "The THROHPUT Code: Thermohydraulic Heat Pipe Modeling," in *Trans. of 5th Symposium on Space Nuclear Power Systems*, CONF–880122–Summs, held in Albuquerque, NM, January 11–14, 1988.

Hall, M. L., and J. M. Doster (1990) "A Sensitivity Study of the Effects of Evaporation/Condensation Accommodation Coefficients on Transient Heat Pipe Modeling," *International Journal of Heat and Mass Transfer*, 33 (3): 465–481.

Hall, M. L., M. A. Merrigan and R. S. Reid (1994) "Status Report on the THROHPUT Transient Heat Pipe Modeling Code," in *Proceedings of the 11th Symposium on Space Nuclear Power and Propulsion*, held in Albuquerque, NM, January 9–13, 1994, AIP Conference Proceedings N°. 301, M. S. El–Genk and M. D. Hoover, Eds., Part 2, pp. 965–970.

Harlow, F. H., and A. A. Amsden (1971) "A Numerical Fluid Dynamics Method for all Flow Speeds," *Journal of Computational Physics*, 8: 197–213.

Harlow, F. H., and J. E. Welch (1965) "Numerical Calculation of Time–Dependent Viscous Incompressible Flow of Fluid with Free Surface," *The Physics of Fluids*, 8 (12): 2182–2189 (December 1965).

Hibbert, S. E., N. C. Markatos, and V. R. Voller (1988) "Computer Simulation of Moving–Interface, Convective, Phase–Change Processes," *International Journal of Heat and Mass Transfer*, 31 (9): 1785–1795.

Hirschfelder, J. O., C. F. Curtiss, and R. B. Bird (1954) *Molecular Theory of Gases and Liquids*, Wiley, New York.

Hirt, C. W., and J. L. Cook (1972) "Calculating Three–Dimensional Flows around Structures and over Rough Terrain," *Journal of Computational Physics*, 10: 324–340.

Ho, C. Y., R. W. Powell, and P. E. Liley (1968) "Thermal Conductivity of Selected Materials," *National Standard Reference Data System – National Bureau of Standards*, NSRD–NBS–16 Part 2 (February 1968).

Hong, J. T., Y. Yamada, and C. L. Tien (1987) "Effects of Non–Darcian and Nonuniform Porosity on Vertical–Plate Natural Convection in Porous Media," *ASME Journal of Heat Transfer*, 109: 356–362 (May 1987).

Huang, P. G., B. E. Launder, and M. A. Leschziner (1985) "Discretization of Nonlinear Convection Processes: a Broad–Range Comparison of Four Schemes," *Computer Methods in Applied Mechanics and Engineering*, 48: 1–24.

Hutchinson, B. R., P. F. Galpin, and G. D. Raithby (1988) "Application of Additive Correction Multigrid to the Coupled Fluid Flow Equations," *Numerical Heat Transfer*, 13: 133–147.

Hutchinson, B. R., and G. D. Raithby (1986) "A Multigrid Method Based on the Additive Correction Strategy," *Numerical Heat Transfer*, 9: 511–537.

Ikeda, Y. (1988) "Effective Thermal Conductivity of Screen Wicks," in *ASME Proceedings of the 1988 National Heat Transfer Conference*, held in Houston, Texas, July 24–27, 1988. HTD–Vol. 96, Vol. 1, pp. 717–722.

Irmay, S. (1958) "On the Theoretical Derivation of Darcy and Forchheimer Formulas," *Transactions, American Geophysical Union*, 39 (4): 702–707.

Irvine, T. F., Jr, and P. E. Liley (1984) *Steam and Gas Tables with Computer Equations*, Academic Press, Inc.

Issa, R. I. (1986) "Solution of the Implicitly Discretised Fluid Flow Equations by Operator Splitting," *Journal of Computational Physics*, 62: 40–65.

Issa, R. I., A. D. Gosman, and A. P. Watkins (1986) "The Computation of Compressible and Incompressible Recirculating Flows by a Non–Iterative Implicit Scheme," *Journal of Computational Physics*, 62: 66–82.

Issacci, F., I. Catton, A. Heiss, and N. M. Ghoniem (1988) "Analysis of Heat Pipe Vapor Dynamics," in *Proceedings of the 25th ASME National Heat Transfer Conference*, held in Houston, TX, 24–27 July 1988, HTD–96, Vol. 1, pp. 361–365.

Issacci, F., I. Catton, and N. M. Ghoniem (1990) "Vapor Dynamics of Heat Pipe Startup," *Proceedings of the 7th Symposium on Space Nuclear Power Systems*, held in Albuquerque, New Mexico, January 7–10, 1990 (ISNPS publisher), CONF–900109, Part 2, pp.1002–1007.

Issacci, F., I. Catton, and N. M. Ghoniem (1991) "Vapor Dynamics of Heat Pipe Startup," *ASME Journal of Heat Transfer*, 113: 985–994 (November 1991).

Ivanovskii, M. N., V. P. Sorokin, and I. V. Yagodkin (1982) *The Physical Principles of Heat Pipes*, translated by R. Berman and G. Rice, Oxford University Press, New York.

Jang, J. H. (1988) *An Analysis of Startup from the Frozen State and Transient Performance of Heat Pipes*, PhD Thesis, Mechanical Engineering, Georgia Institute of Technology, Atlanta, GA, February 1988.

Jang, J. H. (1995) "A Study of Startup Characteristics of a Potassium Heat Pipe from the Frozen State," *Journal of Thermophysics and Heat Transfer*, 9 (1): 117–122.

Jang, J. H., A. Faghri, and W. S. Chang (1989) "Analysis of the Transient Compressible Vapor Flow in Heat Pipes," in *Proceedings of the 1989 ASME National Heat Transfer Conference*, HTD Vol. 110: Numerical Heat Transfer with Personal Computers and Supercomputing, pp. 113–120.

Jang, J. H., A. Faghri, W. S. Chang, and E. T. Mahefkey (1990a) "Mathematical Modeling and Analysis of Heat Pipe Startup from the Frozen State," *ASME Journal of Heat Transfer*, 112: 586–594 (August 1990).

Jang, J. H., W. P. Lucas, K. W. Baker, and A. J. Juhasz (1990b) "Preliminary Report on Copper / Water Heat Pipe Tests at NASA Lewis Research Center," in *Proceedings of the 7th Symposium on Space Nuclear Power Systems*, held in Albuquerque, NM, January 7–10, 1990 (ISNPS publisher), Part 2, pp. 982–987.

Jeppson, D. W., et al. (1978) *Lithium Literature Review: Lithium Properties and Interactions*, Hanford Engineering Development Laboratory, report HEDL–TME 78–15 UC–20 (April 1978).

Kemme, J. E. (1966) *Heat Pipe Capability Experiments*, Los Alamos Scientific Laboratory Report LA–3585–MS (accession number N67–19015), Los Alamos, NM (October 1966).

Kemme, J. E., E. S. Keddy, and J. R. Phillips (1978) "Performance Investigations of Liquid–Metal Heat Pipes for Space and Terrestrial Applications," in *Proceedings of the 3rd International Heat Pipe Conference*, Paper N°. AIAA–78–431, pp. 260–267.

Kennard, E. H. (1938) *Kinetic Theory of Gases*, McGRAW–HILL Book Company, Inc., New York and London.

Kladias, N., and V. Prasad (1989) "Natural Convection in Horizontal Porous Layers: Effects of Darcy and Prandtl Numbers," *ASME Journal of Heat Transfer*, 111: 926–935 (November 1989).

Klein, D. B. and I. Catton (1987) "Transient Analysis of Heat Pipe Vapor Dynamics," in *Trans. of 4th Symposium on Space Nuclear Power Systems*, CONF–870102–Summs., held in Albuquerque, NM, 12–16 January 1987, pp. 377–380.

Krupiczka, R. (1967) "Analysis of Thermal Conductivity in Granular Materials," *International Chemical Engineering*, 7 (1): 122–144 (January 1967).

Kuramae, M. (1992) "Heat Transfer Characteristics of Water Heat Pipes in Conjunction with Freezing or Melting of Working Fluid," *Advances in Heat Pipe Science and Technology*, M. A. Tongze (Ed.), International Academic Publishers, pp. 244–249.

Ochterbeck, J. M. and G. P. Peterson, AIAA *J. of Thermophysics and Heat Transfer*, 7 (1), 127–132 (1993).

Kvernvold, O., and P. A. Tyvand (1980) "Dispersion Effects on Thermal Convection in Porous Media," *Journal of Fluid Mechanics*, 99: 673–686.

Lai, F. C., and F. A. Kulacki (1991) "Non–Darcy Mixed Convection along a Vertical Wall in a Saturated Porous Medium," *ASME Journal of Heat Transfer*, 113: 252–255 (February 1991).

Lax, P. D. (1954) "Weak Solutions of Nonlinear Hyperbolic Equations and their Numerical Computation," *Communication on Pure and Applied Mathematics*, 7:159–193.

Lee, S. L. (1989a) "A Strongly Implicit Solver for Two–Dimensional Elliptic Differential Equations," *Numerical Heat Transfer*, Part B, Vol. 16, pp. 161–178.

Lee, S. L. (1989b) "Weighting Function Scheme and its Application on Multidimensional Conservation Equations," *International Journal of Heat and Mass Transfer*, 32 (11): 2065–2073.

Lee, S. L., and R. Y. Tzong (1991) "An Enthalpy Formulation for Phase–Change Problems with a Large Thermal Diffusivity Jump across the Interface," *International Journal of Heat and Mass Transfer*, 34 (6): 1491–1502.

Léger, D. (1980) *Propriétés Physico–Chimiques du Lithium*, Division de Chimie, Département de Chimie Appliquée et d'Études Analytiques, Report DCAE/SCECF/SECF/80–56, CEA–Saclay, France (February 1980).

Leonard, B. P. (1979) "A Stable and Accurate Convective Modelling Procedure Based on Quadratic Upstream Interpolation," *Computer Methods in Applied Mechanics and Engineering*, 19: 59–98.

Levec, J., and R. G. Carbonell (1985) "Longitudinal and Lateral Thermal Dispersion in Packed–Beds," *AIChE Journal*, 31 (4): 581–602 (April 1985).

Levich, V. G., and V. S. Krylov (1969) "Surface–Tension–Driven Phenomena," *Annual Review of Fluid Mechanics*, 1:293–316.

Liles, D. R., and Wm. H. Reed (1978) "A Semi–Implicit Method for Two–Phase Fluid Dynamics," *Journal of Computational Physics*, 26: 390–407.

Lundgren, T. S. (1972) "Slow Flow through Stationary Random Beds and Suspensions of Spheres," *Journal of Fluid Mechanics*, Vol. 51, Part 2, pp. 273–299.

Majumdar, S. (1988) "Role of Underrelaxation in Momentum Interpolation for Calculation of Flow with Non–Staggered Grids," *Numerical Heat Transfer*, 13: 125–132.

Merrigan, M. A. (1985) "Heat Pipe Technology Issues," in *Space Nuclear Power Systems 1984*, 1st Symposium held in Albuquerque, NM, 1984, M. S. El–Genk and M. D. Hoover, Eds., Orbit Book Company, Malabar, FL, Vol. II, pp. 419–426.

Merrigan, M. A., E. S. Keddy, and J. T. Sena (1985) *Transient Heat Pipe Investigations for Space Power Systems*, Los Alamos National Laboratory Report LA–UR–85–3341 (accession number N86–21806), Los Alamos, NM (September 1985).

Merrigan, M. A., E. S. Keddy, and J. T. Sena (1986) "Transient Performance Investigation of a Space Power System Heat Pipe," in *Proceedings of the AIAA/ASME 4th Joint Thermophysics and Heat Transfer Conference*, held in Boston, MA, 2–4 June, 1986, Paper N°. AIAA–86–1273.

Metals Handbook (1979), Vol. 2: Properties and Selection — Nonferrous Alloys and Pure Metals, and Vol. 3, 9th Edition, American Society for Metals, Metals Park, O. H. .

Minkowycz, W. J., E. M. Sparrow, G. E. Schneider, and R. H. Pletcher (1988) *Handbook of Numerical Heat Transfer*, John Wiley & Sons, INC., New York.

Moeller, T., et al. (1980) *Chemistry with Inorganic Qualitative Analysis*, pp. 358–359, Academic Press Inc., New York, N. Y. .

Monchick, L., and E. A. Mason (1961) "Transport Properties of Polar Gases," *The Journal of Chemical Physics*, 35 (5): 1676–1697 (November 1961).

Muskat, M. (1937) *The Flow of Homogeneous Fluids through Porous Media*, McGraw–Hill Book Company, Inc., New York, N. Y. .

Nakayama, A., T. Kokudai, and H. Koyama (1990) "Non–Darcian Boundary Layer Flow and Forced Convective Heat Transfer over a Flat Plate in a Fluid–Saturated Porous Medium," *ASME Journal of Heat Transfer*, 112: 157–162 (February 1990).

Neale, G., and W. Nader (1974) "Practical Significance of Brinkman's Extension of Darcy's Law: Coupled Parallel Flows within a Channel and a Bounding Porous Medium," *The Canadian Journal of Chemical Engineering*, 52: 475–478 (August 1974).

Ochterbeck, J. M., and G. P. Peterson (1993) "Freeze–Thaw Characteristics of a Copper/Water Heat Pipe: Effects of Noncondensible Gas Charge," *AIAA Journal of Thermophysics and Heat Transfer*, 7 (1), 127–132.

Ohse, R. W. Editor (1985) *Handbook of Thermodynamic and Transport Properties of Alkali Metals*, International Union of Pure and Applied Chemistry, Blackwell Scientific Publications, Oxford.

Ozisik, N. M. (1980) *Heat Conduction*, Wiley–Interscience, New York, chapter 10.

Patankar, S. V. (1980) *Numerical Heat Transfer and Fluid Flow*, Hemisphere Publishing Company, Washington, DC.

Patankar, S. V. (1986) *Efficient Numerical Techniques for Complex Fluid Flows*, Turbine Engine Hot Section Technology, NASA CP–2444, Cleveland, Ohio (accession number N89–12894).

Patankar, S. V. (1988) "Recent Developments in Computational Heat Transfer," *ASME Journal of Heat Transfer*, 110: 1037–1045 (November 1988).

Patankar, S. V., and D. B. Spalding (1972) "A Calculation Procedure for Heat, Mass and Momentum Transfer in Three–Dimensional Parabolic Flows," *International Journal of Heat and Mass Transfer*, 15: 1787–1806.

Peaceman, D. W., and H. H. Rachford (1955) "The Numerical Solution of Parabolic and Elliptic Differential Equations," *Journal of the Society of Industrial and Applied Mathematics*, 3 (1): 28–41 (March 1955).

Pearson, W. B. (1958) *A Handbook of Lattice Spacings and Structures of Metals and Alloys*, International Series of Monographs on Metal Physics and Physical Metallurgy, Vol. 4, G. V. Raynor, Ed., Pergamon Press.

Peery, J. S., and F. R. Best (1987) "Simulation of Heat Pipe Rapid Transient Performance Using a Multi–Nodal Implicit Finite Difference Scheme," in *Space Nuclear Power Systems 1986*, M. S. El–Genk and M. D. Hoover, Eds., Orbit Book Company, Malabar, FL., Vol. V, pp. 145–150.

Peyret, R., and T. D. Taylor (1983) *Computational Methods for Fluid Flow*, Springer Series in Computational Physics, Springer–Verlag New York Inc..

Plumb, O. A. (1983) "The Effect of Thermal Dispersion on Heat Transfer in Packed Bed Boundary Layers," in *Proceedings of 1st ASME–JSME Thermal Engineering Joint Conference*, held in Honolulu, Hawaii, March 20–24, 1983, Vol. 2, pp. 17–22.

Prakash, C., and S. V. Patankar (1985) "A Control Volume–Based Finite–Element Method for Solving the Navier–Stokes Equations Using Equal–Order Velocity–Pressure Interpolation," *Numerical Heat Transfer*, 8: 259–280.

Prasad, V., N. Kladias, A. Bandyopadhaya, and Q. Tian (1989) "Evaluation of Correlations for Stagnant thermal conductivity of liquid–saturated porous beds of spheres," *International Journal of Heat and Mass Transfer*, 32 (9): 1793–1796.

Preliminary Heat Pipe Testing Program (1981), Final Technical Report DOE/SF/10756, prepared under Contract DE–AC03–79SF 10756 by BECHTEL NATIONAL, INC., San Francisco, CA, for the US Department of Energy, San Francisco Operations Office (March 1981).

Raithby, G. D., and G. E. Schneider (1979) "Numerical Solution of Problems in Incompressible Fluid Flow: Treatment of the Velocity–Pressure Coupling," *Numerical Heat Transfer*, 2: 417–440.

Ramadhyani, S., and S. V. Patankar (1985) "Solution of the Convection–Diffusion Equation by a Finite–Element Method Using Quadrilateral Elements," *Numerical Heat Transfer*, 8: 595–612.

Ransom, V. H., and H. Chow (1987) "ATHENA Heat Pipe Transient Model," in *Trans. of 4th Symposium on Space Nuclear Power Systems*, CONF–870102–Summs., held in Albuquerque, NM, 12–16 January 1987, M. S. El–Genk and M. D. Hoover, Eds., ISNPS, UNM, Albuquerque, NM, pp. 389–392.

Rao, D. V., M. S. El–Genk and A. J. Juhasz (1990) "Transient Model of High–Temperature Heat Pipes," in *Proceedings of the 7th Symposium on Space Nuclear Power Systems*, held in Albuquerque, NM, January 7–10, 1990 (ISNPS publisher), Part 2, pp. 854–861.

Rathjen, K. A., and L. M. Jiji (1971) "Heat Conduction with Melting or Freezing in a Corner, *ASME Journal of Heat Transfer*, 93: 101–109.

Raw, W. Y., and S. L. Lee (1991) "Application of Weighting Function Scheme on Convection–Diffusion Phase–Change Problems," *International Journal of Heat and Mass Transfer*, 34 (6): 1503–1512.

Reinarts, T. R., and F. R. Best (1990) "Water Heat Pipe Frozen and Non–Frozen Startup and Shutdown Transients with Internal Measurements and Visual Observations," in *Proceedings of the 7th Symposium on Space Nuclear Power Systems*, held in Albuquerque, NM, January 7–10, 1990 (ISNPS publisher), Part 2, pp. 1011–1016.

Reynolds, O. (1900) *Papers on Mechanical and Physical Subjects*, Cambridge University Press, London.

Reynolds, W. C. (1979) *Thermodynamic Properties in SI*, Department of Mechanical Engineering, Stanford University, Stanford, CA.

Roache, P. J. (1982) *Computational Fluid Dynamics*, Hermosa Publishers, Albuquerque, NM, 87108.

Roberts, C. C., and K. T. Feldman, Jr. (1972) "Predicting Performance of Heat Pipes with Partially Saturated Wicks," in *Proceedings of the 1972 ASME Winter Annual Meeting*, held in New York, N. Y., 26–30 November 1972, Paper N°. 72–WA/HT–38.

Ross, R. G., P. Andersson, and G. Backstrom (1978) "Effects of H and D order on the Thermal Conductivity of Ice Phases," *Journal of Chemical Physics*, 68 (9): 3967–3972 (May 1978).

Sasaki, A., S. Aiba, and S. Fukusako (1990) "Numerical Study on Freezing Heat Transfer in Water–Saturated Porous Media," *Numerical Heat Transfer*, Part A, 18: 17–32.

Scheidegger, A. E. (1974) *The Physics of Flow through Porous Media*, 3rd Edition, University of Toronto Press.

Schlunder, E. U., Editor–in–Chief (1984) "Physical Properties," *Heat Exchanger Design Handbook*, Vol. 5, Hemisphere Publishing Corporation.

Seo, J. T. (1988) *Transient Analysis of Space Nuclear Power Systems*, a Dissertation submitted in partial fulfillment of the requirements for the PhD Degree in Nuclear Engineering, The University of New Mexico, Albuquerque, NM (May 1988).

Seo, J. T., and M. S. El–Genk (1988) "A Transient Model for Liquid–Metal Heat Pipes," in *Transactions of 5th Symposium on Space Nuclear Power Systems*, CONF–880122–Summs, held in Albuquerque, NM, January 11–14, 1988.

Seo, J. T., and M. S. El–Genk (1989) "A Transient Model for Liquid–Metal Heat Pipes," in *Space Nuclear Power Systems 1988*, M. S. El–Genk and M. D. Hoover, Eds., Orbit Book Company, Malabar, FL., Vol. IX, pp. 405–418.

Settari, A., and K. Aziz (1973) "A Generalization of the Additive Correction Methods for the Iterative Solution of Matrix Equations," *SIAM Journal on Numerical Analysis*, 10 (3): 506–521 (June 1973).

Singh, B. S., A. Dybbs, and F. A. Lyman (1973) "Experimental Study of the Effective Thermal Conductivity of Liquid Saturated Sintered Fiber Metal Wicks," *International Journal of Heat and Mass Transfer*, 16: 145–155.

Spalding, D. B., and H. I. Rosten (1985) *PHOENICS–Beginner's Guide*, CHAM Limited, London, England.

Stark, K. P. (1969) *Transactions of the 1969 Haifa Symposium on Fundamentals of Transport Phenomena in Porous Media*, pp. 86. Ed. IAHR, Elsevier, Amsterdam, 1972.

Stewart, H. B. (1981) "Fractional Step Methods for Thermohydraulic Calculation," *Journal of Computational Physics*, 40: 77–90.

Stewart, H. B., and B. Wendroff (1984) "Review Article. Two–Phase Flow: Models and Methods," *Journal of Computational Physics*, 56: 363–409.

Stewart, W. E., Jr., and K. L. Smith (1985) "Inward Solidification of Water in a Cylinder – An Analytical and Experimental Study," in *Proceedings of the 1985 ASME National Heat Transfer Conference*, held in Denver, CO, 4–7 August 1985, Paper N°. 85–HT–2, pp. 1–7.

Stone, H. L. (1968) "Iterative Solution of Implicit Approximations of Multidimensional Partial Differential Equations," *SIAM Journal of Numerical Analysis*, 5: 530–558.

Tam, C. K. W. (1969) "The Drag on a Cloud of Spherical Particles in Low Reynolds Number Flow," *Journal of Fluid Mechanics*, 38: 537–546.

Tao, W. Q., and E. M. Sparrow (1987) "The Transportive Property and Convective Numerical Stability of the Steady–State Convection–Diffusion Finite–Difference Equation," *Numerical Heat Transfer*, 11: 491–497.

Tilton, D., J. Johnson, J. Gottschlich, and S. Iden (1986) *Transient Response of a Liquid–Metal Heat Pipe*, Air Force Wright Aeronautical Laboratories Report AFWAL–TR–86–2037, Wright Patterson AFB, OH (August 1986).

Tilton, D. (1987) *Transient Response of a Liquid–Metal Heat Pipe*, Master's Thesis, the University of Kentucky, Lexington, Kentucky.

Tolubinsky, V. I., E. N. Shevchuk, and V. D. Stambrovsky (1978) "Study of Liquid–Metal Heat Pipes Characteristics at Startup and Operation Under Gravitation," in *Proceedings of the 3rd International Heat Pipe Conference*, Paper N°. AIAA–78–434, pp. 274–282.

Touloukian, Y. S., Editor (1970) *Thermophysical Properties of Matter, the TPRC Data*, Vol. 1: Thermal Conductivity — Metallic Elements and Alloys; Vol. 4: Specific Heat — Metallic Elements and Alloys, Plenum Publishing Corporation.

Touloukian, Y. S., Editor (1975) *Thermophysical Properties of Matter, the TPRC Data*, Plenum Publishing Corporation.

Tournier, J.–M., and M. S. El–Genk (1991) "Heat Pipe Transient Model for Space Applications," in *Proceedings of the 8th Symposium on Space Nuclear Power*

Systems, held in Albuquerque, NM, January 6–10, 1991 (ISNPS publisher), Part 2, pp. 857–868.

Tournier, J.–M., and M. S. El–Genk (1992) "HPTAM Heat Pipe Transient Analysis Model: an Analysis of Water Heat Pipes," in *Proceedings of the 9th Symposium on Space Nuclear Power Systems*, held in Albuquerque, NM, January 12–16, 1991, American Institute of Physics, New York, NY, AIP Conference Proceeding No. 246, Part 3, pp. 1023–1037.

Tournier, J.–M., and M. S. El–Genk (1994a) "A Segregated Solution Technique for Simulating the Transient Operation of Heat Pipes," *Numerical Heat Transfer*, Part B: Fundamentals, 25: 331–355.

Tournier, J.–M., and M. S. El–Genk (1994b) "A Heat Pipe Transient Analysis Model," *International Journal of Heat and Mass Transfer*, 37 (5): 753–762.

van Doormaal, J. P., and G. D. Raithby (1984) "Enhancements of the SIMPLE Method for Predicting Incompressible Fluid Flows," *Numerical Heat Transfer*, 7: 147–163.

Vargaftik, N. B. (1975) *Tables on the Thermophysical Properties of Liquids and Gases, in Normal and Dissociated States*, 2nd Edition, Hemisphere Publishing Corporation, Washington, DC.

Veinberg, A. K. (1967) "Permeability, Electrical Conductivity, Dielectric Constant and Thermal Conductivity of a Medium with Spherical and Ellipsoidal Inclusions," *Soviet Physics–Doklady* , 11 (7): 593–595 (January 1967).

Voller, V. R., and C. Prakash (1987) "A Fixed Grid Numerical Modeling Methodology for Convection–Diffusion Mushy Region Phase–Change Problems," *International Journal of Heat and Mass Transfer*, 30 (8): 1709–1719.

Ward, J. C. (1964) "Turbulent Flow in Porous Media," *Journal of the Hydraulics Division* (Proceedings of the American Society of Civil Engineers), Vol. HY5, pp. 1–12 (September 1964).

Weast, R. C., Editor–in–Chief (1986) *CRC Handbook of Chemistry and Physics*, 66th Edition, 1985–86, CRC PRESS, Inc.

Weiss, D. W., L. A. Stickler, and W. E. Stewart, Jr. (1991) "The Effect of Water Density Extremum on Heat Transfer within a Cylinder Containing a Heat–Generating Porous Medium," *Int. Comm. Heat Mass Transfer*, 18 (2): 259–271.

Whitaker, S. (1977) "Simultaneous Heat, Mass, and Momentum Transfer in Porous Media: A Theory of Drying," in *Advances in Heat Transfer* (Edited by T. F. Irvine, Jr. and J. P. Hartnett), Vol. 13, pp. 119–203. Academic Press, New York (1977).

Whitaker, S. (1986) "Local Thermal Equilibrium: An Application to Packed–Bed Catalytic Reactor Design," *Chemical Engineering Science*, 41 (8): 2029–2039.

Wolff, F., and R. Viskanta (1988) "Solidification of a Pure Metal at a Vertical Wall in the Presence of Liquid Superheat," *International Journal of Heat and Mass Transfer*, 31 (8): 1735–1744.

Woloshun, K. A., M. A. Merrigan, and E. D. Best (1989) "HTPIPE – A Steady–State Heat Pipe Analysis Program," in *Space Nuclear Power Systems 1988*, M. S. El–Genk and M. D. Hoover, Eds., Orbit Book Company, Malabar, FL., Vol. IX, pp. 395–403.

Yanenko, N. N. (1971) *The Method of Fractional Steps*, Springer–Verlag, New–York.

APPENDIX A. MODELING OF HEAT AND MASS TRANSFERS IN POROUS MEDIA

Since the early work of Darcy in the nineteenth century, extensive investigations have been conducted on flow and heat transfer through porous media, covering a broad range of different fields and applications, such as ground–water hydrology, petroleum reservoir and geothermal operations, packed–bed chemical reactors, transpiration cooling and building thermal insulation. The first section of this appendix (Section A-1) describes the necessary governing equations for modeling the flow of liquid in the porous wick of the heat pipe. The Brinkman–Forchheimer–extended Darcy's flow equations approach the empirical representation of the flow in a porous medium (the Forchheimer–extended Darcy flow model) as the permeability of the porous wick, K, decreases, and reduce to the standard Navier–Stokes equations as K goes to infinity.

The next section (A-2) focuses on the heat transfer in a partially frozen porous medium, which contains a mixture of three phases: the solid and liquid phases of the working fluid, and the solid matrix of the wick. The volume–averaged homogeneous enthalpy formulation is best suited for modeling this difficult problem. This method offers several advantages: (a) it employs a fixed–grid numerical scheme; (b) it accounts for the complicated interfacial structures of the various constituents and is valid for any volume fractions of the wick porous matrix and the liquid and frozen phases of the working fluid; and (c) it does not necessitate implicit tracking of the liquid–solid interface.

Finally, analytical expressions of the hydrodynamic and thermal properties of the heat pipe wick are presented in the last two sections of this appendix, and checked using experimental measurements.

A-1. MODELING OF FLOW THROUGH POROUS MEDIA

Most analytical studies of flow through porous media have dealt primarily with a mathematical formulation based on Darcy's law, which neglects the effects of solid boundaries and inertial forces on fluid flow through porous media. To account for these effects, Forchheimer and Brinkman extended Darcy's law, and other investigators introduced the transient and convective inertia effects into their generalized flow equation.

The form of the Brinkman–Forchheimer–extended Darcy's flow equations can be partly justified through analytical volume–averaging of the microscopic conservation equations, which provides a mean to identify the apparent viscosity in the Brinkman's term. It is then postulated that Darcy's term and Forchheimer's extension are the necessary constitutive relationships to model the unknown terms arising from the volume–averaging process.

A-1.1. Darcy's Law

The steady flow of a fluid through a fully–saturated homogeneous isotropic porous medium is described by the empirical Darcy's equation (Darcy 1856):

$$\vec{\nabla}P = \rho\vec{F} - \frac{\mu\vec{q}}{K} \quad , \tag{A-1}$$

where

P, ρ and μ are the pressure (Pa), density (kg/m^3) and dynamic viscosity ($kg/m.s$) of the fluid, respectively,

F is the external acceleration (body forces, such as gravity, in m/s^2),
K is the permeability of the porous medium (m^2), and
q denotes the mean (area–averaged) filter velocity within the medium (m/s).

Since it neglects any inertial and turbulent effects, Darcy's law is valid for very slow flow conditions only. The inertial effect becomes important for high–porosity media or high Rayleigh number regimes.

A-1.2. Forchheimer's Extension

For (unidirectional) high–velocity laminar and turbulent flows in a porous medium, it was first suggested by Osborne Reynolds (1900) and later by Muskat (1937) that the axial pressure gradient might be represented by the form:

$$-\frac{dP}{dz} = a\mu q + b\rho q|q| \quad , \tag{A-2}$$

where a and b are constant for a given porous medium. The following explanation

(Beavers and Sparrow 1969) may be offered to justify the form of Equation (A-2). For a very slow flow, it is well established that the pressure gradient is a linear function of the filter velocity q, and the coefficient a is the reverse of the permeability (see Equation A-1). At higher velocities, departures from Darcy's law are due to inertial effects. The inertial effects are reckoned as being proportional to ρq^2. The linear superposition of the viscous and inertial effects embodied in Equation (A-2) cannot be justified on purely theoretical grounds, nor can the assumption that b is independent of the velocity q. These aspects of the proposed relationship require experimental justification. An analysis by Ward (1964) showed that $b = C/\sqrt{K}$, where C is a dimensionless constant which has been evaluated experimentally by various investigators. Ward (1964) found that for a large variety of porous media C could be taken as a constant equal to approximately 0.55. Despite the original belief that the "inertia coefficient" C was a universal constant, it is now generally accepted that C is a function of the microstructure of the porous medium (Beavers and Sparrow 1969).

Equation (A-2) can be rewritten in terms of the inertia coefficient as:

$$-\frac{dP}{dz} = \frac{\mu q}{K} + \frac{C}{\sqrt{K}}\rho q|q| \quad . \tag{A-3}$$

The second term on the right–hand side of Equation (A-3) is commonly referred to as the *Forchheimer's extension*. As apparent from Equation (A-3), the ratio of pressure gradient to filter velocity is a linear function of the velocity, so that K and C can be easily determined from measurements of static pressure drops and mass flow rates by fitting a straight line to the data. Indeed, experimental investigations (Ergun 1952; Ward 1964; and Beavers and Sparrow 1969) for uni–directional flows of water and gases through packed columns and fibrous materials showed the axial pressure distribution to be a linear function of z.

In the literature, it is a common practice to express the pressure drop in terms of a friction factor. Defining the characteristic dimension of a porous medium as the square root of the permeability $\sqrt{K}$, the Fanning friction factor f_a and the Reynolds number Re have the following expressions:

$$f_a = \frac{\sqrt{K}}{\rho q^2}\left|\frac{dP}{dz}\right| \quad , \qquad \mathrm{Re} = \frac{\rho\sqrt{K}|q|}{\mu} \quad . \tag{A-4}$$

Identifying Equations (A-3) and (A-4) gives the following expression for f_a :

$$f_a = \frac{\sqrt{K}}{\rho q^2}\left(\frac{\mu|q|}{K} + C\frac{\rho q^2}{\sqrt{K}}\right) = \frac{1}{\mathrm{Re}} + C \quad . \tag{A-5}$$

It was found experimentally that f_a varies inversely with the Reynolds number in the laminar flow regime (Darcy flow) and becomes a constant at high Reynolds numbers . As apparent from Equation (A-5), there is no distinct division between laminar, transition and turbulent flows in porous media.

Ergun (1952) used experimental data on the flow of gases (CO_2, N_2, CH_4 and H_2) through beds of granular solids of various shape (various–sized spheres, sand and pulverized coal) and derived the following expressions for the permeability and inertia coefficient of packed particle columns:

$$K = \frac{D_m^2}{150}\frac{\varepsilon^3}{(1-\varepsilon)^2} \quad , \qquad C = \frac{1.75}{\sqrt{150}}\frac{1}{\varepsilon\sqrt{\varepsilon}} = \frac{0.143}{\varepsilon\sqrt{\varepsilon}} \quad , \tag{A-6}$$

where D_m is a characteristic dimension which represents the mean diameter of the particles. The mean particle diameter is generally that of a sphere having same specific surface S_v as the particles in the bed. For a sphere of radius R :

$$S_v = \frac{4\pi R^2}{\frac{4}{3}\pi R^3} = \frac{3}{R} \quad , \tag{A-7}$$

and

$$D_m = \frac{6}{S_v} \quad . \tag{A-8}$$

Needless to say, while the determination of S_v presents no problem for packed columns of identical particles, it is technically difficult for porous media (Ergun 1952). A simple consideration of theoretical possibilities of the structure of porous media makes one realize that a general correlation between porosity and permeability cannot exist. It is obviously quite possible for two porous media of the same porosity to have entirely different permeabilities.

A much used modification of Kozeny's theory for the permeability of porous media was postulated by Carman who derived the so–called *Kozeny–Carman* equation:

$$K = \frac{1}{5S_v^2}\frac{\varepsilon^3}{(1-\varepsilon)^2} = \frac{D_m^2}{180}\frac{\varepsilon^3}{(1-\varepsilon)^2} \quad . \tag{A-9}$$

Other models have been proposed (see the excellent critical review of Scheidegger, 1974). However, the Kozeny–Carman equation is widely used nowadays since it fits experimental data for a large variety of porous media. Note that Equation (A-6) recommended by Ergun is identical in form, with a slightly different constant (150 instead of 180; a value of 175 can also be found in the literature). Despite the facts that hydraulic radius theories utterly fail to describe anisotropic structured bodies such as stiff–fissured clays and highly porous fibrous media, the Kozeny–Carman equation is usually assumed to be unquestionable and the method of determining the specific area S_v of powders by measurement of permeability (with the use of Equations A-3 and A-9) has achieved considerable popularity.

A-1.3. Brinkman's Extension

It is apparent that Darcy's Equation (A-1) neglects the viscous shear stresses acting on a volume element of fluid; only the damping force of the porous medium has been retained, thus Darcy's law is only valid for low–permeability (low–porosity) media. Therefore, there is a need for an equation that is valid for high–permeability media and which reduces to the Navier–Stokes equation as $K \rightarrow +\infty$. The well–known Navier–Stokes equation for steady flow in a fluid phase, *with negligible inertia terms*, has the following form:

$$\vec{\nabla}P = \rho\vec{F} + D\vec{i}v\,\bar{\bar{\tau}} \quad , \tag{A-10}$$

where $\bar{\bar{\tau}}$ is the deviatoric stress tensor. For linear fluids (Newtonian), the deviatoric stress tensor has the following form:

$$\bar{\bar{\tau}} = 2\mu\left[\bar{\bar{D}} - \frac{1}{3}(\text{div}\,\vec{U})\,\bar{\bar{I}}\right] = \mu\left[\overline{\overline{\nabla\vec{U}}} + \left(\overline{\overline{\nabla\vec{U}}}\right)^{T} - \frac{2}{3}(\text{div}\,\vec{U})\,\bar{\bar{I}}\right], \qquad \text{(A-11)}$$

and $\overrightarrow{\text{Div}}\,\bar{\bar{\tau}}$ reduces to $\mu\Delta\vec{U}$ for incompressible fluids ($\text{div}\,\vec{U} = 0$). Based on this analysis, Brinkman (1947) modified Darcy's law in the following way:

$$\vec{\nabla}P = \rho\vec{F} - \frac{\mu\vec{q}}{K} + \mu'\Delta\vec{q} \quad , \qquad \text{(A-12)}$$

which has the advantage of approximating Equation (A-1) for low–permeability materials and Equation (A-10) for large values of K. The factor μ' is an effective dynamic viscosity which may differ from the fluid viscosity μ. Neale and Nader (1974) showed that in some instances assigning μ' the value of μ provided a satisfactory correlation of experimental data. This simplification was therefore recommended and appeared to be an established practice. However, it is uncertain which apparent viscosity μ' one should use, the fluid viscosity μ, or a viscosity that accounts for the concentration of the particles as Einstein's correction does for dilute suspensions ($\mu'/\mu = 1+2.5x(1-\varepsilon)$).

Lundgren (1972) attempted to resolve this issue by extending a statistical formulation to the problem of a fixed bed of spheres. His predictions for μ'/μ, however, differ strongly from that obtained by Einstein and from $\mu'/\mu = 1/\varepsilon$ when ε <0.7. It is not clear which of these correlations is more accurate for low values of ε.

Tam (1969) pointed out that, whenever the spatial length scale is much greater than $\delta = \sqrt{(K\mu'/\mu)}$, Brinkman's term in Equation (A-12) is negligible. For large systems, this means that Darcy's law is valid only outside of a boundary layer of thickness δ.

Neale and Nader (1974) pointed out that since the Brinkman's Equation (A-12) contains the macroscopic shear stress, it is fully compatible with the existence of boundary layer regions within porous media. Moreover, although the effective thickness of such regions is usually quite small (in the order of $\sqrt{K}$), their effects on unobstructed external flows can be surprisingly significant. Outside the boundary layer region, the macroscopic shear term in the Brinkman equation is negligible, indicating that Darcy's original law is valid everywhere except in the immediate vicinity of permeable surfaces.

By introducing the Forchheimer and Brinkman's extensions into Darcy's law, a generalized flow equation for flow through porous media can be written as:

$$\vec{\nabla}P = \rho\vec{F} - \frac{\mu\vec{q}}{K} - \frac{C}{\sqrt{K}}\rho|q|\vec{q} + \mu'\Delta\vec{q} \quad . \tag{A-13}$$

It is a common practice to define the Darcy number *Da* and Forchheimer number *Fo* as:

$$Da = \frac{K}{L^2} \quad , \qquad \text{and} \qquad Fo = \frac{C\sqrt{K}}{L} = C\sqrt{Da} \quad , \tag{A-14}$$

where L is a characteristic length of the porous region (such as its thickness). Georgiadis and Catton (1986, 1988) noted that Brinkman's term has negligible effect on the onset of cellular Bénard convection if $Da < 10^{-3}$. The magnitude of *Da* expresses the ratio (Brinkman's term)/(Darcy drag) away from the solid boundaries. Near these boundaries, the Brinkman term is significant because the shear increases to accommodate the no–slip condition.

A-1.4. Transient and Convective Inertia Terms

An attempt to deduce the "turbulent" form of the Forchheimer flow equation was made by Irmay (1958). This author retained *all* the inertia terms of the Navier–Stokes equations in the microscopic flow channels and then built up a hydraulic radius model in a manner similar to that of Kozeny (Scheidegger 1974):

$$-\frac{dP}{dz} = a\mu q + b\rho q|q| + c\rho\frac{\partial U}{\partial t} \quad . \tag{A-15}$$

Irmay obtained $c = 1$ for the Kozeny model. After using the Dupuit–Forchheimer assumption (which relates the interstical velocity U to the filter velocity q as: $q = \varepsilon U$), Irmay's work resulted into adding the transient term $\frac{\rho}{\varepsilon}\frac{\partial q}{\partial t}$ on the right–hand side of Equation (A-2). This corresponded to the equation already postulated by Polubarinova–Kochina.

Other investigators have supported the introduction of new convective inertia terms in Equation (A-15), but have shown that the role of these additional terms is negligible for low–permeability porous media. Later, Stark (1969) showed that, at high–flow velocity the pressure deviates from that predicted by Equation (A-15). Stark proved that this deviation was due to the convective inertia terms in the Navier–Stokes equations.

Therefore, by introducing the transient term and convective inertia terms in Equation (A-13), the following empirical general flow equation for flow through porous media is obtained:

$$\frac{\rho}{\varepsilon}\frac{\partial \vec{q}}{\partial t} + \text{inertia terms} = \rho\vec{F} - \vec{\nabla}P - \frac{\mu\vec{q}}{K} - \frac{C}{\sqrt{K}}\rho|q|\vec{q} + \mu'\Delta\vec{q} \quad . \tag{A-16}$$

A-1.5. Local Volume–Averaging Technique

Developing a correct formulation of the problem of convection through porous media remains a point of major contention in the literature. Fortunately, it is possible to derive analytically general macroscopic balance equations that describe the flow and heat transfer in porous media, through volumetric averaging of the microscopic conservation equations. A comparison of these more general equations with the empirical equations mentioned above gives some insight into the righteousness of the various heuristic extensions that were derived somewhat independently. Such a comparison provides a means to identify the apparent viscosity μ' in the Brinkman's term. Another advantage of the volume–averaging formulation is that it offers an insight into the assumptions involved.

Following the analysis of Gray and O'Neill (1976; see also Cheng 1978), a two–phase system is considered in which α denotes the fluid phase and β the solid matrix. The porous medium is assumed to be fully–saturated. The averaging volume V is composed of both the α and the β phase such that $V = V_\alpha + V_\beta$, where V_α and V_β are the volumes of the phases α and β in V, respectively. A phase average of some quantity ψ in the α phase may now be defined by:

$$\langle\psi_\alpha\rangle \equiv \frac{1}{V}\int_V \psi_\alpha \, dV \quad , \tag{A-17}$$

where ψ_α refers to the value of ψ in the α phase and is defined to be zero in the β phase. An average formed by integration over only one phase (e. g., the α phase) is called an intrinsic phase average and is defined by:

$$\langle \psi_\alpha \rangle^\alpha \equiv \frac{1}{V_\alpha} \int_{V_\alpha} \psi_\alpha \, dV = \frac{1}{V_\alpha} \int_V \psi_\alpha \, dV \quad . \tag{A-18}$$

The second equality comes naturally since ψ_α is nul in the β phase. If the fraction of the total volume occupied by the fluid phase α is denoted by $\varepsilon = V_\alpha / V$, then it is apparent from Equations (A-17) and (A-18) that:

$$\langle \psi_\alpha \rangle = \varepsilon \langle \psi_\alpha \rangle^\alpha \quad . \tag{A-19}$$

When ψ_α refers to the local fluid velocity, we can identify the filter velocity q and the average pore velocity U with the phase average and intrinsic phase average of ψ_α respectively, so that Equation (A-19) provides a mathematical verification of the Dupuit–Forchheimer postulate ($q = \varepsilon U$).

Now it is assumed that the conventional Navier–Stokes equations for compressible fluid describe the flow in the pores of the microstructure, and these equations are integrated over the volume V. In order for the averaging process to lead to meaningful results, the characteristic length l of the elementary volume V must be such that $d << l << L$, where d is a microscopic characteristic length over which significant variations in the point quantities occur, and L is a macroscopic characteristic length of the porous medium. Averages of derivatives can be related to the derivatives of averages by the theorems of Whitaker and Gray. The averages of products can be expressed in terms of the product averages by the following relation (Gray and O'Neill 1976; and Cheng 1978):

$$\langle \psi_\alpha \varphi_\alpha \rangle^\alpha = \langle \psi_\alpha \rangle^\alpha \langle \varphi_\alpha \rangle^\alpha + \langle \tilde{\psi}_\alpha \tilde{\varphi}_\alpha \rangle^\alpha \quad , \tag{A-20a}$$

where the *tild* notation denotes the deviation of a quantity from its phase average, that is:

$$\tilde{\psi}_\alpha \equiv \psi_\alpha - \langle \psi_\alpha \rangle^\alpha \quad . \tag{A-20b}$$

After integrating the Navier–Stokes equation and performing all necessary analytical transformations, Gray and O'Neill (1976) simplified the resulting macroscopic momentum equations by assuming that density gradients at the microscopic level are very small in comparison to the corresponding velocity gradients, and that the viscosity of the fluid is approximately constant within the averaging volume V. These assumptions are appropriate for slow flows of liquids through porous media, in which thermal and pressure gradients are not too large. At this point, their motion equation takes the form:

$$\frac{\rho}{\varepsilon}\frac{\partial \vec{q}}{\partial t} + \frac{\rho}{\varepsilon^2}\vec{\vec{\nabla}}\vec{q}\,\vec{q} = \rho\vec{F} - \vec{\nabla}P + \frac{\mu}{\varepsilon}\Delta\vec{q} + \text{other terms} \quad , \tag{A-21}$$

where

$$\rho \equiv \langle \rho_\alpha \rangle^\alpha \quad , \quad P \equiv \langle P_\alpha \rangle^\alpha \quad , \text{ and } \quad \vec{q} \equiv \langle \vec{U}_\alpha \rangle = \varepsilon \langle \vec{U}_\alpha \rangle^\alpha = \varepsilon \vec{U} \quad . \tag{A-22}$$

The other terms (which are not reproduced here) involve the deviations of the fluid velocity and pressure from their intrinsic averages, and a surface integral (over the fluid–solid interfacial surface in the volume V) which accounts for the phase–averaged viscous drag of the solid on the fluid.

In a similar manner as for the derivation of the turbulent flow equations, constitutive relationships must be obtained to represent these other terms in a useful and practical manner. For the flow of a Newtonian fluid through an isotropic medium, Gray and O'Neill showed that the macroscopic momentum equation can be reduced to an equation containing only five medium constants (porosity and permeability are two of them), that could be evaluated from experiments. For our purpose, a comparison of the empirical Equation (A-16) with Equation (A-21) suggests that the additional inertia and viscous terms in Equation (A-21) can be represented by the Darcy–Forchheimer extension. Therefore, the equation of motion for a Newtonian fluid through a fully–saturated isotropic porous medium reads:

$$\frac{\rho}{\varepsilon}\frac{\partial \vec{q}}{\partial t} + \frac{\rho}{\varepsilon^2}\vec{\vec{\nabla}}\vec{q}\,\vec{q} = \rho\vec{F} - \vec{\nabla}P - \frac{\mu\vec{q}}{K} - \frac{C}{\sqrt{K}}\rho|q|\vec{q} + \frac{\mu}{\varepsilon}\Delta\vec{q} \quad . \tag{A-23}$$

It is apparent that the flow Equation (A-23) is consistent with the Brinkman–Forchheimer–

extended Darcy flow model, where the apparent viscosity μ' has the value μ/ε. It is also consistent with the postulates of Irmay concerning the transient term and that of other investigators concerning the convective inertia term. The final attractive feature of Equation (A-23) is that it approaches the empirical representation of flow in a porous medium (the Forchheimer–extended Darcy flow model) as the permeability, K, decreases, and reduces to the standard Navier–Stokes equations as the porosity ε goes to 1 and the permeability goes to infinity; consequently, this equation connects the two theories. These arguments justify the fact that Equation (A-23) has been used with success in recent years to model the flow of liquids in porous media (Beckermann and Viskanta 1988; Kladias and Prasad 1989; Nakayama et al. 1990; Sasaki et al. 1990).

In the next section, the governing equations for modeling the heat transfer in a partially frozen porous medium are described.

A-2. MODELING OF HEAT TRANSFER IN A PARTIALLY–FROZEN POROUS MEDIUM

While the modeling of flow in porous media involves only one phase, the liquid, modeling of the heat transfer in a thawing or freezing wick structure is a priori more complex since heat is conducted through the solid matrix and the frozen and liquid phases. Two different numerical formulations have been developed to solve multidimensional convection/ diffusion solid–liquid phase–change problems, the temperature–based method and the volume–averaged enthalpy method. In the temperature based method (Wolff and Viskanta 1988; and Bergman and Webb 1990), the temperature is the sole dependent variable and the energy conservation equations are written separately for the liquid and frozen regions. This formulation requires the specification of interfacial conditions on temperature, velocity and heat transfer at the phase–change boundary. This renders the use of a fixed grid difficult; instead deforming grids or transformed coordinate systems are required to transform the time–dependent physical domain occupied by the melt into a time–independent rectangular domain. While such front tracking formulation is accurate in locating the phase–change boundary, computational complexities and excessive mesh distortion usually preclude its use in cases involving a distorted solid–liquid interface (for example due to natural convection in the liquid phase).

In the enthalpy formulation (Gray and O'Neill 1976; Cheng 1978; Voller and Prakash 1987; Beckermann and Viskanta 1988), the enthalpy is used as a dependent variable along

with the temperature, and there is no need to satisfy explicitly interfacial conditions at the phase–change boundary.

A-2.1. Volume–Averaged Homogeneous Enthalpy Formulation

The first step is to derive an enthalpy conservation equation for each phase (the porous matrix, and liquid and frozen phases of the working fluid). Such equations can be empirical in nature, or derived analytically from statistical theory (Scheidegger 1974) or volume–averaging technique (Gray and O'Neill 1976; Whitaker 1977 and 1986; Cheng 1978; Levec and Carbonell 1985). These equations contain some unknown convective and dispersive terms, which involve the deviations of the fluid velocity and temperatures from their intrinsic averages, as well as surface integrals of temperatures and interphasic exchange quantities over the separative interfaces between the three phases.

The interphasic exchange terms can be treated in two different approaches (Combarnous and Bories 1975; Cheng 1978; Levec and Carbonell 1985). In the first approach, labeled the *continuous solid phase model*, a distinction is made between the phases intrinsic average temperatures, and effective heat transfer coefficients are introduced to model the heat exchange terms between phases. However, it is difficult to represent interphase heat fluxes in terms of film heat transfer coefficients when convective transport is small compared to conduction. The second approach, known as the *homogeneous model*, forms the evolution equation of the overall spatial average temperature by adding the energy equations associated with each phase; in this process, the various interphasic exchange terms simply cancel each others.

Considering that buoyancy–induced and surface–tension–driven liquid flows are characterized by relatively low convective transport rates, one is encouraged to assume that conductive transport is sufficient to eliminate significant temperature differences between the separate phases (we are not considering the case of internal heat generation). In such cases, the evolution equation can be expressed in terms of the overall spatial average temperature only, with the assumption of *local thermal equalibrium* between phases (Cheng 1978; and Whitaker 1986), stating that the intrinsic phase averages of temperatures are equal.

For our purpose of modeling heat transfer in the porous region of the heat pipe, we choose to use the homogeneous model derived from the volume–averaging of the microscopic

enthalpy conservation equations, assuming local thermal and hydrodynamic equalibrium. The advantages of this procedure are that the resulting evolution equation accounts for the complicated interfacial structures of the various constituents and is valid for any volume fractions of the wick porous matrix and the liquid and solid phases of the working fluid. Hence, this approach offers the advantage that the entire domain can be treated as a single region governed by only one conservation equation (Beckermann and Viskanta 1988). In other words, the same equation can be used for the melt as for the fully solidified regions. Also, as mentioned before, unlike empirical methods, a rigorous analytical averaging process could offer additional insight into the assumptions involved.

The homogeneous enthalpy conservation equation for modeling the heat transfer within a partly–frozen liquid–saturated porous medium is easily derived following the procedure outlined by Cheng (1978). It is further assumed that the frozen fluid phase is not moving and that the porous matrix of the medium is fixed, so that only the liquid velocity is non–zero. The microscopic enthalpy conservation equations are integrated over the volume V for each phase, and the unknown terms associated with each particular phase are modeled by introducing *dispersion* thermal coefficients (conductivities).

Several investigators have tried to justify the form of the closure relationships for the unknown terms. Levec and Carbonell (1985) have shown that the unknown terms could be expressed in terms of known quantities through the introduction of various tortuosity, dispersive, convective and heat exchange coefficients, resulting in a quite complex set of equations. Whitaker (1986) has used order–of–magnitude analysis to derive the constraints that must be satisfied in order that the dispersion–thermal–coefficient closure relationships provide a reasonable description of the heat transport process in a packed–bed catalytic reactor. His work has led to a series of constraints which unfortunately are based on estimates only. It must be noted that the closure problem encountered is extremely complex and quite similar to that arising in turbulence modeling, and experimentation seems to be the only reasonable mean to validate the constitutive models. While Cheng (1978) introduced scalar dispersion coefficients, Whitaker (1977, section III.B) developed several arguments which led to the modeling of all the unknown terms with a second–order effective–thermal–conductivity tensor, that consists of a conductive part and a dispersive part.

Using Whitaker's approach, the addition of the volume–averaged enthalpy conservation equations associated with each phase leads to the following homogeneous enthalpy conservation equation:

$$\frac{\partial}{\partial t}\left[\varepsilon\gamma\left(\rho h\right)_S + \varepsilon(1-\gamma)\left(\rho h\right)_L + (1-\varepsilon)\left(\rho h\right)_m\right] + \operatorname{div}\left[\left(\rho h\right)_L \vec{q}\right] = \frac{\partial P_L}{\partial t} + \vec{q}.\vec{\nabla}P_L + \operatorname{div}\left[\overline{\overline{K}}_{eff}\vec{\nabla}T\right] + \frac{1}{\varepsilon}\Phi_L \quad , \tag{A-24}$$

where the subscripts S, L and m refer to the frozen phase, liquid phase and solid matrix respectively, ε is the porosity (void fraction) of the porous matrix, and γ is the fraction of the frozen fluid in the voids of the porous matrix; and

$$\rho_\alpha \equiv \left\langle \rho_\alpha \right\rangle^\alpha, \quad h_\alpha \equiv \left\langle h_\alpha \right\rangle^\alpha, \quad \text{and} \quad \vec{q} \equiv \left\langle \vec{U}_L \right\rangle = \varepsilon(1-\gamma)\left\langle \vec{U}_L \right\rangle^L = \varepsilon(1-\gamma)\vec{U} \ . \tag{A-25}$$

Equation (A-24) is derived assuming local thermal and hydrodynamic equalibrium between the three phases, which can be written (Cheng 1978):

$$\left\langle P_S \right\rangle^S = \left\langle P_L \right\rangle^L = \left\langle P_m \right\rangle^m = \left\langle P \right\rangle \equiv P_L \ , \quad \text{and}$$
$$\left\langle T_S \right\rangle^S = \left\langle T_L \right\rangle^L = \left\langle T_m \right\rangle^m = \left\langle T \right\rangle \equiv T \ . \tag{A-26}$$

The volume–averaged homogeneous enthalpy method offers several advantages: (a) it employs a fixed–grid numerical scheme; (b) it accounts for the complicated interfacial structures of the various constituents (Equation A-24) and is valid for any volume fractions of the wick porous matrix and the liquid and frozen phases of the working fluid; and (c) it does not necessitate implicit tracking of the liquid–solid interface. This method is also preferred because of its simplicity, particularly since the change–of–phase is only one of the processes involved in the physical operation of heat pipes.

A-2.2. Effective Thermal Conductivity Tensor

The effective–thermal–conductivity tensor is the sum of a stagnant conduction part and a thermal dispersion part (Cheng 1978):

$$\overline{\overline{K_{eff}}} = \overline{\overline{K}}' + \overline{\overline{K_D}} \quad , \tag{A-28}$$

where the stagnant tensor is diagonal when expressed in the appropriate orthogonal curvilinear coordinate system, and the dispersion tensor possesses a priori nine non–zero coefficients which depend on the Reynolds and Prandtl numbers. The experimental and/or analytical determination of the components of this tensor represents a somewhat unreasonable task, even for the case of transversely or fully isotropic porous media. Because of these difficulties it is only recently that investigators have considered these effects.

Kvernvold and Tyvand (1980) studied analytically the influence of hydrodynamic dispersion on thermal convection in porous media, and have shown that a better agreement between theoretical prediction and experimental data could be obtained if the thermal dispersion effects were taken into account properly. Plumb (1983), Hong et al. (1987), and Lai and Kulacki (1991) studied the effect of transverse thermal dispersion on both forced and buoyancy–induced boundary layers along a heated vertical wall, for situations where inertial effects are likely to be dominant. Since few data on thermal dispersion are available in the literature, these authors approximated thermal dispersion by hydrodynamic dispersion. They recognized that this representation is not suitable for a porous medium that transports significantly larger amounts of energy compared to the fluid alone, such as a highly permeable porous matrix whose thermal conductivity is higher than that of the fluid (Kladias and Prasad 1989). Available experimental data suggested that the longitudinal dispersion diffusivity is directly proportional to the Peclet number, while the transverse dispersion diffusivity is on the order of 1/7 to 1/3 of the longitudinal value. Despite the fact that such modeling of the dispersion coefficients is overly simplified, these investigators have shown that thermal dispersion effects may become very important when flow inertia is prevalent.

Georgiadis and Catton (1988a and 1988b) developed a stochastic phenomenological model for fully–saturated isotropic packed beds. The interstitial fluid velocity was decomposed into the sum of the mean ensemble–averaged velocity and a random fluctuating component, as is done in the theory of turbulence. They assumed that thermal equalibrium prevails and their closure procedure leads to the appearance of a (eddy) hydrodynamic contribution to thermal conductivity that was also identified by Levec and Carbonell (1985). Georgiadis and Catton then generalized their transport equation for unidirectional flows to the case of a

general three–dimensional system, and obtained an expression for the second–order dispersion tensor. They found that for steady convective heat transfer, the effective thermal conductivity depends linearly on the local Peclet number based on the characteristic dimension D_m (mean size of the particles), the porosity and the thermal diffusivity of the fluid. While the agreement with experimental data is encouraging, the authors pointed out that dispersion effects cannot be neglected a priori even for natural convection in porous media where the velocities are low. They conceded that measured thermophysical properties for the fluid–solid mixture should be used when possible; this applies to the values of porosity, permeability, stagnant thermal conductivity and dispersivity.

It is apparent, then, that the thermal dispersion coefficients are complex functions of flow variables and physical structure of the porous medium in question, and the determination of these coefficients is still a very challenging problem. Because we are only concerned with very slow buoyancy–induced and surface–tension–driven liquid flows through the porous wick of heat pipes, heat conduction is the only significant mode of heat transfer in this region and we would expect the dispersion tensor to be negligible with respect to the stagnant conductive tensor (Singh et al. 1973). For these practical reasons, we assume that the thermal dispersion coefficients are equal to zero.

The following subsections deal with the properties of wire–screened wicks and isotropic porous media. The properties of interest are volume porosity, permeability, effective pore size and effective thermal conductivity of the wicks.

A-3. CONSERVATION OF MASS

The homogeneous continuity equation is derived in the same manner as described in Section A-2.1 by following the procedure outlined by Cheng (1978), and reads:

$$\frac{\partial}{\partial t}\left[\varepsilon\gamma\rho_S + \varepsilon(1-\gamma)\rho_L + (1-\varepsilon)\rho_m\right] + \operatorname{div}\left[\rho_L \vec{q}\right] = 0 \quad . \tag{A-27}$$

Again, the addition of the volume–averaged mass conservation equations associated with each phase eliminates the need to consider the mass transfer between the liquid and solid fluid phases during the freeze–and–thaw process.

The following sections of this appendix describe the hydrodynamic and thermal properties of porous wicks, which are of common use in heat pipes.

A-4. HYDRODYNAMIC PROPERTIES OF WIRE-SCREENED WICKS

Wire screens are used extensively as the capillary structure in heat pipes because they are commercially available in a wide variety of materials and meshes, and are easily implemented. An important issue associated with modeling of heat pipes is determining the properties of the wick, such as porosity, permeability and effective pore radius.

Figure A-1a depicts a standard square–mesh woven wire screen, of thickness $t = 2d$. The mesh number N is defined as the number of openings per unit length:

$$N = \frac{1}{L} = \frac{1}{w + d} \quad , \tag{A-29}$$

where d is the wire diameter, L is the mesh size and w is the width of the openings. In practice, N is expressed in inch^{-1} and ranges between 40 and 300 inch^{-1}. Below 40 inch^{-1}, the wick is not capable of developing sufficient capillary effect, due to the large pores. Above 300 inch^{-1}, the wick is not sufficiently rigid to be of practical use.

Because the woven screen is somewhat loosely wrapped, the effective thickness of one layer, t, is larger than twice the wire diameter, by an effective interlayer clearance η:

$$t = 2d + \eta = 2d(1 + \beta) \quad . \tag{A-30}$$

The equivalent normalized clearance (Ikeda 1988), β, is defined as $\beta = \eta / (2d)$, and ranges typically between 10% and 75%. The three parameters, N, d, and β completely define the geometry of a wire–screened wick.

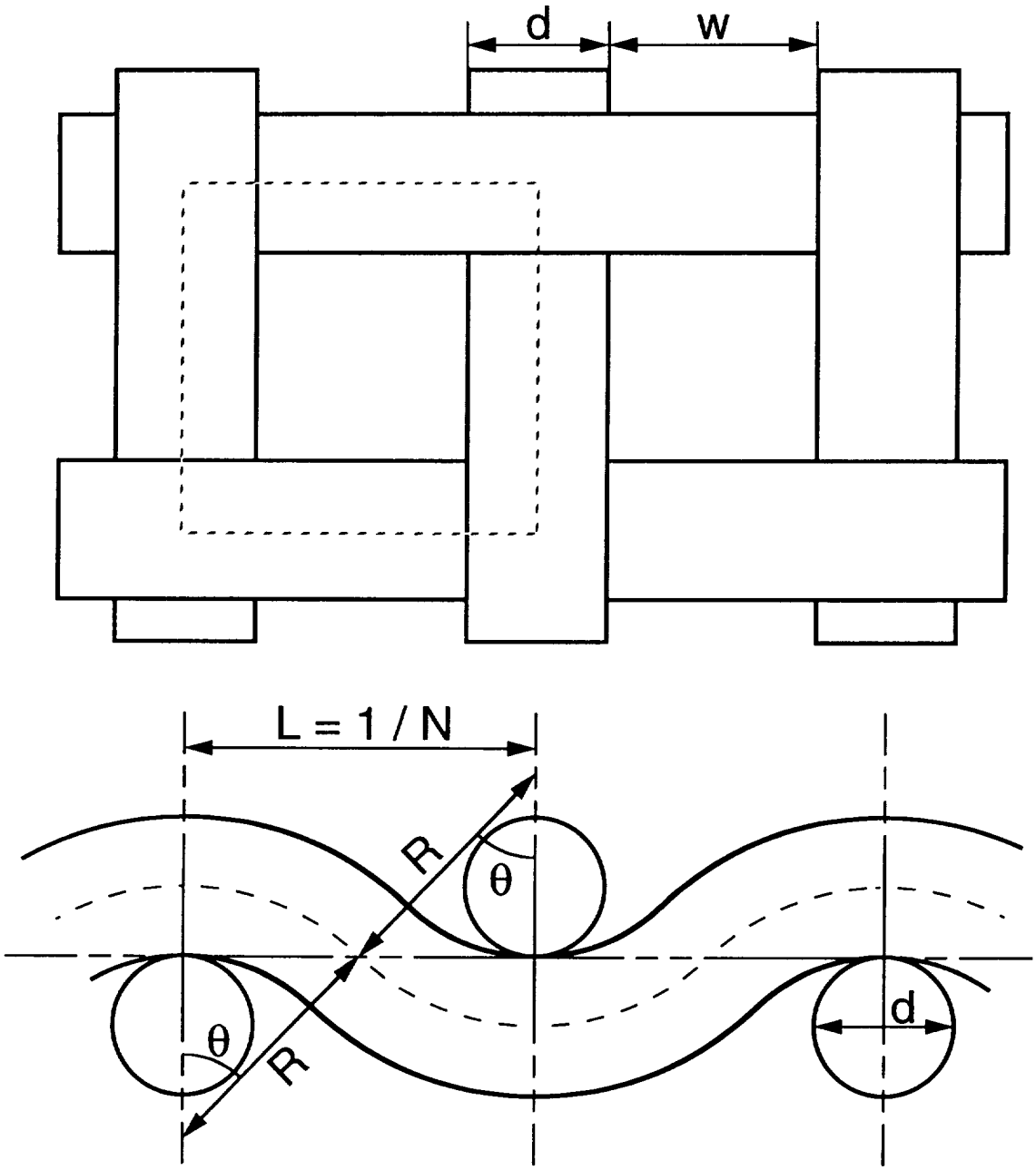

FIGURE A-1. Schematic of a Woven Wire Screen (Top and Front Views).

A-4.1. Surface Porosity of Wire–Screened Wick

As shown in Figure A-1, the surface porosity of a wire–screened wick is given by:

$$\varepsilon_s = \frac{w^2}{L^2} = \left(1 - \frac{d}{L}\right)^2 = (1-\omega)^2 \quad , \tag{A-31}$$

where $\omega = d/L = Nd$ is the wire diameter–to–mesh size ratio of the screen. The surface porosity of the wick is plotted as a function of ω in Figure A-2.

A-4.2. Coefficient of Shrinkage

The coefficient of shrinkage, S, or crimping factor, accounts for the fact that the woven wires are not straight; S is defined as the effective length of the wires per unit mesh size. With the symbols R and θ denoting the radius of curvature of the wire and the sector angle respectively (see Figure A-1), S can be calculated as:

$$S = \frac{2R\theta}{L} = 2R\theta N \quad . \tag{A-32}$$

Furthermore, R and θ are related by the following trigonometric relations:

$$R\sin\theta = \frac{L}{2} \quad , \tag{A-33a}$$

$$R\cos\theta = R - \frac{d}{2} \quad . \tag{A-33b}$$

Adding the squares of Equations (A-33a) and (A-33b) gives:

$$R^2\left(\cos^2\theta + \sin^2\theta\right) = \frac{L^2}{4} + \left(R^2 - Rd + \frac{d^2}{4}\right) \quad ,$$

or

$$\frac{R}{L} = \frac{1}{4}\left(\omega + \frac{1}{\omega}\right) \quad . \tag{A-34}$$

For computational efficiency, it is useful to calculate the tangent of the half–angle $\alpha = \theta/2$. The following trigonometric equations relate α and θ:

$$\begin{aligned} \sin\theta &= 2\cos\alpha\sin\alpha \quad , \\ \cos\theta &= 2\cos^2\alpha - 1 \quad , \end{aligned} \tag{A-35}$$

so that *tan* α) can be written in terms of the cosine and sine of θ as:

$$\tan(\alpha) = \frac{\cos\alpha\sin\alpha}{\cos^2\alpha} = \frac{\sin\theta}{1+\cos\theta} \quad . \tag{A-36}$$

Substituting Equations (A-33a) and (A-33b) into Equation (A-36), and making use of Equation (A-34) to eliminate the radius of curvature R gives finally:

$$\tan(\alpha) \equiv \tan\left(\frac{\theta}{2}\right) = \omega \quad . \tag{A-37}$$

Using Equations (A-34) and (A-37) into Equation (A-32) allows to express the coefficient of shrinkage, S, as a function of the wire diameter–to–mesh size ratio only:

$$S = \left(\omega + \frac{1}{\omega}\right) \mathrm{Arc}\tan(\omega) \quad . \tag{A-38}$$

As shown in Figure A-3, S ranges between 1 and 1.21. The geometrical limit $\omega = 1/\sqrt{3}$, corresponds to the tightest possible configuration of the screen (for which $R = d$, and $\theta = 60^{o}$).

A-4.3. Volume Porosity of Wire–Screened Wick

The volume of a one–layer square–mesh screen with surface area ($L_x L_y$) is given by:

$$\begin{aligned} V_w &= \left(NL_x\right)\left(SL_y A_w\right) + \left(NL_y\right)\left(SL_x A_w\right) \\ &= 2SNA_w\left(L_x L_y\right) \quad , \end{aligned} \tag{A-39}$$

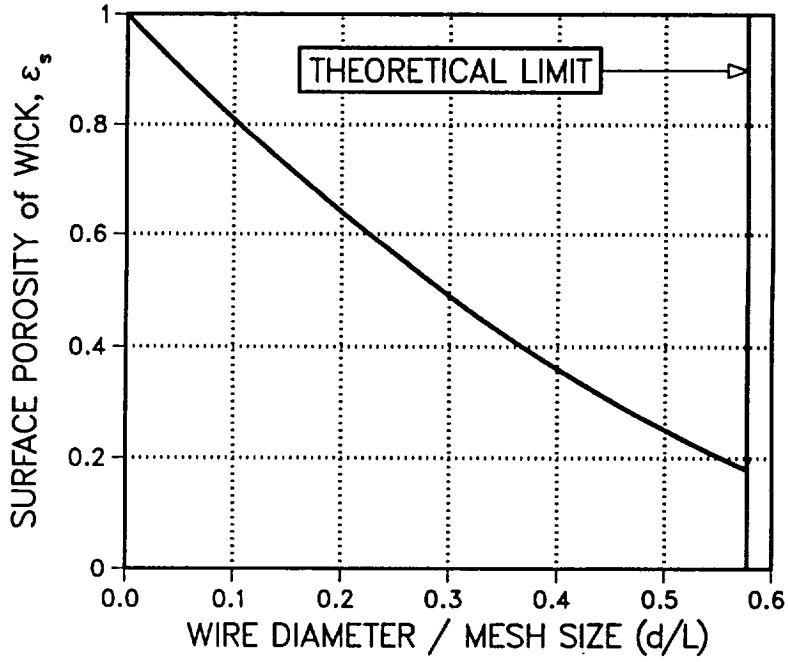

FIGURE A-2. Surface Porosity of a Screen Wick as a Function of Wire Diameter–to–Mesh Size Ratio.

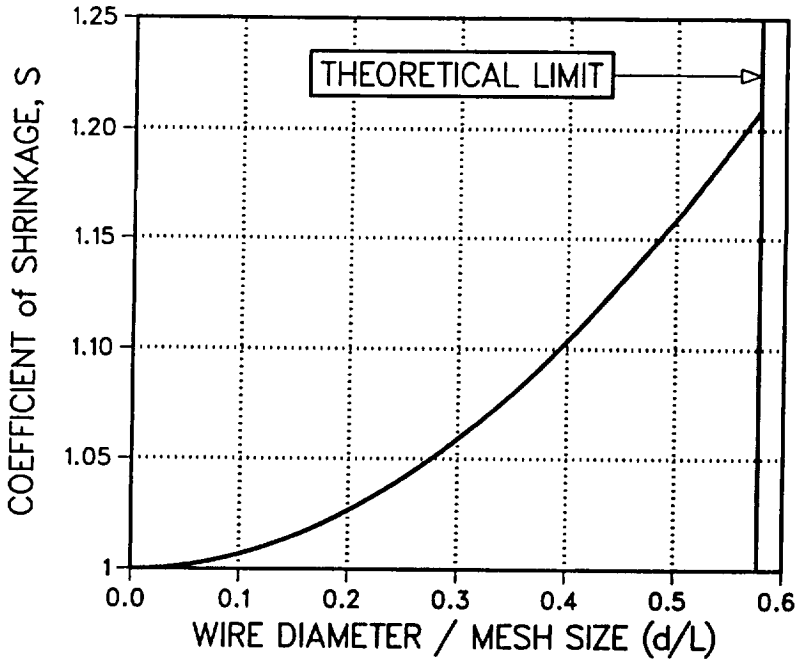

FIGURE A-3. Coefficient of Shrinkage of a Screen Wick as a Function of Wire Diameter–to–Mesh Size Ratio.

where $A_w=\pi d^2/4$, the cross–sectional area of the wire. If we neglect the degree of intermeshing between adjacent layers, the volume porosity of the screen wick is:

$$\varepsilon = 1 - \frac{V_w}{(L_x L_y)t} = 1 - \frac{SN\pi d^2}{2}\frac{1}{2d(1+\beta)} = 1 - \frac{\pi}{4}\frac{\omega}{1+\beta}S(\omega) \quad . \tag{A-40}$$

Figure A-4 shows ε as a function of $\omega = Nd$ and the normalized clearance β of the wick. The volume porosity of the wick increases with the clearance, and decreases with increasing wire diameter–to–mesh size ratio. Note that the porosity of a wire–screened wick is always greater than 0.452, unless the multi–layered screen is intermeshed. This geometrical limit ($\omega = 1/\sqrt{3}, w/d = (\sqrt{3}-1)/4$) corresponds to the tightest possible configuration of the screen (for which $R=d$, and $\theta=60^o$, Figure A-1). Because of the interweaving of the wire rods, the separation distance between two parallel rods must be at least the diameter d of the woven transverse rod. If the degree of wrapping is uncertain (that is the normalized clearance β is unknown), assuming $\beta = 0$ for a tightly wrapped wick is conservative, since it has higher flow resistance (lower permeability) than a loosely wrapped wick.

A-4.4. Permeability of Wire–Screened Wick

Experimental data on tightly wrapped screen wicks for the wick permeability and inertia coefficient have been correlated by the modified Blake–Kozeny equation (Ivanovskii et al. 1982, page 194):

$$K = \frac{d^2}{122}\frac{\varepsilon^3}{(1-\varepsilon)^2} \quad , \qquad C = \frac{2.07}{\sqrt{122}}\frac{1}{\varepsilon\sqrt{\varepsilon}} \quad , \tag{A-41}$$

where d is the wire diameter. It is apparent that the permeability K and inertia coefficient C given by Equation (A-41) are identical in form to that given by the Erguns' Equation (A-6) and the Kozeny–Carman Equation (A-9). If the degree of wrapping is uncertain, using the formula for a tightly wrapped wick (Equation A-41) provides a conservative approach since the tightly wrapped screens have higher flow resistance (lower permeability) than their loosely wrapped counterparts.

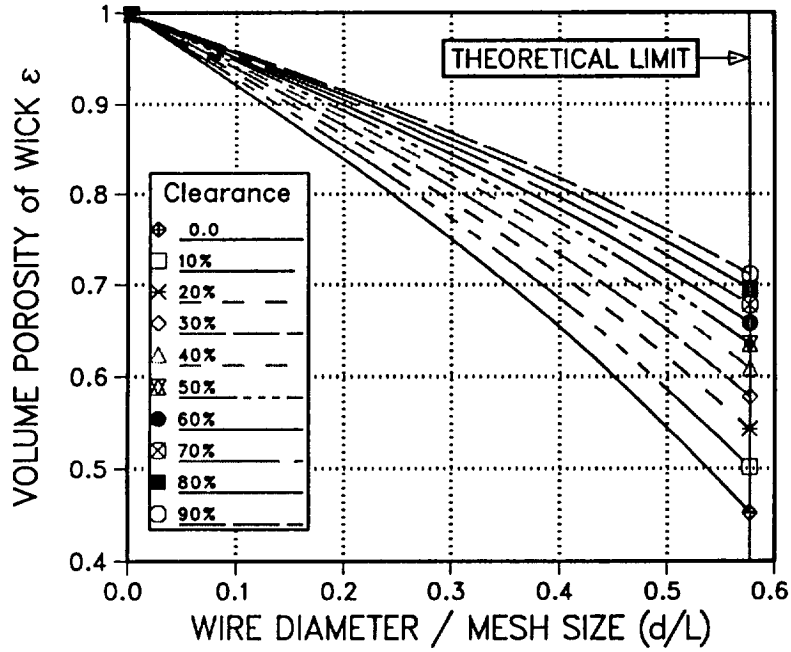

FIGURE A-4. Volume Porosity of Screen Wicks as a Function of Wire Diameter–to–Mesh Size Ratio and Normalized Clearance.

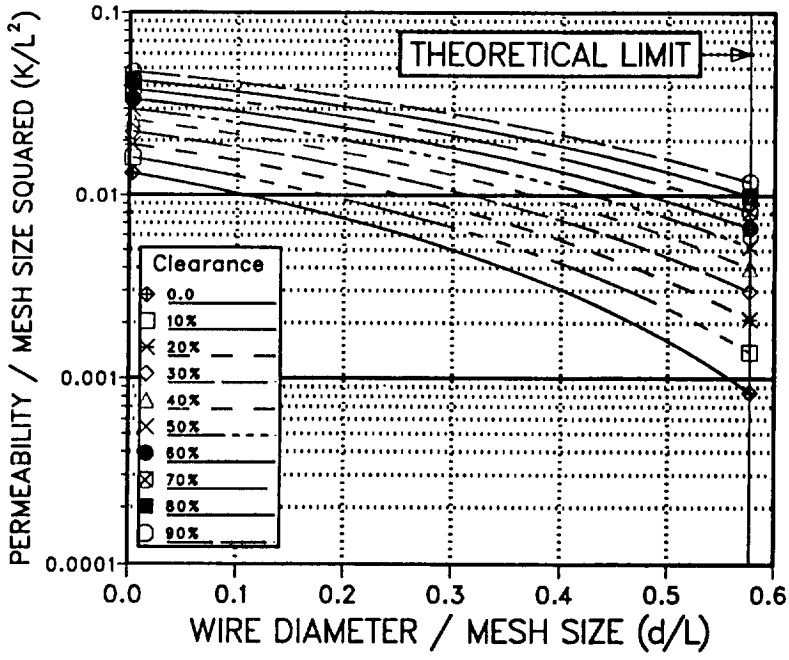

FIGURE A-5. Normalized Permeability of Screen Wicks as a Function of Wire Diameter–to–Mesh Size Ratio and Normalized Clearance.

The normalized permeability of the wick with respect to the mesh size has the form:

$$KN^2 = \frac{K}{L^2} = \frac{\omega^2}{122} \frac{\varepsilon^3}{(1-\varepsilon)^2} \quad . \tag{A-42}$$

Since the coefficient of shrinkage S (given by Equation A-38) and the volume porosity ε (calculated from Equation A-40) are functions of the wire diameter–to–mesh size ratio ω and the normalized clearance β of the wick, the normalized permeability given by Equation (A-42) is also a function of these two variables. Figure A-5 shows that the normalized permeability of the wick increases with the clearance, and decreases with increasing wire diameter–to–mesh size ratio; it has a minimum value of 8.5×10^{-4}.

A-4.5. Verification of Wire–Screened Wick Model

Equations (A-40) and (A-42) were verified using measured characteristics of wire–screened wicks found in the literature (Ikeda 1988; Dunn and Reay 1978; Chang 1990; Ferrell et al. 1973). These data included mesh number, wire diameter, pore size, volume porosity and permeability, and are collected in Table A-1. The last column of this table shows the volume porosity and permeability calculated using the model described in this section, Equations (A-40) and (A-42). The equivalent normalized clearance was chosen to match the porosity (or the permeability) given in the reference. Results showed that these equations can predict the porosity (within 5%) and permeability (within 25%) of wire–screened wicks quite well, except for very coarse meshes ($N < 60$ inch^{-1}).

A-4.6. Effective Pore Radius of a Wire–Screened Wick

The effective pore size of one layer of wire–screened wick is equal to one–half the screen opening size (Figure A-1), and is a function of the wire diameter d and the mesh number N:

$$R_p = \frac{w}{2} = \frac{L-d}{2} \quad . \tag{A-43}$$

For multilayered screens, smaller pores could form in between the various layers, depending on the degree of compression, distortion and intermeshing of the layers. The dependence of the effective pore radius on the depth in the wick was experimentally

TABLE A-1. Comparison of Calculated and Measured Porosity and Permeability for various Square–Mesh Wire Screens.

Reference	screen wick parameters N (in^{-1})	d (μm)	d / L =Nd[c]	R_p (μm)	from reference ε	K (m^2)	calculated parameters K^c (m^2)	ε^c	$\beta^\dagger$
Dunn and Reay (1978)									
Nickel 50	50	203μ[c]	0.40	152.μ*	0.625	6.63×10^{-10}	7.74×10^{-10}	0.65	0
Nickel 100	100	123μ[c]	0.484	65.5μ*	—	1.52×10^{-10}	1.65×10^{-10}	0.60	10%
Nickel 200	200	47μ[c]	0.37	40μ	0.689	6.2×10^{-11}	6.7×10^{-11}	0.69	5%
SS 200	200	66μ[c]	0.52	30.5μ*	—	7.71×10^{-11}	7.8×10^{-11}	0.65	35%
Ferrell et al. (1973)									
SS 40	40	254μ[†]	0.40	190.5μ[c]	0.69	3.7×10^{-10}	1.2×10^{-9}	0.65	0
SS 100	100	123μ[†]	0.484	65.5μ[c]	0.63	2.06×10^{-10}	2.3×10^{-10}	0.63	20%
SS 150	150	70μ[†]	0.413	49.5μ[c]	0.68	8.0×10^{-11}	1.1×10^{-10}	0.675	10%
SS 200	200	50.8μ[†]	0.40	38.1μ[c]	0.69	5.4×10^{-11}	6.8×10^{-11}	0.683	10%
Chang (1990)									
SS 40	40	254μ	0.40	190.5μ	0.69	—	1.8×10^{-9}	0.69	12%
SS 100	100	114μ	0.449	70μ	0.63	—	2.1×10^{-10}	0.63	10%
Copper 100	100	114μ	0.449	70μ	0.69	—	3.8×10^{-10}	0.69	30%
SS 150	150	66μ	0.39	52μ	0.68	—	1.2×10^{-10}	0.68	8%
SS 200	200	53μ	0.417	37μ	0.69	—	8.2×10^{-11}	0.69	20%
SS 250	250	41μ	0.40	30.5μ	0.735	—	7.8×10^{-11}	0.735	32%
SS 400	400	25.4μ	0.40	19.0μ	0.706	—	2.0×10^{-11}	0.70	15%
Noren Heat Pipe Co.									
d=0.0028 in	100[†]	71.1μ	0.28	91.4μ[c]	—	—	3.4×10^{-10}	0.77	0
d=0.0024 in	150	61.0μ	0.36	54.2μ[c]	0.70	—	1.1×10^{-10}	0.70	2%
d=0.0020 in	200[†]	50.8μ	0.40	38.1μ[c]	—	—	4.8×10^{-11}	0.65	0
d=0.0016 in	250	40.6μ	0.40	30.5μ[c]	0.65	—	3.1×10^{-11}	0.65	0

*: Reference 3.21 gives pore diameter, not pore radius.

†: Assumed by present author. [c]: Calculated by present author.

verified by Roberts and Feldman (1972) for water heat pipes using two layers of stainless steel and copper wire–screens. At higher than expected dryout heat transfer rates, these investigators observed that the liquid level receded down to the second layer, at a depth of about 59% of the wick thickness (measured from the wall), and stopped there. At this depth, the L–V interface encountered a pore size 20% smaller than that of a single layer, and the wick could provide enough capillary suction to sustain the liquid level.

While the dependence of the effective pore radius on the depth in a multilayered wick has been recognized experimentally, predicting analytically this dependence is a very difficult problem. Therefore, it is assumed in this work that the capillary capability of the wick is uniform within the wick and given by an effective pore radius of one–half the screen opening size. In this case, the total wick thickness or distribution wick thickness is sum of the thicknesses of the various layers. Figure A-6 shows the effective pore radius R_p of the screen wick as a function of the wire diameter d and the mesh number N. It is important to note that for a given mesh number, the smallest pore size is obtained at the geometrical limit ($\omega = 1/\sqrt{3}$, $R_p / d = (\sqrt{3}-1)/2$), which corresponds to the tightest screen configuration possible. This geometrical limit is inherent to the interweaving of the wire rods. The separation distance between two parallel rods is at least the diameter d of the woven transverse rod (the limit arises for $R = d$, and $\theta = 60^{o}$; see Figure A-1)

A-4.7. Relationship Between Mesh Number and Wire Diameter

Figure A-6 shows that the pore radius R_p is a strong function of the wire diameter d. Therefore, it is not possible to estimate R_p and the other properties of the screen wick accurately if the wire diameter is not known, which is often the case. To remedy this difficulty, values of the wire diameter were collected from Table A-1, which are of common use by screen wicks manufacturers (Ikeda 1988; Dunn and Reay 1978; Chang 1990; Ferrell et al. 1973). Using this information, the wire diameter was correlated as a function of mesh number as:

$$d = -8.65 + \frac{12{,}637.}{N} - \frac{84{,}867.}{N^2} \quad , \tag{A-44}$$

where d is expressed in micrometers (μm) and N is in $inch^{-1}$. The manufacturing values of the wire diameter that were selected for the least–square regression are collected in Table A-2, and are compared with the values given by Equation (A-44).

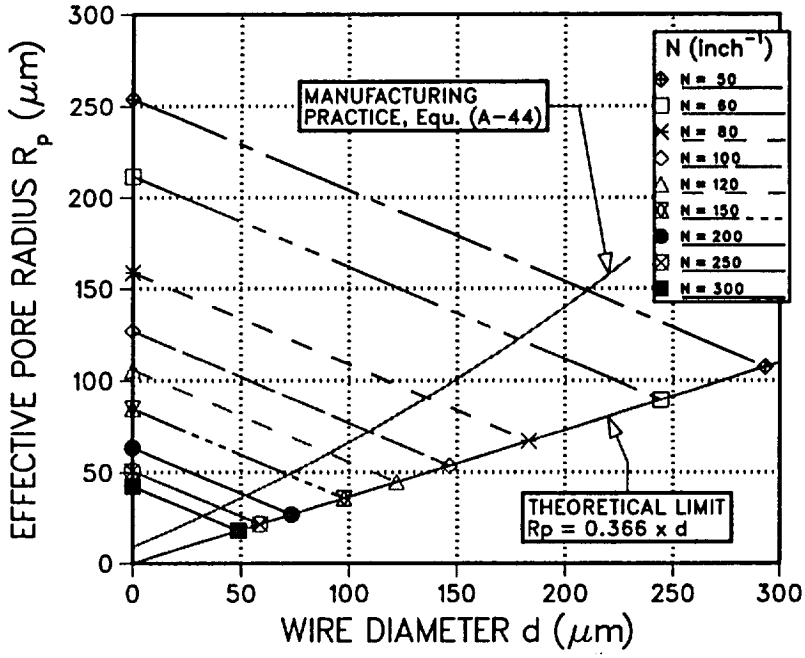

FIGURE A-6. Effective Pore Radius of the Screen Wick as a Function of Wire Diameter and Mesh Number.

When the wire diameter of the screen wick is not known, it is recommended to use the value predicted by the empirical relation, Equation (A-44). In such case, the effective pore radius of the wick is a function of *d* only, and this function is represented in Figure A-6 by the curve labeled "manufacturing practice".

TABLE A-2. Comparison of Common Manufacturing Values of the Wire Diameter with Correlation Equation (A-44), as a Function of Mesh Number.

Mesh # N (inch^{-1})	40	50	100	150	200	250	400
d (μm), Table A-1	254	210	114	66	50.8	40.6	25.4
d (μm), Equ. A-44	254.2	210.1	109.2	71.8	52.4	40.5	22.4

A-5. EFFECTIVE THERMAL CONDUCTIVITY OF POROUS WICK

A great deal of work has been done on the determination of the effective thermal conductivity of porous media saturated with liquid. The stagnant effective thermal conductivity of porous media, k_{eff}, depends on the structure of the porous medium as well as the thermal conductivities and volume fractions of the constituents. In this section, several analytical models and experimental data for the effective thermal conductivity of wire–screen meshes, packed beds of spheres and homogeneous wicks are reviewed.

A-5.1. Theoretical Models of Effective Thermal Conductivity

Chi (1976) has reviewed various analytical models for evaluating the effective thermal conductivity of common heat pipe wick structures, such as wire screens, packed–bed of spheres, cubic array of truncated spheres and rectangular grooves. The *parallel* and *series* theoretical models define the upper and lower limits for the effective thermal conductivity k_{eff} (Combarnous and Bories 1975). The parallel model is valid for a porous medium structured like a set of alternate strata of fluid and solid parallel to the main heat flux:

$$k_{eff} = \varepsilon k_f + (1-\varepsilon)k_m \quad , \tag{A-45}$$

where ε is the volume fraction of liquid, k_f is the thermal conductivity of the fluid (in the solid or liquid phase), and k_m is the thermal conductivity of the wick solid matrix. The lower limit of the effective thermal conductivity is given by the series model:

$$\frac{1}{k_{eff}} = \frac{\varepsilon}{k_f} + \frac{1-\varepsilon}{k_m} \quad . \tag{A-46}$$

In 1891, Maxwell obtained an expression for the effective conductivity of randomly packed and sized cylinders (Singh et al. 1973) as:

$$\frac{k_{eff}}{k_f} = \frac{(k_m + k_f) + (1-\varepsilon)(k_m - k_f)}{(k_m + k_f) - (1-\varepsilon)(k_m - k_f)} = \frac{\psi + (1-\varepsilon)}{\psi - (1-\varepsilon)} \quad . \tag{A-47}$$

where

$$\psi = \frac{k_m + k_f}{k_m - k_f} \quad . \tag{A-48}$$

In 1892, Rayleigh developed a series solution for the thermal conductivity of a square array of identical cylinders using potential theory (Chang 1990):

$$\frac{k_{eff}}{k_f} = 1 - \frac{2(1-\varepsilon)}{-\psi + (1-\varepsilon) + \frac{0.036(1-\varepsilon)^4}{\psi} + \frac{0.0134(1-\varepsilon)^8}{\psi} \cdots} \quad . \tag{A-49}$$

Because the absolute value of ψ is always greater than or equal to 1, the terms of order $(1\text{-}\varepsilon)^4$ and higher can be neglected in Equation (A-49). In this case, Rayleigh's equation reduces to Maxwell's Equation (A-47). Indeed, it is found that Equations (A-47) and the truncated series (A-49) give identical results for volume porosities ε greater than 0.25.

Ikeda (1988) derived a new correlation for the effective thermal conductivity of a plain woven screen wick, in which the wire diameter, mesh number, coefficient of shrinkage and inter–layer clearance were included as variables. Ikeda matched his correlation to experimental data for wire screens to obtain the volume porosity and the normalized clearance β of the wicks (these two quantities are related by Equation A-40). Unfortunately, the values of the inter–layer clearance he obtained by this method were much larger than that calculated from the measured thicknesses of the screens. Ikeda's work was therefore non–conclusive.

Chang (1990) developed a simple theoretical model for the effective thermal conductivity of fluid–saturated wire screens in terms of wire diameter, mesh number, total thickness of wick and number of layers, and compared his model with existing correlations and experimental data available in the literature. Chang found that all the models tend to deviate from the measured values as the conductivity ratio k_m / k_L increases above 1. For a conductivity ratio ranging between 24 (liquid water and stainless–steel screen) and 623 (liquid water and copper screen), Maxwell's Equation (A-47) for a random arrangement of distributed cylinders was accurate within 25% (air data excluded). Chang's correlation gave slightly better results in some cases, but did not exhibit any significant improvement over Maxwell's, as it was only 20% accurate for copper screens saturated with liquid

water. Furthermore, Chang's equation included a free geometric parameter that is difficult to estimate.

Maxwell also derived an expression for a continuous liquid phase containing randomly dispersed and randomly–sized solid spheres (Chi 1976) as:

$$\frac{k_{eff}}{k_f} = \frac{(k_m + 2k_f) + 2(1-\varepsilon)(k_m - k_f)}{(k_m + 2k_f) - (1-\varepsilon)(k_m - k_f)} = \frac{\varphi + 2(1-\varepsilon)}{\varphi - (1-\varepsilon)} \quad . \tag{A-50}$$

where

$$\varphi = \frac{k_m + 2k_f}{k_m - k_f} \quad . \tag{A-51}$$

However, because Maxwell did not take into account the interaction between the spherical inclusions, his solution is admissible only when the conductivity ratio k_m / k_f is much less than 1 or for porous media with large volume porosity. In order that the action of the spheres may not produce effects depending on their interference, their radii must be small compared with their distances, therefore, the wick volume porosity must be large. When the thermal conductivity of the solid inclusions is greater than that of the liquid, Equation (A-50) underpredicts the effective thermal conductivity of the wick, as demonstrated by experimental data for the magnetic permeability of ferromagnetic inclusions dispersed in a nonmagnetic material (Veinberg 1967).

By taking account the interaction of the inclusions, Veinberg (1967) derived the following transcendental equation valid for any concentration of spherical solid inclusions and any matrix–to–fluid thermal conductivity ratio:

$$\varepsilon\left(\frac{k_{eff}}{k_f}\right)^{1/3} = \frac{k_m - k_{eff}}{k_m - k_f} \quad . \tag{A-52}$$

Following a similar procedure, Veinberg (1967) also obtained the effective thermal conductivity of an isotropic aggregate of randomly oriented ellipsoidal inclusions.

Prasad et al. (1989) measured the stagnant thermal conductivity of several liquid–saturated porous beds of spheres and evaluated the accuracy of the parallel model and other

correlations available in the literature. These authors observed that these correlations (except the parallel model Equation A-45) were quite capable of predicting reasonable values for k_{eff} as long as $k_m > k_f$; however, none of the correlations investigated by Prasad and coworkers were suitable when the solid thermal conductivity was significantly lower than the fluid thermal conductivity. Also, the agreement was generally not good for a gas–filled porous medium. Based on their experimental data, Prasad et al. (1989) recommended the use of Krupiczka's model for liquid–saturated beds of granular solids.

Krupiczka (1967) solved analytically the two–dimensional Laplace equation for two simple geometries: a stack of parallel cylinders of volume porosity 0.215, and a simple cubic array of spheres of porosity 0.476. Then he extrapolated his results to intermediate volume porosities using experimental data available in the literature, and obtained the following correlation:

$$\frac{k_{eff}}{k_f} = \left(\frac{k_m}{k_f}\right)^n, \quad \text{where}$$

$$n = 0.280 - 0.757\,\mathrm{Log}_{10}(\varepsilon) - 0.057\,\mathrm{Log}_{10}\left(\frac{k_m}{k_f}\right) \quad . \tag{A-53}$$

A-5.2. Comparison of Theoretical Models with Experimental Data

Krupiczka (1967) collected experimental data for beds of granular solids in liquid water, oil, aqueous solutions of glycerol and ethyl alcohol, and various gases. The matrix–to–fluid conductivity ratio k_m / k_L ranged between 1 and 1650. Krupiczka's correlation deviated by as much as 70% for gas–filled beds, but performed reasonably well (within 25%) for liquid–saturated packed beds. However, because of the methodology used, Equation (A-53) is only valid for volume porosities ε ranging between 0.2 and 0.5.

For the liquid and frozen phases of liquid metals (sodium, potassium and lithium) and structural materials compatible with these fluids (stainless steel, nickel, niobium, molibdenum, tungsten and zirconium), the matrix–to–fluid conductivity ratio ranges between 0.1 and 3.5. For these combinations of fluids and materials, Equations (A-45)–(A-47), (A-50) and (A-52) reduce approximately to the thermal conductivity of the liquid phase, and are suitable (Figures A-7 and A-8). This is because liquid–metals have high thermal conductivity, similar to that of the structural materials which are compatible

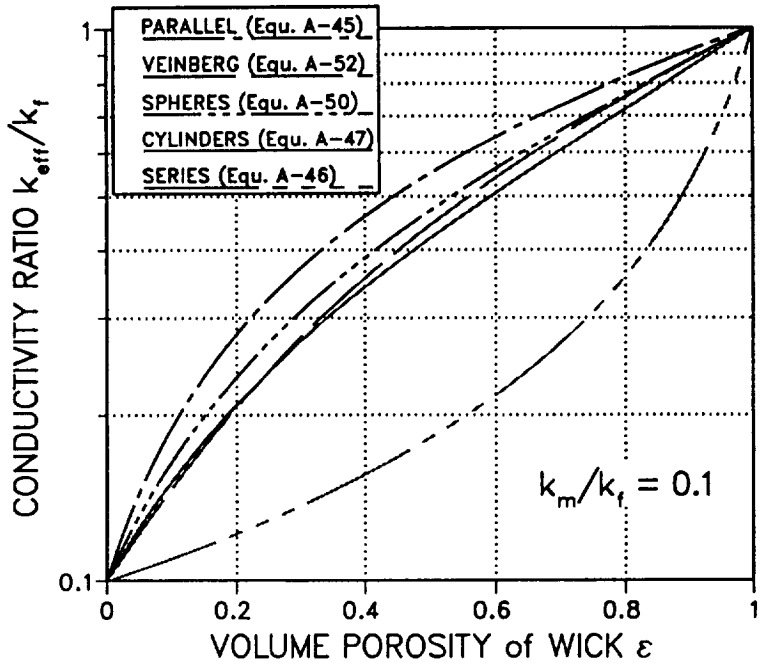

FIGURE A-7. Effective Thermal Conductivity of Wicks for a Conductivity Ratio $k_m / k_f = 0.1$ as a Function of Volume Porosity.

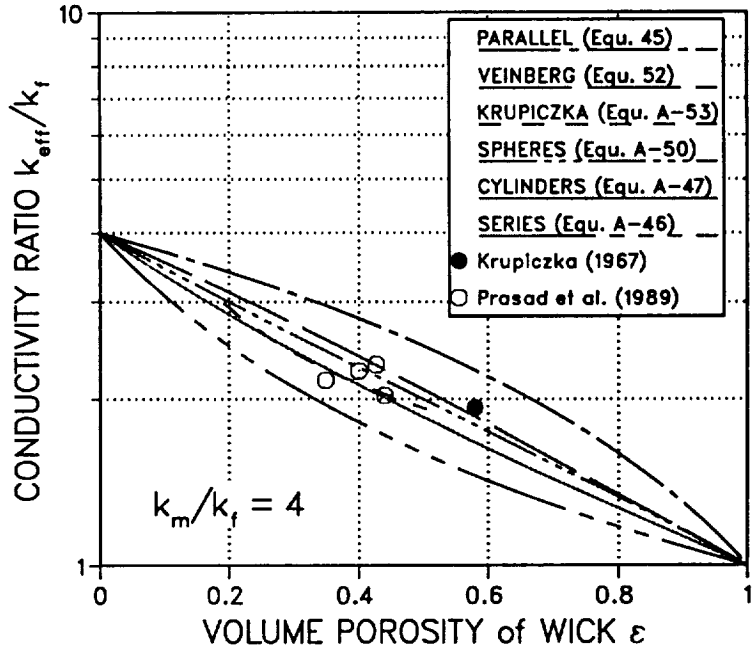

FIGURE A-8. Effective Thermal Conductivity of Wicks for a Conductivity Ratio $k_m / k_f = 4$ as a Function of Volume Porosity.

with these fluids. The situation, however, is very different for non–liquid metal working fluids, when the fluid thermal conductivity is significantly lower than that of the matrix. For example, liquid water has a poor thermal conductivity (0.63 W / m.K) compared to that of the metallic wick matrix, usually copper (392 W / m.K), or stainless–steel (15.4 W / m.K).

The models presented above for the effective thermal conductivity of porous wicks are compared with experimental data available in the literature. Chang (1990) and Ikeda (1988) reported experimental data for the transverse thermal conductivity of wire–screened wicks, and Krupiczka (1967) collected experimental data for beds of granular solids in liquid water, oil, aqueous solutions of glycerol and ethyl alcohol, and various gases; the matrix–to–fluid conductivity ratio k_m / k_f ranged between 1 and 1650. Veinberg (1967) reported experimental data for the magnetic permeability of ferromagnetic inclusions dispersed in a nonmagnetic material. Singh et al. (1973) and Ferrell et al. (1973) also studied experimentally the effective thermal conductivity (parallel to the felting plane) of water–saturated stainless–steel sintered fiber wicks, sintered powders and screen meshes.

Results for wicks with matrix–to–fluid conductivity ratio of 0.1, 4, 24 (water–stainless steel), 75 and 623 (water–copper) are shown in Figures A-7 to A-11, respectively. As shown in Figures A-11 and A-9, the effective thermal conductivity of copper and stainless–steel wicks saturated with liquid water is a strong function of wick porosity, and various models give very different values. The *parallel* and *series* theoretical models define the extreme range in which the real value of the wick effective conductivity k_{eff} is found.

Figures A-7 to A-11 show that Maxwell's Equation (A-50) and Veinberg's model for randomly distributed spheres give identical results for large volume porosity. For porosities less than 0.8, Maxwell's model underpredicts the effective thermal conductivity of the wick. Veinberg's Equation (A-52) is valid for any concentration of spherical solid inclusions as Veinberg took into account the interaction of the inclusions in the derivation of his correlation. Also, Maxwell's Equation (A-50) and Veinberg's Equation (A-52) give almost identical results for wicks with conductivity ratio k_m / k_f less than 1 (Figure A-7), as the heat conducted through the connected inclusions of solid plays a less important role in this case.

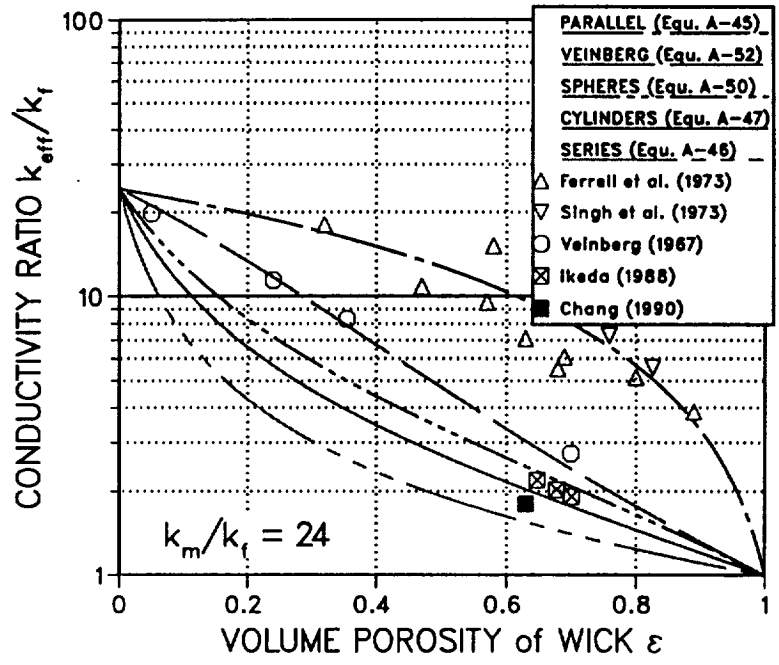

FIGURE A-9. Effective Thermal Conductivity of Wicks for a Conductivity Ratio $k_m / k_f = 24$ (Water–Stainless Steel) as a Function of Porosity.

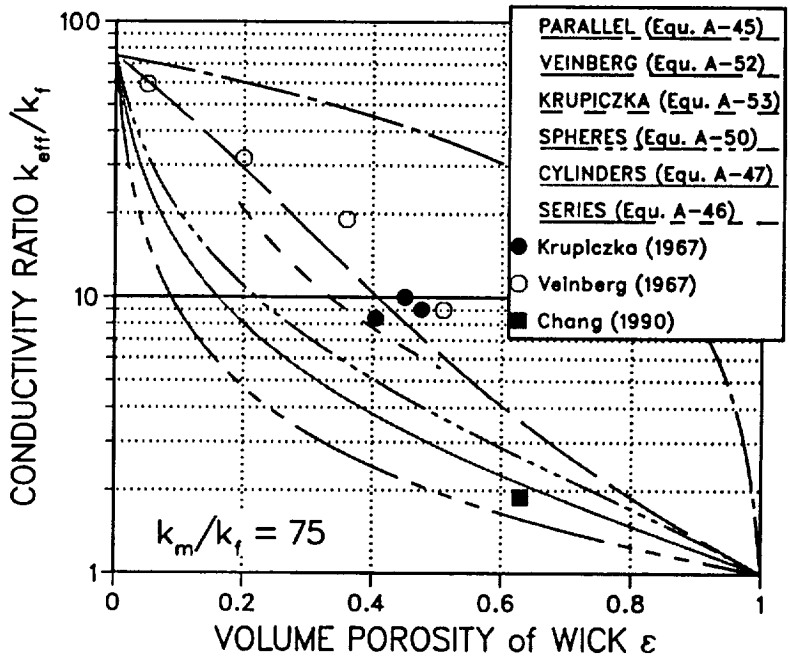

FIGURE A-10. Effective Thermal Conductivity of Wicks for a Conductivity Ratio $k_m / k_f = 75$ as a Function of Volume Porosity.

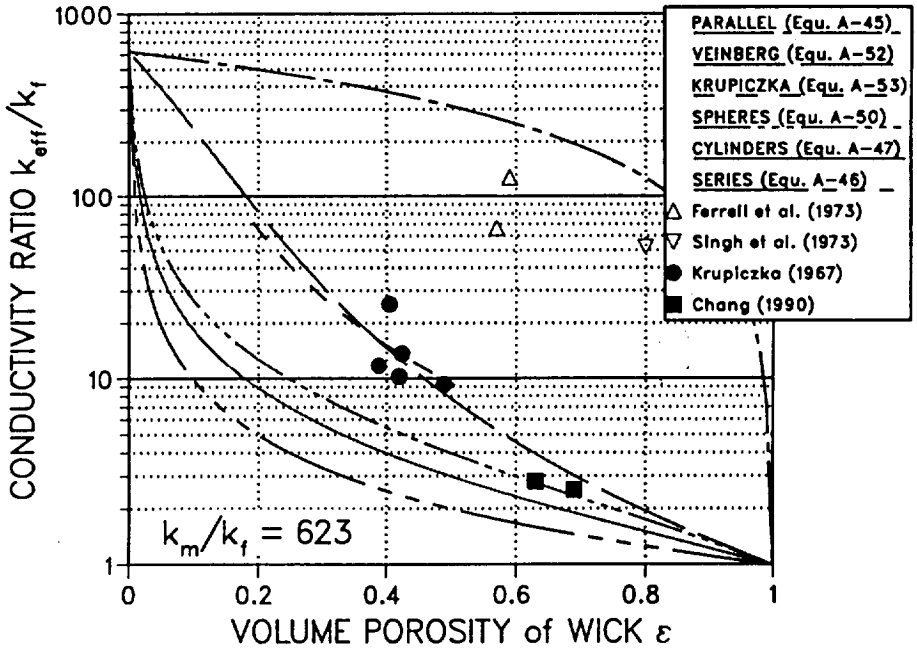

FIGURE A-11. Effective Thermal Conductivity of Wicks for a Conductivity Ratio $k_m / k_f = 623$ (Water–Copper) as a Function of Volume Porosity.

As shown in Figures A-7 to A-11, Maxwell's Equation (A-47) for distributed cylinders gives consistently lower effective thermal conductivities than his model for distributed spheres (Equation A-50). Figures A-10 and A-11 show that Krupiczka's model (Equation A-53) gives results very similar to that obtained from Veinberg's model (Equation A-52) for beds of spherical granulars. This agreement validates the use of Veinberg's correlation for porous beds of spheres.

For a conductivity ratio ranging between 24 (liquid water and stainless–steel screen) and 623 (liquid water and copper screen), Maxwell's Equation (A-47) is the most accurate for calculating the effective radial thermal conductivity of wire–screened wicks. The model of Veinberg compares very well with experimental data for ferromagnetic inclusions dispersed in a nonmagnetic material and for beds of spherical particles. Therefore, Equation (A-52) is best for calculating the effective thermal conductivity of isotropic porous media such as ceramic powders and packed beds of spheres.

Finally, the effective axial thermal conductivity of water–saturated stainless–steel sintered fiber wicks, sintered powders and screen meshes is well predicted by the parallel model,

Equation (A-45). As shown in Figure A-9 and A-11, the effective axial conductivity of screen meshes saturated with water is at least four times the effective radial conductivity. It is therefore important to evaluate these two conductivities independently in HPTAM in order to accurately predict the effect of axial conduction in heat pipes using low–temperature working fluids, such as water. For liquid–metal heat pipes with wire–screened wicks however, Equations (A-45) and (A-52) for axial and radial conductivities give very similar results (Figures A-7 and A-8), suggesting that, unlike in water heat pipes, components of the wick effective conductivity are almost equal in liquid–metal heat pipes.

Based on the results of this section, Maxwell's Equation (A-47) for distributed cylinders is chosen to calculate the effective radial thermal conductivity of wire–screened wicks in HPTAM, while the parallel model, Equation (A-45), is selected for calculating the axial thermal conductivity of such wicks. The model of Veinberg (Equation A-52) for distributed spheres is preferred for calculating the effective thermal conductivity of isotropic porous media such as ceramic powder, metallic felt or sintered metal.

APPENDIX B. FREE–MOLECULE AND TRANSITION FLOWS REGIMES

During the startup of fully–thawed, high–temperature heat pipes (utilizing liquid–metal working fluids), free–molecule and transition flow regimes arise in the vapor region.

Section (B-1) reviews some fundamentals of the kinetic theory of gases. Sections (B-2) to (B-6) describe the methodology used to estimate the effective molecular diameter of heat pipe working fluids. This information is necessary for evaluating the mean free path of the vapor molecules.

B-1. MEAN FREE PATH AND KINETIC THEORY

Assuming that molecules are effectively small hard spheres of diameter σ, Maxwell derived the following expression for the average distance traveled by molecules between collisions:

$$\lambda = \frac{1}{\sqrt{2}\pi\sigma^2 n} \quad , \tag{B-1}$$

where n is the number of molecules per unit volume (Dushman and Lafferty 1962, p. 28; Cunningham and Williams 1980, p. 70; note the mistake of using the word "radius" for "diameter" in the text). n is related to the vapor–phase density by $n = N_a.\rho_v/M$, where M is the molecular weight.

To draw the flow charts for the various heat pipe working fluids of interest, namely, lithium, sodium, potassium and water, it is necessary to estimate the effective molecular diameter σ of these fluids in order to calculate the mean free path of the vapor molecules.

B-2. EVALUATION OF THE MOLECULAR DIAMETER OF SPHERICAL NON–POLAR MOLECULES

There are three methods reviewed for determining the molecular diameter σ of spherical non–polar molecules (they do not apply for water), namely, the transport coefficient method, the van der Waals method, and the close–packed solid–phase density method, which are described in the following sections.

B-2.1. Transport Coefficient Method (Dynamic Viscosity)

From kinetic theory (Cunningham and Williams 1980, chapter 2), the dynamic viscosity of a gas can be calculated as:

$$\mu_v = \frac{1}{2} mnv_a\lambda \ , \tag{B-2}$$

where the mean average molecular velocity v_a is given as:

$$v_a = \sqrt{\frac{8kT}{\pi m}} \tag{B-3}$$

(note in Dushman and Lafferty 1962, chapter 1, the mistake of using the factor 1/3 instead of 1/2 in Equation (B-2), due initially to a calculation error of Maxwell! See Cunningham and Williams 1980, pp. 255–256, for more details). Combining Equations (B-2) and (B-3) gives the following expression for the viscosity of the gas in terms of the temperature and the gas molecular mass m and molecular diameter σ:

$$\mu_v = \frac{1}{2} mn \frac{\sqrt{\frac{8kT}{\pi m}}}{\sqrt{2}\pi\sigma^2 n} = \frac{1}{\pi\sigma^2}\sqrt{\frac{mkT}{\pi}} \ . \tag{B-4}$$

A more sophisticated approach leads to the following expression of μ_v for a pure gas composed of rigid, elastic and nonattracting spherical molecules of diameter σ and mass m (Dushman and Lafferty 1962, p. 28):

$$\mu_v = \frac{5}{16\sigma^2}\sqrt{\frac{mkT}{\pi}} \ . \tag{B-5}$$

It is well–known, however, that two molecules attract each other when they are far apart and repel each other when they come close together. These intermolecular forces are commonly described by a potential energy function characterized by the two parameters σ and ε (ε is the maximum energy of attraction between a pair of molecules). For spherical non–polar molecules, the Lennard–Jones potential applies, leading to a modification of equation (B-5) as (Monchick and Mason 1961, p. 1678):

$$\mu_v = \frac{5}{16\sqrt{\pi}\sigma^2}\frac{\sqrt{mkT}}{\Omega^*(T^*)} \quad . \tag{B-6}$$

Substituting $M = mN_a$, and evaluating π, k and N_a, we find:

$$\mu_v = \frac{5}{16\sqrt{\pi}}\left(\frac{k}{N_a}\right)^{1/2}\frac{\sqrt{MT}}{\sigma^2\Omega^*} = 8.4415 \times 10^{-25}\frac{\sqrt{MT}}{\sigma^2\Omega^*} \quad . \tag{B-7}$$

If σ in expressed in Angstrøm (Å) and M in gr/mol, Equation (B-7) reads as (Hirschfelder et al. 1954, p. 528):

$$\mu_v = 8.4415 \times 10^{-25}\frac{(10^{-3})^{1/2}}{(10^{-10})^2}\frac{\sqrt{\tilde{M}T}}{\tilde{\sigma}^2\Omega^*} = 266.94 \times 10^{-8}\frac{\sqrt{\tilde{M}T}}{\tilde{\sigma}^2\Omega^*} \quad . \tag{B-8}$$

Ω^* is a dimensionless corrector factor function of the dimensionless temperature $T^*=kT/\varepsilon$. The function Ω^* can be expressed in terms of T^* as (Hirschfelder et al. 1954, p. 1126):

$$\Omega^*(T^*) \approx 0.73122 + \frac{0.95922}{T^*} - \frac{0.102}{T^{*2}} \quad , \qquad \text{for} \quad 0.3 \le T^* \le 5.0 \tag{B-9}$$

Equation (B-8) has been verified experimentally for various non–polar gases (Hirschfelder et al. 1954, pp. 560–563). The Principle of Corresponding States (Hirschfelder et al. 1954, pp. 244–247) leads to $T_c^* = 1.3$, which is in good agreement with experimental data for Ne, Ar, Xe, N_2, O_2 and CH_4 (Hirschfelder et al. 1954, p. 303). Hence, T^* may be calculated as:

$$T^* = 1.3\frac{T}{T_c} \quad . \tag{B-10}$$

Using experimental data for the dynamic viscosity of the vapor phase μ_v, it is then a simple exercise to determine the molecular diameter σ through the use of Equations (B-8)–(B-10).

B-2.2. Van der Waals Method

From Dushman and Lafferty (1962), p. 37, the molecular diameter is given directly in terms of the molar volume b_0 as:

$$\sigma^3 = 7.929 \times 10^{-25} \times b_0 \ , \tag{B-11}$$

where

$$b_0 = \frac{R_g T_c}{8 P_c} \ . \tag{B-12}$$

B-2.3. Close-Packed Solid-Phase Density (metallic fluids)

Knowing the structure and the density of the close-packed solid-phase of the working fluid, it is possible to calculate the lattice parameters and deduce the molecular diameter σ (molecules are modeled as hard-spheres, and close-packed means the nearest neighboring molecules are touching each other in the structure). In this section, *a* refers to the cubic lattice parameter (the side of the reference cube) and *b* is the distance between centers of the nearest neighboring molecules in the structure, which is equal to σ in the case of a close-packed structure.

B-2.3.1. *Close-Packed Simple Cubic Lattice (6 nearest neighbors):*

$a = b = \sigma$.

One molecule occupies a volume of σ^3 , so that:

$\rho_S = m/\sigma^3$, and:

$$\sigma = \left(\frac{m}{\rho_s}\right)^{\frac{1}{3}} \ . \tag{B-13}$$

B-2.3.2. *Close-Packed Body-Centered Cubic Lattice:*

$$b^2 = 3\left(\frac{a}{2}\right)^2 = \frac{3}{4} a^2 = \sigma^2 \ , \ \text{so that} \quad a = \frac{2}{\sqrt{3}} \sigma \ . \tag{B-14}$$

The body–centered molecule has 8 nearest neighbors and a volume a^3 contains $1+8x(1/8) = 2$ molecules, so that the density is $\rho_S = 2m/a^3$, and:

$$\sigma = \frac{\sqrt{3}}{4^{1/3}} \left(\frac{m}{\rho_s}\right)^{\frac{1}{3}} \quad . \tag{B-15}$$

B-2.3.3. *Close–Packed Face–Centered Cubic Lattice*:

$b = \frac{a}{\sqrt{2}} = \sigma$, and $a = \sqrt{2}\,\sigma$.

A corner–molecule has 12 nearest neighbors and a cube of side *a* centered on it contains $1+12x(1/4) = 4$ molecules , so that the density is $\rho_S = 4m/a^3$, and:

$$\sigma = 2^{1/6}\left(\frac{m}{\rho_s}\right)^{\frac{1}{3}} \quad . \tag{B-16}$$

TABLE B-1. Some Properties of Heat Pipe Working Fluids (Vargaftik 1975, Reynolds 1979, and Schlunder 1984).

working fluid	M (gr/mol)	Tmelt (K)	ρ_S* (kg/m^3)	T_C (K)	P_C (MPa)
lithium	6.94	453.7	534.0	3,200 ± 600	70.0 ± 14.0
potassium	39.10	336.4	862.0	2,225 ± 25	16.4 ± 0.3
sodium	22.99	371.0	971.2	2,510 ± 20	31.0 ± 6.0
water	18.016	273.15	916.8	647.3	22.1 ± 0.03

*: densities at room–temperature (except for ice), from Weast 1986; and ASM Metals 1981.

B-3. EVALUATION OF THE MOLECULAR DIAMETER OF LITHIUM

B-3.1. Transport Coefficient Method (Dynamic Viscosity)

We found that the most appropriate vapor–phase viscosity correlation is that of Vargaftik (1975) for monoatomic vapor, with a molecular diameter $\sigma = 3.0$ Å (we used $T_c = 3{,}800$ K as recommended by Reynolds 1979). The kinetic theory agrees with experimental values to within $\pm 8\%$ in the temperature range $1{,}000\ \text{K} \leq T \leq 2{,}000\ \text{K}$.

B-3.2. Van der Waals Method

Using the critical values listed in Table B-1, we find $2.94\ \text{Å} < \sigma < 3.82\ \text{Å}$.

B-3.3. Close–Packed Solid–Phase Density

Solid lithium has a body–centered cubic type of structure above 80 K and undergoes a spontaneous transition to a close–packed hexagonal structure at 80 K. Using the literature value of $a = 3.5092$ Å (Pearson 1958; and Jeppson et al. 1978), we find:

$$\sigma = \frac{\sqrt{3}}{2}\, a = 3.039\ \text{Å} \quad .$$

Substituting the room–temperature density of solid lithium (Table B-1) in Equation (B-15), we find $\sigma = 3.038$ Å, which is almost identical.

Finally, compilation of these results leads to the following selection:
$\sigma(\text{Li}) = 3.0 \pm 0.1$ Å, resulting in an uncertainty in the mean free path λ of $\pm 6.3\%$.

B-4. EVALUATION OF THE MOLECULAR DIAMETER OF POTASSIUM

B-4.1. Transport Coefficient Method (Dynamic Viscosity)

We found that the best vapor–phase viscosity fits are that of Vargaftik (1975) for saturated vapor with a molecular diameter $\sigma = 3.93$ Å , and that used in SNPSAM (Seo 1988) and HTPIPE (Woloshun et al. 1989) models with $\sigma = 4.26$ Å .

B-4.2. Van der Waals Method

Using the critical values listed in Table B-1, we find $4.77 \text{ Å} < \sigma < 4.87 \text{ Å}$.

B-4.3. Close–Packed Solid–Phase Density

Solid potassium has a body–centered cubic type of structure which is maintained without transformation down to 0 K (Pearson 1958). Using the room–temperature density of solid potassium (Table B-1) in Equation (B-15), we find $\sigma = 4.608$ Å , which is the value listed in Table B-2 for room–temperature.

Finally, compilation of these results leads to the following selection:
$\sigma(K) = 4.44 \pm 0.18$ Å , resulting in an uncertainty in the mean free path λ of $\pm$ 8.6%.

TABLE B-2. Lattice Parameters of Solid Potassium at Various Temperatures.

T	5 K	78 K	293 K
a (Å) *	5.225	5.247	5.321
σ (Å) #	4.525	4.544	4.608

*: lattice parameters *a* compiled from Pearson (1958).

#: molecular diameter calculated with Equ. B-14, assuming close–packed structure.

B-5. EVALUATION OF THE MOLECULAR DIAMETER OF SODIUM

B-5.1. Transport Coefficient Method (Dynamic Viscosity)

We found that the best vapor–phase viscosity fits are that of Vargaftik (1975) for saturated vapor with a molecular diameter $\sigma = 2.83$ Å , and that used in SNPSAM (Seo 1988) and HTPIPE (Woloshun et al. 1989) models with $\sigma = 3.45$ Å .

B-5.2. Van der Waals Method

Using the critical values listed in Table B-1, we find $3.81 \text{ Å} < \sigma < 4.37 \text{ Å}$.

B-5.3. Close–Packed Solid–Phase Density

Solid sodium has a body–centered cubic type of structure, and undergoes a spontaneous partial martensitic transformation to a close–packed hexagonal structure on cooling below 36 K (Pearson 1958). Using the room–temperature density of solid sodium (Table B-1) in Equation (B-15), we find $\sigma = 3.710$ Å , which is close enough to the values listed in Table B-3.

Finally, compilation of these results leads to the following selection:
$\sigma(\text{Na}) = 3.58 \pm 0.13$ Å , resulting in an uncertainty in the mean free path λ of $\pm$ 7.7%.

TABLE B-3. Lattice Parameters of Solid Sodium at Various Temperatures.

T	5 K	78 K	87 K	293 K
a (Å) *	4.225	4.238	4.249	4.291
σ (Å) #	3.659	3.670	3.680	3.716

*: lattice parameter *a* compiled from Pearson (1958).

#: molecular diameter calculated with Equ. B-14, assuming close–packed structure.

B-6. EVALUATION OF THE MOLECULAR DIAMETER OF WATER

The viscosity formula for non–polar gases (Equation B-6), based on the Lennard–Jones potential, cannot be applied with confidence to gases consisting of polar or highly elongated molecules, because of the highly angle–dependent force fields that exist between such molecules (H_2O, NH_3, CH_3OH, NOCl,...). For polar molecules, the most widely used intermolecular energy potential is the Stockmayer potential, sum of the Lennard–Jones function and an additional angle–dependent term to account for the electrostatic interaction of the two dipoles (Hirschfelder et al. 1954, @1.3). The second and third virial coefficients for water have been computed for this potential function by Rowlinson (σ = 2.65 Å, ε/k = 380 K, Hirschfelder et al. 1954, p. 214; also Eisenberg and Kauzmann 1969, p. 51).

Rowlinson also used a potential function similar to Stockmayer's but with the repulsive energy proportional to r^{-12} and with an additional term describing dipole–quadripole forces (Hirschfelder et al. 1954, pp. 225–227; also Eisenberg and Kauzmann 1969, p. 52). For water vapor, he found σ = 2.725 Å, ε/k = 356 K . Although the agreement between calculated and experimental second virial coefficients was not improved, the derived parameters are certainly more reliable when the dipole–quadripole interaction is included. In particular the value of σ determined from the modified potential function is much closer to the intermolecular distance in ice: the separation of hydrogen–bonded molecules in ordinary ice is 2.76 Å, and the distance between nearest neighboring molecules in ice polymorphs may vary from 2.74 Å to 2.87 Å (Eisenberg and Kauzmann 1969, p. 48, 85).

For very high energy collisions, where the repulsive forces are more important than the attractive forces, it is a fairly good approximation to replace the angle–dependent contribution in the Stockmayer potential by an expression for the interaction of two–point dipoles that are perfectly aligned. For water vapor, Krieger (Hirschfelder et al. 1954, pp. 597–599) found σ = 2.824 Å, ε/k = 230.9 K .

Some other models have also been proposed for calculating the viscosity (and other transport coefficients) of polar gases. The Sutherland model (Hirschfelder et al. 1954, pp. 565–567) is not appropriate for water vapor. Monchick and Mason (1961) have calculated the collision integrals for the Stockmayer potential for polar gases and have compared their model with viscosity experimental data. For water vapor, they found the potential parameters values listed in Table B-4, using different methods.

Finally, by using the critical values listed in Table B-1 for water, the van der Waals method gives $\sigma = 2.89$ Å .

By compiling all these results we obtain 2.52 Å < σ(H2O) < 2.89 Å. However, we expect the molecular diameter of water to be greater than 2.74 Å, which is the smallest distance between neighboring molecules in ice, and we choose:

> σ(H2O) = 2.8 ± 0.1 Å, resulting in an uncertainty in the mean free path λ of ± 7.5%.

TABLE B-4. Energy Potential Parameters for Water Vapor as Determined by Monchick and Mason (1961) from Various Fitting Methods.

METHOD	σ (Å)	ε/k (K)
graphical method	2.52	775.
least square (rec.)	2.71	506.
non–polar gas	2.65	800.
free fit	2.80	260.

APPENDIX C. AN OVERVIEW OF NUMERICAL TECHNIQUES

This appendix reviews several efficient and advanced numerical techniques, and discuss their performance, respective merits and drawbacks. Section C-1 reviews several discretization schemes for the convection and diffusion fluxes. Sections C-2 and C-3 discuss the merits of finite–element and finite–difference methods and describe the non–staggered and staggered grid arrangements. Section C-4 shows the equivalence of under–relaxation and transient formulations, and demonstrates that the time–dependent formulation is always preferable. Section C-5 describes the very popular SIMPLE, SIMPLER and SIMPLEC finite–difference iterative solution techniques, in which the velocity components and pressure are calculated in a sequential or *segregated* manner. The residual norm reduction technique described in Section C-6 provides an optimum pressure under–relaxation factor for the convergence of the SIMPLE–type strategies. The effective parabolic block correction technique is described in section C-7. This procedure was developed to solve two–dimensional incompressible parabolic flow problems very efficiently by a marching technique in the flow direction, and can be extended to the solution of two–dimensional steady compressible flows. In contrast with the pressure–velocity coupling, the temperature–velocity coupling which arises in natural convection and temperature–driven incompressible flow problems has received little attention. Galpin and Raithby developed the Coupled–Equation Line–Solver iterative technique for the solution of such incompressible buoyancy–driven flow problems (section C-8). Sections C-9 and C-10 describe the very efficient line–by–line iterative technique, additive block–correction (ACM) method and additive–correction multigrid procedure for the solution of five–point linear systems which arise from the discretization of conservation equations on a two–dimensional domain. The advantages of ACM over the Brandt–type multigrid algorithms are reviewed in section C-11. The last section (C-12) reviews the non–iterative splitting methods, such as the Alternating Direction Implicit (ADI) approximations to solve multi–dimensional flow problems, the Marker–And–Cell formulation (MAC) and other projection algorithms to resolve the pressure–velocity coupling of the Navier–Stokes equations, and the non–iterative PISO procedure (Pressure–Implicit with Splitting of Operators) of Issa. These non–iterative splitting procedures have been considered to speed up calculations and reduce the complexity of programmation as well as storage requirements.

C-1. DIFFUSION/CONVECTION DISCRETIZATION SCHEMES

As is well known, the numerical solution of convection–diffusion problems is rendered difficult because of a numerical instability that occurs when the convective transport dominates the transport by diffusion. The difficulty manifests itself by producing unrealistic oscillatory or "wiggly" solutions whenever the mesh size exceeds a critical value (Ramadhyani and Patankar 1985). Although mesh refinement might overcome the problem, very often the resulting increase in computational cost is excessive. This difficulty has been recognized and overcome by practitioners of finite–difference and finite–element techniques through the use of upwind and hybrid schemes, some of which have the attractive feature of being unconditionally stable. Success in overcoming the stability problem has been achieved, however, at the expense of accuracy. Most upwind and hybrid schemes suffer from severe false (numerical) diffusion when the flow direction is at an angle to the grid lines (Patankar 1980). False diffusion tends to augment the transport in the direction normal to the local streamline, and can cause quite erroneous inferences to be drawn, particularly when transport models (such as models of turbulence) themselves are being studied.

The well–known power–law differentiating scheme (PLDS) of Patankar and Spalding (Patankar 1980) is based on the exact solution of one–dimensional steady diffusion–convection problems with constant properties, and performs well in flow regions in which the velocity field aligns closely with the mesh lines, when convection is primarily balanced by streamwise diffusion rather than cross–stream diffusion or sources. That is, the power–law scheme does not respond correctly to lateral diffusion. The Quadratic Upstream–Weighted Interpolation scheme (QUICK) of Leonard (1979) is third–order accurate in space and establishes implicitly the coupling between the flow components, even so it superposes one–dimensional approximations. Huang, Launder and Leschziner (1985) have shown that for a two–dimensional irrotational corner flow, both the power–law scheme and QUICK give a very accurate flow field, primarily because of the special nature of this flow in which the velocity components are coupled through the pressure but not through convection. However PLDS does not insure formal conservation of the stagnation pressure. The study of these authors leaves no doubt that PLDS should not be used unless the mesh can be closely aligned with the flow path lines, like in the case of a boundary layer flow. QUICK emerges as one of the most successful schemes for incompressible steady flows. It is a scheme attractively simple to incorporate into a solution algorithm and, for the typical mesh densities employed, requires only some 65% more computing time

than PLDS. Because the QUICK scheme results in an unusual nine–point matrix, a modified line–by–line technique with alternating sweep directions, which treats implicitly the four closest neighbors only, must be used to overcome convergence difficulties (Huang, Launder and Leschziner 1985). The investigation of several authors shows that high–order schemes such as QUICK significantly reduce false numerical diffusion but can produce wiggles and often fail to converge. In particular Tao and Sparrow (1987) showed that QUICK is stable only for grid Peclet numbers less than 8/3. For all these reasons, and considering the particular flow geometry of interest, that in a heat pipe, it is appropriate and preferable to use the power–law differencing scheme of Patankar to discretize the convection–diffusion fluxes.

C-2. STAGGERED GRID ARRANGEMENTS

In incompressible flow problems, there is no explicit equation that governs the pressure distribution. It is indirectly specified via the continuity equation. When the correct pressure field is substituted into the momentum equations, the resulting velocity field also satisfies the continuity equation (Patankar 1980). One way to handle this indirect specification of pressure is to attempt a direct simultaneous solution of the whole set of discretized momentum and continuity equations. In practical problems, however, this technique would require a very large amount of computer storage and time, even when specialized sparse matrix solvers are employed. Another possibility is elimination of the pressure from the overall formulation, but these methods cannot be easily extended to compressible and unsteady flow situations, and are not well suited for problems in which boundary conditions are prescribed on the pressure. It is therefore desirable to use iterative solution techniques in which the velocity components and pressure are calculated in a sequential or segregated manner (Baliga and Patankar 1983).

Although the continuity constraint is used to determine the pressure, only gradients of pressure appear in the momentum equations (and the pressure does not appear explicitly in the continuity equation). Because of this, if the pressure is interpolated using linear shape functions, only pressure differences between alternate grid points are involved in the overall system of equations (Prakash and Patankar 1985). Hence the equations reveal no difference between a uniform and a "checkerboard" pressure fields. Such a spurious pressure distribution is unacceptable, and is prevented in finite difference methods by using a staggered grid arrangement.

On a staggered grid, the momentum and continuity equations are discretized by using two different families of control volumes. Mass fluxes across the faces of the momentum control volumes are extrapolated in order to insure that mass is strictly conserved over these volumes. For these reasons, the method entails specification and calculation of a relatively extensive amount of geometrical and topological information.

C-3. NON–STAGGERED GRIDS AND FINITE–ELEMENTS

In a finite–difference discretization method, a "checkerboard" pressure field can develop as an acceptable solution if the velocity components and the pressure are located at the same grid positions (Patankar 1980). Since such pressure fields are undesirable, one uses a staggered grid, which completely eliminates the "checkerboard" pressure field. In the staggered grid, the velocity components are stored at displaced or staggered locations such that the pressure drop between two pressure nodes can be used to "drive" the velocity component located between them. Methods such as SIMPLE and its variants all use the staggered grid arrangement. Although the staggered grid eliminates this major difficulty, it introduces some inconvenience which becomes more serious when the method is extended to curvilinear non–orthogonal coordinates. Similarly, since there is no direct counterpart of the staggered grid in the finite–element method, one has to resort to unequal–order interpolation, which reduces the accuracy of the overall solution (Patankar 1988). These reasons provide the motivation for the search for methods with non–staggered grid or equal–order interpolation.

Although the non–staggered grid methods appear satisfactory on the surface, a number of them suffer from a subtle drawback: the solution produced by them depends on the values of the under–relaxation factors or the size of the time step. This feature is obviously very undesirable. That the non–staggered grid methods have this characteristic has been recognized by Patankar and other authors for quite some time. Recently, Majumdar (1988) has described this phenomena and proposed a remedy for it. Incidentally, the same drawback is present in some of the finite–element methods with equal–order interpolation.

The finite–element method provides close approximation of curved boundaries, a systematic and general way of modeling boundary conditions, and a versatile algorithm (Banaszek 1989). For these reasons, the finite–element method has become a more and more popular numerical tool in field theory problems, despite its greater programming complexity compared to the finite–difference methods.

By contrast, finite–difference methods are simple to formulate, can easily be extended to two or three dimensions, and require considerably less computational work and storage requirement than finite–element methods (for equivalent number of nodes). For these reasons, it is preferable to discretize the flow conservation equations using the finite–difference method, based on the control–volume integration. The control–volume approach has the following advantages: (a) it is simple to implement and amenable to easy physical interpretation; (b) the solution obtained by this approach satisfies global conservation, even on a non–uniform grid.

C-4. EQUIVALENCE OF UNDER–RELAXATION AND TRANSIENT FORMULATIONS

As is well known when dealing with steady–state problems, the resulting discretization equations can be solved directly by some relaxation algorithm such as a point or line Gauss–Seidel solver, or the steady–state solution can be obtained as asymptotic values of an associated unsteady problem. Moreover, by using the unsteady formulation, it is possible to solve both the steady and transient problems with the same code. When it is chosen to solve the steady–state equations directly, heavy under–relaxation is usually necessary to resolve the non–linearities and couplings, and it can be shown that relaxing the steady–state equations is equivalent to the transient formulation. To illustrate this point, consider the discretized form of the two–dimensional transient axial momentum equation:

$$(\rho \mathrm{Vol})^z \frac{v_{i,j} - v_{i,j}^n}{\Delta t} + aE^z (v_{i+1,j} - v_{i,j}) + aW^z (v_{i-1,j} - v_{i,j}) + aN^z (v_{i,j+1} - v_{i,j}) + aS^z (v_{i,j-1} - v_{i,j}) = S^z \ ,$$

which can be rewritten as:

$$aP^z v_{i,j} + aE^z v_{i+1,j} + aW^z v_{i-1,j} + aN^z v_{i,j+1} + aS^z v_{i,j-1} = \tilde{S}^z \ , \qquad \text{(C-1a)}$$

where

$$aP^z = \frac{(\rho Vol)^z}{\Delta t} - \left(aE^z + aW^z + aN^z + aS^z\right), \text{ and } \tilde{S}^z = S^z + \frac{(\rho Vol)^z}{\Delta t} v_{i,j}^n . \qquad \text{(C-1b)}$$

Introducing the coefficient aP* and the factor E (van Doormaal and Raithby 1984) defined by:

$$aP^* = -(aE^z + aW^z + aN^z + aS^z) > 0 , \text{ and } E = \frac{aP^*}{(\rho Vol)^z} \Delta t = \frac{\Delta t}{\Delta t^*} , \qquad \text{(C-2)}$$

Equation (C-1) is equivalent to:

$$\left(1 + \frac{1}{E}\right) aP^* v_{i,j} + aE^z v_{i+1,j} + aW^z v_{i-1,j} + aN^z v_{i,j+1} + aS^z v_{i,j-1} = S^z + \frac{aP^*}{E} v_{i,j}^n . \qquad \text{(C-3)}$$

By contrast, the steady–state discretized equation has the following form:

$$aP^* v_{i,j} + aE^z v_{i+1,j} + aW^z v_{i-1,j} + aN^z v_{i,j+1} + aS^z v_{i,j-1} = S^z . \qquad \text{(C-4)}$$

To resolve the non–linearities and the couplings between the flow equations, Equation (C-4) must be under–relaxed. Introducing the relaxation factor α, the relaxed version of Equation (C-4) has the form (Patankar 1980):

$$v_{i,j} = v_{i,j}^n + \alpha \left\{ \frac{1}{aP^*} (S^z - aE^z v_{i+1,j} - aW^z v_{i-1,j} - aN^z v_{i,j+1} - aS^z v_{i,j-1}) - v_{i,j}^n \right\} , \qquad \text{(C-5)}$$

or:

$$\frac{aP^*}{\alpha} v_{i,j} + aE^z v_{i+1,j} + aW^z v_{i-1,j} + aN^z v_{i,j+1} + aS^z v_{i,j-1} = S^z + \frac{1 - \alpha}{\alpha} aP^* v_{i,j}^n . \qquad \text{(C-6)}$$

Clearly, Equations (C-3) and (C-6) are identical if the relaxation factor α is taken to be $\alpha = E/(E+1)$. Note that the characteristic time step Δt^* corresponding to E=1 is the maximum stability limit for the explicit discretization version of Equation (C-1). We wish to use values of E in excess of 1 for fast calculation of transient and asymptotic solutions, and this is only possible with implicit discretization schemes such as Equation (C-1). It is also apparent that the E–formulation is preferable than the α–formulation since α is a non–linear compressed function of the time step Δt while E is proportional to Δt. However, it is better to use the unsteady formulation (C-1) because the use of the same time step Δt in all

conservation equations gives a consistent scheme, while the use of the same E factor does not, since Δt^* is different for different transported variables.

In conclusion, it is recommended that the time–dependent approach be adopted in all cases, even if only the steady–state solution is of interest. The solution can be advanced in time by using both explicit and implicit discretizations. Explicit schemes are easily programmed but have a severe stability restriction on the time step ($\Delta t < \Delta t^*$), which may compromise their efficiency. Such a restriction can be (partially) removed by use of an implicit approach such as an ADI factorization, at the expense of an increase in complexity.

C-5. SIMPLE–TYPE PROCEDURES

The papers most relevant to the present subject are those of Harlow and Welch (1965), Harlow and Amsden (1971), and Chorin (1968). These authors all use finite–difference procedures in which the dependent variables are the velocity components and the pressure. The latter is deduced from a Poisson equation which is obtained by the combination of the continuity equation and momentum equations, and the idea is present of a first approximation to the solution, followed by a succeeding correction. The iterative nature of the SIMPLE–type procedures for incompressible flows arises from the following reasons: (a) the equations are non–linear; (b) the continuity and momentum equations are coupled by the pressure; and (c) a direct solution of the finite–difference equations, even when they are linear, is time consuming (Patankar and Spalding 1972).

In the formulation for fluid flow, only the procedure for incompressible flows is described here. The method has been extended to compressible flows, but those details do not necessarily mean flows with constant density; the density can be a function of temperature and concentration. The term incompressibility refers to the effect of pressure on density. Since the calculation procedure described does not directly account for the pressure–density coupling, it is considered to be applicable only to flows at low Mach numbers (Patankar, in Minkowycz et al. 1988, p. 216).

The momentum conservation equations for two–dimensional incompressible flows can be discretized by successive–substitution linearization of the convective terms:

$$aP^r u_{i,j} + aE^r u_{i+1,j} + aW^r u_{i-1,j} + aN^r u_{i,j+1} + aS^r u_{i,j-1} = C^r(P_{i,j} - P_{i+1,j}) + S^r \ , \qquad \text{(C-7a)}$$

$$aP^z\, v_{i,j} + aE^z\, v_{i+1,j} + aW^z\, v_{i-1,j} + aN^z\, v_{i,j+1} + aS^z\, v_{i,j-1} = C^z(P_{i,j} - P_{i,j+1}) + S^z\,, \qquad \text{(C-7b)}$$

$$(A_r u)_{i,j} - (A_r u)_{i-1,j} + (A_z v)_{i,j} - (A_z v)_{i,j-1} = 0 \quad . \qquad \text{(C-7c)}$$

The resulting momentum and continuity linear equations involve the velocity components u,v and the pressure field P as the dependent variables (as a rule, all omitted subscripts should be read as i,j). The pressure–velocity elliptical coupling can be resolved by the SIMPLE–type pressure correction techniques (Raithby and Schneider 1979), originally derived by Patankar and Spalding, which proceed as follows. Starting with a guessed stared pressure field, the momentum conservation Equations (C-7a) and (C-7b) are solved for the stared velocity components:

$$aP^r\, u^*_{i,j} + aE^r\, u^*_{i+1,j} + aW^r\, u^*_{i-1,j} + aN^r\, u^*_{i,j+1} + aS^r\, u^*_{i,j-1} = C^r\left(P^*_{i,j} - P^*_{i+1,j}\right) + S^r\,, \qquad \text{(C-8a)}$$

$$aP^z\, v^*_{i,j} + aE^z\, v^*_{i+1,j} + aW^z\, v^*_{i-1,j} + aN^z\, v^*_{i,j+1} + aS^z\, v^*_{i,j-1} = C^z\left(P^*_{i,j} - P^*_{i,j+1}\right) + S^z\,. \qquad \text{(C-8b)}$$

Because this new velocity field does not satisfy the continuity equation (C-7c), these velocities and the pressure field must be corrected:

$$u = u^* + u'\,,\quad v = v^* + v'\,,\quad \text{and} \quad P = P^* + P' \quad . \qquad \text{(C-9)}$$

The momentum correction equations relate the velocity and pressure corrections and are obtained by subtracting Equations (C-8a) and (C-8b) from Equations (C-7a) and (C-7b) respectively:

$$aP^r\, u'_{i,j} + aE^r\, u'_{i+1,j} + aW^r\, u'_{i-1,j} + aN^r\, u'_{i,j+1} + aS^r\, u'_{i,j-1} = C^r\left(P'_{i,j} - P'_{i+1,j}\right)\,, \qquad \text{(C-10a)}$$

$$aP^z\, v'_{i,j} + aE^z\, v'_{i+1,j} + aW^z\, v'_{i-1,j} + aN^z\, v'_{i,j+1} + aS^z\, v'_{i,j-1} = C^z\left(P'_{i,j} - P'_{i,j+1}\right). \qquad \text{(C-10b)}$$

After suitable simplifications of the momentum correction equations, a pressure correction equation is derived as follows: the momentum equations are used to express the velocity components in terms of the pressure correction field, and the velocities appearing in the continuity Equation (C-7c) are eliminated. This procedure leads to the construction of an elliptical Poisson equation that is solved for the pressure correction field. This pressure correction field is used to correct the velocity field, but is not used usually to correct the

pressure field, so that a separate equation is used to evaluate the pressure field. The pressure correction step corrects the velocity field to yield a new velocity field which satisfies exactly the mass conservation constraint, while the pressure field is corrected so as to satisfy the momentum conservation equations in an average, "most–consistent" way. At this point a distinction must be made between passive and active pressure update methods. In the passive PULS algorithm (Pressure Update from Least–Square residual minimization), the corrected velocity field is inserted into the momentum conservation equations and the pressure at a particular location is chosen so that a linear combination of the squares of the four momentum residuals surrounding this particular location is minimum. The weighting factors must depend on the cell dimensions as recommended by Briley (1974). Raithby and Schneider (1979) have shown that such a passive pressure update procedure still achieves convergence for large time steps. The advantage of this method is that the coefficients of the pressure update matrix are dependent on the grid dimensions only and need to be calculated only once. It is then possible to perform a matrix inversion once for the entire problem, so that the pressure update steps will be very inexpensive in CPU time. This is all the more important that the iterative solution of the Poisson equation requires many more iterations to reach a given accuracy than do the momentum equations, and can take up to 80% of the total computing time in some cases.

In the active pressure update SIMPLE (Semi–Implicit Method for Pressure–Linked Equations) and SIMPLEC (SIMPLE–Consistent) algorithms , the same pressure correction field is used to update both the velocity field and the pressure field. SIMPLE neglects the off–diagonal velocity corrections in Equations (C-10), while SIMPLEC approximates these corrections by $u'_{i,j}$ in Equation (C-10a) and by $v'_{i,j}$ in Equation (C-10b). The resulting approximate correction momentum equations take the form:

$$\left(A_r u'\right)_{i,j} = D^r\left(P'_{i,j} - P'_{i+1,j}\right) \quad ,$$

$$\left(A_z v'\right)_{i,j} = D^z\left(P'_{i,j} - P'_{i,j+1}\right) \quad , \tag{C-11}$$

with

$$D^r = \frac{A_r C^r}{aP^r} \quad \text{and} \quad D^z = \frac{A_z C^z}{aP^z} \tag{C-11a}$$

for SIMPLE, and

$$D^r = \frac{A_r C^r}{aP^r + aE^r + aW^r + aN^r + aS^r} \quad \text{and} \quad D^z = \frac{A_z C^z}{aP^z + aE^z + aW^z + aN^z + aS^z} \tag{C-11b}$$

for SIMPLEC. Making use of Equations (C-9) and (C-11) in the continuity Equation (C-7c) gives the following pressure correction equation:

$$aP\ P'_{i,j} + aE\ P'_{i+1,j} + aW\ P'_{i-1,j} + aN\ P'_{i,j+1} + aS\ P'_{i,j-1} = S^p \quad , \tag{C-12}$$

where

$$\begin{aligned} aP_{i,j} &= D^r_{i,j} + D^r_{i-1,j} + D^z_{i,j} + D^z_{i,j-1} \ , \\ aE_{i,j} = -\ D^r_{i,j} \ , \quad aW_{i,j} &= -\ D^r_{i-1,j} \ , \quad aN_{i,j} = -\ D^z_{i,j} \ , \quad aS_{i,j} = -\ D^z_{i,j-1} \ , \\ \text{and} \quad S^p_{i,j} &= -\left[\left(A_r u^*\right)_{i,j} - \left(A_r u^*\right)_{i-1,j} + \left(A_z v^*\right)_{i,j} - \left(A_z v^*\right)_{i,j-1}\right] \ . \end{aligned} \tag{C-13}$$

Because of the inconsistency in the simplifications of the momentum correction equations made by SIMPLE, this algorithm requires that the pressure is under–relaxed. The SIMPLEC algorithm of van Doormaal and Raithby (1984) uses a consistent simplification of the momentum correction equations and does not require any pressure under–relaxation. The SIMPLER (SIMPLE–Revised) algorithm of Patankar (1980) operates slightly differently. A stared velocity field is assumed and the off–diagonal correction velocities are neglected in the momentum equations, as in SIMPLE, so that Equations (C-7) are rewritten:

$$aP^r u_{i,j} + aE^r u^*_{i+1,j} + aW^r u^*_{i-1,j} + aN^r u^*_{i,j+1} + aS^r u^*_{i,j-1} = C^r\left(P_{i,j} - P_{i+1,j}\right) + S^r \ , \tag{C-14a}$$

$$aP^z v_{i,j} + aE^z v^*_{i+1,j} + aW^z v^*_{i-1,j} + aN^z v^*_{i,j+1} + aS^z v^*_{i,j-1} = C^z\left(P_{i,j} - P_{i,j+1}\right) + S^z \ . \tag{C-14b}$$

These momentum equations are used to express the velocity components in terms of the pressure field, and the velocities appearing in the continuity equation are eliminated. The resulting elliptical Poisson equation is solved for the pressure field. At this point a pressure correction field is computed using the SIMPLE procedure and the stared velocities are corrected as before. However, the pressure is not corrected and the pressure field computed in the first step is taken as the new pressure field. Note that in SIMPLER the Poisson equation for the new pressure field is identical to the pressure correction equation except for the source term, which is different. One of the advantages of SIMPLER is that

if the guessed stared velocity field happened to be the correct one, the pressure equation would yield the correct pressure field. SIMPLER internally generates a pressure field that is compatible with the velocity field, and this procedure has a much better rate of convergence than SIMPLE, even so the computational work per iteration is increased by about 60%. Van Doormaal and Raithby (1984) pointed out that when diffusion and convection phenomena are dominated by pressure gradients and source terms, the consistent approximation in SIMPLEC becomes exact so that this procedure should be used. This applies to flow systems with large pressure gradients such as flows in porous media and heat exchangers. Also SIMPLEC is easy to program and performs as well or better than SIMPLER in terms of CPU time and storage requirements. Note that SIMPLE–type algorithms are appropriate when pressure–velocity couplings are predominant. For buoyancy–induced flows or strong temperature effects, efficient treatment of the pressure–velocity coupling becomes of less consequence.

C-6. RESIDUAL NORM REDUCTION TECHNIQUE

When using the SIMPLE–type pressure update procedures, the velocity field must usually be under–relaxed to resolve the non–linearities in the momentum equations, while the pressure correction is also under–relaxed when inconsistent approximations are made such as in SIMPLE. Chatwani and Turan (1991) have proposed an improvement of SIMPLE–type strategies by selecting the pressure correction under–relaxation factor based on the minimization of global residual form. After solving the pressure correction equation for P' and after the velocity field has been corrected according to the procedure, the new pressure field is under–relaxed as $P = P^* + \alpha P'$, and the momentum residuals are formed as:

$$R^r = S^r - \left[aP^r u_{i,j} + aE^r u_{i+1,j} + aW^r u_{i-1,j} + aN^r u_{i,j+1} + aS^r u_{i,j-1}\right] - C^r\left[\left(P^*_{i,j} + \alpha P'_{i,j}\right) - \left(P^*_{i+1,j} + \alpha P'_{i+1,j}\right)\right] = \tilde{R}^r - \alpha C^r\left(P'_{i,j} - P'_{i+1,j}\right) \qquad \text{(C-15a)}$$

$$R^z = S^z - \left[aP^z v_{i,j} + aE^z v_{i+1,j} + aW^z v_{i-1,j} + aN^z v_{i,j+1} + aS^z v_{i,j-1}\right] - C^z\left[\left(P^*_{i,j} + \alpha P'_{i,j}\right) - \left(P^*_{i,j+1} + \alpha P'_{i,j+1}\right)\right] = \tilde{R}^z - \alpha C^z\left(P'_{i,j} - P'_{i,j+1}\right) \quad . \qquad \text{(C-15b)}$$

The global residual norm (assuming equal weight for all node points) is:

$$G = \sum_{i,j} \left(R_r^2 + R_z^2\right) \quad ,$$

and can be minimized with respect to the relaxation factor α by setting the derivative of G to zero:

$$\frac{\partial G}{\partial \alpha} = -2 \sum_{i,j} \left\{ \begin{array}{l} C^r \left(P'_{i,j} - P'_{i+1,j} \right) \left[\tilde{R}^r - \alpha C^r \left(P'_{i,j} - P'_{i+1,j} \right) \right] \\ + C^z \left(P'_{i,j} - P'_{i,j+1} \right) \left[\tilde{R}^z - \alpha C^z \left(P'_{i,j} - P'_{i,j+1} \right) \right] \end{array} \right\} = 0 \quad ,$$

so that the optimum relaxation factor α is given by:

$$\alpha = \frac{\sum_{i,j} \left\{ C^r \tilde{R}^r \left(P'_{i,j} - P'_{i+1,j} \right) + C^z \tilde{R}^z \left(P'_{i,j} - P'_{i,j+1} \right) \right\}}{\sum_{i,j} \left\{ \left[C^r \left(P'_{i,j} - P'_{i+1,j} \right) \right]^2 + \left[C^z \left(P'_{i,j} - P'_{i,j+1} \right) \right]^2 \right\}} \quad . \tag{C-16}$$

Therefore, no empirical information is needed for the pressure relaxation factor, as the code will automatically select the optimum value at each iteration level. Even for those cases where no improvement in the convergence is obtained, the proposed method takes the guesswork out of trying to specify α. It is believed that performance of the method can be improved by reevaluating the momentum equation coefficients with the updated (corrected) velocities before applying the minimization criterion. Note that the present residual norm reduction technique is different from the PULS algorithm (Raithby and Schneider 1979) which formulates a Poisson equation for the pressure on the basis of minimization of local residuals and thus can encounter convergence difficulties. The present algorithm is based on improvements in the pressure correction algorithm in a global sense and faces no convergence difficulties.

Note that this residual norm reduction technique recommended by Patankar (1986) is easily extended to all dependent variables. The solution procedure of the linearized equations predicts a change (or correction) in the dependent variables. Instead of accepting this change as it is, it is multiplied by a constant α, a kind of under– or over–relaxation factor. The value of this factor is found by requiring that the norm of the residual vector (i.e., the sum of the squares of the residuals of all the equations) be a minimum. This minimization search produces a kind of "optimum" relaxation of the dependent variables.

C-7. EFFECTIVE PARABOLIC BLOCK CORRECTION PROCEDURE

Braaten and Patankar (1989) have proposed an effective Parabolic Block Correction (PBC) procedure to accelerate the convergence of the solution of two–dimensional incompressible flow. This procedure makes use of the fact that incompressible parabolic flow problems can be solved in a very efficient manner by a marching technique in the flow direction, technique which requires little computer storage and CPU time, as described by Raithby and Schneider (1979). A flow is parabolic in the axial direction z if axial diffusion is negligible and the radial pressure gradient is small compared with the axial pressure drop. This situation arises usually when an incompressible fluid is flowing in a tube with no recirculation. The PBC technique proceeds as follows. Consider the axial momentum conservation Equation (C-7b), which is reproduced here for convenience:

$$aP^z v_{i,j} + aE^z v_{i+1,j} + aW^z v_{i-1,j} + aN^z v_{i,j+1} + aS^z v_{i,j-1} = C^z(P_{i,j} - P_{i,j+1}) + S^z \,. \qquad \text{(C-7b)}$$

The procedure consists in correcting the axial velocity components and the pressures by marching in the flow direction, say by increasing j, so that $v_{i,j-1}$ is known from the previous line correction step. In the spirit of the parabolic approximation, the flow is not influenced by the downstream neighbor, so that $v_{i,j+1}$ is evaluated explicitly from the previous iteration; also the pressure variation in the cross–stream direction is neglected compared to the streamwise pressure changes, and corrections of pressures ΔP_j are uniform along the line j+1. With these approximations, Equation (C-7b) reduces to:

$$aW^z v_{i-1,j} + aP^z v_{i,j} + aE^z v_{i+1,j} = C^z\left[P^*_{i,j} - \left(P^*_{i,j+1} + \Delta P_j\right)\right] + S^z - aN^z v^*_{i,j+1} - aS^z v^*_{i,j-1} \,,$$

or

$$aW^z v_{i-1} + aP^z v_i + aE^z v_{i+1} = - C^z \Delta P + \tilde{S}^z \,, \qquad \text{(C-17)}$$

where the stared quantities refer to the best available estimates, and subscripts j are dropped since unnecessary. Because of the linear form of Equation (C-17), it is easy to verify that the solution of this system can be written: $v_i = \hat{v}_i + \Delta P f_i$, where $\hat{v}_i$ and f_i are solutions of the system:

$$aW^z \hat{v}_{i-1} + aP^z \hat{v}_i + aE^z \hat{v}_{i+1} = \tilde{S}^z \,, \qquad \text{(C-18a)}$$

$$aW^z f_{i-1} + aP^z f_i + aE^z f_{i+1} = - C^z \,. \qquad \text{(C-18b)}$$

Equations (C-18) are easily solved using the efficient TDMA tridiagonal matrix solver of Thomas. It is more efficient to combine the solution of Equations (C-18a) and (C-18b) since one set of the TDMA recursive coefficients is not dependent on the source term and is therefore identical for both systems. Finally, ΔP is calculated by requiring that mass is globally conserved over the cells of line j. Summation of the mass balance equations over the line j gives an equation of the following form:

$$\dot{m} = \sum_{i=1}^{Nr} \rho A_i^z v_i = \left(\sum_{i=1}^{Nr} \rho A_i^z f_i \right) \Delta P + \sum_{i=1}^{Nr} \rho A_i^z \hat{v}_i \ , \qquad \text{(C-19)}$$

which gives ΔP in terms of the most recent updates of the velocity field, $\hat{v}_i$ and f_i. After the correction procedure has been applied to every line of constant j in increasing order, it can be repeated in the radial direction. While the use of PBC is slightly more expensive than one double sweep of the line–by–line iterative technique, this procedure alone is capable of solving the entire problem if the flow is of boundary–layer type, and can significantly improve the rate of convergence of the solution algorithm in the case of an almost parabolic flow, such as in a heat pipe where radial pressure gradients and axial diffusion phenomena are small or negligible.

Connell and Stow (1986) have extended the pressure–update procedure to the solution of two–dimensional steady compressible flows. The first step of a typical iteration consists of solving the continuity and momentum equations for the pressure and velocity fields by using an Extended Pressure Correction procedure (EPC). The energy equation is then solved for the temperatures, and densities are updated as a function of pressures and temperatures by using the equation of state. Connell and Stow have tested various EPC procedures and have retained EPC–2A as their most stable and efficient algorithm, which requires about 20 to 40% less CPU time than SIMPLE. The procedure consists of performing one or two internal iterations of SIMPLE type, whose purpose is to explicitly account for the off–diagonal velocity corrections in the momentum correction equation. The first internal iteration proceeds exactly as SIMPLE: the off–diagonal velocity corrections are neglected in the momentum correction equation, the pressure correction equation is formed and solved, and the corresponding off–diagonal velocity corrections are computed. Their new value is used explicitly in the momentum correction Equations (C-10) and the process is repeated. While EPC–2A does not require any under–relaxation of the velocity field, the pressure field must be relaxed. It is apparent that the use of the

consistent velocity correction approximation of Van Doormaal and Raithby (1984) should strongly improve the efficiency of the algorithm and remove the need for pressure under–relaxation. The new procedure is obtained by simply using SIMPLEC instead of SIMPLE for the internal iterations of the extended pressure correction procedure. Connell and Stow pointed out that because the discrete equations are coupled and non–linear, there is little point in solving them exactly during each iteration. Only the Poisson equation for the pressure corrections must be solved within a certain accuracy for the procedure to converge correctly.

C-8. THE CELS SOLVER FOR TREATING THE TEMPERATURE–VELOCITY COUPLING

In contrast with the pressure–velocity coupling, the temperature–velocity coupling which arises in natural convection and temperature–driven incompressible flow problems has received little attention. Note that incompressible flows does not necessarily mean flows with constant density; the density can be a function of temperature and concentration. The term incompressibility refers to the effect of pressure on density. Since the calculation procedure described does not directly account for the pressure–density coupling, it is considered to be applicable only to flows at low Mach numbers (Patankar, in Minkowycz 1988, pp. 216). Galpin and Raithby (1986) identified two different forms of the temperature–velocity coupling for buoyancy–driven flows: (a) the temperature appears implicitly in the momentum equations through the Boussinesq approximation; (b) the velocity components appear in the energy equation through the advective energy transport terms. In forced–convection flows, coupling (a) is negligible, that is the velocity field does not depend on the temperature and can be computed separately, while the temperature field is strongly dependent on the velocity profiles through coupling (b). In pure natural convection (temperature–driven convection) flow, coupling (a) is particularly strong, and coupling (b) can be significant also. For very slow flows such as in a porous medium, coupling (b) is negligible, that is the temperature field is independent of the flow field and can be computed separately.

Because the conservation equations are non–linear, they must be linearized in the first place, and two different practices have been extensively used. In the successive substitution linearization, the unknown coefficients are simply evaluated from the currently available values of the dependent variables, as it is done in SIMPLE–type algorithms. This standard linearization decouples the momentum and energy equations, which is convenient

for the solution of the system, but usually requires heavy under–relaxation to avoid divergence since it does not accurately mimic the physics of the flow. In the Newton–Raphson (NR) linearization technique, the anticipated change in the coefficients is taken into account via their first derivative with respect to the dependent variables ($uT \approx u^nT + uT^n - u^nT^n$). This more accurate NR linearization practice has a significantly higher rate of convergence, at the expense of an increased computational effort due to the coupling of the momentum and energy equations. When the current estimates of the solution are close to the exact solution, the NR technique is very efficient. But for initial guesses that are far from the solution, this linearization technique often fails to converge, as observed by Patankar (1986). The same author has devised a very satisfactory technique, called the hybrid linearization method, which employs the standard linearization until the norm of the residuals decreases below a certain value, and then switches to the NR linearization until the final convergence of the solution. By combining this hybrid linearization method with a direct solution solver (sparse–matrix LU decomposition) and a residual norm reduction technique (after each iteration, the optimum under–relaxation factor is computed by minimizing the norm of the residuals), Patankar (1986) was able to obtain a converged solution in only 25 iterations for a flow with a Rayleigh number of 10^7 when a zero initial guess was used for all variables. For the first time, the same author obtained solutions for Rayleigh numbers as high as 10^9 (with a Prandtl number of 0.71) when solutions for a lower Rayleigh number were used as the initial guess. Iterative methods such as SIMPLER failed to converge even after 1000 iterations.

Galpin and Raithby (1986) have applied the NR linearization technique to the momentum and energy conservation equations for incompressible buoyancy–driven flows and obtained:

$$aP^r u_{i,j} + aE^r u_{i+1,j} + aW^r u_{i-1,j} + aN^r u_{i,j+1} + aS^r u_{i,j-1} = C^r(P_{i,j} - P_{i+1,j}) + S^r + aP^{rT} T_{i,j} + aE^{rT} T_{i+1,j} \quad , \qquad \text{(C-20a)}$$

$$aP^z v_{i,j} + aE^z v_{i+1,j} + aW^z v_{i-1,j} + aN^z v_{i,j+1} + aS^z v_{i,j-1} = C^z(P_{i,j} - P_{i,j+1}) + S^z + aP^{zT} T_{i,j} + aN^{zT} T_{i,j+1} \quad , \qquad \text{(C-20b)}$$

$$aP^T T_{i,j} + aE^T T_{i+1,j} + aW^T T_{i-1,j} + aN^T T_{i,j+1} + aS^T T_{i,j-1} = S^T + aE^{Tr} u_{i,j} + aW^{Tr} u_{i-1,j} + aN^{Tz} v_{i,j} + aS^{Tz} v_{i,j-1} \quad , \qquad \text{(C-20c)}$$

$$(A_r u)_{i,j} - (A_r u)_{i-1,j} + (A_z v)_{i,j} - (A_z v)_{i,j-1} = S \quad . \qquad \text{(C-20d)}$$

Galpin and Raithby have compared the standard (ST) and Newton–Raphson (NR) linearization techniques by solving the system of Equations (C-20) exactly at each step (by using a direct solver), to isolate the effects of the temperature–velocity coupling. They have considered the natural convection flow in a polar annulus for three different fluids: air (Pr = 0.71), glycerin (Pr = 13,000) and Mercury (Pr = 0.025). These authors have observed like Patankar that the NR linearization technique works only when the general sense of the flow is established (good "initial" solution) since it assumes that extrapolation from the previous solution is reasonable over the prescribed time step. For $Pr \geq 1$, ST–direct converges only for small time steps, while NR–direct converges faster for a wider range of time steps. For fluids with low Prandtl number, the temperature profile is established mainly by conduction, so that the advective coupling (b) is weak and standard linearization is suitable to solve the system of Equations (C-20). For flows of moderate or high Prandtl numbers and high Rayleigh numbers, a bidirectional sensitivity (couplings (a) and (b)) is retained, and proper treatment of the temperature–velocity coupling via the Newton–Raphson linearization is important. Galpin and Raithby (1986) have extended the Coupled–Equation Line–Solver (CELS) iterative method to the solution of the coupled system of Equations (C-20). This algorithm solves simultaneously for u, v, P and T along lines of control volumes, iteratively improving the solution by sweeping line by line across the entire domain in alternating directions, very much as does the line–GS solver or ADI technique for a scalar variable. Careful attention is paid in the formulation to ensure that mass is rigidly conserved, so that iterations are required only to improve the satisfaction of the linear momentum and energy conservation equations. The j–row updating of the CELS technique proceeds as follows. By retaining implicitly only the dependent variables with a subscript j (the variables with subscripts j-1 or j+1 are evaluated explicitly and incorporated into the source terms), the system of Equations (C-20) reduces to:

$$aP^r u_{i,j} + aE^r u_{i+1,j} + aW^r u_{i-1,j} = C^r (P_{i,j} - P_{i+1,j}) + \tilde{S}^r + aP^{rT} T_{i,j} + aE^{rT} T_{i+1,j} \ , \qquad \text{(C-21a)}$$

$$aP^z v_{i,j} + aE^z v_{i+1,j} + aW^z v_{i-1,j} = C^z P_{i,j} + \tilde{S}^z + aP^{zT} T_{i,j} \ , \qquad \text{(C-21b)}$$

$$aP^T T_{i,j} + aE^T T_{i+1,j} + aW^T T_{i-1,j} = \tilde{S}^T + aE^{Tr} u_{i,j} + aW^{Tr} u_{i-1,j} + aN^{Tz} v_{i,j} \ , \qquad \text{(C-21c)}$$

$$(A_r u)_{i,j} - (A_r u)_{i-1,j} + (A_z v)_{i,j} = \tilde{S} \ . \qquad \text{(C-21d)}$$

Equation (C-21d) can be used to express the v components of the velocity field in terms of

the u components, and the v components are eliminated in Equation (C-21b) to give an equation for the pressure in terms of the u components and the temperature:

$$C^z P_{i,j} = aE^{Pr} u_{i+1,j} + aP^{Pr} u_{i,j} + aW^{Pr} u_{i-1,j} + aWW^{Pr} u_{i-2,j} + \widetilde{S}^P - aP^{zT} T_{i,j} \quad . \qquad \text{(C-22)}$$

Equation (C-22) is used to eliminate the pressures in Equation (C-21a), which gives a linear equation pentadiagonal in u and bidiagonal in T. Finally, the v component of the velocity is eliminated in Equation (C-21c) by using Equation (C-21d), which results in a linear equation tridiagonal in T and bidiagonal in u. These two linear equations can be efficiently solved by the coupled pentadiagonal u, tridiagonal T matrix PT–TDMA algorithm (Galpin and Raithby 1986). After calculation of T and u, Equation (C-22) is used to evaluate the pressure P while v is obtained from Equation (C-21d). The CELS algorithm is performed successively on rows of increasing j, and the last line $j = Nz$ requires a special treatment: (a) the v components of the velocity field are calculated from the boundary conditions; (b) the u components of the velocity field are calculated using the mass balance over each control volume (Equation C-21d); (c) the last interior v–momentum Equation (C-21b) is used to evaluate the pressure; (d) finally the temperatures are computed from the solution of the tridiagonal Equation (C-21c). Note that by sweeping along lines of constant j in increasing order (from j=1 to Nz), mass conservation is enforced exactly after each sweep, even if the velocity and pressure fields have not converged yet. Because CELS decouples the pressure between the lines j, the convergence of the solver is slowed. To remedy this problem, a block correction of pressure is performed after each sweep, by correcting the pressure levels of each line j by δP_j (Galpin, van Doormaal and Raithby 1985). The constraint that determines δP_j is that the v–momentum Equations (9b) are satisfied on the average along the line j :

$$\sum_{i=1}^{Nr} \left[aP^z v_{i,j} + aE^z v_{i+1,j} + aW^z v_{i-1,j} + aN^z v_{i,j+1} + aS^z v_{i,j-1} - S^z - aP^{zT} T_{i,j} - aN^{zT} T_{i,j+1}\right]$$

$$= \sum_{i=1}^{Nr} C^z\left(P_{i,j} + \delta P_j - P_{i,j+1}\right) = \sum_{i=1}^{Nr} C^z (P_{i,j} - P_{i,j+1}) + \delta P_j \sum_{i=1}^{Nr} C^z \quad . \qquad \text{(C-23)}$$

Then all pressures on line j are corrected, starting from line Nz-1 to line 1, in decreasing order. Galpin and Raithby (1986) found that for large time steps, NR–CELS performed better than a line Gauss–Seidel solver combined with SIMPLEC or SIMPLER, the latter being very sensitive to the size of the time step. In contrast, the computational time

required by NR–CELS to reach the steady–state flow solution is a smooth and decreasing function of the time step.

C-9. THE LINE–BY–LINE ITERATIVE TECHNIQUE

The five–point finite–difference equations can be solved by repetitive use of TDMA in the first and second coordinate directions (TDMA double–sweep or line Gauss–Seidel method). The advantage of this solver is that it gives nearly the exact solution after only one double–sweep when the coefficients in one direction are much smaller (or greater) than the coefficients in the other direction (Patankar and Spalding 1972). This situation arises for strongly anisotropic problems, of for isotropic problems which must be discretized on grids of very large aspect ratios. The double–sweep can be repeated a few times to obtain greater accuracy.

Because the solution of the pressure correction elliptical equation can represent as much as 80% of the total computational cost, it is a high priority to solve the Poisson equation in an efficient manner. The line–by–line iterative technique of Patankar has the combined advantages of simplicity and low–storage requirement. The rate of convergence of this technique depends crucially on the treatment of the off–line dependent variables, and van Doormaal and Raithby (1984) have proposed a modification of the line–by–line technique to accelerate its performance.

C-10. ADDITIVE BLOCK–CORRECTION METHOD

Settari and Aziz (1973) have proposed a single partitioning method of acceleration of convergence for stratified or heterogeneous problems. This Additive Block–Correction (ABC) can be applied after a certain number of iterations of any iterative method used to solve the following linear system of equations:

$$\mathbf{R} = \mathbf{S} - [A]\,\mathbf{T} = 0 \quad , \tag{C-24}$$

where [A] is a NxN matrix, **S** is the source term vector of dimension N and **T** is the dependent variable vector. Now we consider a complete partition of $I_N = \{1,2,...,N\}$ constituted of M blocks I_p (p=1 to M) with $M \leq N$; we associate one unknown correction α_p with each partition or block, and we define the correction vector δ such that $\delta_i = \alpha_p$

for $i \in I_p$. If we denote by **T** the current approximation of the solution of Equation (C-24) and require that the average residual on every block or partition is zero, we obtain:

$$\sum_{i \in I_p} \left\{ [A](\mathbf{T}+\delta) - \mathbf{S} \right\}_i = 0, \quad \text{for} \quad p = 1 \ \text{to} \ M. \tag{C-25}$$

For the row–partition of a five–point linear system obtained from the discretization of conservation equations on a two–dimensional domain $N_r \times N_z$, Equation (C-25) can be rewritten:

$$\sum_{i=1}^{N_r} \left\{ \begin{array}{r} aP_{i,j}\left(T_{i,j}+\alpha_j\right) + aW_{i,j}\left(T_{i-1,j}+\alpha_j\right) + aE_{i,j}\left(T_{i+1,j}+\alpha_j\right) \\ + aN_{i,j}\left(T_{i,j+1}+\alpha_{j+1}\right) + aS_{i,j}\left(T_{i,j-1}+\alpha_{j-1}\right) - S_{i,j} \end{array} \right\} = 0,$$

$$\text{for} \quad j = 1 \ \text{to} \ N_z \ . \tag{C-26}$$

The correction vector α of dimension N_z is solution of the following tridiagonal linear system:

$$bS_j\, \alpha_{j-1} + bP_j\, \alpha_j + bN_j\, \alpha_{j+1} = Q_j, \quad \text{for} \quad j = 1 \ \text{to} \ N_z, \tag{C-27a}$$

where

$$bS_j = \sum_{i=1}^{N_r} aS_{i,j}\ , \quad bP_j = \sum_{i=1}^{N_r} (aP+aW+aE)_{i,j}\ , \quad bN_j = \sum_{i=1}^{N_r} aN_{i,j}\ , \quad \text{and} \quad Q_j = \sum_{i=1}^{N_r} R_{i,j}\ . \tag{C-27b}$$

Hutchinson and Raithby (1986) have studied the rate of convergence of various iterative solvers and showed that the use of a multigrid method based on the additive correction strategy of Settari and Aziz (1973) can dramatically reduce the number of iterations needed.

The use of very dissimilar grid spacings results in strongly anisotropic coefficients. A point Gauss–Seidel solver (GS) reduces the high–frequency modes of the error more effectively than the lowest–frequency components, so that the asymptotic convergence rate of the solver depends on the lowest allowable mode in the error. After the high–frequency modes have been removed, the GS solver appears to "stall" if the grid aspect ratio $C = \Delta z/\Delta r$ is large. It can be observed that one application of the GS solver at location (i,j) is

equivalent to advancing the solution at this point by a time step $\Delta t_{i,j}$, which is the minimum time to transfer information from the explicit–variable nodes (i,j+1), (i+1,j) to the node (i,j). For two–dimensional steady–state diffusion, the time steps to transfer information along the grid lines have the form $\Delta t_r = E\,\Delta r^2$ and $\Delta t_z = E\,\Delta z^2$ respectively, and since $\Delta r << \Delta z$ we have $\Delta t_{i,j} = \Delta t_r$. Since the time necessary to smooth any error component is roughly the time to transfer information over one wavelength, the number of iterations to smooth all allowable error modes in the r–direction is roughly equal to the number of nodes N_r in that direction. However it takes a time $\Delta t_z = C^2\,\Delta t_{i,j}$ to transfer information between two adjacent nodes in the weak coefficient direction z (the smoothing of even the higher–frequency components is therefore extremely expensive in z). The convergence is governed by the lowest admissible Fourier mode of the error because the time step implied by the solver is least effective in smoothing these modes. It is clear that increasing the implicitness of the solver in the strong coefficient direction r will alleviate the problem. In such case $\Delta t_{i,j} \approx \Delta t_z$ and the error is smoothed in about N_Z line–by–line sweeps implicit in the r direction. The use of the row–partition additive correction of Settari and Aziz (1973) will insure a complete propagation of information in the weak coefficient direction z. Such level shift guarantees that the average error along each row j is zero (the residual on every block of the partition is forced to zero), so that the k=0 Fourier mode is eliminated. For this problem, it is then possible to perform a simple two–level Additive–Correction Multigrid procedure (ACM) as follows: point–GS iterations are performed on the fine grid (level 1) as long as the rate of decrease in the norm of the residual is suitable, that is $\|R^{(k+1)}\| \le \mu\,\|R^{(k)}\|$, where μ depends of the rate of smoothing of the high–frequency error of the iterative solver used for the particular problem considered ($\mu = 0.5$ for the point–GS solver applied to the diffusion problem). Then the level–two shift of Settari and Aziz is performed to remove the low–frequency mode of the error, and iterations on the level 1 are resumed. The overall rate of convergence is dominated by the information propagation rate in the weak coefficient direction z. The line–GS solver (line–by–line technique) propagates information at the rate of roughly one node Δz per iteration, while the line–GS solver combined with ACM propagates information across the whole domain on each iteration (information propagation refers to the propagation of Dirichlet–type boundary conditions inside the domain). The point–GS solver requires roughly $C^2\,N_Z$ iterations for propagation across the domain in the weak coefficient direction z, and the rate of convergence of this solver is accelerated to that of the line–GS when it is combined with the ACM strategy.

For variable meshes and flow problems with spatially varying velocities, it may not be possible to orient the line solver in the strong coefficient direction, because it varies. For high–Peclet convection combined with diffusion, the large coefficients are aligned with the flow direction. The propagation of the boundary conditions arises by diffusion normal to the flow (between the stream tubes). The time step implied in the solver is now dominated by the convective time. It takes many such time steps to diffuse information normal to the flow, which causes the iterative solver to stall. In such case, convergence can be enhanced by an additive correction based on stream tube blocks (flow rings).

Because the solution of the additive block correction equations is very inexpensive for two–dimensional problems (the use of row– or ring–shaped blocks leads to a tridiagonal linear system for the block correction vector), it is generally more efficient to perform an ACM correction after each fine grid iteration, since the convergence rate of the overall algorithm is optimized. Inexpensive iterations on the level–two coarse grid rapidly diminish exactly those components of the error (low–frequency) that are so difficult and expensive to reduce by fine–grid iterations alone.

C-11. ACM VERSUS BRANDT–TYPE MULTIGRID ALGORITHM

In the multigrid (MG) method of Brandt (1980, 1984), the conservation equations must be discretized on different (finer to coarser) grids, and difficult decisions must be made concerning the treatment of boundary conditions, the transfer of residuals or the interpolation of the dependent variables, so that this type of algorithm is rather complex to program. By contrast, in the Additive Correction Multigrid method (ACM) proposed by Hutchinson and Raithby (1986), summation of the equations over a block of cells is equivalent to demanding integral conservation over each block or coarse–grid cell, and constrains these choices. Hutchinson and Raithby have shown that ACM was as efficient as MG for Poisson–type problems, while much easier to implement. Numerical tests revealed no performance degradation of ACM with either Neumann or Dirichlet boundary conditions. Unlike the MG algorithm of Brandt, ACM obtains the discretized correction equations for the coarse grid directly from the fine–grid equations by application of the ABC strategy of Settari and Aziz. This distinction is important for two reasons. First, discretization is required on the fine grid only, thus reducing complexity and cost as well as eliminating the possibility of discretization inconsistencies between the coarse and fine grids. Second, because the fine–grid discretization equations are conservative and the coarse–grid correction equations are formed by simply combining the fine–grid equations,

the resulting coarse–grid equations are also conservative. Solution of the coarse–grid equations and subsequent correction of the fine–grid solution field yields a field that is conservative over each block.

C-12. NON–ITERATIVE SPLITTING METHODS

To resolve couplings and non–linearities of the flow conservation equations, iterative methods such as SIMPLE–type pressure–correction algorithms have been used extensively. However, iterative methods are costly and therefore not very attractive for unsteady calculations. Non–iterative splitting procedures have been considered to speed up calculations and reduce the complexity of programmation as well as storage requirements. Originally these methods have been applied to solve multi–dimensional problems as a series of linearized one–dimensional problems.

Consider the two–dimensional heat diffusion equation:

$$\frac{\partial u}{\partial t} = \nu \left\{ \partial_x^2 + \partial_y^2 \right\} u \quad . \tag{C-28}$$

While the explicit discretization of Equation (C-28) is conditionally stable ($2\nu \Delta t \left(\frac{1}{\Delta x^2} + \frac{1}{\Delta y^2} \right) < 1$), the following combined implicit–explicit representation is unconditionally stable if $\theta \geq 1/2$:

$$\frac{u^{n+1} - u^n}{\Delta t} = \nu \left\{ \partial_x^2 + \partial_y^2 \right\} \left[\theta u^{n+1} + (1 - \theta) u^n \right] \quad . \tag{C-29}$$

The Crank–Nicolson scheme is obtained for $\theta = 1/2$ and is second–order accurate in time. While in one dimension the fully–implicit and Crank–Nicolson schemes result in a tridiagonal linear system that can be very efficiently solved with Thomas algorithm, their extension to 2 and 3 space dimensions leads to algebraic equations that contain 5 or 7 unknowns, respectively. Although the resulting equations are still unconditionally stable, they are no longer tridiagonal and they must be solved by direct elimination or iterative procedures, which require a substantially greater computational effort.

C-12.1. Alternating Direction Implicit Approximations (ADI)

To overcome the shortcomings of the common implicit methods for two–dimensional problems, Peaceman and Rachford (1955) and Douglas (1955) have developed a variation of the Crank–Nicolson approximation known as an Alternating Direction Implicit (ADI) method. A number of variations have been proposed. The Peaceman–Rachford ADI form of Equation (C-28) is a two–step scheme which proceeds as follows:

$$\frac{u^* - u^n}{\Delta t/2} = \nu \left[\partial_x^2 u^* + \partial_y^2 u^n\right]$$
$$\frac{u^{n+1} - u^*}{\Delta t/2} = \nu \left[\partial_x^2 u^* + \partial_y^2 u^{n+1}\right] \quad . \tag{C-30}$$

The diffusion term has been split into its two spatial components and each step results in a tridiagonal linear system. This ADI scheme is second–order accurate in time and unconditionally stable for the diffusion equation. However it cannot be extended to 3 dimensions, and Douglas and Gunn (1964) have proposed an ADI scheme that is unconditionally stable and second–order accurate for the three–dimensional diffusion equation. Their algorithm retains these properties of stability and accuracy for any number of commutative splitting operators and for non–commutative operators in two dimensions. As an illustration, the ADI procedure of Douglas and Gunn is applied to the following implicit equation:

$$\frac{u^{n+1} - u^n}{\Delta t} = \{F_1 + F_2\}\left[\theta u^{n+1} + (1-\theta)u^n\right] \ , \tag{C-31a}$$

which can be rewritten:

$$\left\{I - \theta\Delta t\,(F_1 + F_2)\right\} u^{n+1} = \left\{I + (1-\theta)\Delta t\,(F_1 + F_2)\right\} u^n = q^n \quad . \tag{C-31b}$$

The procedure is formed of the following two steps:

$$\left\{I - \theta\Delta t\, F_1\right\} u^* - \left\{\theta\Delta t\, F_2\right\} u^n = q^n \tag{C-32a}$$
$$\left\{I - \theta\Delta t\, F_2\right\} u^{n+1} - \left\{\theta\Delta t\, F_1\right\} u^* = q^n \quad . \tag{C-32b}$$

Subtracting Equation (C-32b) from Equation (C-32a) gives:

$$u^* = \left\{I - \theta\Delta t\, F_2\right\} u^{n+1} + \left\{\theta\Delta t\, F_2\right\} u^n \quad , \tag{C-33}$$

and u* can be eliminated from Equation (C-32a) to yield:

$$\left\{I - \theta\Delta t\,(F_1 + F_2)\right\} u^{n+1} = q^n - \left(\theta\Delta t\right)^2 \{F_1 F_2\}\left(u^{n+1} - u^n\right) . \tag{C-34}$$

It can be seen that the ADI scheme of Douglas and Gunn applied to two–dimensional problems is equivalent to the Jakonov factorization. Equation (C-34) is of the same order of accuracy as Equation (C-31a), and is second–order accurate in time when θ=1/2. For solution efficiency, it is preferable to introduce $\phi = u - u^n$, and rewrite Equations (C-31) as:

$$\phi^{n+1} = \Delta t\,\{F_1 + F_2\}\left[u^n + \theta\phi^{n+1}\right] \quad , \tag{C-35a}$$

or:

$$\left\{I - \theta\Delta t\,(F_1 + F_2)\right\} \phi^{n+1} = \Delta t\,\{F_1 + F_2\}\, u^n \quad . \tag{C-35b}$$

The Jakonov factorization of Equation (C-35b) takes the form:

$$\left\{I - \theta\Delta t\, F_1\right\}\left\{I - \theta\Delta t\, F_2\right\} \phi^{n+1} = \Delta t\,\{F_1 + F_2\}\, u^n \quad , \tag{C-36}$$

which is easily solved by the following two–step scheme:

$$\begin{aligned} \left\{I - \theta\Delta t\, F_1\right\} \phi^* &= \Delta t\,\{F_1 + F_2\}\, u^n \\ \left\{I - \theta\Delta t\, F_2\right\} \phi^{n+1} &= \phi^* \quad . \end{aligned} \tag{C-37}$$

These ADI schemes are very efficient when the operators $\{F_i\}$ are linear.

Douglas and Jones (1963) have proposed various splitting predictor–corrector methods for resolving the non–linearity of the one–dimensional convection–diffusion equation:

$$\frac{\partial u}{\partial t} = \{F + G(u)\}\, u \quad , \tag{C-38}$$

where F is a linear operator (diffusion) and G(u) is non–linear (convection). The first predictor consists in estimating the solution u* at time $(n+1/2)\Delta t$ by using successive substitution linearization of the non–linear operator G. Douglas and Jones have considered the following predictors:

$$\frac{u^* - u^n}{\Delta t/2} = \{F\}\, u^* + \{G(u^n)\}\, u^n \,, \tag{C-39a}$$

$$\frac{u^* - u^n}{\Delta t/2} = \{F\}\left[\frac{u^* + u^n}{2}\right] + \{G(u^n)\}\, u^n \,, \tag{C-39b}$$

$$\frac{u^* - u^n}{\Delta t/2} = \{F + G(u^n)\}\left[\frac{u^* + u^n}{2}\right] . \tag{C-39c}$$

Equation (C-39a) is the Crank–Nicolson predictor, while Equation (C-39b) is a modified Crank–Nicolson predictor. Gary (1964) has proposed a predictor similar to Equation (C-39c) to estimate the solution u* at the new time step $(n+1)\Delta t$:

$$\frac{u^* - u^n}{\Delta t} = \{F + G(u^n)\}\left[\frac{u^* + u^n}{2}\right] . \tag{C-40}$$

After the corrector step is performed, the estimate of the solution $u^{n+1/2}$ at time $(n+1/2)\Delta t$ was taken as u* if one of the predictors (C-39) was used, or as $(u^*+u^n)/2$ if predictor (C-40) was employed, and the solution u^{n+1} at the advanced time was obtained from the following corrector:

$$\frac{u^{n+1} - u^n}{\Delta t} = \left\{F + G\left(u^{n+1/2}\right)\right\}\left[\frac{u^{n+1} + u^n}{2}\right] . \tag{C-41}$$

Gary (1964) has also devised an iterative explicit predictor method for the solution of Equation (C-38):

$$\begin{aligned} u^{(0)} &= u^n \,, \\ \frac{u^{(k+1)} - u^n}{\Delta t} &= \left\{F + G\left(\frac{u^{(k)} + u^n}{2}\right)\right\}\left[\frac{u^{(k)} + u^n}{2}\right] \,, \quad \text{for } k=0 \text{ to } p-1, \\ u^{n+1} &= u^{(p)} \,, \end{aligned} \tag{C-42a}$$

which unfortunately is unstable for certain values of p, and whose admissible time steps are restricted. Gourlay and Morris (1968) have proposed a variation of Gary's unstable predictor that is unconditionally stable:

$$\frac{u^{(0)} - \hat{u}^n}{\Delta t} = \{F + G(u^n)\}\, u^n \quad , \quad \text{where} \quad \hat{u}_i = \frac{u_{i+1} + u_{i-1}}{2} \quad ,$$

$$\frac{u^{(k+1)} - u^n}{\Delta t} = \{F\}\left[\frac{u^{(k+1)} + u^n}{2}\right] + \frac{1}{2}\left[\{G(u^n)\}\, u^n + \left\{G\left(u^{(k)}\right)\right\} u^{(k+1)}\right], \quad \text{for } k=0 \text{ to } p\text{-}1,$$

$$u^{n+1} = u^{(p)} \quad . \tag{C-42b}$$

In practice, 2 iterations (p=2) are sufficient to obtain convergence to the order of accuracy of the overall method. The same authors have extended their algorithm to non–linear two–dimensional problems of the following type:

$$\frac{\partial u}{\partial t} = \{G_1(u) + G_2(u)\}\, u \quad . \tag{C-43}$$

The Crank–Nicolson discretization scheme of Equation (C-43) reads:

$$\frac{u^{n+1} - u^n}{\Delta t} = \frac{1}{2}\left[\left\{G_1(u^{n+1})\right\} u^{n+1} + \{G_1(u^n)\}\, u^n\right] + \frac{1}{2}\left[\left\{G_2(u^{n+1})\right\} u^{n+1} + \{G_2(u^n)\}\, u^n\right] \quad ,$$

or

$$\left\{I - \frac{\Delta t}{2}\left[G_1(u^{n+1}) + G_2(u^{n+1})\right]\right\} u^{n+1} = \left\{I + \frac{\Delta t}{2}\left[G_1(u^n) + G_2(u^n)\right]\right\} u^n \quad , \tag{C-44}$$

which combines temporal and spatial implicitnesses. The approximate Jakonov factorization of Equation (C-44) takes the form:

$$\left\{I - \frac{\Delta t}{2} G_1(u^{n+1})\right\}\left\{I - \frac{\Delta t}{2} G_2(u^{n+1})\right\} u^{n+1} = \left\{I + \frac{\Delta t}{2} G_1(u^n)\right\}\left\{I + \frac{\Delta t}{2} G_2(u^n)\right\} u^n = q^n \; . \tag{C-45}$$

To estimate the operators $\{G_1\}$ and $\{G_2\}$ at the new time step, Gourlay and Morris proposed the following explicit stable predictor:

$$\frac{u^{**} - \tilde{u}^n}{\Delta t} = \left\{G_1\left(u^n\right) + G_2\left(u^n\right)\right\} u^n \quad , \tag{C-46}$$

where $\hat{u}_{i,j} = \frac{1}{4}\left(u_{i+1,j} + u_{i-1,j} + u_{i,j+1} + u_{i,j-1}\right)$ on an uniform grid ($\Delta x = \Delta y$), so that the two–step ADI scheme reduces to:

$$\left\{I - \frac{\Delta t}{2} G_1(u^{**})\right\} u^* = q^n$$
$$\left\{I - \frac{\Delta t}{2} G_2(u^{**})\right\} u^{n+1} = u^* \quad . \tag{C-47}$$

Also, Chorin (1968) has adapted the Peaceman–Rachford predictor–corrector method to the solution of the two–dimensional convection–diffusion transport Equation (C-43):

$$\frac{u^* - u^n}{\Delta t/2} = \{G_1(u^n)\} u^* + \{G_2(u^n)\} u^n$$
$$\frac{u^{n+1} - u^*}{\Delta t/2} = \{G_1(u^*)\} u^* + \{G_2(u^*)\} u^{n+1} \quad . \tag{C-48}$$

The Navier–Stokes equations constitute a system of non–linear coupled partial differential equations for the density, flow field components and temperature. The sequential (or segregated) numerical solution of the corresponding linearized finite–difference equations necessitates that the solution procedure be applied repeatedly to restore the couplings and the non–linearities. If the solution procedure itself is iterative, it is possible that the total number of iterations required is not significantly increased by the couplings and the non–linearities (Ghia, in Minkowycz et al. 1988, p. 306). But this is generally not the case.

To overcome these shortcomings, Briley and McDonald (1975, and 1977) and Beam and Warming (1976) have proposed a block–ADI splitting algorithm for the simultaneous solution of the unsteady compressible Navier–Stokes equations. Unlike the methodology proposed by Gourlay and Morris (1968), terms involving non–linearities at the implicit time level are linearized by Taylor expansion about the solution at the known time level (Newton–Raphson linearization). The result is a system of multidimensional coupled (but linear) difference equations for the dependent variables at the implicit time level. To solve these equations, the ADI factored scheme of Douglas and Gunn is introduced which leads to systems of coupled linear equations having narrow block–banded matrix structures, which can be solved efficiently by standard block–elimination methods. Properties are taken to be constant and the pressure is eliminated as a dependent variable by means of the equation of state (the perfect gas law was used, which is convenient but not essential).

Energy dissipation and cross–derivative viscous terms are treated explicitly for efficient spatial factorization. However, since any number of splitting operators can be used, mixed–derivatives can be treated implicitly within the ADI framework, at the expense of computational efficiency. Anyhow, the explicit treatment of the aforementioned viscous and dissipation terms had no observable adverse effect on stability. Because the conservative form of the compressible Navier–Stokes equations was discretized using a two time level scheme, Briley and McDonald pointed out that the vector of the dependent variables ψ must be taken as $\psi = \{\rho, \rho\mathbf{U}, \rho e\}$ to maintain second–order accuracy in time for the overall scheme (obtained when $\theta = 1/2$). The two–dimensional compressible Navier–Stokes equations can be written in the following condensed form:

$$\frac{\partial \psi}{\partial t} = \mathbf{G}_1(\psi) + \mathbf{G}_2(\psi) \quad , \tag{C-49}$$

where $\mathbf{G_1}$ and $\mathbf{G_2}$ are non–linear multicomponent operators associated with space dimension 1 and 2 respectively, and the implicit–explicit temporal discretization scheme gives the analog of Equation (C-49) as:

$$\frac{\psi^{n+1} - \psi^n}{\Delta t} = \theta \left[\mathbf{G}_1(\psi^{n+1}) + \mathbf{G}_2(\psi^{n+1})\right] + (1-\theta)\left[\mathbf{G}_1(\psi^n) + \mathbf{G}_2(\psi^n)\right] \quad . \tag{C-50}$$

The non–linearity of the operators $\mathbf{G_i}$ is treated via Newton–Raphson linearization:

$$\begin{aligned} \mathbf{G}_i(\psi^{n+1}) &= \mathbf{G}_i(\psi^n) + \left[\frac{\partial \mathbf{G}_i}{\partial \psi}\right]^n \left[\psi^{n+1} - \psi^n\right] + O\left(\Delta t^2\right) \\ &= \mathbf{G}_i(\psi^n) + [\mathbf{A}_i]\left[\psi^{n+1} - \psi^n\right] + O\left(\Delta t^2\right) \quad , \end{aligned} \tag{C-51}$$

where the Jacobians $[\mathbf{A_i}]$ are linear operators. Introducing $\phi = \psi - \psi^n$, and making use of linearization (C-51) into (C-50) leads to the following equation:

$$\left[\mathbf{I} - \theta \Delta t \left(\mathbf{A}_1 + \mathbf{A}_2\right)\right] \phi^{n+1} = \Delta t \left[\mathbf{G}_1(\psi^n) + \mathbf{G}_2(\psi^n)\right] = \mathbf{Q}^n \quad . \tag{C-52}$$

The ADI factored scheme of Douglas and Gunn applied to Equation (C-52) gives:

$$\left[\mathbf{I} - \theta \Delta t \, \mathbf{A}_1\right]\left[\mathbf{I} - \theta \Delta t \, \mathbf{A}_2\right] \phi^{n+1} = \mathbf{Q}^n \quad , \tag{C-53}$$

which is equivalent to the solution of two block–tridiagonal systems:

$$\begin{aligned} \left[\mathbf{I} - \theta\Delta t\, \mathbf{A}_1\right] \phi^{*} &= \mathbf{Q}^{n} \\ \left[\mathbf{I} - \theta\Delta t\, \mathbf{A}_2\right] \phi^{n+1} &= \phi^{*} \ . \end{aligned} \tag{C-54}$$

For two or three dimensional problems, Alternating Direction Implicit (ADI) methods are very attractive: instead of solving a 5–point (or 7–point in three dimensions) linear system, the ADI splitting solves successively 2 or 3 tridiagonal systems. Unfortunately, it has been found that such spatial splitting methods have a rather poor accuracy for disturbances which propagate skew to the coordinate axes. This suggests that a more productive approach would be to split by physical phenomena as well. One step could solve sonic propagation implicitly in all directions, with further steps involving implicit convection terms, possibly split by spatial coordinates. Also, when axial velocities are much larger than transverse velocities, it is advantageous to overcome the convection limit on the time step in the axial direction only.

C-12.2. Marker–And–Cell Formulation and Projection Algorithms

These ideas have been applied by several authors to the pressure–velocity formulation of the Navier–Stokes equations:

$$\begin{aligned} \frac{\partial}{\partial t}(\rho \mathbf{U}) = - \vec{\nabla} P + \vec{\mathrm{Div}}\left[\bar{\bar{\tau}} - (\rho \mathbf{U})\mathbf{U}\right] + \mathbf{F} = - \vec{\nabla} P + \mathbf{G}(\mathbf{U}) \\ \frac{\partial \rho}{\partial t} + \mathrm{div}\,(\rho \mathbf{U}) = 0 \end{aligned} \tag{C-55}$$

where the convection–diffusion non–linear operator **G** has been introduced for simplicity. One of the earliest and most widely used methods for solving the unsteady incompressible version of the system of Equations (C-55) is the Marker And Cell (MAC) method of Harlow and Welch (1965). The method is characterized by the use of a staggered grid and the solution of a Poisson equation for the pressure at every time step. Although the original form of the MAC method has certain weaknesses, the use of a staggered grid and a Poisson equation for the pressure has been retained in many modern methods derived from the MAC method, such as the SIMPLE–type procedures. The method was developed initially for unsteady problems involving free surfaces. To allow the surface location to be

determined as a function of time, markers (massless particles) are introduced in the flow. These markers are convected by the velocity field but play no role in determining the velocity or pressure fields. In the MAC formulation, discretization of the incompressible version of Equations (C-55) gives the following algorithm, written in symbolic vector form:

$$\rho \frac{\mathbf{U}^{n+1} - \mathbf{U}^{n}}{\Delta t} = -\vec{\nabla} P^{n+1} + \mathbf{G}(\mathbf{U}^{n})$$

$$\operatorname{div}\left(\mathbf{U}^{n+1}\right) = 0 \quad . \tag{C-56}$$

By treating the convection–diffusion terms explicitly, the advanced–time velocity field can be expressed in terms of the advanced–time pressure gradient. Substituting the velocity field in the continuity equation gives an elliptical Poisson equation that is solved for the advanced–time pressure field. The MAC method has surprisingly excellent stability characteristics. However, because of the explicit differencing of the convection–diffusion terms in the momentum equations, the time step for stable solution is limited by the constraining parabolic stability criterion (Peyret and Taylor 1983, page 148).

The projection method proposed by Chorin (1968) is closely related to the MAC method. In the present notation the projection method splits the unsteady incompressible momentum equations into two steps by introducing an auxiliary velocity field which is calculated while omitting the pressure gradient term:

$$\rho \frac{\mathbf{U}^{*} - \mathbf{U}^{n}}{\Delta t} = \mathbf{G}(\mathbf{U}^{*}) \tag{C-57a}$$

$$\rho \frac{\mathbf{U}^{n+1} - \mathbf{U}^{*}}{\Delta t} = -\vec{\nabla} P^{n+1} \tag{C-57b}$$

$$\operatorname{div}\left(\mathbf{U}^{n+1}\right) = 0 \quad . \tag{C-57c}$$

Equation (C-57a) is solved using the Peaceman–Rachford ADI splitting, while Equations (C-57b) and (C-57c) are combined and solved by a Dufort–Frankel type relaxation scheme (Chorin 1968). Originally the projection method was formulated on a non–staggered grid. However, Peyret and Taylor (1983) recommended that the projection method be used with a staggered (MAC) grid. In the first mesh used by Chorin, the velocity and pressure are defined at the nodes of the mesh. The advantages of such a mesh are its simplicity and the

fact that the velocity is defined, in particular, on the boundary where this quantity is generally prescribed. On the other hand, one of its disadvantages is that the pressure is also defined on the boundary. Since there is generally no boundary condition for the pressure, it is necessary to devise a special technique to compute the pressure on this boundary. In the staggered MAC grid, the pressure is defined at nodes, while the velocities are defined at the faces between the cells. Therefore, the pressure is no longer defined on the domain boundary, and the same formulas can be used to compute the whole pressure field, so that the Poisson equation for the pressure automatically satisfies the discrete form of the integral mass conservation over the entire physical domain. So it is necessary to employ non–centered differences near the boundary. But this inconvenience is largely balanced by the advantage of the MAC mesh for the pressure computation.

Goda (1979) has used the projection method to obtain the steady viscous flow in two– and three–dimensional driven cavities. This author used an ADI fractional scheme to solve Equation (C-57a), which is conditionally stable due to the non–linearities in the convection–diffusion operator **G**.

Another variant of the basic MAC formulation is that due to Hirt and Cook (1972). In the present notation, an auxiliary velocity field **U*** and a pressure correction P* are obtained from:

$$\rho \frac{\mathbf{U}^* - \mathbf{U}^n}{\Delta t} = - \vec{\nabla} P^n + \mathbf{G}(\mathbf{U}) \qquad \text{(C-58a)}$$

$$\rho \frac{\mathbf{U}^{n+1} - \mathbf{U}^*}{\Delta t} = - \vec{\nabla} P^* \qquad \text{(C-58b)}$$

$$\mathrm{div}\left(\mathbf{U}^{n+1}\right) = 0 \quad . \qquad \text{(C-58c)}$$

The pressure correction is used to insure that U^{n+1} satisfies continuity, and the new pressure is obtained as $P^{n+1} = P^n + P^*$. Hirt and Cook used the above formulation to examine incompressible (laminar) viscous flows past three–dimensional structures.

Harlow and Amsden (1971) extended the MAC method of Harlow and Welch (1965) to the conservative form of the unsteady compressible flow equations. In the present notation, Equations (C-55) were discretized as follows:

$$\frac{(\rho \mathbf{U})^{n+1} - (\rho \mathbf{U})^{n}}{\Delta t} = - \vec{\nabla}\left[\alpha P^{*} + (1-\alpha) P^{n}\right] + \mathbf{G}(\mathbf{U}^{n}) \qquad \text{(C-59a)}$$

$$\frac{\rho^{n+1} - \rho^{n}}{\Delta t} + \operatorname{div}\left[\theta(\rho \mathbf{U})^{n+1} + (1-\theta)(\rho \mathbf{U})^{n}\right] = 0 \quad . \qquad \text{(C-59b)}$$

The Poisson equation for the stared pressure field is obtained from the continuity Equation (C-59b) by making use of Equation (C-59a) to eliminate the advanced time mass fluxes. The advanced–time density is linearized in terms of the stared pressure by using the equation of state:

$$\rho^{n+1} = \rho^{n} + \left(\frac{\partial \rho}{\partial P}\right)_{T}^{n} \left[P^{*} - P^{n}\right] \quad . \qquad \text{(C-59c)}$$

Once the elliptical Poisson equation is solved for the stared pressure field, the advanced–time density is calculated from Equation (C-59c) and the new velocity field is obtained from Equation (C-59a). The energy equation is then solved for the new temperature field and the advanced–time pressure field is calculated as a function of density and temperature from the equation of state. The pressure–velocity coupling algorithm of Harlow and Amsden is very attractive since it applies to any Mach–number flow regimes. However, the time step is limited due to the fact that the convection–diffusion terms in the momentum equations are discretized explicitly.

The splitting algorithm of Harlow and Amsden for compressible flow has been extended by Liles and Reed (1978) and Stewart (1981) to the non–conservative form of the unsteady incompressible flow equations. The time step in the resulting TRAC code is still limited by convection and diffusion. The advantage of the non–conservative form is that it separates the effect of physical phenomena. Each of them, such as convection, diffusion, sonic propagation and interphase exchanges, has its own characteristic time scale. If we wish to evaluate the mechanical stresses following an external laser heating of the heat pipe, tracking the pressure waves is necessary, at least in the early moments since the waves are dying out with time. We would apply explicit differences to sonic propagation terms and compute on a time scale 10^{-3} s. In this case, there is no need for implicit differencing of convection–diffusion terms, but interphase exchanges would probably be the difference implicitly. Clearly, it is important, for efficient difference schemes, to concentrate the computational effort on features of the solution which have practical significance. For

problems where the flow is changing only very slowly with time, or when it is desired to reach the steady flow quickly, large time steps and unconditionally stable fully–implicit schemes may be used. For time steps large enough to justify implicit treatment of convection and diffusion, splittings by physical phenomena and spacial coordinates may be combined.

C-12.3. Non–Iterative PISO Procedure (Pressure–Implicit with Splitting of Operators)

The semi–implicit pressure–velocity algorithms described above are conditionally stable and not particularly accurate because of the approximate way the couplings and non–linearities are treated. Such drawbacks could be removed through the use of fully implicit iterative methods such as SIMPLE or other similar algorithms. Unfortunately, such iterative methods are not very attractive for unsteady flow calculations and not very efficient for the modeling of compressible flows. Recently, Issa (1986) developed PISO (Pressure–Implicit with Splitting of Operators), a non–iterative method whose stability is little impaired by the splitting procedure. PISO has the ability to cope with large time steps, usually larger than the physical time step required to accurately describe the transient evolution of the solution. Note that implicitness of the scheme is required for fast solution calculation since the physical time step is usually very much larger than the time–step stability limit of the explicit discretization scheme. As in the previous pressure–velocity splitting algorithms, the pressure is treated as one of the main variables, so that the incompressibility limit is also correctly handled by PISO.

For simplicity, let us consider first the PISO algorithm as it is applied to solve the discretized incompressible flow equations:

$$\rho \frac{\mathbf{U}^{n+1} - \mathbf{U}^{n}}{\Delta t} = - \vec{\nabla} P^{n+1} + \mathbf{G}(\mathbf{U}^{n+1})$$

$$\text{div}\left(\mathbf{U}^{n+1}\right) = 0 \quad . \tag{C-60}$$

The algorithm consists of a predictor step followed by two successive corrector steps:

$$\rho \frac{\mathbf{U}^* - \mathbf{U}^n}{\Delta t} = - \vec{\nabla} P^n + \mathbf{G}^n(\mathbf{U}^*) \qquad \text{(C-61a)}$$

$$\rho \frac{\widehat{\mathbf{U}} - \mathbf{U}^n}{\Delta t} = - \vec{\nabla} P^* + \mathbf{G}^n(\mathbf{U}^*) \ , \quad \text{div}\,(\widehat{\mathbf{U}}) = 0 \qquad \text{(C-61b)}$$

$$\rho \frac{\mathbf{U}^{n+1} - \mathbf{U}^n}{\Delta t} = - \vec{\nabla} P^{n+1} + \mathbf{G}^n(\widehat{\mathbf{U}}) \ , \quad \text{div}\,(\mathbf{U}^{n+1}) = 0 \ . \qquad \text{(C-61c)}$$

The diffusion–convection operator **G** is non–linear and can be linearized using a standard linearization technique or the Newton–Raphson approximation, or the same predictor–corrector splitting can be used to resolve the non–linearities. The predictor step consists of solving Equation (C-61a) for the stared velocity field. Convection and diffusion terms are treated implicitly. The corrector phase is constituted of two identical pressure correction steps which lead to divergence free velocity fields. The predictor Equation (C-61a) and first corrector Equation (C-61b) are identical to Equations (C-58) for Hirt and Cook's algorithm (1972). The role of the second corrector step (Equation C-61c) is to update the convection/diffusion terms. Issa has shown that a minimum of two corrector steps must be performed before the velocities and pressures thus obtained can be legitimately regarded as solutions. Issa showed that the non–iterative PISO splitting procedure constituted of two corrector steps is third–order accurate in time, which is higher than the order of the two–time step discretization scheme. Convection and diffusion are treated explicitly in the momentum conservation equation so that the Poisson equation for the pressure field is easily formed by substituting the advanced–time velocity field into the continuity equation. Note that the Poisson equation for the pressure should not be derived from the differential form of the momentum and continuity equations, but is obtained from the combination of the discretized forms of these equations for consistency.

As for stability, the exact solution of Equations (C-60) is unconditionally stable since the system is fully implicit. However, the corrector–predictor splitting solves them approximately so that stability may be altered. In any event, the stability will be greatly affected by the non–linearity of the actual system of equations. To remedy this situation, the corrector Equations (C-61b) and (C-61c) are replaced by ones which are intrinsically more stable, by treating the diagonal part $\mathbf{G_0}$ of the convection–diffusion operator **G** implicitly ($\mathbf{G} = G_0\mathbf{I} + \overline{\mathbf{G}}$):

$$\rho \frac{\hat{\mathbf{U}} - \mathbf{U}^n}{\Delta t} - G_0^n \hat{\mathbf{U}} = - \vec{\nabla} P^* + \overline{\mathbf{G}}^n(\mathbf{U}^*) \tag{C-62b}$$

$$\rho \frac{\mathbf{U}^{n+1} - \mathbf{U}^n}{\Delta t} - G_0^n \mathbf{U}^{n+1} = - \vec{\nabla} P^{n+1} + \overline{\mathbf{G}}^n(\hat{\mathbf{U}}) \ . \tag{C-62c}$$

The resulting Equations (C-62b) and (C-62c) possess much smaller error amplification factors for the same time step. Note that the corrector Equations (C-62) are identical in form to Equations (C-14) for the SIMPLE–Revised algorithm of Patankar. Because the equations may not be solved exactly if an iterative solution method is selected, the velocity field may not be exactly divergence free, so that terms of the form div($\mathbf{U}^*$) must be kept in the Poisson equation to avoid mass error accumulation.

Issa has extended the PISO algorithm to solve the following discretized compressible flow equations for a perfect gas:

$$\frac{(\rho \mathbf{U})^{n+1} - (\rho \mathbf{U})^n}{\Delta t} = - \vec{\nabla} P^{n+1} + \mathbf{G}(\mathbf{U}^{n+1}) \tag{C-63a}$$

$$\frac{\rho^{n+1} - \rho^n}{\Delta t} + \text{div}\,(\rho \mathbf{U})^{n+1} = 0 \tag{C-63b}$$

$$\frac{(\rho e)^{n+1} - (\rho e)^n}{\Delta t} = \mathbf{H}(e^{n+1}) - \text{div}\,(P\mathbf{U})^{n+1} + \mathbf{J}(\mathbf{U}^{n+1}) \tag{C-63c}$$

$$P^{n+1} = r\,(\rho T)^{n+1} \ , \ e = e(T) \ , \tag{C-63d}$$

where $\mathbf{G}$ and $\mathbf{H}$ are convection–diffusion operators and $\mathbf{J}$ is the stress work operator. Because the coupling now involves the density and temperature, an additional corrector stage must be incorporated to achieve third–order accuracy in time (however, a two–stage scheme still achieves second–order accuracy in time). The merits of PISO stem largely from its ability to resolve a pressure field free from the influence of errors in div($\mathbf{U}$). Again, the convection–diffusion operators $\mathbf{G}$ and $\mathbf{H}$ are split into their diagonal and off–diagonal parts to enhance the stability of the algorithm. The two–stage scheme consists of the following steps: momentum predictor, first momentum (pressure) corrector, energy predictor and second momentum corrector, which read as:

$$\rho^n \frac{\hat{\mathbf{U}} - \mathbf{U}^n}{\Delta t} - G_0 \hat{\mathbf{U}} = -\vec{\nabla} P^n + \overline{\mathbf{G}}(\hat{\mathbf{U}}) \tag{C-64a}$$

$$\frac{(\rho \mathbf{U})^* - (\rho \mathbf{U})^n}{\Delta t} - \frac{G_0}{\rho^n}(\rho \mathbf{U})^* = -\vec{\nabla} P^* + \overline{\mathbf{G}}(\hat{\mathbf{U}})$$

$$\frac{\rho^* - \rho^n}{\Delta t} + \mathrm{div}\,(\rho \mathbf{U})^* = 0\,, \quad \rho^* = \frac{P^*}{rT^n} \tag{C-64b}$$

$$\frac{(\rho e)^* - (\rho e)^n}{\Delta t} - H_0\, e^* = \overline{\mathbf{H}}(e^*) - \mathrm{div}\,(P\mathbf{U})^* + \mathbf{J}(\mathbf{U}^*) \tag{C-64c}$$

$$\frac{(\rho \mathbf{U})^{**} - (\rho \mathbf{U})^n}{\Delta t} - \frac{G_0}{\rho^*}(\rho \mathbf{U})^{**} = -\vec{\nabla} P^{**} + \overline{\mathbf{G}}(\mathbf{U}^*)$$

$$\frac{\rho^{**} - \rho^n}{\Delta t} + \mathrm{div}\,(\rho \mathbf{U})^{**} = 0\,, \quad \rho^{**} = \frac{P^{**}}{rT^*} \quad . \tag{C-64d}$$

In the two–stage scheme, the stared temperature field is taken as the advanced–time temperature, while the double–stared quantities are taken for the new pressure, density and velocity fields. For the three–stage scheme, two additional steps are performed, an explicit energy corrector, and a third momentum (pressure) corrector:

$$\frac{\rho^{**} e^{n+1} - (\rho e)^n}{\Delta t} - H_0\, e^{n+1} = \overline{\mathbf{H}}(e^*) - \mathrm{div}\,(P\mathbf{U})^{**} + \mathbf{J}(\mathbf{U}^*) \tag{C-64e}$$

$$\frac{(\rho \mathbf{U})^{n+1} - (\rho \mathbf{U})^n}{\Delta t} - \frac{G_0}{\rho^{**}}(\rho \mathbf{U})^{n+1} = -\vec{\nabla} P^{n+1} + \overline{\mathbf{G}}(\mathbf{U}^*)$$

$$\frac{\rho^{n+1} - \rho^n}{\Delta t} + \mathrm{div}\,(\rho \mathbf{U})^{n+1} = 0\,, \quad \rho^{n+1} = \frac{P^{n+1}}{rT^{n+1}} \quad . \tag{C-64f}$$

Note that the stress work in Equation (C-64e) and the off–diagonal part of the convection–diffusion operator in Equation (C-64f) are not reevaluated at the most recent double–stared velocity field for computational efficiency. The fields obtained at the end of the splitting procedure are approximations to the exact ones with a temporal accuracy comparable to or better than the accuracy of the two–level discretization scheme. For a perfect gas, Issa found that the two–stage scheme was second–order accurate in time, while the three–stage scheme was third–order accurate. PISO treats the couplings with the energy and state equations implicitly, so that relatively large time steps can be employed without generation

of instabilities (the time step limitation is dominated by the treatment of the non–linearities since the procedure is non–iterative).

Issa, Gosman and Watkins (1986) have demonstrated that PISO is of good temporal accuracy, is faster than common iterative techniques for transient flow calculations, is stable for large time steps (hence as efficient as SIMPLEC for steady problems) and applicable to compressible flow regimes as well. The non–linearity arising from the dependency of the convection–diffusion operators **G** and **H** on the field variables themselves is handled by evaluating their linearized coefficients from the old time level values. Although this practice is only first–order accurate in time it is of the same order of accuracy as the Euler temporal difference scheme, and is therefore consistent with it. If a Crank–Nicolson type discretization scheme is employed, which is second–order accurate in time, the non–linearities can be resolved within the same accuracy by using the same splitting algorithm.